

# **Flow-Induced Crystallisation of Polymers Containing Nucleant Particles**

*A Thesis for the Degree of Doctorate of Philosophy*

by

**Andrew William Phillips**  
**BSc / BEng (Hons. I)**

Department of Materials Engineering  
Monash University  
Clayton, Victoria, 3800  
Australia

Submitted May 2011

## **Declaration**

I, Andrew Phillips, declare that this thesis is my own work and has not been submitted in any form for another degree or diploma at any university or other institute of tertiary education. Information derived from the published and unpublished work of others has been acknowledged in the text and a list of references is given in the bibliography.

Under the Copyright Act 1968, this thesis must be used only under the normal conditions of scholarly fair dealing. In particular no results or conclusions should be extracted from it, nor should it be copied or closely paraphrased in whole or in part without the written consent of the author. Proper written acknowledgement should be made for any assistance obtained from this thesis.

I certify that I have made all reasonable efforts to secure copyright permissions for third-party content included in this thesis and have not knowingly added copyright content to my work without the owner's permission.



## Abstract

Thermoplastic polyolefins are typically processed into their final form by injection moulding or extrusion technologies. These processes impart complex flow and temperature histories to the solidifying polymer which in turn can dramatically alter the final physical properties of the component. In particular, if the flow intensity is sufficient, a highly anisotropic crystalline architecture, termed shish-kebab can form. A highly oriented thread-like core is considered to form first (shish), which then provides a template for the formation and growth of oriented chain folded crystalline lamellae (kebabs). Therefore, shish formation is one the key components to understanding morphology development under flow conditions. The crystallisation of semicrystalline polymers is further complicated by the intentional addition of nucleating agents. Nucleants are used to enhance or override polymer crystallisation with the aim of (a) speeding up processing and (b) altering the solid-state morphology and hence final properties of the produced component. However, their influence on flow-induced crystallisation, in particular on shish formation and relaxation, are currently not well understood. Accordingly, the present study aimed to provide new insight into how nucleating agents influence flow-induced crystallisation.

This project employed in-situ time-resolved small and wide angle x-ray scattering (rheo-SAXS/WAXS) and Fourier transform infrared spectroscopy (rheo-FTIR) techniques to investigate shish formation and relaxation as well as the morphology development during subsequent crystallisation. Complementary morphological information was obtained using optical microscopy (OM), scanning electron microscopy (SEM) and differential scanning calorimetry (DSC) techniques. Isotactic polypropylene (iPP) was selected as the model matrix material due to its following advantageous characteristics: its general relevance to industrial processes, its convenient range of crystallisation kinetics and its ability to form different crystalline polymorphs. Four particulate nucleating agents which had substantially different effects on the iPP matrix, were investigated.



During shear flow, surprising sharp meridional streaks were observed in conjunction with the more commonly observed equatorial streaks in the SAXS patterns. No associated lamellar scattering was observed in the SAXS patterns and no crystalline reflections were observed in the WAXS patterns. These results showed that shish contain non-crystalline structural singularities along their length while they form. This provides strong evidence that shish initially form from the aggregation of point-like nuclei into oriented threads. This view contradicts the classical view that shish form from the densification of extended chains or segments of extended chains produced by an abrupt coil-to-stretch transition.

All nucleants examined in this thesis (a) decreased the critical shear rate required to form shish and (b) for a given shear rate, increased the density and dimension of shish formed. Therefore, the experimental results revealed that particles assist shish formation under flow conditions. Particle aspect ratio was shown to have the greatest influence on shish formation. This was explained by the manner in which different shaped particles interact with the flow field and modify the local strain environment near the surface of the particle.

iPP is known to crystallise in three polymorphic forms:  $\alpha$ -iPP (monoclinic),  $\beta$ -iPP (trigonal) and  $\gamma$ -iPP (orthorhombic). The specific phase formed and its associated morphology is known to have a large influence on the final properties of the component. Therefore, the combined influence of flow condition and nucleant on the polymorphic behaviour of iPP was also investigated in this study. In pure iPP, flow was found to induce  $\beta$ -iPP. However, flow was surprisingly found to suppress  $\beta$ -iPP in nucleated material, even when the nucleant specifically induced high quantities of  $\beta$ -iPP during crystallisation in the absence of flow. In addition, the combined influence of flow and nucleant was found to promote  $\gamma$ -iPP. These results therefore have important implications for the processing of iPP containing nucleants, the addition of which can influence both the level of orientation achieved as well as the specific crystalline phases formed in the final component.

## Table of contents

<b>Declaration</b>	i
<b>Abstract</b>	iii
<b>Table of contents</b>	v
<b>Acknowledgments</b>	xi
<b>Chapter 1 - Introduction</b>	1
1.1 Preamble	1
1.2 Aim of the thesis	6
1.3 Outline of the presented research	7
1.31 Flow-induced crystallisation of pure iPP	7
1.32 Flow-induced crystallisation of iPP containing $\beta$ -iPP nucleating agents	7
1.33 Shish formation and relaxation in iPP containing $\alpha$ -iPP nucleating agents	8
<b>Chapter 2 - Literature review</b>	11
2.1.0 Introduction	11
2.2.0 Crystallisation from quiescent polymer melts containing foreign particles	13
2.2.1 Classical nucleation theory	13
2.2.2 Homogeneous versus heterogeneous nucleation	15
2.2.3 Crystallisation kinetics	17
2.2.4 Control of polymer crystallisation using additives	19
2.3.0 Crystallisation from stressed polymer melts containing foreign	25
2.3.1 Chain dynamics of entangled polymers	25
2.3.2 Formation of the shish-kebab structure	30
2.3.3 Combined influence of flow and foreign particles on polymer crystallisation	36
2.4.0 Hierarchical structure and properties of iPP	42
2.4.1 Hierarchical structure of $\alpha$ -iPP	43
2.4.2 Hierarchical structure of $\beta$ -iPP	45
2.4.3 Hierarchical structure of $\gamma$ -iPP	49
2.4.4 Structure of smectic-iPP	50
2.4.5 Physical and mechanical properties of iPP	51
2.5.0 Conclusions	57

<b>Chapter 3 - Experimental methods</b>	59
3.1.0 Introduction	59
3.2.0 Sample preparation and thermal-shear profile	60
3.2.1 Isotactic polypropylene matrix	61
3.2.2 Nucleating agent preparation and compounding technique	62
3.3.3 Thermal-shear profile	64
3.3.0 Analytical techniques	68
3.3.1 X-ray scattering experiments	68
3.3.1.1 Beamline 20B, the Australian National Beamline Facility	72
3.3.1.2 Powder Diffraction beamline, Australian Synchrotron	72
3.3.1.3 SAXS/WAXS beamline, Australian Synchrotron	73
3.3.1.4 X-ray data reduction	74
3.3.1.5 X-ray data analysis	75
3.3.2 Fourier transform infrared spectroscopy	83
3.3.3 Differential scanning calorimetry	84
3.3.4 Microscopy	87
3.3.4.1 Characterisation of ex-situ nucleant particles	87
3.3.4.2 Polarised optical microscopy	87
3.3.4.3 Characterisation of etched samples	88
<b>Chapter 4 - Crystallisation and melting of oriented parent - daughter lamellae in sheared isotactic polypropylene</b>	91
4.1.0 Introduction	91
4.2.0 Experimental	93
4.2.1 Sample preparation and thermal-shear profile	93
4.2.2 Analytical techniques	95
4.3.0 Results	96
4.3.1 Quiescent crystallisation of iPP	96
4.3.2 Parent-daughter model in sheared $\alpha$ -iPP	97
4.3.3 Crystallisation of sheared iPP	103
4.3.4 Melting of sheared iPP	109

4.4.0 Discussion	112
4.4.1 Updated flow-induced crystallisation model of $\alpha$ -iPP	112
4.4.2 Thermal stability of sheared iPP	113
4.5.0 Conclusions	118
<b>Chapter 5 - Polystyrene as a versatile nucleating agent for polypropylene</b>	119
5.1.0 Introduction	119
5.2.0 Experimental	121
5.2.1 Sample preparation and thermal-shear profile	121
5.2.2 Analytical techniques	122
5.3.0 Results	122
5.3.1 Characterisation of iPS particles	124
5.3.2 Influence of iPS particles on iPP morphology	126
5.3.3 Influence of iPS particles on iPP crystallisation kinetics	132
5.3.4 Influence of iPS particles on the melting of iPP crystals	135
5.4.0 Discussion	137
5.4.1 Morphology of iPS particles	137
5.4.2 Crystallisation from a quiescent melt	138
5.4.3 Crystallisation from a sheared melt	140
5.5.0 Conclusions	142
<b>Chapter 6 - Influence of shear flow on the morphology development of <math>\beta</math> nucleated iPP</b>	143
6.1.0 Introduction	143
6.2.0 Experimental	144
6.2.1 Sample preparation and thermal-shear profile	144
6.2.2 Analytical techniques	145
6.3.0 Results	146
6.3.1 Characterisation of CaSub particles	146
6.3.2 Influence of flow condition on iPP polymorphism	150
6.3.3 Influence of flow condition on the orientation of iPP	154
6.3.4 Ex-situ microscopy of permanganate etched samples	158
6.3.5 Morphology development during crystallization	160
6.3.6 In-situ melting experiments	168

6.4.0 Discussion	171
6.4.1 Melting of $\beta$ -iPP crystals	171
6.4.2 Orientation development in sheared iPP containing $\beta$ -iPP nucleating particles	172
6.4.3 Inter-relation of shear flow and nucleant loading level on $\beta$ -iPP formation	177
6.5.0 Conclusions	182
<b>Chapter 7 - Influence of shear flow on the morphology development of         <math>\alpha</math> nucleated isotactic polypropylene</b>	185
7.1.0 Introduction	185
7.2.0 Experimental	187
7.2.1 Sample preparation and thermal-shear profile	187
7.2.2 Analytical techniques	188
7.3.0 Results	189
7.3.1 Characterisation of nucleant particles	189
7.3.2 Ex-situ microscopy of permanganate etched samples	193
7.3.3 Influence of nucleant and flow condition on iPP polymorphism	197
7.3.4 Influence of nucleant and flow condition on iPP orientation	201
7.3.5 Morphology development during crystallisation	207
7.3.6 In-situ melting experiments	214
7.4.0 Discussion	218
7.4.1 Thermal stability of shish in nucleated iPP	218
7.4.2 Orientation development in sheared iPP containing $\alpha$ -iPP nucleating particles	219
7.4.3 Inter-relation of shear flow and nucleant loading level on $\gamma$ -iPP formation	222
7.4.4 Flow-induced $\beta$ -iPP formation in the presence of $\alpha$ -iPP nucleants	226
7.5.0 Conclusions	227

<b>Chapter 8 - Shish formation and relaxation in sheared isotactic polypropylene containing nucleating particles</b>	229
8.1.0 Introduction	229
8.2.0 Experimental	231
8.2.1 Sample preparation and thermal-shear profile	231
8.2.2 Analytical techniques	232
8.3.0 Results	233
8.3.1 Observation of shish before, during and after shear flow	233
8.3.2 Quantitative investigation of shish during and after shear flow	238
8.3.3 Particle-induced and flow-induced conformational ordering	248
8.3.4 Crystallisation of sheared and relaxed iPP containing nucleating particles	252
8.4.0 Discussion	258
8.3.1 Influence of nucleants on the quiescent melt	258
8.4.2 Formation of shish during shear flow	260
8.4.3 Stability of shish after shear flow	263
8.4.4 Particle assisted shish formation	266
8.5.0 Conclusions	269
<b>Chapter 9 - Concluding remarks</b>	271
9.1 Influence of flow conditions and nucleant particles on iPP polymorphism	271
9.2 Influence of flow conditions and nucleant particles on shish formation	273
<b>References</b>	277
<b>Appendix 1 - Matrix material information</b>	295
<b>Appendix 2 - Published research</b>	303



## Acknowledgments

The author would like to thank his supervisors, Associate Professor Graham Edward (Monash University) and Dr Peng-wei Zhu (Monash University) for their patience, encouragement and assistance during the course of the experimental program and preparation of the thesis.

The author would also like to acknowledge the following people for their many important contributions to this work. The assistance of Dr Chitiur Hadinata (Autodesk) and Mrs Amita Bhatia (Monash University) for their help in manning synchrotron experiments, including some very long nights, was very much appreciated. The help of Dr Stephen Mudie, Dr Nigel Kirby and Dr Adrian Hawley (from the Australian Synchrotron) for their assistance with the synchrotron experiments and modification of the SAXS15id software was invaluable. The author would like to acknowledge the assistance from Dr. Jan Ilavsky (Advanced Photon Source Argonne National Laboratory) for modifying the Nika software package, without which the automated azimuthal integration of two-dimensional x-ray scattering profiles would not have been possible. Finally, the author would also like to thank George Theodossiou (Monash Centre for Electron Microscopy) for his help in preparing the SEM images.

The author would like to thank the following institutions for their financial support during the course of this project. The Co-operative Research Centre for Polymers (CRC-P) for not only providing scholarship funding, but also for providing a vast array of career development and networking opportunities. The Monash Silver Jubilee Scholarship (MSJS) provided by Monash University was appreciated. As too was the scholarship top up provided by Autodesk. The assistance from the Royal Australian Chemical Institute (RACI) Polymer Division for the financial contribution toward attending the 26<sup>th</sup> Annual Meeting of the Polymer Processing Society (PPS-26) in Banff, Canada was also greatly appreciated



A considerable portion of this research was undertaken on the SAXS/WAXS and Powder Diffraction beamlines at the Australian Synchrotron, Victoria, Australia. In addition some of this research was undertaken at the Australian National Beamline Facility at the Photon Factory in Japan, operated by the Australian Synchrotron. We acknowledge the Linkage Infrastructure, Equipment and Facilities Program of the Australian Research Council for financial support (proposal number LE0989759) and the High Energy Accelerator Research Organisation (KEK) in Tsukuba, Japan, for operations support.

Finally, the author would like to thank his family for their support in this project. In particular the author would like to thank his long suffering wife, Belinda, who not only graciously proof read the draft papers as well as this thesis, but also had to endure being a “PhD widow” during the final stages of the thesis.

# Chapter 1

## Introduction

### 1.1 Preamble

Thermoplastic polyolefins are commodity materials made from simple alkene monomers (i.e.  $C_nH_{2n}$ ). Thermoplastic polyolefins are inert materials which can be processed to possess an exceptionally wide variety of properties. Consequently they find numerous and diverse applications in areas such as: consumer packaging, fibres for textiles, structural members, pipelines and in biomedical and electronic materials. The vast majority of the thermoplastic polyolefins produced on a tonnage basis are polyethylene (PE) and polypropylene (PP), with 79 Mt/pa and 45 Mt/pa produced in 2007 respectively [1].

PE is the simplest polyolefin and is produced in three main varieties: low density PE (LDPE) (21 Mt/pa), linear LDPE (LLDPE) (22 Mt/pa) and high density PE (HDPE) (36 Mt/pa) [1]. Commercial LDPE has a density range of 0.915–0.94 g/cm<sup>3</sup> and was first produced by Imperial Chemistry Industries (ICI) in 1939. The material was highly branched which reduces the chains ability to crystallise, leading to good ductility and impact properties. The manufacture of HDPE became possible with the discovery of organometallic catalysis by Ziegler [2-3] and Natta [4], who were awarded the Nobel prize in chemistry (1963) for their work. Having significantly less branches than LDPE, HDPE has a higher density of between 0.945-0.96 g/cm<sup>3</sup> and can more completely crystallise, improving both its strength and modulus. Copolymerisation of ethylene with short chain alkenes (e.g. 1-butene, 1-hexene, 1-octene) produces the substantially linear LLDPE which has densities between 0.915–0.925 g/cm<sup>3</sup>. LLDPE products have higher impact and strength properties than LDPE.

PP is the next simplest polyolefin. The location of the methyl group along the polymer backbone changes the polymers ability to crystallise and therefore has a dramatic influence on the properties of PP. The most common commercial form of PP is isotactic PP (iPP), first discovered by Natta in 1955 [3]; where the methyl groups are all on the same side of

the main chain. This leads to relatively high crystallinities which gives the polymer a good combination of physical, mechanical and thermal properties. Atactic PP (aPP), where the methyl groups are randomly distributed either side of the backbone, is produced in much lower volumes than iPP. Due to the random arrangement of side groups, aPP is amorphous and has poor mechanical properties. aPP is a soft material which finds uses in adhesives and sealants. When the methyl groups alternate along the backbone, syndiotactic PP (sPP) is formed. sPP is not produced in large volumes and has a crystallinity far less than iPP. Developments in homogeneous metallocene catalysis over the last few decades now allow efficient control of regio- and stereo-regularities, molecular weight and molecular weight distribution and co-monomer incorporation. This has widened further the application range of PP.

An overwhelming majority of thermoplastic polyolefins are processed into their final form in the molten state by multi-stage manufacturing processes such as injection moulding, blow moulding and extrusion. In these processes individual polymer chains receive a complex and inhomogeneous history of thermal (temperature gradients & cooling rates) and mechanical (flow & pressure) conditions. In turn, the crystallisation process is influenced by the thermo-mechanical history during processing as this dictates the conformation of individual polymer chains and the number of available nuclei prior to the onset of crystallisation. A wide variety of morphologies and, consequently, properties are thus formed depending on processing conditions and location within the component. Understanding the link between processing and morphology will allow for more tightly controlled and optimised properties, as well as reduced processing defects.

For example, in the injection moulding process molten polymers are exposed to varying levels of shear flow and temperature profiles prior to crystallisation. The resulting morphology is substantially different from that observed under quiescent (i.e. without concurrent deformation) crystallisation conditions. Typically, a multi-layer ‘skin-core’ structure is formed [5-7], **Figure 1.1**. Rapid cooling at the surface produces a thin amorphous skin. Low cooling rates and strain fields in the core allow relaxation of chain molecules and a predominantly spherulitic structure is formed. Between the skin and core regions, a highly sheared zone forms which produces very anisotropic molecular

arrangements. In particular, a “shish-kebab” structure, a special kind of polymer crystalline assembly, can form under certain moulding conditions [8-17]. In this structure a highly oriented thread-like core composed of extended chains (shish) forms first, which then provides a template for the formation and growth of oriented chain folded crystalline lamellae (kebabs). The dimensions and specific morphologies of these zones have a significant influence on the physical, optical and mechanical properties of the final moulded article [18-19].

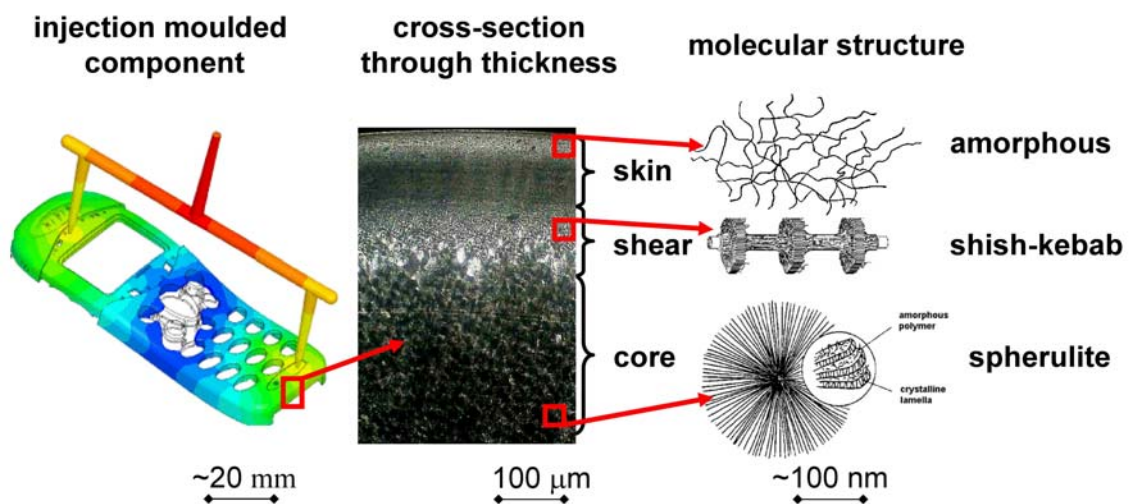


**Figure 1.1.** Optical cross-section viewed using polarized light of a typical injection moulded component highlighting the typical zones and microstructure formed. Image of mobile phone cover courtesy of Autodesk.

The formation of shish-kebab structures are associated with high molecular and crystalline orientation. High molecular orientation has been associated with improved tensile modulus and strength along the orientation direction as well as improved fracture properties across the orientation direction [20-22]. One of the most cited practical uses of intentionally high orientation, is in living hinges. In living hinge applications, the high molecular orientation which exists across the hinge promotes increased fatigue life [23]. Nevertheless, there are two important negative consequences of orientation. The first is that oriented molecules enhance differential shrinkage during solidification, which in turn increases the likelihood of dimensional instability and warpage [24-25]. The second is that the orientated structures invariably lead to anisotropic physical and optical properties. Anisotropic properties are undesirable from structural and aesthetic points of view where uniform properties in all

directions are important. Most importantly warpage and dimensional stability are rarely tolerable in consumer products.

Crystallisation and the subsequent development of morphology is further complicated by the intentional addition of a large range of polymer additives which are included for various industrial reasons [26-27]. Nucleating agents are one of the most common classes of additives to include in a polymers formulation, due to their ability to control the crystallisation process. Nucleating agents are added to polymers to (a) improve the rate of crystallisation and therefore the productivity and (b) alter the solid-state morphology with the aim of improving the moulded components physical, optical and mechanical properties. Although the action of many common nucleating agents is well understood in the quiescent condition [28-32], their role during flow-induced crystallisation has received comparatively little attention.

To understanding the influence of processing conditions and nucleating agents, it is desirable to follow individual chains in-situ from their equilibrium coiled state to being crystallised in an oriented form under conditions representative of industrial processes. **Table 1.1** summarises some of the advantages and disadvantages of the main experimental techniques which can probe the orientation or conformation of polymer molecules in-situ. A significant proportion of the experiments conducted lately have been performed on suitably designed parallel plate rheometers (such as the Linkam CSS450) which allow for controlled thermal-shear profiles and in-situ observation. These rheometers have been shown to be easily adaptable for in-situ observations using a wide range of techniques such as: optical microscopy (OM) [33-34], turbidity and birefringence measurement [35], small angle light scattering (SALS) [35-36], small and wide angle x-ray scattering (SAXS/WAXS) [14], small angle neutron scattering (SANS) [37-38] and Fourier transform infrared spectroscopy (FTIR) [39-41]. The main disadvantage of these rheometers is that in practice they only are able to access moderate shear intensities ( $\sim 100 \text{ s}^{-1}$ ); far below those typically observed in commercial polymer processing operations ( $> 1000 \text{ s}^{-1}$ ). This raises the important question of their applicability to industrial processes. In spite of this disadvantage, a great deal has been learnt from the results obtained from these techniques.

**Table 1.1.** Advantages and disadvantages of the main experimental techniques which can probe the orientation or conformation of polymer molecules in-situ.

Technique	Phases characterised	Sample thickness	Advantages	Disadvantages
Wide angle x-ray scattering (WAXS)	Mainly crystalline	~ 1 mm	Very accurate	Cost, lengthy data analysis
Small angle x-ray scattering (SAXS)	Mainly crystalline	~ 1 mm	Very accurate	Cost, lengthy data analysis
Small angle neutron scattering (SANS)	Amorphous	~ 1- 10 mm	Very accurate, allows determinations of radius of gyration	Very costly, requires deuteration of sample
Small angle light scattering (SALS)	Average of both	< 1 mm	Simple and rapid	Requires optically transparent samples
Infrared spectroscopy (IR)	Crystalline or amorphous	Transmission < 500 $\mu\text{m}$ (mid IR) < 5 mm (near IR)	Provides conformational information, rapid, suitable for online measurement	Overlap of bands, need to know angle of the transition moment to determine orientation
Raman	Crystalline or amorphous	Typically < 500 $\mu\text{m}$	Provides conformational information, rapid, suitable for online measurement	Tedious calculation required
Birefringence	Average of both	< 1 mm	Simple, rapid, suitable for online	Requires optically transparent samples
Nuclear magnetic resonance spectroscopy (NMR)	Crystalline or amorphous	< 1 mm	May resolve intra- and inter-molecular interactions	Structure must be known, requires high magnetic anisotropy
Fluorescence	Amorphous	< 1 mm	May be used for online measurement	Requires use of dye, difficult interpretation
Acoustics	Average of both	10 mm	Suitable for online measurement	Requires structural model to interpret data

## 1.2 Aim of the thesis

The aim of this thesis is to examine how nucleant particles influence the flow-induced crystallisation of iPP. Specifically the impact nucleant particles have on: the formation and relaxation of flow-induced nuclei, subsequent crystallisation kinetics and the development of final morphology of iPP will be examined. These will be probed using a range of time and spatially resolved techniques. In particular, in-situ simultaneous wide and small angle x-ray scattering will be the primary characterisation technique. A commercial grade of iPP was chosen as the model matrix polymer for the following reasons: its general relevance to industrial processes; its convenient range of crystallisation kinetics, which reduces the minimum time resolution needed to perform in-situ experiments; and the ability of iPP to form a variety of different crystalline and mesomorphic phases. Pure iPP and iPP containing various loadings of two intentional  $\alpha$ -iPP and two intentional  $\beta$ -iPP nucleating agents were investigated. These nucleants are:

- Intentional  $\alpha$ -iPP nucleating agents
  - Sodium benzoate (SB)
  - Bicyclo[2.2.1]heptane-2,3-dicarboxylic acid (HPN)
- Intentional  $\beta$ -iPP nucleating agents
  - Isotactic polystyrene (iPS)
  - Calcium salt of suberic acid (CaSub)

### 1.3 Outline of the presented research

This thesis is organised as follows. **Chapter 2** presents a review of the relevant literature including the current understanding regarding crystallisation from both quiescent and sheared melts, with particular emphasis placed on the influence of foreign particles. **Chapter 2** also includes a review of the hierarchical structure and properties of iPP, which is used as the matrix material in this study. **Chapter 3** summarises the main experimental procedures used in this thesis. **Chapter 4** through **Chapter 8** comprises the results and discussions obtained from this study, and these are described in more detail in the next three sections. Finally, **Chapter 9** summarises the main conclusions drawn from this work as well as points to possible directions future research could take.

#### *1.31 Flow-induced crystallisation of pure iPP*

In **Chapter 4** the influence of shear flow on the crystallisation of pure iPP is examined. In particular the unique parent-daughter (PD) lamellar branching phenomenon in  $\alpha$ -iPP is investigated. It is important to have a thorough understanding of the PD lamellar branching phenomenon as it is an inherent property of  $\alpha$ -iPP crystallisation and can significantly influence the measurement of orientation. **Chapter 4** presents a simple procedure for investigating the individual contributions of PD lamellar using WAXS. The procedure is then used to investigate PD lamellar branching during crystallisation and melting.

#### *1.32 Flow-induced crystallisation of iPP containing $\beta$ -iPP nucleating agents*

The usual crystalline form of iPP is a chiral  $3_1$  helix. This allows iPP to crystallise into a variety of crystalline and mesomorphic forms ( $\alpha$ -iPP,  $\beta$ -iPP,  $\gamma$ -iPP and smectic-iPP) depending on the specific crystallisation conditions.  $\alpha$ -iPP is thermodynamically the most stable crystalline form and exhibits good strength, due to its tight interlocking PD lamellar structure. However its toughness, particularly low temperature toughness, is quite poor.  $\beta$ -iPP on the other hand is less thermodynamically stable but has significantly improved toughness compared to  $\alpha$ -iPP. The addition of specific  $\beta$ -iPP



nucleating agents are commonly used to obtain significant quantities of  $\beta$ -iPP [42-48]. It is generally thought that specificity of the nucleant towards  $\beta$ -iPP is due to the formation of an epitaxial relationship with the  $\beta$ -iPP crystal. However, flow-induced crystallisation conditions have been suspected to counter the nucleating effect of  $\beta$ -iPP nucleating agents.

**Chapter 5** investigates polystyrene as a new class of polymeric nucleating agents for iPP. The morphology of isotactic polystyrene particles embedded into an iPP matrix were altered by selective heat treatment to be either semicrystalline or amorphous. Under quiescent conditions, it was shown that crystalline iPS particles selectively nucleated  $\beta$ -iPP, while amorphous iPS particles selectively nucleated  $\alpha$ -iPP. These results imply that the surface of the particle controls the crystallisation of iPP under quiescent conditions.

The crystalline iPS particles could however only nucleate a moderate amount  $\beta$ -iPP under the chosen crystallisation conditions. This makes investigation of the kinetics of  $\beta$ -iPP formation in nucleated material under a wide range of flow-induced crystallisation conditions more difficult. To address this, **Chapter 6** performs a detailed investigation of the morphology development and crystallisation kinetics of sheared iPP in the presence of the highly efficient  $\beta$ -iPP nucleating agent CaSub. The results revealed that the presence of the foreign particles assisted the formation of flow-induced nuclei, which then specifically nucleated  $\alpha$ -iPP. The creation of the additional flow-induced nuclei suppressed the heterogeneous nucleation effect from the surface of the particle.

### ***1.33 Shish formation and relaxation in iPP containing $\alpha$ -iPP nucleating agents***

In **Chapter 6** it was established that the addition of foreign particles leads to a synergistic increase in the numbers of flow-induced nuclei. Furthermore, the addition of the foreign nucleant particles was shown to decrease the flow intensity required to form oriented structures. Previously, it was thought that the surface of the particles stabilised extended chain conformations which then lead to increased numbers of nuclei [49-51]. However, particle shape has also been implicated, suggesting a different mechanism may be in operation [52]. In **Chapter 7** and **Chapter 8** the formation and relaxation of

shish in the presence of two commercial  $\alpha$ -iPP nucleants was studied. The two nucleants selected (SB and HPN) had similar chemical compositions and sizes but had different particle aspect ratios and substantially different abilities to induce heterogeneous nuclei.

**Chapter 7** provides a detailed investigation on the influence of SB and HPN particles on the flow-induced crystallisation of iPP. The results show that addition of both particles modified the local strain environment during shear flow. It was revealed that particle aspect ratio was a more important factor than the nucleation efficiency of the particle in terms of assisting shish formation. Interestingly, the combined effect of shear flow and nucleant was found to be very effective at inducing the  $\gamma$ -iPP phase.

**Chapter 8** furthers the investigation presented in **Chapter 7** by examining the dynamics of shish formation and relaxation during and after shear flow at temperatures well above the lamellae melting point of iPP containing SB and HPN particles. The results show that particle rotation during shear flow controls many aspects of shish formation. Furthermore, strong evidence is presented which shows that shish initially form, in a stepwise way, by the aggregation of point-like nuclei into oriented threads, contrary to the widely held view that shish form via an abrupt coil-to-stretch transition.



## Chapter 2

### Literature review

#### 2.1.0 Introduction

The discovery of the chain folded lamella by Andrew Keller in 1957 showed that most polymer crystals rarely reach a state of thermodynamic equilibrium [53-54]. This revealed that polymer crystallisation is dominated by kinetics effects, which dictate the formation of crystal nuclei and the diffusion of stems to the growing crystal. In the majority of polymer crystals, the long chains fold back and forth on themselves to form thin plate-like crystalline lamella. The lamellar thickness is typically significantly less than the length of the fully extended chain. In lamella, bonding along the chains is covalent, while bonding between chains is van der Waals type bonding. This causes the tensile modulus perpendicular and transverse to the chain to differ by some two orders of magnitude. In many polymers lamella units typically organise into complex hierarchical structures. For example in polyethylene (PE) and isotactic polypropylene (iPP) crystallised under quiescent (i.e. without concurrent deformation) conditions, the lamellae form long ribbons which can be twisted about their molecular axis and radiate out from a central point and form a spherulitic structure [7, 55]. The lamella and ribbons are connected by tie chains which are incorporated into adjacent lamella and ribbons. The inter-lamella and inter-ribbon region is amorphous and consists of tie chains, chain ends, loose loops, and unincorporated ends.

External flow fields, such as those produced during injection moulding, are well known to create molecular extension and orientation in polymer melts. This leads to significant changes in the crystallisation kinetics, and the development of morphology [10, 17]. For example, flow can change a spherulite structure which forms under quiescent conditions, to an oriented one containing the molecular assembly termed ‘shish-kebab’ [14]. This change invariably alters physical, optical and mechanical properties of the polymer. Inclusion of foreign particles in polymer formulation further complicates this picture by altering flow profiles as well as morphology development. At the heart of these changes is what happens

to the chain conformation during flow, and in the presence of particles. Ideally, it would be desirable to follow a single chain configuration from its equilibrium random coil to an oriented state, however this is experimentally difficult to achieve in real time under conditions typical of industrial processes.

The following chapter aims to systematically review the influence of both the presence of foreign particles and the imposition of flow on the development of morphology in semicrystalline polymers. In addition, the hierarchical structure and properties of the different crystalline forms of iPP, which is used as the model matrix material in this thesis, are reviewed. The review is organised as follows:

The first part of this review focuses on the quiescent crystallisation of polymer melts containing foreign particles. This section begins with a brief review of classical nucleation theory. The current state of the debate regarding the mechanism of the early stages of polymer crystallisation is then summarised. Finally, the influence of foreign particles on polymer crystallisation is thoroughly examined.

The second part of this review will examine the crystallisation from stressed polymer melts containing foreign particles. The first section will summarise the current understanding of the effect of flow on the chain dynamics of entangled polymers. The subsequent section will investigate the formation of the shish-kebab structure including the conditions required for their formation and their possible formation mechanism. The final section will review the influence of particles on shish-kebab formation.

The last part of this review will describe the known crystalline forms of iPP. This will include: the crystal structure, the lamellar scale architectures and the thermodynamic and mechanical properties of each phase.

## 2.2.0 Crystallisation from quiescent polymer melts containing foreign particles

### 2.2.1 Classical nucleation theory

When the temperature of a polymer is below that of the melting point of an unconstrained, infinitely large crystal (i.e. the equilibrium melting point) ( $T_m^0$ ) of that polymer, the crystal state has a lower free energy than its corresponding liquid state, as shown schematically in **Figure 2.1a**. The Gibbs free energy ( $G$ ), can be defined as the difference between the enthalpy ( $H = U + pV$ ) and entropy ( $S$ ) according to:

$$G(T, p) = (U + pV) - TS \quad \text{Equation 2.1}$$

where  $U$  is the internal energy,  $p$  is the pressure,  $V$  is the volume and  $T$  is the temperature of the system. The first derivative of the Gibbs free energy therefore reveals that a discontinuous transition must occur at  $T_m^0$  to  $V$ ,  $H$  and  $S$ , **Figure 2.1b**. In the melt, entropy dominates. Crystallisation results in the regular arrangement of chains which are locked into rigid position and is therefore associated with a negative entropy change. However, for a reaction to occur spontaneously there must be an overall negative change in  $G$ . The close packed arrangement of chains in the crystal maximises the attractive forces and increases the density, which results in a large reduction in enthalpy.

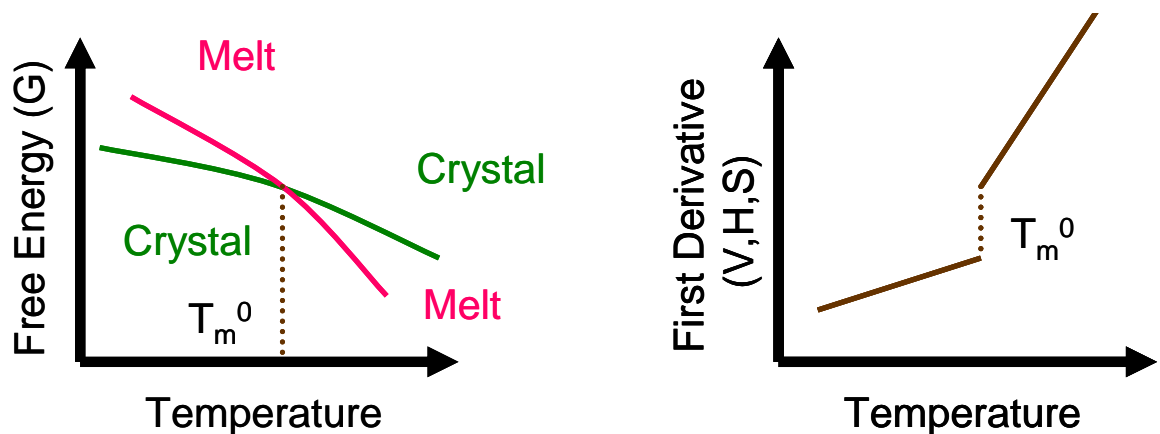


**Figure 2.1.** Effect of temperature on thermodynamic variables of semicrystalline polymers around the equilibrium melting temperature ( $T_m^0$ ) (a) Gibbs free energy (b) entropy and volume.

From the above thermodynamic considerations, the driving force for nucleation is then the Gibbs free energy difference between the crystal and the liquid ( $\Delta G$ ). Under quiescent conditions, the activation energy for homogeneous nucleation can be taken as [56]:

$$E = \frac{16\pi}{3} \frac{\sigma^3}{\Delta G} \quad \text{Equation 2.2}$$

where  $\sigma$  is the activation energy per unit necessary to form the interface between the liquid and the nucleus. At low super cooling,  $\Delta G$  is proportional to the degree of super cooling ( $\Delta T = T_m^0 - T$ ) and to the melting entropy ( $\Delta S_m$ ). Therefore,

$$E \cong \frac{\sigma^3}{\Delta S_m^2 \Delta T^2} \quad \text{Equation 2.3}$$

Although conditions may exist where the crystal phase is thermodynamically more stable, to form a crystal implies the formation of a new interface. The necessary formation of the interface then decreases the enthalpic gain of forming a crystal. Therefore, these two opposing forces leads to an energy barrier which needs to be overcome to form the initial nucleolus which eventually will grow into a crystal. Small nuclei will then appear and redissolve due to statistical fluctuations. However, when a nuclei reaches a critical size the bulk enthalpy contribution, which is favourable, becomes larger than the surface energy contribution, which is detrimental, and the nuclei can then grow spontaneously into a crystal, **Figure 2.2**.

The classical nucleation theory described here still dominates the field of crystallisation. However, there are a number of important limitations to the theory, the most important being that the internal and surface structure of the nuclei may be significantly different to the bulk crystal. For example, it has been suggested that crystallisation in many polymers is preceded by the formation of metastable bundles consisting of roughly parallel stems with

the length of a few chain atoms [57]. This therefore raises the important question as to what the correct values for the bulk free energy and surface free energy of the nuclei would be.

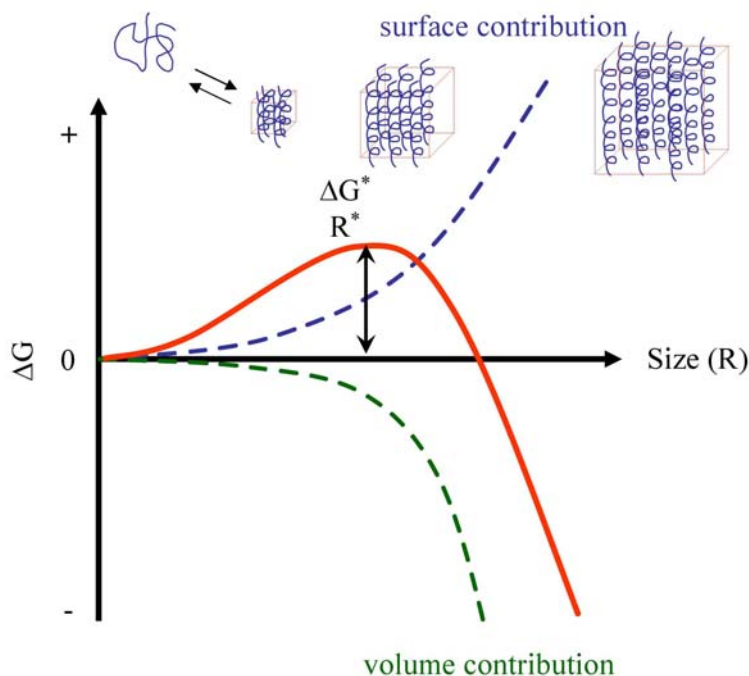


**Figure 2.2.** Dependence of the Gibbs free energy for crystallisation ( $\Delta G$ ) with aggregate size ( $R$ ), shown as a solid red line. Variation in  $\Delta G$  depends on two opposing factors, the energy required to create new surface, and the reduction in entropy due to the regular arrangement of stems.  $\Delta G^*$  and  $R^*$  are the free energy barrier and the size of a critical nucleus for nucleation to spontaneously occur. At low  $R$  ( $R < R^*$ ), transient aggregates form and redissolve, while for large  $R$  ( $R > R^*$ ) nuclei can grow spontaneously into stable crystals.

### 2.2.2 Homogeneous versus heterogeneous nucleation

The formation of stable crystal structures from a supercooled melt is generally considered a two step process: nucleation and growth. Crystal growth occurs by the deposition of chain segments to the crystal, and is governed to a large extent by the diffusion coefficient of the chain segments and the redispersion of chains at the crystal growth front. Crystal growth will be covered in further detail in the following section. Nucleation involves the cooperative ordering of chain segments to form nuclei above a critical size. The first nuclei



to form from the supercooled melt (primary nucleation) can occur by two different mechanisms: (1) a liquid-liquid phase separation (homogeneous nucleation) and (2) by nucleation on pre-existing nuclei (heterogeneous nucleation). Historically, it has been considered that heterogeneous nucleation occurred in the majority of cases, as even relatively pure materials will have a reasonable population of heterogeneous nuclei (e.g. dust, left over polymerisation catalyst, etc) which provide sites for nuclei formation. However, over the last decade a considerable number of studies have found a variety of evidence that homogeneous nucleation may also play an important role in many industrially significant polymers.

The bulk of the recent experimental evidence which supports the case for homogenous nucleation comes from in-situ simultaneous small and wide angle x-ray scattering (SAXS/WAXS) experiments. In the classical picture of heterogeneous nucleation Bragg peaks (WAXS) are expected to form after an induction period. SAXS accompanies the WAXS due to the formation of regular crystal and amorphous lamella layers. Therefore no SAXS is expected to form during the induction period. However, a number of studies have shown that SAXS can form before the formation of Bragg peaks. Furthermore, the SAXS scattering in these experiments initially increased exponentially and could be fitted to the Cahn-Hilliard (C-H) theory for spinodal decomposition [58]. This “SAXS before WAXS” phenomenon and C-H kinetics during initial crystallisation have now been reported for a number of industrially important semicrystalline polymers such as: iPP [59-61], PE [61] and polyethylene terephthalate (PET) [62-63].

Olmsted et al. provided a theoretical basis for the spinodal assisted crystallisation of semicrystalline polymers [64]. Central to this theory is a coupling between density and chain conformation. This coupling should occur as segments of the ‘correct’ (helical) conformation should pack more densely than those with random conformations. Under appropriate conditions, this coupling can then induce a liquid-liquid binodal within the equilibrium liquid-crystalline solid coexistence region. Compared to the amorphous melt, the denser liquid would be closer to the final density and conformations found in the crystal phase and thus, would be expected to have a lower energy barrier to crystallisation. This simple model allows the prediction and explanation of a range of testable consequences.

For instance, spinodal scattering is most commonly observed in sheared polymer melts. This can be rationalised by the shear flow orienting and increasing the persistence length of the polymer segments, thereby promoting the formation of the denser phase.

Nevertheless, a number of criticisms have been levelled at the scattering experiments which support homogeneous type mechanisms. One of the key criticisms of the simultaneous SAXS/WAXS studies is that the lag time between the intensity increase in the SAXS region and the occurrence of crystalline reflection in the WAXS region is due to the low concentration of crystals present. Therefore, the scattered intensity from crystals in the WAXS region is too small to detect above the background and amorphous halo. Hsiao et al. reported simultaneous SAXS/WAXS and laser light scattering (LS) experiments on iPP and found that although SAXS scattering did precede the WAXS scattering, the early evolution of crystallinity measured by SAXS, WAXS and LS followed the same Avrami equation [65]. This strongly suggests that the early stages of crystallisation followed classical nucleation and growth. Recently, Panine et al. [66] investigated the early crystallisation of iPP using a high brilliance x-ray scattering method coupled with very sensitive detectors. In these experiments Panine surprisingly found the nucleation and growth of crystalline moieties prior to the occurrence of significant SAXS intensity. In another study Wang performed in-situ small angle neutron scattering (SANS) experiments on solution crystallised PE and also found no evidence for spinodal-like density fluctuation [67]. Wang suggested the existence of the early emergence of SAXS peak may be due to the over subtraction of the background.

### 2.2.3 Crystallisation kinetics

Assuming that the rate of nucleation is governed by the Arrhenius equation, the rate of nucleation ( $k(T)$ ) can be expressed by the following relation:

$$k(T) = Ae^{\left[ \frac{-C\sigma^3}{T_x \Delta T^2 \Delta S_m^2} \right]} \quad \text{Equations 2.4}$$

where A and C are constants.

The Hoffman-Lauritzen theory can be used to describe the crystal growth rate [68]. The temperature dependent growth rate for a spherulite ( $G(T_m)$ ) is described by **Equation 2.5**:

$$G(T_m) = G_0 e^{\left(\frac{-U^*}{R(T-T_\infty)}\right)} e^{\left(\frac{K_g}{T\Delta T}\right)} \quad \text{Equation 2.5}$$

where  $G_0$  is a pre-exponential velocity vector which contains constants which are not strongly dependant on temperature,  $K_g$  is the secondary nucleation exponent which incorporates such things as the fold energy,  $U^*$  is the apparent activation energy of motion for a polymer chain,  $R$  is the gas constant,  $T$  is the crystallisation temperature and  $T_\infty$  is the temperature at which molecular displacement becomes impossible. The actual crystallisation rate will then be a combination of **Equation 2.4** and **Equation 2.5** which represent the contributions from nuclei formation and the growth of crystal structures.

Although the Hoffman-lauritzen theory explains the kinetics of crystallisation in molecular terms, the overall crystallisation kinetics (nucleation and growth) of polymers is often modelled using the Avrami equation:

$$1 - \chi_{rel} = e^{-kt^n} \quad \text{Equation 2.6}$$

where  $\chi_{rel}$  is the crystallisation fraction at time ( $t$ ),  $k$  is the bulk crystallisation constant and  $n$  is the Avrami exponent. Assuming the nucleation and crystal growth rates are invariant, the value of  $n$  can give important information about the growth conditions and growth geometry. The growth geometry for various crystallisation and nucleation conditions have been reported by Mandelkern [69] and are summarised in **Table 2.1**. The wide range of values obtained shows that the  $n$  value does not define a unique nucleation growth geometry and therefore complementary analysis is often required to interpret the meaning of  $n$ .

**Table 2.1.** Avrami exponent (n) for various types of nucleation and growth geometries.

Data taken from Mandelkern [69]. \* All nuclei active at  $t = 0$ .

Growth habit	Linear growth		Diffusion controlled growth	
	Steady state	$t = 0^*$	Steady state	$t = 0$
Sheaf-like	6	5	3.5	2.5
Sphere-like	4	3	2.5	1.5
Disk-like	3	2	2	1
Rod-like	2	1	1.5	0.5

#### **2.2.4 Control of polymer crystallisation using additives**

Polymer crystallisation is complicated by the intentional addition of a wide variety of substances (e.g. minerals, organic salts, and organics) to polymer formulations. For the most part these substances are added in particulate form. Through their influence on such things as crystallisation kinetics and the final morphology of the polymer, these substances can have a large influence on the economics of the produced components by altering production rates, as well as the physical, optical and mechanical properties of the final products. These substances influence polymer crystallisation in two main ways: by influencing crystal growth rates or by influencing crystal nucleation rates. Recent investigations have suggested that a range of common additives may retard crystal growth rates by inhibiting chain diffusion to the crystal growth front [70-71]. Nevertheless, it is usually assumed that crystal growth rates are relatively insensitive to foreign substances and that their overriding influence is in providing sites for heterogeneous nucleation, thereby enhancing nucleation. The following provides a summary of the advances which have been made to further understand heterogeneous nucleation on the surface of foreign particles.

If the polymer can interact with and ‘wet’ the surface of a particle, then the interfacial free energy of a nuclei forming on it can be reduced. For example, when the contact angle is  $90^\circ$ , it can be shown that the size of the hemispherical nucleolus forming on the surface (heterogeneous nucleation) is half that of the spherical nucleolus forming in the bulk (homogeneous nucleation) [72]. The nucleation barrier on a flat surface is then  $\Delta F^*_{\text{flat}} = \Delta F^*_{\text{homo}}/2$ , where  $\Delta F^*$  is the free energy barrier to nucleation. Thus nucleation is favoured on flat surfaces even if they are inert.

If attractive forces are sufficient, the polymer molecules may get physically adsorbed onto the foreign surface. The configuration of these adsorbed molecules may then be confined reducing their free volume. The accompanying reduction in entropy would then lower the activation energy required to form nuclei of critical size [32]. This ‘soft epitaxy’ mechanism has recently been employed by Li et al. to explain the size dependence of nucleation in nano-composites of PE containing carbon nanotubes (CNT) of various diameters, **Figure 2.3** [73]. For small CNT diameters, PE lamellae grew exclusively with the surface orthogonal to the CNT axis. However, as the CNT diameter was increased, lamellae were observed to nucleate in multiple orientations suggesting a change in nucleation mechanism to normal epitaxy. Li et al. explained the new growth mechanism observed on the small diameter CNT by the adsorption and confinement of the PE molecules on the surface of the CNT. This resulted in the cooperative alignment of the chain and the CNT axis. Therefore in this model, strict lattice matching is thought not to be required.

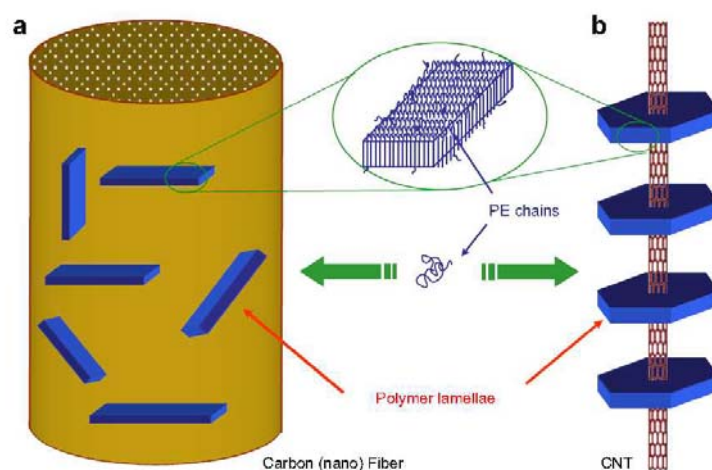


**Fig. 6.** Schematic representation of the "size-dependent soft epitaxy" mechanism. (a) For large-diameter CNFs, PE lamellae are randomly orientated on the fiber surface. (b) For small-diameter CNTs, soft epitaxy dictates the parallel orientation between PE chains and the CNT axis, leading to an orthogonal orientation between CNT and PE lamellae [72].

**Figure 2.3.** Suggested mechanism for the size dependant soft epitaxy described by Li et al. [73].

The interfacial free energy, and therefore the activation energy to form a nuclei of critical size can be further reduced if there is a good match between structural features (linear arrays or gratings with regular periodicity) on the nucleating surface and characteristic distances within the polymer crystal. The ‘epitaxy’ formed results in the growth of the

polymer crystal along one or more strictly defined crystallographic directions and thus an orientation relationship between the two phases is formed. Generally it is thought that a misfit between the polymer unit cell and the repeat distance on the nucleant surface should be less than 10-15 % for epitaxial nucleation to be significant [74]. However in practice, it has been found that a wide range of structurally diverse surfaces can act as nucleating agents for the one polymer.

Wittmann and Lotz performed electron diffraction studies on substrate-PE bilayers and showed that the crystal planes of PE in which the characteristic repeat distances best matched the periodicity in the structural features on the surface of the nucleant became the contact plane in the epitaxial relationship [75]. This leads to six possible epitaxial matches (three each for the monoclinic and orthorhombic PE phases) with characteristic repeat distances between  $\approx 4$  and  $\approx 9.4$  Å being able to nucleate PE [75]. A similar study performed by Mathieu et al. found that the (010) contact plane of  $\alpha$ -iPP and  $\gamma$ -iPP unit cells are made of the same highly symmetrical, lozenge shaped array of methyl group [76-77]. Mathieu et al. showed that the lozenge can interact with surfaces with periodicities  $\approx 4.2$  Å,  $\approx 5$  Å and  $\approx 6.6$  Å, which match periodicities normal to the lozenge long diagonal, short diagonal and to its cell edges respectively, **Figure 2.4**. In addition, Stocker et al. showed that a substrate periodicity of  $\approx 6.5$  Å [78] and an orthogonal geometry of the contact phase is able to specifically nucleate  $\beta$ -iPP.

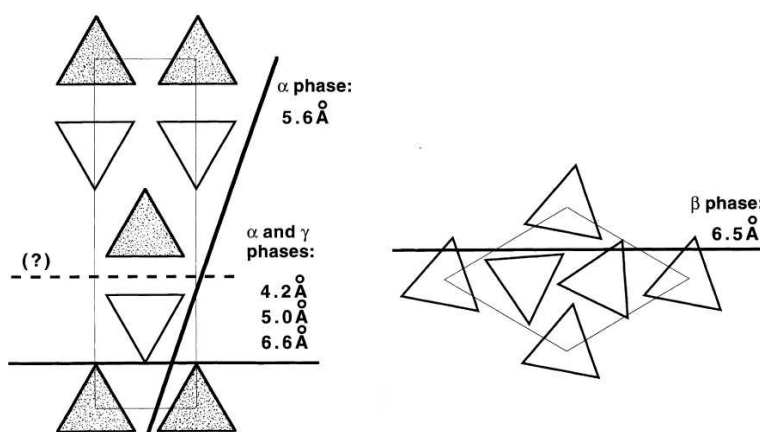
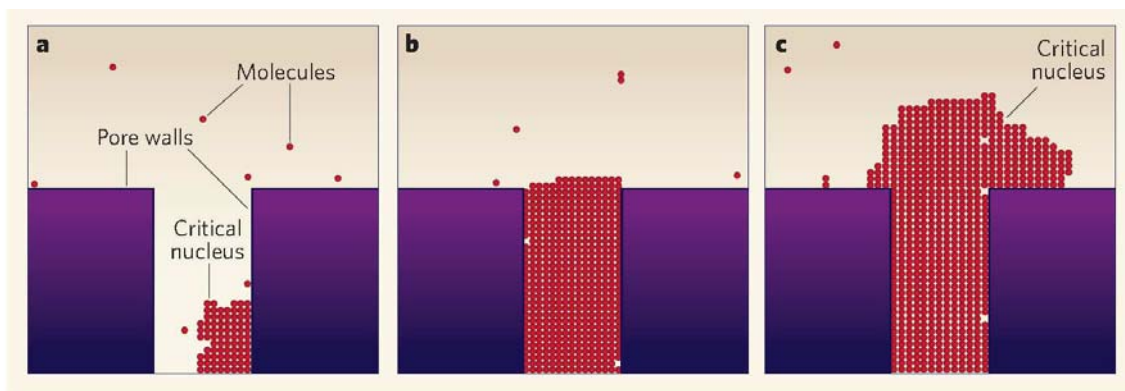


Fig. 7. Schematic summary of the epitaxies observed so far for the various crystal phases of isotactic polypropylene, and the corresponding lattice periodicities and specific crystal phase involved. Helices of opposite hands are shown shaded and unshaded, respectively. Setting angles of the  $\beta$  phase are as determined in Ref. [13]. For  $\alpha$ iPP, the alternate (010) plane illustrated in Fig. 2c might be added to this diagram (broken line), but no evidence for its role as a contact plane has been obtained so far.

**Figure 2.4.** Known epitaxial relationships for iPP. Mathieu et al. [76].

Chayen et al.'s breakthrough study on the effect of mesoporous seeds on protein crystallisation showed that porous surfaces can further promote nucleation [79]. Page and Sear provided a possible explanation based on classical nucleation theory for the increased nucleation in porous materials [72], **Figure 2.5**. In a pore, it is possible for a forming nuclei to be in contact with more than one surface simultaneously (i.e. a corner). For example, a nuclei forming in a tight corner which makes a contact angle of  $90^\circ$  on an equivalent flat surface would be a quarter that of a spherical nucleolus forming in the bulk,  $\Delta F^*_{\text{corner}} = \Delta F^*_{\text{homo}}/4$ . Therefore compared to a flat surface, nucleation in a tight corner further reduces the interfacial energy and therefore lowers the activation energy required to form a nuclei of critical size. Such a mechanism would suggest that smaller pores would aid nucleation, as long as the pore is larger than the molecular diameter. However, crystallisation into the bulk only proceeds when the pore is filled to the top, where it can act as a 'self seed'. In this case a larger pore would promote nucleation. These opposing dependencies on pore size result in an optimum pore diameter where nucleation rates are maximal. The influence of pore size predicted by Page and Sear has been experimentally confirmed by Shin et al. who investigated PE crystallising in cylindrical alumina nano-pores [80]. They found that the nucleation rate increased with decreasing pore diameter. However, Shin et al. also found that the crystallinity reduced as the degree of confinement tightened. Although not studied in their investigation, this reduced crystallinity would be expected to reduce crystallisation breakout from the pore.

Another implication of crystal nucleation occurring in pores is the possibility of the external confinement of the pore influencing the crystal structure. Ha et al. investigated the polymorphic behaviour of amino acids confined to different sized nano-pores [81]. Ha found that crystal nucleation and polymorph selectivity was indeed influenced by the confinement provided by the nano-pores. Ha et al. speculated that the influence of pore size on the polymorphism was likely to be due to critical size constraints imposed on the forming nuclei. It is not inconceivable that a similar effect could also occur in many semicrystalline polymers which show polymorphism. However, as yet no such studies have been reported in the literature.



**Figure 1 | Crystal nucleation in a pore.** Page and Sear<sup>2</sup> propose a model to explain why porous materials induce protein crystallization. **a**, The pore walls weakly attract the molecules to be crystallized. Crystals start to grow in the corners of the pore when a critical nucleus of molecules forms. **b**, The crystal grows until the pore is filled. **c**, Another critical nucleus of molecules forms on the outside of the pore, which allows the ‘breakout’ of a bulk crystal from the pore. The rates of nucleus formation and breakout vary independently according to the width of the pore.

**Figure 2.5.** Suggested model for the nucleation in and out of pores. Taken from Frenkel [82].

In addition to the nucleation mechanisms described previously, the curvature of the particle surface can have important implications for polymer crystallisation. Cacciuto et al. performed Monte Carlo simulations to study how smooth spherical particles influenced crystallisation in a suspension of hard colloidal spheres [83], **Figure 2.6**. Three regimes of nuclei formation were described depending on the radius of the particle. Small spheres were found to generate large numbers of topological defects in the nuclei growing on them which inhibited their formation. The particle size therefore needed to be above a well defined minimum to effectively promote crystallisation. On the other hand large spheres, which can be considered to be relatively flat on the scale of the growing nuclei, were found to be highly effective at generating nuclei which then remained attached to the particle surface. When the particle size was between these two extremes, the particles were found to act as nuclei factories. At some point in time, pre-critical nuclei growing on these intermediate sized particles break away from the particle wall and the critical nuclei is formed in the bulk. The detachment allows space for new nuclei to form and thus a large number of nuclei may be created within the material. The particle size can therefore have important consequences for the size distribution of crystallites formed by heterogeneous nucleation.



Large, flat particles would promote large crystals, while the large number of nuclei generate by intermediate sized particles should result in small crystals.

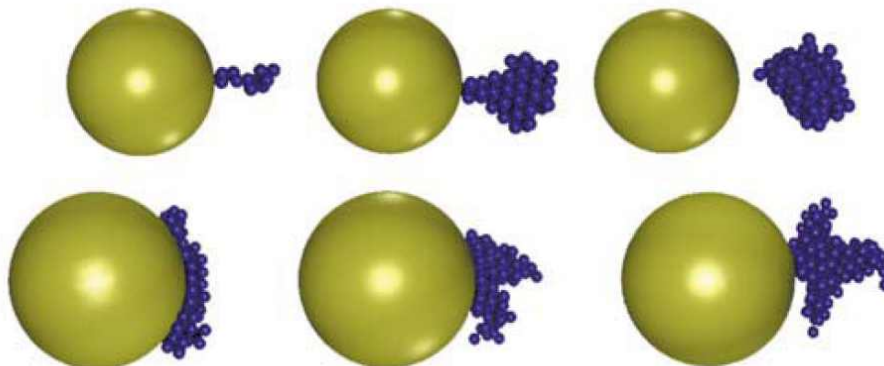


**Figure 4** Snapshot sequence of crystal nucleation on spherical seeds. The seeds have radii  $R_s = 5\sigma$  (top) and  $7\sigma$  (bottom). From left to right the sizes of the nuclei are, respectively,  $N \approx 10$ ,  $\approx 50$  and  $\approx 100$  for the sphere of radius  $R_s = 5\sigma$  and  $N \approx 60$ ,  $\approx 80$  and  $\approx 120$  for the sphere of radius  $R_s = 7\sigma$ . The above phenomenon should be observable in confocal microscopy studies of seeded crystallization in a colloidal suspension.

**Figure 2.6.** From Cacciuto et al. showing simulated nuclei growing on particles of different radii [83].

Recent experimental observations support the simulation work by Cacciuto et al. [83]. D’Haese et al. studied the effect of zinc oxide nano-particle size on the quiescent crystallisation of iPP, and found that the nucleation efficiency of the particle increased with increasing particle size [84]. Zhu et al. studied the influence of two particulate colourants, which had very different surface curvatures, on the quiescent crystallisation of iPP [49, 85]. Zhu and co-workers found that the colourant with the flat surface was a highly effective nucleant, and increased the lamellar thickness. On the other hand, the colourant with the curved surface did not appreciably influence nucleation or lamellar thickness.

## 2.3.0 Crystallisation from stressed polymer melts containing foreign particles

### 2.3.1 Chain dynamics of entangled polymers

The application of external flow or stress fields to entangled polymer melts can lead to orientation and extension of large segments of, or even the entire, polymer molecule. These extended chains can then dramatically alter the development of morphology during subsequent crystallisation. The following section examines the current understanding of the chain dynamics which occur in entangled linear polymer melts during and after flow.

De Gennes provided the theoretical background for chain extension in dilute solutions of polymer molecules under different flow conditions [86]. At the heart of de Gennes' theory was the concept of an abrupt transition of the originally unoriented molecules in random coil configurations to oriented molecules in extended chain conformations. This coil-to-stretch transition occurs without the formation of stable intermediate states, once a critical extensional deformation rate ( $\dot{\epsilon}_c$ ) was reached. De Gennes argued that such an abrupt transition would occur because the hydrodynamic interactions, which act to resist the unravelling of the molecule, decrease rapidly as the polymer is stretched. Therefore, when the deformation rate exceeds the chain relaxation rate, defined by the inverse of the chain Rouse time (i.e.  $\dot{\epsilon}_c > 1/\tau_R$ ), the chains will stretch to a fully extended state.

Keller et al. noted that the flow-induced morphologies in solution were similar to those found in entangled melts and reasoned from their similarity that a coil-to-stretch transition also occurred in entangled melts [10]. In their original experiments, extensional flow fields were created using an opposing jet device and the chain orientation was measured by optical birefringence. In these experiments, Keller found evidence for the existence of a coil-to-stretch transition in entangled melts, by showing a sharp upturn in birefringence at a critical strain rate ( $\dot{\epsilon}_c$ ). Furthermore, Keller found that  $\dot{\epsilon}_c$  scaled with the molecular weight ( $M$ ) according to the relation:

$$\dot{\epsilon}_c \propto M^{-\beta}$$

**Equation 2.7**

where  $\beta$  is a constant related to the Rouse time. This relation shows that longer chains can become extended using lower strain rates and hence under weaker flow intensities. Therefore in polydisperse melts subjected to a fixed strain rate just above  $\dot{\gamma}_c$ , only the longest chains in the distribution will become extended and accordingly a bimodal distribution of chain extensions will result. Dukovski and Muthukumar revealed that molecular weight was however not the only determining factor for a chain to become extended in a given flow field by showing that a chains' initial conformation also influenced the dynamics of chain extension [87].

The majority of the early experiments were performed using elongational flow. Shear flow was considered to be insufficient to allow the complete extension of molecules due to the rotational component counteracting the elongational component of the flow. However, many studies have revealed that simple shear flow can also induce significant chain extension in entangled polymer melts [10, 14, 17]. Keller hypothesised that a similar transition also existed at a critical shear rate ( $\dot{\gamma}_c$ ) and would occur between entanglement constraints imposed by the surrounding molecules [10].

The relaxation of entangled extended polymer molecules can be described by the reptation theory first presented by de Gennes [88] and later expanded by Doi and Edwards [89]. Reptation theory assumes that the large scale motion of the relaxing polymer chains are constrained by the topology of neighbouring chains. This results in the chains relaxing in a snake-like motion (reptation) along an imaginary tube formed by these neighbouring molecules. This constrained motion leads to a characteristic relaxation time, termed the disengagement or reptation time ( $\tau_d$ ), for a chain to diffuse through one tube length. This simple theory explains a number of important experimental observations including: a nonzero second normal stress difference in simple shear flow, the origin of shear thinning due to the alignment in flow of the tubes, and the approximate scaling of  $\tau_d \propto M^3$ .

Nevertheless, there are several deficiencies in this simple model. Most notably, numerous experimental studies revealed that the reptation time in fact scales as  $\tau_d \propto M^{3.4}$  [90-93].

This has led to proposals for the inclusion of a number of additional processes into the Doi-Edwards model to account for the experimental results. **Figure 2.7** illustrates the regimes of flow intensity in which these different processes are thought to dominate [94]. In polydisperse systems, the release of the constraints imposed by the neighbouring molecules as they reptate away during the reptation of the main chain along the tube is important [95]. This “constraint release” (CR), otherwise known as double reptation, is thought to be important under weak flow conditions where the deformation rate is less than the Rouse time. However, under strong flows the relative motion of molecules in the velocity gradient is thought to lead to the release of entanglements, thereby permitting further chain relaxation [94]. This is termed “convective constraint release” (CCR). In addition, under intense flow conditions chain “stretch” also can become important [89]. Another important relaxation mechanism, termed “contour length fluctuations” (CLF) is the inclusion of more complicated modes of chain relaxation which leads to fluctuations of the path length of the occupied tube segments [93]. The impact of CLF is that it leads to faster relaxation of the chain ends than when reptation is considered alone. Milner and McLeish showed theoretically that the inclusion of CLF on the overall melt viscosity alone could account for the  $M^{3.4}$  dependence [90]. Although long predicted by theory, only recently has the existence of the CR [96] and CLF [97] phenomenon in entangled polymer melts been confirmed by direct observation using neutron spin echo (NSE) spectroscopy of labelled PE chains.

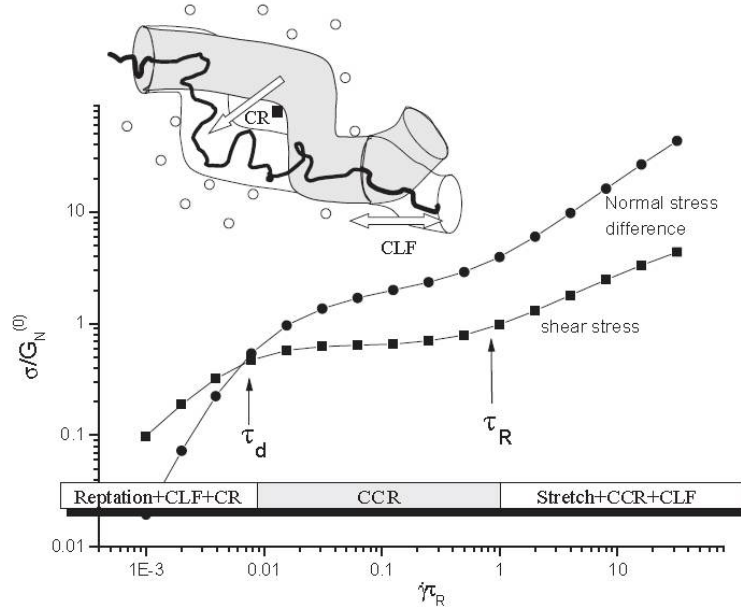


**Fig. 1.** Schematic illustration of the shear rates at which the various tube-dynamic processes dominate. Plotted are both the shear stress  $\sigma_{xy}$  and normal stress difference  $\sigma_{xx} - \sigma_{yy}$  with shear rate, where  $x$  and  $y$  are Cartesian components. Reptation (moderated by CLF) dominates a pseudo-Newtonian regime at low rates, until CCR causes the shear stress nearly to plateau when shear rates are faster than reptation. At high rates faster than the slowest CLF mode, the chains start to stretch and shear stress rises again. Inset: The three physical processes of polymer dynamics in a constraining tube. Under reptation, the whole chain takes diffusive steps along the tube in a random direction (solid line). Under CLF, the chain end explores new tube configurations through longitudinal fluctuations of the total entangled tube length, but without requiring center-of-mass (reptation) motion. Under CR, an entanglement with a neighboring chain (shown by the solid square) may disappear, allowing effective conformational relaxation of that part of the tube, again without reptation of the test chain itself. Tube configuration before relaxation is shaded; after relaxation, light.

**Figure 2.7.** Regimes of flow intensity in which different reptation processes dominate. Taken from Bent et al. [94].

The simple reptation time for a linear monodisperse entangled chain can be calculated with the simple Doi-Edwards model using the following relation:

$$\tau_d = 3\tau_e Z^3 \quad \text{Equation 2.8}$$

where  $\tau_e$  is the relaxation time of a single entanglement strand and  $Z$  is the number of entanglements per chain (i.e. the chain length divided by the mean entanglement length). When CLF effects are taken into account the relation becomes:

$$\tau_d = 3\tau_e Z^3 [1 - \kappa Z^{-0.5}]^2 \quad \text{Equation 2.9}$$

where  $\kappa$  is a constant found to be close to unity [91]. The Rouse time ( $\tau_R$ ), which can be considered to be the retraction time of the tube, can be determined from the following equations:

$$\tau_R = \frac{\tau_d}{3Z} \quad \text{Equation 2.10}$$

or

$$\tau_R = \tau_e Z^2 \quad \text{Equation 2.11}$$

Both  $\tau_R$  and  $\tau_d$  require the determination of the entanglement relaxation time ( $\tau_e$ ), which can be calculated from the Kuhn step length ( $b$ ), the tube diameter ( $a$ ) and the monomeric friction coefficient ( $\zeta_0$ ) [89-92]:

$$\tau_e = \frac{\xi_0 a^4}{3\pi^2 K_B T b^2} \quad \text{Equation 2.12}$$

where  $K_B$  is the Boltzmann constant and  $T$  is the absolute temperature. The relationships between the characteristic lengths  $a$  and  $b$  with the equilibrium random coil features, i.e  $a^2 = M_e \langle R^2 \rangle / M$  and  $b^2 = m_0 \langle R^2 \rangle / M$  allows  $\tau_e$  to be expressed as:

$$\tau_e = \frac{\xi_0 \frac{\langle R^2 \rangle}{M} M_e^2}{3\pi^2 K_B T m_0} \quad \text{Equation 2.13}$$

where  $\langle R^2 \rangle / M$  is the ratio of the monodisperse chain end-to-end distance and the molecular weight for an ideal equilibrium random coil,  $M_e$  is the average molecular weight between topological constraints and  $m_0$  is the monomers molecular weight. Therefore if the quantities  $\langle R^2 \rangle / M$ , the monomeric friction coefficient and the entanglement length are

known, the characteristic relaxation times of polymer chains in a monodisperse melt can be determined.

### **2.3.2 Formation of the shish-kebab structure**

If the flow intensity imposed on an entangled melt is sufficient, a highly anisotropic crystalline architecture termed shish-kebabs can form [8-17]. It is generally considered that a highly oriented thread-like core composed of extended chains or chain segments (shish), that can be in amorphous, crystalline or mesomorphic states, forms first. The shish then provide a template for the growth of oriented chain folded crystalline lamellae which grow perpendicular to the long axis of the shish (kebabs). The formation of shish has been implicated in influencing many of the important physical and mechanical properties of the produced polymer [18-19]. Accordingly, the formation of shish is critical to understanding morphology and property development in a wide range of processes such as injection moulding and extrusion technologies. In the first part of this section, the conditions required to initiate shish formation are examined. In the second part of the section, the various mechanisms proposed in the literature for how the shish entities form are summarised and compared. Finally, the current understanding of the growth of kebabs on the shish core is briefly reviewed.

A critical flow intensity is known to be required to form the shish-kebab structure. It has been widely established that the deformation rate needs to be of sufficient intensity such that the longest chains in the system can become extended [10]. However, the shish entities are known to be composed of many chains and therefore an additional amount work must be necessary to bring the extended chains together. Using a specially designed apparatus which could apply a defined amount of mechanical work, Janeschitz-Kriegl et al. showed that a critical amount of work was required for the transition from point-like nuclei to thread-like nuclei (shish) [98]. This concept has been recently extended by Mykhaylyk et al. who took advantage of the shear rate gradient found in parallel plate rheometry samples to characterise the specific flow conditions required to induce the shish-kebab structure in a range of polyolefins [12-13], **Figure 2.8**. In essence, a critical amount of mechanical work ( $w_b$ ) was needed to be applied at deformation rates exceeding the inverse of the Rouse time

of the longest chains in the system. Above a critical shear rate ( $\dot{\gamma}_{\min}$ ), the critical work was found to be independent of shear rate due to the saturation of extended chains. However, at shear rates below  $\dot{\gamma}_{\min}$ , the required critical work was found to increase with decreasing shear rate due to a decrease in the population of extended chains.

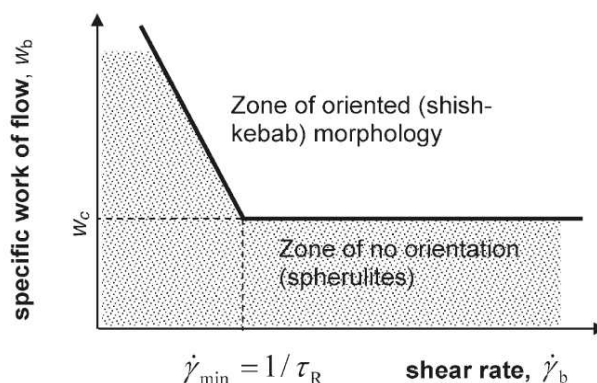


**Figure 16.** Schematic diagram of flow conditions required for the formation of oriented (shish kebab) morphology in a polymer melt. The solid line dividing the diagram into two zones (zone of orientation and zone of no orientation) corresponds to a plot of the boundary specific work required for the formation of oriented nuclei (shish),  $w_b$ , as a function of the boundary shear flow rate,  $\dot{\gamma}_b$ . The critical specific work,  $w_c$ , indicates the minimum amount of the specific work required for the formation of oriented nuclei at the chosen thermodynamic parameters. The minimum shear rate  $\dot{\gamma}_{\min}$  indicates the flow rate below which the concentration of molecules in a stretched state is decreased.

**Figure 2.8.** Schematic diagram illustrating the flow conditions where shish-kebab and spherulite structures dominate. Mykhaylyk et al. [13].

Although the specific flow conditions for shish formation have been identified, the mechanism responsible for the initial shish formation is still under debate. The proposed mechanisms broadly fall into three groups: (a) shish form directly from extended chains or chain segments produced via an abrupt coil-to-stretch transition [10, 14, 87, 99]; (b) shish nucleate from pre-existing nuclei and then grow by the addition of new chain segments [30, 33-34, 100-102]; and (c) shish form, in discrete steps, by the aggregation of point-like nuclei into oriented threads [98, 103-106]. **Figure 2.9** summarises the essential components of each of these mechanisms schematically. It is worthwhile to point out here that these three mechanisms are not necessarily mutually exclusive and more than one mechanism could lead to the formation of shish under a given set of processing conditions.



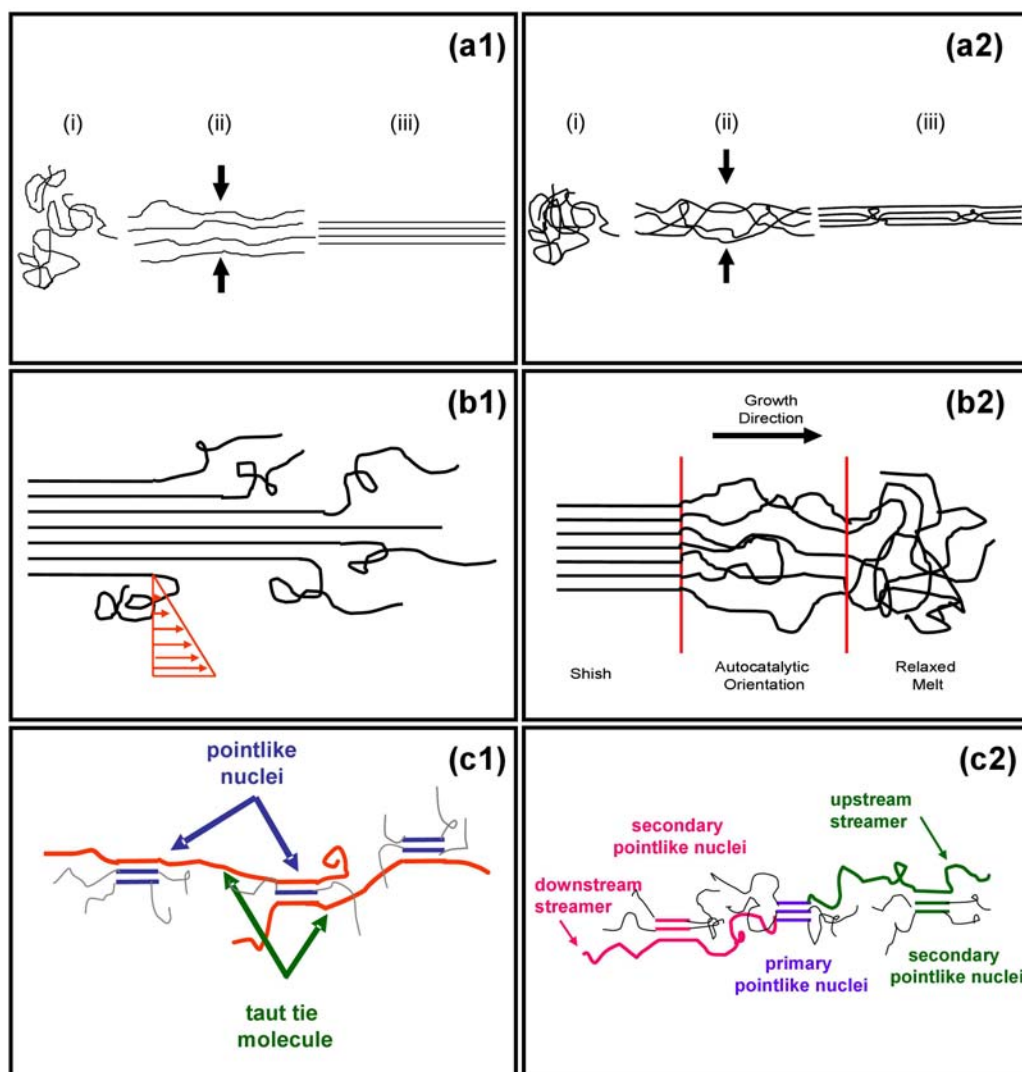


**Figure 2.9.** Schematic diagrams illustrating six possible mechanisms for initial shish formation. **(a)** (i) The originally coiled chains (ii) become extended by the flow via an abrupt coil-to-stretch transition before (iii) undergoing densification into the shish. **(a1)** Structure formation when coil-to-stretch results in the chains adopting fully extended chain conformations and **(a2)** when the chains extend as a cooperative network. **(b)** Shish growth from pre-existing nuclei. **(b1)** Unrolling of polymer coils attached to the nuclei and **(b2)** autocatalytic growth of shish at their free ends. **(c)** Shish formation by the accumulation of point-like nuclei into oriented threads. **(c1)** Oriented threads form when tie molecules connecting adjacent point-like nuclei are pulled taut by the flow and **(c2)** the flow field leads to coiled up free ends of chains attached to primary flow-induced nuclei to unravel up and down stream, promoting secondary nuclei formation. Flow direction is horizontal. See in-text for more detail.

Keller et al. [10] explained shish formation around the abrupt coil-to-stretch proposed by de Gennes, **Figure 2.9a1**. In the model, a given flow field will result in the longest chains becoming extended as if in relative isolation and align along the flow direction. These extended chains then migrate together and undergo densification into the final shish structure. Some time after the shish are formed, nearby chains which remained coiled crystallise on the shish template and form kebabs. The seminal modelling work performed by Dukovski & Muthukumar [87] showed how the shish densification may occur. Once the chains drift close together to form an initial overlap region, the overlap then rapidly propagates along the length of the extended chains. Nevertheless, it was unclear how these chains which are extended in isolation could diffuse the necessary distance in the short time required for shish formation. An alternative densification mechanism was recently put forward by Kimata et al. who performed thorough SANS experimentation on shish formation in sheared iPP [37]. By selectively deuterating different lengthed chains, Kimata et al. found that long chains were not overrepresented in the shish entities. They put forward the hypothesis that only the long chains become extended by the flow. These long chains which have higher average segmental orientation then recruit neighbouring smaller chains to form the shish structure.

Keller et al. [10] also noted that in an entangled melt it may not be the whole chain which becomes fully extended but rather sections of the chain between entanglement points, **Figure 2.9a2**. This idea was further supported by a superb experiment performed by Hsiao et al. on a blend of crystallising ultra-high molecular weight polyethylene (UHMWPE) and non-crystallising PE matrix [99]. Using scanning electron microscopy (SEM) and in-situ SAXS they observed the formation of multiple interconnected shish in sheared UHMWPE. The formation of these multiple shish then strongly pointed to the coil-to-stretch transition occurring in sections of stretched UHMWPE chain which form part of an entangled network.

Pennings et al. [101-102] suggested that shish growth along their longitudinal direction was the main mechanism of shish formation, **Figure 2.9b1**. In this picture flow leads to the initial formation of point-like nuclei from the densification of flow-induced extended chain

segments. Nearby chains adsorb onto the surface of these point-like nuclei and then, due to the difference in relative velocity between the attached and free chain ends, get unravelled and extended by the flow field. These extended chain segments then promote the longitudinal growth of the nuclei through subsequent densification and rearrangement processes. Yamazaki et al. extended this work by showing that a critical shear rate was required to overcome the conformational relaxation of chains at the growth front [34]. In a separate paper, Yamazaki and co-workers also proposed that shish could grow in an analogous way perpendicular to the flow direction [33]. In this model, the lateral growth was achieved by the repeated adsorption of chains onto the lateral surface of the shish followed by their subsequent extension along the flow direction. Therefore in this picture, for both lateral and longitudinal growth to occur, an external flow field was thought to be required.

By studying deformed films of isotactic polystyrene (iPS) using transmission electron microscopy (TEM), Petermann et al. observed that the presence of obstacles altered the growth direction of shish. This suggested the presence of a flow field may not be necessary for shish formation [30]. From these results Petermann et al. hypothesised that shish could also grow by an autocatalytic process, by the self-induced alignment of chain sections at the tip of the growing shish cores in the absence of flow, **Figure 2.9b2**. In this way, shish can grow provided their growth rate is fast enough to counter chain relaxation at the tip of the shish, and that folded chains are not incorporated into the shish. In an elegant experiment, Lieberwirth et al. [100] confirmed the original work of Petermann et al. by selectively deforming a super cooled melt of iPP. Lieberwirth showed that shish nucleated in the deformed region and grow into the undeformed region of the melt. Although this work confirmed that shish could grow without a flow field, the presence of an external flow field would enhance the alignment of chain sections, thereby increasing growth rates.

Hoffman and Clark [105-106] explained shish formation in an entirely different way. They argued that kebabs are nucleated off specific sites along the core of the shish and that these provide information about structural singularities in the backbone of the shish. In their theory the shish are thought to originate with the accumulation of multiple aligned point-like nuclei along the length of a flow elongated molecule. These point-like nuclei can be

thought of as small bundles of roughly parallel chains which show intermediate order between amorphous and crystalline states [107]. The result is a row of aligned point-like nuclei interlinked with taut tie molecules which form the basis of the shish precursors. Janeschitz-Kriegl et al. supported this general mechanism by noting that the slope of a plot of the log of the number of point-like nuclei per cubic metre versus the log of mechanical work yielded a slope of 2 [98]. This implies that the creation of new point-like nuclei during flow can not be independent of the number of nuclei already present. Therefore a longer range interaction between point-like nuclei must exist. They put forward a hypothesis that shish could only form once a critical number of point-like nuclei is reached. Heeley et al. proposed a variation on this mechanism, where the point-like nuclei act as effective cross links under shear flow [104], **Figure 2.9c1**. In this model individual molecules participate in multiple point-like nuclei, which effectively pin them. The pinning provided by the point-like nuclei retards relaxation of extended chains and allows the tie molecules to be pulled taut by the flow. The taut tie molecules then provide the basis of the shish precursor.

An alternative accumulation mechanism was proposed by Seki et al. [103], who suggested that molecules which adsorb onto the surface of point-like nuclei would get rapidly extended up or down stream for the original point-like nuclei by the flow, **Figure 2.9c2**. These “streamers”, although not fully extended, would have increased segmental orientation and therefore would lead to increased point-like nuclei formation up and down stream of the original point-like nuclei. The process would then be rapidly repeated to form the shish precursors.

At a sufficient under cooling, the shish provide nucleation sites for folded chain lamellae which grow laterally away from the shish wall. Early studies revealed two types of kebabs [10]. The first type, termed macrokebabs, could be selectively melted or dissolved in an appropriate solvent. Conversely, the second type which were termed microkebabs, were found to have similar thermal and chemical stability to the shish. The difference was explained by the microkebabs being formed around cilia which were also incorporated into the shish core, while the macrokebabs were thought to have grown on the microkebabs and were therefore not directly attached to the shish. Nevertheless, both types of kebabs may

not be formed in all cases. Zhu and Edward reported that high cooling rates could suppress the transition to macrokebab in injection moulded iPP resulting in shish-kebab composed entirely of microkebabs [108]. In addition, the simulation work of Dukovski and Muthukumar did not reveal any evidence for microkebab formation and macrokebabs were epitaxially nucleated on the shish surface [87].

The epitaxial nucleation of macrokebabs on the shish surface raises the important question as to what is the minimum shish diameter which can induce the shish-kebab structure. Hu et al. performed Monte Carlo simulations to examine the effect of one aligned and extended single chain in a solution of unoriented chains [15]. Hu's simulation demonstrated that it was indeed possible for a single chain to nucleate chain folded lamellae. This shows there may be no lower limit of the shish diameter which can form the shish-kebab structure. Nevertheless, at the time of writing, this surprising result has yet to be confirmed by experiment.

### ***2.3.3 Combined influence of flow and foreign particles on polymer crystallisation***

The presence of foreign particles can dramatically alter the final crystalline morphology of semicrystalline polymers under flow-induced crystallisation conditions. The combined influence of flow and particles has been shown to lead to a synergistic increase in the number of flow-induced nuclei [43, 52, 109-112]. This leads to increased crystallisation rates and therefore finer crystalline morphologies. The presence of particles has also been shown to reduce the flow intensity required to form the shish-kebab morphology [33-34, 49-50, 84, 112-116]. A range of particle characteristics have been suggested to influence this particle assisted flow-induced nuclei formation, including the particles: curvature [49-50], size [84], shape [52] and the affinity of the polymer molecules to the particle [115]. However, a detailed picture for how this may occur is not yet available. In addition, the heterogeneous nucleation effects observed under quiescent conditions can be suppressed or interrupted by even mild flow conditions [42-43]. Accordingly, through their large impact on the final morphology, the addition of particles can have important implications for the final properties of polymer articles processed under flow-induced crystallisation conditions. The first part of this section provides a thorough review of the proposed mechanisms of

how the particles assisted formation of flow-induced nuclei could occur. The final part of this section illustrates some of the possible consequences the additional flow-induced nuclei have for morphology and property development.

A number of mechanisms have been proposed to account for the observed interactions of particles and flow, **Figure 2.10**. One possible influence is that the surface of a particle could stabilise the extended conformation of oriented molecules, retarding their relaxation and thereby assisting the densification of flow-induced nuclei, **Figure 2.10a**. García-Gutiérrez et al. investigated the influence of single walled carbon nanotubes (SWCNT) on the flow-induced crystallisation of poly(butylene terephthalate) (PBT) [51]. García-Gutiérrez found that even under quiescent crystallisation conditions, the addition of a small amount of SWCNT acted as pseudo shish and a template for the formation of oriented crystalline lamellae perpendicular to their surface. However, they found that the fraction of oriented material increased dramatically when shear flow was applied and attributed the behaviour to shish being stabilised on the surface of the SWCNT. In another study, Zhu and co authors investigated the influence of two colorants, which had different surface curvatures, on the morphology distribution of injection moulded iPP [49-50]. Zhu found that the colourant particle with the curved surface did not appreciably influence shish-kebab formation, while the colourant with the flat surface promoted shish-kebab formation, even under mild flow intensities. Zhu proposed that the different surface contact, which would arise with different curvature, played a significant role in shish-kebab formation. In this model, flat surfaces provide many contact points which stabilise extended chain conformation and therefore promote shish formation. On the other hand, the number of contact points for an extended linear molecule would be reduced on a curved surface. This would allow the extended state to relax or be perturbed by the surrounding flow.

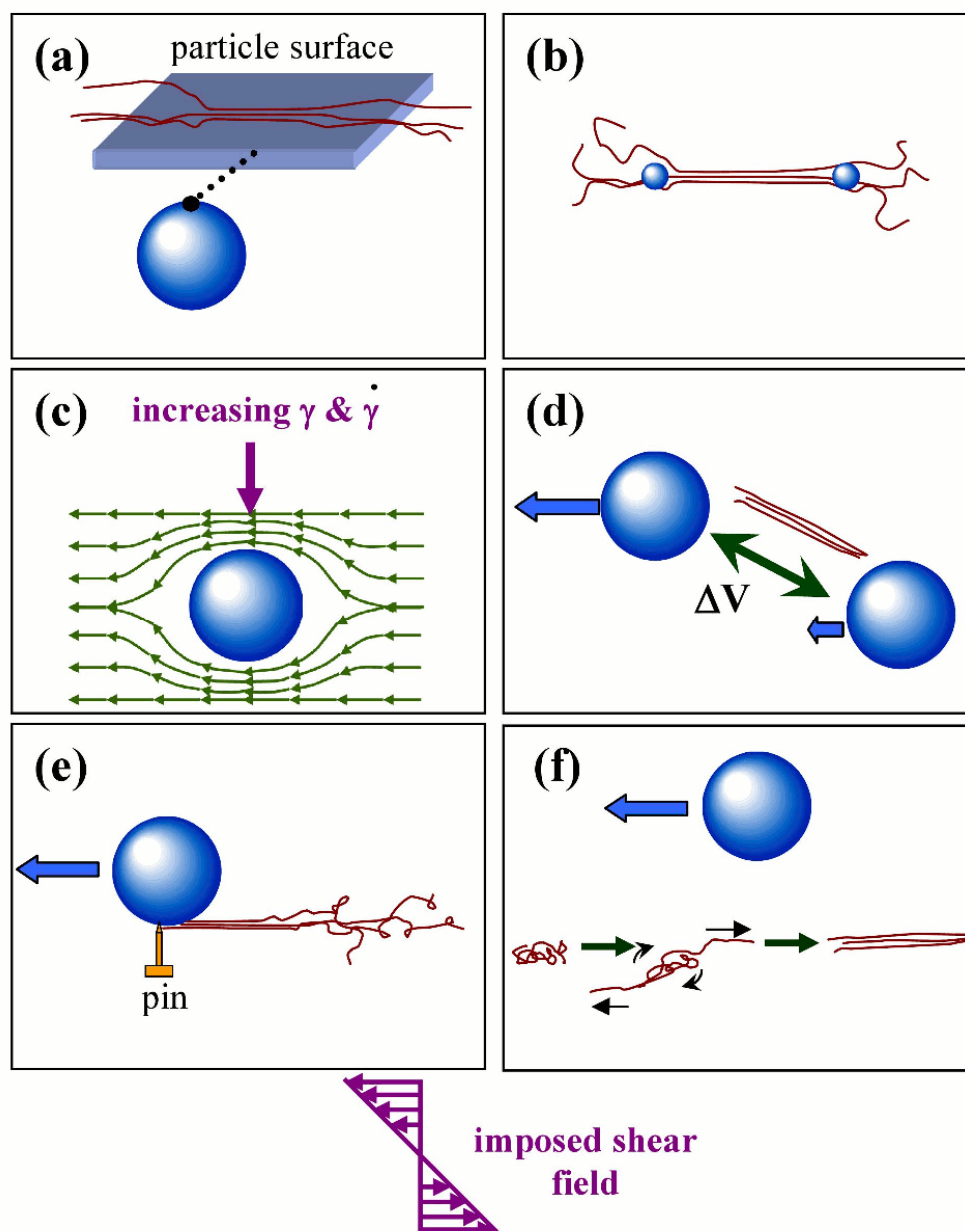


**Figure 2.10.** Schematic representation of six possible mechanisms for particle assisted shish formation. **(a)** Stabilisation of extended conformations on the surface of particles. **(b)** Retarded relaxation of extended conformations by increasing the number of physical cross-links. **(c)** Increased strain and strain rate near the particle caused by flow of matrix around the particle. **(d)** Separation of nearby particles leading to increased elongation flow between the two particles. **(e)** One end of a molecule is adsorbed and pinned on the surface of particle, while the other end is extended by the flow. **(f)** Long range perturbation of a molecules streamline by the motion of a passing particle. Refer in-text for more details.

It has also been suggested that particles which strongly interact with the polymer could act as additional physical cross-links, promoting chain extension during flow and retarding the relaxation of extended chain conformations after flow is ceased. The resultant greater number of chains in extended chain conformations would then accelerate shish formation, **Figure 2.10b**. Fu et al. added nanostructured polyhedral oligomeric silsesquioxane (POSS) to iPP and found its presence promoted shish formation but also resulted in a decrease in the long period [116]. Fu suggested this behaviour was consistent with the POSS acting as physical cross-links which retarded relaxation of extended chains. In another study, Kelarakis et al. added modified carbon nanofibers (MCNFs) to iPP and found that at the very early stages of crystallisation, the amount of oriented crystals increased with increasing concentration of MCNF [117]. Kelarakis attributed this behaviour to MCNFs hindering the motion of chains, which would retard the relaxation of extended chain conformations. Recently, Patil et al. investigated the formation of shish in a linear polyethylene containing two different nano-particles (SWCNT and zirconia), which were found to have substantially different affinities for the polymer molecule [115]. Patil showed that the nano-particles which strongly interacted with the polymer molecule promoted shish formation, while the nano-particle which did not interact with the polymer molecule disrupted shish formation. Patil ascribed this behaviour to the strongly interacting particles anchoring the polymer chains which then significantly increased the number of chains in extended conformations during flow. On the other hand, the weakly interacting nano-particles disrupted the chain extension processes during flow.

Hwang et al. [118] advocated that polymer molecules flow around the particles (i.e. there exists a velocity difference ( $\Delta V$ ) between the particle and matrix), and this flow difference leads to an increase in both the strain and strain rate near the exposed sides of the particle (**Figure 2.10c**). The constriction caused by the polymer molecules having to flow around the particle would also lead to an increase in the elongational component of shear flow. Furthermore, Hwang suggested the elongational component of shear flow would be further increased in the region between two nearby but separating particles (**Figure 2.10d**). Real space imaging of the expected morphology gradient near a particle should be able to confirm such hypotheses.



Jerschow and Janeschitz-Kriegl noted an increase in the size of the oriented surface layer of iPP exposed to duct flow when methyldibenzylidene sorbitol (MDBS) was added [112]. They proposed that the increase orientation was due to polymer molecules being adsorbed onto the surface of the nucleant, effectively pinning one part of a molecule. During subsequent shear flow, the free ends of the molecule are easily stretched due to the differential in the flow field, accelerating the formation of shish (**Figure 2.10e**). Yamazaki and co-authors provided further evidence for this type of mechanism when investigating the formation of shish in sheared iPP and PE melts using polarised optical microscopy [33-34]. They observed thread-like nuclei only formed at artificial sites or ‘pins’, such as dust particles within the melt or on the surface of the shear cell.

Under simple shear flow conditions the rotational rate and extensional rate are equal, and therefore the rotational component is just sufficient to counteract the elongation component of the flow from stretching out the polymer chains. Harlen and Koch proposed that particles can tip this balance in the favour of the extensional component promoting favourable conditions for the coil-to-stretch transition to occur, **Figure 2.10f** [119]. As a particle moves past a polymer molecule, its velocity disturbs the molecule out of its initial streamline due to the slightly different flow histories along the length of the molecule. As the molecule now lies over a broader range of streamlines, the molecule is able to interact more strongly with the flow field and become stretched along the flow direction.

An interesting consequence of the formation of additional flow-induced nuclei in the presence of particles has recently been revealed by Huo et al. [43]. Huo investigated the flow-induced crystallisation of iPP containing an intentional  $\beta$ -iPP nucleating agents. As discussed later in this chapter, shear flow is known to induce the formation of  $\beta$ -iPP. Huo found that the application of shear flow indeed led to the formation of  $\beta$ -iPP in pure iPP and iPP containing small concentrations of the  $\beta$ -iPP nucleant ( $< 0.1\text{wt}\%$ ). However, at higher loading levels shear flow was found to suppress  $\beta$ -iPP formation. They rationalised that this amazing result was due to the combined shear flow and particles altering the concentration of oriented  $\alpha$ -iPP nuclei, which are thought to initiate a  $\alpha$ -iPP to  $\beta$ -iPP growth transition. At low shear rates, the presence of the nucleant particles promoted the

formation of oriented  $\alpha$ -iPP nuclei, while at higher shear rates the nucleant particles suppressed oriented  $\alpha$ -iPP nuclei. However, such a model has yet to be experimentally confirmed.

Chen et al. observed a similar phenomenon under oscillatory shear conditions and proposed an alternative explanation for the suppression of  $\beta$ -iPP at the higher shear rates [42]. The more intense flow fields in the nucleated samples would lead to a mechanical strain-induced transition from the metastable  $\beta$ -iPP to the more stable  $\alpha$ -iPP. The results presented therefore have important implications for the processing of polymers containing a wide variety of additives, the inclusion of which can dramatically alter the morphology and thus properties of the polymer component.

## 2.4.0 Hierarchical structure and properties of iPP

Natta and Corfidini showed that the usual crystal form of iPP has each polymer molecule arranged as a  $3_1$  helix [120]. The helix is chiral and can exist in either the right or left hand configuration. This chirality allows for three different crystalline phases:  $\alpha$ -iPP (monoclinic),  $\beta$ -iPP (trigonal),  $\gamma$ -iPP (orthorhombic) as well as the mesomorphic smectic-iPP, **Figure 2.11**. In this section the hierarchical structure and the physical and mechanical properties of each iPP phase are reviewed.

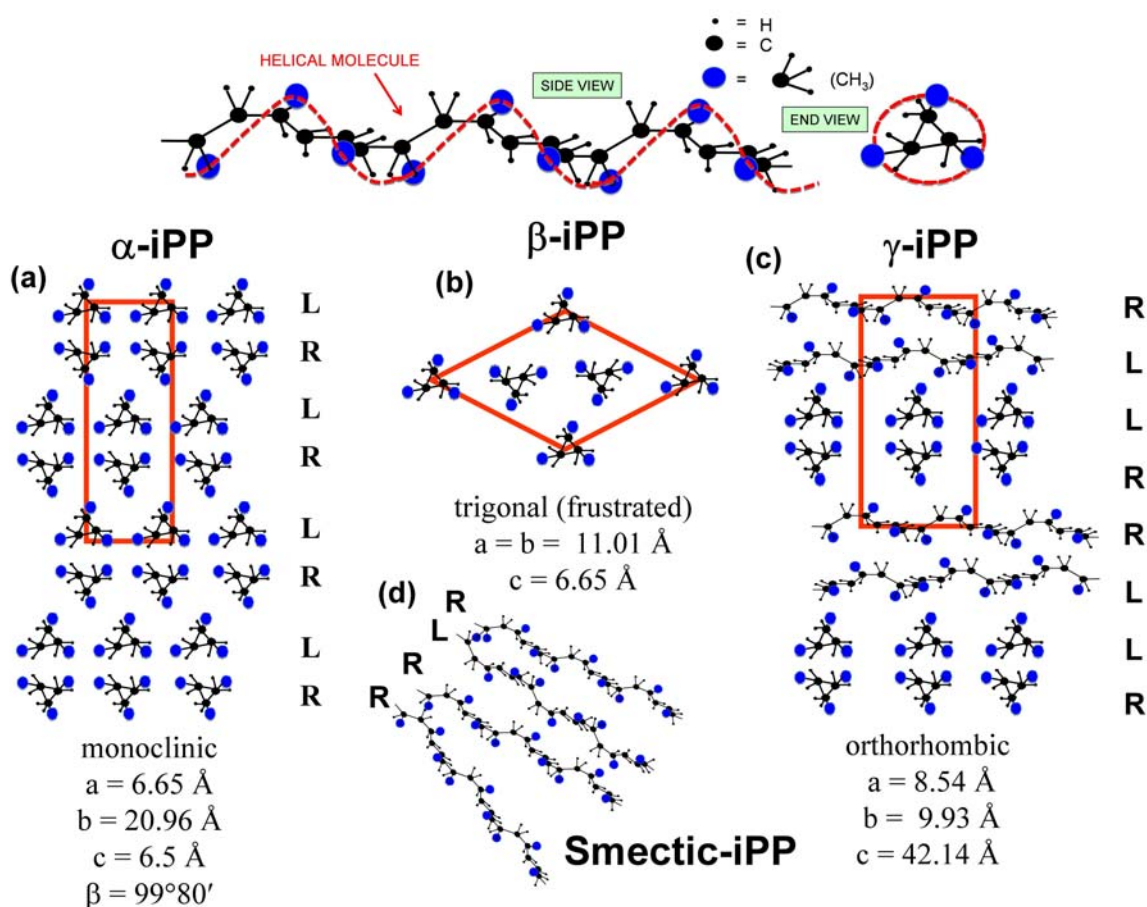


**Figure 2.11.** The crystal structures of iPP. (a) monoclinic  $\alpha$ -iPP consisting of alternating antichiral layers, (b) trigonal isochiral  $\beta$ -iPP with frustrated packing, (c) orthorhombic  $\gamma$ -iPP structure proposed by Bruckner and Meille [121] and (d) a schematic illustration of the mesomorphic- or smectic-iPP.

### 2.4.1 Hierarchical structure of $\alpha$ -iPP

The  $\alpha$  crystalline phase is by far the most common phase of iPP. Its structure was first determined by Natta and Corfidini in 1960 [120] to be monoclinic with cell parameters  $a = 6.65 \text{ \AA}$ ,  $b = 20.96 \text{ \AA}$ ,  $c = 6.5 \text{ \AA}$  and  $\beta = 99^\circ 80'$ . The crystal structure is made up of alternating sheets of left and right handed helices, where neighbouring sheets are arranged in such a way that the tip of each sheet inter-penetrates. Interestingly, it appears that this regular arrangement of stems can sometimes get mixed up and two adjacent sheets with the same chirality are possible. This leads to a dramatic reorientation of the chain axis from the substrate layer (parent) by the  $\beta$  angle of  $\alpha$ -iPP monoclinic unit cell ( $99^\circ 80'$ ) forming a branch [122]. A daughter lamella may then form from this initial nucleus.

The orientation relation between parent and daughter lamellae was first determined by Keith and Padden [123], who showed that the  $a_2$ -axis and  $c_2$ -axis of the daughter lamellae ( $L_D$ ) are aligned along the  $c_1$ -axis and the  $a_1$ -axis of the parent lamellae ( $L_P$ ) respectively, **Figure 2.12**. This is termed a parent-daughter relationship (PD). In this thesis the  $a$ ,  $b$  and  $c$  axes of the parent lamellae are identified by the subscript 1 ( $a_1$ ,  $b_1$ ,  $c_1$ ), and the axes of the daughter lamellae by the subscript 2 ( $a_2$ ,  $b_2$ ,  $c_2$ ). PD lamellar branching has been observed over a wide range of crystallisation conditions: melt [37, 124-128], solution [129], thin films [130-132] and the sheared region of injection mouldings [6, 113-114, 133].

PD lamellar branching has been found not to occur at high [134] ( $>160^\circ \text{C}$ ) or low crystallisation temperatures [135] ( $< 90^\circ \text{C}$ ). Lotz proposed that this alteration in the lamellar branching frequency could be explained by the alterations of the morphological features of the epitaxial site with temperature [136]. Lotz reasoned that a flat surface, of at least the size of the forming embryo, must be available for the molecular stems to be deposited at right angles to the normal chain-axis direction of the substrates  $\alpha(010)$  face. Therefore surfaces which are rough or crenelated are unlikely to be suitable sites for the epitaxial nucleation of daughter lamellae. Lotz hypothesised that at higher temperatures the crenellation occurs due to the lenticular shape of the growing  $\alpha$ -iPP lamellae, while at low temperatures the crenellation is induced by a high rate of secondary nucleation.

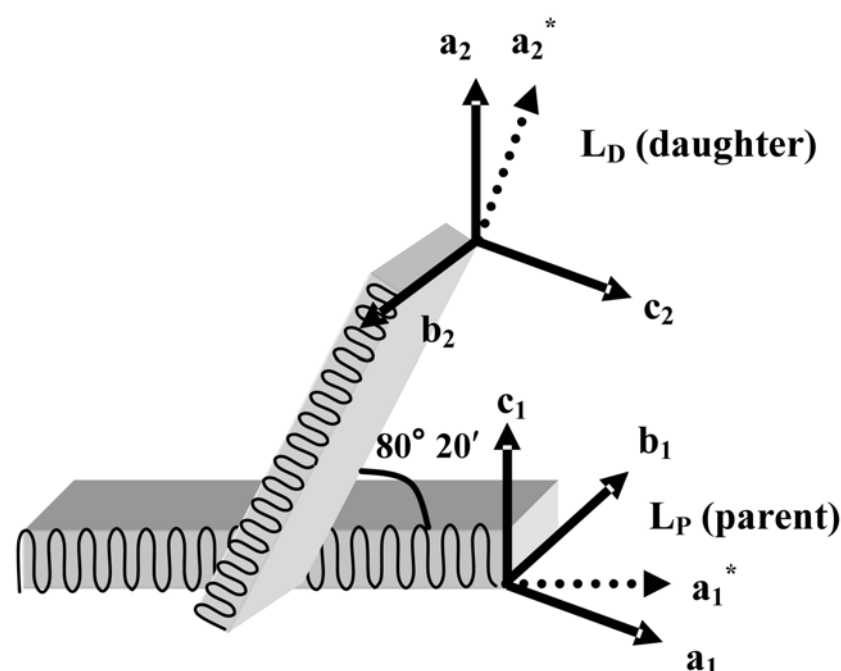


**Figure 2.12.** Generalised model for the oriented parent-daughter structure found in sheared isotactic polypropylene.

The change in the frequency of PD lamellar branching with temperature has been shown to lead to a change in the morphology of the iPP spherulites when crystallisation takes place at different isothermal crystallisation temperatures. Keith and Padden showed that spherulites grown below 134 °C generally exhibited a slightly positive birefringence (i.e.  $n_{\text{radial}} > n_{\text{tangential}}$ ), while spherulites grown above 138 °C have a negative birefringence (i.e.  $n_{\text{tangential}} > n_{\text{radial}}$ ) [137]. Furthermore, spherulites grown in the range 134 °C – 138 °C displayed what was termed a mixed birefringence, where radial sections have either positive or negative birefringence. A recent review by Yang suggests this transition is due to a change in the spherulite structure, **Figure 2.13** [138]. At low temperatures the PD lamellar structure dominates the spherulite. In this structure, the daughter lamellae are always tangential to the radial parent lamellae and therefore the spherulites contain roughly equal contributions from both radial and tangentially oriented chains. Conversely at high temperatures, the spherulites are composed almost entirely of radial lamellae, and therefore have a greater proportion of tangentially oriented chains. Intermediate temperatures lead to core-shell structures where the PD lamellar structure formed in the core gradually gives

way to being dominated by radial lamellae with increasing distance from the core. Nevertheless, the reason why such a transition occurs is not well understood.

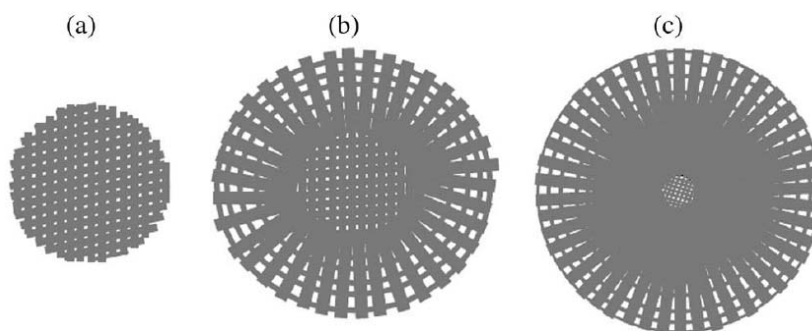


**Figure 4** Three different spherulite structures. (a) cross-hatched, (b) cross-hatched lamellae surrounded by radial lamellae, (c) radial lamellae with small cross-hatched core.

**Figure 2.13.** Influence of crystallisation temperature on the structure of  $\alpha$ -iPP spherulites. From Yang [138].

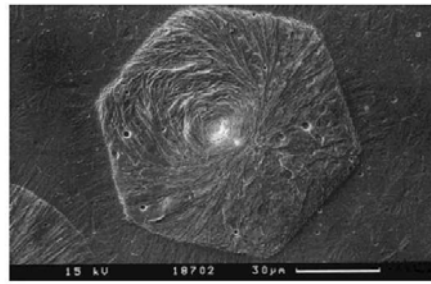
#### 2.4.2 Hierarchical structure of $\beta$ -iPP

The  $\beta$  phase of iPP was first identified in 1959 by Padden and Keith [137]. Originally  $\beta$ -iPP was thought to have a hexagonal structure with parameter  $a = b = 19 \text{ \AA}$  and  $c = 6.5 \text{ \AA}$  [139], however this large cell was thought to contain nine chains and it was unclear how such a large number of chains would be arranged in the unit cell.  $\beta$ -iPP was later determined to possess a frustrated structure with a trigonal unit cell containing three isochiral helices and parameters  $a = b = 11.01 \text{ \AA}$  and  $c = 6.5 \text{ \AA}$  [140-141]. Numerous methods have been developed to produce significant quantities of  $\beta$  phase such as: crystallisation in a temperature gradient [142] and flow-induced crystallisation [143-147], particularly in oscillation mode [42, 148-149]. Nevertheless, by far the most effective method of inducing high contents of  $\beta$ -iPP is by the addition of specific  $\beta$  nucleating agents [42-46, 48, 150]. The selectivity of these agents has been shown to be related to an epitaxial relationship between the substrate and the  $\beta$ -iPP unit cell [76-78].

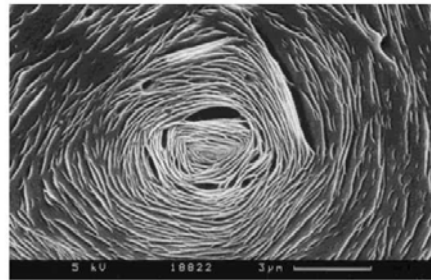
The hierarchical structure of  $\beta$ -iPP has been comprehensively reviewed by Varga [151]. Compared to  $\alpha$ -iPP spherulites,  $\beta$ -iPP spherulites generally have strongly negatively

birefringence. When crystallised below 120 °C, radial type spherulites are formed in which the lamellae do not twist as they grow away from the core. Conversely at temperatures up to 135 °C, banded type spherulites are favoured, where regular twisting of lamellae leads to successive light and dark regions. Nucleated samples often contain immature spherulites (also known as quasi-spherulites), which are in the transition between hedritic and spherulitic structure. Hedritic structures have been defined as regular polygonal formation when viewed from at least one direction, and in the case of polymers consist of clusters of chain folded lamellar crystallites [44]. In  $\beta$ -iPP the hedrites take the form of hexagonal clusters of lamellae when viewed flat-on (hexagonites), **Figure 2.14**. Due to the formation of branches at screw dislocations, flow cup arrangements are often found in the centre of the hexagonites. When the same hexagonite is viewed in the lateral direction, the lamellae appear as long rods which then transform into oval shaped (ovalite) structures (**Figure 2.15**) due to the splaying of their initial parallel arrangement.

Many studies have reported growth transitions from  $\beta$ -iPP to  $\alpha$ -iPP ( $\beta\alpha$  bifurcation). Although  $\beta$ -iPP is a metastable phase, it has been found to grow 20-70% faster than the thermodynamically stable  $\alpha$ -iPP under certain conditions [142]. A cross over point has been found at both low and higher temperature where the growth rate of  $\alpha$ -iPP exceeds that of  $\beta$ -iPP and thus there exists a 'temperature window' where  $\beta$ -iPP can be formed in significant quantities. In isothermal crystallisation experiments in which they performed temperature jumps, Varga and co-workers showed that the higher temperature growth transition occurred at  $\approx 141$  °C [134]. The low temperature growth kinetics are much harder to probe due to the extremely high growth rates. Nevertheless, the existence of a low temperature  $\beta$ -iPP to  $\alpha$ -iPP growth transition, which indicates a transition to higher  $\alpha$ -iPP growth rates, was shown by Lotz et al. during stepwise crystallisation experiments to be  $\approx 105$  °C [135]. In addition, growth transitions from  $\alpha$ -iPP to  $\beta$ -iPP ( $\alpha\beta$  bifurcation) have also been observed. These  $\alpha$ -iPP to  $\beta$ -iPP growth transitions have only been found to occur under certain conditions such as crystallisation in a temperature gradient [142] or under flow-induced crystallisation conditions [143-147].



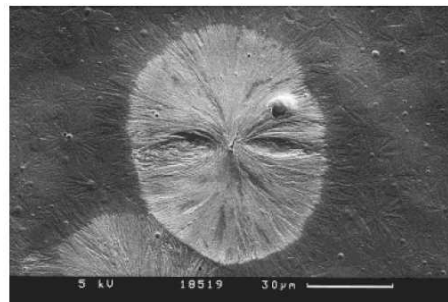
(a)



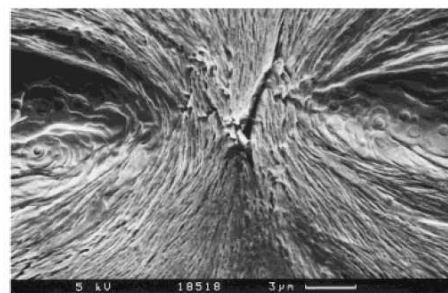
(b)

**Figure 13** SEM micrographs taken of (a)  $\beta$ -hexagonite and (b) its magnified center;  $T_c = 141^\circ\text{C}$ ; 0.1 wt % Ca-Pim.

**Figure 2.14.**  $\beta$ -iPP hexagonite viewed face-on. Taken from Varga et al. [44].



(a)



(b)

**Figure 14** SEM micrographs on an ovalite developed from (a) a needle crystal (hexagonite standing on edge) and (b) a structural detail;  $T_c = 141^\circ\text{C}$ ; 0.1 wt % Ca-Pim.

**Figure 2.15.**  $\beta$ -iPP hexagonite viewed in the lateral direction. Taken from Varga et al. [44].



The molecular mechanisms responsible for these unique growth transitions are not yet fully known. Lotz and co-workers initiated the  $\beta$ -iPP to  $\alpha$ -iPP growth transition on  $\beta$ -iPP single crystals using a temperature jump [152]. This resulted in the formation of numerous  $\alpha$ -iPP single phase crystals which had a specific orientation relationship to the original  $\beta$ -iPP crystal, **Figure 2.16**. Lotz showed that the  $\alpha$ -iPP crystals were oriented such that their  $ac$   $\alpha(010)$  faces were parallel to the  $\beta(110)$  of the  $\beta$ -iPP single crystals. This reveals that the transition site was between the densely packed  $\alpha(040)$  and  $\beta(110)$  planes, which are both composed of isochiral helices and which have an inter-helix distance of 6.5 Å and 6.35 Å, respectively. Therefore only small perturbations are needed to swap between either phase. Although the possibility of the same relationship being involved in the reverse transition can not be ruled out, due to experimental difficulties its existence has yet to be verified. An alternative mechanism for the  $\alpha$ -iPP to  $\beta$ -iPP transition was put forward by Li et al. who suggested that smectic bundles would be favourable sites for  $\beta$ -iPP nuclei [153]. Li argued that the random ordering of helices in these bundles would make the formation of  $\alpha$ -iPP nuclei which have a strict left-right handed helical packing unfavourable compared to isochiral  $\beta$ -iPP nuclei.

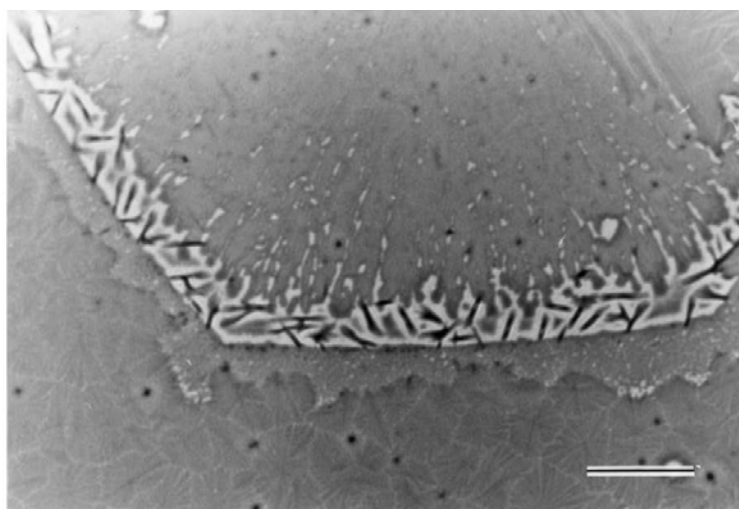


**Figure 5** Phase contrast optical micrograph of a hexagonal single crystal of  $\beta$ iPP crystallized at 125°C for 10 min, and at 145°C for 60 min.  $\alpha$  phase crystals have developed at the edge, but inside the  $\beta$  phase crystal contour, in the form of elongated laths, extended in the  $a^*$  axis of the unit-cell. Note the characteristic orientation of these laths either parallel, or at 60° to the  $\{110\}$  edges of the hexagonal  $\beta$ iPP single crystal. Scale bar: 20  $\mu$ m

**Figure 2.16.** Phase contrast optical micrograph showing epitaxial growth of  $\alpha$ -iPP on  $\beta$ -iPP. Taken from Lotz [152].

### 2.4.3 Hierarchical structure of $\gamma$ -iPP

The rarer  $\gamma$ -iPP was first identified by Addink and Beintema in 1961 [154].  $\gamma$ -iPP has an orthorhombic unit cell with parameters  $a = 8.54 \text{ \AA}$ ,  $b = 9.93 \text{ \AA}$  and  $c = 42.41 \text{ \AA}$ . Packing is comprised of systematic isochiral bilayers, which are tilted  $80^\circ$  or  $100^\circ$  from one another [121, 155]. This structure leads to two unique properties: (a) it is the only polymer crystal structure to have non-parallel chains and (b) it allows for the epitaxial nucleation of  $\gamma$ -iPP on  $\alpha$ -iPP and vice versa. Nucleation of  $\gamma$ -iPP is thought to occur when the isotactic sequence length becomes very short [156-157].  $\gamma$ -iPP can accordingly be promoted by methods which increase the number or uniformity of defects, or amplify their effect such as: crystallisation under high pressures [158-160], polymerisation processes which produce high stereo-defects and/or regio-defects [161-163], co-polymerisation with other olefins [164-165], addition of powerful nucleating agents [166-168], and under flow-induced crystallisation conditions [165, 169].

The few studies which have reported the hierarchical structure of  $\gamma$ -iPP spherulites suggest they are composed of bundle-like or feather-like entities, which like  $\alpha$ -iPP spherulites, possess a positive birefringence [159, 168]. As with  $\alpha$ -iPP spherulites this optical characteristic suggests that the bundle-like entities are made up of radiating primary lamellae, from which epitaxial growth of daughter  $\gamma$ -iPP has occurred. The primary lamellae are typically  $\alpha$ -iPP, however Mezghani and Phillips have also reported the self-epitaxy of  $\gamma$ -iPP [159]. Epitaxial nucleation of  $\alpha$ -iPP on  $\gamma$ -iPP (i.e.  $\gamma$ -iPP lamellar branching) has been shown by Lotz [9] and De Rosa [161] to occur on the ac surface of the mother  $\alpha$ -iPP lamellae, **Figure 2.17**.

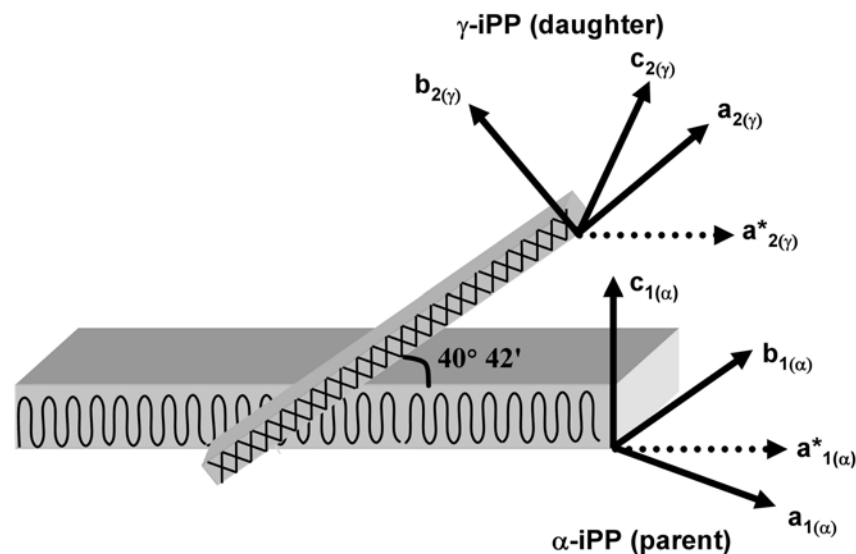


**Figure 2.17.** Generalised model for the orientation relationship between  $\alpha$ -iPP and  $\gamma$ -iPP lamellae.

#### 2.4.4 Structure of smectic-iPP

Along with the more well known crystalline phases, Natta and Cordini reported the formation of mesomorphic- or smectic-iPP [120]. Although the exact nature and structure of the phase is not well known, it is generally thought that the phase is composed of small clusters of roughly parallel helices with a random assembly of helical hands [170-171]. Due to smectic-iPP possessing an intermediate degree of ordering between crystalline and amorphous phases, it is often invoked as an intermediary in iPP crystallisation schemes. Smectic-iPP is usually found under rapid quenching conditions when cooled below 80 °C [120, 170-171]. Recently, smectic-iPP has been reported to also form in iPP nano-droplets approaching the usual lamellar thickness of iPP [172-173]. In this case, smectic-iPP is thought to be promoted by the external geometrical confinement compressing the spacing between chains which results in a loss of the positional registry along the chain-axis.

#### 2.4.5 Physical and mechanical properties of iPP

**Table 2.2** summarises some of the characteristic physical properties of the three crystalline forms of iPP. Compared to  $\alpha$ -iPP,  $\beta$ -iPP generally has a lower observed melting point ( $T_m$ ) and equilibrium melting temperature ( $T_m^0$ ), crystal density ( $\rho_c$ ), enthalpy of fusion ( $\Delta H_f$ ) and lamellar surface energy ( $\sigma_e$ ). Whereas compared to  $\alpha$ -iPP,  $\gamma$ -iPP has generally comparable  $T_m^0$ ,  $\rho_c$  and  $\sigma_e$  but substantially lower  $\Delta H_f$ . A wide range of values have been reported for the thermodynamic properties of iPP polymorphs. Some of the variation in the measured values can be explained by differences between the polymers examined, such as molecular weight [174]. However, a much larger influence are the differences in the experimental method used. For example, compared to using a non-linear Hoffman-Weeks approach, using a linear Hoffman-Weeks approach can underestimate determination of  $T_m^0$  for both  $\alpha$ -iPP [175] and  $\beta$ -iPP [176].

All three iPP polymorphs show tensile stress-strain behaviour characteristics of most semicrystalline polymers, exhibiting three regions: elastic deformation at low strain up to the yield point, formation of neck at intermediate strain, and propagation of the neck to break at high strain. A summary of the typical mechanical properties of the three crystalline forms of iPP is provided in **Table 2.3**. The only major difference between deformation of  $\beta$ -iPP and  $\alpha$ -iPP is the propagation of the neck, where  $\alpha$ -iPP has relatively constant neck stress, while the stress during necking for  $\beta$ -iPP slightly increases as the neck propagates [151]. This has been found to lead to a much more diffuse neck in  $\beta$ -iPP, **Figure 2.18**.

The modulus and yield stress of  $\beta$ -iPP are slightly lower than  $\alpha$ -iPP [151]. This is intriguing as  $\beta$ -iPP has been shown to have a higher crystallinity [44], which is generally thought to improve both yield stress and modulus, than  $\alpha$ -iPP. Phillips et al. suggested the higher resistance to deformation of  $\alpha$ -iPP could be, at least in part, due its tight interlocking cross-hatched parent-daughter morphology [177].

**Table 2.2.** Summary of the main physical properties of the three crystalline forms of iPP

Property	Unit	M <sub>w</sub> (10 <sup>3</sup> g/mol)	α-iPP	β-iPP	γ-iPP	Method	Reference
Equilibrium melting temperature (T <sub>m</sub> <sup>0</sup> )	°C	64	186.1			Gibbs-Thomson plot	[178]
		257	186.1		187.2	Non-linear Hoffman-Weeks	[158]
		200		192		Linear Hoffman-Weeks	[179]
		-		184		-	[27]
		-		177.3		Linear Hoffman-Weeks	[176]
		-		209.2		Non-linear Hoffman-Weeks	[176]
		367	205			Linear Hoffman-Weeks	[85]
		-	186			Linear Hoffman-Weeks	[180]
		260	185			Non-linear Hoffman-Weeks	[175]
		257			194	Linear Hoffman-Weeks	[160]
		23	183.7			Gibbs-Thomson plot	[174]
		263	187.7			Gibbs-Thomson plot	[174]
Observed melting temperature (T <sub>m</sub> )	°C	-	~ 165	~155		-	[27]
		257			~160	-	[158]
Enthalpy of fusion (ΔH <sub>f</sub> )	J/g	257	209.0		144.8	Clapeyron equation	[158]
		257			150	DSC-WAXS	[158]
		-	177.0	168.5		DSC-WAXS	[181]
		200	221(16)	192(8)		DSC	[179]
		-		113(11)		-	[27]
Lamellar surface energy (σ <sub>e</sub> )	mJ/m <sup>-2</sup>	257	52.2		51.7	Clapeyron equation	[158]
		257			53.6	DSC-WAXS	[158]
		257			55.2	Dilatometry-WAXS	[160]
		-	67.6	55.2		DSC-Optical	[182]
Crystal density (ρ <sub>c</sub> )	g/cm <sup>3</sup>	257	0.936		0.933	-	[158]
		-	0.936	0.921		-	[27]
Amorphous density (ρ <sub>a</sub> )	g/cm <sup>3</sup>	-	0.858	0.858	0.858	-	[27]

**Table 2.3.** Summary of the mechanical properties of the three crystalline forms of iPP.

Property	Unit	$\alpha$ -iPP	$\beta$ -iPP	$\gamma$ -iPP	Method	Reference
Modulus (E)	GPa	2	1.8		Tensile	[151]
		0.91		0.82	Tensile	[183]
		1.3	1.13		Compression	[184]
				2.25	Compression	[185]
				1.88	Flexure	[186]
Yield Stress (YS)	MPa	36.5	29.5		Tensile	[151]
		50	36		Compression	[184]
				86	Compression	[185]
				38.9	Flexure	[186]
		19.8		21.4	Tensile	[183]
Ultimate Stress (UTS)	MPa	39.5	44		Tensile	[151]
		430	280		Compression	[184]
				214	Compression	[185]
Elongation at break (TE)	%	420	480		Tensile	[151]
		51		238	Tensile	[183]
Fracture toughness ( $K_{IC}$ )	MPa m <sup>1/2</sup>	2.2	2.6		Charpy v-notch	[187]
Fracture toughness ( $G_c$ )	kJ/m <sup>2</sup>	6.2	9.3		Charpy v-notch	[187]
		2.4	4.9		Izod v-notch	[188]
		7.8		10.6	Izod v-notch	[189]

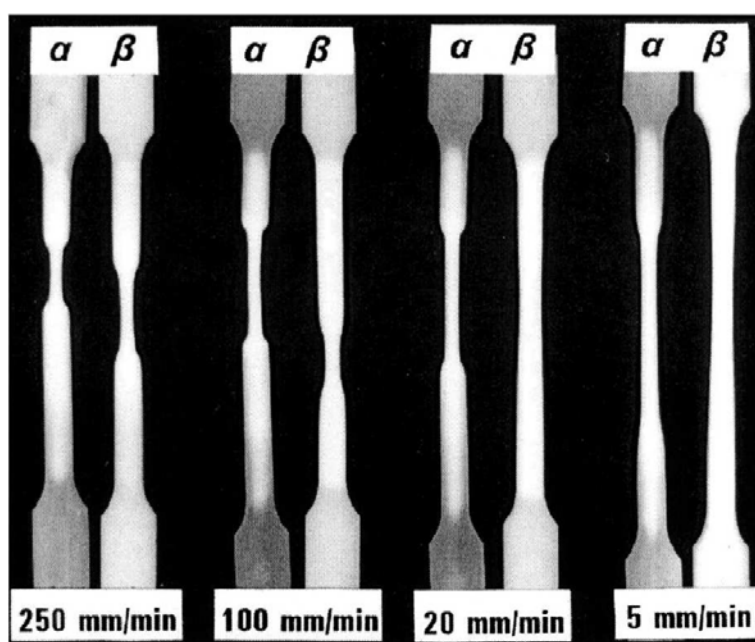


**Figure 21.** Character of necking of  $\alpha$ - and  $\beta$ -nucleated iPP at different deformation rate.

**Figure 2.18.** Difference in necking behaviour of  $\alpha$ -iPP and  $\beta$ -iPP. Taken from Varga [151].

When tested at ambient temperatures,  $\beta$ -iPP has been shown to have a higher tensile strength and total elongation compared to  $\alpha$ -iPP. Deformation of  $\beta$ -iPP has been shown

to lead to a strain-induced  $\beta$ -iPP to  $\alpha$ -iPP phase transformation [184, 190-191]. Therefore one possible reason for the higher strength and ductility is that a strain-induced  $\beta$ - $\alpha$  transformation leads to the formation of a stronger  $\alpha$ -iPP phase in the case of the former, and increased strain due to transformation plasticity in the latter. Another possible reason is the increased number of tie molecules between lamellae in  $\beta$ -iPP morphologies changing the crazing behaviour. This mechanism will be discussed in greater detail in conjunction with the higher observed toughness of  $\beta$ -iPP.

Although  $\beta$ -iPP has a lower melting temperature, the heat distortion temperature of  $\beta$ -iPP is higher than  $\alpha$ -iPP. Varga has explained the higher heat distortion temperature of  $\beta$ -iPP due to the formation of a more stable  $\alpha$ -iPP phase created by a  $\beta$ - $\alpha$  recrystallisation process that takes place at elevated temperatures [151]. The tight interlocking parent-daughter morphology found in  $\alpha$ -iPP spherulites has also been suggested to yield higher chemical resistance compared to  $\beta$ -iPP spherulites [192].

Due to difficulties in preparing large homogeneous samples with high  $\gamma$ -iPP contents, relatively few studies have been performed to date on the tensile properties of  $\gamma$ -iPP. Using a novel high pressure mould design, Mezghani et al. successfully prepared several specimens of pure  $\gamma$ -iPP for further morphological and tensile analysis [183]. **Figure 2.19** shows typical stress-strain curves of  $\gamma$ -iPP formed at higher pressure compared to the  $\alpha$ -iPP formed under the same conditions but at lower pressure. Compare to  $\alpha$ -iPP,  $\gamma$ -iPP was found to have a slightly lower modulus but somewhat higher yield stress compared to  $\alpha$ -iPP. However, compared to  $\alpha$ -iPP,  $\gamma$ -iPP was found to have a five fold increase in ductility. Mezghani speculated that the increased ductility could be explained by the different crazing tendencies of the two phases. In particular it was speculated that a significantly greater number of tie molecules exist in  $\gamma$ -iPP between adjacent lamellae and these tie molecules stabilise micro-crazes during the latter stages of deformation.

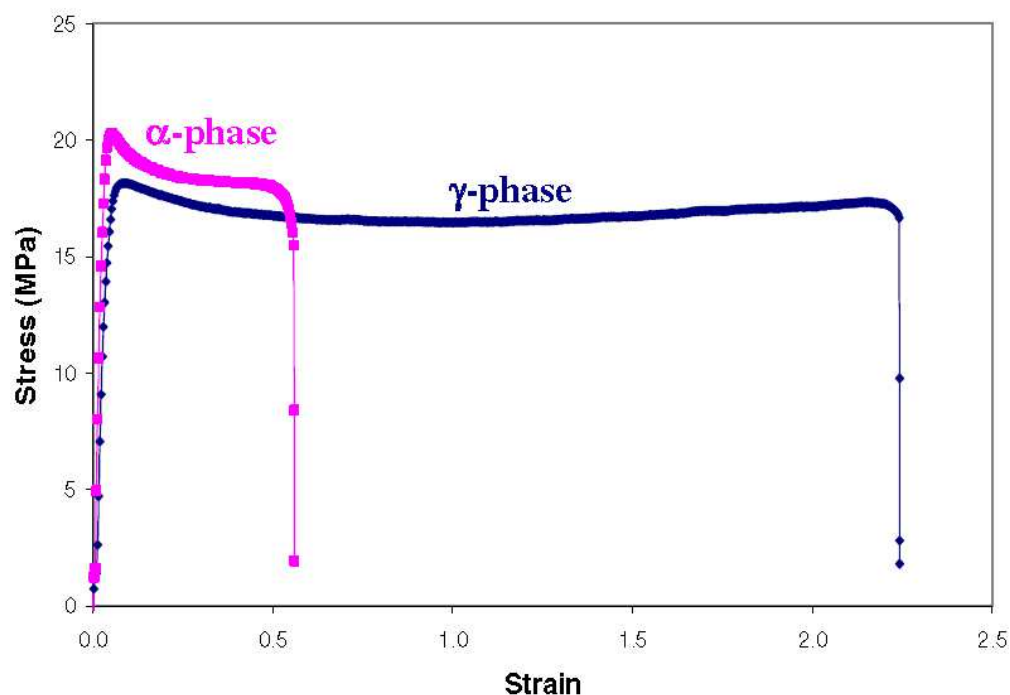


**Figure 4.5:** Typical stress-strain curves of the  $\alpha$ - and  $\gamma$ -phases.

**Figure 2.19.** Typical stress-strain curves of  $\alpha$ -iPP and  $\gamma$ -iPP. From Mezghani et al. [183].

Compared to other commodity semicrystalline polymers such as PE and PET, the fracture toughness, in particular the low temperature toughness, of  $\alpha$ -iPP is relatively low. This low toughness seriously limits the range of applications iPP can be used in. The toughness of  $\beta$ -iPP has generally been found to be superior to that of  $\alpha$ -iPP [151, 187-189]. A range of hypotheses have been put forward to explain the improved toughness of the  $\beta$ -iPP phase. The often cited reason for the improved toughness of  $\beta$ -iPP is the energy dissipated during deformation by the strain-induced  $\beta$ -iPP to  $\alpha$ -iPP or the  $\beta$ -iPP to smectic-iPP transformations [184, 193-194]. Jacoby et al. proposed this was due to the coupling between the crystallites and the amorphous phase being lower in  $\beta$ -iPP compared to  $\alpha$ -iPP [195]. Karger-Kocsis et al. provided further support of this hypothesis by showing  $\beta$ -iPP had superior mechanical dampening behaviour under impact loading [196]. More recently, it has been suggested that the superior toughness of the  $\beta$ -iPP phase is related to its peculiar morphology, in particular the arrangement of tie molecules between adjacent lamella. By altering the final molten temperature ( $T_f$ ) before crystallisation, Luo et al. systematically varied the supramolecular structure of the produced  $\beta$ -iPP spherulite, and hence the connectivity between crystallites, without



appreciably changing the total and  $\beta$ -iPP crystallinity [188]. The different  $\beta$ -iPP morphologies produced ( $\beta$ -spherulites,  $\beta$ -transcrystalline entities and flower agglomerates of  $\beta$ -iPP crystallites), which progressively had higher concentrations of tie molecules, were shown to have yield improvements in toughness. This strongly suggests that the toughness of iPP is controlled by the connectivity between crystallites.

$\gamma$ -iPP has also been found to exhibit enhanced toughness compared to  $\alpha$ -iPP. Na et al. investigated the fracture toughness of an iPP copolymer (3.7% ethylene content) subjected to two different cooling rates from the quiescent melt [189]. A cooling rate of 1 °C/min produced plaques rich in  $\gamma$ -iPP, while samples quenched in air produced samples rich in  $\alpha$ -iPP. Na showed that the enhanced fracture toughness of  $\gamma$ -iPP was due to a combination of enhanced craze density ahead of the crack tip as well as suppressed void formation. Similar to the explanation put forward by Luo et al. for  $\beta$ -iPP [188], Na suggested that the superior toughness of  $\gamma$ -iPP was due the higher number of tie chains connecting neighbouring lamellae.

## 2.5.0 Conclusions

Polymer processing technologies such as injection moulding and extrusion invariably leads to flow fields which are now well known to elongate and orientate polymer chains in the entangled melt. The conformation of the chains determines the subsequent morphological development during crystallisation and therefore the physical, optical and mechanical properties of the final polymer article. At the heart of these changes is the formation of long thread-like entities (shish) which template the formation of oriented crystalline chain folded lamellae (kebabs). Accordingly, the formation and subsequent stability of shish during and after flow is the key to understanding morphology development under conditions representative of industrial processes. Although the formation of the shish-kebab structure has been widely investigated over the last half century, the shish formation mechanism is still under intense debate.

Polymer products invariably have a range of additives included in their formulations for a variety of commercial and consumer reasons. These additives, often added in particulate form, further complicate the development of morphology. The addition of these particulate additives have been shown to lead to a synergistic increase in the number of flow-induced nuclei that are formed by flow. Furthermore, the presence of particles has also been shown to reduce the flow intensity required to form the shish-kebab morphology. A range of particle characteristics, such as particle curvature, size, shape and affinity for the polymer molecule, have been suggested to influence the formation of shish. Nevertheless, the mechanisms which govern how particles influence the initial shish formation, the stability of shish and the subsequent growth of kebabs are currently not well understood.

Isotactic polypropylene (iPP) was identified as an ideal candidate material to study due to its relatively simple structure, convenient range of crystallisation kinetics, and general applicability to industrial processes. Isotactic polypropylene is also an interesting model material to study due to its ability to form a range of different crystalline and mesomorphic forms depending on the specific formulation (chain architecture and additive profile) and processing conditions (temperature, pressure and mechanical work). In particular, the rare  $\beta$ -iPP (tetragonal) and  $\gamma$ -iPP (orthorhombic)

forms of iPP show promise for improved mechanical properties over the more common  $\alpha$ -iPP (monoclinic).

Flow-induced crystallisation conditions have been shown to induce reasonable quantities of  $\beta$ -iPP. It has been shown that an  $\alpha$  to  $\beta$  growth transition or  $\alpha\beta$  bifurcation occurs on the surface of oriented  $\alpha$ -iPP row nuclei. Nevertheless, the nature of the nucleation sites responsible for  $\beta$ -iPP nucleation is still under debate. Large quantities of  $\beta$ -iPP can be produced by specific  $\beta$ -iPP nucleating agents. However, the epitaxial nucleation of  $\beta$ -iPP on the surface of the nucleant under quiescent conditions has been shown to be suppressed by flow. This is at odds with the previously mentioned increase in  $\beta$ -iPP under flow-induced-crystallisation conditions. The processes controlling this interesting behaviour therefore need to be identified.

Historically the formation of reasonable quantities of  $\gamma$ -iPP have only been able to be achieved when crystallisation was carried out under high pressure. Recently, it has been discovered that application of intense shear flow or the presence of very powerful nucleating agents can also increase the  $\gamma$ -iPP content. However, the combined influence of nucleant and shear flow on the formation of  $\gamma$ -iPP has yet to be investigated.

Consequently, there is a need for a comprehensive study which can investigate the combined influence of flow conditions and common polymer additives on the entire crystallisation process. Such a study should allow for more rational choice of polymer formulations and more optimised processing conditions, which ultimately will improve product properties and reduce processing costs.

## Chapter 3

### Experimental methods

#### 3.1.0 Introduction

To achieve the goal of examining how nucleant particles influence the flow-induced crystallisation of isotactic polypropylene (iPP) requires time-resolved observations to be performed in-situ during and after the application of flow. In the present work, these in-situ observations were made using a parallel plate rheometer, which was modified to allow simultaneous small and wide angle x-ray scattering (rheo-SAXS/WAXS) and Fourier transfer infrared spectroscopy (rheo-FTIR) experiments to be performed during an imposed thermal-shear profile. However, both SAXS/WAXS and FTIR techniques require a structural model for meaningful interpretation. Therefore additional direct observation techniques such as polarised optical microscopy (POM) and scanning electron microscopy (SEM) as well as complementary techniques such as differential scanning calorimetry (DSC) were employed to confirm the structural models used to interpret the SAXS/WAXS and FTIR data.

This chapter is divided into two sections. The first section outlines the material preparation techniques, including: the matrix material and nucleants used, the mixing techniques employed and the sample nomenclature. The first section also describes the apparatus and protocols used to control the thermal-shear profile imposed on the sample. The second section summarises the analytical techniques used in this work. Firstly the instrument configurations and data analysis of the time-resolved rheo-SAXS/WAXS and rheo-FTIR setups are described in detail. Finally, a description of the complementary experiments which include: DSC, POM and SEM is provided. In addition to what is described in this chapter, more specific experimental details can be found in the separate experimental sections at the start of **Chapters 4-8**.

### 3.2.0 Sample preparation and thermal-shear profile

#### 3.2.1 Isotactic polypropylene matrix

iPP is a common semicrystalline polymer which is typically processed into its final form by a variety of processing technology such as injection moulding and extrusion. It is typically produced through the polymerisation of propylene gas in the presence of Ziegler-Natta or metallocenic catalysts, **Figure 3.1**. The specific type of catalyst and the processing conditions used can greatly influence the molecular architecture such as the degree of chain branching or the distribution of stereo- and regio-errors along the main chain.

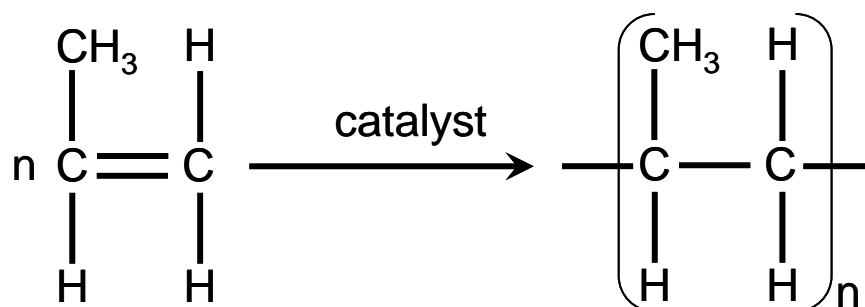


**Figure 3.1.** Schematic illustration of the polymerisation of polypropylene from propylene.

The polymer used was an iPP homopolymer manufactured by Borealis (HD601CF). This grade was chosen due to its low intentional additive profile and as it has been extensively investigated by our group. In particular HC601CF contains no calcium stearate, which has previously been shown to induce an unwanted high temperature smectic phase [197]. The grade data sheet supplied by Borealis (**Appendix 1A**) states the average weight molecular weight ( $M_w$ ) and the average number molecular weight ( $M_n$ ) were 367 000 g/mol and 74 000 g/mol, respectively ( $M_w/M_n = 4.96$ ). Further analysis conducted by Polymer Standard Services Inc. (**Appendix 1B**) on the polymer beads found the  $M_w$  and  $M_n$  were 427 000 g/mol 91 500 g/mol, respectively ( $M_w/M_n = 4.66$ ). This suggests that the actual molecular weight distribution may be shifted to slighter higher molecular weights than the grade average. Small variations in the molecular weight from batch to batch are not unexpected in commercially processed

material. The molecular weight distribution measured by Polymer Standards Services Inc. is considered to be the most relevant and is shown in **Figure 3.2**. **Table 3.1** summarises the properties of the material.

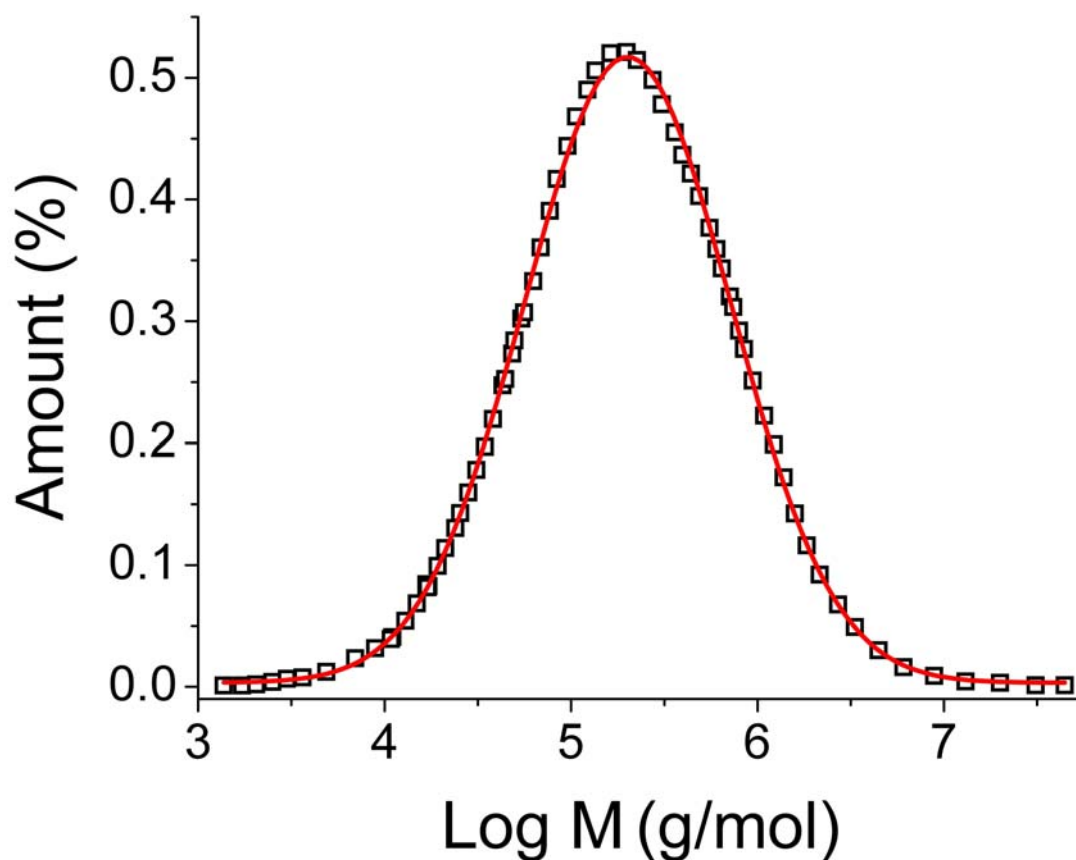


**Figure 3.2.** Molecular weight (M) distribution of HD601CF. The trend line is a log-normal fit.

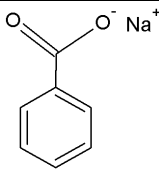
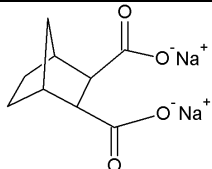
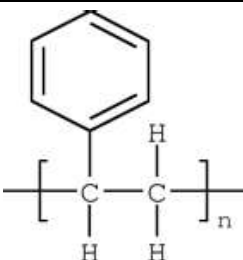
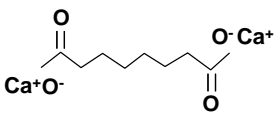
**Table 3.1.** Material properties for the iPP matrix material (Borialis HD601CF). Data taken from the grade sheet supplied by Borealis (**Appendix 1A**).

Material property	Method	Typical value
Density	ISO 1183	900 - 910 kg/m <sup>3</sup>
Melt Flow Rate	ISO 1133	8 g / 10 min
Melting temperature (DSC)	ISO 3146	162 - 166 °C
Vicat softening temperature A50, (10 N)	ISO 306	154 °C
Instrumented puncture test	ISO 7765-2	12 J / 1000 N
Tensile Strength	ISO 527-3	30 - 50 MPa
Tensile Modulus	ISO 527-3	650 - 750 MPa
Isotactic index (FTIR)	Ratio (998/973)	0.95

### 3.2.2 Nucleating agent preparation and compounding technique

Five nucleant particles were added to the iPP matrix material: amorphous isotactic polystyrene (iPS(amorphous)), crystalline isotactic polystyrene (iPS(crystalline)), Calcium suberate (CaSub), bicyclo[2.2.1]heptane-2,3-dicarboxylic acid, trade name HPN-68 (HPN) and sodium benzoate (SB). No additional processing aids or antioxidants were added to stabilise the matrix material during processing. The naming convention, chemical structure of the nucleants and the loadings used in this thesis are provided in **Table 3.2**. In addition, the specific properties of the nucleants are summarised in **Table 3.3**.

**Table 3.2.** Overview of the samples used in this work.

Code	Nucleant		Concentration (wt%)	Chapter
iPP(control)	-		-	Chapters 4-8
iPP(self seed)	self seed		-	Chapters 6-8
iPP(0.05SB)		sodium benzoate (SB)	0.05	Chapters 7-8
iPP(0.10SB)			0.10	
iPP(0.50SB)			0.50	
iPP(1.00SB)			1.00	
iPP(0.05HPN)		bicyclo[2.2.1]heptane-2,3-dicarboxylic acid (HPN)	0.05	Chapters 7-8
iPP(0.10HPN)			0.10	
iPP(0.50HPN)			0.50	
iPP(1.00HPN)			1.00	
iPP(iPS <sub>(crystalline)</sub> )		crystalline isotactic polystyrene (iPS <sub>(crystalline)</sub> )	2.0	Chapter 5
iPP(iPS <sub>(amorphous)</sub> )		amorphous isotactic polystyrene (iPS <sub>(amorphous)</sub> )	2.0	
iPP(0.02CaSub)		calcium suberate (CaSub)	0.02	Chapter 6
iPP(0.05CaSub)			0.05	
iPP(0.10CaSub)			0.10	
iPP(0.50CaSub)			0.50	
iPP(1.00CaSub)			1.00	

The iPS used in this work was manufactured by Scientific Polymer Products Inc. It had an isotactic index greater than 90% and  $M_w = 400,000$  g/mol. Before being compounded into the iPP matrix, the iPS powder was heated in a vacuum oven at 180 °C for 5 h to induce a high degree of crystallinity, then sieved through a 100 µm mesh to further reduce the average grain size of the particles.

CaSub was synthesised in house using reagents acquired from Sigma-Aldrich according to the procedure described by Varga et al. [44]. CaSub has been shown have one of the highest selectivity's for β-iPP of all known β-iPP nucleants, and can, under appropriate conditions, produce samples composed almost entirely of β-iPP [151]. CaSub was made by mixing an equimolar amount of sodium hydroxide (NaOH) dissolved in distilled water to a stirred dilute solution of suberic acid ( $C_8H_{14}O_4$ ) in ethanol at room temperature. An equimolar amount of calcium chloride ( $CaCl_2$ ) was then added to the sodium solution to obtain the calcium salt. The white precipitate was filtered, washed in ethanol and dried at 220 °C overnight to remove crystal water from the produced powder. The density of the powder was measured in ethanol (20 °C) and found to be  $1.62 \pm 0.03$  g/cm<sup>3</sup>. The powder was then milled in a ball mill (9 mm diameter) for 8 hours to yield a fine powder of CaSub.

HPN was obtained from Milliken and was used in its “as received” form. Apart from the active ingredient, the formulation contained two additional components: 13-docosenamide (z) and amorphous silicon dioxide. Both these additives were included in the formulation to inhibit agglomeration of the particle from moisture outside the polymer. HPN has been shown to have one of the highest nucleation potency of all known α-iPP nucleants [166-168].

The SB used in this study was obtained from Sigma-Aldrich in a purity of greater than 99%. A novel dispersion technique was employed to obtain a fine distribution of small needle-like SB particles in the iPP matrix. The coarse particles were ground using a mortar and pestle, then dissolved in a small amount of boiling de-ionised water. The concentrated solution was then sprayed onto the surface the molten polymer during the initial stages of mixing. In this procedure, the water quickly boils off leaving a fine



distribution of needle-like SB particles which are then dispersed into the matrix material.

**Table 3.3.** Summary of nucleants used in this experiment. \* decomposition temperature.

Nucleant	Supplier	Density (g/cm <sup>3</sup> )	Melting Temperature (°C)
iPS(amorphous)	Scientific Polymer Products	1.056 [198]	-
iPS(crystalline)	Scientific Polymer Products	1.08 [199]	~ 225
CaSub	In house synthesis	1.62	450* [44]
HPN	Milliken	1.65 [200]	352.85* [200]
SB	Sigma-Aldrich	1.44[201]	436 [201]

Various loadings of the nucleants were added to molten iPP at 175 °C in a Haake Rheocord 90 batch mixer. Before addition of the polymer, the batch mixer was held at temperature for 10 minutes to allow thermal equilibrium to be reached. 45 g of the polymer pellets were added in one step and mixed for 60 s to allow time for the polymer to melt. The nucleant was then added in one step and the polymer and nucleant were mixed for a further 300 s. A mixing speed of 60 RPM was used throughout the entire process. The polymer was then force cooled to prevent excessive degradation. The material was removed from the batch mixer and compression moulded to a thickness of 1.5 mm at 190°C for 300 s. 12 mm diameter disks were then cut from the compression moulded material to be used for further analysis.

### 3.3.3 Thermal-shear profile

In this work a Linkam CSS450 parallel plate shear cell was used to precisely control the thermal-shear profile. **Figure 3.3** shows a schematic diagram of the shear cells inner workings. The thermal profile was controlled by heating units in the lid and base. The shear profile was applied to the sample by rotating the bottom plate using a precision stepping motor. The shear rate ( $\dot{\gamma}$ ) was controlled by adjusting the sample thickness (d) and the angular velocity ( $\omega$ ) of the bottom plate. The shear strain ( $\gamma$ ) was controlled by adjusting the shear time ( $t_\gamma$ ). The shear rate and strain were calculated at a given radius (r) from the centre of the disk by **Equation 3.1** and **Equation 3.2**, respectively.

$$\dot{\gamma} = \frac{\omega r}{d}$$

**Equation 3.1**

and

$$\gamma = \frac{\omega r}{d} t_\gamma$$

**Equation 3.2**

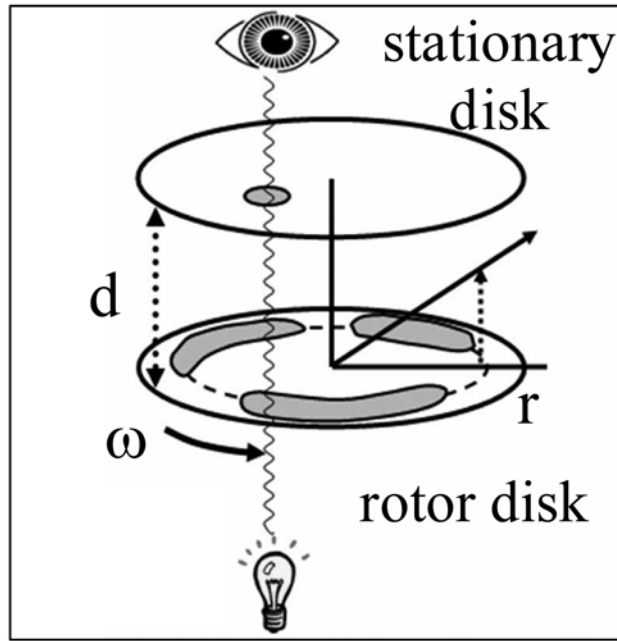


**Figure 3.3.** Schematic diagram of the inner workings of the Linkam parallel plate shear cell.

In-situ observations of the sample during the imposed thermal-shear profile are made through small apertures in the lid and base of the Linkam, which allow light to be transmitted through the sample to the detector. The apertures are circles 3 mm in diameter and are located 7.5 mm from the centre of rotation. The sample being investigated is held in place by window material, which was specific to the wavelength of light used for in-situ observations. For optical investigations, two 2 mm thick disks of fused quartz are used, while for infrared investigations two 2 mm thick disks of zinc selenide (ZnSe) were used. Further adaptations were made to the shear cell for x-ray scattering investigations. A 2 mm thick steel bottom plate which contained three 3 mm wide slots, and a 2 mm thick top plate which contained one 3 mm circular aperture (the

gray shaded regions in **Figure 3.3**) replaced the standard quartz windows. 50  $\mu\text{m}$  thick films of kapton<sup>TM</sup> were then used to keep the sample in place during the experiments. To limit surface nucleation influencing the results, the window materials were manufactured to have a fine surface polish, and care was taken to avoid contamination and scratching of the windows during experimentation.

To ensure reproducible results between the different setups, the temperature and shear profile were externally calibrated. The temperature was calibrated using additional thermocouples inserted at various locations in the melt. **Table 3.4** shows the average melt temperature measured using the additional thermocouple versus the set point temperature. This analysis revealed that both the melt temperature and the set point temperature were in line for the quartz windows over a wide temperature range. However, the melt temperature was on average +0.5 °C higher than the set point temperature with the ZnSe windows in place and -4.6 °C lower with the steel/kapton<sup>TM</sup> windows in place. These average values were used to adjust the temperature to ensure the reproducibility of the temperature profile between the different experimental setups. The shear strain was calibrated by the selective addition of a dye to the melt followed by the application of a controlled step shear. The position of the dye was then measured and compared against the expected position under perfect shear conditions. All experimental setups examined produced the same nominal shear strain as measured from the dye. Furthermore, the measured shear strain was in accordance with the expected shear strain indicating that wall slip did not occur to an appreciable extent.

**Table 3.4.** Comparison of Linkam CSS450 set point temperature versus melt temperature measured using external thermocouple when different window material are used.

Set point (°C)	Quartz (°C)	Metal/Kapton <sup>TM</sup> (°C)	ZnSe (°C)
220.0	220.2 ± 0.1	215.6 ± 0.1	220.6 ± 0.1
210.0	209.9 ± 0.1	205.4 ± 0.1	210.4 ± 0.1
200.0	199.9 ± 0.1	195.6 ± 0.1	200.8 ± 0.1
190.0	189.9 ± 0.1	185.5 ± 0.1	190.0 ± 0.1
180.0	179.9 ± 0.1	175.7 ± 0.1	180.4 ± 0.1
170.0	170.3 ± 0.1	165.3 ± 0.1	170.5 ± 0.1
160.0	160.0 ± 0.1	154.9 ± 0.1	160.5 ± 0.1
150.0	149.8 ± 0.1	144.8 ± 0.1	150.5 ± 0.1
140.0	139.9 ± 0.1	134.6 ± 0.1	140.4 ± 0.1
130.0	130.0 ± 0.1	125.7 ± 0.1	130.3 ± 0.1
120.0	120.0 ± 0.1	115.6 ± 0.1	120.6 ± 0.1
110.0	109.9 ± 0.1	105.5 ± 0.1	110.4 ± 0.1
100.0	99.9 ± 0.1	95.6 ± 0.1	100.5 ± 0.1
<b>mean difference (°C)</b>	<b>0.0 ± 0.1</b>	<b>-4.6 ± 0.1</b>	<b>0.5 ± 0.1</b>

The general experimental protocol used in this work was as follows:

- Place the sample, which is in the form of a 12 mm disk into the shear cell held at 220 °C.
- Compress the sample slowly to the working distance at a rate of 0.01 mm/s. This ensures that the shear rate imposed on the samples during the compression phase was always less than 0.3 s<sup>-1</sup>.
- Hold the sample at 220 °C for a least 300 s to erase the previous thermal-shear profile.
- Cool to the isothermal temperature at 0.5 °C/s.
- Apply a shear pulse of defined shear rate and shear strain.
- Hold at the isothermal temperature until the end of the experiment.
- Cool to room temperature at 0.5 °C/s.

The specific thermal-shear profiles used in this work are described in further detail in the experimental sections at the beginning of **Chapters 4-8**.

### 3.3.0 Analytical techniques

#### 3.3.1 X-ray scattering experiments

X-ray scattering techniques are widely employed to characterise the morphology of semicrystalline polymers. WAXS is commonly used to determine parameters such as: crystallinity, crystallite dimensions, phase composition, and molecular orientation. SAXS can be used to provide information on: the crystallinity, the long period and lamellar thickness, and the crystallite orientation. WAXS and SAXS scattering from most semicrystalline polymers is relatively weak, therefore large beam dimensions and long exposure times are typically required when conventional x-ray sources are used. To overcome this, synchrotron radiation was used as the source of x-ray radiation in the present work. The advantages of using a synchrotron source over a conventional source are the considerably high incident flux and beam culmination obtained with the synchrotron source. This significantly improves data quality, and allows time- and spatially-resolved experiments to be performed.

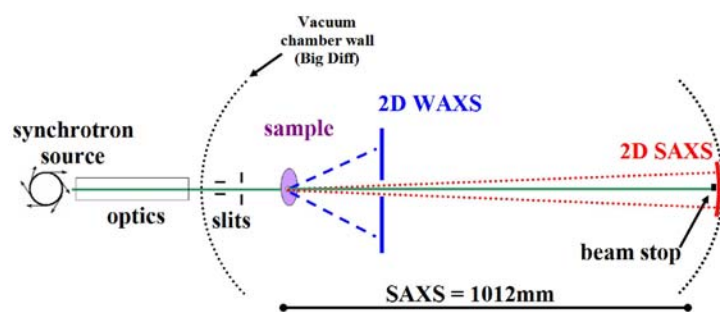
SAXS and WAXS patterns are typically represented as a function of the intensity versus the scattering vector. The scattering vector ( $q$ ) was calculated by the following formula:

$$q = 4\pi \sin \theta / \lambda$$

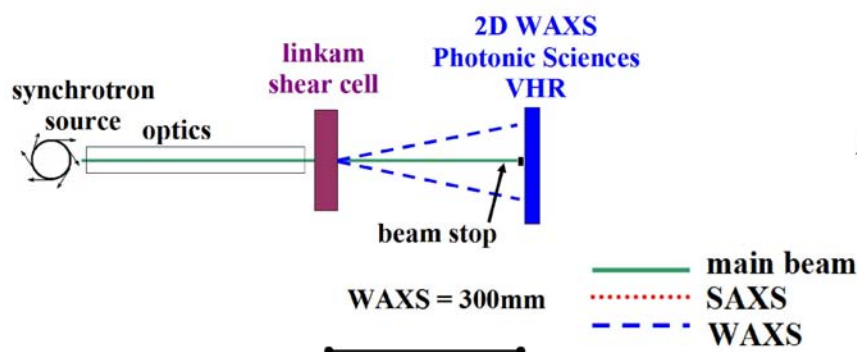
**Equation 3.3**

where  $2\theta$  is the scattering angle and  $\lambda$  is the incident wavelength.

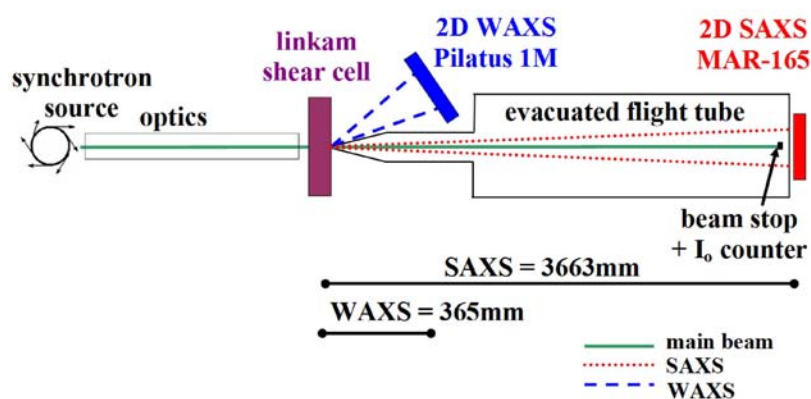
In this study, x-ray scattering experiments were performed at: the Australian National Beamline Facility (ANBF), beamline 20B at the Photon Factory, Tsukuba, Japan; the Powder Diffraction beamline at the Australian Synchrotron, Melbourne Australia; and the SAXS/WAXS beamline at the Australian Synchrotron, Melbourne Australia. A summary of the main features of each experimental setup and the detector systems used are provided in **Table 3.5** and **Table 3.6** respectively. Schematic diagrams of the experimental setups are also provided in **Figure 3.4**. The basic experimental setups are described in the following sections. Further details can also be found in the experimental sections in **Chapters 4-8**.



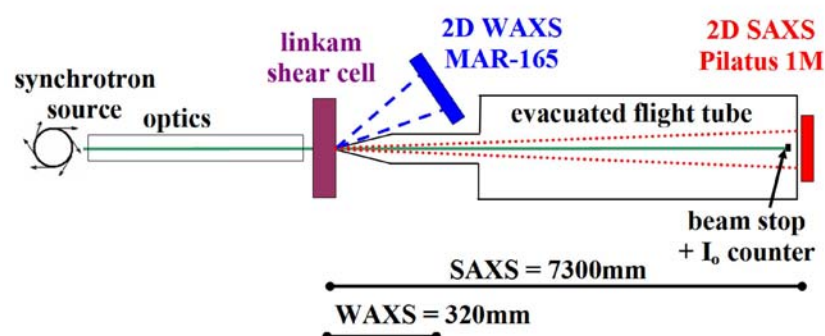
BL20B  
Australian National  
Beamline Facility



Powder Diffraction  
Australian Synchrotron



SAXS/WAXS(1)  
Australian Synchrotron



SAXS/WAXS(2)  
Australian Synchrotron

**Figure 3.4.** Schematic diagrams of the experimental x-ray scattering setups used in this thesis.

**Table 3.5.** Summary of the main experimental parameters used in the x-ray scattering experiments. Minimum time resolution ( $\Delta t$ ), wavelength ( $\lambda$ ), exposure time ( $t_{\text{exp}}$ ), azimuthal angle covered ( $\phi$ ), minimum scattering vector ( $q_{\text{min}}$ ). \* Azimuthal coverage determined at  $q = 1 \text{ \AA}^{-1}$ .

Beam Line	Date Performed	Simultaneous SAXS/WAXS	$\Delta t$ (s)	$\lambda$ (Å)	Beam Size ( $\mu\text{m}$ )	WAXS Parameters				SAXS Parameters			
						Camera length (mm)	Detector	$t_{\text{exp}}$ (s)	$\phi$ (deg)	Camera length (mm)	Detector	$t_{\text{exp}}$ (s)	$q_{\text{min}}$ ( $\text{\AA}^{-1}$ )
BL 20B ANBF	November 2008 June 2009	Y	0	2	200	110	IP BAS 2000	~ 300	360	1012	IP BAS 2000	~ 300	0.0080
Powder Diffraction AS	August 2008	N (WAXS only)	15	0.82	1000	300	PS VHR	~ 5	360	-	-	-	-
SAXS/WAXS(1) AS	July 2009	Y	5.2	1.48	250 x 150	365	Dectris Pilatus 1M	1 s	~70°	3663	MAR-165	1	0.0031
SAXS/WAXS(2) AS	May 2010	Y	5.6	1.34	200 x 100	320	MAR 165	1 s	90°	7300	Dectris Pilatus 1M	1	0.0028

**Table 3.6.** Summary of detector systems used in the x-ray scattering experiments.

Detector		Pixel Size (mm)	Dynamic Range (orders of magnitude)	Frame Rate (Hz)	Readout time (ms)	Count Rate (x-ray/s)	Detector dimensions (mm)
Dectris - Pilatus 1M	Multi-module (10 modules in 2 x 5 array with 7 x 17 pixel gap between each). Rectangular.	172	6	30	30	$> 2 \times 10^6$	169 x 179
MAR-165	Single module, i.e. no gaps in active area. Circular.	80	3-4	1	4000	$0.4 \times 10^6$	165
Photonic Science VHR	Single module, i.e. no gaps in active area. Circular.	32	5	33	3000	NA	166
BAS 2000	reusable two-dimensional film. Rectangular.	100	5	NA	NA	unlimited	100 x 200



### 3.3.1.1 Beamline 20B, the Australian National Beamline Facility

Experiments were performed at the Australian National Beamline Facility (ANBF) beamline 20B, in November 2008 and June 2009. Beamline 20B is installed on a bending magnet port at the Photon Factory, Tsukuba, Japan and delivers monochromatic synchrotron x-rays in the energy range of 4.5–20 keV to the experimental hutch. The main component of the instrument is a multi-configuration vacuum diffractometer. Fuji film image plates with a pixel size of 100  $\mu\text{m}$  were used as the detector system. Complete two-dimensional WAXS images were taken at a camera length of 110 mm in flat plate geometry. A 20 mm diameter hole was located in the centre of the WAXS plate which allowed for simultaneous capture of complete two-dimensional SAXS images. SAXS images were taken at a camera length of 1012 mm in cylindrical geometry, with the image plates mounted in the circular diffractometer. The two-dimensional intensity data was extracted from the image plates using a BAS2000 scanner. The SAXS image plates were protected from the main beam intensity by a homemade beamstop  $\sim 2$  mm in diameter mounted on the  $2\theta$  arm.

All experiments used a square-shaped microbeam which had dimensions of 200  $\mu\text{m}$  x 200  $\mu\text{m}$ . A wavelength of 2.0  $\text{\AA}$  was employed to record the two-dimensional SAXS/WAXS patterns. In order to account for decay in the ring current, the exposure time was normalized to the ring current. Typical exposure times for both SAXS/WAXS experiments ranged from 180 – 600 s. All samples investigated on Beamline 20B were ex-situ samples previously prepared prior to arriving at the synchrotron. A calibrated motorised sample stage allowed for scanning of the x-ray microbeam across the radius of the sheared disks.

### 3.3.1.2 Powder Diffraction beamline, Australian Synchrotron

In-situ two-dimensional rheo-WAXS experiments were performed on the Powder Diffraction beamline in August 2008. The Powder Diffraction beamline is located on a bending magnet port and delivers monochromatic radiation over an energy range of 5–30 keV. Wallwork et al. have provided a general description of the Powder Diffraction beamline [202]. The Linkam CSS450 was mounted on the beamline using a specially constructed stand. The stand allowed for easy removal and accurate replacement of the shear cell during sample change-over. A Photonic Science VHR CCT detector was used

to record the two-dimensional WAXS patterns in flat plate geometry. Beam dimensions of  $1000\text{ }\mu\text{m} \times 1000\text{ }\mu\text{m}$ , a wavelength of  $0.82\text{ }\text{\AA}$ , a camera length of 126 mm and 15 s exposure time were employed throughout the experiment. The read out time of the detector was approximately 3 s. Beam current was logged every 150 s to allow for image normalisation.

#### 3.3.1.3 SAXS/WAXS beamline, Australian Synchrotron

Two series of in-situ two-dimensional rheo-SAXS/WAXS experiments were performed at the SAXS/WAXS beamline. The first was performed in July 2009 (SAXS/WAXS(1)), while the second was performed in May 2010 (SAXS/WAXS(2)). The source for the SAXS/WAXS beamline is an in-vacuum 3 m undulator which can deliver monochromatic radiation over the energy range 5-20 KeV. Kirby et al. have provided a general description of the SAXS/WAXS beamline [203]. The Linkam CSS450 was mounted on the beamline using the stand described in the previous section. The setup employed a flat plate with the detector surface perpendicular to the main beam for SAXS detection, while an inclined flat plate detector offset to the main beam was used for WAXS detection. The focal point of the WAXS detector was set up such that it intersected the main beam at the sample. The setup allowed for in-situ investigations with a considerable amount of the scattering intensity around the azimuth in the WAXS region to be captured, whilst simultaneously capturing complete SAXS patterns.

In SAXS/WAXS(1) series of experiments, the WAXS detector was the Dectris - Pilatus 1M, while the SAXS detector was the MAR-165. The Dectris - Pilatus 1M detector has a considerable dead space at the bottom of the detector which limited how close the detector could be placed to the main beam, thereby reducing the azimuthal coverage which could be obtained. Nevertheless, this setup allowed for an azimuthal coverage of  $\sim 70^\circ$  in the WAXS region at  $q = 1\text{ }\text{\AA}^{-1}$ . Beam dimensions of  $250\text{ }\mu\text{m} \times 150\text{ }\mu\text{m}$ , a wavelength of  $\lambda = 1.48\text{ }\text{\AA}$ , and an exposure time of 1 s were employed throughout both experiments. The minimum time resolution between successive images was 5.2 s.

In the SAXS/WAXS(2) series of experiments, the SAXS/WAXS detectors were swapped. The MAR-165 detector has a much smaller dead space at the bottom of the detector which allowed it to be brought closer to the main beam. This allowed the azimuthal coverage in these experiments to be increased to 90° in the WAXS region at  $q = 1 \text{ \AA}^{-1}$ . Beam dimensions of 200  $\mu\text{m}$  x 100  $\mu\text{m}$ , a wavelength of  $\lambda = 1.34 \text{ \AA}$ , and an exposure time of 1 s were employed throughout both experiments. The minimum time resolution between successive exposures was 5.6 s.

In both experiments, the shear cell was rotated such that the equatorial scattering was always captured. Scattering without the specimen was recorded to enable background correction and all images were normalised to the main beam intensity which was measured by a scintillation counter mounted in the beamstop. Geometry refinements were performed with the aid of the calibration standard silver behenate (AgBeh).

#### 3.3.1.4 X-ray data reduction

Automated transformation of the raw two-dimensional scattering patterns to one-dimensional intensity profile were performed using two software packages. The Nika set of macros for Igor Pro were used to reduce all two-dimensional SAXS data as well as the WAXS data obtained from BL20B at ANBF and the powder diffraction beamline at the Australian synchrotron. The SAXS15id software which runs on the IDL Virtual Machine platform was used exclusively to reduce the data from the off axis WAXS detector in the SAXS/WAXS(1) and SAXS/WAXS(2) experiments. Images were normalised using either the main beam current (BL20B and PD) or using the scattered intensity measured at the SAXS detector (SAXS/WAXS(1) and SAXS/WAXS(2)) before background, dark field and mask images were subtracted.

In both software packages, two types of transformation were employed on the processed images to achieve the required one-dimensional SAXS/WAXS intensity profiles. **Figure 3.5** summaries the steps involved in both processes. In the first type of transformation, segments of various angular breadth in the azimuthal direction were directly integrated to yield the change in intensity as a function of the scattering vector. In the second type of transformation, the processed two-dimensional images were first

converted from Cartesian (x-y) coordinates to polar (q- $\phi$ ) coordinates. Boxes with a fixed breadth of scattering vectors were then integrated to yield intensity as a function of azimuthal angle.

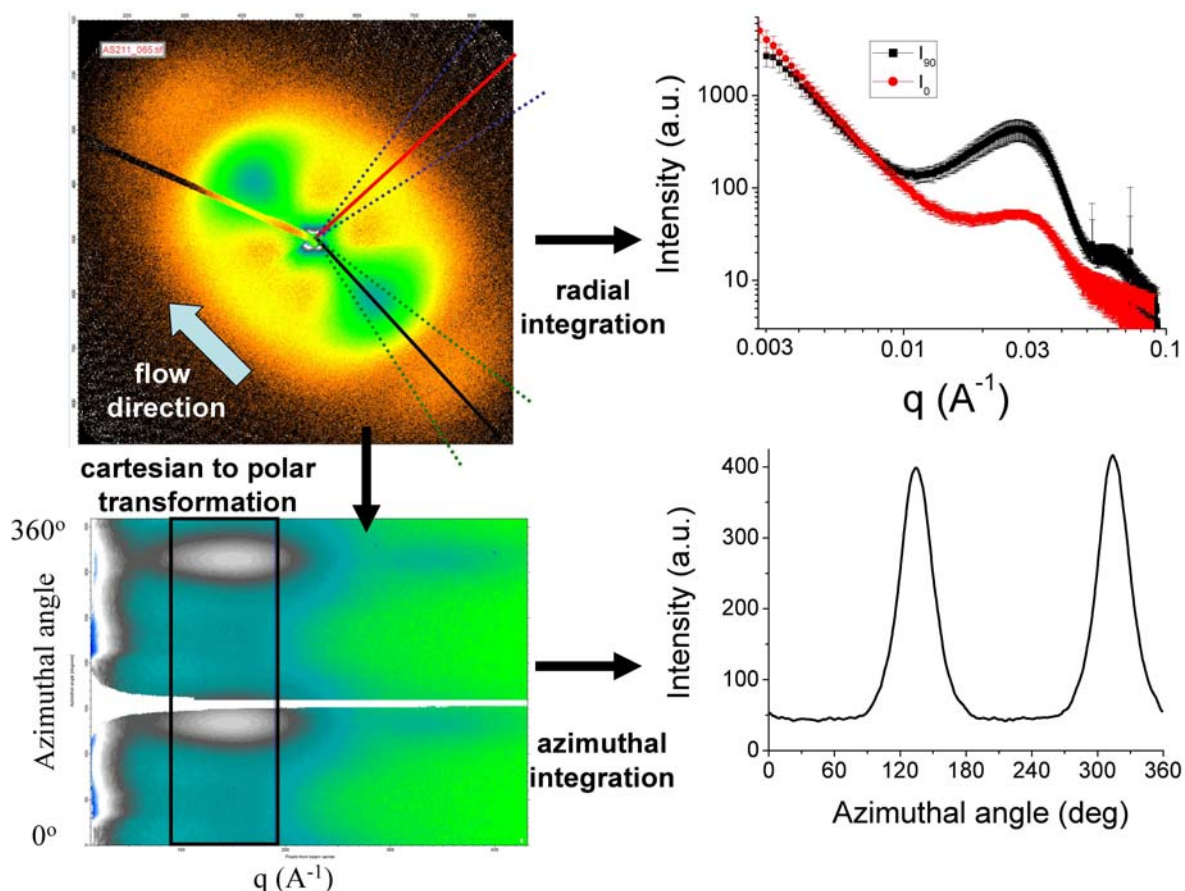


**Figure 3.5.** Example of the two transformation procedures used to obtain one-dimensional intensity profiles from the raw two-dimensional patterns.

### 3.3.1.5 X-ray data analysis

The following section describes some of the main methods used to analyse the experimentally derived SAXS/WAXS patterns. Scattering in the wide angle regions is predominantly from crystalline planes and therefore WAXS is highly sensitive to the proportion and orientation of crystalline phases. A volume crystallinity index for iPP ( $\chi_v$ ) was determined by separating out the amorphous and crystalline contributions to the total scattering of a circularly integrated WAXS intensity profile along  $q$  between  $0.8 \text{ \AA}^{-1} \leq q \leq 1.8 \text{ \AA}^{-1}$  and  $0 \leq \phi \leq 360^\circ$ . Automated procedures were employed to deconvolute the scattering profiles using the fitykc© software package. Three Gaussian curves centred at  $q = 1.0 \text{ \AA}^{-1}$ ,  $1.2 \text{ \AA}^{-1}$  and  $1.45 \text{ \AA}^{-1}$  were used to account for the

amorphous scattering. Seven Gaussian curves were used to account for the major crystalline scattering peaks observed between  $0.9 \text{ \AA}^{-1} \leq q \leq 1.6 \text{ \AA}^{-1}$ . An example of the fit obtained is provided in **Figure 3.6**. The volume crystallinity index was then estimated by:

$$\chi_v = \frac{A_{\text{crystalline}}}{A_{\text{crystalline}} + A_{\text{amorphous}}} \quad \text{Equation 3.4}$$

where  $A_{\text{crystalline}}$  is the area of the seven crystalline Gaussian curves and  $A_{\text{amorphous}}$  is the area of the three amorphous Gaussian curves.

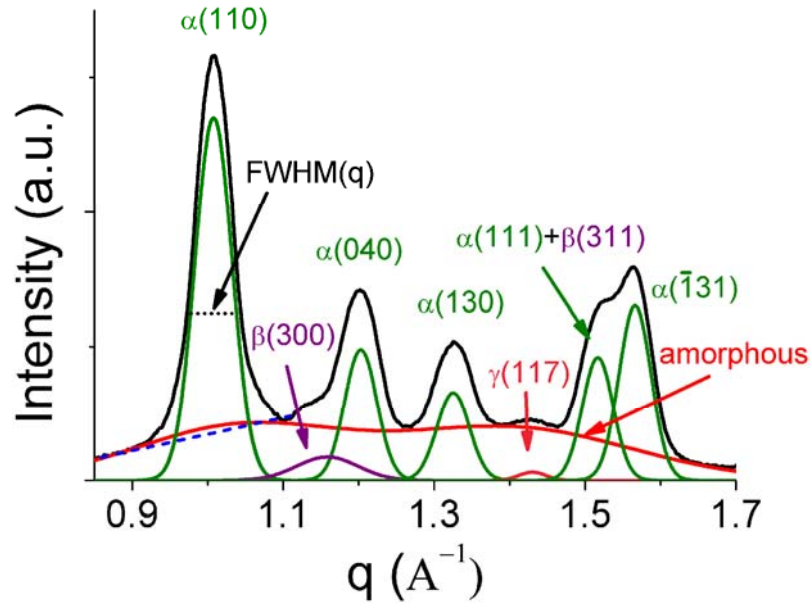


**Figure 3.6.** WAXS intensity profile along the scattering vector ( $q$ ) showing the main isotactic polypropylene crystalline reflections present. Shear rate  $80 \text{ s}^{-1}$ .

The  $\beta$ -iPP crystallinity ( $\chi_\beta$ ) and  $\gamma$ -iPP crystallinity ( $\chi_\gamma$ ) indices were estimated using the Turner-Jones method [139, 204]:

$$K_\beta = \frac{A_\beta(300)}{A_\beta(300) + A_\alpha(110) + A_\alpha(040) + A_\alpha(130)} \quad \text{Equation 3.5}$$

$$\chi_\beta = K_\beta \chi_v \quad \text{Equation 3.6}$$

$$K_{\gamma} = \frac{A_{\gamma}(117)}{A_{\gamma}(117) + A_{\alpha}(130)} \quad \text{Equation 3.7}$$

$$\chi_{\gamma} = K_{\gamma} \chi_v \quad \text{Equation 3.8}$$

where  $A_{\beta}(300)$ ,  $A_{\alpha}(110)$ ,  $A_{\alpha}(040)$ ,  $A_{\alpha}(130)$  and  $A_{\gamma}(117)$  are the areas of the reflections indicated in **Figure 3.6**.

The  $\alpha$ -iPP crystallinity ( $\chi_{\alpha}$ ) can then be estimated from the following relation:

$$\chi_{\alpha} = \chi_v - \chi_{\beta} - \chi_{\gamma} \quad \text{Equation 3.9}$$

The breadth of the desmeared crystalline peaks can yield information about the crystal perfection and the crystal size. The lamellar thickness of the iPP samples was calculated from the WAXS data using the Scherrer equation [205]:

$$\langle L_{hkl} \rangle = \frac{K\lambda}{\beta_{hkl} \cos \theta_{hkl}} \quad \text{Equation 3.10}$$

where  $L_{hkl}$  is the crystallite size in the direction perpendicular to the diffraction plane ( $hkl$ ),  $K$  is the crystallite shape factor (0.89), and  $\beta_{hkl} = (\beta_{hkl}^2 - b_0^2)^{1/2}$ , with  $B_{hkl}$  being the peak width at half maximum intensity and  $b_0$  the instrumental resolution. The assumption in the Scherrer equation is that all the line broadening of reflections results from the finite crystallite size, and therefore the lamellar thickness estimation can be considered an upper bound.  $\langle L_{001} \rangle$  has to be estimated from the reflections  $\alpha(111)$ ,  $\alpha(041)$ , and  $\alpha(\bar{1}31)$  due to the absence of a pure reflection of the form  $\alpha(00l)$ . The thickness of crystalline lamellae,  $\langle L_{001} \rangle$ , can be calculated from the reflection  $\alpha(\bar{1}31)$  by the following equation:

$$\langle L_{001} \rangle = L_{\bar{1}31} \cos \omega = \frac{K\lambda}{\beta_{\bar{1}31} \cos \theta_{\bar{1}31}} \cos \omega \quad \text{Equation 3.11}$$

where  $\omega$  is an angle between the lattice planes  $\alpha(001)$  and  $\alpha(\bar{1}31)$ . Using the crystal unit cell of the  $\alpha$ -form crystal ( $a = 6.66 \text{ \AA}$ ,  $b = 20.96 \text{ \AA}$ ,  $c = 6.5 \text{ \AA}$ ,  $\beta = 99^\circ 80'$ , and  $\alpha$  and  $\gamma = 90^\circ$ ) [120], the value of  $\omega$  was calculated to be  $57.89^\circ$ .

Scattering in the wide angle region is also highly sensitive to crystalline orientation. **Figure 3.7a** shows a typical oriented two-dimensional WAXS pattern ( $0 < \varphi < 90$ ) from an iPP sample crystallised under flow-induced crystallisation condition. The concentric rings which are typically found in isotropic materials condense into arcs at various locations around the azimuth. Azimuthal intensity profiles from the three main crystalline phases present,  $\alpha(110)$ ,  $\alpha(040)$ ,  $\beta(300)$  &  $\gamma(117)$  are shown in **Figure 3.7b**. These azimuthal intensity profiles were used to estimate the crystalline orientation for  $\alpha$ -iPP,  $\beta$ -iPP, and  $\gamma$ -iPP.

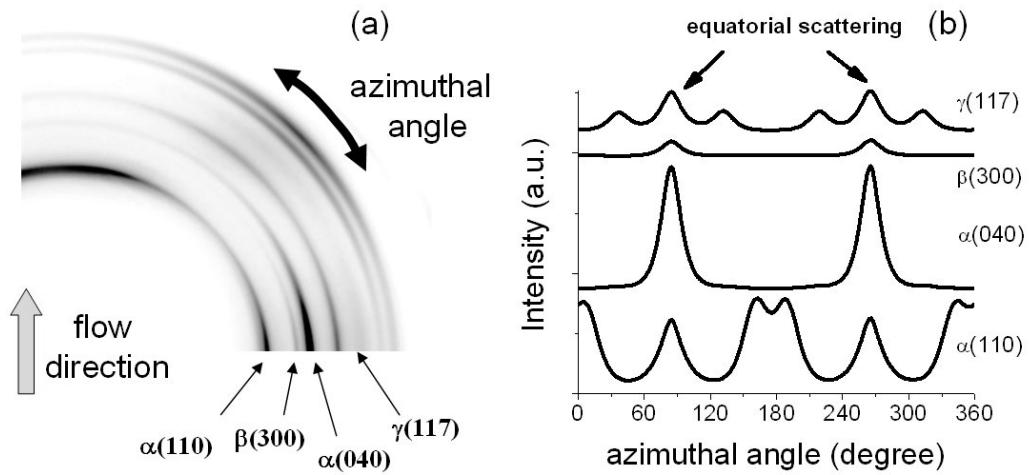


**Figure 3.7.** (a) Typical two-dimensional oriented WAXS pattern. (b) Azimuthal intensity profiles of the main  $\alpha$ -iPP,  $\beta$ -iPP and  $\gamma$ -iPP reflections.

The crystalline orientation parameter ( $f_h$ ) can be quantitatively measured from the WAXS data using the Herman's orientation function according to the equation:

$$f_h = \frac{3\langle \cos^2 \varphi \rangle - 1}{2} \quad \text{Equation 3.12}$$

where  $\varphi$  is an angle between the direction within the crystal of interest (e.g. c-axis of the  $\alpha$ -iPP phase) and the reference direction (e.g. flow direction).  $\langle \cos^2 \varphi \rangle$  can be defined according to the equation:

$$\langle \cos^2 \varphi \rangle = \frac{\int_0^{\frac{\pi}{2}} I(\varphi) \cos^2 \varphi \sin \varphi \, d\varphi}{\int_0^{\frac{\pi}{2}} I(\varphi) \sin \varphi \, d\varphi} \quad \text{Equation 3.13}$$

The physical meaning of the Herman's orientation function is that  $f_h$  has a value of unity when all the crystals are aligned along the reference direction, which is coincident with the flow direction in the present study. When all the crystals are aligned perpendicular to the reference direction,  $f_h$  adopts a value of -0.5. Whereas for a completely random orientation of crystals,  $f_h$  is 0.

The following work is primarily concerned with the orientation of the molecular chain axis (c-axis) with respect to the flow direction of  $\alpha$ -iPP crystals. Assuming the oriented structures have rotational symmetry around the flow direction, the angles which the  $\alpha$ -iPP c-axis ( $\sigma$ ), a-axis ( $\omega$ ) and b-axis ( $\mu$ ) make to the flow direction can be given by the following equations:

$$f_{c[\alpha]} = \frac{3\langle \cos^2 \sigma \rangle - 1}{2} \quad \text{Equation 3.14}$$

$$f_{a(\alpha)} = \frac{3\langle \cos^2 \omega \rangle - 1}{2} \quad \text{Equation 3.15}$$

$$f_{b(\alpha)} = \frac{3\langle \cos^2 \mu \rangle - 1}{2} \quad \text{Equation 3.16}$$

with:

$$f_{a(\alpha)} = f_{c(\alpha)} + f_{b(\alpha)} \quad \text{Equation 3.17}$$

There is no pure reflection from the c-axis in  $\alpha$ -iPP. However,  $f_{c(\alpha)}$  can be calculated using Wilchinsky's method [206] from the unit cell geometry and the scattered intensities from the  $\alpha(110)$  and  $\alpha(040)$  reflections.



$$\langle \cos^2 \sigma \rangle = 1 - 1.099 \langle \cos^2 \varphi_{\alpha(110)} \rangle - 0.901 \langle \cos^2 \varphi_{\alpha(040)} \rangle \quad \text{Equation 3.18}$$

$f_{b(\alpha)}$  for  $\alpha$ -iPP crystals can be calculated directly from the  $\alpha(040)$  reflection using the equation:

$$\langle \cos^2 \mu \rangle = \langle \cos^2 \varphi_{\alpha(040)} \rangle \quad \text{Equation 3.19}$$

The a-axis orientation ( $f_{a(\alpha)}$ ) can then be obtained from **Equation 3.17**.

In the present experiment there is not sufficient experimental data to calculate the  $\beta$ -iPP orientation in the same way as was possible for  $\alpha$ -iPP. This is due to the insufficient separation of the main  $\beta$ -iPP peaks from the main  $\alpha$ -iPP reflections to allow accurate measurement of their azimuthal intensity profile. Nevertheless, in order to compare the development of the orientation of the  $\beta$ -iPP to the  $\alpha$ -iPP orientation, a crude estimation of  $\beta$ -iPP orientation was determined from the average square cosine of the  $\beta(300)$  reflection  $\langle \cos^2 \varphi_{\beta(300)} \rangle$  according to **Equation 3.12**. This parameter is roughly comparable to the  $f_{b(\alpha)}$  parameter.

$$f_{h(\beta)} = \frac{3 \langle \cos^2 \varphi_{\beta(300)} \rangle - 1}{2} \quad \text{Equation 3.20}$$

In a similar manner the  $\gamma$ -iPP orientation was estimated from the average square cosine of the  $\gamma(117)$  reflection  $\langle \cos^2 \varphi_{\gamma(117)} \rangle$ .

$$f_{h(\gamma)} = \frac{3 \langle \cos^2 \varphi_{\gamma(117)} \rangle - 1}{2} \quad \text{Equation 3.21}$$

Another way to characterise the orientation of the different crystalline phases of iPP is to determine the crystalline oriented fraction ( $\Phi_c$ ) [207-208]. **Figure 3.8** illustrates the general principle of separating out contributions from oriented and unoriented crystals

as well as background contributions from the  $\alpha(110)$ ,  $\beta(300)$  and  $\gamma(117)$  azimuthal intensity profiles. The crystalline oriented fraction can then be determined from:

$$\Phi_c = \frac{\text{oriented crystalline scattering}}{\text{total integrated area} - \text{background scattering}} \quad \text{Equation 3.22}$$

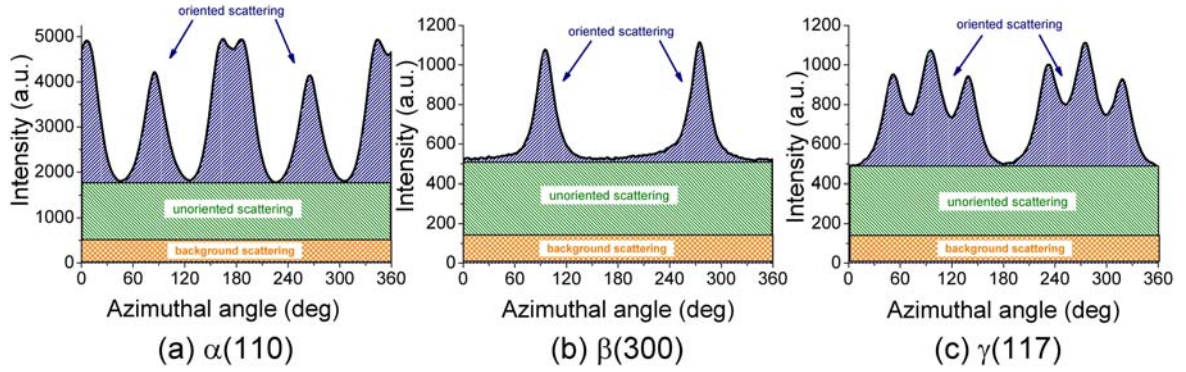


**Figure 3.8.** Separation of the oriented, unoriented and background contributions to the azimuthal intensity profile of (a)  $\alpha(110)$ , (b)  $\beta(300)$  and (c)  $\gamma(117)$  azimuthal intensity profiles.

Small angle x-ray scattering arises from the inhomogeneous nature of the material being examined. Therefore the development during crystallisation and melting of structures such as shish or crystalline lamellae can also be probed using SAXS. A convenient method is to determine the total integrated intensity ( $I$ ) as a function of scattering vector.  $I$  determined in this way is proportional to the total volume ( $V$ ) and the electron density contrast ( $\Delta\rho$ ) of the scattering species. As SAXS is sensitive to the anisotropy present within the sample, the integrated intensity is often determined along a particular sector of the two-dimensional profile. In this work two  $20^\circ$  sectors are extracted from the SAXS patterns, one centred on the equator ( $I_0$ ), while the other centred on the meridian ( $I_{90}$ ). An illustration of this procedure is shown in **Figure 3.5**.  $I_0$  and  $I_{90}$  can then be determined from the following equation:

$$I = \int_{q_{\min}}^{q_{\max}} \int_{\varphi-10^\circ}^{\varphi+10^\circ} I(q, \varphi) dq d\varphi \quad \text{Equation 3.23}$$

**Equation 3.12** is most commonly used to calculate the molecular orientation from WAXS, however it can also be used to determine the degree of lamellar orientation ( $f_{h(\text{SAXS})}$ ) [19, 21-22]. To limit other contributions to the azimuthal intensity profile such as from shish, the integration is performed over a defined range of  $q$ -values (typically  $0.015 \leq q \leq 0.5 \text{ \AA}^{-1}$ ) as illustrated in **Figure 2.3**. The lamellar orientation was then determined from:

$$f_{h(\text{SAXS})} = \frac{3\langle \cos^2 \varphi_{\text{SAXS}} \rangle - 1}{2} \quad \text{Equation 3.24}$$

In this case when  $f_{h(\text{SAXS})}$  is unity, all lamellar normals are perfectly parallel to the flow direction, while when  $f_{h(\text{SAXS})}$  is zero, the lamellar normals are randomly distributed.

Similar to the method used to determine the crystalline oriented fraction, the oriented fraction of lamellae ( $\Phi_L$ ) can be determined from the background corrected azimuthal intensity profile as shown in **Figure 3.9** and using the following relation:

$$\Phi_L = \frac{\text{oriented lamellar scattering}}{\text{total integrated area}} \quad \text{Equation 3.25}$$

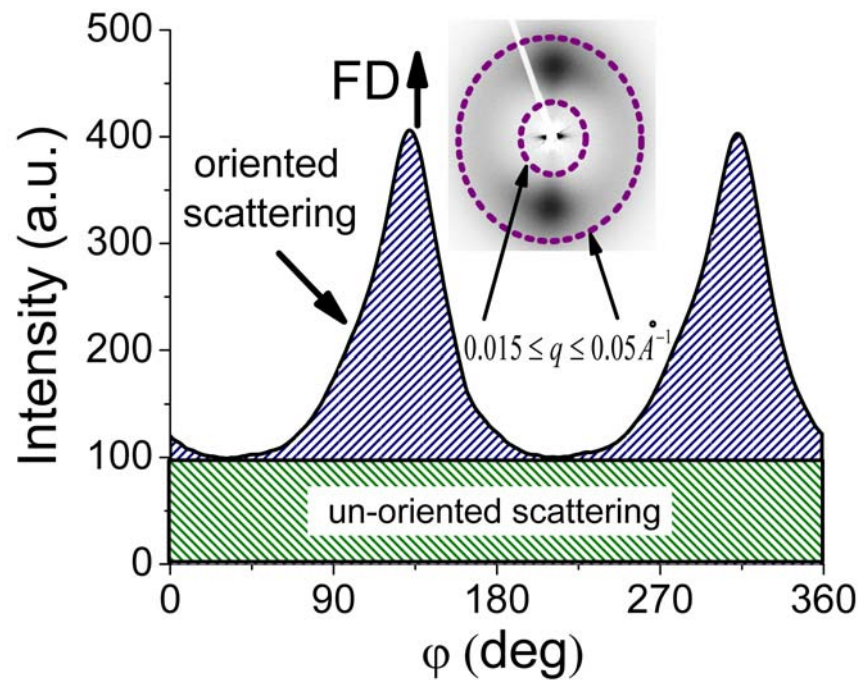


**Figure 3.9.** Plot of background subtracted intensity versus azimuthal angle ( $\varphi$ ) showing the method used to determine the oriented fraction of lamellae ( $\Phi_L$ ).

### 3.3.2 Fourier transform infrared spectroscopy

FTIR covers a range of techniques which can be used to qualitatively and quantitatively characterise the structure of semicrystalline polymers. For example, FTIR can be used to investigate the degree of crystallinity, the degree of molecular conformation and the segmental orientation of the crystalline and amorphous phases. In the present work, in-situ rheo-FTIR experiments were performed to investigate the presence of nucleants on development of conformational order of the iPP molecules before, during and after shear flow.

Rheo-FTIR experiments were performed on a Perkin-Elmer GX. The setup is shown in **Figure 3.10**. The hard but relatively brittle ZnSe glass used for the window material allows for the samples spectrum to be recorded between  $17\,000\text{ cm}^{-1}$  and  $700\text{ cm}^{-1}$ . An auto polariser can also be fitted ahead of the sample environment to allow orientation studies to be performed. The FTIR experiments were performed over a wavenumber range of  $2000\text{--}700\text{ cm}^{-1}$ , with a resolution of  $4\text{ cm}^{-1}$  and optical path difference (OPD) velocity of  $0.2\text{ cm/s}$ . These parameters allowed for a minimum time resolution between successive measurement points of  $3.2\text{ s}$ . An empty cell was used as the background. The route mean squared intensity of the melt immediately prior to shear was used to normalise the data.

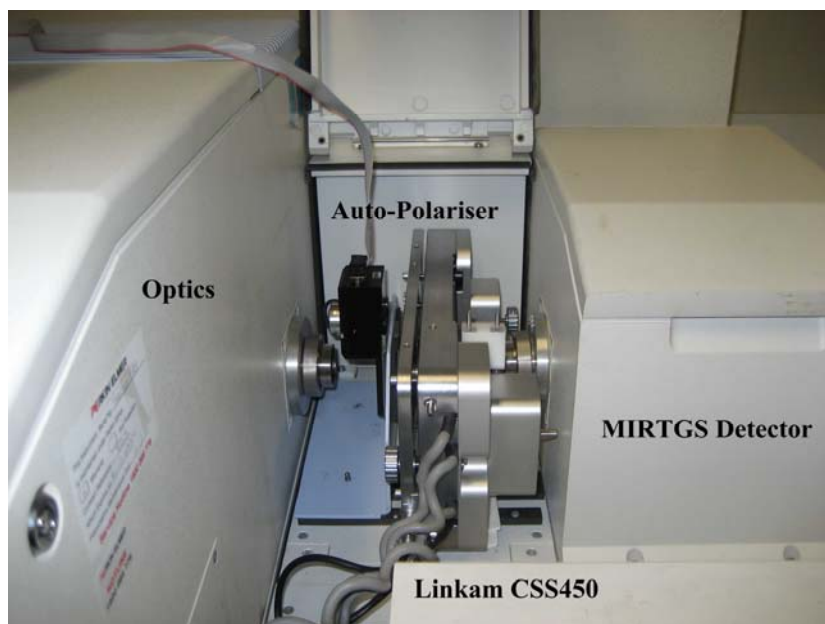


**Figure 3.10.** In-situ rheo-FTIR experimental setup.

### 3.3.3 Differential scanning calorimetry

DSC covers a range of thermal techniques which measure the difference in heat flow between a sample pan and a reference pan as a function of temperature or time. In this thesis, DSC experiments were primarily used to characterise the influence of nucleants on the crystallisation kinetics and melting behaviour of iPP.

DSC experiments were performed using a Perkin-Elmer DSC-7 with attached intercooler. Sample size was ~5 mg. High purity indium (melting onset = 156.60 °C) and high purity zinc (melting onset 419.47 °C) references were used for temperature calibration. Transition energy was calibrated using high purity indium (heat of fusion = 28.45 J/g). All samples were run under a nitrogen atmosphere and had baselines subtracted before data analysis. Samples were run in triplicate. Uncertainty in the parameters measured by DSC was assessed by calculating the standard error of the three measurements and the 95.4% confidence interval was reported.

The weight percent crystallinity ( $\chi_{DSC}$ ) of the sample was determined from melting endotherms measured at a heating rate of 0.17 °C/s according to the following relation:

$$\chi_{DSC} = \frac{\Delta H}{\Delta H_0} \quad \text{Equation 3.26}$$

where  $\Delta H$  is the enthalpy of fusion determined by the integrating the area under the baseline corrected thermogram and  $\Delta H_0$  is the heat of fusion of the equivalent pure crystal.

Two parameters were determined to characterise the influence of the nucleants on the quiescent crystallisation kinetics. The nucleation efficiency of the particles was determined according to the method proposed by Fillon et al. [209-210]. This method assumes that the best nucleant are self seeds, i.e. small crystal fragments made of the polymers crystals formed by partial melting. The peak crystallisation temperature during continuous cooling of a self nucleated polymer is considered as the upper bound,

while the crystallisation temperature of the pure polymer is considered the lower bound.

**Figure 3.11** illustrates the procedure.

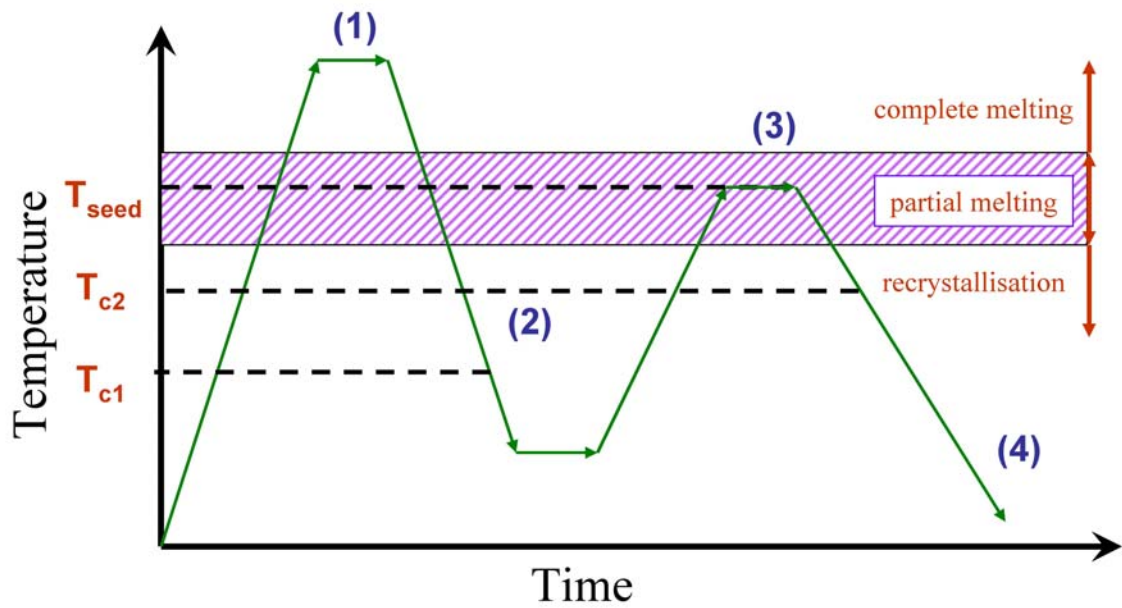


**Figure 3.11.** Thermal protocol used to determine the nucleation efficiency (NE).

Four thermal steps are required for self nucleation. (1) The sample is heated to 220 °C for 300 s to erase the previous thermal history. (2) A standard crystallisation state is created by cooling the sample to 50 °C at 0.17 °C/s (lower crystallisation temperature ( $T_{c1}$ )). (3) The sample is then heated to the partial melting temperature ( $T_{seed}$ ) and held there for 300 s. (4) The sample is then immediately cooled to 50 °C at 0.17 °C/s (upper crystallisation temperature ( $T_{c2}$ )). The nucleation efficiency (NE) can then be calculated according to the following equation:

$$NE = \frac{T_{cNA} - T_{c1}}{T_{c2} - T_{c1}} \quad \text{Equation 3.27}$$

where ( $T_{cNA}$ ) is the crystallisation temperature of the polymer samples containing the nucleating particles. Slight variations in  $T_{seed}$  can lead to large fluctuations in  $T_{c2}$ , therefore the correct determination of the self seed temperature is critical for reliable results to be obtained. If the self seed temperature is too low, recrystallisation occurs, while if the temperature is too high then the sample melts completely. In this experiment recrystallisation was observed at temperatures below 166.5 °C, while

complete melting occurred at 170 °C, **Figure 3.12**. From this analysis, the value for  $T_{\text{seed}}$  was selected to be 167 °C.

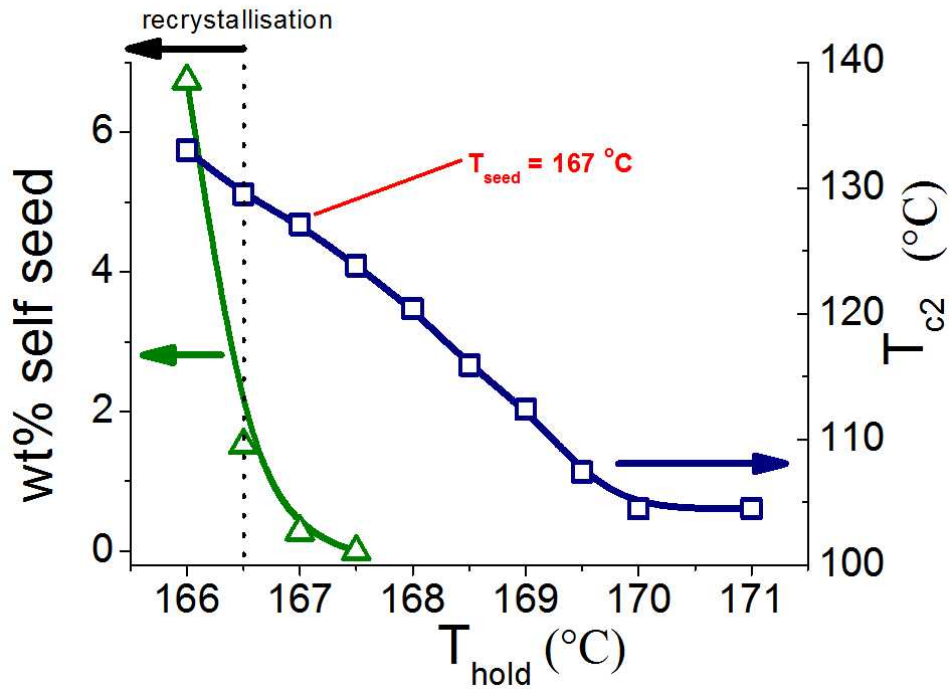


**Figure 3.12.** Plot of hold temperature ( $T_{\text{hold}}$ ) versus the upper crystallisation temperature ( $T_{c2}$ ) and the wt% of self seed, showing the basis for the selection of the self seed temperature ( $T_{\text{seed}}$ ).

Another kinetic parameter which is commonly used to characterise the effectiveness of a nucleant is its ability to decrease the activation energy for crystallisation ( $\Delta E$ ).  $\Delta E$  can be determined from the Kissinger model according to the equation:

$$\frac{d \left[ \ln \left( \frac{CR}{T_c^2} \right) \right]}{d \left( \frac{1}{T_c} \right)} = - \frac{\Delta E}{R} \quad \text{Equation 3.28}$$

where,  $T_c$  is the peak crystallisation temperature with the cooling rate (CR) and  $R$  is the universal gas constant (8.314 J/K mol). In this work,  $\Delta E$  was calculated by fitting a line of best fit to a plot of  $\frac{1}{T_c}$  versus  $\ln \left( \frac{CR}{T_c^2} \right)$  using data collected from four different cooling rates: 0.08 °C/s, 0.17 °C/s, 0.33 °C/s and 0.5 °C/s.

### 3.3.4 Microscopy

#### 3.3.4.1 Characterisation of ex-situ nucleant particles.

A JEOL JSM-7001F field emission scanning electron microscope (FESEM) operating in secondary electron mode was used to image the nucleant particles ex-situ. The ex-situ particles were supported on carbon tape, coated to 10 Å thick with gold / platinum and imaged at an acceleration voltage of 15 kV, a probe current of 6 amps and working distance of 10 mm.

#### 3.3.4.2 Polarised optical microscopy

POM can give important information about the structure of a polymer. Polarised light can interact with electromagnetically anisotropic structures present within the polymer and can therefore give information about the crystalline morphology as well as any molecular orientation present. In this work, two POM techniques were employed to characterise the produced samples.

In-situ POM of samples within the Linkam CSS450 shear cell were taken on a Nikon 80i microscope in transmission mode using a Nikon DS-Fi1 CCD camera. The setup allowed for time resulted images with a minimum time resolution between successive images of 5 s.

Ex-situ polarised optical macro images of the sheared disks were made using a home made polariscope, **Figure 3.13**. A fluorescent light box was used as the light source. The sample to be imaged was sandwiched between crossed polarising films. A 14 megapixel Olympus FE-4030 CCD camera mounted 150 mm above the light box was then used to record the images.



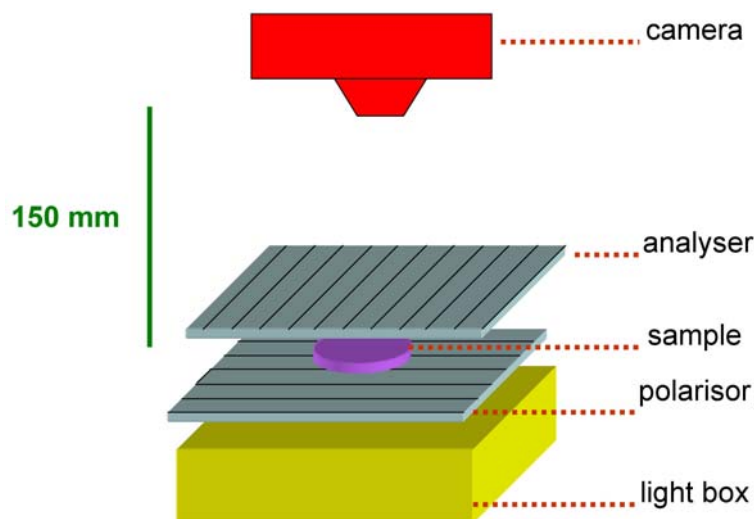


**Figure 3.13.** Setup of the polariscope used to record macro images of the sheared disks.

#### 3.3.4.3 Characterisation of etched samples

The permanganic etching technique first proposed by Olley et al. [211] has been found to be of great benefit in uncovering the microstructure of polyolefines [177, 192, 212]. An improved version of this technique for use with bulk specimens, proposed by Park et al. [213], was used in this thesis. Radial sections from the samples were immersed in a vigorously stirred solution of 3wt% potassium permanganate ( $\text{KMnO}_4$ ), 64.7wt% concentrated sulphuric acid ( $\text{H}_2\text{SO}_4$ ) and 32.9wt% ortho-phosphoric acid ( $\text{H}_3\text{PO}_4$ ) for 7 hours. This solution preferentially etches away the amorphous regions in the polymer leaving the crystalline lamellae largely intact. After etching, specimens were quenched in cool hydrogen peroxide ( $\text{H}_2\text{O}_2$ ), washed in distilled water, and underwent acetone sonification for 15 minutes to remove any artefacts from the etching process. An advantageous consequence of the etching procedure was that it removed a considerable amount of material ( $\sim 100\ \mu\text{m}$ ) from the free surfaces. This revealed the core of the samples which is more representative of what was observed in the scattering and FTIR experiments.

The spherulite scale morphology of the etched surfaces was imaged using reflected optical microscopy (ROM). An Olympus PMG3 microscope with a differential interference optic attachment was used to take the micrographs. Higher magnifications of the lamellar morphology were achieved with the FESEM previously described. Samples were coated with a 10 Å thick with gold / platinum coating and imaged at an

acceleration voltage of 15 kV, a probe current of 6 amps and working distance of 10 mm. However, significant degradation of the polymer was observed at higher magnifications. For subsequent investigations, the degradation was reduced by using a lower acceleration voltage of 5 kV with the same probe current and working distance.



## Chapter 4

### Crystallisation and melting of oriented parent - daughter lamellae in sheared isotactic polypropylene

#### 4.1.0 Introduction

To fully appreciate the morphology development of isotactic polypropylene (iPP) in the presence of foreign particles, it is necessary to have a thorough understanding of the morphology of pure iPP. In this chapter the unique hierarchical structure of iPP is investigated under quiescent crystallisation and flow-induced crystallisation conditions. Morphology characterisation is performed with a range of in-situ and ex-situ characterisation techniques.

Natta and Corradini showed that the usual crystal form of iPP has each polymer molecule arranged as a  $3_1$  helix [120]. The helix is chiral and can exist in either the right or left hand configuration. This chirality allows for four different crystalline phases:  $\alpha$ ,  $\beta$ ,  $\gamma$  and the smectic phase. The  $\alpha$  crystalline phase ( $\alpha$ -iPP) is by far the most common phase. Its monoclinic crystal structure is made up of alternating sheets of left- and right-handed helices. Interestingly, it appears that this regular arrangement of stems can sometimes break down and it is possible to have two adjacent sheets with the same chirality. This leads to a dramatic reorientation of the chain axis from the substrate layer (parent) by the  $\beta$  angle of  $\alpha$ -iPP monoclinic unit cell ( $99^\circ 80'$ ) forming a branch [122]. A daughter lamella may then form from this initial nucleus.

This parent-daughter lamellar branching phenomenon has been observed over a wide range of crystallisation conditions and is therefore considered to be a general property of  $\alpha$ -iPP crystallisation. The parent-daughter relationship (PD) is such that the daughter lamellae ( $L_D$ ) are aligned along the  $c_1$ -axis and the  $a_1$ -axis of the parent lamellae ( $L_P$ ). In this thesis the a-, b- and c-axes of the parent lamellae are identified by the subscript 1 ( $a_1$ ,  $b_1$ ,  $c_1$ ), and the axes of the daughter lamellae by the subscript 2 ( $a_2$ ,  $b_2$ ,  $c_2$ ). The nature of the PD structure has been thought to influence important properties such as fatigue life [23], resistance to deformation [177], and surface properties such as wear

and adhesion [50]. Thus a greater understanding of this structure may allow for tailored microstructures to be produced, extending the range of properties available for industrial applications.

Parent and daughter lamellae are however inherently difficult to study separately in in-situ environments due to their many structural similarities. However, by allowing the material to crystallise in an oriented form, such as under flow-induced crystallisation conditions, a bimodal orientation of lamellae is developed and the individual contributions of PD lamellae can be observed by wide angle x-ray scattering (WAXS). Coupled with an appropriately designed shear cell and an intense x-ray source, this permits PD lamellae to be investigated in-situ during important physical processes like crystallisation and melting. In the first part of this chapter the morphology of iPP crystallised under quiescent crystallisation conditions is briefly reviewed. Then the basis and procedure for separating the individual oriented PD lamellae contributions to the two-dimensional WAXS profile is introduced. In the following section this procedure will be applied to further understand oriented PD lamellar branching during isothermal crystallisation from a sheared melt. In the final section of the chapter, the relative thermal stability of the oriented PD lamellae will be determined to identify the multiple melting peaks which are commonly observed during non-isothermal differential scanning calorimetry (DSC) thermograms of sheared iPP. The melting thermograms will then be used to investigate the effect of flow conditions on lamellar thickness / perfection.

Some of the results presented in this chapter have been previously published in the proceeding of the 25<sup>th</sup> *Annual Meeting of the Polymer Processing Society (PPS-25)* [214] and in *The Australian Journal of Chemistry* [215]. A copy of these papers are included in **Appendix 2**.

## 4.2.0 Experimental

### 4.2.1 Sample preparation and thermal-shear profile

The thermal-shear profile was designed to simulate, as close as practically possible, conditions found in typical industrial processes prior to the onset of crystallisation. For example in the injection moulding process short-lived and intense shear fields are typically imposed to the supercooled melt near the cold mould wall [113-114]. Furthermore, solidification in injection moulded parts occurs under relatively high cooling rates and large temperature gradients. However in this study, crystallisation was carried out under isothermal conditions after the application of a short shear pulse to a supercooled melt. This allows for more simplified and detailed quantitative analysis of the crystallisation kinetics and morphology development.

The thermal-shear profile used in this experiment is shown in **Figure 4.1a**. Disks 12 mm in diameter of the compression moulded material were heated to 220 °C and compressed slowly to the working distance of 0.5 mm at 0.01 mm/s. The compressed disks were held at the melting temperature for 300 s to erase any previous history. The isotropic nature of the melt after this treatment was confirmed by WAXS and polarised optical microscopy. Samples were then cooled as quickly as practically possible to the isothermal crystallisation temperature ( $T_c$ ) of 135 °C at 0.5 °C/s. A brief controlled step shear was immediately applied for 1 s with shear rates between 0-80 s<sup>-1</sup>. Shear rates greater than 80 s<sup>-1</sup> were not able to be investigated in this study due to the appearance of flow instabilities (melt fracture) at shear rates greater than 80 s<sup>-1</sup>. In all cases the samples were held at the crystallisation temperature for long enough for the crystallisation rate to be effectively negligible. The samples were then cooled at 0.5 °C/s to 50 °C and held there for 5 min. The sample was then heated at constant rate at 0.17 °C/s to 200 °C. A heating rate of 0.17 °C/s was chosen to limit reorganisation or recrystallisation influencing the shape of the melting peaks as observed by Paukkeri and Lehtinen [216].

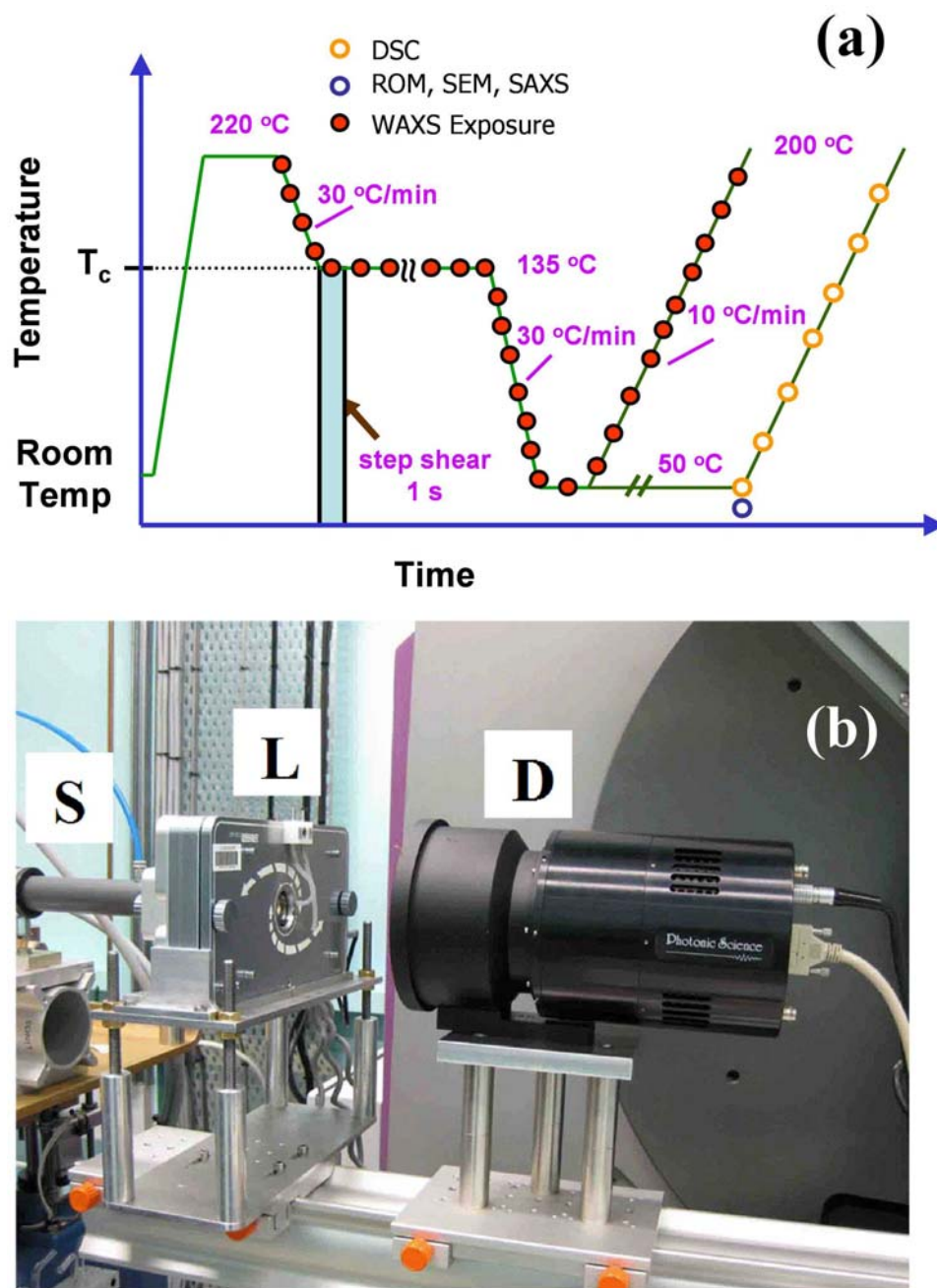


**Figure 4.1.** (a) Schematic representation of the thermal-shear profile used in this chapter. Coloured circles represent when SAXS/WAXS, ROM, SEM and DSC measurements were taken. (b) rheo-WAXS experiment on the Powder Diffraction beam line at the Australian Synchrotron. Synchrotron source (S), Linkam shear cell (L) and detector (D).

## 4.2.2 Analytical techniques

Small angle x-ray scattering (SAXS) experiments were performed at the Australian National Beamline Facility (ANBF) at the Photo Factory in Tsukuba, Japan. The experimental setup was described in detail in **Chapter 3.3.1.1**. In-situ two-dimensional rheo-WAXS experiments were performed on the Powder Diffraction beam line at the Australian Synchrotron [202], **Figure 4.1b**. The experimental setup was described in detail in **Chapter 3.3.1.2**. The volume ( $\chi_v$ ),  $\beta$ -iPP ( $\chi_\beta$ ) and  $\gamma$ -iPP ( $\chi_\gamma$ ) crystallinity indices were estimated according to the produces specified in **Chapter 3.3.1.5**.

Ex-situ samples were etched for 7 h in the permanganate solution described in **Chapter 3.3.4**. Reflected optical micrographs (ROM) of the etched surfaces were taken on an Olympus PMG3 microscope with a differential interference optic attachment. Higher magnification of the etched surfaces was achieved with a JEOL JSM-7001F field emission scanning electron microscope (SEM) operating in secondary electron mode. Samples were coated to 10 Å thick with gold / platinum and imaged at 50 000 x magnification at an acceleration voltage of 5 kV.

DSC experiments were performed on the fully crystallised iPP samples using a Perkin-Elmer DSC-7 at heating rates of 0.17 °C/s. The width of the sectioned pieces along the radius of the disk was 1.5 mm which corresponds to a shear rate resolution in the DSC samples of  $\pm 5 \text{ s}^{-1}$ . The Thompson-Gibbs relationship was used to calculate the average lamellar thickness ( $\langle L \rangle$ ) of a polymer sample from the peak melting temperature ( $T$ ) in their DSC thermogram according to the equation [217]:

$$\langle L \rangle = \frac{2\sigma_e}{\Delta H_f \rho_c} \left( \frac{T_0}{T_0 - T} \right) \quad \text{Equation 4.1}$$

where the melting temperature of crystallites with infinite thickness [174],  $T_0 = 187.7$  °C, the lamellae surface energy [174],  $\sigma_e = 52.2 \text{ mJ/m}^2$ , the density of the crystalline phase [218],  $\rho_c = 0.936 \text{ g/cm}^3$ , and the melting enthalpy of a perfect crystal [181],  $\Delta H_f = 177.0 \text{ J/g}$ .



### 4.3.0 Results

#### 4.3.1 Quiescent crystallisation of iPP

In this section the morphology of iPP crystallised under quiescent conditions is briefly investigated. iPP samples which had been isothermal crystallised at 135 °C without prior deformation of the melt were etched in the permanganate solution and viewed using ROM and SEM. The etching procedure selectively removes the amorphous phase leaving the crystalline regions largely intact. **Figure 4.2** shows the hierarchical structure of quiescent crystallised iPP. When viewed under optical light, large spherulite structures composed of long ribbons radiating out from a central core were observed, **Figure 4.2a**. Closer inspection of the spherulites using SEM reveal two regions, **Figure 4.2b-d**. In the core of the spherulite a cross-hatched structure consisting of parent and daughter lamellae of similar size was observed. On the other hand, with increasing distance from the core the morphology transitioned to thicker radial lamellae (parent) being the dominant lamellar structure, with smaller daughter lamellae being observed lamellae between the larger parent lamellae. Similar core-shell spherulite structures to what was observed here have previously been observed during isothermal crystallisation at temperatures between 132 - 152 °C [127, 138, 219].

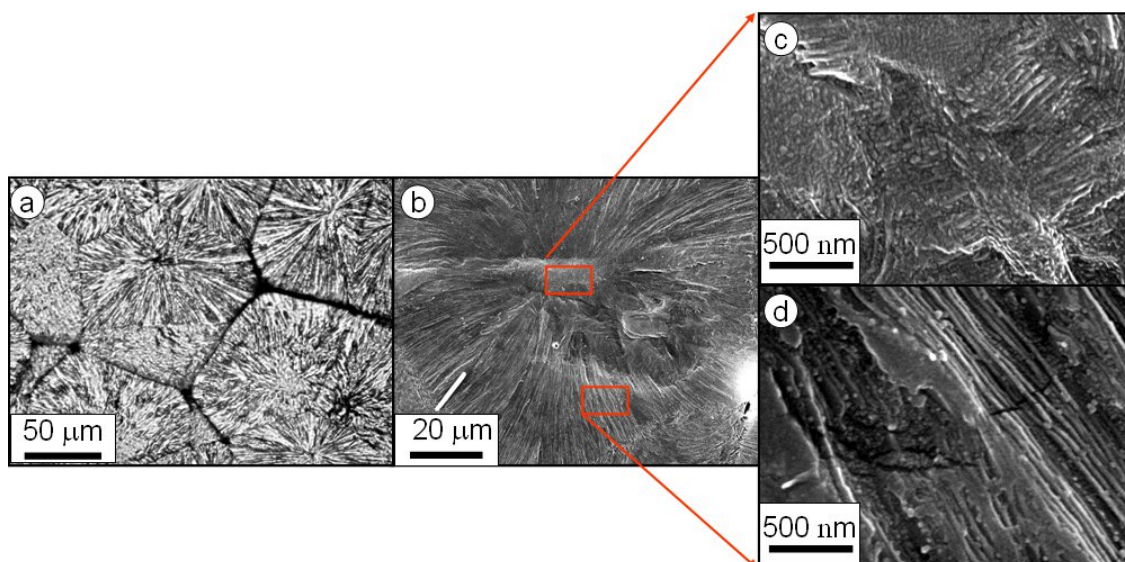


**Figure 4.2.** (a) ROM and (b), (c) & (d) SEM images of permanganate etched surfaces crystallised at 135 °C. Indicative locations of (c) & (d) are shown by the small red boxes in (b). Quiescent condition.

Two-dimensional WAXS and SAXS patterns of the quiescent crystallised sample are shown in **Figure 4.3**. In the WAXS region only the 5 main reflections of  $\alpha$ -iPP were present, indicating the sample was composed almost entirely of the  $\alpha$ -iPP crystalline form. This was also confirmed by DSC. In the SAXS region a single broad halo was observed consistent with lamellae structures with a range of thicknesses. Uniform concentric rings observed in the WAXS pattern are evidence of randomly aligned molecular chain c-axis (the molecular chain helix axis for iPP). Similarly, the uniform halo shape SAXS pattern was observed, indicating random orientated lamellae. The results presented in this section show that although the PD structure can be investigated in the ex-situ condition, PD lamellae can not be separated using x-ray scattering when crystallised in the quiescent condition.

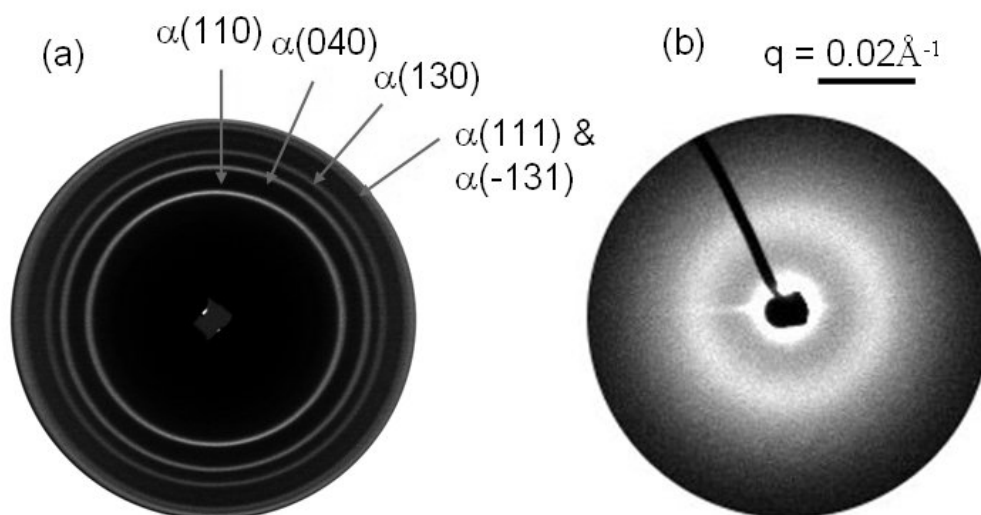


**Figure 4.3.** (a) Two-dimensional wide angle x-ray scattering (WAXS) and (b) small angle x-rays scattering (SAXS) patterns of iPP crystallized isothermally at 135 °C. Quiescent condition.

#### 4.3.2 Parent-daughter model in sheared $\alpha$ -iPP

In this section the basis and procedure for the separation of oriented PD lamellae contribution to the two-dimensional WAXS profiles will be presented. To fully understand the x-ray scattering patterns and derive quantitative information, it is necessary to have a detailed structural model. A generalised model of the oriented PD lamellar structure is provided in **Figure 4.4**. In the model, highly oriented thread-like assemblies (commonly referred to as shish) which are composed of extended chains are

aligned along the flow direction. Depending on a range of factors, the chains can be in an amorphous, mesomorphic or crystalline state [14]. The shish provide nucleation sites for parent lamellae (kebabs) which grow radially out from the shish with their  $c_1$ -axis (chain folding axis) aligned along the flow direction. Epitaxial nucleation of daughter lamellae can then occur on the  $ac$  faces of the parent lamellae. In the model, the  $c_2$ -axis of the daughter lamellae is related to  $c_1$ -axis of the parent lamellae by the  $\beta$  angle of  $\alpha$ -iPP monoclinic unit cell ( $99^\circ 80'$ ).

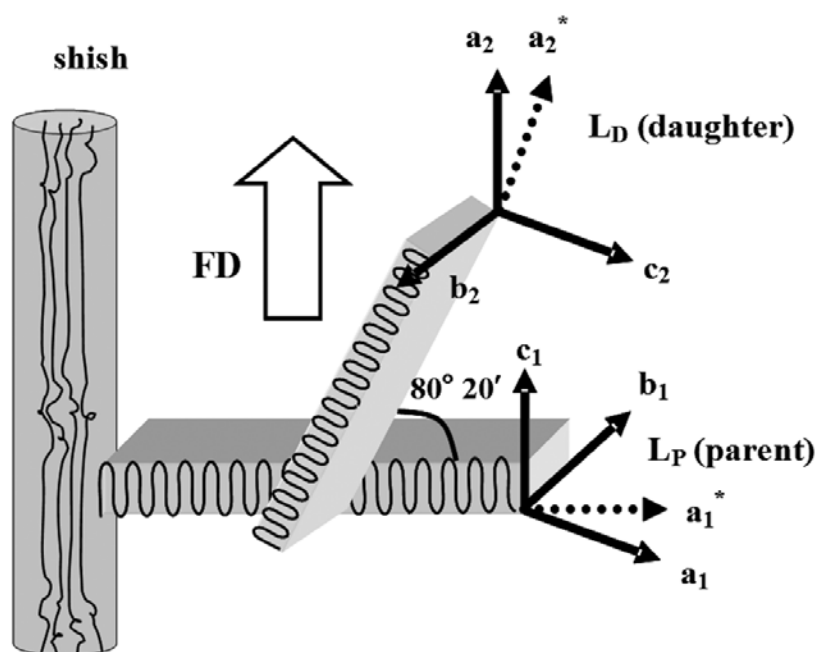


**Figure 4.4.** Generalised model for the oriented parent-daughter structure found in sheared isotactic polypropylene.

To confirm the proposed structural model, the surface of a sample sheared for 1s at a shear rate of  $80 \text{ s}^{-1}$  was etched in the permanganate solution and investigated by ROM and SEM. In reflected light many highly oriented thread-like structures, consistent with the presence of shish, were observed to be aligned along the flow direction, **Figure 4.5a**. Some small spherulites were also observed between the shish. At higher magnification the shish were heavily etched possibly revealing they were regions of lower order than the surrounding material. Extending radially from the shish were primary lamellae (parent) which tended to become thinner with increasing distance from the shish core, **Figure 4.5b**. Smaller lamellae consistent with daughter lamellae filled the space between neighbouring parent lamellae. The thickness of the oriented parent and daughter lamellae were found to be  $126 \pm 7 \text{ \AA}$  and  $95 \pm 9 \text{ \AA}$  respectively. The

planes of the daughter lamellae were found to be inclined  $80 \pm 2^\circ$  to the parent lamellae. These results confirm the proposed structural model.

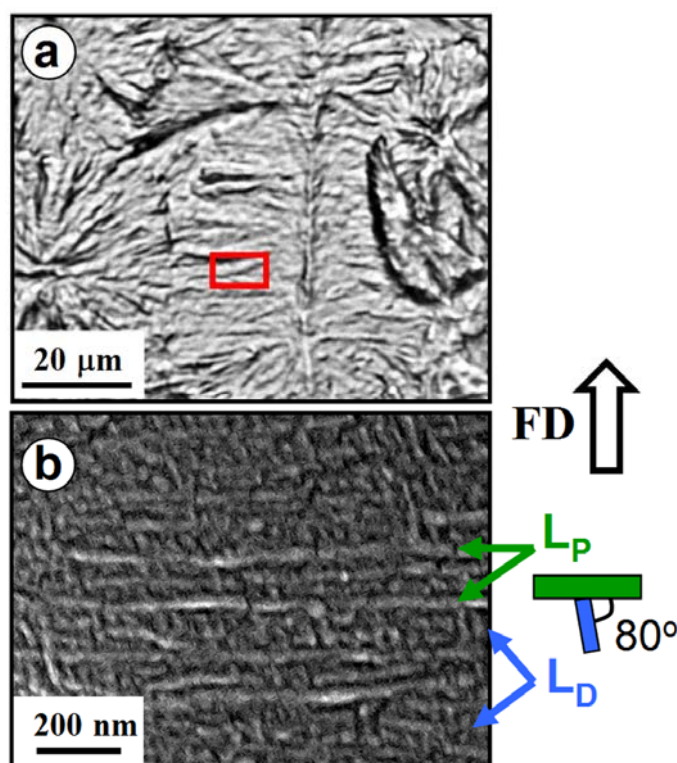


**Figure 4.5.** (a) ROM and (b) SEM images of permanganate etched surfaces. Indicative location of (b) is shown by the small red box in (a) (shear time = 1 s, shear rate =  $80 \text{ s}^{-1}$ , shear temperature =  $135^\circ\text{C}$ ).

SAXS is a widely used and powerful technique to investigate the large scale structures that form in semicrystalline polymers. SAXS experiments were performed to further investigate the morphology of sheared  $\alpha$ -iPP as well as to assess its potential as a tool to follow the individual contributions of PD lamellae during crystallisation and melting. **Figure 4.6a** shows a typical two-dimensional SAXS pattern of a sheared  $\alpha$ -iPP ex-situ sample in the fully crystallised condition. Corresponding one-dimensional azimuthal intensity profiles as function of scattering angle at intervals of  $q = 0.0012 \text{ \AA}^{-1}$  as well as an azimuthal intensity profile averaged between  $0.006 \text{ \AA}^{-1} \leq q \leq 0.05 \text{ \AA}^{-1}$  are shown in **Figure 4.6b** and **Figure 4.6c** respectively. The observed scattering was broadly consistent with the proposed structural model. The model predicts that parent lamellae should scatter along the meridian, while daughter lamellae should scatter in a bimodal distribution either side of the equator. An increase in scattering intensity was indeed

observed in the meridional regions, however instead of the predicted bimodal distribution, a single low intensity broad peak was observed along the equator.

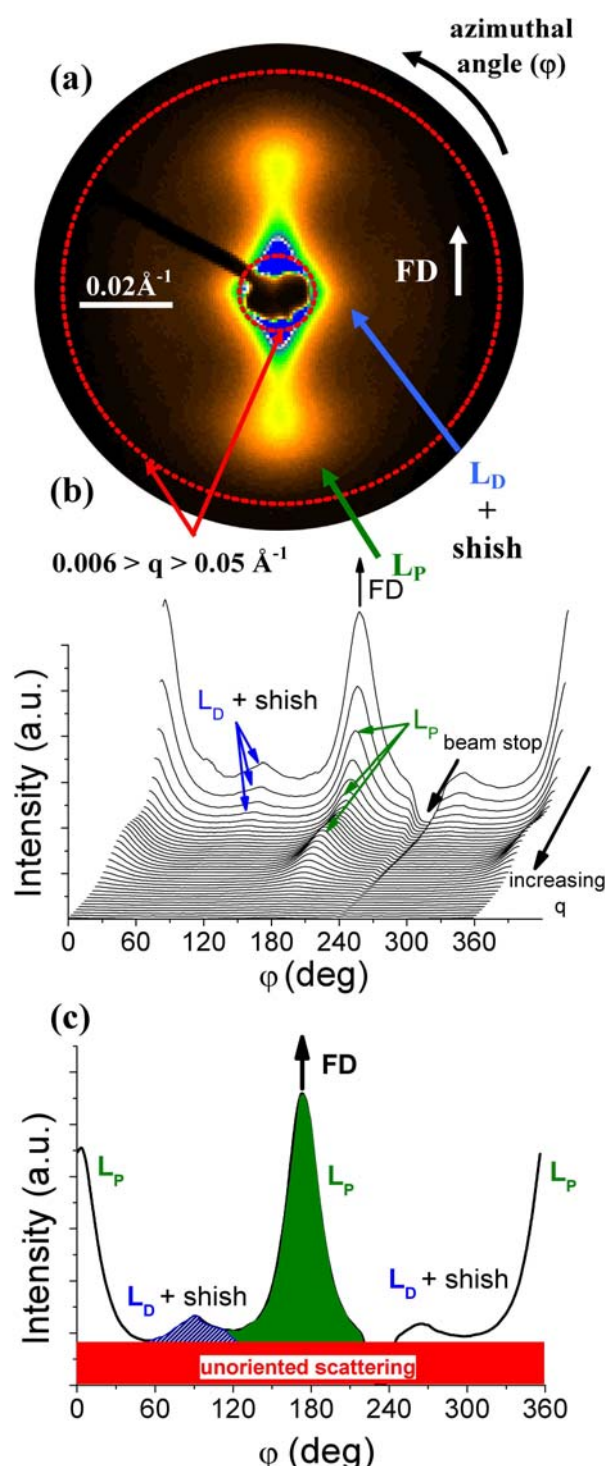


**Figure 4.6.** (a) Typical two-dimensional SAXS pattern of sheared  $\alpha$ -iPP. (b) Corresponding azimuthal intensity profiles at scattering vector intervals of  $q = 0.0012 \text{ \AA}^{-1}$  and (c) average azimuthal intensity profile. The scattering profiles in (b) and (c) are both between the scattering vectors indicated in (a). Oriented parent ( $L_P$ ) and daughter ( $L_D$ ) lamellae (shear time = 1 s, shear rate =  $80 \text{ s}^{-1}$ , shear temperature =  $135 \text{ }^\circ\text{C}$ ).

Possible explanations for the absence of the bimodal distribution could be (a) the low azimuthal resolution of the setup at low  $q$  where the daughter lamellae would scatter leading to one broad peak being observed along the equator and (b) the presence of oriented shish aligned with their long axis along the flow direction, which would also scatter to the equatorial region and contribute to the observed scattering. Although the low azimuthal resolution would not necessarily preclude the use of SAXS to study many aspects of PD lamellar branching, the influence of shish on the observed scattering cannot easily be accounted for. Therefore their presence would make accurate deconvolution of the individual parent and daughter contributions to the two-dimensional SAXS patterns difficult and SAXS was not pursued further.

An in-situ two-dimensional WAXS pattern given the same thermo-shear profile as SAXS pattern is shown in **Figure 4.7a**. The first 5 rings of  $\alpha$ -iPP are clearly visible. The azimuthal angle ( $\varphi$ ) where scattering should occur according to the model described in **Figure 4.4** can be calculated using the method described by Kakudo and Kasai [220]:

$$\cos(\delta) = \cos(\theta)\cos(90 - \varphi) \quad \text{Equation 4.2}$$

where  $\delta$  is the angle the crystalline plane normal makes with the flow direction and  $\theta$  is the Bragg angle. The model correctly predicts broad features of the diffraction pattern. For the  $\alpha(110)$  reflection, parent lamellae should diffract along the equator, while daughters should diffract close to the meridian (as diffraction occurs perpendicular to the  $c$ -axis). According to the proposed model for daughter lamellae,  $\delta_D = 19.7^\circ$  which equates to a predicted  $\varphi_D = 70.7^\circ$ . However, the measured  $\varphi_D$  was closer to  $76^\circ$ . The discrepancy can be explained if the lamellae are assumed to curve. This is discussed in further detail in the next section. For the  $\alpha(040)$  reflection, both parent and daughter lamellae should diffract along the equator, as both their  $b$ -axes are perpendicular to the flow direction. Therefore, due to the clear separation of parent and daughter contributions, the  $\alpha(110)$  reflection is ideally suited to monitor oriented PD lamellae contributions to crystallisation and melting. The scattering around the  $\alpha(110)$  profile can be further deconvoluted to separate out scattering due to the amorphous halo and scattering due to unoriented lamellae ( $L_U$ ). The amorphous contribution to scattering in



this region was estimated by fitting a straight line to the minimum either side of the  $\alpha(110)$  peak in a WAXS intensity profile integrated along  $q$  as shown in **Figure 3.6**. A typical  $\alpha(110)$  azimuthal intensity profile of sheared iPP is shown in **Figure 4.7b**, and highlights the individual  $L_P$ ,  $L_D$  and  $L_U$  contributions as well as the amorphous contribution to the total scattered intensity.

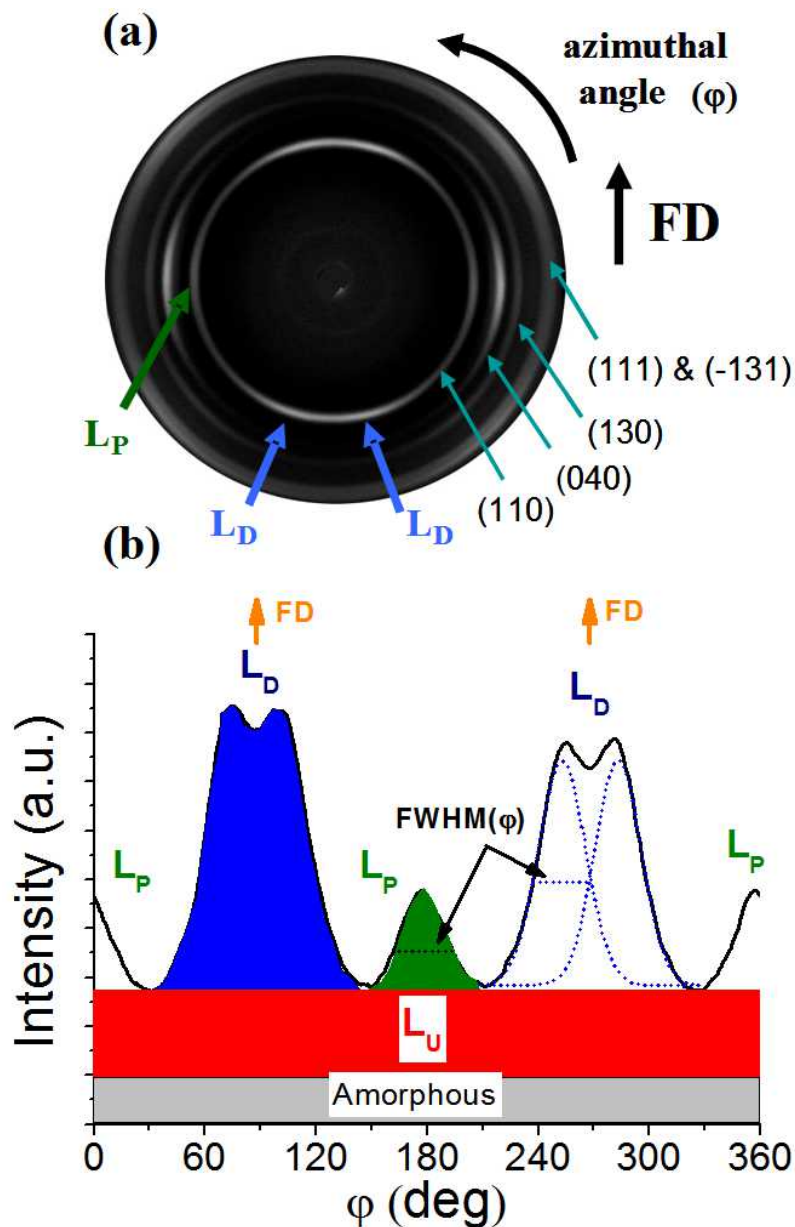


**Figure 4.7.** (a) Typical two-dimensional WAXS patterns and (b) intensity profile as a function of azimuthal angle ( $\phi$ ) for the  $\alpha(110)$  reflection highlighting the contribution of oriented parent ( $L_P$ ), daughter ( $L_D$ ) lamellae and unoriented ( $L_U$ ) lamellae as well as the amorphous region (shear time = 1 s, shear rate =  $80 \text{ s}^{-1}$ , shear temperature =  $135 \text{ }^\circ\text{C}$ ).

An idea of the relative concentration of the daughter lamellae ([D]) can be obtained by calculating the ratio of the integrated intensity under the (110) reflection according to the following equation [133]:

$$[D] = \frac{L_D}{L_D + L_P} \quad \text{Equation 4.3}$$

This analysis does not provide an absolute concentration value [221] but rather can be used to indicate the change in relative concentration.

### 4.3.3 Crystallisation of sheared iPP

Although the structure of PD lamellae has been widely studied in a range of ex-situ samples, the crystallisation of PD lamellae under conditions typical of industrial processes has received comparatively little attention. Industrial processes such as injection moulding lead to large shear gradients throughout the part. These greatly complicate crystallisation kinetics and the subsequent development of morphology when compared to quiescent conditions. In this section the growth of oriented PD lamellae will be characterised in-situ during isothermal crystallisation after the application of a moderate step shear.

**Figure 4.8** shows a birds eye view of the changes that occur to the WAXS intensity profile along the scattering vector as well as the azimuthal intensity profile of the  $\alpha(110)$  peak during crystallisation after a step shear for 1 s at a shear rate  $80 \text{ s}^{-1}$ . Before the step shear no crystallinity and no azimuthal dependence of intensity were observed. In the first exposure after the application of the step shear ( $\sim 15 \text{ s}$  after the step shear), crystallisation had begun as shown by the formation of the characteristic  $\alpha$ -iPP peaks. Crystallisation quickly progressed and reached saturation  $\sim 200 \text{ s}$  after the step shear. At the early stage of crystallisation the azimuthal intensity profile of the  $\alpha(110)$  peak took on the characteristic appearance of the oriented PD structure described previously. The ratio of the height of parent to daughter lamellae was significantly more at the early stages compared to the later stages of crystallisation. This confirms that parent lamellae form before daughter lamellae.



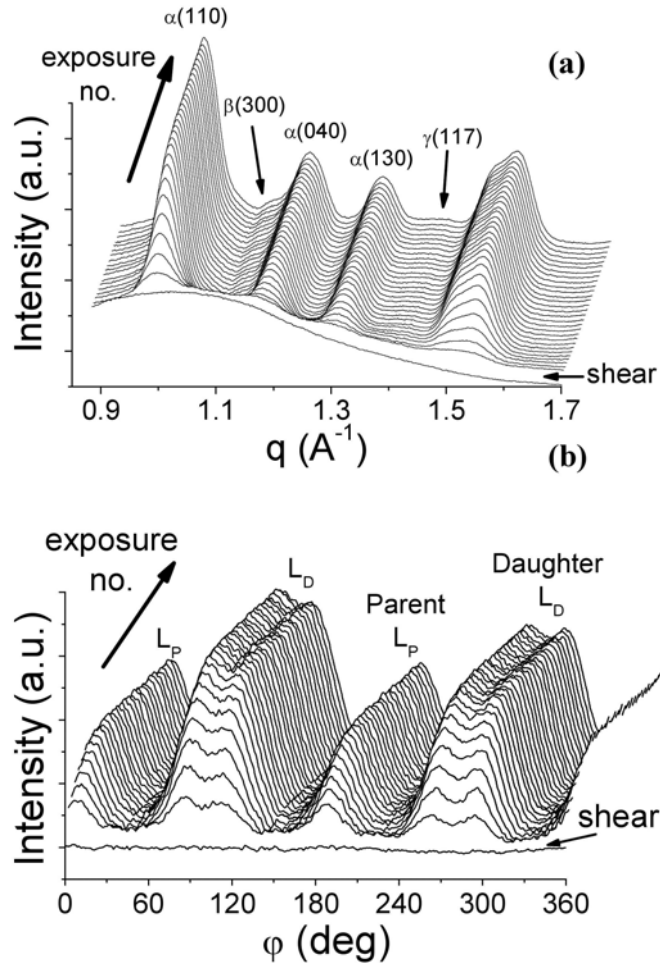


**Figure 4.8.** Bird's eye view of the changes that occur to (a) the WAXS intensity profile ( $q$ ) and (b) the azimuthal ( $\phi$ ) intensity profile of the  $\alpha(110)$  reflection during crystallisation (shear time = 1 s, shear rate =  $80 \text{ s}^{-1}$ , shear temperature =  $135^\circ\text{C}$ ).

The kinetics of crystallisation were further probed by plotting the relative proportion of the parameters:  $\chi_v$ ,  $L_P$ ,  $L_D$ ,  $L_U$  defined by the ratio ( $\chi_{rel}$ ) against time:

$$\chi_{rel} = \frac{Q(t)}{Q(\infty)} \quad \text{Equation 4.4}$$

where  $Q(t)$  is the instantaneous and  $Q(\infty)$  is the final value of the parameter in the fully crystallised conditions. Quantitative information about the crystallisation kinetics and growth geometry were obtained by fitting the crystallisation data to the Avrami model:

$$1 - \chi_{rel} = e^{-kt^n} \quad \text{Equation 2.6}$$

where  $k$  is the bulk crystallisation constant and  $n$  is the Avrami exponent. The crystallisation half time ( $t_{0.5}$ ) was taken as the time at which the model line intersected  $\chi_{rel} = 0.5$ . The assumption used in this analysis is that the measured parameters derived from the reflected intensity, (i.e.  $Q(t)$  and  $Q(\infty)$ ) are linearly proportional to the actual volume fraction of the parameter. The results are shown in **Figure 4.9**. Reasonably good fits were obtained for all parameters emphasising the general applicability of the model to all lamellae contributions to the total crystallinity. The analysis also demonstrates that the oriented PD lamellae form well before the unoriented lamellae.

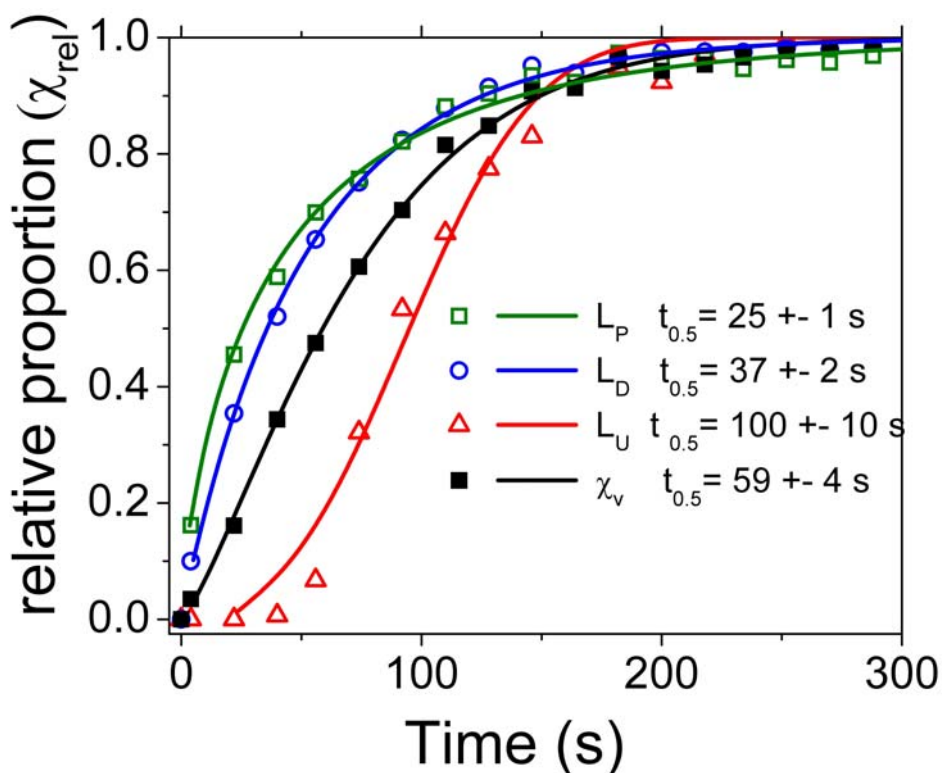


**Figure 4.9.** Relative proportion ( $\chi_{rel}$ ) of the parent ( $L_P$ ), daughter ( $L_D$ ), unoriented ( $L_U$ ) lamellae contributions to total crystalline scattering ( $\chi_v$ ) during the initial stages of crystallisation (shear time = 1 s, shear rate =  $80 \text{ s}^{-1}$ , shear temperature =  $135 \text{ }^\circ\text{C}$ ).

The Avrami exponent can give important information about the crystallisation conditions. The Avrami exponent was determined in the primary crystallisation region from the gradient of the linear region of a plot of  $\ln(\ln(1/1 - \chi_{rel}))$  versus  $\ln(t)$ . At low conversions there is a significant uncertainty in determining  $\chi_{rel}$ . Significant deviation from the model also occurs in the latter stages of crystallisation which has been attributed to the occurrence of secondary crystallisation [222]. Therefore the Avrami

exponent was determined by fitting a straight line to the linear region between these two extremes. The Avrami exponent in this way contains information about both nucleation and growth conditions. In heterogeneous nucleation where crystal growth is not diffusion controlled, the Avrami exponent is related to the dimension of crystal growth: with  $n = 3$  indicating spherical growth,  $n = 2$  indicating disk-like growth and  $n = 1$  indicating rod-like growth. Furthermore, if growth is controlled by the diffusion of chain segments to the lamellae growth front then the crystal growth rate should be proportional to the square root of time [99]. This has been shown to lead to Avrami exponents which are less than 1 [223-224]. Often non-integer values of the Avrami exponent are obtained which can indicate the presence of more than one growth geometry during crystallisation. The results of this analysis are shown in **Figure 4.10**.

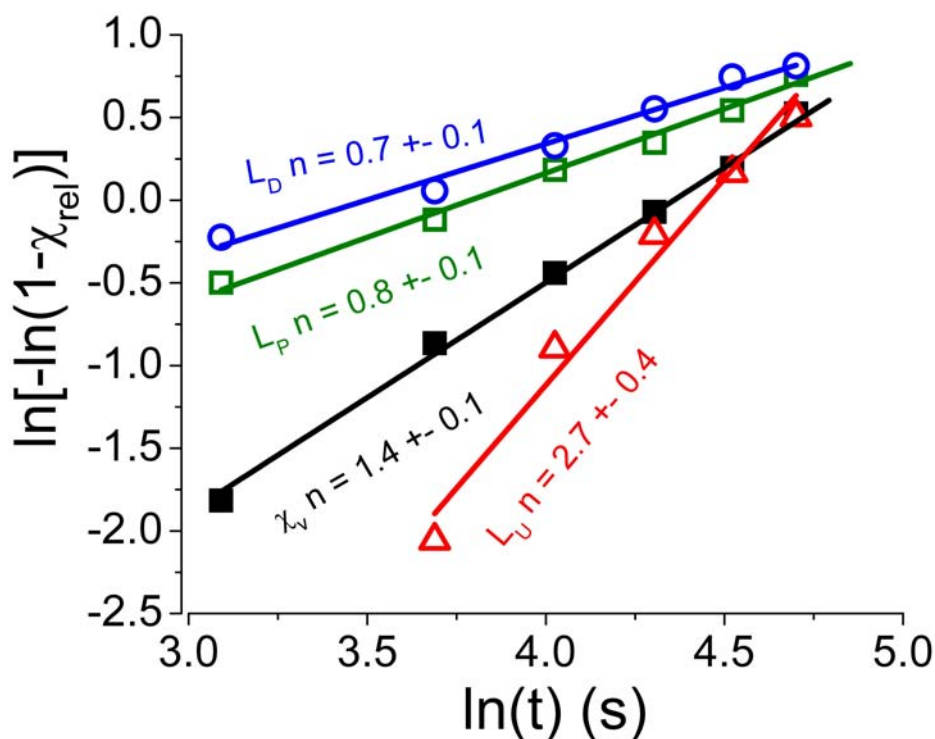


**Figure 4.10.** Avrami plots of the crystallisation data and corresponding Avrami exponent ( $n$ ) for parent ( $L_P$ ), daughter ( $L_D$ ) and unoriented ( $L_U$ ) lamellae and for total crystallinity ( $\chi_v$ ) (shear time = 1 s, shear rate =  $80 \text{ s}^{-1}$ , shear temperature =  $135 \text{ }^\circ\text{C}$ ).

The unoriented lamellae had an Avrami exponent of  $2.7 \pm 0.4$  which indicates they grew in an almost spherical way. This result is consistent with the unoriented lamellae being mainly in the small spherulites observed in **Figure 4.5**, which would show three dimensional growth characteristics. The Avrami exponent of the oriented PD lamellae was significantly less than 1. This demonstrates both oriented parent and daughter

lamellae growth is highly constrained suggesting athermal nucleation conditions and diffusion controlled growth of lamellae. Similar results have been obtained from rheo-SAXS experiments which investigate the early growth of kebabs [99, 225]. Daughter lamellae ( $n = 0.7 \pm 0.1$ ) were found to have a slightly smaller Avrami exponent than parent lamellae ( $n = 0.8 \pm 0.1$ ) illustrating their growth is somewhat more constrained. Constraint in this case could be due to a combination of (a) the reduced diffusion of chains segments to the crystal growth front from chains also being incorporated in neighbouring lamellae and (b) from microstructural constraint caused by the impingement of neighbouring lamellae. The Avrami exponent determined for  $\chi_v$  was  $1.4 \pm 0.1$  and represents an average of unoriented and oriented lamellae growth.

The growth of PD lamellae during primary crystallisation was further investigated by plotting the full width at half maximum of the parent, daughter and unoriented lamellae contributions to the  $\alpha(110)$  peak along the scattering vector (FWHM(q)), **Figure 4.11a**. Sectors of  $10^\circ$  width in the azimuthal direction and centred at  $0^\circ$  for parent,  $76^\circ$  for daughter and  $37^\circ$  for unoriented lamellae were used for the analysis. According to **Equation 3.10** the FWHM(q) of the x-ray reflection from a crystal plane is inversely proportional to the number of periodic planes, which is approximated as the crystal size in the direction normal to the corresponding plane. Therefore the FWHM(q) can give an indication of the thickness of lamellae during crystallisation. During the early stages of crystallisation ( $<100$  s) the FWHM(q) of all lamellae decrease rapidly showing that as crystallisation progressed the thickness of the lamellae increased substantially. This demonstrates that lamellae thickening along the chain fold direction is an important growth mechanism at the early stages of crystallisation. The final FWHM(q) of the three lamellae indicated that unoriented lamellae are thinner than daughter lamella which are thinner than parent lamellae. The full width at half maximum of the parent and daughter contributions to the  $\alpha(110)$  can also be probed during crystallisation along the azimuthal angle (FWHM( $\phi$ )), **Figure 4.11b**. The FWHM( $\phi$ ) gives information about the angular dispersion of the crystallites, with a higher FWHM( $\phi$ ) indicating a larger angular spread. As crystallisation progressed, the FWHM( $\phi$ ) of both parent and daughter lamellae increased. This can be explained by curving and twisting of lamellae as they grow. Further information about the curvature of daughter lamellae as they grow can be obtained by comparing the observed scattering angle with the angle where scattering

should occur according to **Equation 4.2** and the structural model presented in **Figure 4.4**. The results are presented in **Figure 4.11c** and show  $\varphi_D$  increased rapidly from the model predicted value of  $70.7^\circ$  during the initial stages of crystallisation before reaching an equilibrium value. The increase in the observed scattering angle shows the planes of daughter lamellae curve towards the flow direction as they grow, further indicating highly constrained growth of daughter lamellae.

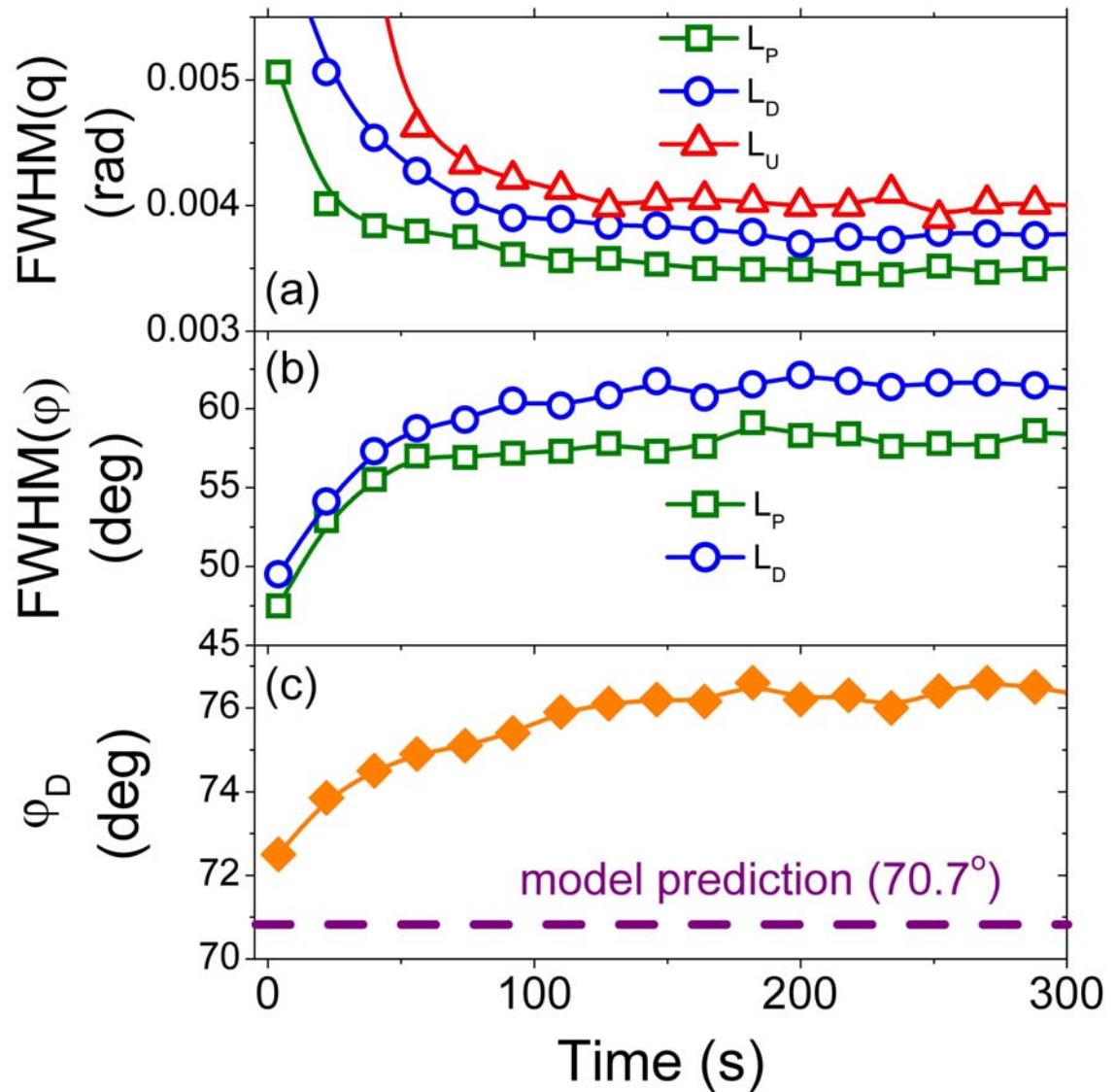


**Figure 4.11.** (a) Full width at half maximum of the  $\alpha(110)$  reflection along scattering angle (b) along the azimuthal angle FWHM( $\varphi$ ) highlighting individual contributions from parent, ( $L_P$ ) daughter, ( $L_D$ ) and unoriented ( $L_U$ ) lamellae. (c) The azimuthal angle daughter lamellae scatter to ( $\varphi_D$ ) on the  $\alpha(110)$  reflection as a function of time during the initial stages of crystallisation (shear time = 1 s, shear rate =  $80 \text{ s}^{-1}$ , shear temperature =  $135^\circ\text{C}$ ).

#### 4.3.4 Melting of sheared iPP

Further information may be obtained about the oriented PD structure during melting. In particular multiple melting peaks are often observed in the DSC thermograms of sheared iPP, however their origin is uncertain. In this section the oriented PD structure is investigated during a simulated DSC melting cycle.

DSC melting thermograms of the sheared samples are shown in **Figure 4.12**. In the sample crystallised in the absence of shear flow, appreciable melting was observed to begin around 160 °C, peaking in a broad single peak centred at 175.0 °C. Increasing the shear rate up to 20 s<sup>-1</sup> decreased the peak position and also resulted in the peak becoming narrower. At 30 s<sup>-1</sup> a bimodal distribution of melting temperatures was observed by the high temperature peak centred at 169.4 °C and the lower temperature peak centred at 165.0 °C. At this shear rate the formation of oriented structures were observed by both ROM and WAXS measurements. Increasing the shear rate above 30 s<sup>-1</sup> resulted in a steady increase in both peak temperatures, but particularly the high temperature peak. Additionally, the relative size of the lower temperature peak increased with respect to the high temperature peak with increasing shear rate.

In-situ melting of a sheared iPP sample under the same nominal conditions as the DSC experiments was then performed. The temperature dependence of the  $\alpha(110)$  azimuthal intensity profile during melting is shown in **Figure 4.13**. Initially increasing temperature led to a decrease in the intensity from daughter lamellae while the intensity from parent lamellae stayed relatively constant. It was not until a temperature of 173°C that the intensity from the parent lamellae began to decrease appreciably. At this stage the peak heights of both daughter and parent lamellae were roughly similar. The relative amount of daughter lamellae during this period was determined (**Figure 4.14a**) and clearly demonstrates that daughter lamellae melt before parent lamellae. During melting the angle daughter lamellae scatter to on the  $\alpha(110)$  was observed to decrease approaching the model value of 70.7° , **Figure 4.14b**. This last point again indicates that the daughter lamellae curve and get thinner as they grow away from their parent lamellae. In this case melting occurs at the extremities first, progressing at higher temperatures toward their parent lamellae.

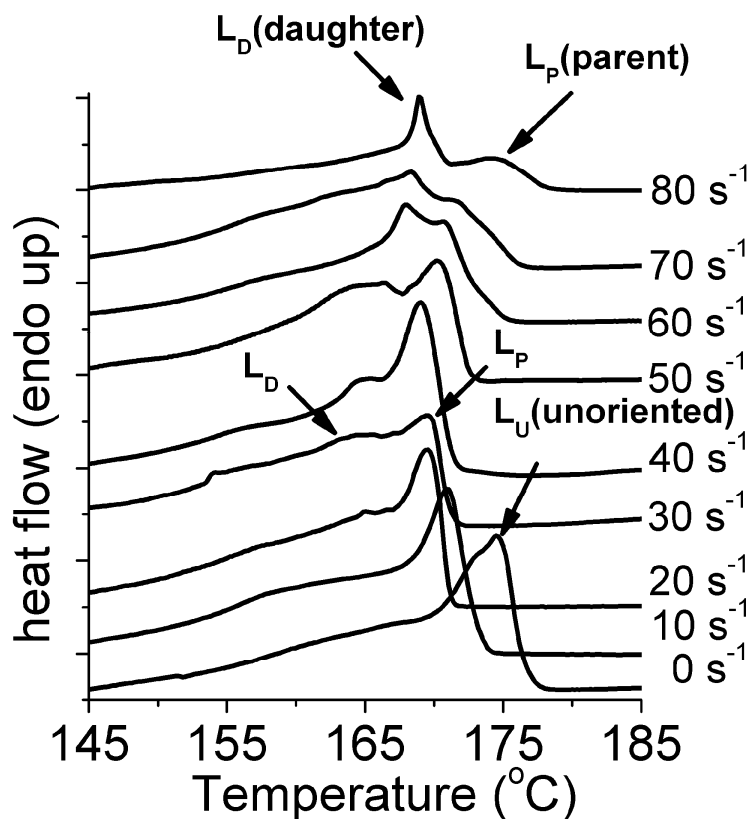


**Figure 4.12.** Melting DSC thermograms of samples subjected to shear rates between 0-80 s<sup>-1</sup>. Heating rate is 0.17 °C/s.

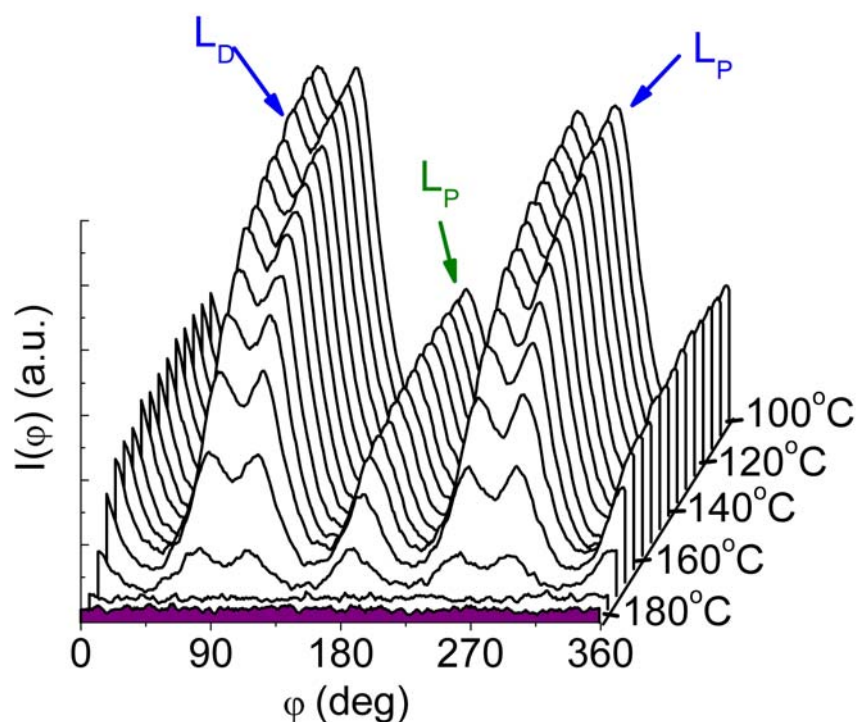


**Figure 4.13.** Intensity for the (110) reflection  $I(\phi)$  as a function of azimuthal angle ( $\phi$ ) during melting of a previously sheared sample (shear time = 1 s, shear rate = 80 s<sup>-1</sup>, shear temperature = 135 °C, heating rate = 0.17 °C/s).

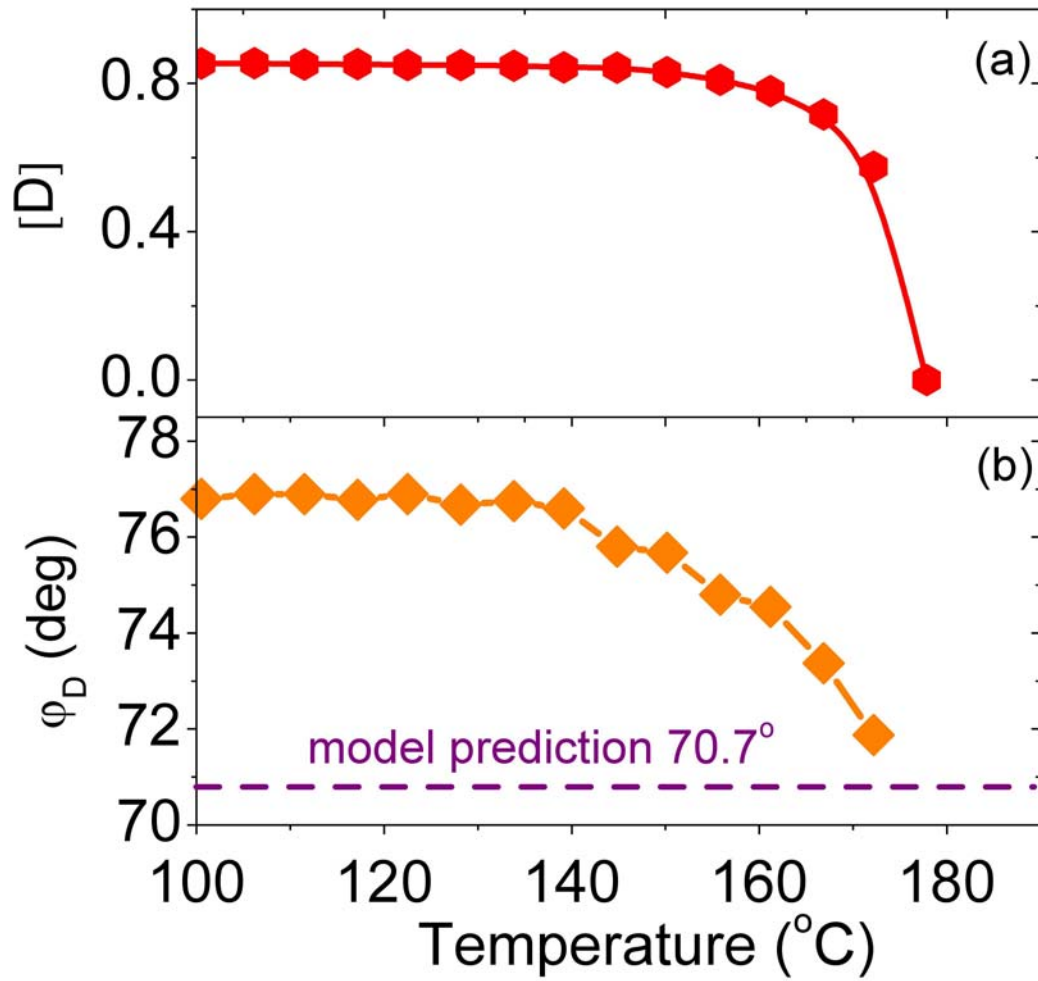


**Figure 4.14.** (a) The relative concentration of oriented daughter lamellae ( $[D]$ ) and (b) The azimuthal angle daughter lamellae scatter to ( $\phi_D$ ) on the  $\alpha(110)$  reflection during the melting of a previously sheared sample (shear time = 1 s, shear rate =  $80 \text{ s}^{-1}$ , shear temperature =  $135 \text{ }^\circ\text{C}$ , heating rate =  $0.17 \text{ }^\circ\text{C/s}$ ).



## 4.4.0 Discussion

### 4.4.1 Updated flow-induced crystallisation model of $\alpha$ -iPP

The information presented in this chapter can now be used to update the PD branching contribution to the flow-induced crystallisation model for iPP, **Figure 4.15**. Parent lamellae radiate out from the central shish much like a flattened spherulite. Growth occurs primarily along the  $a^*$ -axis, resulting in individual lamellae being much longer than they are thick. Similarly, daughter lamellae grow from the parent lamellae with their initial growth rate being much faster along the  $a^*$ -axis direction than any other, however due to their sequential formation which results in reduced diffusion of chains to the crystal growth front from chains being also incorporated into nearby lamellae, the daughter lamellae are thinner and less perfect than parent lamellae. Due to impingement on adjacent parent lamellae, daughter lamellae are not as long as parent lamellae. As the daughter lamellae grow they curve towards the flow direction. It is thought that this occurs due to the influence of adjacent daughter lamellae which confine their growth direction. Such confinement-induced orientation has previously been observed in polymer crystallising between inorganic fibres [221, 226] or in narrow epoxy channels [227]. Amorphous and tie chains fill the space between the crystalline regions leading to the formation of the tight interlocking PD structure.

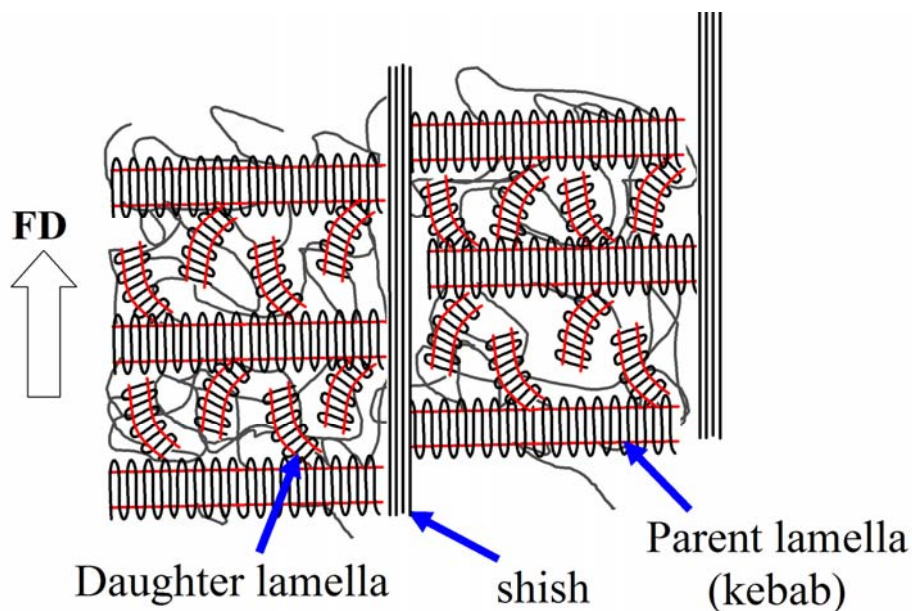


**Figure 4.15.** Updated flow-induced crystallisation model for iPP. Orientation relationship between parent and daughter lamellae illustrated in **Figure 4.4**.

#### 4.4.2 Thermal stability of sheared iPP

Multiple melting peaks are often observed in the DSC melting thermograms of sheared iPP. A likely explanation is that the thinner daughter lamellae melt at a lower temperature than the parent lamellae. Experimental evidence supporting the lower thermal stability of daughter lamellae has been gained mainly in samples crystallised under quiescent conditions which are composed predominantly of spherulites. For example by: transmission electron microscopy (TEM) measurements of the lamellar thickness of fully crystallised material [126] and partially melted samples [125, 127] and birefringence measurements made during the melting of spherulites [128]. These experiments are complicated by the unique PD structure which leads to the thickness of radial parent lamellae becoming thicker with increasing distance from the core of  $\alpha$ -iPP spherulite [125]. This is thought to be due to the morphological constraint from the relatively higher number of branched lamellae suppressing thickening of the radial parent lamellae towards the core of the spherulite, as shown schematically in **Figure 4.16**. Nevertheless, multiple melting peaks are not uncommon in the DSC thermographs of iPP and their occurrence has been explained by a number of other different competing processes. For instance: different crystalline phases [228-229], recrystallisation [180, 216, 230] and differences in crystal perfection / thicknesses [127, 231]. Recently, Wang et al. investigated the melting behaviour of PD lamellae in thin films in-situ using environmental atomic force microscopy (AFM) [130]. They concluded that PD lamellae essentially formed and melted at the same time and multiple melting was due to recrystallisation phenomenon. However, the long time between images ( $\sim 30$  minutes) would have substantially limited the selectivity of their experiment. In this section the relative thermal stability of the oriented PD lamellae will be determined to show the multiple melting peaks observed in the melting curves of sheared iPP are due to the oriented PD lamellar structure. The assignment of the peaks will then be used to determine the influence of shear rate on lamellar thickness.

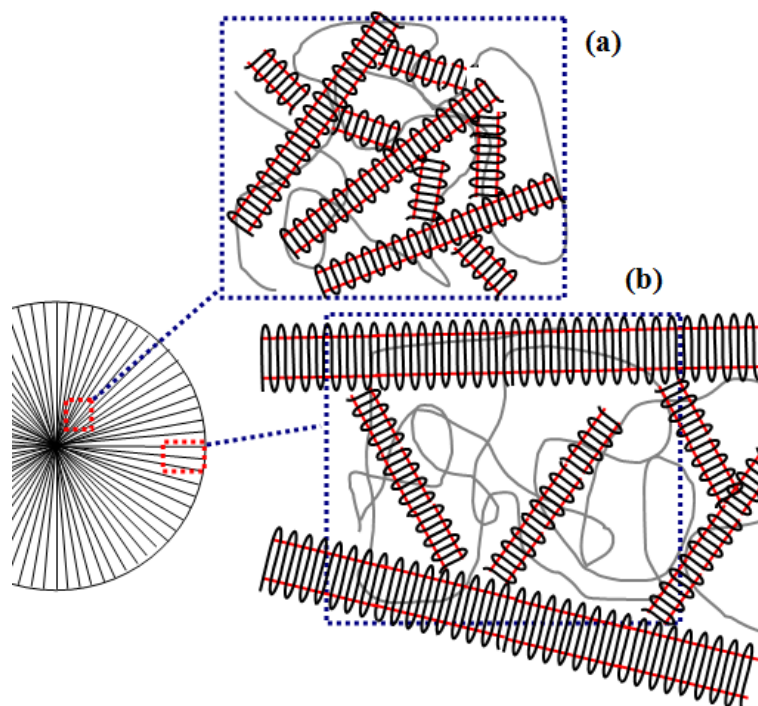


**Figure 4.16.** Schematic diagram of an iPP spherulite showing a) impingement of tangential (daughter) lamellae restricting the isothermal thickening of the radial (parent) lamellae in the centre region of the spherulite and b) the outer region of the spherulite where considerably greater thickening can take place before impingement of tangential lamellae occurs.

Clearly the DSC melting curves presented in **Figure 4.12** are greatly complicated under SIC conditions. Using the unique evidence provided by the in-situ time resolved rheo-WAXS technique the origin of the two melting peaks observed in the DSC thermograms can now be determined. **Figure 4.17** shows the DSC curve at the highest shear rate of  $80 \text{ s}^{-1}$  plotted on the same curve as the relative proportion of the different contributions to the total crystallinity. The volume fractions of both  $\beta$ -iPP and  $\gamma$ -iPP were small with  $\chi_b = 0.02$  and  $\chi_\gamma = 0.08$  and therefore these would be unlikely to account for the observed multiple melting behaviour. Furthermore, both  $\beta$ -iPP and  $\gamma$ -iPP melted well before the low temperature peak and therefore melting by  $\beta$ -iPP or  $\gamma$ -iPP can be ruled out. The smooth drop in the relative proportion of total crystallinity suggests recrystallisation processes are not occurring to a significant extent in this experiment. Unoriented lamellae melted at too low a temperature are therefore also unable to account for the observed multiple melting behaviour. Daughter lamellae however, can clearly be seen to melt at a lower temperature than parent lamellae. In addition, the

melting temperature of PD lamellae observed by WAXS closely corresponds to the melting temperature observed by DSC. This demonstrates that the bimodal distribution observed in the sheared DSC curves above  $30 \text{ s}^{-1}$  arises from two different populations of lamellar thickness. In this case the thicker parent lamellae give rise to the high temperature peak and the thinner daughter lamellae give rise to the low temperature peak.

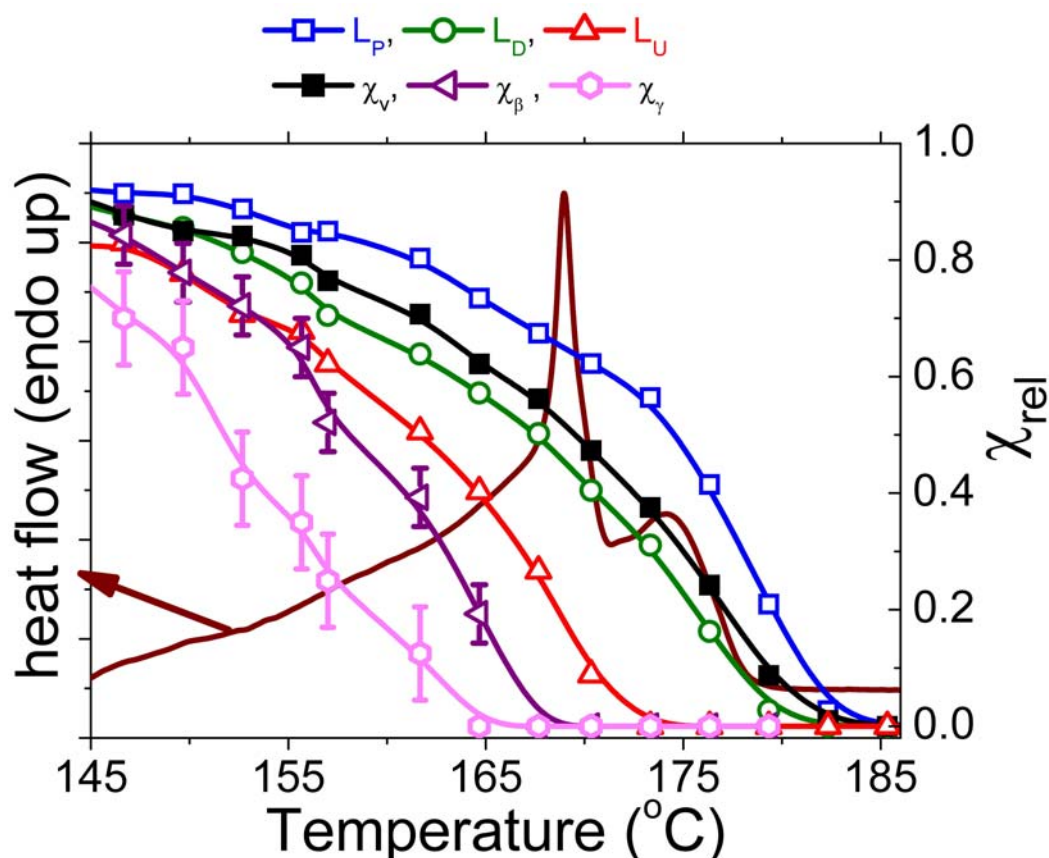


**Figure 4.17.** Overlay of DSC thermogram with the relative proportion ( $\chi_{rel}$ ) of the various contributions to the total crystallinity ( $\chi_v$ ) determined from the WAXS patterns during melting of a previously sheared sample. Parent ( $L_P$ ), daughter ( $L_D$ ), unoriented ( $L_U$ ) lamellae,  $\beta$ -iPP crystallinity ( $\chi_\beta$ ),  $\gamma$ -iPP crystallinity ( $\chi_\gamma$ ) (shear time = 1 s, shear rate =  $80 \text{ s}^{-1}$ , shear temperature =  $135 \text{ °C}$ , heating rate =  $0.17 \text{ °C/s}$ ).

The clear bimodal distribution of lamellar thickness observed at shear rates greater than  $30 \text{ s}^{-1}$  is at odds with what is observed in samples crystallised below  $30 \text{ s}^{-1}$  where a single broad peak is observed. This can be explained by the unique structure of the  $\alpha$ -iPP spherulites which leads to an increase in the lamellar thickness of radial parent lamellae with increasing distance from the spherulite core as previously explained. The

effect is evident in the lower shear rate DSC thermograms presented in **Figure 4.12** (0-30 s<sup>-1</sup>) which show a decrease in the peak position and therefore the average lamellar thickness with increasing shear rate. It is well known that shear flow will increase the average number of nucleation sites [7, 232] thereby decreasing the spherulite size obtained. This would result in a narrowing of the difference in lamellar thickness in the spherulite morphology and therefore the lamellar distribution for parent and daughter lamellae essentially overlap, leading to one peak being observed in the DSC thermograms. As will be shown in **Chapter 6**, a shear rate of 30 s<sup>-1</sup> is the minimum necessary to induce shish under these conditions. The formation of shish then results in a substantially different geometrical arrangement of the crystallites and it is this that allows the parent lamellae to thicken relatively unhindered resulting in the observed difference in melting point.

Now that the origin of the two melting peaks observed by DSC has been confirmed, the measured peak melting temperature can be used to separate the influence of shear rate on the individual PD lamellar thickness for shear rates greater than 30 s<sup>-1</sup> using **Equation 4.1**. The results from this analysis are shown in **Figure 4.18** and are compared to the lamellar thickness determined from WAXS using **Equation 3.10** and SEM. Although the overall trends were the same between the different experimental approaches, a difference in the magnitude of the lamellae thickness between the different techniques was observed. However, this discrepancy is not unexpected due to the different theoretical approaches used in each to estimate lamellar thickness. The results show that up to a shear rate of 30 s<sup>-1</sup> the lamellar thickness decreased in line with the decrease in the spherulite size as described previously. Above a shear rate of 30 s<sup>-1</sup> the parent lamellae were found to thicken more readily than daughter lamellae, particularly at the higher shear rates. From a thermodynamic stand point this is unexpected as an increase in the free energy would increase the degree of under-cooling achieved and according to **Equation 4.1** the lamellae thickness should decrease. However, it is believed that the results can be explained by a mechanistic argument. The increase in shear rate leads to an increase in the number of suitably oriented chain segments aligned along the flow direction. This should not only increase the lamellar thickness but also would lead to increased crystal perfection by increasing the diffusion of chain segments to the crystal growth front. Similar anisotropic behaviour of crystal growth has recently been observed during isothermal crystallisation in the presence of a

flow field [233]. It is unclear at this stage why the thickness of the daughter lamellae also increased slightly with increasing shear rate, though the observed change is small and could possibly be accounted for by experimental uncertainty.

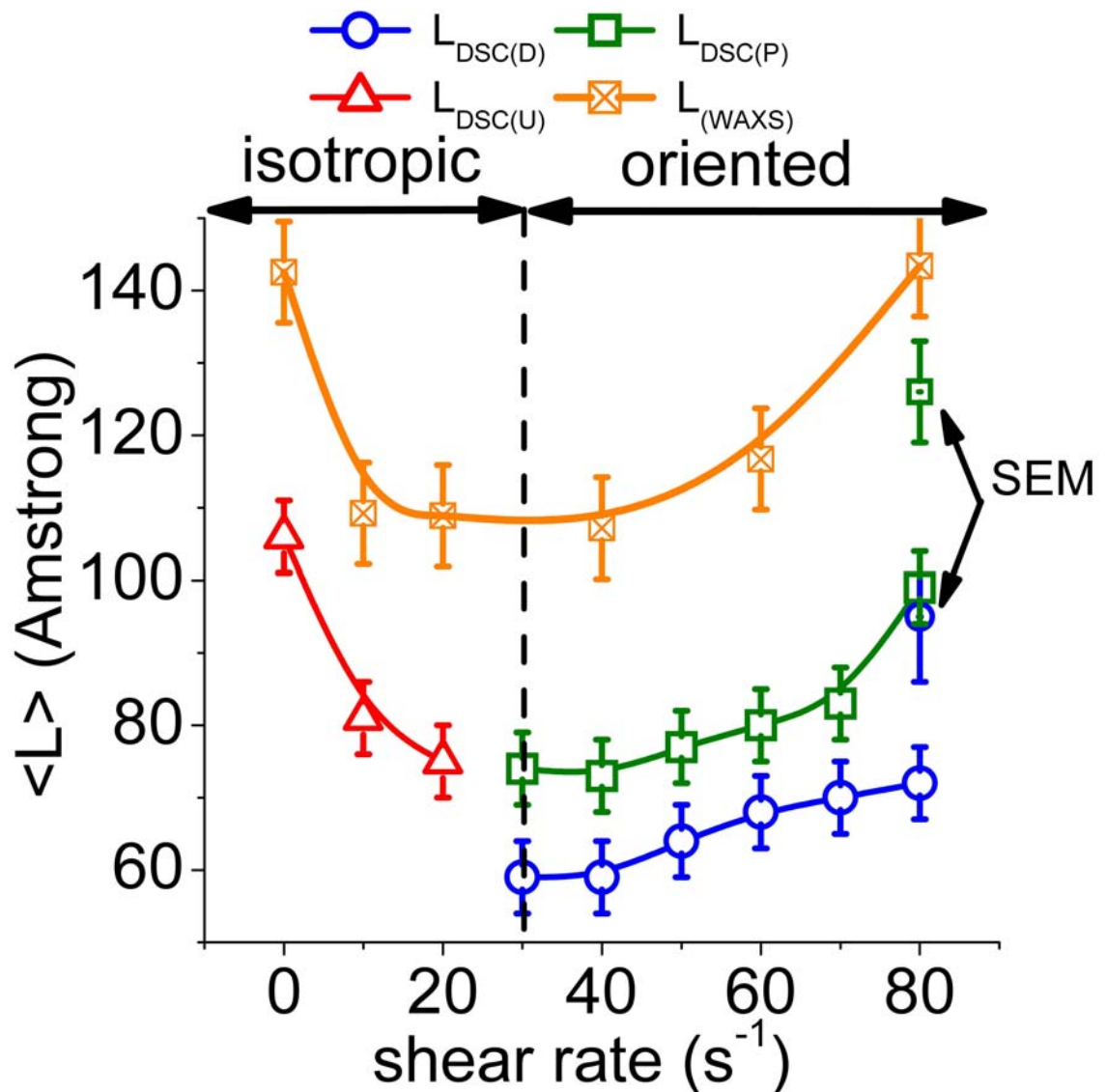


**Figure 4.18.** Average lamellar thickness as a function of shear rate calculated using the Thompson-Gibbs equation of the melting peaks depicted in **Figure 4.12** along with the lamellar thickness calculated using the Scherrer equation and by SEM.

#### 4.5.0 Conclusions

A simple procedure was developed that allowed the individual contributions from parent and daughter (PD) lamellae to be probed using wide angle x-ray scattering (WAXS). The contribution of oriented PD lamellae to the crystallisation, and melting of sheared  $\alpha$ -iPP was then characterised using time resolved rheo-WAXS. The findings from this chapter are briefly summarised as follows.

During crystallisation oriented parent lamellae were observed to form before daughter lamellae consistent with the long held view on their epitaxial nucleation mechanism. Growth of both oriented PD lamellae was highly constrained, indicating athermal nucleation and diffusion controlled growth conditions. Furthermore, the planes of the daughter lamellae were found to curve toward the flow direction with increasing distance from their parent lamellae. The direction of curvature was explained by the influence of adjacent daughter lamellae confining their grow direction.

Along with their growth being more constrained than parent lamellae during isothermal crystallisation, the daughter lamellae were also observed to melt at a lower temperature due to them being thinner and/or less perfect than parent lamellae. These differences are thought to arise from their sequential formation which results in reduced diffusion of chains to the crystal growth front due to chains being also incorporated into nearby lamellae. The difference in parent and daughter lamellar thickness / perfection was then used to assign the multiple melting behaviour observed in the DSC thermograms.

A U-shaped dependence of lamellar thickness was observed with increasing shear rate and was explained by changes that occurred to the morphology above and below the transition to an oriented structure at a shear rate of  $\sim 30 \text{ s}^{-1}$ . Below  $30 \text{ s}^{-1}$  the decreased in lamellar thickness was related to the decrease in spherulite size, consistent with the unique behaviour of  $\alpha$ iPP spherulite in which the radial lamellae are thicker with increasing distance from the core of the spherulites. Above  $30 \text{ s}^{-1}$  the increase in lamellar thickness was thought to be due to the increase in the number of suitably oriented extended chain segments aligned along the flow direction prior to the onset of crystallisation increasing the diffusion of chain segments to the crystal growth front.

## Chapter 5

### Polystyrene as a versatile nucleating agent for polypropylene

#### 5.1.0 Introduction

Natta and Corfidini showed that the usual crystal form of isotactic polypropylene (iPP) has each polymer molecule arranged as a  $3_1$  helix [120]. The helix is chiral and can exist in either the right or left hand configuration. This chirality allows for four different crystalline phases:  $\alpha$ -iPP (monoclinic) [120],  $\beta$ -iPP (trigonal) [137, 140-141],  $\gamma$ -iPP (orthorhombic) [154] and the mesomorphic smectic-iPP [120].  $\alpha$ -iPP is by far the most common and occurs under a wide variety of crystallisation conditions.  $\beta$ -iPP has received considerable attention due to its promising mechanical properties, such as improved fracture toughness and elongation at break [151, 187]. However,  $\beta$ -iPP is thermodynamically less stable and is therefore more difficult to obtain under conditions typically found in industrial processes.

Numerous methods have been developed to produce significant quantities of  $\beta$ -iPP such as: crystallisation in a temperature gradient [142]; flow-induced crystallisation [143-147], particularly in oscillation mode [42, 148-149]; and by the addition of specific  $\beta$ -iPP nucleating agents [42-48]. Of these methods, large fractions of  $\beta$ -iPP are most easily attained by the addition of specific  $\beta$ -iPP nucleating agents. Historically these agents have been derived from low molecular weight crystallisable compounds, which can broadly be divided into two categories. The first category includes aromatic compounds such as  $\gamma$ -quinacridone [45] (Red Pigment E3B), while the second category includes compounds derived from group IIA metal salts such as lanthanum carbide (LaC) and calcium carbonate ( $\text{CaCO}_3$ ) [43] and Ca salts of pimelic and suberic acid [44]. The selectivity of these agents can be described by a *two dimensional lattice matching theory* [76-78, 234]. Central to this theory is that a reasonable epitaxial match, at least within 10%, exists between the repeat distance in the iPP unit cell and the corresponding nucleating surface. Recently, two amorphous polymeric nucleating agents, styrene acrylonitrile (SAN) and polystyrene (PS) were shown to also selectively nucleate  $\beta$ -iPP [47-48]. However, it is unclear how an epitaxial theory could explain the nucleation mechanism of these amorphous polymers. These polymeric nucleating



agents have the advantage of being relatively cheap and easy to process and therefore show good commercial potential. However, any explanation for the nucleation mechanism of these amorphous polymers is at best tentative.

The methyl groups of the iPP would most likely interact with the phenyl groups of PS [234] and therefore the arrangement of the phenyl groups would be important to understanding any epitaxial relationship between the two. The structure of amorphous polystyrene has been extensively studied [198, 235-240]. The most comprehensive model proposed to date shows the phenyl groups micro-segregate into stacks [240]. Although the stacks are disordered, the phenyls within the stacks not only show significant positional registration with neighbouring phenyls within the same stack but neighbouring stacks show also significant positional registration with each other. The repeat distance between adjacent phenyl groups in the same stack is  $\sim 5$  Å. Isotactic polystyrene (iPS), being a stereoregular polymer, allows the iPS molecules to crystallise in the form of a  $3_1$  helix [199]. Micro-segregation of the phenyls into regular stacks is also a feature of crystalline iPS, with the repeat distance between adjacent phenyl groups within each stack being 6.65 Å. If epitaxy is significant, the change in the arrangement of phenyls between the amorphous and crystalline states of iPS should lead to a change in iPP crystallisation behaviour. Accordingly, in this chapter the morphology of iPS particles embedded in an iPP matrix were varied to be either semicrystalline (iPS<sub>crystalline</sub>) or amorphous (iPS<sub>amorphous</sub>) and their influence on the isothermal quiescent crystallisation of iPP was then studied.

Shearing the melt prior to the onset of crystallisation further complicates the crystallisation of iPP in the presence of nucleating agents. Most importantly shear flow increases the number of flow-induced point and thread-like (shish) nuclei which can increase crystallisation kinetics as well as template the formation of oriented crystalline and lamellar structures [8-17]. The addition of a variety of nucleating agents has been found to increase the density of shish for a given set of crystallisation conditions [241] and it is suspected that their presence can significantly reduce the activity of any nucleating agents present [42-43]. For these reasons, crystallisation after a moderate step shear was also studied.

Some of the results presented in this chapter have previously been published in Polymer [242]. A copy of this paper is included in **Appendix 2**.

## 5.2.0 Experimental

### 5.2.1 Sample preparation and thermal-shear profile

The polymeric nucleating agent used was a fine powder of iPS ( $> 90\%$  isotactic) manufactured by Scientific Polymer Products Inc. with the average weight molecular weight,  $M_w = 400,000$  g/mol. The sample naming convention is described in **Table 3.2**. The iPS was heated in a vacuum oven at  $180\text{ }^{\circ}\text{C}$  for 5 h to induce a high degree of crystallinity then sieved through a  $100\text{ }\mu\text{m}$  mesh to further reduce the average grain size of the particles. 2 wt% of the refined iPS powder was compounded into molten iPP according to the procedures described in **Chapter 3.2.2**.

Two thermal pre-treatments were applied above and below the equilibrium melting point of iPS ( $T_m^0(\text{iPS}) = 242\text{ }^{\circ}\text{C}$ ) [243] to yield samples where the morphology of the iPS was predominantly amorphous or semicrystalline, **Figure 5.1**. Amorphous iPS in a matrix of iPP (iPP(iPS<sub>amorphous</sub>)) was produced by heating the master batch to  $280\text{ }^{\circ}\text{C}$  for 180 s then quickly cooling it to room temperature at  $0.5\text{ }^{\circ}\text{C/s}$ , while crystalline iPS in a matrix of iPP (iPP(iPS<sub>crystalline</sub>)) was produced by heating the material to  $200\text{ }^{\circ}\text{C}$  for 180 s before cooling too room temperature. Control material (iPP<sub>control</sub>) containing no nucleating agent was prepared under the same conditions as iPP(iPS<sub>crystalline</sub>) and iPP(iPS<sub>amorphous</sub>). The crystallisation kinetics of the iPP<sub>control</sub> material prepared by both routes was found to be similar showing degradation of the iPP matrix was not significant under the experimental conditions. All samples were then reheated to  $200\text{ }^{\circ}\text{C}$ , compressed to the required gap thickness and held there for at least 180 s to eliminate the previous thermal history of the iPP matrix. Samples were cooled to the isothermal crystallisation temperature of  $135\text{ }^{\circ}\text{C}$  at  $0.5\text{ }^{\circ}\text{C/s}$ . Crystallisation from the quiescent melt and after a moderate step shear with a shear rate of  $80\text{ s}^{-1}$  and duration of 1 s were studied. In all cases the samples were held at the crystallisation temperature for long enough for the crystallisation rate to be effectively negligible. Samples were then cooled at  $0.5\text{ }^{\circ}\text{C/s}$  to room temperature.

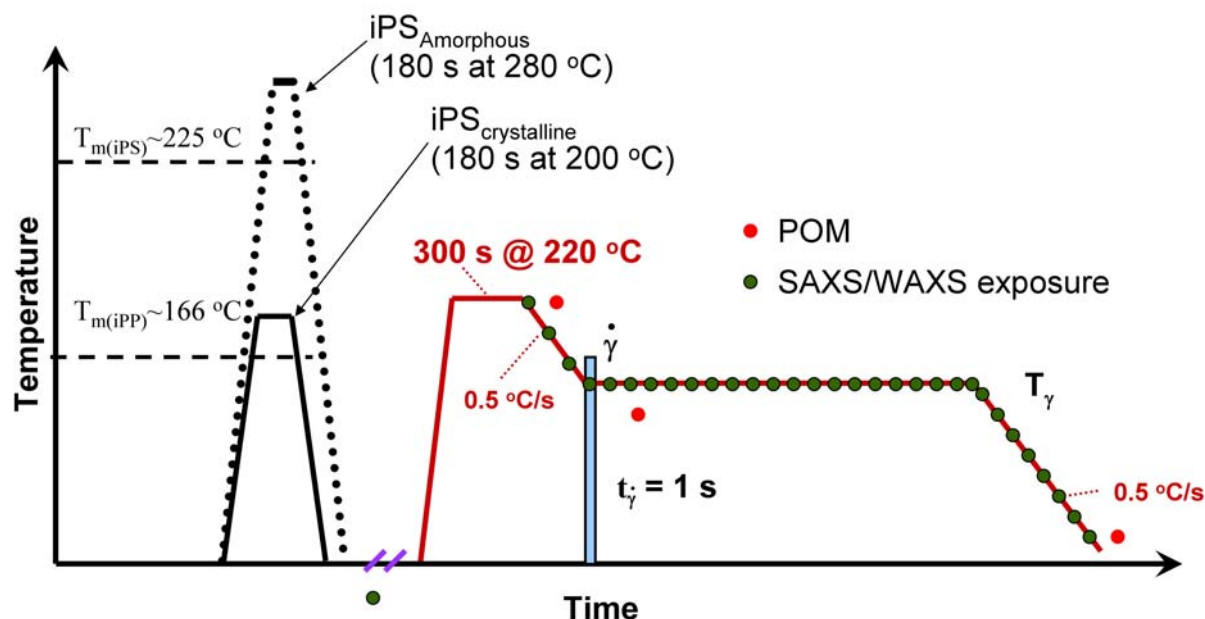


**Figure 5.1.** Schematic representation of the thermal-shear profile used in this experiment.

Additional heat treatments, identical to those experienced by iPP(iPS<sub>crystalline</sub>) and iPP(iPS<sub>amorphous</sub>) were performed to prepare iPS samples of sufficient size for ex-situ x-ray analysis. The crystalline iPS material was designated (iPS<sub>crystalline</sub>), while the amorphous iPS material was designated (iPS<sub>amorphous</sub>).

### 5.2.2 Analytical techniques

In-situ simultaneous two-dimensional small and wide angle x-ray scattering experiments (rheo-SAXS/WAXS) were performed on the SAXS/WAXS beamline (SAXS/WAXS(1)) at the Australian Synchrotron. The experimental setup was described in detail in **Chapter 3.3.1.3**. The setup allowed for in-situ investigations with a considerable amount of the scattering intensity around the azimuth ( $\varphi \sim 70^\circ$ ) in the WAXS region to be captured whilst simultaneously capturing complete SAXS patterns. Additional WAXS experiments were performed on ex-situ iPS samples that had been subjected to similar thermal treatments to that experienced in the shear cell. The experiments were performed at the Australian National Beamline Facility (ANBF) beamline 20B, Tsukuba, Japan. The experimental setup was described in detail in **Chapter 3.3.1.1**.

Polarised optical micrographs (POMs) were taken on a Nikon 80i microscope using a Nikon DS-Fi1 CCD camera at a shear cell gap thickness of 50  $\mu\text{m}$ . Differential scanning calorimetry (DSC) experiments were performed on the fully crystallised iPP samples using a Perkin-Elmer DSC-7 using a heating rate of 0.17  $^{\circ}\text{C/s}$ . Heating scans were also performed on the ex-situ iPS material which had experienced similar conditions to that which the compounded material experienced in the shear cell. Enthalpy of fusion,  $\Delta H$ , was determined by integrating the area under the baseline corrected thermogram. Percentage crystallinity of iPS was calculated from **Equation 3.26** where  $\Delta H_0^{\text{iPS}}$  for iPS was taken as 86.59 J/g [244]. The density of the crystalline and amorphous phases were taken as 1.08 g/cm<sup>3</sup> [199] and 1.056 g/cm<sup>3</sup> [198] respectively.

### 5.3.0 Results

#### 5.3.1 Characterisation of iPS particles

A survey was conducted to establish the homogeneity and dispersion of iPS particles in the iPP matrix and to investigate the influence of the selective heat treatment on the morphology of the iPS particles. The distribution of equivalent spherical diameters ( $D$ ) of the  $iPS_{\text{crystalline}}$  and  $iPS_{\text{amorphous}}$  particles in the iPP matrix was determined by taking 10 POMs of each sample and applying standard image analysis techniques to determine  $D$  for each particle. The results are presented in **Figure 5.2a**. The analysis showed a very similar distribution of diameters for iPS particles in both  $iPP(iPS_{\text{amorphous}})$  and  $iPP(iPS_{\text{crystalline}})$  material with the average equivalent spherical diameter  $D_{\text{ave}}$  for both being  $\sim 16 \mu\text{m}$ . The influence of the selective thermal pre-treatments on the morphology of the iPS particles can be illustrated by following the changes that occurred to same iPS particle after heat treatment. Initially, the iPS particle embedded in the iPP matrix was heated to  $200^\circ\text{C}$  for 180 s ( $iPP(iPS_{\text{crystalline}})$ ), **Figure 5.2b**. In this condition the particle showed high birefringence and was of irregular shape. The same particle was then heated to  $280^\circ\text{C}$  for 180 s ( $iPP(iPS_{\text{amorphous}})$ ), **Figure 5.2c**. After this treatment the particle lost its birefringence and tended to become slightly more rounded in appearance.

**Figure 5.3** shows the scattered intensity versus scattering vector ( $q$ ) of the two iPS samples given similar thermal profiles to that which the master batch of 2 wt% iPS in iPP was subjected in the shear cell. For clarity the  $iPS_{\text{crystalline}}$  curve is offset from  $iPS_{\text{amorphous}}$ . The WAXS profile of  $iPS_{\text{amorphous}}$  shows two broad amorphous peaks centred at  $q = 0.68 \text{ \AA}^{-1}$  and  $1.45 \text{ \AA}^{-1}$ , while seven crystalline peaks were superimposed onto the two amorphous peaks in the  $iPS_{\text{crystalline}}$  profile. A volume crystallinity index ( $\chi_v$ ) for the ex-situ iPS samples was determined by separating out the amorphous, crystalline and background contributions to scattering between  $0.4 \text{ \AA}^{-1} \leq q \leq 4 \text{ \AA}^{-1}$ , similar to the procedure outlined previously for iPP in **Chapter 4.2.5**.

The crystallinity determined by x-ray was  $\chi_v = 23 \pm 1 \%$ . The crystallinity determined by DSC was in close agreement  $\chi_{v(\text{DSC})} = 25 \pm 2 \%$ . No crystallinity was observed in  $iPS_{\text{amorphous}}$  by DSC or x-ray techniques.

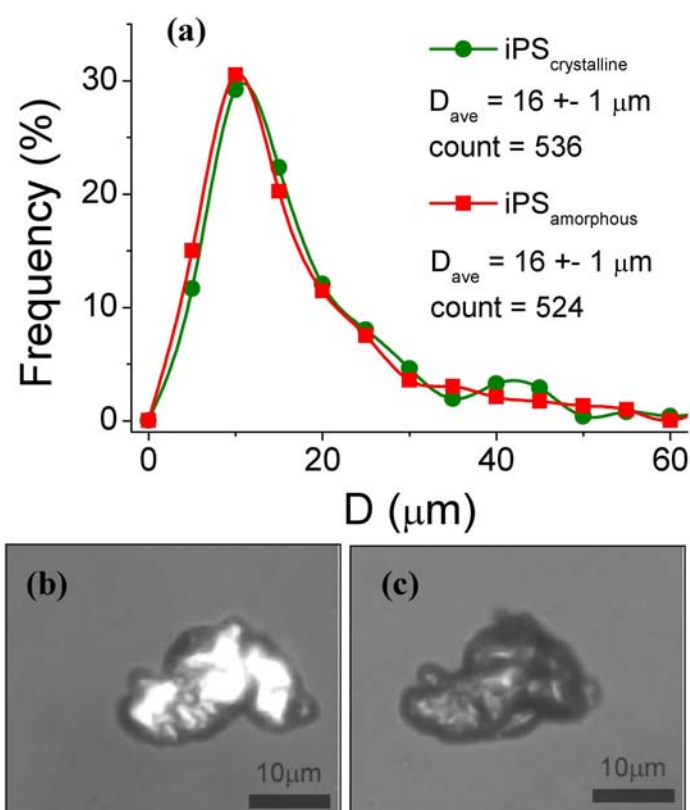


**Figure 5.2.** (a) Distribution of the equivalent spherical diameter ( $D$ ) for iPS particles in iPP( $\text{iPS}_{\text{crystalline}}$ ) and iPP( $\text{iPS}_{\text{amorphous}}$ ) material. POM image of a typical iPS particle in the iPP matrix held at (b) 200 °C for 180 s, and (c) the same particle held at 280 °C for 180 s.

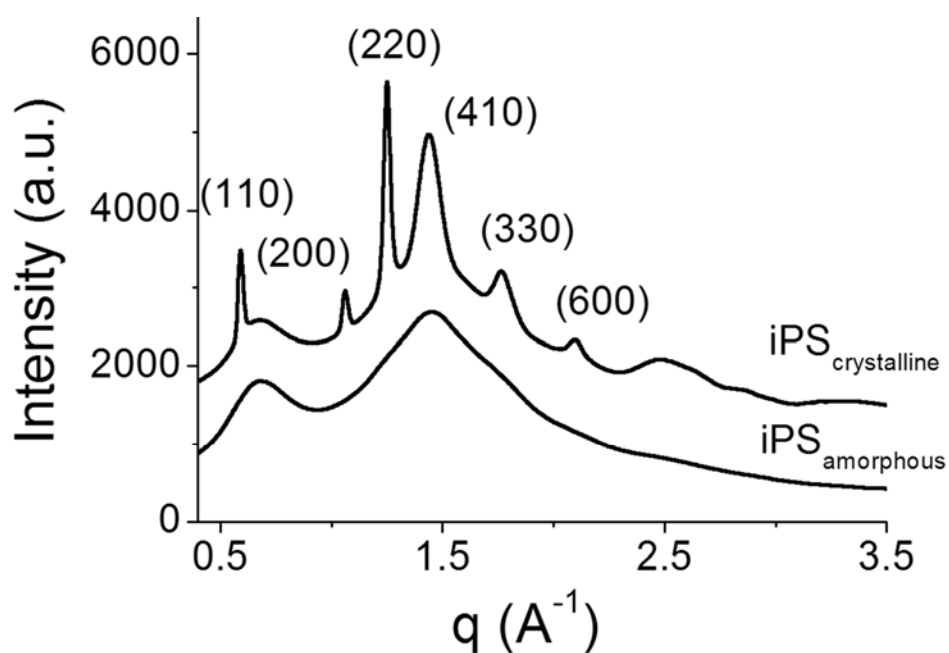


**Figure 5.3.** Intensity as a function of scattering vector ( $q$ ) for ex-situ  $\text{iPS}_{\text{crystalline}}$  and  $\text{iPS}_{\text{amorphous}}$  material.

### 5.3.2 Influence of iPS particles on iPP morphology

POMs were taken while the iPP was in the molten (200 °C) and crystalline states **Figure 5.4**. During crystallisation the surface of the iPS<sub>crystalline</sub> particles were covered by a negatively birefringent phase characteristic of  $\beta$ -iPP spherulites. Many nucleation points were observed and crystal growth appeared to be columnar. The identification of  $\beta$ -iPP was confirmed by heating the material in-situ. The phase covering the iPS<sub>crystalline</sub> particle melted at ~155 °C while the surrounding material melted at ~169 °C. Under the same conditions no negatively birefringent phase could be observed in either the iPP(iPS<sub>amorphous</sub>) or iPP<sub>control</sub> samples. The presence of both morphologies of iPS also substantially reduced the  $\alpha$ -iPP spherulite size when compared to the iPP<sub>control</sub>.

POM images of the three samples immediately after the application of shear are shown in **Figure 5.5**. In iPP(control), a small number of thread-like nuclei aligned along the flow direction were present in combination with a number of point-like nuclei. The thread-like structures appeared to have formed before the point-like nuclei and are consistent with the formation of shish-kebab structures. In both iPP(iPS<sub>crystalline</sub>) and iPP(iPS<sub>amorphous</sub>) the particles appeared to tumble and move more slowly than the surrounding melt during shear flow. Compared to iPP(control), increased numbers of thread-like structures were observed in both iPP(iPS<sub>crystalline</sub>) and iPP(iPS<sub>amorphous</sub>). The thread-like structure appeared to form around the edges of the particles. In addition, the thread-like structures were also observed to form behind both varieties of iPS particle. Unlike in the quiescent condition no  $\beta$ -iPP could be distinguished in any of the sheared samples.

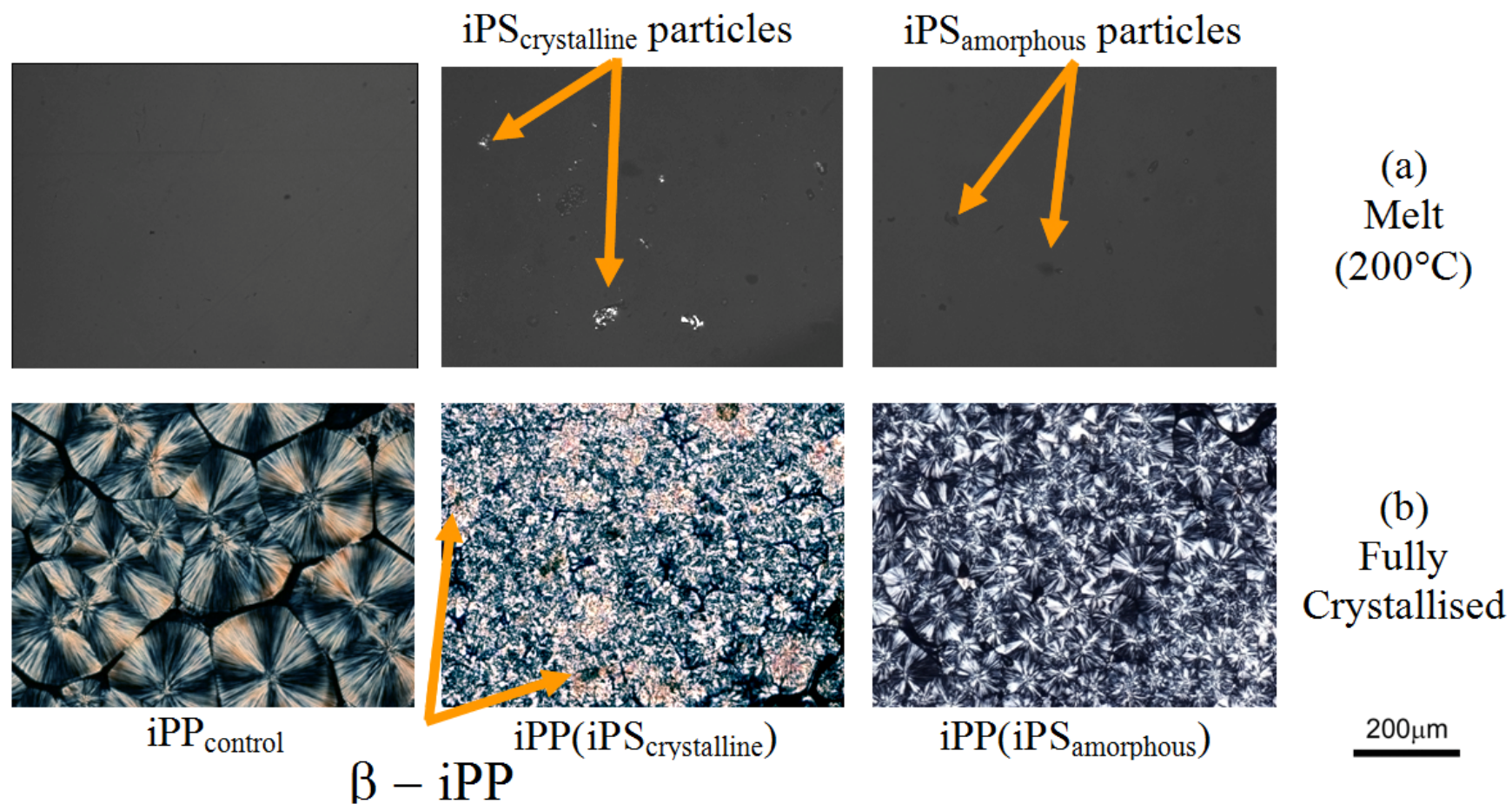


**Figure 5.4.** Polarised optical micrographs taken of (a) the iPP melt and (b) after isothermal crystallisation at 135°C under quiescent conditions.



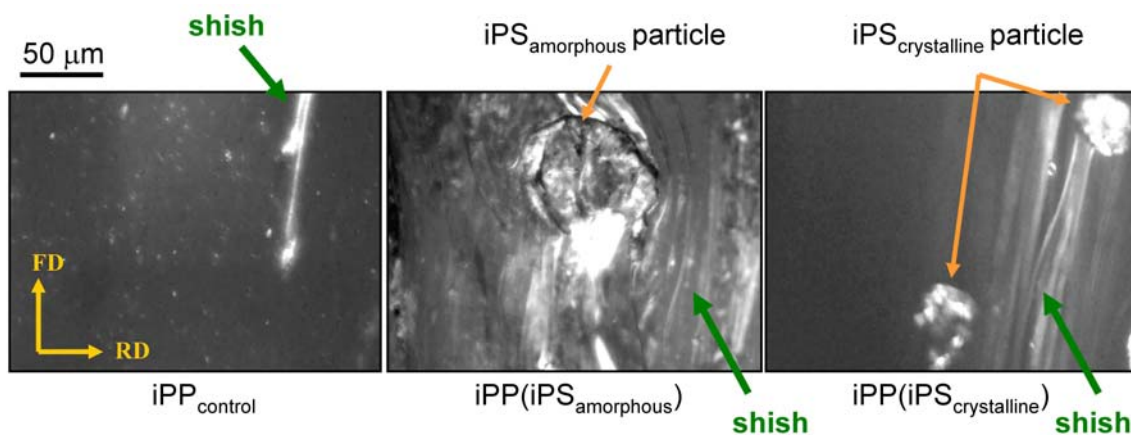


**Figure 5.5.** Polarised optical micrographs taken in the first 30 s after the imposition of shear flow (shear time = 1 s, shear rate =  $80 \text{ s}^{-1}$ , shear temperature =  $135 \text{ }^{\circ}\text{C}$ ). Flow direction is vertical.

One-dimensional WAXS profiles after the samples were fully crystallised from the quiescent state and after a moderate step shear are shown in **Figure 5.6**. Automated procedures were employed to deconvolute the scattering profiles using the fity<sup>k</sup>© software package. Three Gaussian curves centred at  $q = 1.0 \text{ } \text{\AA}^{-1}$ ,  $1.2 \text{ } \text{\AA}^{-1}$  &  $1.45 \text{ } \text{\AA}^{-1}$  were used to account for the amorphous scattering. Seven Gaussian curves were used to account for the major crystalline scattering peaks observed between  $0.9 \text{ } \text{\AA}^{-1} \leq q \leq 1.6 \text{ } \text{\AA}^{-1}$ . The volume crystallinity index ( $\chi_v$ ) and the relative amount of  $\beta$ -iPP ( $K_\beta$ ) were determined using the methods described in **Chapter 3.3.1.5** and **Equation 3.4** and **Equation 3.5**, respectively. The  $\chi_v$  and  $K_\beta$  values are presented in **Table 5.1**. In the quiescent condition iPP(iPS<sub>crystalline</sub>) contained a mixture of  $\beta$ -iPP ( $K_\beta = 0.26$ ) and  $\alpha$ -iPP while both iPP(iPS<sub>amorphous</sub>) and iPP<sub>control</sub> samples did not show any  $\beta$ -iPP. This supports the POMs shown in **Figure 5.4**. Shearing the melt prior to crystallisation led to all samples having a small amount of  $\beta$ -iPP. Both iPP(iPS<sub>crystalline</sub>) and iPP(iPS<sub>amorphous</sub>) had essential the same  $\beta$ -iPP contents with  $K_\beta \sim 0.08$ - $0.09$ , while iPP<sub>control</sub> had a slightly smaller value  $K_\beta = 0.04$ .

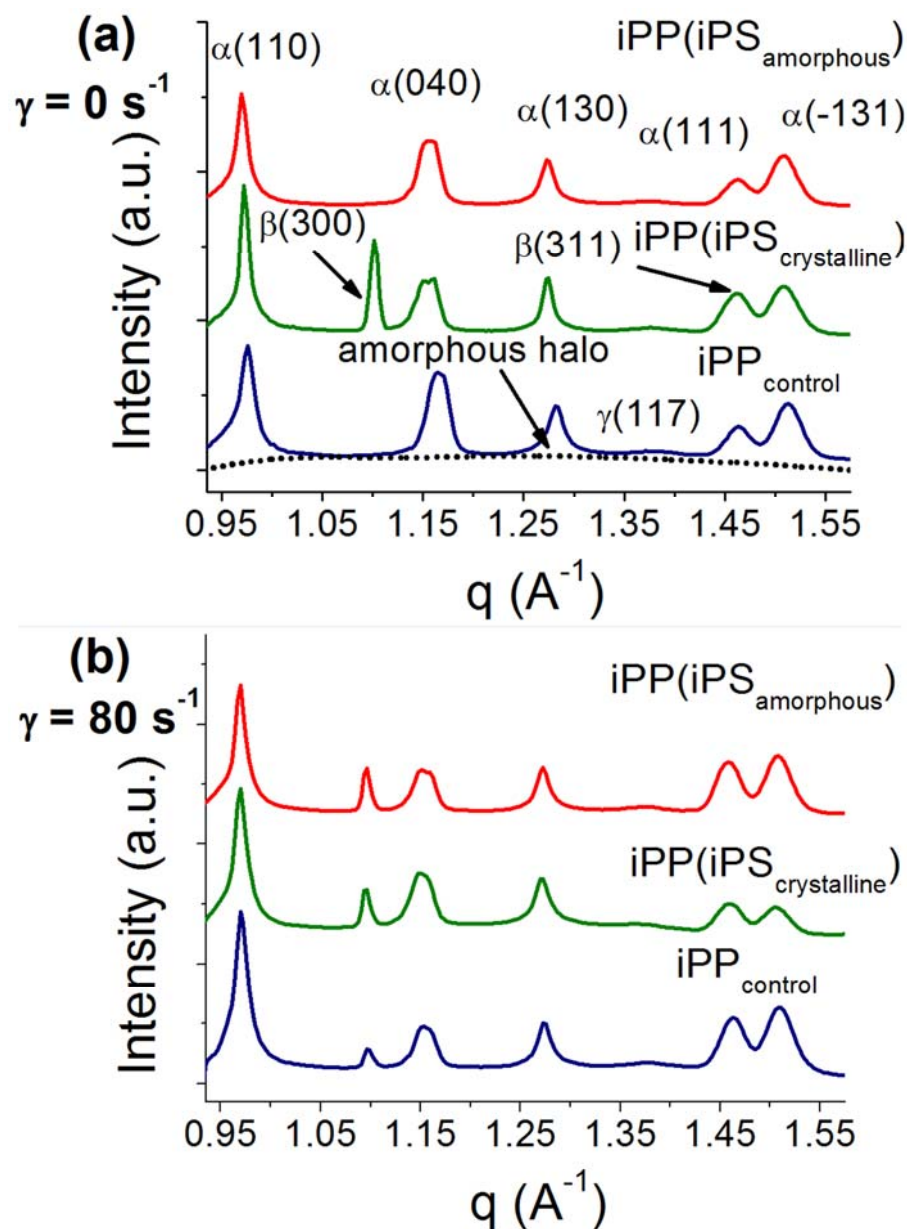


**Figure 5.6.** Intensity as a function of scattering vector ( $q$ ) for fully crystallised material (a) in the quiescent condition and (b) after a moderate step shear (shear time = 1 s, shear rate =  $80 \text{ s}^{-1}$ , shear temperature =  $135 \text{ }^{\circ}\text{C}$ ).

**Table 5.1.** Volume crystallinity ( $\chi_v$ ), relative amount of  $\beta$ -iPP ( $K_\beta$ ) crystallisation half time ( $t_{0.5}$ ) and Avrami exponent ( $n$ ) under quiescent crystallisation conditions and after a moderate step shear (shear time = 1 s, shear rate =  $80 \text{ s}^{-1}$ , shear temperature =  $135 \text{ }^\circ\text{C}$ ).

Material	Condition	$\chi_v$ (%)	$K_\beta$ (%)	$t_{0.5}$ (s)	$n$
iPP <sub>control</sub>	Quiescent	$56 \pm 1$	$\sim 0$	$753 \pm 8$	$3.0 \pm 0.2$
iPP(iPS <sub>crystalline</sub> )		$63 \pm 1$	$26 \pm 1$	$223 \pm 3$	$2.7 \pm 0.1$
iPP(iPS <sub>amorphous</sub> )		$53 \pm 1$	$\sim 0$	$278 \pm 4$	$3.1 \pm 0.1$
iPP <sub>control</sub>	Sheared	$60 \pm 1$	$4 \pm 1$	$115 \pm 2$	$2.4 \pm 0.1$
iPP(iPS <sub>crystalline</sub> )		$61 \pm 1$	$8 \pm 1$	$73 \pm 1$	$1.9 \pm 0.1$
iPP(iPS <sub>amorphous</sub> )		$61 \pm 1$	$9 \pm 1$	$83 \pm 1$	$2.0 \pm 0.1$

Two-dimensional SAXS patterns after quiescent crystallisation and in the fully crystallised state are presented in **Figure 5.7a**. These patterns show that the lamellar structure produced from quiescent conditions are essentially isotropic. SAXS patterns taken immediately after the application of shear flow ( $< 5 \text{ s}$ ) and after crystallisation had come to completion are shown in **Figure 5.7b & c** respectively. For iPP<sub>control</sub>, additional sharp scattering streaks were observed at low scattering vectors in the equatorial region immediately after the application of shear flow. These streaks persisted throughout the crystallisation process and were observed in the final fully crystallised material. The formation of the streaks was quickly followed by an increase in scattering intensity in the meridional position. This type of scattering is consistent with a shish kebab model [14, 37, 113], where the equatorial scattering is due to oriented thread-like nuclei (shish) and the meridional scattering is due to epitaxial nucleated lamellae with their chain axis aligned along the flow direction (kebabs). Isotropic scattering was also observed and is assumed to be due to randomly oriented lamellae. The equatorial scattering formed immediately after shear flow was much stronger and extended to higher scattering angles for the materials containing both morphologies of iPS. Equally the meridional scattering was more pronounced and there was less isotropic scattering in these samples.

The oriented fraction of lamellae ( $\Phi_L$ ) of the sheared samples in the fully crystallised condition was determined using the procedures described in **Chapter 3.3.1.5** and **Equation 3.25**. The results are shown at the bottom of **Figure 5.7**. It was found that  $\Phi_L$  for the material containing both iPS morphologies was more than twice that of iPP<sub>control</sub>.

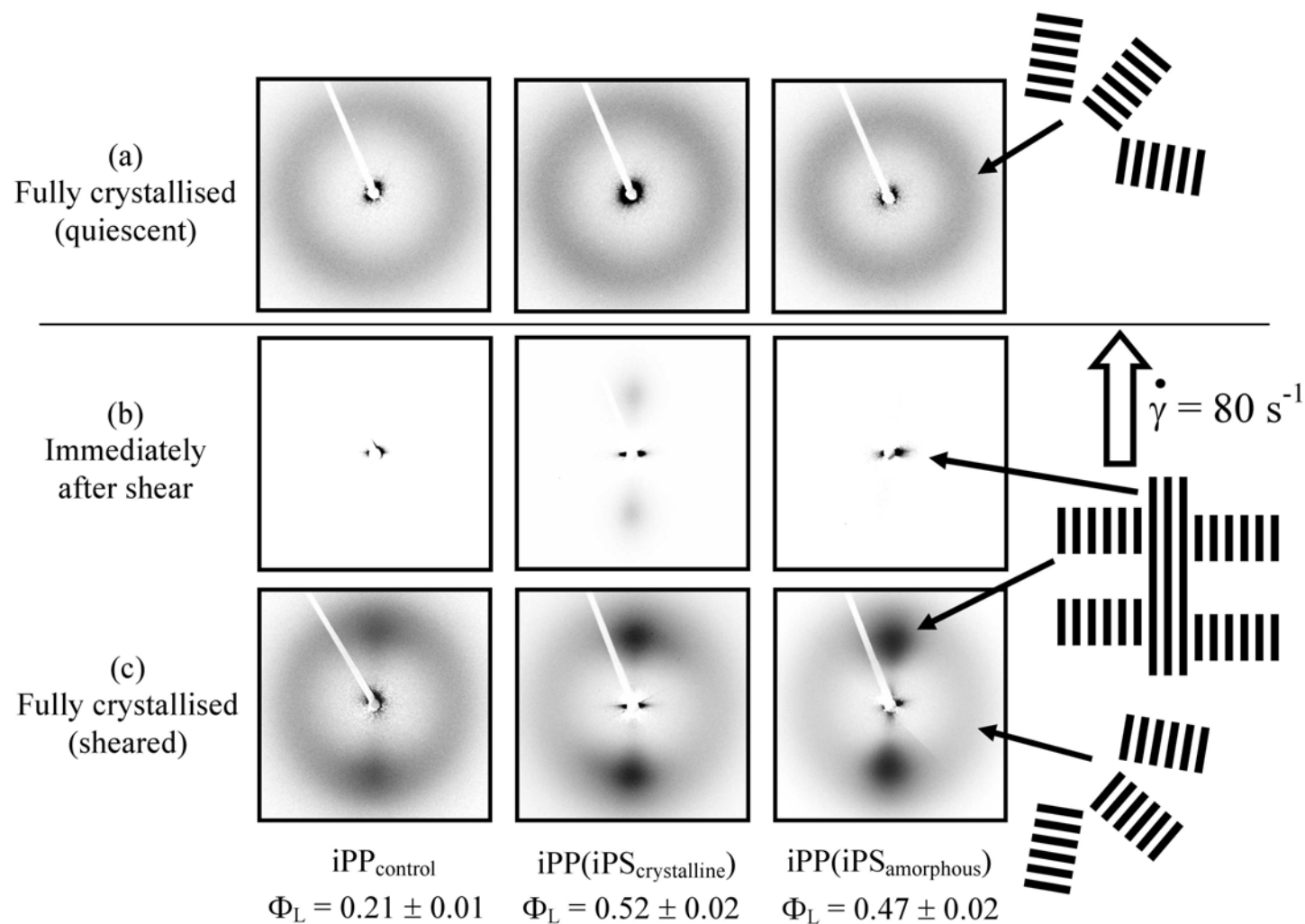


**Figure 5.7.** Two dimensional SAXS images taken (a) in the fully crystallised condition after quiescent crystallisation, (b) immediately after the application of shear flow, and (c) in the fully crystallised condition after a moderate step shear (shear time = 1 s, shear rate =  $80 \text{ s}^{-1}$ , shear temperature =  $135 \text{ }^{\circ}\text{C}$ ). Oriented fraction of lamellae ( $\Phi_L$ ) is provided for the fully crystallised material after a moderate step shear.

The material containing  $iPS_{\text{crystalline}}$  had a slightly higher  $\Phi_L$  than the material containing  $iPS_{\text{amorphous}}$ , although more detailed studies would be needed to test whether this is significant.

### 5.3.3 Influence of $iPS$ particles on $iPP$ crystallisation kinetics

The kinetics of crystallisation were probed by plotting the relative crystallinity ( $\chi_{\text{rel}}$ ) versus time, **Figure 5.8**. The relative crystallinity was determined by dividing the instantaneous crystallinity ( $\chi(t)$ ) by the total crystallinity of the fully crystallised material ( $\chi(\infty)$ ). Quantitative information about the crystallisation kinetics and growth geometry was obtained by fitting the crystallisation data to the Avrami model presented in **Chapter 4.4.3** and using **Equation 4.12**. The crystallisation half time ( $t_{0.5}$ ) was taken as the time at which the model line intersected  $\chi_{\text{rel}} = 50\%$ . Compared to the  $iPP_{\text{control}}$ ,  $t_{0.5}$  was dramatically reduced in the presence of both  $iPS$  morphologies, with  $t_{0.5}$  for  $iPP(iPS_{\text{crystalline}})$  being slightly less than  $iPP(iPS_{\text{amorphous}})$ , Table 1. The crystallisation kinetics from a sheared melt were significantly faster, up to 6 times for  $iPP_{\text{control}}$ , than for the quiescent condition. The  $t_{0.5}$  for both  $iPS$  morphologies after the moderate step shear were significantly reduced compared to the  $iPP_{\text{control}}$ .  $iPP(iPS_{\text{crystalline}})$  had a slightly shorter  $t_{0.5}$  than  $iPP(iPS_{\text{amorphous}})$ .

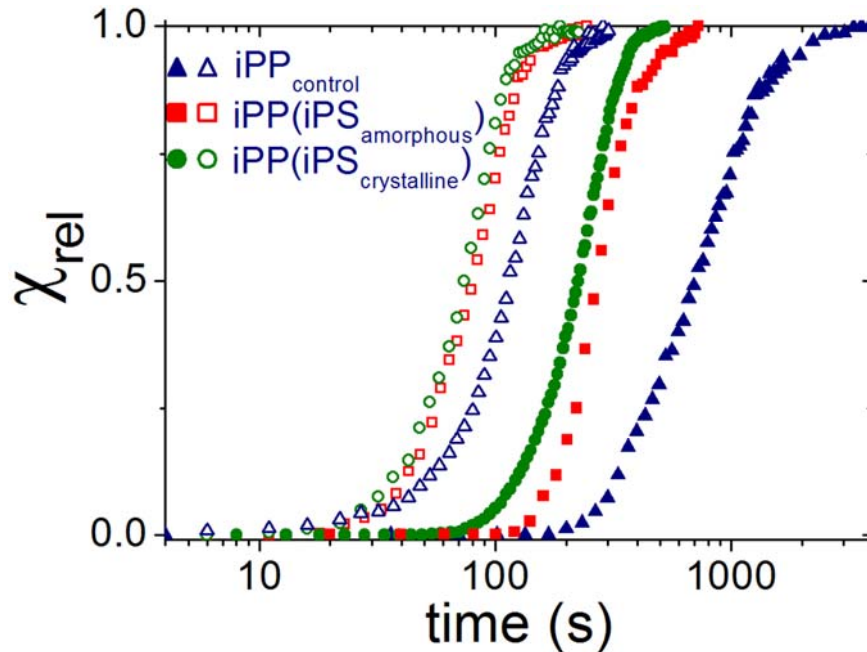


**Figure 5.8.** Relative crystallinity ( $\chi_{\text{rel}}$ ) for the three samples during quiescent crystallisation (solid symbols) and after a moderate step shear for 1 s (open symbols) (shear time = 1 s, shear rate =  $80 \text{ s}^{-1}$ , shear temperature =  $135^\circ\text{C}$ ).

The Avrami exponent was determined in the primary crystallisation region from the gradient of the linear region of a plot of  $\ln(\ln(1/(1-\chi_{rel})))$  versus  $\ln(t)$ . At low conversions there is a significant uncertainty in determining  $\chi_{rel}$  by the above method. Significant deviation from the model also occurs in the latter stages of crystallisation which has been attributed to the occurrence of secondary crystallisation [222]. Therefore the Avrami exponent was determined by fitting a straight line to the linear region between these two extremes as shown in **Figure 5.9**. In heterogeneous nucleation the Avrami exponent is related to the dimension of crystal growth: with  $n = 3$  indicating spherical growth,  $n = 2$  indicating disk-like growth, and  $n = 1$  indicating rod-like growth. Furthermore, a reduction in the Avrami exponent can also occur under confined growth conditions [223-224]. Often non-integer values of the Avrami exponent are obtained indicating the presence of more than one growth geometry during crystallisation. The Avrami exponents determined by this method are summarised in **Table 5.1**. In the quiescent condition both iPP<sub>control</sub> and iPP(iPS<sub>amorphous</sub>) had Avrami exponents close to 3 which is indicative of the spherulite growth observed in **Figure 5.4**. iPP(iPS<sub>crystalline</sub>) had a slightly smaller exponent ( $n \sim 2.7$ ) which may be due to the observed columnar growth of  $\beta$ -iPP from the surface of the iPS<sub>crystalline</sub> particles. After the moderate step shear the Avrami exponent of all samples was reduced with iPP<sub>control</sub> having  $n \sim 2.4$  and the iPP containing both morphologies of iPS being close to  $n \sim 2$  i.e. disk-like growth. This result is consistent with the SAXS results presented in **Figure 5.7**.

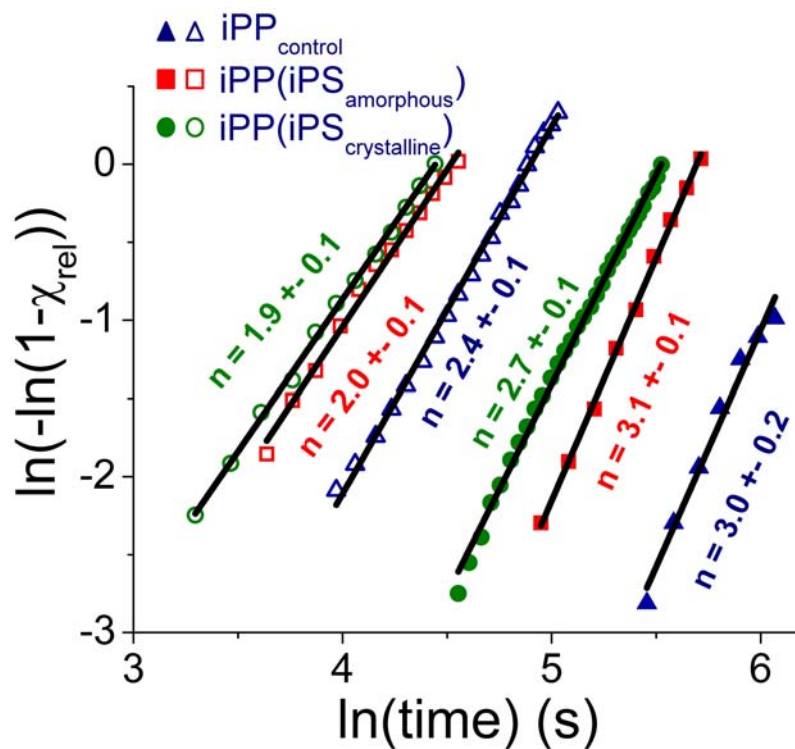


**Figure 5.9.** Avrami plots of the crystallisation data for the three samples during quiescent crystallisation (solid symbols) and after a moderate step shear (open symbols) (shear time = 1 s, shear rate = 80 s<sup>-1</sup>, shear temperature = 135 °C).

The different initial thermal treatments used to produce iPP(iPS<sub>crystalline</sub>) and iPP(iPS<sub>amorphous</sub>) may lead to different amounts of degradation, which could impact the measured crystallisation kinetics. A thorough examination was performed to determine the influence of the thermal pre-treatment temperature on the iPP matrix isothermal crystallisation kinetics using DSC, **Figure 5.10**. In this experiment samples were put through the same thermal profiles used in the previous experiments except the original thermal pre-treatment temperature ( $T_1$ ) was varied between 180 – 320 °C, **Figure 5.10a**. The final homogenisation temperature ( $T_2$ ) was kept constant at 200°C and the time to peak exothermal heat flux ( $t_p$ ) was determined as a measure of the isothermal crystallisation kinetics at 135 °C ( $T_3$ ), **Figure 5.10b**. **Figure 5.10c** shows that the crystallisation kinetics remained constant when the thermal pre-treatment temperatures was increased up to 300 °C. This is higher than the maximum 280 °C used in the study. These results are consistent with those obtained by Alfonso et al. [245]. However, when iPP(iPS<sub>crystalline</sub>) was subjected to the same thermal profile  $t_p$  decreased during the temperature range 210-280 °C consistent with the melting point of iPS, **Figure 5.10d**. These results therefore show that the higher thermal pre-treatment temperature used to

produce iPP(iPS<sub>amorphous</sub>) material did not result in the iPP matrix undergoing degradation which would significantly affected the crystallisation kinetics. Furthermore, the observed transition in the iPP(iPS<sub>crystalline</sub>) sample shows that the transition in morphology from iPS<sub>crystalline</sub> to iPS<sub>amorphous</sub> has a significant influence on the crystallisation kinetics of iPP.

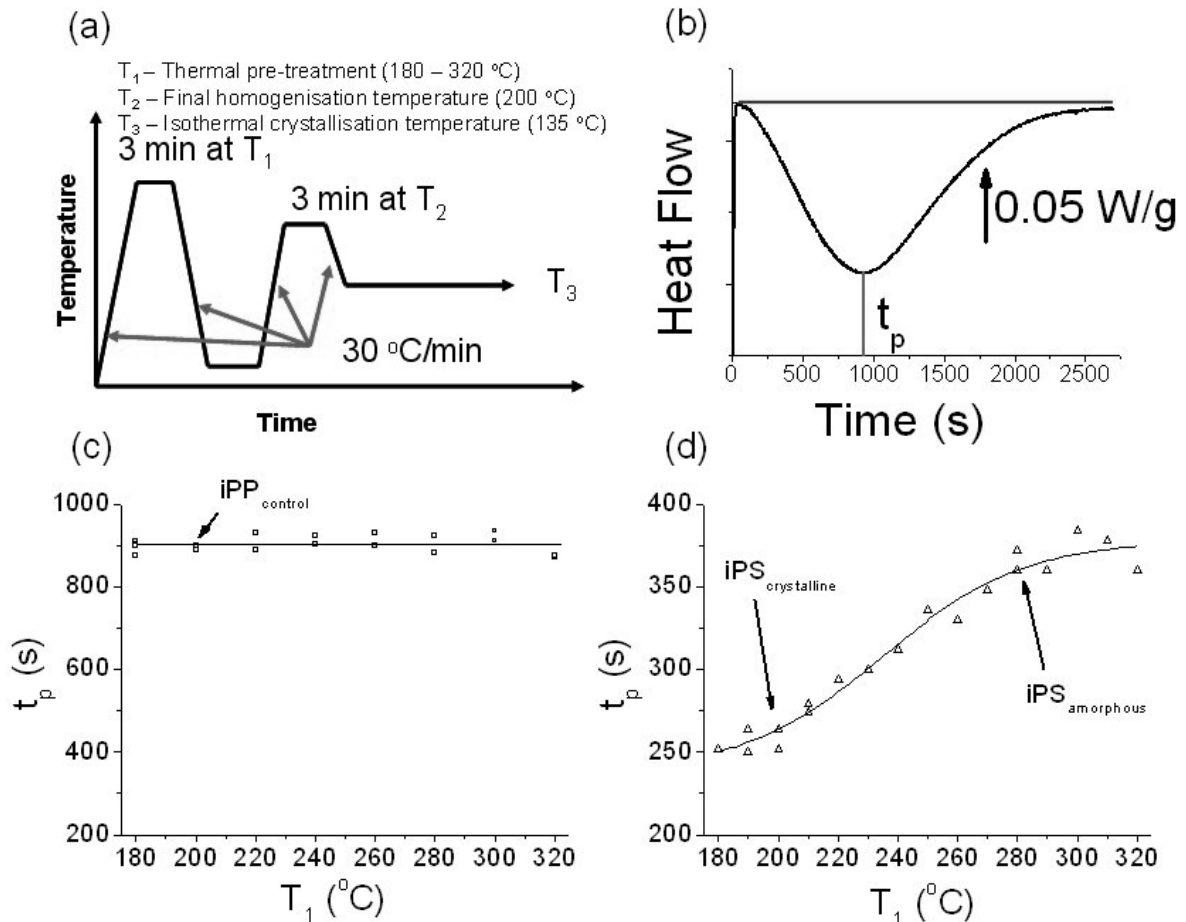


**Figure 5.10.** (a) Thermal profile used to investigate the influence of preheat treatment on the crystallisation kinetics. (b) DSC trace of the isothermal crystallisation of iPP showing the definition of the peak exothermal heat flux ( $t_p$ ). The influence of the thermal pre-treatment temperature ( $T_1$ ) on  $t_p$  for (c) iPP<sub>control</sub> and (d) iPS<sub>(crystalline)</sub>.

#### 5.3.4 Influence of iPS particles on the melting of iPP crystals

Samples for DSC analysis were sectioned from the fully crystallised disks after the selected thermal-shear profile. The arc was approximately 1mm along the radius which in the sheared samples corresponded to shear rate range of  $\sim 10 \text{ s}^{-1}$ . DSC heating scans of the three iPP samples after quiescent crystallisation are shown in **Figure 5.11a**. All samples showed an obvious endothermic peak between 165 °C and 170 °C due to  $\alpha$ -iPP. The iPP(iPS<sub>crystalline</sub>) sample showed an additional peak at 156.2 °C which is in the



temperature range for  $\beta$ -iPP. The application of a moderate step shear complicated the heating scans further, **Figure 5.11b**. All samples showed a similar sized shallow peak in the  $\beta$ -iPP temperature range at  $\sim 155$  °C. The  $\alpha$ -iPP peaks of iPP(iPS<sub>crystalline</sub>) and iPP(iPS<sub>amorphous</sub>) samples split into at least two separate endothermic peaks. In the previous chapter the origin of these two peaks was shown to be due to the different thickness / perfection of oriented parent and daughter lamellae, which are characteristic of  $\alpha$ -iPP crystallisation. A small peak in the melting profiles at higher temperatures ( $\sim 225$  °C) due to the 2wt% crystalline iPS was observed in both the sheared and un-sheared iPP(iPS<sub>crystalline</sub>) samples. The position and area of these peaks were consistent with the presence of 2 wt% iPS<sub>crystalline</sub>.

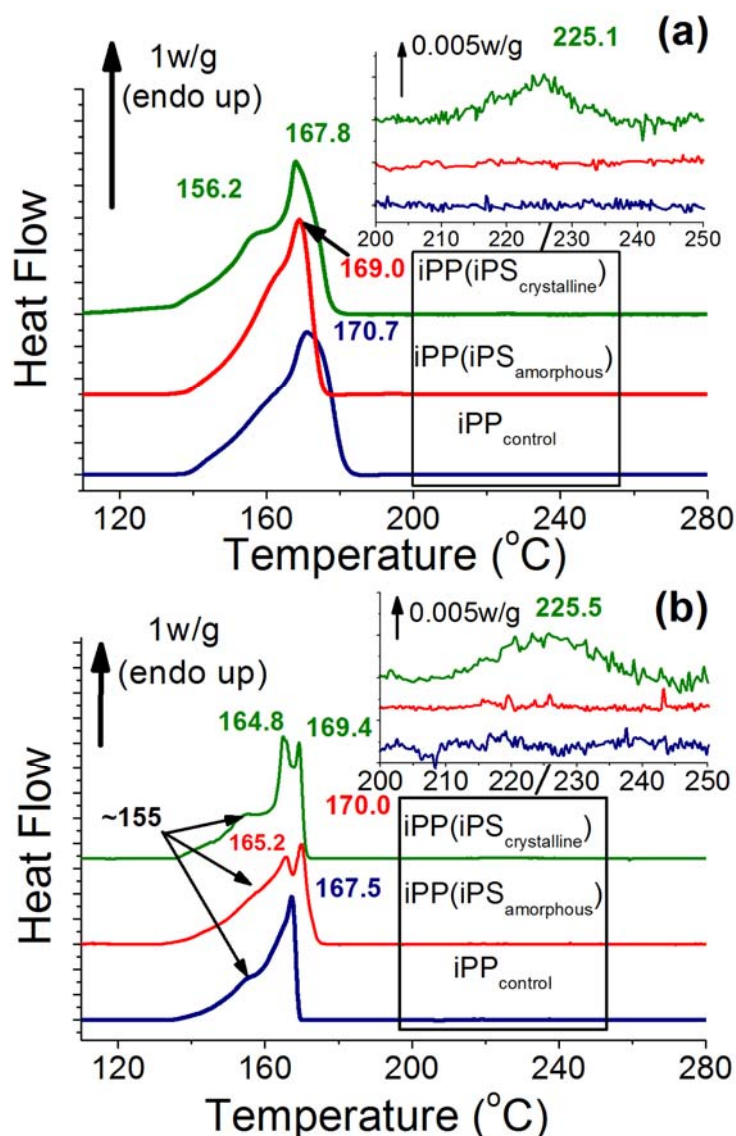


**Figure 5.11.** Ex-situ DSC heating scans after (a) quiescent crystallisation and (b) after a moderate step shear (shear time = 1 s, shear rate =  $80 \text{ s}^{-1}$ , shear temperature = 135 °C). The insert is a magnification of the high temperature region from 200 °C to 250°C.

## 5.4.0 Discussion

### 5.4.1 Morphology of iPS particles

Like most polymer pairs, on blending, polypropylene and polystyrene are essentially immiscible. This results in the iPS remaining as discrete particles at the end of both heat treatments. Ex-situ x-ray analysis of material which had been given essentially the same thermal profile as experienced in the shear cell shows that the crystallinity of the iPS<sub>crystalline</sub> particles was reasonably high at ( $\chi_v = 23 \pm 1$  %) while iPS<sub>amorphous</sub> particles showed no discernable crystallinity. The particle morphology of the originally crystalline iPS particles was irregular. Their morphology is however only slightly altered by heating them above their melting point where they tend to become more spherical. The crystalline order observed at the lower temperature is destroyed, and due to the sluggish crystallisation kinetics of iPS, they remain essentially amorphous during the subsequent isothermal crystallisation of iPP. This was confirmed by the DSC measurements presented in **Figure 5.11**.

The non-polar methyl groups on iPP molecules would interact with iPS through their phenyl groups [234]. Therefore, the arrangement of phenyl groups in the crystal and amorphous state is important in understanding how the morphology of iPS would influence the crystallisation of iPP. Crystalline iPS has been shown to form a  $3_1$  helix with a rhombohedral unit cell (on hexagonal parameters  $a = b = 21.90$  Å and  $c = 6.65$  Å) [199]. The phenyl groups within this crystal structure form into parallel stacks with the repeat distance between adjacent phenyl groups within the same stack being 6.65 Å apart.

Amorphous iPS also shows considerable short range order due to the steric interactions of the bulky phenyl groups dominating chain conformation and packing. This ordering is evident by the two broad peaks centred at  $q = 0.68$  Å<sup>-1</sup> (polymerisation peak) and  $1.45$  Å<sup>-1</sup> (amorphous halo) in the WAXS profiles shown in **Figure 5.3**. The conformation of the polystyrene chains in the amorphous state has been extensively studied, primarily by diffraction techniques [198, 235-238]. By comparing experimentally derived radial distribution function (RDF) with those calculated from structural models, early studies, such as those by Katada [235], Yeh [236], Wecker et al. [198] and Schubach et al. [237] suggested the PS chains undergo orderly packing with

neighbouring chains being roughly parallel to one another. The distance between adjacent chains was thought to be about 9 – 10 Å, while the distance between adjacent phenyl groups on the same chain, as well as between neighbouring chains was ~ 5 Å. Adams et al. performed a detailed conformational study of amorphous PS and indicated that this type of packing could be achieved if the chain adopted a disordered helical arrangement [238], although the conformational parameters presented were in contradiction to those indicated by conformational energy calculations [239].

Even though these models could explain broadly the features of the scattering profile of amorphous PS, they could not account for the unusual position and temperature dependence of the polymerisation peak which increases in intensity with increasing temperature. This issue was overcome by the super chain model proposed by Mitchell and Windle [240]. In their model, micro-segregation of the phenyl groups occurs whereby the phenyls form into stacks as if they were flexible super chains. The stacks are similar to that found in crystalline iPS, being locally parallel to one another but are more highly disordered. The backbone does not form a helix but rather adopts a random configuration with as many as 6 chain segments being able to contribute to the same region of the stack. The distance between adjacent phenyls in the stacks is ~ 5 Å, and the distance between adjacent super chains is ~9 Å. Transmission electron microscopy (TEM) suggests that the ordered regions range in size from 15-45 Å [236]. It should be emphasised here that the order found in amorphous iPS is not long range in the accepted meaning of the term.

#### ***5.4.2 Crystallisation from a quiescent melt***

The experimental results show that the presence of both morphologies of iPS substantially influenced the quiescent crystallisation of iPP. iPS<sub>crystalline</sub> particles were covered by β-iPP but their presence also increased the overall crystallisation kinetics and resulted in a substantial decrease in the spherulite size of α-iPP spherulites further away from the particles. iPS<sub>amorphous</sub> particles did not induce β-iPP. However, like iPS<sub>crystalline</sub> their presence also resulted in increased crystallisation kinetics and smaller α-iPP spherulite size. Therefore it can be concluded that morphologically, iPS<sub>crystalline</sub> selectively nucleates β-iPP and iPS<sub>amorphous</sub> nucleates α-iPP. On the other hand, both

$iPS_{\text{crystalline}}$  and  $iPS_{\text{amorphous}}$  increase the crystallisation rate of iPP with the influence of  $iPS_{\text{crystalline}}$  on crystallisation kinetics of iPP being more significant.

One possible explanation for these results is as follows: the conformational changes that occur to the iPS molecule during crystallisation result in a change in the epitaxial relationship between iPS and iPP. In helical polymers such as iPP it is considered that there are two possible ways a substrate can interact with the helix: a) via the interstrand distance as found in  $\alpha$ -iPP &  $\gamma$ -iPP or b) by the repeat distance between adjacent chains as found in  $\beta$ -iPP [78]. The contact plane of  $\alpha$ -iPP (010) consists of a lozenge shaped array of methyl groups [76]. Compounds with substantially different repeat distances have been found to interact with this array and act as effective  $\alpha$ -iPP nucleants (4.2 Å, 5.0 Å, & 6.6 Å) [76].  $\beta$ -iPP on the other hand has been found to interact with only one repeat distance ( $\sim 6.5$  Å) but it also requires an orthogonal cell geometry [77-78]. In this case it is thought that the  $\sim 5.0$  Å repeat distance between adjacent phenyls in  $iPS_{\text{amorphous}}$  would lead to nucleation of  $\alpha$ -iPP while the 6.65 Å repeat distance between adjacent phenyls in  $iPS_{\text{crystalline}}$  would lead to nucleation of  $\beta$ -iPP, **Figure 5.12**.

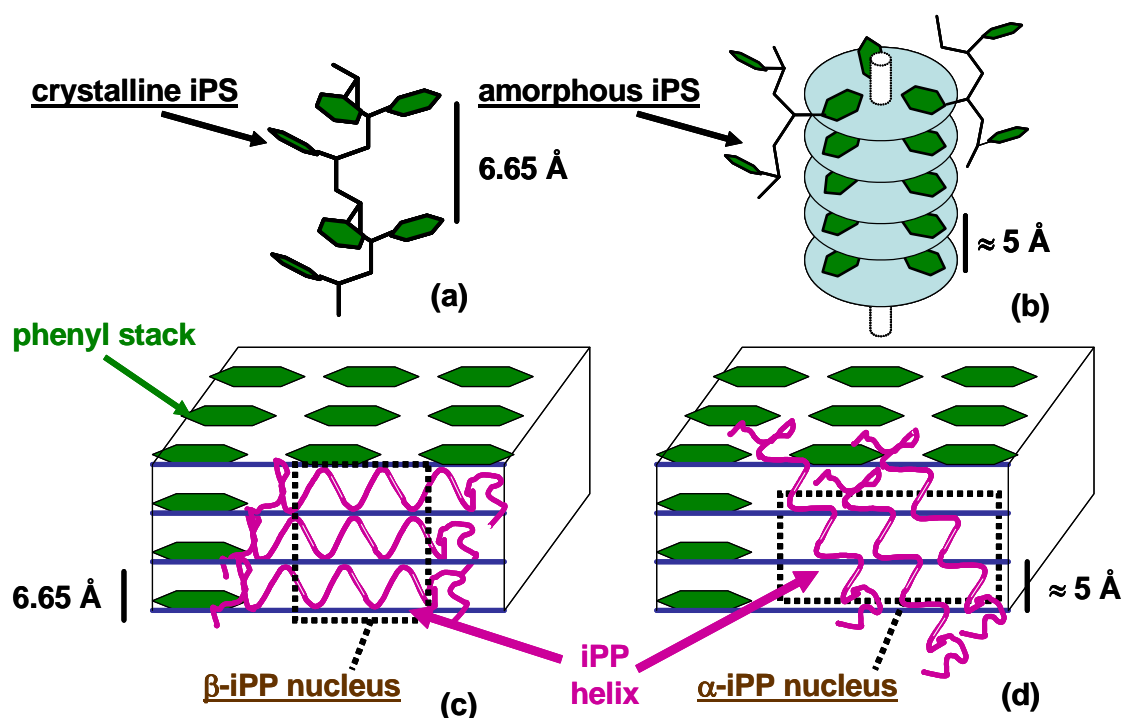


**Figure 5.12.** Isotactic polystyrene molecules (iPS) in (a) the crystalline and (b) the amorphous state, highlighting the difference in the repeat distance between adjacent phenyl groups which form channels on the materials surface. Influence of distance between these channels on the nucleation of isotactic polypropylene (iPP) (c)  $\beta$ -iPP nucleation and (d)  $\alpha$ -iPP nucleation.

### 5.4.3 Crystallisation from a sheared melt

Over the last few years considerable effort has been focused on understanding the formation of shish in sheared polymer melts. The addition of nucleating agents is expected to further complicate the formation of shish. However, a detailed explanation for the influence of nucleating agents on the formation of shish is yet to be determined. In this experiment, a considerably greater intensity and an extension to high scattering angles of the sharp equatorial streak was observed immediately after the application of shear in the presence of both iPS morphologies. Furthermore, the addition of both varieties of iPS particle increased the number of thread-like nuclei immediately after shear when observed using polarised light. These results show that the presence of the iPS particles assisted the formation of shish. The increased numbers of shish in the samples containing the iPS particles then substantially increase the number of active nuclei, and thereby accelerated the crystallisation kinetics when compared to iPP<sub>control</sub>. Similar observations have been made in wide variety of previous studies [33-34, 49-50, 84, 112-116]. Nevertheless, the mechanism by which this occurs is not well understood. A similar number of shish were formed in both iPP(iPS<sub>crystalline</sub>) and iPP(iPS<sub>amorphous</sub>) samples as highlighted by the similarly intense equatorial streaks in the SAXS patterns and similar  $\Phi_L$  and  $t_{0.5}$  values. This indicates that epitaxy does not play a dominant role in assisting the formation of shish. Rather, increased shish formation was observed to be forming near the sides of the particle, which would be exposed to the highest shear flow, as well as in the wake the particle makes as it moved through the matrix. This suggests that both iPS<sub>crystalline</sub> and iPS<sub>amorphous</sub> particles modify the local strain environment by amplifying the shear strain and shear rate near the particle. This higher flow intensity would then promote the formation of shish, leading to the observed higher density of shish in the presence of both particles.

The application of shear flow led to a similar  $\beta$ -iPP content for all three samples. Sheared melts are widely known to encourage the formation of  $\beta$ -iPP. It has been shown that an  $\alpha$ -iPP to  $\beta$ -iPP growth transition or  $\alpha\beta$  bifurcation occurs on the surface of oriented  $\alpha$ -iPP row nuclei [146]. Nevertheless, the nature of the nucleation sites responsible for  $\beta$ -iPP nucleation is still under debate. Lotz showed that an epitaxial relationship was involved in the reverse  $\beta$ -iPP to  $\alpha$ -iPP transition and suggested the same epitaxy might also occur during  $\alpha\beta$  bifurcation [152]. Sun et al. suggested that an

orientation window exists for the iPP molecule in the molten state which enables the nucleation of  $\beta$ -iPP [145]. On the other hand, Li et al. argued that shear flow can induce the formation of smectic ordered domains, and that growth of  $\beta$ -iPP should be easier than  $\alpha$ -iPP from these flow-induced smectic bundles [153]. Although the application of the step shear resulted in the formation of  $\beta$ -iPP for iPP<sub>control</sub> and iPP(iPS<sub>amorphous</sub>) samples, the step shear decreased the  $\beta$ -iPP content for iPP(iPS<sub>crystalline</sub>) material, **Figure 5.6**. The selective nucleation of  $\beta$ -iPP from iPS<sub>crystalline</sub> particles observed during quiescent crystallisation is therefore seemingly suppressed by the step shear. Similar behaviour has been observed by Huo et al. [43] who used WAXS and POM to investigate the influence of shear rate on the  $\beta$ -iPP content of an iPP nucleated by selective  $\beta$ -iPP nucleating agent (LaC + CaCO<sub>3</sub>). Hou argued that shear flow increases the number of active nuclei which selectively nucleate  $\alpha$ -iPP. This seemed to be at odds with the well known increase in  $\beta$ -iPP content during flow-induced crystallisation of iPP that occurs through  $\alpha\beta$  bifurcation [144-146]. Therefore it was unclear whether shear flow, in the presence of a selective  $\beta$ -iPP nucleating agent, suppressed the formation of oriented  $\alpha$ -iPP crystals or instead promoted them to the extent that that  $\beta$ -iPP growth from  $\alpha\beta$  bifurcation would be unfavourable.

The results presented here indicate that the addition of both morphologies of iPS considerably increased the number of shish that form immediately after the application of shear flow. Moreover, the shish appeared to form in increasing numbers closer to the particles. As shown by the increase in crystallisation kinetics, which are significantly faster than found in the quiescent condition, the shish are very effective at nucleating  $\alpha$ -iPP. Therefore it can be concluded that their presence completely overwhelms the epitaxial crystallisation process at the surface of the particles, resulting in high proportions of oriented  $\alpha$ -iPP crystals.

### 5.5.0 Conclusions

The morphology of isotactic polystyrene (iPS) particles which had been added to a matrix of isotactic polypropylene (iPP) were successfully varied in-situ by selective heat treatment to be either semicrystalline iPP(iPS<sub>crystalline</sub>) or amorphous iPP(iPS<sub>amorphous</sub>). Isothermal crystallisation of iPP in the presence of iPS particles of both morphologies, (iPP(iPS<sub>crystalline</sub>) and iPP(iPS<sub>amorphous</sub>)), and a control (iPP<sub>control</sub>) were then studied under quiescent conditions as well as after a moderate step shear. From the results obtained the following was concluded:

Under quiescent conditions iPS<sub>crystalline</sub> was found to selectively nucleate the  $\beta$ -iPP while iPS<sub>amorphous</sub> was found to nucleate  $\alpha$ -iPP. The results were explained by difference in the morphology of the two varieties of iPS particle, in particular the distance between adjacent phenyl groups, which is important for any epitaxial relationship between iPP and iPS.

During crystallisation after a moderate step shear, both morphologies of iPS resulted in a substantial increase in the density of shish compared to iPP<sub>control</sub>. The greater amount of shish increased crystallisation kinetics and promoted the formation of more oriented  $\alpha$ -iPP lamellae.

Similar numbers of shish were observed under flow-induced crystallisation conditions in the presence of both morphologies of iPS particles indicating that epitaxy did not play a significant role in assisting the formation of shish. Rather, shish were observed to form close to the surface of the particle where the shear flow would be the highest if there was a velocity difference between the particle and the matrix. This suggests that the particles assist shish formation by modifying the local strain environment.

After shear flow the amount of  $\beta$ -iPP was similar for all samples. In particular, the amount of  $\beta$ -iPP reduced for iPP(iPS<sub>crystalline</sub>) compared to the quiescent condition. This suggests the action of  $\beta$ -iPP nucleating agents are suppressed by shear flow.

## Chapter 6

### **Influence of shear flow on the morphology development of $\beta$ nucleated iPP**

#### **6.1.0 Introduction**

In the previous chapter, only a moderate amount of the trigonal  $\beta$  form of isotactic polypropylene ( $\beta$ -iPP) ( $K_\beta = 0.26$ ) was produced by the crystalline isotactic polystyrene (iPS<sub>crystalline</sub>) particles. This relatively low  $\beta$ -iPP content makes further detailed investigations into the dynamics of  $\beta$ -iPP formation under flow-induced crystallisation conditions less accurate. To address this, the present chapter will investigate the influence of a highly selective  $\beta$ -iPP nucleant, calcium suberate (CaSub). CaSub particles have been shown have one of the highest selectivity for  $\beta$ -iPP of all known  $\beta$ -iPP nucleating agents, and can, under appropriate conditions, produce samples composed almost entirely of  $\beta$ -iPP [44, 151]. In the present chapter the combined influence of CaSub loading level and flow conditions on the development of iPP morphology and orientation is characterised. This information will allow new insight to be gained on the mechanism of flow-induced formation of  $\beta$ -iPP as well as the mechanism of flow-induced suppression of  $\beta$ -iPP in the presence of  $\beta$ -iPP nucleating particles.



## 6.2.0 Experimental

### 6.2.1 Sample preparation and thermal-shear profile

Calcium suberate (CaSub) was synthesised according to the procedures described in **Chapter 3.2.2**. The sample naming convention is described in **Table 3.2**. The thermal-shear profile used in this chapter is shown in **Figure 6.1**. The disks were heated to 220 °C and slowly compressed to a working distance of 0.5 mm at 0.01 mm/s. The compressed disks were held at temperature for 300 s to erase the previous thermal history. The isotropic nature of the melt was confirmed by in-situ small and wide angle x-ray scattering (rheo-SAXS/WAXS) as well as ex-situ SAXS/WAXS and etched samples viewed under reflected light after quiescent crystallisation. The samples were cooled from 220 °C to the isothermal crystallisation temperature of 135 °C at 0.5 °C/s. A short controlled step shear was then applied to the melt for 1 s at shear rates between 0-80 s<sup>-1</sup>. Higher shear rates than 80 s<sup>-1</sup> were not investigated due to the appearance of flow instabilities and melt fracture in some samples. The samples were then held at the crystallisation temperature until the crystallisation rate was effectively negligible and then cooled to 50 °C at a rate of 0.5 °C/s. The sample was then heated at 0.17 °C/s to 220 °C, held there for 300 s before quiescent crystallisation was carried out at 135 °C.

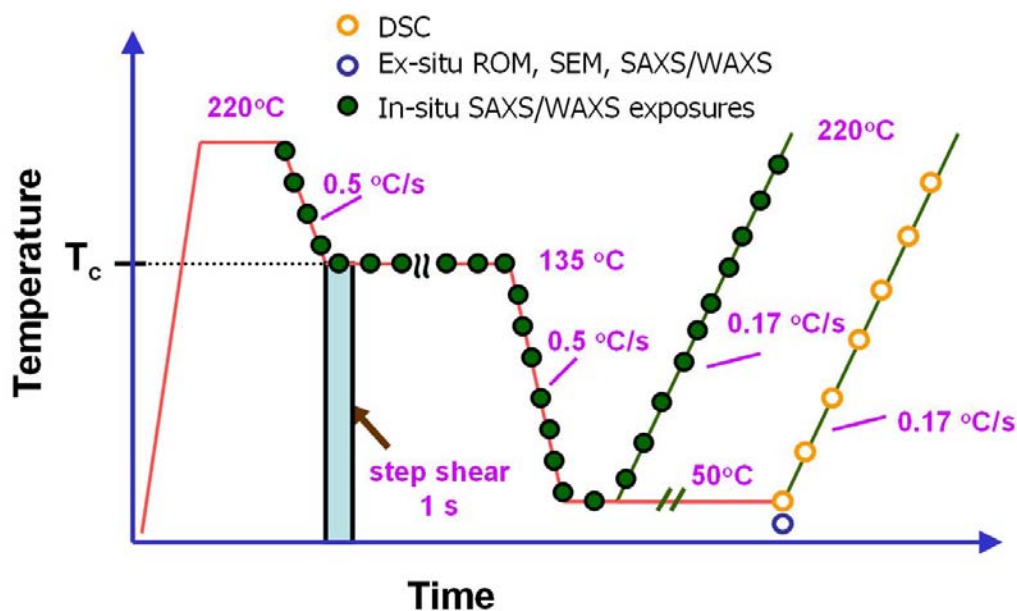


**Figure 6.1.** Schematic illustration of the thermal-shear profile used in this chapter.

### 6.2.2 Analytical techniques

Two varieties of simultaneous SAXS/WAXS experiments were used in this chapter. The first type were performed on ex-situ samples and aimed to understand the influence of shear rate on the final crystalline morphology and orientation. In these experiments a range of shear rates was obtained from one sample by scanning the synchrotron microbeam along the radius of disks sheared for 1 s at an angular velocity ( $\omega = 3.3$  rad/s). In this way, a wide range of shear rates between 0-80 s<sup>-1</sup> could be investigated in the same sample with a shear rate resolution of  $\pm 1$  s<sup>-1</sup>. The second type investigated the development of morphology in-situ during the imposed thermal-shear profile using simultaneous rheo-SAXS/WAXS.

Ex-situ simultaneous SAXS/WAXS experiments were performed at the Australian National Beamline Facility (ANBF) in Tsukuba, Japan. The experimental setup was described in detail in **Chapter 3.3.1.1.** and allowed for simultaneous collection of complete SAXS/WAXS patterns. In-situ simultaneous rheo-SAXS/WAXS experiments were performed on the SAXS/WAXS beam line at the Australian Synchrotron (SAXS/WAXS(1)). The experimental setup was described in detail in **Chapter 3.3.1.3.** The setup allowed for in-situ investigations with a considerable amount of the scattering intensity around the azimuth ( $\varphi \sim 70^\circ$ ) in the WAXS region to be captured whilst simultaneously capturing complete two-dimensional SAXS patterns.

In addition, the ex-situ samples were etched for 7 h in the permanganate solution described in **Chapter 3.3.4.** Reflected optical micrographs (ROM) of the etched surfaces were taken on an Olympus PMG3 microscope with a differential interference optic attachment. Higher magnification of the etched surfaces was performed with a JEOL JSM-7001F field emission scanning electron microscope (SEM) operating in secondary electron mode. Samples were coated to 10 Å thick with gold / platinum and imaged at an acceleration voltage of 5 kV. In-situ images of the particles in the polymer matrix were made under polarised light using a Nikon 80i microscope and a Nikon DS-Fi1 CCD camera. Differential scanning calorimetry (DSC) experiments were performed on a Perkin-Elmer DSC-7 using the procedures described in **Chapter 3.3.3.** Melting experiments were performed on samples sectioned from the sheared disks at heating rates of 0.17 °C/s.

### 6.3.0 Results

#### 6.3.1 Characterisation of CaSub particles

In this section the morphology and dispersion of the produced CaSub particles in the iPP matrix is characterised using in-situ polarised optical microscopy (POM) and ex-situ SEM techniques. The influence of the CaSub particles on the quiescent crystallisation and subsequent melting behaviour of iPP is then characterised using DSC.

A survey was conducted to determine the morphology of the produced CaSub particles and their dispersion in the iPP matrix. The method produced fine equiaxed CaSub particles, which exhibited flat faceted surfaces, **Figure 6.2a**. In-situ POM images of the produced CaSub particles after being compounded into the molten iPP matrix indicated the CaSub particles were well dispersed by the mixing technique and did not appear to have aggregated, **Figure 6.2b**. The particle size distribution of the produced CaSub particles was determined from five individual SEM images using standard image analysis techniques, **Figure 6.3**. From this analysis the average dimension of the particles was determined to be  $350 \pm 20$  nm.

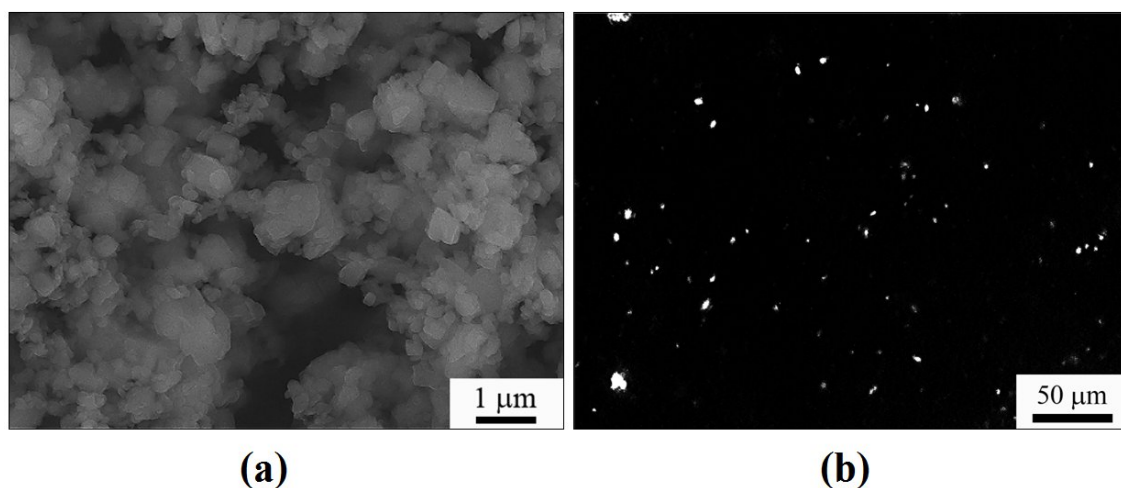


**Figure 6.2.** (a) SEM image of ex-situ CaSub particles, (b) in-situ POM image of CaSub particles in iPP(1.0CaSub).

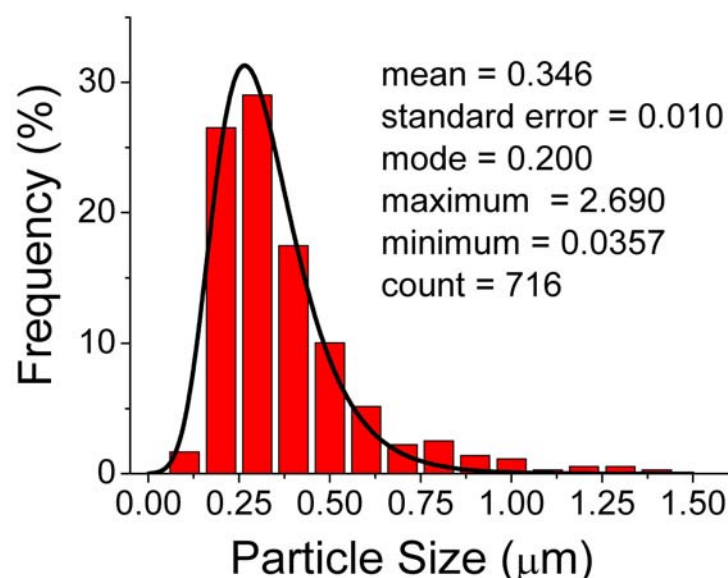
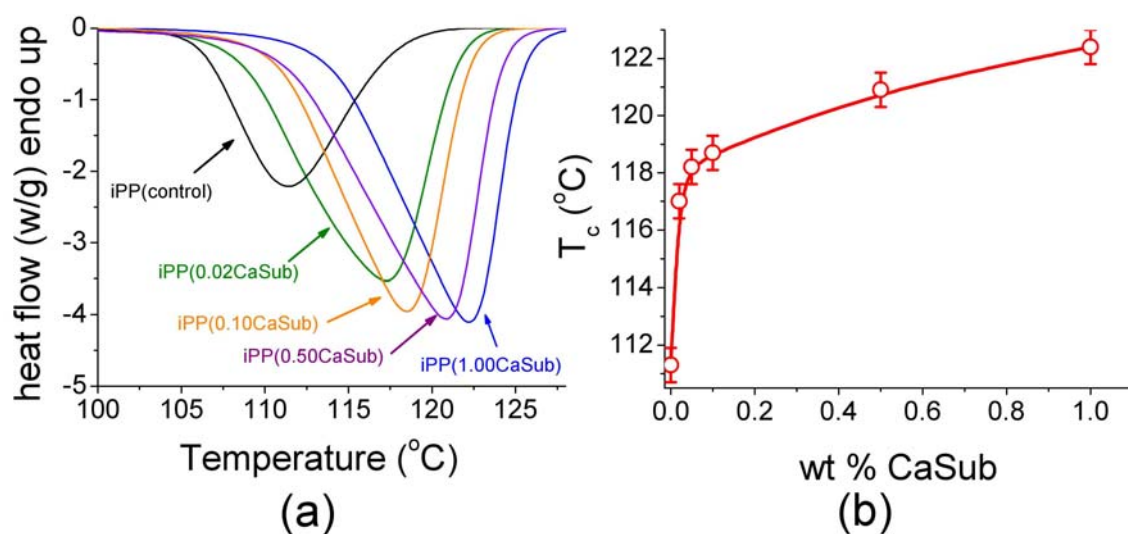


**Figure 6.3.** Particle size distribution of the produced CaSub particles.

**Figure 6.4a** shows the DSC crystallisation curves obtained after holding the sample at 220 °C for 300 s before being continuously cooled at 0.17 °C/s to 50 °C. All samples showed one broad exothermic peak. The peak crystallisation temperature ( $T_c$ ) for each sample was obtained from the minimum in the exothermic crystallisation peak and the results are plotted in the insert in **Figure 6.4b**. For iPP(control)  $T_c$  was  $111.3 \pm 0.3$  °C. The addition of only 0.02 wt% CaSub resulted in a substantial shift towards higher temperatures with  $T_c = 117.0 \pm 0.3$  °C. Additional increases in CaSub loading level resulted in smaller increases in  $T_c$ , however no saturation point was reached in the range of loadings investigated. This further indicates that aggregation of CaSub particles was not significant at the loading levels investigated.

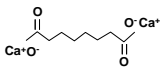
The influence of CaSub loading on the nucleation efficiency (NE) is summarised in **Table 6.1**. NE increased with increasing loading level consistent with the increased number of heterogeneous nucleation sites which would become available. The influence of CaSub loading level on the activation energy for crystallisation ( $\Delta E$ ) is provided in **Figure 6.5**. The range of values determined for  $\Delta E$  were comparable to values previously reported in the literature [85, 168, 246]. All  $\Delta E$  values were negative (i.e. the crystallisation rate decreased with increasing temperature). This is consistent with crystallisation in this temperature regime being largely diffusion controlled.  $\Delta E$  was found to decrease with increasing loading level. This indicates that crystallisation

(nucleation and/or growth) in the presence of CaSub particles is thermodynamically more favourable compared to iPP(control).



**Figure 6.4.** (a) Selected differential scanning calorimetry (DSC) cooling curves. (b) The influence of CaSub loading level on peak crystallisation temperature ( $T_c$ ).

**Table 6.1.** Summary of CaSub particles' influence on the quiescent crystallisation of isotactic polypropylene. Crystallisation temperature ( $T_c$ ), nucleation efficiency (NE).

Sample	Chemical Structure	average dimensions (nm)	Loading (wt%)	surface area (m <sup>2</sup> /g)	$T_{c,NA}$ (°C)	NE (%)
iPP		350 ± 20	0	-	111.3 ± 0.3	0
iPP(self seed)			~0.15	-	142.7 ± 0.3	100
iPP(0.02CaSub)			0.02	0.004	117.0 ± 0.3	18 ± 1
iPP(0.05CaSub)			0.05	0.010	118.2 ± 0.3	22 ± 1
iPP(0.10CaSub)			0.10	0.019	118.7 ± 0.3	24 ± 1
iPP(0.50CaSub)			0.50	0.096	120.9 ± 0.3	31 ± 1
iPP(1.00CaSub)			1.00	0.191	122.4 ± 0.3	36 ± 1

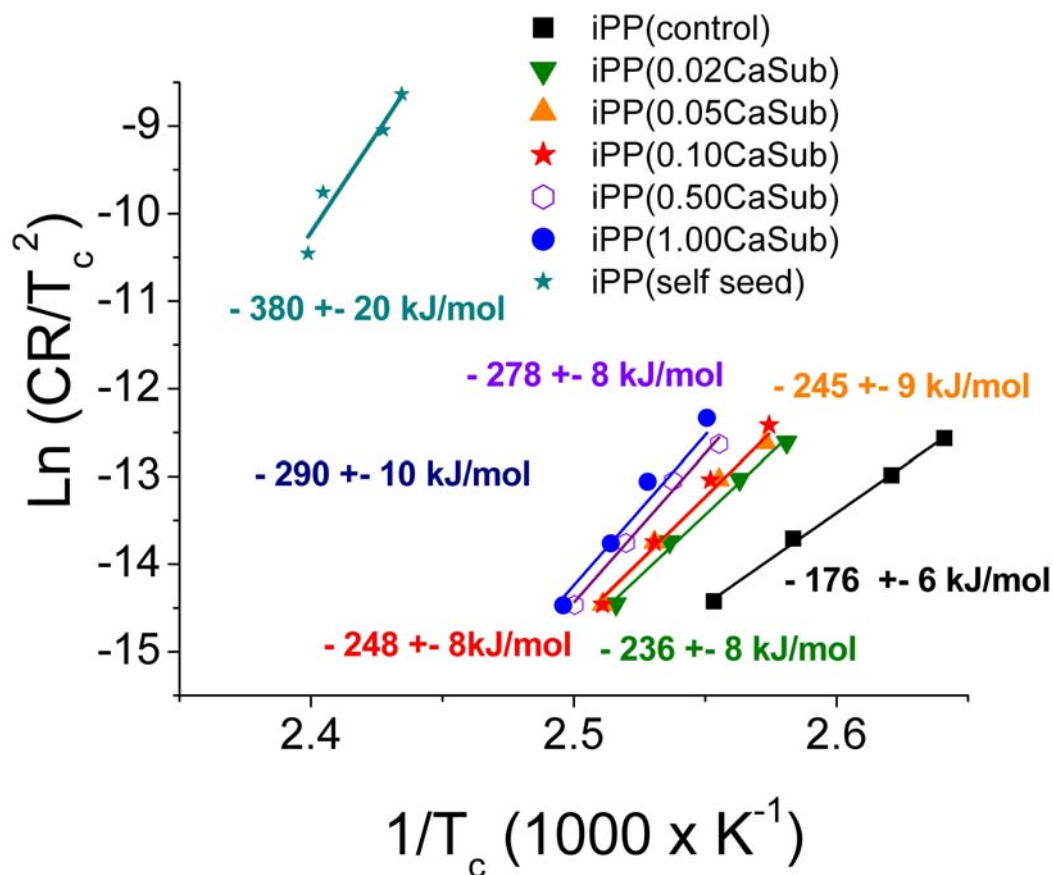


**Figure 6.5.** Kissinger plot showing the influence of CaSub loading level on the activation energy for crystallisation ( $\Delta E$ ).

**Figure 6.6** shows the melting thermogram after crystallisation presented in **Figure 6.4a**. iPP(control) showed one broad peak with a maximum at  $166.9 \pm 0.3$  °C consistent with the melting of  $\alpha$ -iPP crystals. The addition of 0.02 wt% resulted in the formation of two additional overlapping peaks at lower temperature, centred at  $149.0 \pm 0.3$  °C and  $153.4 \pm 0.3$  °C. These peaks are consistent with the melting of  $\beta$ -iPP crystals. The high temperature peak also increased to a slightly higher temperature,  $169.5 \pm 0.3$  °C, in comparison to iPP(control). Further increases in loading of CaSub resulted in only small increases in the relative size of the low temperature peaks compared to the higher temperature peak. Due to the clear separation of the  $\alpha$ -iPP and  $\beta$ -iPP melting peaks an attempt was made to quantify the  $\alpha$ -iPP ( $\chi_{\alpha(\text{DSC})}$ ) and  $\beta$ -iPP ( $\chi_{\beta(\text{DSC})}$ ) crystallinities by integrating the area under the respective peaks and using the thermodynamic parameters provided in **Table 2.2**. The results are shown in **Table 6.2**. Increasing the CaSub loading level generally increased the  $\beta$ -iPP crystallinity. However, the measured volume crystallinity ( $\chi_{v(\text{DSC})}$ ) for the nucleated samples also increased with CaSub loading level.

This led to unrealistically high values approaching unity. The results presented in this section show that only small additions of CaSub dramatically alter the morphology of iPP.

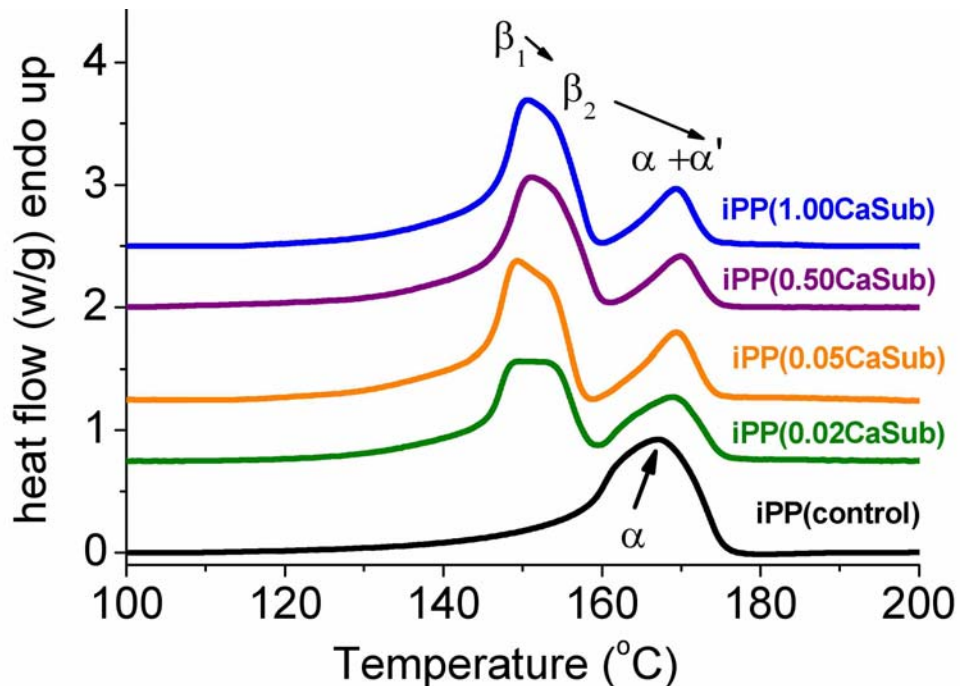


**Figure 6.6.** DSC melting curves after quiescent crystallisation. Heating rate 0.17 °C/s.

**Table 6.2.** Indices for the  $\alpha$ -iPP ( $\chi_{\alpha(\text{DSC})}$ ),  $\beta$ -iPP ( $\chi_{\beta(\text{DSC})}$ ) and volume ( $\chi_{v(\text{DSC})}$ ) crystallinity determined from the DSC melting curves shown in **Figure 6.6**.

Sample	$\chi_{\beta(\text{DSC})}$	$\chi_{\alpha(\text{DSC})}$	$\chi_{v(\text{DSC})}$
iPP(control)		$0.65 \pm 0.03$	$0.65 \pm 0.03$
iPP(0.02CaSub)	$0.63 \pm 0.04$	$0.16 \pm 0.02$	$0.79 \pm 0.06$
iPP(0.05CaSub)	$0.78 \pm 0.04$	$0.12 \pm 0.01$	$0.90 \pm 0.05$
iPP(0.50CaSub)	$0.69 \pm 0.03$	$0.14 \pm 0.01$	$0.83 \pm 0.04$
iPP(1.00CaSub)	$0.83 \pm 0.05$	$0.13 \pm 0.01$	$0.96 \pm 0.06$

### 6.3.2 Influence of flow condition on iPP polymorphism

In this section the influence of shear rate and CaSub loading level on iPP polymorphism was investigated using ex-situ simultaneous SAXS/WAXS. Selected two-dimensional SAXS/WAXS images are shown in **Figure 6.7**. For clarity, the SAXS region is enlarged relative to the WAXS region. Under quiescent conditions all samples showed concentric circles in the WAXS and SAXS regions. This revealed that both the crystalline and lamellar orientation distributions were isotropic. In the WAXS patterns



of iPP(control) only reflections from  $\alpha$ -iPP and  $\gamma$ -iPP were observed. However, the addition of CaSub particles changed the crystalline form to being predominantly  $\beta$ -iPP, although weak  $\alpha$ -iPP crystalline reflections were still observed. These results are broadly consistent with the DSC results presented previously and show that CaSub is a powerful  $\beta$ -iPP nucleating agent.

The application of even low intensity shear flow substantially altered the SAXS/WAXS patterns. For the iPP(control), shear flow led to the formation of additional  $\beta$ -iPP reflections, while in the samples containing CaSub particles, increasing shear rate led to the suppression of  $\beta$ -iPP reflections present under quiescent conditions. In all samples above a critical shear rate, oriented crystalline and lamellae structures were detected in the WAXS and SAXS patterns respectively. In the WAXS region, the  $\alpha(110)$ ,  $\alpha(040)$  &  $\alpha(130)$  reflection concentrated into arcs in the equatorial region. This indicates a general alignment of the c-axis (molecular chain helix axis) along the flow direction as these rings are all (hk0) form and are therefore parallel to the  $\alpha$ -iPP c-axis. The  $\alpha(110)$  and  $\alpha(130)$  showed additional intensity concentrations away from the equator consistent with the formation of  $\alpha$ -iPP daughter lamellae as discussed in **Chapter 4.3.2**. The critical shear rate where the oriented crystalline structures were detected reduced with the addition of CaSub. In pure iPP the shear rate was  $30 \text{ s}^{-1}$  while the addition of 0.05 wt % and 1.0 wt% CaSub reduced the shear rate to  $20 \text{ s}^{-1}$  and  $10 \text{ s}^{-1}$  respectively.

The  $\beta(300)$  and  $\gamma(117)$  reflections also became oriented above a critical shear rate. For the  $\beta(300)$  reflection an increase in scattering occurred along the equator. This indicates the c-axis of the  $\beta$ -iPP crystals is also aligned along the flow direction. Once oriented, the  $\gamma(117)$  reflection was observed to concentrate into three peaks, with one peak centred on the equator and another two peaks inclined  $\sim 40^\circ$  either side of equator. This is consistent with  $\gamma$ -iPP crystals being oriented in the parallel chain axis orientation [161]. Further details of the orientation relationship of  $\gamma$ -iPP are discussed in the next chapter (**Chapter 7.3.4**). For all samples, the critical shear rate required to induce  $\beta$ -iPP and  $\gamma$ -iPP orientation was more than for  $\alpha$ -iPP. However, similar to  $\alpha$ -iPP, the critical shear rate required to induce  $\beta$ -iPP and  $\gamma$ -iPP orientation was substantially reduced with increasing loading of CaSub particles.



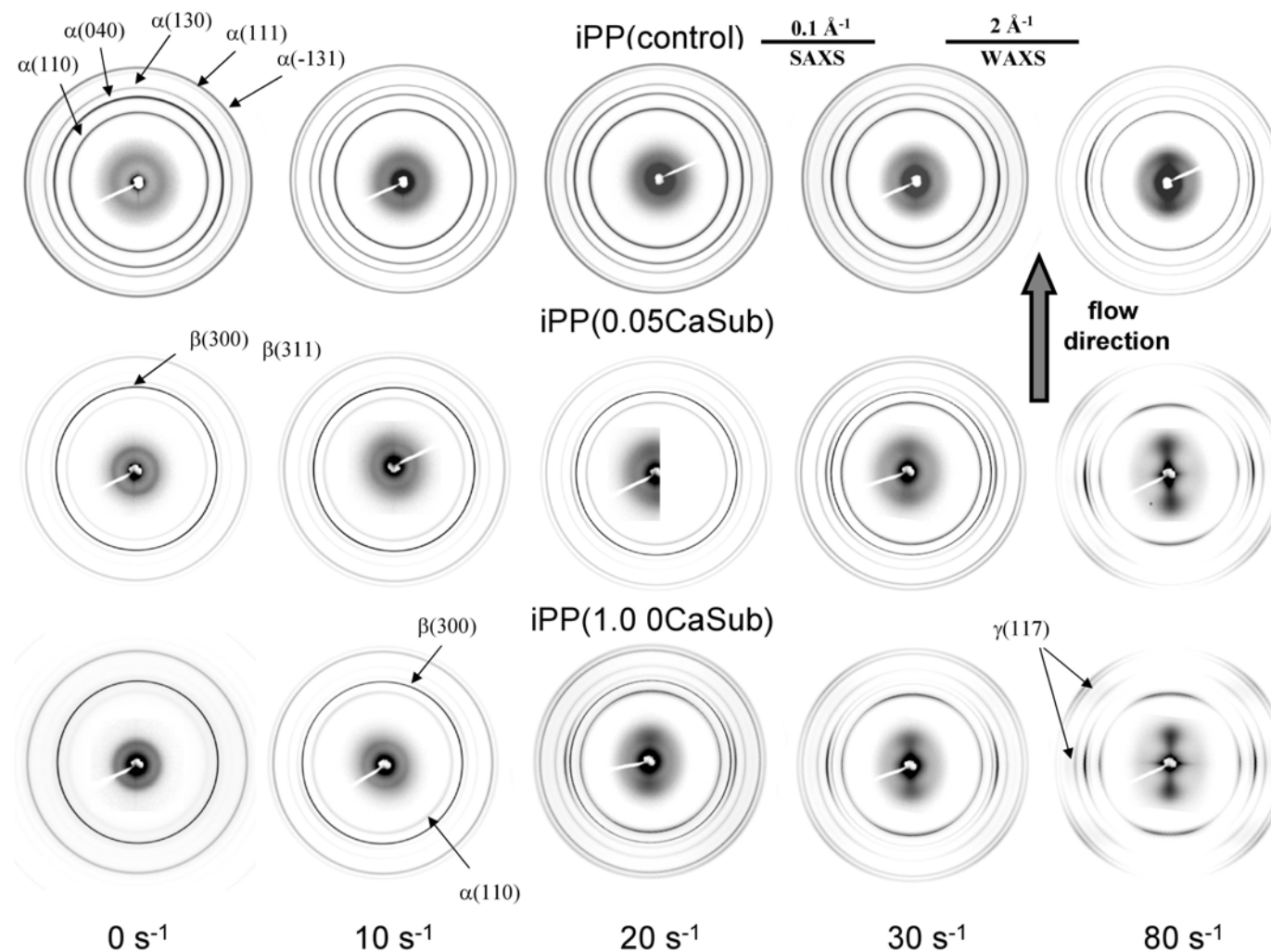


**Figure 6.7.** Simultaneous SAXS/WAXS images at different shear rates and CaSub loading level (shear time = 1 s, shear temperature = 135 °C).

In the SAXS region, above a critical shear rate the concentric rings concentrated into lobes in the meridian (kebabs). Furthermore, at higher shear rates sharp equatorial streaks were observed close into the beamstop (shish). Along with the previously described WAXS patterns, these SAXS patterns are in agreement with the formation of the shish-kebab structure described in **Chapter 4.3.2**. The addition of CaSub particles reduced the shear rate required to observe oriented structures in the SAXS patterns from  $30 \text{ s}^{-1}$  for iPP(control) to  $20 \text{ s}^{-1}$  for iPP(0.05CaSub) to  $10 \text{ s}^{-1}$  for iPP(1.00CaSub).

For iPP(control), the orientation of the  $\alpha$ -iPP c-axis and lamellar normal coincided with the flow direction and the long axis of the shish. Although the  $\alpha$ -iPP c-axis and lamellar normals coincided for the samples containing CaSub particles, they were both slightly inclined toward the flow direction and the long axis of the shish. In the sample containing iPP(0.05CaSub) and iPP(1.00CaSub) the offset angle was  $3^\circ$  and  $5^\circ$  respectively. This reveals that some portion of lamellar growth in the sample containing CaSub particles occurred at an inclination to the shish wall.

To further probe the evolution of crystalline morphology with shear rate and CaSub loading level, the  $\alpha$ -iPP ( $\chi_\alpha$ ),  $\beta$ -iPP ( $\chi_\beta$ ),  $\gamma$ -iPP ( $\chi_\gamma$ ) and volume ( $\chi_v$ ) crystallinity indices were determined from the WAXS patterns according to the procedures outlined in **Chapter 3.3.1.5**. The results are plotted in **Figure 6.8a-d**. For iPP(control), initially increasing the shear rate led to an increase in  $\chi_\beta$  which reached a peak at  $30 \text{ s}^{-1}$ . Further increases in shear rate resulted in a steady decline in  $\chi_\beta$ . The application of shear flow to the samples containing CaSub resulted in a substantial decrease in the  $\chi_\beta$  level observed under quiescent crystallisation conditions. There was an unexpected dependence on CaSub loading level, with the observed decrease in  $\chi_\beta$  with increasing shear rate occurring more slowly as the loading level was reduced. This resulted in the  $\chi_\beta$  content at the highest shear rates increasing with decreasing loading of CaSub particles. Increasing the shear rate did not appreciably influence  $\chi_\gamma$  for iPP(control). No measurable  $\chi_\gamma$  was observed for the samples containing CaSub particles for shear rates below  $10 \text{ s}^{-1}$ . However with increasing shear rate above  $20 \text{ s}^{-1}$ ,  $\chi_\gamma$  increased, approaching the  $\chi_\gamma$  level of iPP(control). For iPP(control), the shear rate did not appreciably alter  $\chi_v$ . For the samples containing CaSub particles, a slightly higher  $\chi_v$  was observed for shear rates below  $10 \text{ s}^{-1}$ .

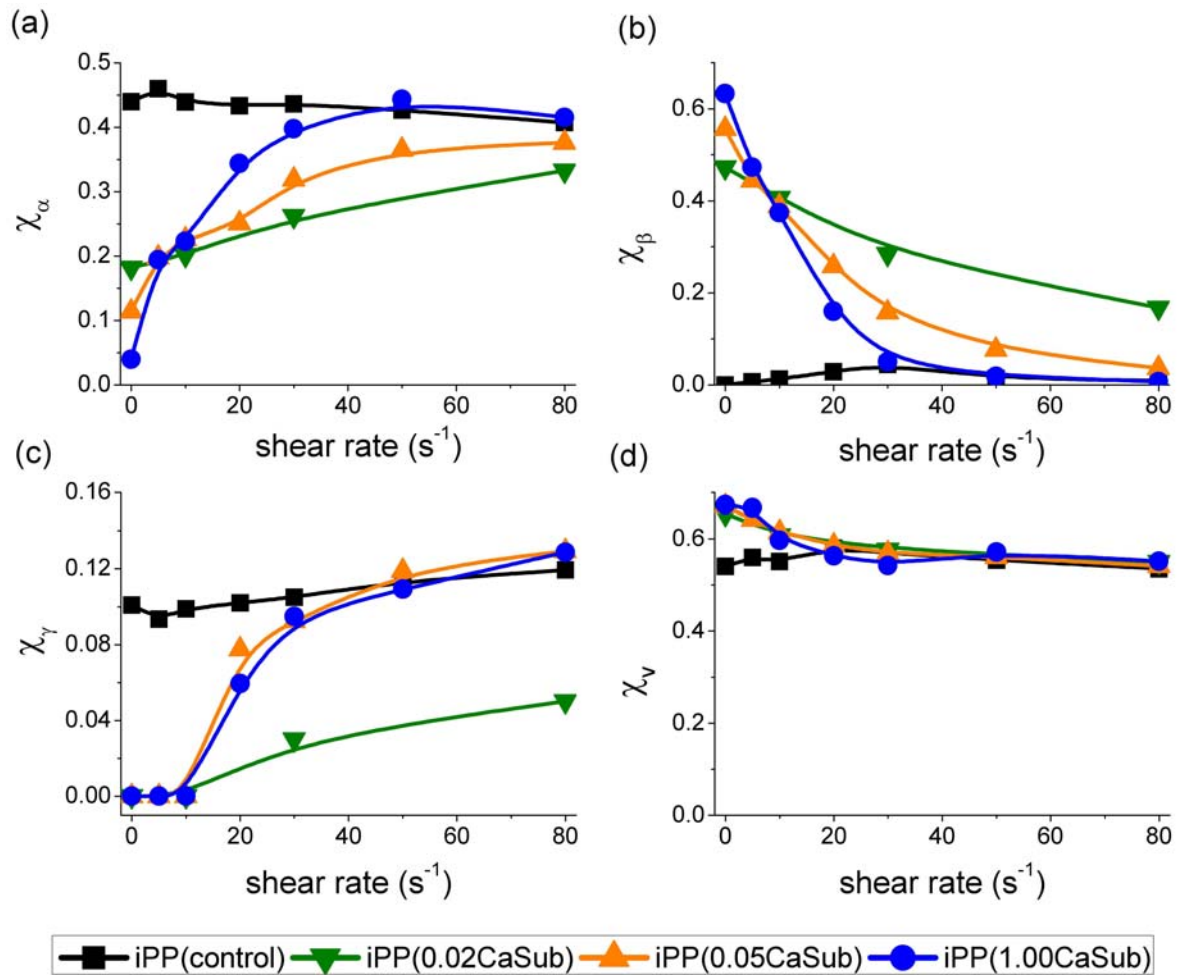


**Figure 6.8.** Influence of shear rate and loading level on (a)  $\alpha$ -iPP ( $\chi_{\alpha}$ ), (b)  $\beta$ -iPP ( $\chi_{\beta}$ ), (c)  $\gamma$ -iPP ( $\chi_{\gamma}$ ) and (d) volume ( $\chi_v$ ) crystallinity indices (shear time = 1 s, shear temperature = 135 °C).

### 6.3.3 Influence of flow condition on the orientation of iPP

**Figure 6.9** shows the influence of shear rate and CaSub loading level on the Herman's orientation function of the c-axis ( $f_{c(\alpha)}$ ), b-axis ( $f_{b(\alpha)}$ ) and a-axis ( $f_{a(\alpha)}$ ) of the  $\alpha$ -iPP crystals determined according to the procedures described in **Chapter 3.3.1.5**. No orientation was observed until a critical shear rate. Above this shear rate  $f_{c(\alpha)}$  was always positive and increased with increasing shear rate. This showed that the flow induced the c-axis of the crystals (molecular chain helix axis) to become aligned along the flow direction.  $f_{c(\alpha)}$  is influenced by the formation of the oriented PD lamellar structure. As discussed in **Chapter 4.3.2** the PD lamellar structure contains a bimodal distribution of lamellae where the crystalline c-axis of daughter lamella are essentially

perpendicular to the crystalline c-axis of their parent lamella. Therefore the presence of daughter lamella reduces the measured  $f_{c(\alpha)}$  value. Above the critical shear rate  $f_{b(\alpha)}$  was always negative and decreased with increasing shear rate. This is due to the b-axis of both parent and daughter lamellae being inclined perpendicular to the flow direction. For all samples  $f_{a(\alpha)}$  did not change appreciably, perhaps decreasing slightly at higher shear rates and loading levels. This may indicate the a-axis of  $\alpha$ -iPP crystal was not oriented by flow. However,  $f_{a(\alpha)}$  is also influenced by the relative concentration of orientated parent and daughter lamellae, which also have near perpendicular a-axes.

The addition of CaSub particles decreased the critical shear rate required to detect measurable  $\alpha$ -iPP orientation. For iPP(control) a critical shear rate of  $30 \text{ s}^{-1}$  was needed to induce oriented structures. In iPP(0.05CaSub) the critical shear rate was  $20 \text{ s}^{-1}$  while in iPP(1.00CaSub) it was  $10 \text{ s}^{-1}$ . Furthermore, for a given set of processing conditions, increasing CaSub loading resulted in a considerable increase in  $f_{c(\alpha)}$  as well as a decrease of  $f_{b(\alpha)}$ . This confirms that the addition of CaSub particles substantially increased the orientation of  $\alpha$ -iPP crystals.

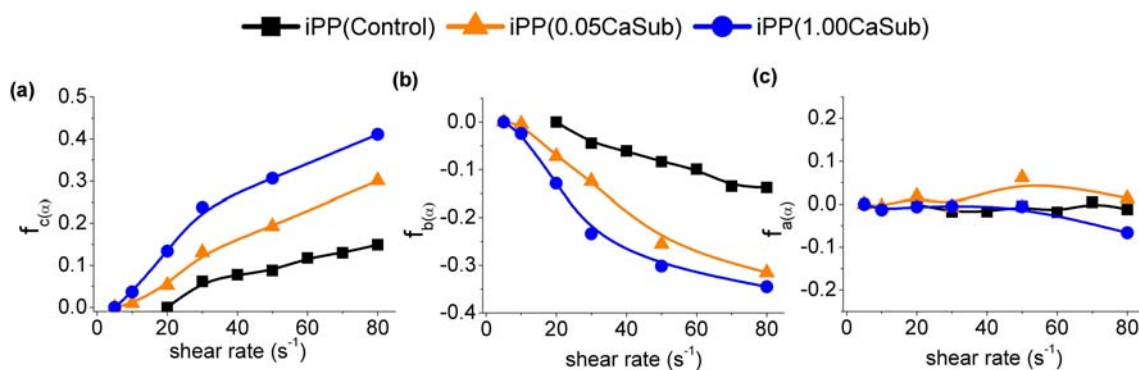


**Figure 6.9.** Influence of shear rate of the Herman's orientation for  $\alpha$ -iPP for samples containing different loading levels of CaSub nucleant agent (shear time = 1 s, shear temperature =  $135^\circ\text{C}$ ).

The influence of shear rate and loading level on orientation of  $\beta$ -iPP crystals ( $f_{h(\beta)}$ ) is shown in **Figure 6.10a**. The critical shear rate required to attain  $\beta$ -iPP orientation was slightly higher than that observed for  $\alpha$ -iPP orientation. For iPP(control) a shear rate of  $50 \text{ s}^{-1}$  was required, while for iPP(0.05CaSub) and iPP(1.00CaSub) it was  $30 \text{ s}^{-1}$  and  $20 \text{ s}^{-1}$  respectively. The  $\beta(300)$  plane is perpendicular to the  $\beta$ -iPP c-axis and therefore a decrease in  $f_{h(\beta)}$  is expected when the chain axis becomes aligned along the flow

direction. Increasing the loading of CaSub generally resulted in lower  $f_{h(\beta)}$  values compared to iPP(control). This indicates increased  $\beta$ -iPP c-axis orientation in these samples. However, at high shear rates  $f_{h(\beta)}$  was somewhat lower in iPP(0.05CaSub) compared to iPP(1.00CaSub).

The influence of nucleant loading level and shear rate on the orientation of the  $\gamma$ -iPP crystals ( $f_{h(\gamma)}$ ) is shown in **Figure 6.10b**. Above the critical shear rate required to observe  $\gamma$ -iPP orientation, the value of  $f_{h(\gamma)}$  decreased with increasing shear rate. This is expected as the  $\gamma(117)$  plane is nearly perpendicular to the one half of the chains which are oriented along the flow direction in the parallel chain-axis orientation. Increasing loading of CaSub particles decreased  $f_{h(\gamma)}$  compared to iPP(control). This shows that for a given set of processing conditions, the addition of CaSub particles also increased the orientation of  $\gamma$ -iPP.

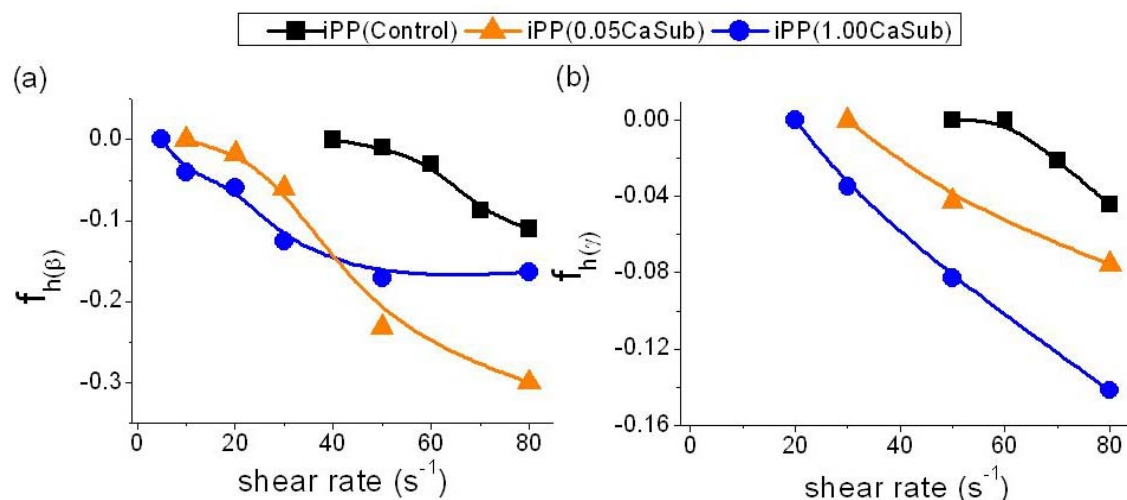


**Figure 6.10.** Influence of shear rate of the Herman's orientation for (a)  $\beta$ -iPP and (b)  $\gamma$ -iPP for samples containing different loading levels of CaSub nucleant agent (shear time = 1 s, shear temperature = 135 °C).

The influence of shear rate and CaSub loading level on the lamellar orientation was also investigated. **Figure 6.11** shows the influence of shear rate on the azimuthal intensity profile for iPP(control) and iPP containing CaSub. The absence of any intensity variation with azimuthal angle indicates that the lamellar orientation was isotropic, while variations in the azimuthal profile may indicate the presence of lamellar orientation. Further quantitative assessment of the level of lamellar orientation was performed by calculating the lamellar orientation parameter ( $f_{h(SAXS)}$ ) using **Equation**

**3.24** and the method described in **Chapter 3.3.1.5**. The results are shown in **Figure 6.12**. In iPP(control), no lamellar orientation was observed until a shear rate of  $30 \text{ s}^{-1}$ . Increasing the shear rate resulted in an increase in intensity along the meridian indicating an increase in lamellae with normals oriented along the flow direction. The addition of CaSub decreased the critical shear rate required to observed lamellar orientation consistent with that observed in the WAXS results. The critical shear rate required to observe lamellar orientation was  $20 \text{ s}^{-1}$  and  $10 \text{ s}^{-1}$  for iPP(1.00CaSub) and iPP(0.05CaSub), respectively. For a given set of processing conditions, the addition of CaSub also resulted in an increase in the relative height of the meridional peak and the magnitude of  $f_{h(\text{SAXS})}$  compared to iPP(Control). This indicated increased lamellar orientation in the presence of CaSub particles. At higher shear rates, and especially for the higher loading level, an increase in oriented scattering was also observed in the equatorial region. This scattering could be due to either oriented daughter lamellar or shish. Although signifying higher lamellar orientation, its presence may account for the observed reduction in the  $f_{h(\text{SAXS})}$  values of the nucleated samples at the higher shear rates.

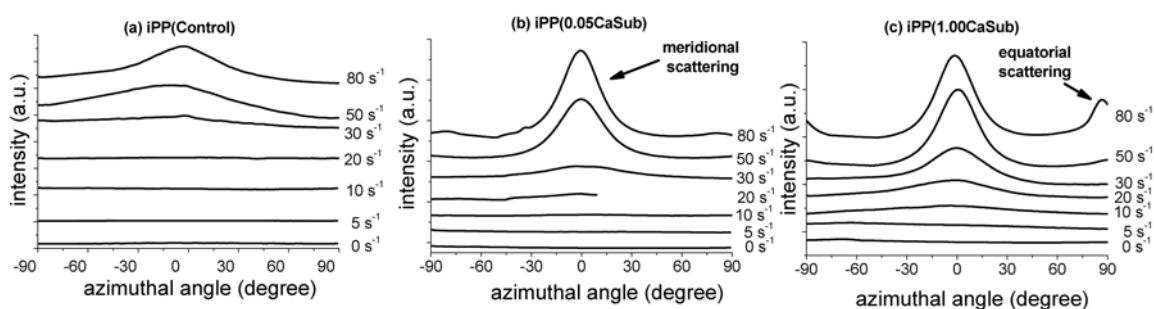


**Figure 6.11.** Small angle x-ray scattering azimuthal intensity profile as a function of shear rate (shear time = 1 s, shear temperature =  $135^\circ\text{C}$ ).

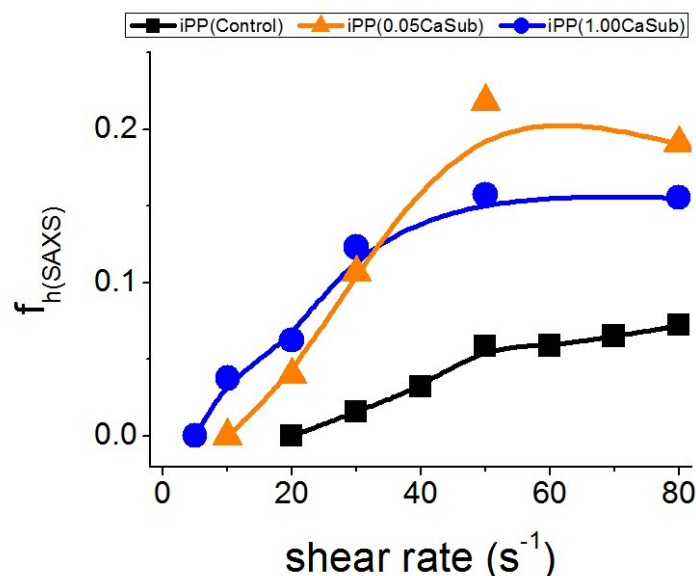


**Figure 6.12.** Influence of shear rate and loading level on the lamellar orientation function ( $f_{h(\text{SAXS})}$ ) (shear time = 1 s, shear temperature = 135 °C).

#### 6.3.4 Ex-situ microscopy of permanganate etched samples

In this section etched samples of iPP(control) and iPP(1.00CaSub) isothermally crystallised at 135 °C under quiescent conditions as well as after a moderate step shear were investigated using ROM and SEM. **Figure 6.13** shows representative SEM micrographs of the samples crystallised under quiescent conditions. Both micrographs are near the centre of the disk and are imaged through the thickness direction. Examination of the micrographs revealed characteristic hierarchical structures in both samples. The spherulites in iPP(control) were significantly larger than those found in iPP(1.00CaSub) which had an oval shape. Significant differences were observed between the inner structure of the spherulites in the two samples. iPP(control) spherulites showed a core-shell type structure as described previously in **Chapter 4.3.1**, and is consistent with them being  $\alpha$ -iPP spherulites. Alternatively, the neighbouring lamellae in the core of the iPP(1.00CaSub) spherulites were almost parallel in the centre. However, with increasing distance along the major axis they splayed due to lamellar branching to form an oval-like structure. Along the minor axis of the spherulite a flower cup arrangement was observed. This morphology is consistent with the spherulites in iPP(1.00CaSub) sample being  $\beta$ -iPP [44, 151].



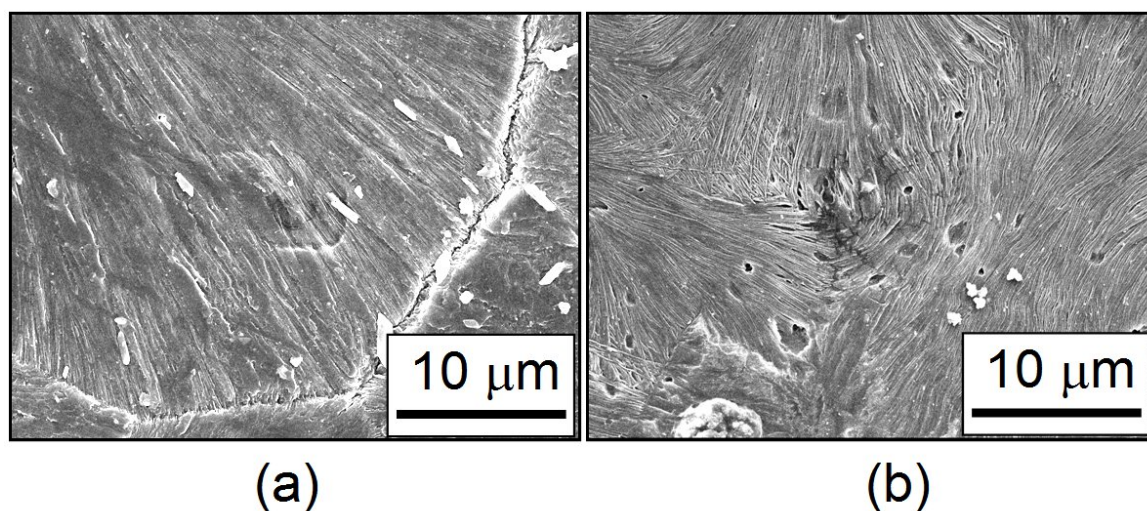


**Figure 6.13.** Scanning electron micrographs of the morphology of (a) iPP(Control) and (b) iPP(1.00CaSub) crystallised under quiescent conditions at 135 °C.

The ROM and SEM micrographs of samples crystallised under flow-induced conditions are shown in **Figure 6.14**. The ROM images revealed the shish in both samples were aligned with their long axis along the flow direction. However, the addition of CaSub particles substantially increased the number of shish and perhaps slightly decreased their alignment along the flow direction compare to iPP(control). At higher magnification the shish appeared to be highly etched, which could possibly indicate they are a region of lower order or higher internal stress. Interestingly, at higher magnification it appeared that the shish core was not straight, but rather it took a meandering path. Furthermore, in some cases the shish core appeared to have formed small branches. The shish in iPP(1.00CaSub) were more contorted and had more branches compare to iPP(control). Extending approximately 90° from the shish wall were primary lamellae (kebabs). Further out from the shish the primarily lamellae appeared to have curved to avoid impingement from neighbouring lamellae which formed at different regions along the meandering shish. The direction of the curvature of the lamellar normal was generally toward the flow direction. Smaller secondary lamellae (daughters), which were inclined  $80 \pm 2^\circ$  to the primary lamellae, filled the space between the primary lamellae. In both samples, small spherulites were also observed between the shish-kebab structures. The spherulites in the iPP(1.00CaSub) sample were much smaller but more numerous compared to those in iPP(control).





information about growth geometry was obtained by fitting the crystallisation data to the Avrami model according to the procedure outlined in **Chapter 2.2.3** and using **Equation 2.6** to obtain the Avrami exponent ( $n$ ). The influence of shear rate and CaSub loading level on these parameters is provided in **Table 6.3**.

The development of crystallinity of iPP(control) and the samples containing different loading levels of CaSub is presented in **Figure 6.15**. Increasing the loading level decreased  $t_{0.1}$  and  $t_{0.5}$  highlighting increased rates of crystallisation in the presence of CaSub. This is consistent with the non-isothermal DSC parameters presented in **Table 6.1**. In the samples containing CaSub particles,  $\beta$ -iPP crystals were universally found to have formed before  $\alpha$ -iPP crystals. This is the reason for the higher volume fraction of  $\beta$ -iPP in the samples containing CaSub.

Flow led to a marked decrease in  $t_{0.1}$  and  $t_{0.5}$  for  $\chi_v$ , **Figure 6.16**. The increased crystallisation rates implies the formation of additional flow-induced nuclei. Flow in the presence of the CaSub particles however did not significantly reduce  $t_{0.1}$  for  $\beta$ -iPP crystals, **Table 6.3**, yet flow did reduce  $t_{0.1}$  for the  $\alpha$ -iPP crystals. This resulted in a substantial delay from the time when the first  $\alpha$ -iPP crystals appeared to when the first  $\beta$ -iPP crystals appeared, **Figure 6.17**. This delay is the primary reason for the reduction in  $\chi_\beta$  content in these samples.

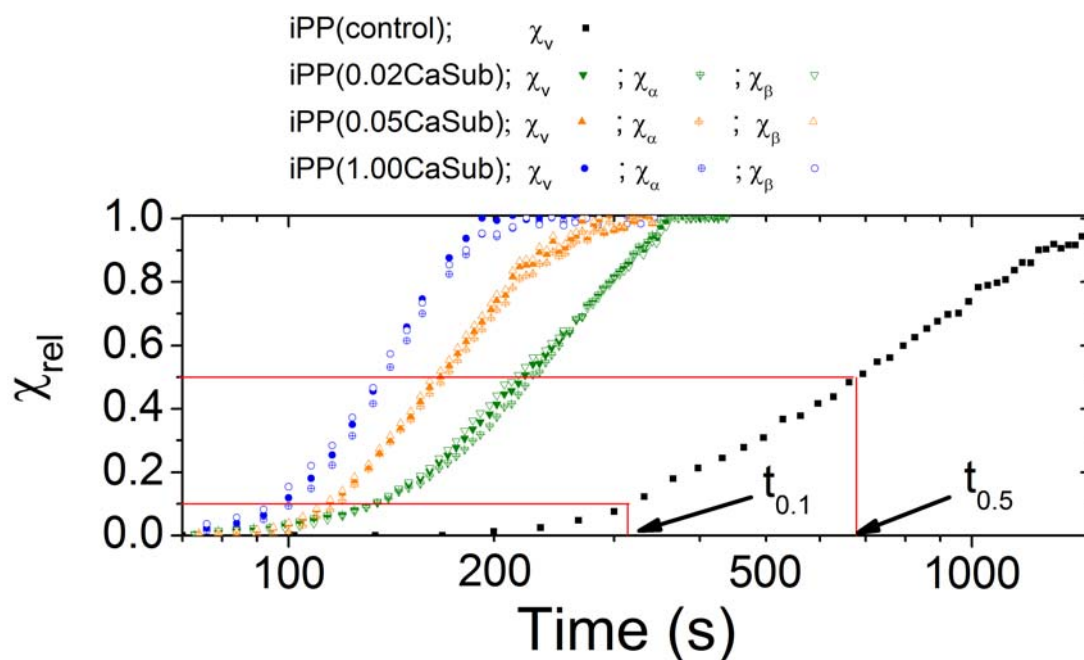


**Figure 6.15.** Changes in the relative crystallinity ( $\chi_{rel}$ ) of the  $\alpha$ -iPP ( $\chi_\alpha$ ) and  $\beta$ -iPP ( $\chi_\beta$ ) contributions to the volume crystallinity ( $\chi_v$ ) during quiescent crystallisation at 135 °C.

**Table 6.3.** Influence of shear rate and Ca-Sub loading level on the time to reach 10% conversion ( $t_{0.1}$ ), 50 % conversion ( $t_{0.5}$ ) and the Avrami exponent ( $n$ ) for  $\alpha$ -iPP ( $\chi_\alpha$ ),  $\beta$ -iPP ( $\chi_\beta$ ) and volume contributions ( $\chi_v$ ) to WAXS scattering (shear time = 1 s, shear temperature = 135 °C).

Material	shear rate (s <sup>-1</sup> )	$\chi_\alpha$			$\chi_\beta$			$\chi_v$		
		$t_{0.1}$ (s)	$t_{0.5}$ (s)	$n$	$t_{0.1}$ (s)	$t_{0.5}$ (s)	$n$	$t_{0.1}$ (s)	$t_{0.5}$ (s)	$n$
iPP(control)	0	340 ± 4	753 ± 8	3.1 ± 0.2	-	-	-	340 ± 4	753 ± 8	3.0 ± 0.2
	10	186 ± 2	371 ± 4	2.9 ± 0.1	296 ± 9	450 ± 20	2.8 ± 0.1	186 ± 2	371 ± 4	2.9 ± 0.1
	30	94 ± 1	176 ± 2	2.7 ± 0.1	98 ± 1	177 ± 2	2.9 ± 0.1	94 ± 1	176 ± 2	2.8 ± 0.1
	80	61 ± 1	114 ± 2	2.4 ± 0.1	97 ± 1	127 ± 1	3.2 ± 0.2	61 ± 1	115 ± 2	2.4 ± 0.1
iPP(0.02CaSub)	0	140 ± 2	228 ± 3	2.9 ± 0.2	135 ± 3	217 ± 4	2.5 ± 0.2	137 ± 3	222 ± 5	2.6 ± 0.2
	10	70 ± 2	110 ± 3	2.6 ± 0.2	89 ± 2	133 ± 3	3.0 ± 0.1	74 ± 1	130 ± 3	3.0 ± 0.1
	30	48 ± 5	98 ± 8	2.5 ± 0.1	78 ± 1	119 ± 1	2.9 ± 0.2	57 ± 2	112 ± 3	2.7 ± 0.1
	80	36 ± 1	93 ± 1	2.2 ± 0.1	73 ± 1	119 ± 1	3.1 ± 0.2	38 ± 1	98 ± 1	2.4 ± 0.1
iPP(0.05CaSub)	0	120 ± 3	170 ± 4	2.8 ± 0.3	110 ± 2	161 ± 2	2.3 ± 0.1	112 ± 2	166 ± 2	2.4 ± 0.1
	10	77 ± 2	149 ± 4	2.7 ± 0.3	105 ± 1	157 ± 2	3.1 ± 0.1	92 ± 1	157 ± 2	3.0 ± 0.1
	30	47 ± 1	102 ± 2	2.3 ± 0.1	82 ± 1	120 ± 1	3.1 ± 0.2	69 ± 1	115 ± 2	2.7 ± 0.2
	80	35 ± 1	70 ± 1	1.9 ± 0.1	65 ± 1	93 ± 1	3.4 ± 0.1	40 ± 1	72 ± 1	2.0 ± 0.1
iPP(1.00CaSub)	0	102 ± 2	140 ± 2	2.6 ± 0.1	92 ± 2	134 ± 2	2.3 ± 0.1	100 ± 2	138 ± 2	2.3 ± 0.1
	10	69 ± 1	118 ± 1	2.6 ± 0.1	75 ± 1	120 ± 1	2.7 ± 0.1	75 ± 1	120 ± 1	2.7 ± 0.1
	30	57 ± 1	113 ± 2	2.5 ± 0.1	82 ± 1	122 ± 1	3.0 ± 0.1	67 ± 1	116 ± 2	2.6 ± 0.1
	80	29 ± 1	86 ± 4	1.6 ± 0.1	81 ± 1	127 ± 1	3.3 ± 0.2	29 ± 1	86 ± 4	1.7 ± 0.1

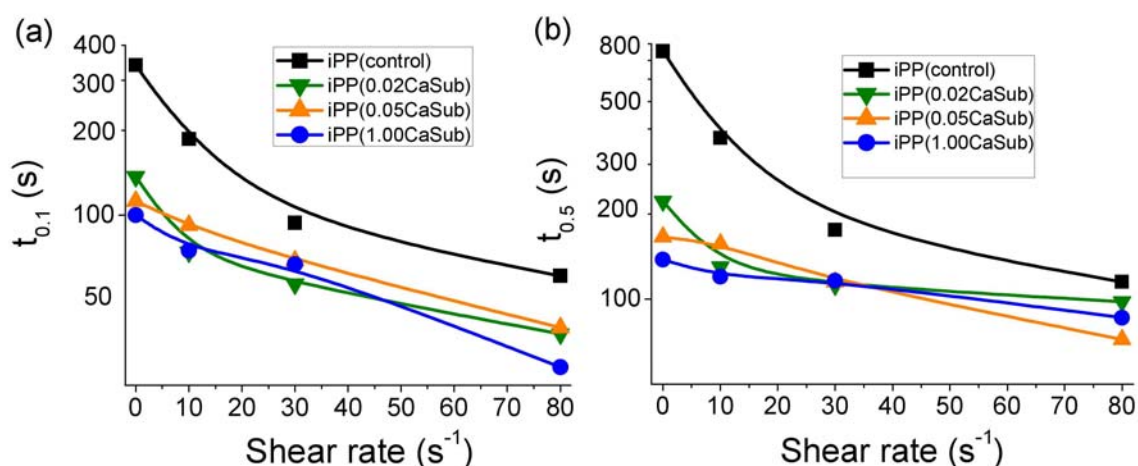


**Figure 6.16.** Influence of shear rate and loading level of CaSub on (a) the induction time ( $t_{0.1}$ ) and (b) the crystallisation half time ( $t_{0.5}$ ) of the volume crystallinity ( $\chi_v$ ) (shear time = 1 s, shear temperature = 135 °C).

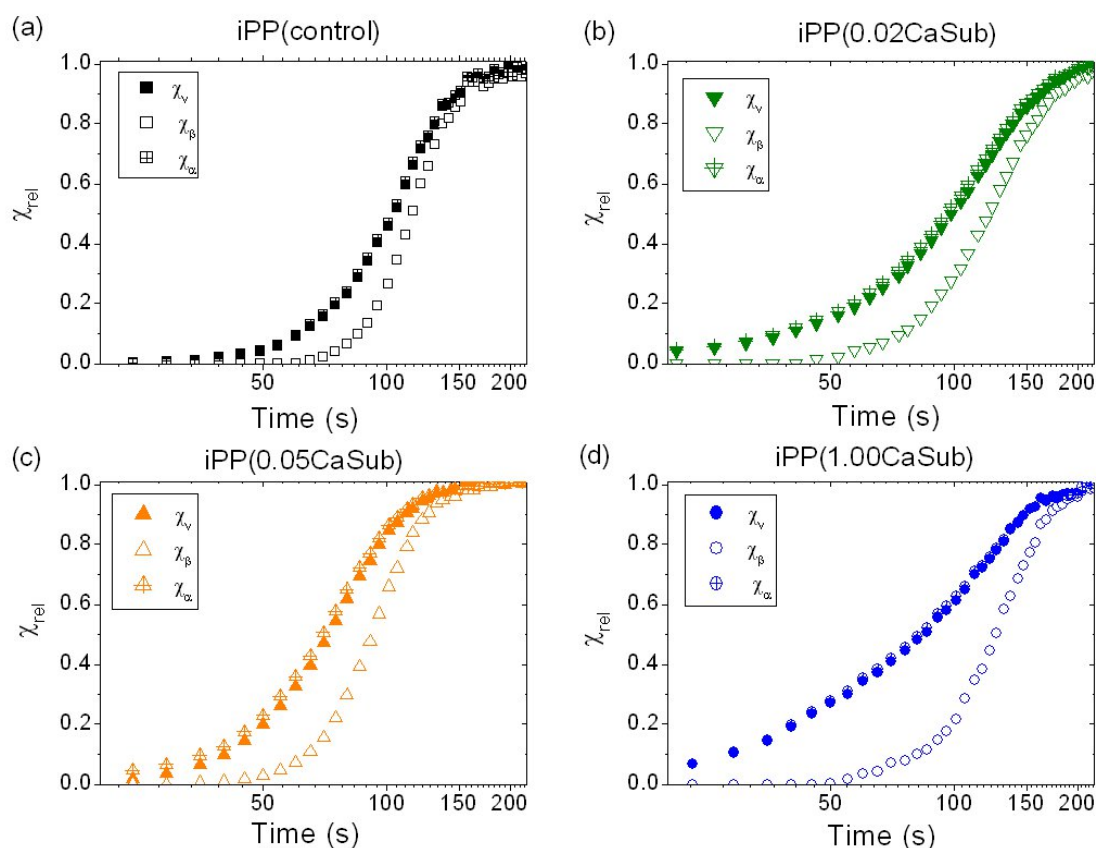


**Figure 6.17.** Changes in the relative crystallinity ( $\chi_{rel}$ ) of  $\alpha$ -iPP ( $\chi_\alpha$ ) and  $\beta$ -iPP ( $\chi_\beta$ ) contributions to the volume crystallinity ( $\chi_v$ ). (a) iPP(control), (b) iPP(0.02CaSub), (c) iPP(0.05CaSub) and (d) iPP(1.00CaSub) (shear rate = 80 s<sup>-1</sup>, shear time = 1 s, shear temperature = 135 °C).

**Table 6.3** shows the influence of shear rate and CaSub loading level on the Avrami exponent. In iPP(control) crystallised under quiescent conditions the Avrami exponent for  $\chi_v$  was  $\sim 3$  indicating a spherical growth geometry. This is consistent with the spherulites presented in **Figure 6.13**. The addition of CaSub particles reduced the Avrami exponent for  $\chi_v$ . The reduction in  $\chi_v$  was due primarily to the reduction in the  $\chi_\beta$  component. It is worth noting here that as well as signifying a change in the growth geometry, a reduction in the Avrami exponent can indicate confined growth conditions [85, 247]. Therefore in combination with the spherulites observed in **Figure 6.13** this result suggests that confined  $\beta$ -iPP crystallisation occurred on the surface of the CaSub particles. Increasing shear rate led to a reduction in the Avrami exponent for  $\chi_v$  component for all samples to around to  $\sim 2$  i.e. disk-like growth. The reduction was greater with increasing CaSub loading level. This is consistent with the growth geometry changing from spherulite to the shish-kebab type morphology presented in **Figure 6.14**. The reduced Avrami exponent was due entirely to the reduction in the  $\chi_\alpha$  component. Interestingly, in iPP(control) the Avrami exponent of  $\chi_\beta$  did not change appreciably with increasing shear rate, while in the nucleated samples it increased with increasing shear rate. This indicates that the mechanism of  $\beta$ -iPP formation in the presence CaSub particles changes under flow-induced crystallisation conditions. Indeed, the similar Avrami exponent for the  $\chi_\beta$  component of all samples at the high shear rates alludes to similar growth conditions of  $\beta$ -iPP for all samples.

Further analysis was performed on sheared iPP(control) to investigate the development of orientation of the  $\alpha$ -iPP and  $\beta$ -iPP crystallites during crystallisation. The orientation of each phase was characterised by calculating the oriented fraction of crystallites ( $\Phi_c$ ) according to the method described in **Chapter 3.3.1.5**. The results are presented in **Figure 6.18**. The oriented fraction of  $\alpha$ -iPP crystallites was the highest at the early stages of crystallisation. The oriented fraction of  $\alpha$ -iPP crystallises was then observed to decrease during crystallisation, before reaching a plateau of 0.26. On the other hand  $\beta$ -iPP crystallites were essentially unoriented at the start of crystallisation. The fraction of oriented  $\beta$ -iPP crystallites then increased as crystallisation progressed, before reaching a plateau of 0.15.

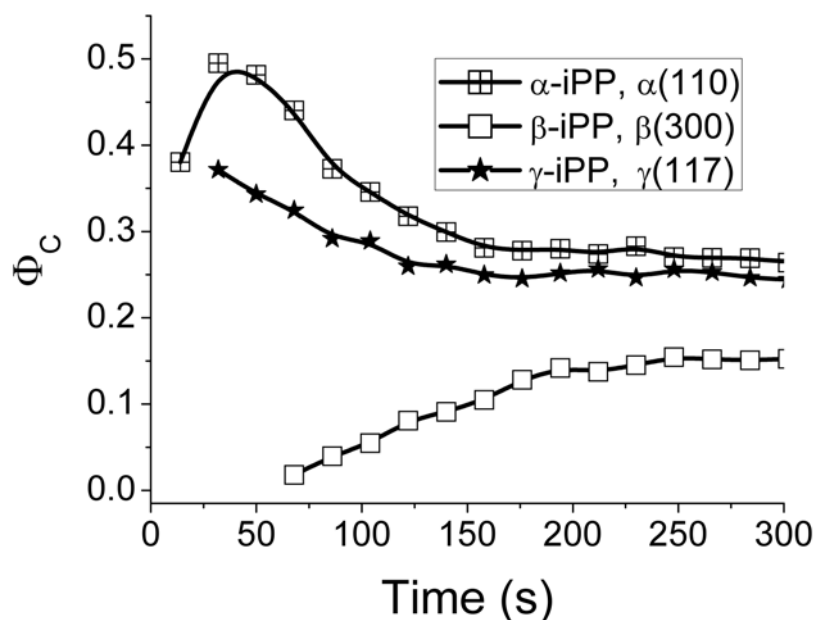


**Figure 6.18.** Development of the oriented fraction of crystals ( $\Phi_c$ ) for  $\alpha$ -iPP,  $\beta$ -iPP and  $\gamma$ -iPP during crystallisation in iPP(control) (shear rate =  $80 \text{ s}^{-1}$ , shear time = 1 s, shear temperature  $135^\circ\text{C}$ ).

**Figure 6.19** shows the influence of the addition of various loading of CaSub particles on the two-dimensional SAXS patterns at selected times after then end of shear flow. For all samples, immediately after the flow stopped sharp equatorial streaks were observed, which are indicative of the formation of shish aligned with their long axis along the flow direction. Increasing the loading level increased the relative intensity of the equatorial streak as well as extended the scattering to larger scattering vectors. This confirms that the addition of CaSub particles increases the number and density of the shish. After an induction period scattering was observed along the meridian and increased as time progressed. This meridional scattering is consistent with the formation of chain folded lamellae (kebabs) with normals aligned close to the flow direction. In all samples the meridional maximum did not start exactly on the meridian and were not  $90^\circ$  to the equatorial streaks. This indicates that the kebab normals are initially inclined to the plane of the shish. The addition of CaSub appeared to increase this inclination.

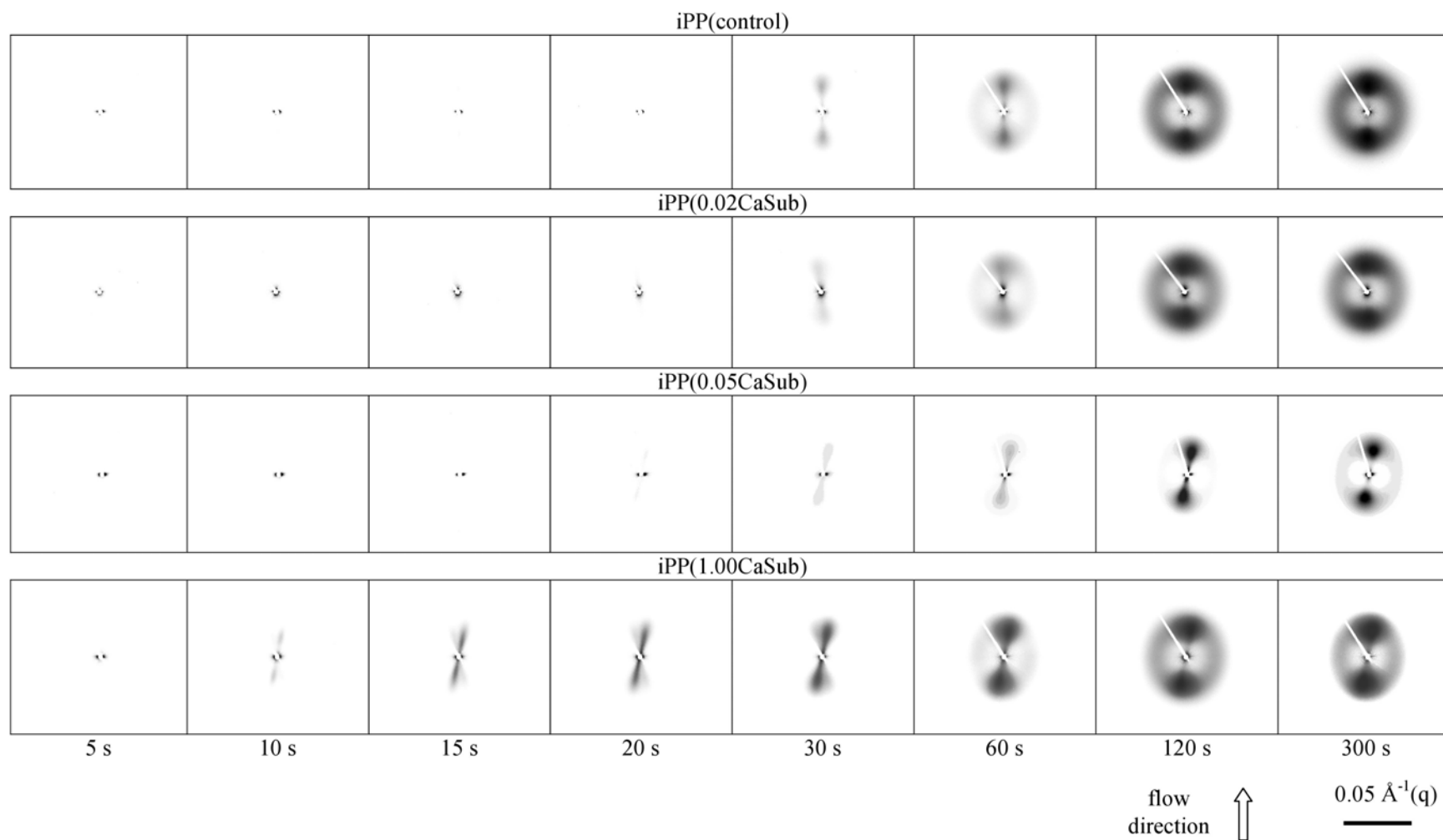


**Figure 6.19.** Two-dimensional SAXS patterns of pure iPP and iPP containing various loading levels of CaSub particles at selected times after shear flow (shear rate =  $80 \text{ s}^{-1}$ , shear time = 1 s, shear temperature =  $135 \text{ }^{\circ}\text{C}$ ). Flow direction is vertical.

Quantitative measurements were performed to further investigate the nucleation and growth of oriented lamellae, **Figure 6.20**. The position of the meridional peak gives information about the direction the average kebab normal makes to the flow direction. **Figure 6.20a** confirms that for all samples, the first kebabs to form did not have their normals aligned along the flow direction, but instead were slightly inclined. As crystallisation progressed and the kebabs grew, the lamellae normals in all samples tended to become more aligned along the flow direction. This can be explained by the kebab normals curving towards the flow direction. Increasing the loading of CaSub particles substantially increased the magnitude of the initial inclination as well as increased the final average inclination of kebab normals to the flow direction.

The oriented fraction of lamellae ( $\Phi_L$ ) was determined according to the procedures previously detailed in **Chapter 3.3.1.5** and using **Equation 3.25**. All samples showed the highest  $\Phi_L$  at the first stages of crystallisation, **Figure 6.20b**. As crystallisation progressed,  $\Phi_L$  decreased. This can be explained by the highly oriented kebabs growing first followed by the nucleation and growth of unoriented lamellae at latter stages. Both the initial  $\Phi_L$  immediately after shear flow was applied and the final  $\Phi_L$  after crystallisation had essentially finished were dramatically increased with increasing CaSub loading. This is consistent with the higher density of shish observed in these samples.

The full width at half maximum (FWHM( $\varphi$ )) of the meridional peak along the azimuthal direction was also determined to determine the distribution of lamellae normals during crystallisation, **Figure 6.20c**. For each data point the azimuthal intensity profile was fitted using a Gaussian function and its FWHM( $\varphi$ ) was obtained. A smaller value of FWHM( $\varphi$ ) indicates a narrower distribution of oriented lamellae normals [49]. For all samples, the FWHM( $\varphi$ ) increased during crystallisation, further indicating that the kebabs curved as they grew.

The development of the lamellar orientation function during crystallisation was also investigated, **Figure 6.20d**. The magnitude of the lamellar orientation is related to the individual components presented in **Figure 6.20a-c**.  $f_{h(\text{SAXS})}$  decreased as crystallisation



progressed for all samples. This is primarily due to the large drop in  $\Phi_L$  but also, to a smaller extent, the increase in  $\text{FWHM}(\varphi)$ .

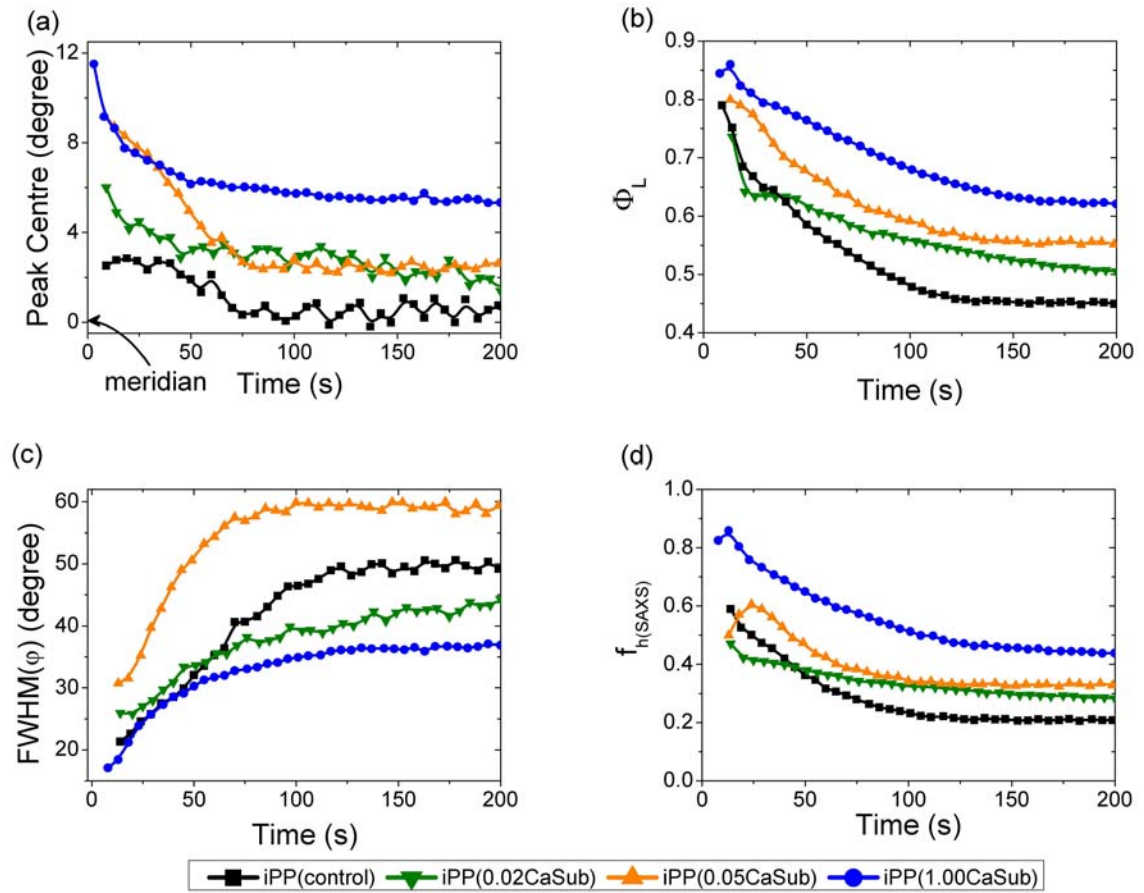


**Figure 6.20.** Influence of CaSub loading level on (a) the position of meridional maximum, (b) the oriented fraction of lamellae ( $\Phi_L$ ), (c) the full width at half maximum (FWHM) of kebabs and (d) the lamellar orientation function during isothermal crystallisation (shear rate =  $80 \text{ s}^{-1}$ , shear time = 1 s, shear temperature =  $135^\circ\text{C}$ ).

### 6.3.6 In-situ melting experiments

In the experiments described in this section, previously crystallised samples are re-melted then recrystallised. The experiments are performed to confirm (a) the origin of the multiple melting peaks observed in the DSC thermograms in **Figure 6.6** and (b) to confirm that the  $\beta$ -iPP selectivity of the CaSub particles is not destroyed by the imposed thermal-shear profile.

**Figure 6.21a** shows the changes that occurred to the integrated intensity of  $\alpha(110)$  and  $\beta(300)$  reflections during melting. During melting of the iPP(control) sample, the area

of the  $\alpha(110)$  reflection remained relatively constant until  $\sim 150$  °C where it then steadily decreased until it had completely disappeared at 174 °C. Conversely, the  $\alpha(110)$  intensity for the iPP(1.00CaSub) sample increased slightly over the range 150 – 160 °C before decreasing rapidly and finally disappearing at 176 °C. The area of the  $\beta(300)$  reflection initially remained relatively constant up to 144 °C before decreasing rapidly and disappearing altogether by 164 °C.

**Figure 6.21b** shows the changes that occurred to the FWHM(q) of the  $\alpha(110)$  and  $\beta(300)$  reflections during melting. The FWHM(q) can indicate the change in the relative size of the crystallites according to the Scherrer equation (**Equation 3.10**). During melting of iPP(control), the FWHM(q) of the  $\alpha(110)$  reflection decreased during heating up to 171 °C before increasing rapidly again during the later stages of melting. This can be explained by the melting of the smaller and less perfect lamellae followed by the eventual melting of the smaller lamellae at higher temperature. The trend in the FWHM(q) of the  $\alpha(110)$  of the iPP(1.00CaSub) sample was similar for iPP(control) at low and high temperatures. However, the FWHM(q) briefly increased between 150 °C and 160 °C. This is the same temperature range as the observed increase in  $\alpha(110)$  peak intensity and would appear to indicate the formation of additional small  $\alpha$ -iPP crystals. The FWHM(q) of the  $\beta(300)$  reflection showed a plateau between 135-145°C which would also be consistent with the formation of additional  $\beta$ -iPP crystals.

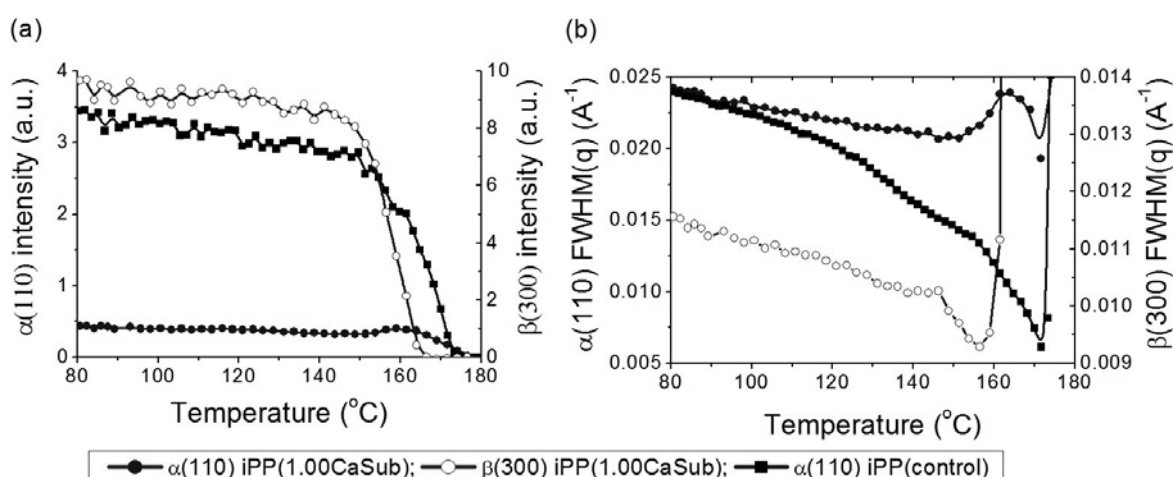


**Figure 6.21.** Influence of temperature on (a) the relative intensity and (b) the full width at half maximum (FWHM) of the  $\alpha(110)$  and  $\beta(300)$  reflections during melting of quiescently crystallised material.

**Figure 6.22** shows the influence of CaSub loading level on  $\chi_\beta$  after three different thermal-shear treatments. The first treatment (1) is the sample crystallised under quiescent conditions at 135 °C. The second treatment (2) is the sample crystallised at 135 °C after a 1 s shear at shear rate 80 s<sup>-1</sup>. The third treatment (3) takes the sheared samples after treatment 2, re-melts them at 220 °C for 300 s, followed by quiescent recrystallisation at 135 °C. A similar  $\chi_\beta$  was observed after treatment 1 and 3 for all samples. This result shows that the structure of the CaSub particle is not appreciably influenced by the flow conditions. Furthermore, this result confirms that the samples' previous thermal-shear history can be erased by treatment at 220 °C for 300 s.

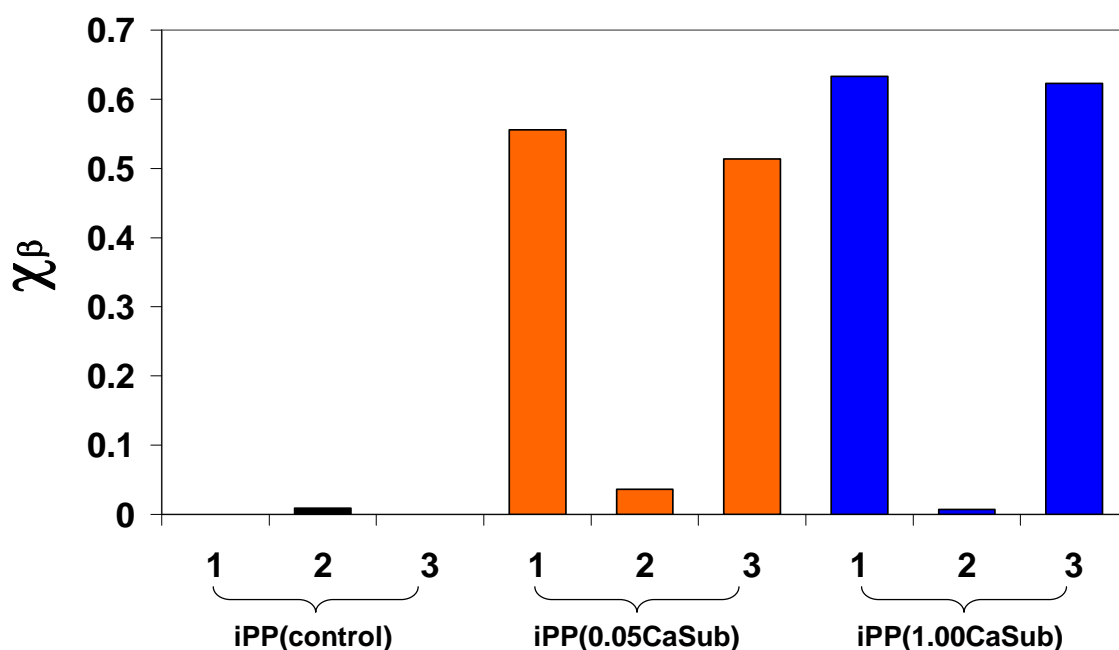


**Figure 6.22.**  $\beta$ -iPP crystallinity after (1) quiescent crystallisation at 135 °C, (2) flow-induced crystallisation at 135 °C (shear rate = 80 s<sup>-1</sup>, shear time = 1 s) and (3) samples from 2 remelting at 220 °C for 300 s followed by quiescent crystallisation at 135 °C.

## 6.4.0 Discussion

### 6.4.1 Melting of $\beta$ -iPP crystals

In this section the origin of the multiple melting peaks of the nucleated samples observed in the DSC thermogram presented in **Figure 6.6** is addressed. This will allow the reason for discrepancy of the DSC and WAXS derived values for  $\chi_\beta$  and  $\chi_\alpha$  to be determined. At low temperature (149-154 °C) two overlapping peaks were observed in the DSC thermograms. The results from the in-situ x-ray scattering experiments during melting show that the  $\beta(300)$  peak area stayed relatively constant until  $\sim 150$  °C. However, the FWHM(q) reached a plateau from 140 – 150 °C. These results indicate that  $\beta$ -iPP underwent recrystallisation before melting. Two recrystallisation processes have previously been presented in the literature: lamellar thickening and/or perfection ( $\beta\beta'$  recrystallisation) and recrystallisation taking place at a unit cell level by transiting the melt state similar to the  $\alpha_1$ - $\alpha_2$  phase transition [230] ( $\beta_1$ - $\beta_2$  phase transition). The first is associated with crystallisation from low  $T_c$  ( $< 120$  °C) while the latter is associated with crystallisation at high  $T_c$  ( $>135$  °C) [151]. If recrystallisation by lamellar thickening was responsible, it would be expected that the FWHM(q) would decrease during crystallisation. However, the result suggests that additional small  $\beta$ -iPP crystals were being formed. Accordingly, the results support the view that  $\beta$ -iPP recrystallisation occurred through the formation of a new  $\beta$ -iPP phase ( $\beta_2$ ).

In the nucleated samples a single broad peak was observed in the DSC thermograms at  $169.5 \pm 0.3$  °C consistent with the melting of  $\alpha$ -iPP crystals. Interestingly, when measured by DSC  $\chi_{\alpha(\text{DSC})}$  did not change appreciably with increasing loading level of CaSub particles. However,  $\chi_\alpha$  varied from  $\chi_\alpha = 0.04$  to  $\chi_\alpha = 0.19$  for iPP(0.02CaSub) to iPP(1.00CaSub) respectively when measured by WAXS. The presence of the high temperature peak can be explained by the  $\beta\alpha'$  recrystallisation phenomenon first investigated by Varga [151]. At  $\sim 150$  °C both the  $\alpha(110)$  peak area and FWHM(q) increased over a 10 °C interval. This can only be explained by the creation of additional  $\alpha$ -iPP crystals which are somewhat smaller than the  $\alpha$ -iPP crystals already present. Similar observations using in-situ WAXS have previously been reported [248-249]. It is thought that when the sample is cooled below a critical temperature ( $T_R^* \sim 105$  °C) a

small quantity of finely dispersed  $\alpha$ -iPP crystals are formed within the  $\beta$ -iPP crystals due to secondary crystallisation. When the sample is reheated these  $\alpha$ -iPP crystals act as nuclei for  $\beta\alpha'$  recrystallisation. Asano & Fujiwara suggested that because of the large difference in crystal structure between  $\beta$ -iPP and  $\alpha$ -iPP this transition also occurs via the melt state by successive unfolding, melting and recrystallisation [190].

An important implication of the  $\beta_1$ - $\beta_2$  and  $\beta\alpha'$  transitions is that their influence makes it difficult to reliably quantify the amount of  $\beta$ -iPP and  $\alpha$ -iPP crystals present using DSC. This fact may explain the rather large measured crystallinity values presented in **Table 6.2**. Additionally, these processes, which would vary substantially with different processing conditions could also be at least partly responsible for the large spread in the measured thermodynamic properties of  $\beta$ -iPP presented in **Table 2.2**.

#### ***6.4.2 Orientation development in sheared iPP containing $\beta$ -iPP nucleating particles***

In this section the factors which influence the development and distribution of the final crystalline and lamellar orientation in sheared iPP containing  $\beta$ -iPP nucleating particles are examined. This will then be used to gain a better understanding of the influence CaSub particles have on the flow-induced crystallisation of iPP.

**Figure 6.23** summarises the key factors which influence the final orientation distribution in the present experiment. In all samples investigated, the overwhelming majority of crystallisation was observed to occur after the cessation of shear flow. This highlights that the final orientation is determined to a large extent by the competitive growth from the point-like and thread-like (shish) nuclei present at the start of crystallisation. Shear flow above a critical shear rate led to the formation of shish which were generally aligned with their long axis along the flow direction. It is well known that shish provide a template for the nucleation of oriented chain folded lamellae (kebabs) which grow into the melt [10-17]. On the other hand point-like nuclei promote unoriented lamellae growth. In the present experiment point-like nuclei arise principally from two sources. The first is the intentional addition of the foreign CaSub particles which act as heterogeneous nuclei, while the second is the formation of additional flow-induced point-like nuclei. It is worthy to note here that small shish can also be considered to act as point-like nuclei if their long dimension is considerably smaller

than the distance between adjacent nuclei. Factors which influence the relative amount of nucleation from point-like nuclei and nuclei sites along the shish are the total surface area available for nucleation (density and dimensions) and the quality of the nucleation surface (epitaxial match) of each. In the present experiment oriented lamellae were observed to form before unoriented lamellae, highlighting that shish nuclei are more numerous and/or are of higher quality than the point-like nuclei present.

Apart from competitive growth between point-like and shish nuclei, several additional factors may influence the final orientation distribution. Lamellar branching phenomena (particularly the parent-daughter lamellar branching observed in iPP) will tend to reduce the final crystalline c-axis and lamellar normal orientation along the flow direction. The curving and twisting of oriented lamellae as they grow away from the shish such as that observed in **Figure 6.20c** will also reduce orientation by broadening the crystalline c-axis and lamellar normal orientation distributions. Other important factors which impact the final orientation are the initial orientation distribution of the shish as well as the local orientation of the nucleation sites along the shish backbone. Both of these are important as lamellae nucleation is a local event, with initial lamellae growth occurring roughly perpendicular to the shish wall.

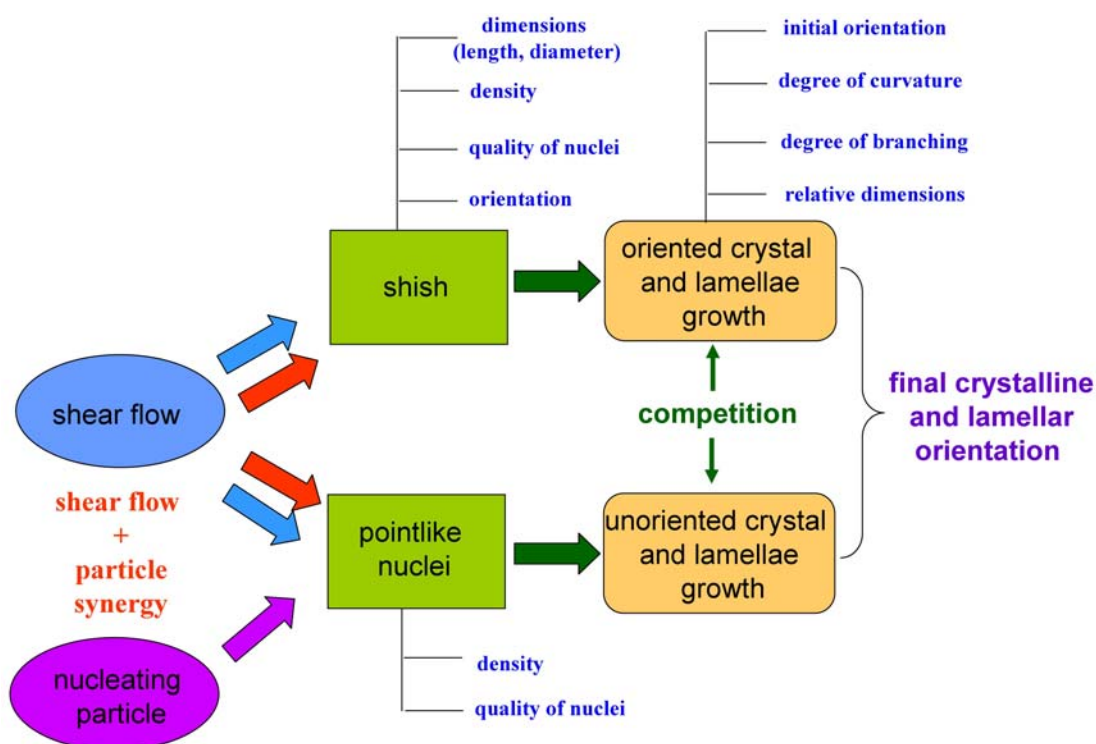


**Figure 6.23.** Summary of factors contributing to the final crystalline and lamellar orientation of semicrystalline polymers crystallised under flow-induced crystallisation and in the presence of nucleation particles.

The addition of CaSub particles was shown to reduce the critical shear rate required to induce oriented morphologies. Furthermore, the SEM images presented in **Figure 6.14** showed that the addition of CaSub particles substantially increased the density of the shish formed. Therefore it can be concluded that the addition of the CaSub particles assisted the formation of shish. This higher density of shish is responsible for the significantly higher crystalline and lamellar orientation observed in these samples.

Even with the high density of shish in the sheared iPP(1.00CaSub) sample, numerous small spherulites were still observed in the micrographs in **Figure 6.14**. The unoriented lamellae within these spherulites were not primarily  $\beta$ -iPP, but rather were  $\alpha$ -iPP. Therefore their origin is not related to the heterogeneous sites on the surface of the CaSub particles which specifically nucleates  $\beta$ -iPP. These unoriented  $\alpha$ -iPP crystals must then be from the formation of additional flow-induced point-like nuclei. Therefore, in addition to assisting the formation of shish, the presence of the CaSub particles also assisted the formation of additional flow-induced point-like nuclei. These point-like nuclei compete with the shish nuclei, lowering the total crystalline and lamellar orientation. The underlying mechanism responsible for this particle assisted shish and point-like nuclei formation will be discussed in **Chapter 8.4.4** where all the available information from chapters 5-8 is brought together.

The simultaneous SAXS/WAXS results presented in **Figure 6.6** revealed that in the samples containing CaSub particles the kebab normals were slightly inclined to the flow direction and the long axis of the shish. Zhu et al. observed a similar phenomenon in the skin region of injection moulded samples containing sodium benzoate particles [113]. In that study, inclined lamellae were only observed in the presence of the sodium benzoate particles and therefore the presence of the particles was thought to be a necessary condition for their formation. In the present study, the inclined lamellae were also only observed in the presence of the CaSub particles in the final fully crystallised condition, in agreement with the findings of Zhu et al. However, the results presented in **Figure 6.20a**, which plots the development of lamellar normal during crystallisation, show inclined lamellae are also formed in the iPP(control) sample, albeit only in the early stages of crystallisation and to a much lesser degree than the samples containing CaSub particles. Therefore this phenomenon does not necessarily require the presence of particles, though their presence does appear to amplify it.

The origin of this interesting phenomenon is summarised in **Figure 6.24**. The SEM micrographs in **Figure 6.14** show the shish in iPP(control) and iPP(1.00CaSub) are highly aligned along the flow direction. However on closer inspection, they take a meandering path and in places branching appears to have occurred. Kebabs are widely considered to nucleate locally on or at least very near to the shish wall and grow rapidly outwards nearly perpendicular to the shish wall. Therefore the initial growth direction of the kebab will be highly sensitive to the local alignment of the shish wall. The reason the shish take a meandering path instead of a straight one is not entirely certain. One possibility is that the shish relax after the flow stops. However, the increased meandering observed in the samples containing CaSub particles which had faster crystallisation kinetics would make this scenario less likely. Another possibility is the formation of small and highly local flow instabilities, or secondary flows. The secondary flows would act to locally perturb the shish while they are forming. The influence of secondary flow on the forming shish could also explain why the addition of the CaSub particles increased the meandering of the shish. A number of studies have shown that the addition of isotropic particles to viscoelastic fluids greatly complicate the flow environment [118, 250]. A possible example of how the flow could be disturbed near the particle is shown in **Figure 6.24b**. Therefore increased secondary flow near particles may account for the observed increase in shish meandering and subsequent lamellar inclination.

Interestingly, the inclination of the kebab normal was significantly larger at the first stages of crystallisation and decreased as crystallisation progressed. This behaviour indicates increased alignment of the kebab normal along the flow direction as crystallisation progressed. It is proposed that this behaviour can be accounted for by a confinement-induced orientation mechanism, **Figure 6.25**. At some point neighbouring lamellae which have different inclinations to the flow direction will impinge upon one another. The diffusion rate of chains to the growth front will be reduced near the impingement point due to chains being incorporated into nearby lamellae. Therefore faster growth rates would be achieved if the lamellae alter their growth direction. Similar confinement-induced alignment of lamellae normal was also observed during the growth of oriented daughter lamellae in **Chapter 4.3.3**.



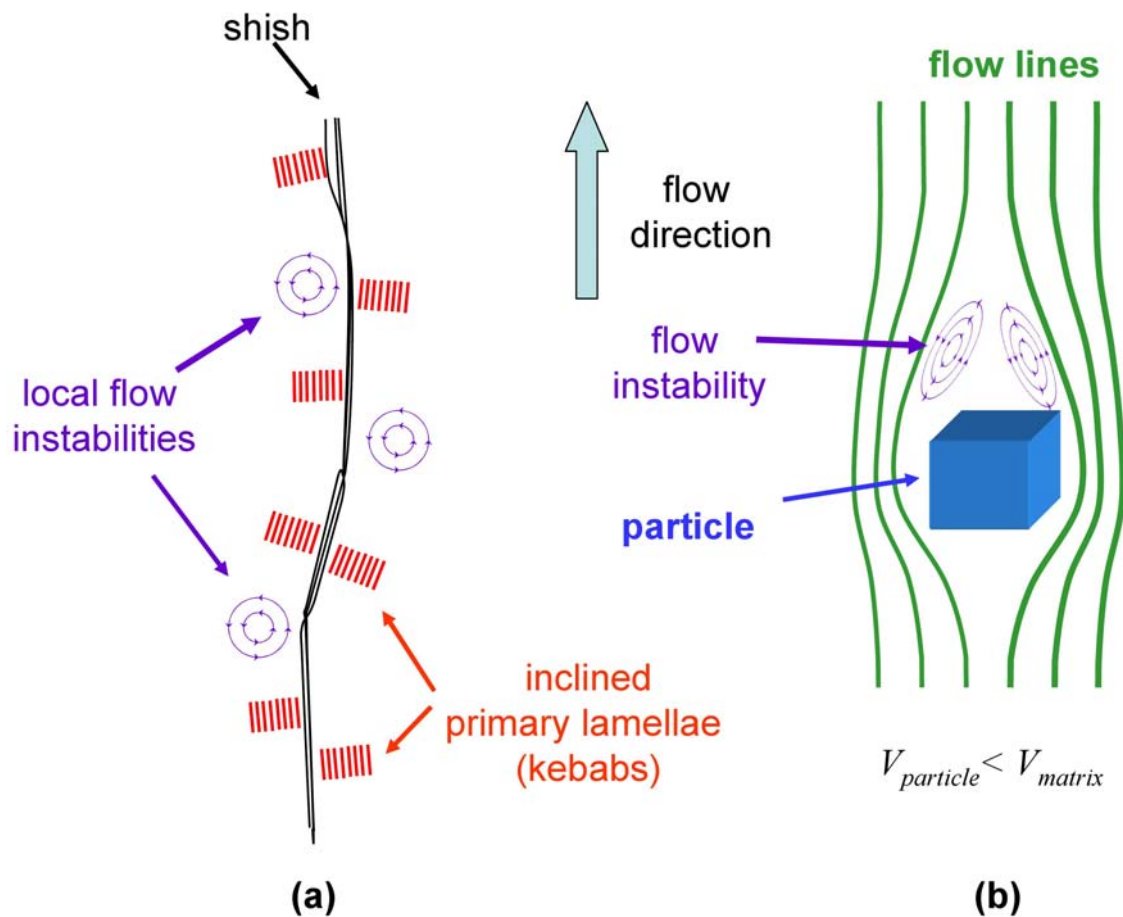


**Figure 6.24.** (a) Origin of inclined lamellae and (b) example of complex flow around particles.

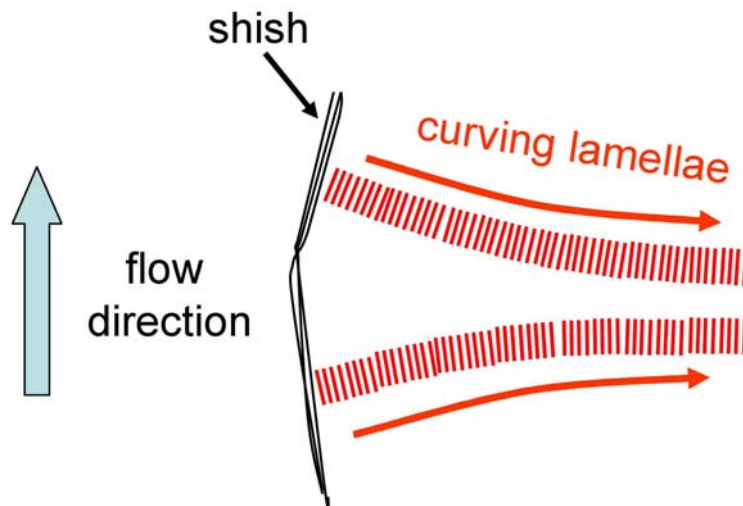


**Figure 6.25.** Mechanism of confinement induced orientation of lamellae growing from meandering shish.

#### ***6.4.3 Inter-relation of shear flow and nucleant loading level on $\beta$ -iPP formation.***

The application of shear flow to a supercooled iPP melt has been demonstrated to induce  $\beta$ -iPP in a variety of different situations. For example: in plate rheometry experiments [43, 144, 251], in the shear region of injection mouldings [113, 133, 147], in fibre pull experiments [145-146] as well as under oscillatory shear conditions [42, 148-149]. Although the conditions for  $\beta$ -iPP formation have been widely examined, the mechanism responsible for flow-induced formation of  $\beta$ -iPP are still under intense debate. Previously studies have suggested that shear flow leads to the formation of shish-kebab ( $\alpha$ -iPP row structures) and the surface of these row structures provide nucleation sites for an  $\alpha$ -iPP to  $\beta$ -iPP growth transition ( $\alpha\beta$  bifurcation) [144, 146, 151]. Once formed, these  $\beta$ -iPP nuclei can form a layer rich in  $\beta$ -iPP only as long as the kinetic requirement for higher  $\beta$ -iPP growth rate than  $\alpha$ -iPP is achieved (i.e. between 105 °C – 141 °C) [9, 151]. Therefore the formation of  $\alpha$ -iPP row structure were thought to be necessary to induce  $\beta$ -iPP nuclei. In the present work,  $\beta$ -iPP in iPP(control) was observed to form after  $\alpha$ -iPP, supporting this hypothesis. However, the results presented in this chapter are not entirely consistent with this view. No crystalline and lamellar orientation was detected below shear rates of 30 s<sup>-1</sup>. Yet  $\beta$ -iPP was detected in iPP(control) down to shear rates of 5 s<sup>-1</sup> and indeed peaked at 30 s<sup>-1</sup>. Therefore, it can be concluded that oriented  $\alpha$ -iPP row structures were not necessary to induce  $\beta$ -iPP.

Steady state shear experiments performed by Somani et al. noted a concurrent increase in  $\beta$ -iPP content with the increase in the amount of oriented  $\alpha$ -iPP crystals [144]. Therefore it can be speculated that the formation of  $\beta$ -iPP is related to the chain orientation in the melt. A simple relation between chain orientation and  $\beta$ -iPP content would suggest that it should be possible to induce very high concentrations of  $\beta$ -iPP using appropriate flow conditions, though in practice an upper limit of 65-70%  $\beta$ -iPP appears to exist [144]. In the present experiment the  $\beta$ -iPP content of iPP(control) peaks at a shear rate of 30 s<sup>-1</sup> before decreasing for higher shear rate. However, increasing the shear rate was observed to generally increase the number of shish suggesting a more complicated influence of flow on  $\beta$ -iPP formation. A similar dependence of shear rate was recently observed by Sun et al. who investigated the formation of  $\beta$ -iPP in the area adjacent to a Kevlar fibre embedded in an iPP matrix [145]. By varying the fibre pulling

rate, different polymorphic morphologies were produced in the area adjacent to the fibre. The different pulling rates were thought to induce different levels of iPP chain orientation. Therefore Sun et al. concluded that an orientation window of the iPP molecules in the molten state exists, which could preferentially nucleate  $\beta$ -iPP. Extended chains by themselves would be unlikely to be effective nuclei. However, flow is also known to promote and extend helical conformation along the chain back bone [107]. These helical sections may then coalesce with others from neighbouring chains to form small stable bundles which could then act as point-like nuclei [39]. Li et al. argued that if these bundles possess mesomorphic ordering, then the formation of  $\alpha$ -iPP nuclei which have a strict left-right handed helical packing, would be unfavourable compared to  $\beta$ -iPP nuclei [153]. Therefore, under certain conditions these mesomorphic nuclei could promote the formation of isochiral  $\beta$ -iPP nuclei.

The results presented in this chapter showed that increasing the shear rate increased the number of flow-induced nuclei. However, it can also be expected that increasing the shear rate would improve the quality of nuclei, increasing their size as well as their perfection. Indeed, it has recently been shown that increasing the flow intensity, can transform the structure of flow-induced nuclei from mesomorphic to crystalline [252]. Accordingly, the results presented in this chapter are broadly consistent with the  $\beta$ -iPP formation mechanism proposed by both Li et al. [153] and Sun et al. [145]. At low to intermediate shear rates mesomorphic point-like nuclei are formed, some of which possess the necessary structure to preferentially nucleate  $\beta$ -iPP. At higher shear rates, large and more ordered nuclei are formed which preferentially nucleate  $\alpha$ -iPP. This raises the important question as to what exactly is the mesomorphic structure, which can serve as  $\beta$ -iPP sites.

At higher shear rates, it was observed that the  $\beta$ -iPP crystals became oriented with their chain axis aligned along the direction of flow. However, previous studies have shown  $\beta$ -iPP crystals possess a random orientation when induced by flow [144]. Furthermore, the presence of oriented  $\beta$ -iPP seemed to be at odds with the original nuclei being mesomorphic bundles, which would essentially act as point-like nuclei. This discrepancy can be explained by the results presented in **Figure 6.18** which show an increase in  $\beta$ -iPP orientation as crystallisation progressed, rather than the decrease

observed in  $\alpha$ -iPP orientation. This shows that  $\beta$ -iPP initially nucleant randomly, but then become oriented as they grow. It is proposed that the orientation of  $\beta$ -iPP can be explained by the influence of nearby oriented  $\alpha$ -iPP growth fronts. The growth front would act to confine the growth direction of the  $\beta$ -iPP spherulites. The suggested sequence of the confinement-induced orientation is shown in **Figure 6.26**.

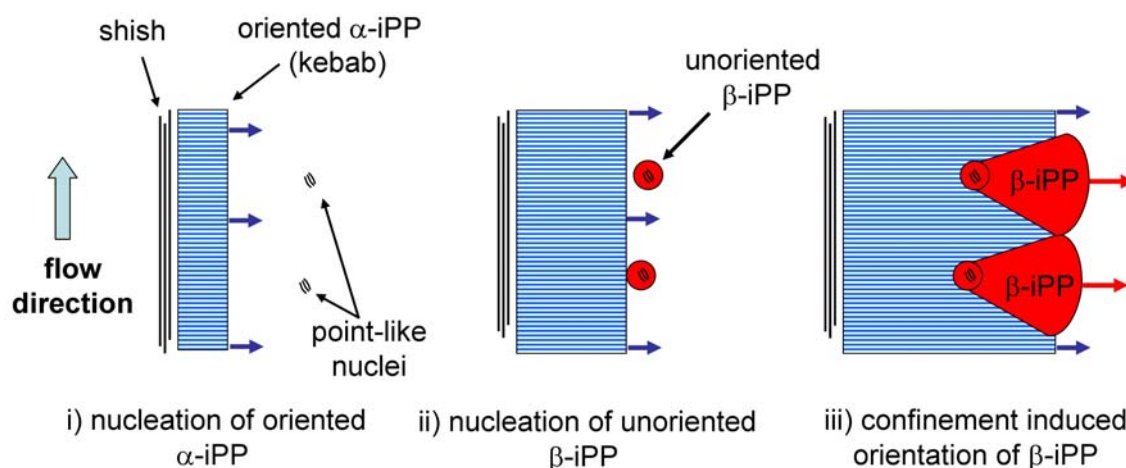


**Figure 6.26.** Nucleation and growth of  $\beta$ -iPP under flow-induced crystallisation conditions.

The addition of CaSub particles was shown to induce a large concentration of  $\beta$ -iPP when crystallised under quiescent conditions. However, shear flow was shown to unexpectedly suppress  $\beta$ -iPP formation. This has important implications for the processing of iPP containing intentional  $\beta$ -iPP nucleating agents and therefore the origin of this phenomenon needs further clarification. A possible explanation could be that the flow somehow alters the morphology of CaSub particles, rendering them incapable of nucleating  $\beta$ -iPP. To verify this hypothesis, a sheared sample containing CaSub particles was re-melted (**Figure 6.21**), to erase the previous thermal history. The sample was then allowed to recrystallise under quiescent conditions. This sample had almost the same  $\beta$ -iPP content as the sample originally crystallised under quiescent conditions. Therefore the possibility of flow permanently influencing the particles nucleation ability can be ruled out.

Deformation of  $\beta$ -iPP has been shown to lead to a strain-induced  $\beta$ -iPP to  $\alpha$ -iPP phase transformation [184, 190-191]. This transformation is thought to occur by a solid state mechanism requiring the reversal of helical hands in  $\beta$ -iPP crystal [191]. Therefore,

another potential explanation is that the flow converts small  $\beta$ -iPP nuclei into  $\alpha$ -iPP nuclei. However, in the present work no  $\beta$ -iPP crystals were detected under quiescent condition for any sample for at least 35 s. This suggests that no  $\beta$ -iPP crystals had formed when the shear pulse was applied and thus any strain-induced  $\beta$ -iPP to  $\alpha$ -iPP phase transition can also be ruled out.

Another possible explanation is that the flow creates additional nuclei which specifically nucleate  $\alpha$ -iPP and compete with  $\beta$ -iPP nucleation from the surface of the CaSub particles. Increase the shear rate was shown to change the growth mechanism of both crystalline phases. In particular, the growth geometry of  $\beta$ -iPP became less constrained under flow conditions, suggesting that the  $\beta$ -iPP formed under flow conditions did not nucleate on the surface of the CaSub particles as it did under quiescent conditions. Rather the  $\beta$ -iPP in the nucleated material formed in a similar way to that found in sheared iPP(control). This shows that the flow suppressed the epitaxial mechanism observed under quiescent conditions.

Flow in the presence of Ca-Sub particles was observed to changed the order of crystallisation from  $\beta$ -iPP nucleating first under quiescent conditions to  $\alpha$ -iPP nucleating first under flow-induced conditions. Concurrently, flow also substantially reduced the induction time for the formation of both crystals, suggesting new more powerful nuclei were formed. For a given shear rate above the critical shear rate required to form shish, the addition of CaSub particles was shown to increase the density of shish. Shish are well known to be highly effective substrates from which oriented  $\alpha$ -iPP form crystals can nucleate on. Their presence would therefore completely overwhelm the epitaxial crystallisation on the surface of CaSub particles. A large reduction in  $\beta$ -iPP was also recorded at low shear rate where shish-kebab structures were not detected. The flow-induced suppression of  $\beta$ -iPP in this range can be explained by the formation of flow-induced point-like nuclei, which, if being of sufficient quality, would also selectively nucleate  $\alpha$ -iPP. Therefore it is proposed that it is the formation of additional flow-induced nuclei that preferentially nucleate  $\alpha$ -iPP which is responsible for the flow-induced suppression of  $\beta$ -iPP in the presence of specific  $\beta$ -iPP nucleating agents.

A surprising influence of CaSub loading level on the amount of  $\beta$ -iPP was observed. Under quiescent conditions, and at low shear rates, the  $\beta$ -iPP content predictably increased with increasing loading level. However, at high shear rates the opposite trend was observed with lower loading levels resulting in higher  $\beta$ -iPP contents. If flow-induced nuclei formation occurred principally on or near to the surface of the particle then a 1:1 influence of loading level and  $\beta$ -content would be expected. This would lead to no loading dependence. Therefore this interesting observation implies the existence of a correlation effect between nearby particles which further enhances flow-induced nuclei formation. A possible mechanism is that two separating particles would create additional strain in the region between them if they are close to one another. The contribution from these nearby separating particles would accordingly increase as the average inter-particle distance decreases (i.e. increasing loading level). The increased strain and thus nuclei formed would then further suppress nucleation from the surface of the particles.

Throughout this chapter it has been shown, that varying the loading level of  $\beta$ -iPP nucleating agent and flow conditions can radically alter the crystalline morphology and molecular orientation of iPP. In combination with precise knowledge of the flow history, this information may allow new and innovative morphology characteristics to be produced. For example, in injection moulding or extrusion processes the shear rate and shear strain profile varies through the thickness. In conjunction with specific  $\beta$ -iPP nucleation agents, this profile may allow for new skin-core morphologies to be produced. In the skin layer the particles may promote highly oriented  $\alpha$ -iPP structures which can improve strength. In the core, the lower shear rates and slower solidification may promote large volume fractions of tough  $\beta$ -iPP via nucleation from the surface of the particle. Products produced in this way may exhibit improvements in both strength and toughness.

## 6.5.0 Conclusions

This chapter investigated the influence of shear flow on the morphology development and crystallisation kinetics of isotactic polypropylene (iPP) containing various loadings of the specific  $\beta$ -iPP nucleating agent calcium suberate (CaSub). From the results obtained the following was concluded:

In the present study the formation of shish was found to be the primary source of oriented crystalline and lamellar structures. The presence of point-like nuclei, either from the heterogeneous sites on the surface of CaSub particles or the formation of flow-induced point-like nuclei, was found to lead to unoriented crystalline and lamellar structures. The competitive growth from the shish and point-like nuclei was found to be the main factor which influenced the final crystalline and lamellar orientation.

The addition of CaSub particles was shown to (a) reduce the flow intensity required to induce shish and (b) for a given flow intensity substantially increase the volumetric density of shish. This shows that the addition of CaSub particles assisted the formation of shish. The higher number of shish formed then resulted in much higher levels of crystalline and lamellar orientation in the samples containing CaSub particles compared to iPP(control).

In addition to assisting in the formation of shish, the presence of the CaSub particles was also observed to assist in the formation of additional flow-induced point-like nuclei. These point-like nuclei nucleated unoriented  $\alpha$ -iPP lamellae which grew in competition with oriented lamellae nucleated from shish, thereby limiting the final orientation achieved.

It was observed that the kebabs did not initially form perpendicular to the long axis of the shish, but were inclined. The addition of CaSub particles increased the initial inclination of the lamellae from  $\sim 3^\circ$  in iPP(control) to  $\sim 12^\circ$  in iPP(1.00CaSub). The inclination was explained by the locally contorted path the shish take through the matrix.

In iPP(control) a shear rate of at least  $30 \text{ s}^{-1}$  was necessary to induce crystalline and lamellar orientation. However,  $\beta$ -iPP was formed at shear rates as low as  $5 \text{ s}^{-1}$ . This shows that oriented  $\alpha$ -iPP crystals are not necessary to induce  $\beta$ -iPP as previously thought. Rather it was proposed that flow-induced mesomorphic point-like nuclei preferentially nucleate  $\beta$ -iPP.

The  $\beta$ -iPP content of iPP(control) reached a peak at  $30 \text{ s}^{-1}$  before decreasing with increasing shear rate. The influence of shear rate on  $\beta$ -iPP formation was explained by changes in the density and quality of the flow-induced nuclei formed. At shear rates below  $30 \text{ s}^{-1}$ , increasing shear rate increased the number of bundles which could nucleate  $\beta$ -iPP, while at higher shear rates, nuclei with increased quality were formed which preferentially nucleated  $\alpha$ -iPP.

The  $\beta$ -iPP selectivity observed under quiescent conditions of the CaSub particles was observed to be depressed when crystallisation was carried out under flow-induced conditions. This interesting phenomenon was explained by CaSub particles assisting the formation of additional flow-induced nuclei. The nuclei then selectively nucleated the  $\alpha$ -iPP phase suppressing the  $\beta$ -iPP nucleation mechanism on the surface of the particle.





### **Influence of shear flow on the morphology development of $\alpha$ nucleated isotactic polypropylene**

#### **7.1.0 Introduction**

The crystallisation of polymers is complicated by the inclusion of a wide range of particulate additives in polymer formulations such as: nucleating agents, colourants and reinforcing agents. Under quiescent conditions these heterogeneous particles can act as nucleation sites, enhancing crystal nucleation and thereby influencing crystallisation kinetics and the final morphology of the polymer. The number of active heterogeneous nucleation sites is strongly related to factors which influence the particle surface area available for nucleation. The most common factors affecting this are the concentration and dispersion of particles in the polymer matrix. Yet many other particle characteristics have also been implicated in influencing the nucleation of polymers under quiescent conditions such as: epitaxy [76-78], particle size [84], particle curvature [83, 85] and porosity [79].

Foreign particles can also dramatically alter the crystallisation kinetics and the development of morphology under flow-induced crystallisation conditions. The combined effect of flow and particles has been suggested to yield a synergistic increase in the number of active nuclei, raising crystallisation rates further than their individual contribution [43, 52, 109-112]. Furthermore, the addition of particles has been shown to decrease the flow intensity required to form the shish-kebab structure [33-34, 49-50, 84, 112-116]. A number of particle characteristics have been suggested to influence the formation of flow-induced nuclei. Zhu and co-authors [49-50] suggested a particles surface curvature may influence the stability of shish formed on the particles surface. D'Haese et al. [84] investigated the influence of particle size under a wide range of shear flow conditions. D'Haese found that the critical shear rate for shish formation decreased with increasing particle size. However, the influence of the nucleation efficiency of the particles, which also increased with particle size, could not be ruled out. Recently, Patil et al. [115] observed that single wall carbon nanotubes (SWCNT) led to increased shish formation, while zirconia nano-particles destabilised shish

formation. Patil explained this by the stronger chain-particle interaction of the SWCNT retarding the relaxation of extended chains compared to the weaker chain-particle interactions of the zirconia nano-particles. Byelov et al. [52] showed that the shape of the particle could influence flow-induced nuclei formation, with anisotropic particles leading to greater numbers of flow-induced nuclei compared to isotropic particles. However, the mechanism responsible for this interesting influence of particle shape was not identified.

It is known that shish are highly stable entities such that they can be super heated compared to the lamellae melting temperature. Pennings and Kiel investigated the melting of polyethylene (PE) shish formed from a stirred solution and found the shish melted  $\sim 15\text{-}20\text{ }^{\circ}\text{C}$  higher than the lamellae melting point [101]. Kimata et al. performed in-situ SANS experiments on a sheared deuterated isotactic polypropylene (iPP) and found the shish structure was stable until at least  $180\text{ }^{\circ}\text{C}$  [37]. This was at least  $14\text{ }^{\circ}\text{C}$  higher than the highest lamellae melting temperature. The precise reason for the higher melting point of shish is still not well understood. One possibility is that extended chain configurations present in the shish impart higher resistance to dissolution. Another possibility is a higher interconnectivity of chains within the shish, which then help to stabilise them. The presence of particles during shish formation or dissolution may further impact their stability. However, the influence of particles on the thermal stability of shish is yet to be established.

In the first part of this chapter the influence of two commercial particulate  $\alpha$ -iPP nucleating agents on the quiescent crystallisation of iPP is characterised to establish their nucleation potential. The combined influence of shear flow condition and nucleant loading level on the development of morphology is then investigated. The information gained will allow for the identification of the particle characteristics which influence the morphology of sheared iPP. In the final part of this chapter the effect of the two nucleants on the thermal stability of shish will be established.

## 7.2.0 Experimental

### 7.2.1 Sample preparation and thermal-shear profile

Two commercial particulate nucleants which specifically nucleate  $\alpha$ -iPP were used in this chapter: sodium benzoate (SB) and bicyclo[2.2.1]heptane-2,3-dicarboxylic acid, trade name HPN-68 (HPN). The sample naming convention is described in **Table 3.2**. The compounding and sample preparation procedures are described in detail in **Chapter 3.2.2**. The thermal-shear profile used in this experiment is shown in **Figure 7.1**. The disks were heated to 220 °C and slowly compressed to a working distance of 0.5 mm at 0.01 mm /s. The compressed disks were held at temperature for 300 s to erase the previous thermal history. The isotropic nature of the melt was confirmed by in-situ small and wide angle x-ray scattering (rheo-SAXS/WAXS) as well as ex-situ SAXS/WAXS and etched samples viewed under reflected light after quiescent crystallisation. The samples were cooled from 220 °C to the isothermal crystallisation temperature (135 °C or 150 °C) at 0.5 °C/s. A short controlled step shear was immediately applied to the melt for 1 s at shear rates between 0-80 s<sup>-1</sup>. The samples were held at the crystallisation temperature until the crystallisation rate was effectively negligible and then cooled to 50 °C at a rate of 0.5 °C/s. The sample was subsequently heated at 0.17 °C/s to 220 °C, held there for 300 s before being isothermal crystallised at 135 °C.

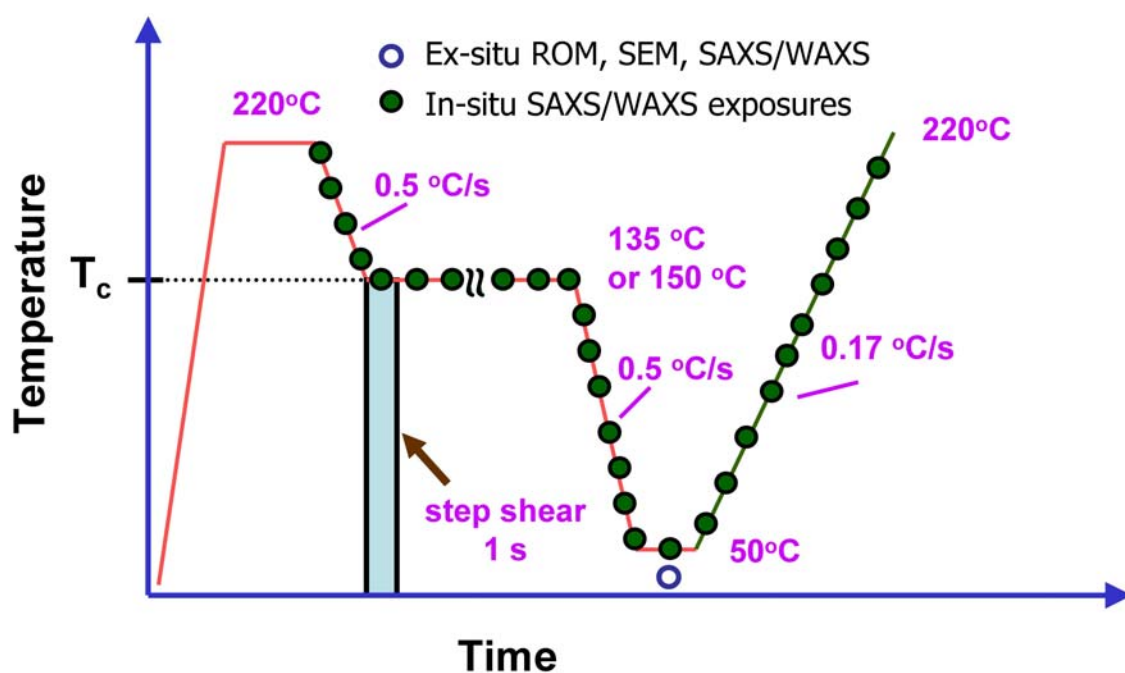


**Figure 7.1.** Schematic illustration of the thermal-shear profile used in this chapter.

### 7.2.2 Analytical techniques

Two varieties of simultaneous SAXS/WAXS experiments were performed. The first type were performed on ex-situ samples and aimed to understand the influence of shear flow condition on the crystalline morphology and orientation. In these experiments a range of shear rates were obtained from one sample by scanning the synchrotron microbeam along the radius of disks sheared for 1 s at an angular velocity ( $\omega = 3.3$  rad/s). In this way shear rates between  $0\text{--}80\text{ s}^{-1}$  could be investigated in the same sample with a shear rate resolution of  $\pm 1\text{ s}^{-1}$ . The second type investigated the development of morphology in-situ. In these experiments simultaneous rheo-SAXS/WAXS measurements were made continuously during the imposed thermal-shear profile.

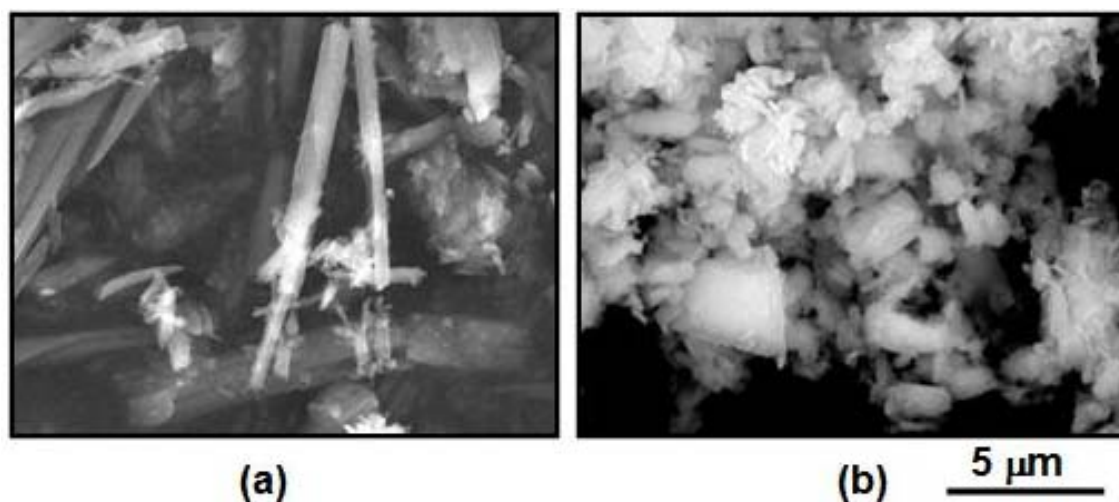
Ex-situ simultaneous SAXS/WAXS experiments were performed at the Australian National Beamline Facility (ANBF) beamline 20B, Tsukuba, Japan. The experimental setup was described in detail in **Chapter 3.3.1.1** and allowed for simultaneous collection of complete SAXS/WAXS patterns. In-situ simultaneous SAXS/WAXS experiments were performed on the SAXS/WAXS beam line at the Australian Synchrotron (SAXS/WAXS(1)). The experimental setup was described in detail in **Chapter 3.3.1.3**. The setup allowed for in-situ investigations with a considerable amount of the scattering intensity around the azimuth ( $\varphi \sim 70^\circ$ ) in the WAXS region to be captured whilst simultaneously capturing complete SAXS patterns.

Ex-situ samples were etched for 7 h in the permanganate solution described in **Chapter 3.3.4**. Reflected optical micrographs (ROM) of the etched surfaces were taken on an Olympus PMG3 microscope with a differential interference optic attachment. Higher magnification of the etched surfaces was performed with a JEOL JSM-7001F field emission scanning electron microscopy (SEM) operating in secondary electron mode. Samples were coated to  $10\text{ \AA}$  thick with gold / platinum and imaged at an acceleration voltage of 5 kV. In-situ images of the particles in the polymer matrix were made under polarised light in the Linkam shear cell using Nikon 80i microscope and a Nikon DS-Fi1 CCD camera. Differential scanning calorimetry (DSC) experiments were performed on a Perkin-Elmer DSC-7 using the procedures described in **Chapter 3.3.3**.

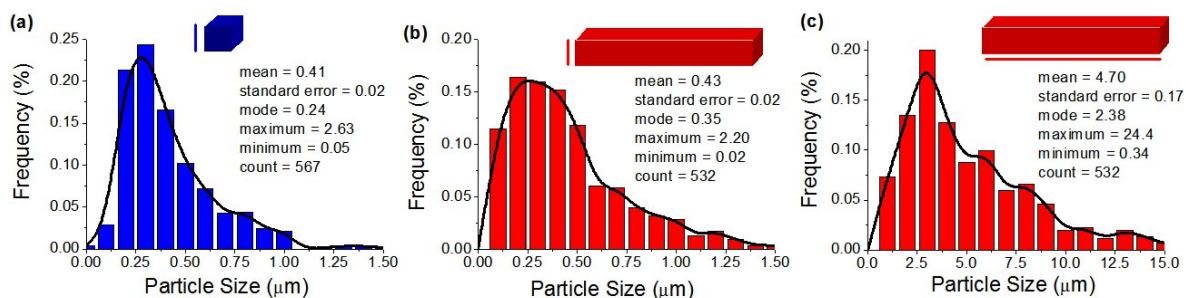
## 7.3.0 Results

### 7.3.1 Characterisation of nucleant particles

In this section the morphology and dispersion of the produced SB and HPN particles in the iPP matrix was characterised using polarised optical microscopy (POM) and SEM. The influence of SB and HPN on the quiescent crystallisation behaviour of iPP was then characterised using DSC. The morphology of the particles before being compounded into the iPP is shown in **Figure 7.2**. The SB particles were highly elongated needle-like particles with an aspect ratio near 10. HPN particles were equiaxed and had an aspect ratio near 1. Both SB and HPN particles exhibited flat faceted surfaces. The particle size distribution was determined using SEM on five separate fields using standard image analysis techniques, **Figure 7.3**. To aid the analysis, the shape of the particles was assumed to be cuboidal, with  $a = b = c$  for HPN particles and  $a = b \neq c$  for SB particles, where  $a$ ,  $b$ , &  $c$  are the side lengths of the particle. From this analysis the average dimension of the particles was  $a = b = c = 0.41 \pm 0.04 \mu\text{m}$  for HPN particles and  $a = b = 0.43 \pm 0.04 \mu\text{m}$  and  $c = 4.7 \pm 0.3 \mu\text{m}$  for SB particles.

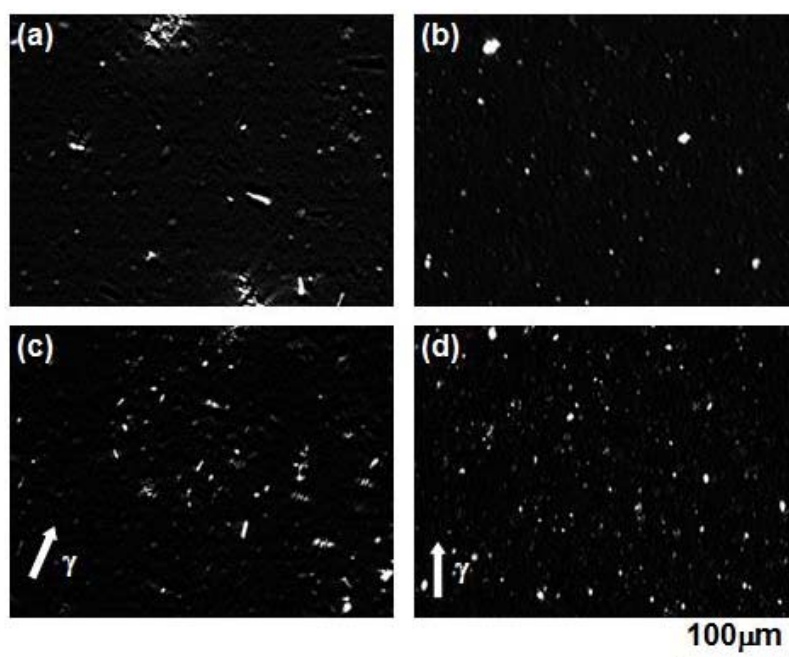


**Figure. 7.2.** Scanning electron micrographs (SEM) of (a) sodium benzoate (SB) and (b) bicyclo[2.2.1]heptane-2,3-dicarboxylic acid (HPN).



**Figure 7.3.** Particle size distribution of (a) HPN, (b) the short axis of SB and (c) the long axis of SB.

POM images were taken of the HPN and SB particles in the molten iPP matrix, **Figure 7.4**. The POM images shown in **Figure 7.4a & b** show that both SB and HPN particles were well dispersed in the iPP matrix by the mixing technique employed. The SB particles however showed some preferred orientation of their long axis along the radial direction of the shear cell in the quiescent condition. This alignment is presumably due to the weak flow field applied to the sample when it was compressed in the initial stages of the experiment. After a 30 s shear at a shear rate of  $80 \text{ s}^{-1}$  and at a temperature of  $181^\circ\text{C}$ , both particles remained well dispersed. The SB particles now showed preferred orientation of their long axis along the flow direction, **Figure 7.4d**.

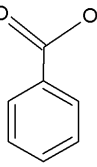
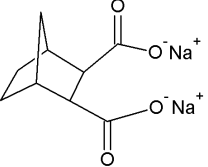


**Figure 7.4.** POM images showing the dispersion of a 1 wt% loading of sodium benzoate (SB) and bicyclo[2.2.1]heptane-2,3-dicarboxylic acid (HPN) in the iPP melt. Quiescent conditions (a) SB (b) HPN. After step shear (c) SB (d) HPN (shear rate =  $80 \text{ s}^{-1}$ , shear time = 30 s, shear temperature =  $181^\circ\text{C}$ ). The arrow indicates the approximate direction of flow.

**Table 7.1** summarises the influence of nucleant type and loading level on the quiescent crystallisation of iPP. The peak crystallisation temperature ( $T_c$ ) for each sample was obtained from the minimum in the exothermic crystallisation peak. The nucleation efficiency (NE) and the activation energy for crystallisation ( $\Delta E$ ) were determined using **Equation 3.27** and **Equation 3.28** respectively. **Figure 7.5** shows the DSC crystallisation curves obtained after holding the sample at 220 °C for 300 s before being continuously cooled at 0.17 °C/s to room temperature. Samples containing both HPN and SB particles showed one broad exothermic peak. Increasing the nucleant loading shifted the crystallisation curves to higher temperatures, with the addition of HPN being more effective than SB when compared at equivalent loading level. Further experiments were performed using three additional cooling rates and the value of  $\Delta E$  was determined from the linear regression of Kissinger plots shown **Figure 7.6**. The influence of nucleant type on quiescent crystallisation was further analysed by plotting NE and  $\Delta E$  as a function of the nucleant surface area, **Figure 7.7**. Increasing the nucleant loading (i.e. nucleant surface area) resulted in an increase in NE. This is simply related to the higher number of heterogeneous sites available for nucleation. All  $\Delta E$  values were negative showing that crystallisation occurs spontaneously under this temperature regime.  $\Delta E$  was found to decrease with increasing nucleant loading. This shows that crystallisation (nucleation and or growth) is energetically more favourable in the presence of both nucleants. The increase in NE, and corresponding decrease in  $\Delta E$ , was more pronounced at lower loadings, however no saturation level was reached in the range of loadings investigated. This latter point further indicates aggregation of the particles was not significant. When compared at a similar nucleant surface area, the addition of HPN was found to be far more effective than SB in terms of raising NE, and lowering  $\Delta E$ . This shows that HPN had a greater ability to nucleate iPP crystals than SB. Indeed, HPN has been shown to have one of the highest NE of all known  $\alpha$ -iPP nucleants [166-168].



**Table 7.1.** Summary of the morphology of the SB and HPN particles used in this investigation and their influence on the quiescent crystallisation of isotactic polypropylene during continuous cooling from the melt. Peak crystallisation temperature ( $T_c$ ), nucleation efficiency (NE), activation energy for crystallisation ( $\Delta E$ ).

sample	chemical structure	nucleant shape	average dimension ( $\mu\text{m}$ )	loading (wt. %)	surface area ( $\text{m}^2/\text{g}$ )	$T_c$ ( $^{\circ}\text{C}$ )	NE (%)	$\Delta E$ (kJ/mol)
iPP(control)	-	-	-	neat	-	$111.3 \pm 0.3$	0	$-176 \pm 6$
iPP(self seed)				self seed	-	$142.7 \pm 0.3$	100	$-380 \pm 20$
iPP(0.05SB)		needle	$0.43 \pm 0.04$ x $4.7 \pm 0.2$	0.05	0.005	$113.3 \pm 0.3$	$6 \pm 1$	$-180 \pm 10$
iPP(0.10SB)				0.10	0.010	$114.5 \pm 0.3$	$11 \pm 1$	$-211 \pm 7$
iPP(0.50SB)				0.50	0.052	$117.6 \pm 0.3$	$21 \pm 1$	$-230 \pm 20$
iPP(1.00SB)				1.00	0.103	$120.6 \pm 0.3$	$30 \pm 1$	$-240 \pm 10$
iPP(0.05HPN)		isotropic	$0.41 \pm 0.4$	0.05	0.007	$124.8 \pm 0.3$	$43 \pm 1$	$-247 \pm 8$
iPP(0.10HPN)				0.10	0.014	$127.2 \pm 0.3$	$49 \pm 1$	$-284 \pm 9$
iPP(0.50HPN)				0.50	0.071	$129.7 \pm 0.3$	$54 \pm 1$	$-314 \pm 7$
iPP(1.00HPN)				1.00	0.141	$132.8 \pm 0.3$	$59 \pm 1$	$-340 \pm 40$

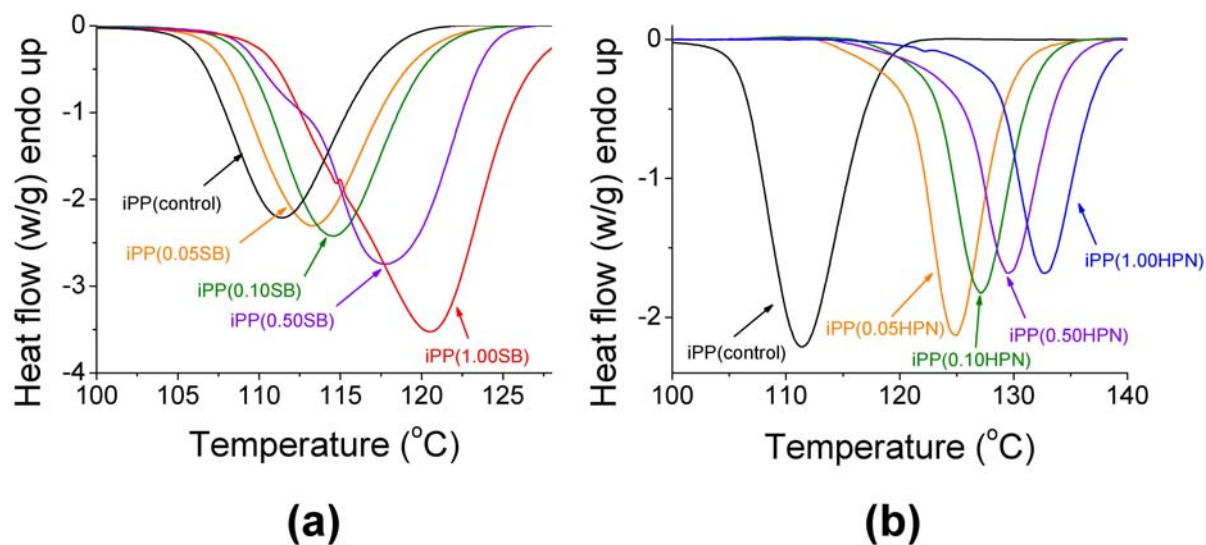


**Figure 7.5.** Selected DSC cooling curves showing the influence of additions of (a) SB and (b) HPN. Cooling rate  $0.17^{\circ}\text{C}/\text{s}$ .

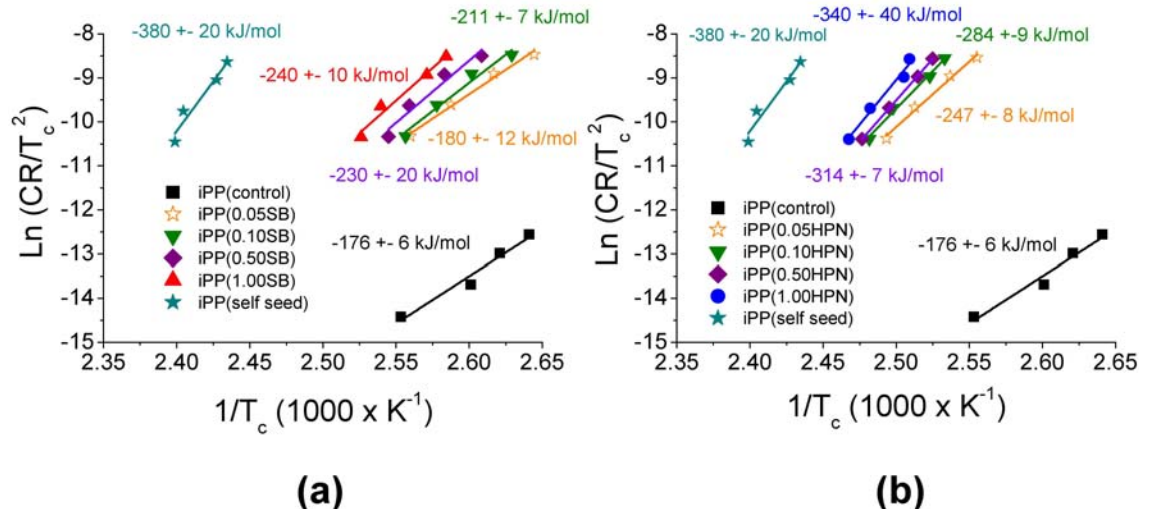


**Figure 7.6.** Kissinger plot showing the influence of loading level on the activation energy for crystallisation ( $\Delta E$ ) (a) SB and (b) HPN. Cooling rate  $0.17^\circ C/s$ .

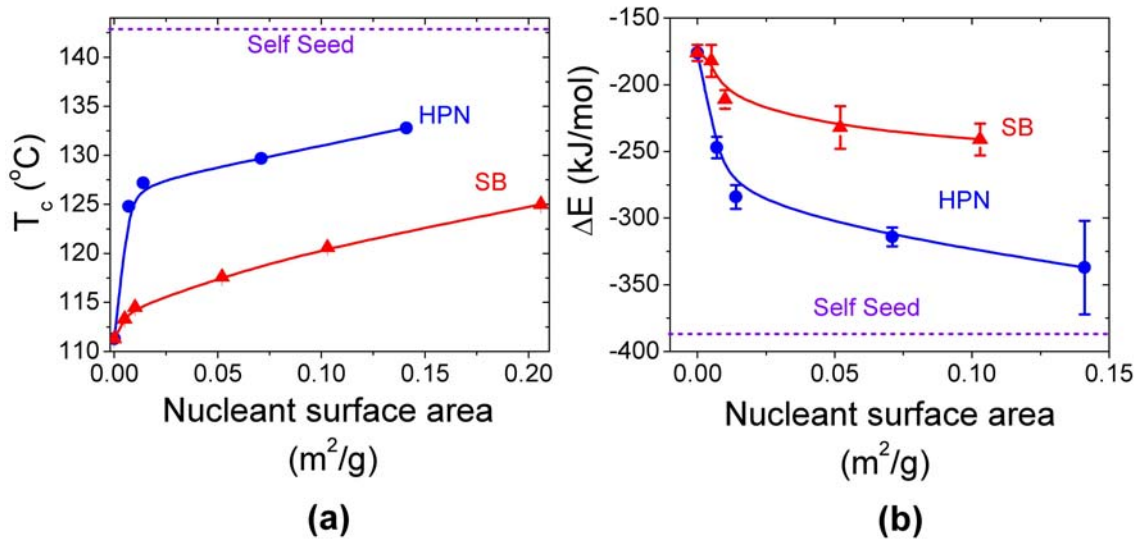


**Figure 7.7.** Influence of the addition of HPN and SB on (a) the peak crystallisation temperature ( $T_c$ ) during continuous cooling at  $0.17^\circ C/s$  and (b) the activation energy for crystallisation ( $\Delta E$ ).

### 7.3.2 Ex-situ microscopy of permanganate etched samples

In this section the influence of shear rate and nucleant type on the spherulite and lamellar scale morphology is imaged using ex-situ ROM and SEM of paramagnetic etched samples. **Figure 7.8** shows the influence of shear rate and nucleant on the spherulite scale morphology viewed under reflected light. The micrographs are imaged through the thickness direction and the flow direction is vertical. iPP(control) crystallised under quiescent conditions exhibited large spherulites. The addition of both

nucleants reduced the size of the spherulites, with HPN being significantly more effective than SB. The spherulite diameter was estimated using the linear intercept method on appropriately scaled micrographs with a minimum of 500 intercepts [253]. The spherulite diameters were  $iPP(\text{control}) = 73 \pm 9 \mu\text{m}$ ,  $iPP(1.00\text{SB}) = 20 \pm 4 \mu\text{m}$ ,  $iPP(1.00\text{HPN}) = 5 \pm 1 \mu\text{m}$ . It is worthwhile to note at this point, that decreasing the spherulite size is one of the main reasons to use nucleators, as reduced spherulite size can decrease haze and increase stiffness of the final product. In  $iPP(\text{control})$ , increasing the shear rate led to a further reduction in the spherulite size. At a shear rate of  $\sim 30 \text{ s}^{-1}$ , long oriented threads aligned along the flow direction (shish) with primary lamellae (kebabs) perpendicular to their long axis appeared. Increasing the shear rate further led to an increase in the length of shish and increased their density. A similar influence of shear rate was observed for both  $iPP(1.00\text{HPN})$  and  $iPP(1.00\text{SB})$  samples. However, the density of the shish was increased and the critical shear rate to observe the shish structure was reduced in the presence of both nucleants.

The lamellar scale morphology of  $iPP(1.00\text{SB})$  and  $iPP(1.00\text{HPN})$  crystallised under quiescent conditions is shown in **Figure 7.9**. Although significantly smaller, the spherulites in  $iPP(1.00\text{SB})$  showed the same core-shell structures observed in  $iPP(\text{control})$  in **Figure 4.2**. In the centre of the spherulite, parent and daughter lamellae of similar size were observed, while further out from the centre, thicker radial parent lamellae became dominant. When the lamellae were viewed ‘edge on’ the planes of the daughter lamellae in both samples made an angle  $81^\circ \pm 2$  to the plane of the parent lamellae. No transition to dominant radial lamellar was observed in the spherulites in the  $iPP(1.00\text{HPN})$ . Rather the spherulites appeared to consist of both parent and daughter lamellae of similar size. Presumably this is due to the high nucleation density preventing the transition of dominant radial lamellae in these samples.

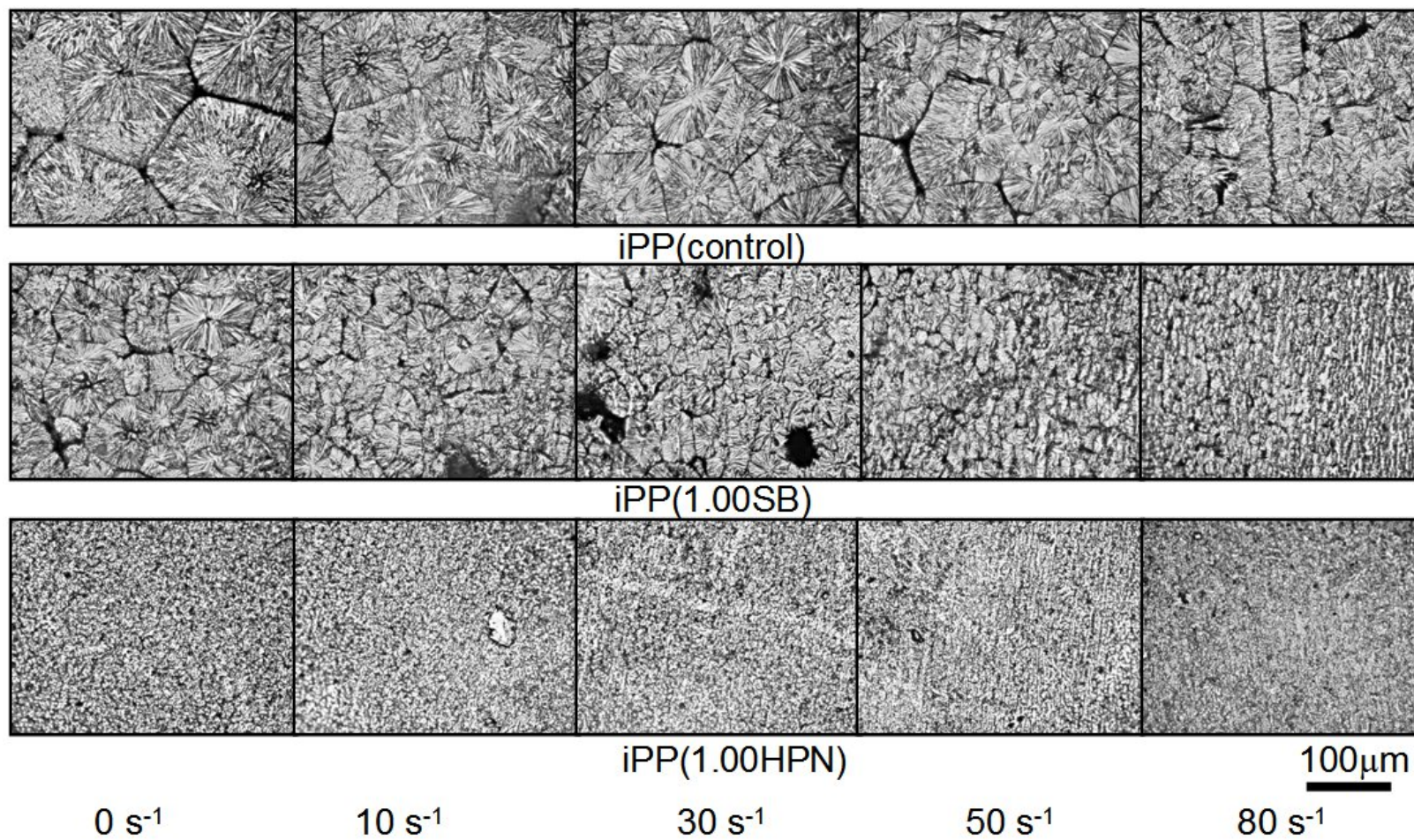


**Figure. 7.8.** Reflected optical micrographs of permanganate etched samples showing the influence of shear rate and nucleant type on the (shear time = 1 s, shear temperature = 135 °C). Flow direction is vertical.



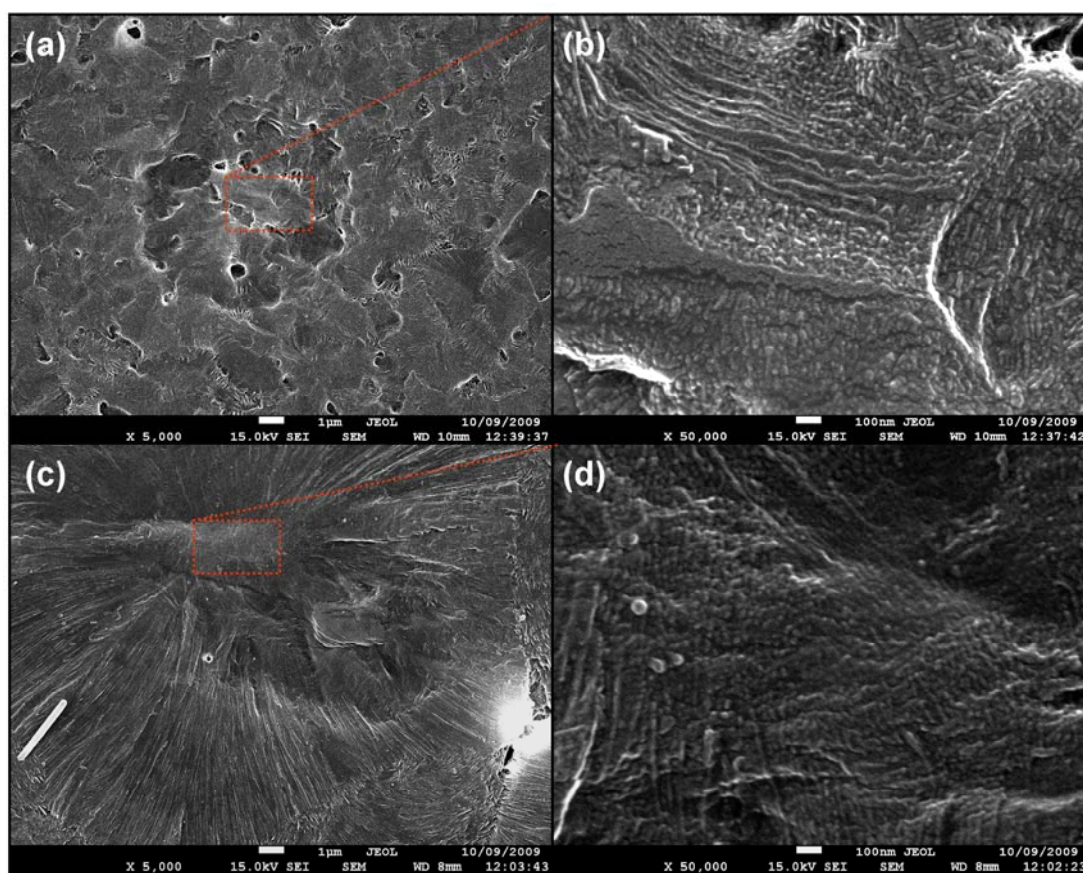


**Figure 7.9.** SEM images of permanganate etched samples isothermally crystallised under quiescent conditions at 135 °C. (a) & (b) iPP(1.00HPN), (c) & (d) iPP(1.00SB). The red boxes in (a) & (c) signify the regions of interest in (a) & (d).

**Figure 7.10a-c** shows the spherulite scale morphology after a moderate step shear. All three samples showed a mix of spherulites and shish-kebab structures. The samples containing both nucleants had a significantly greater density of shish-kebabs and smaller spherulite sizes than iPP(control). Although generally aligned along the flow direction, the shish in all samples took a meandering path. The meandering was more prevalent in iPP(1.00HPN) compared to iPP(control) and iPP(1.00SB). Closer investigation of the lamellar morphology in the area immediately adjacent to the shish was performed, **Figure 7.10d-f**. This revealed thick parent lamellae emanating roughly parallel from the shish wall and with normals broadly aligned along the flow direction. Surprisingly, the parent lamellae in iPP(1.00HPN) samples were significantly contorted compared those in iPP(control) and iPP(1.00SB). In between the parent lamellae of all samples were daughter lamellae inclined  $81^\circ \pm 2$  to their parent lamellae.

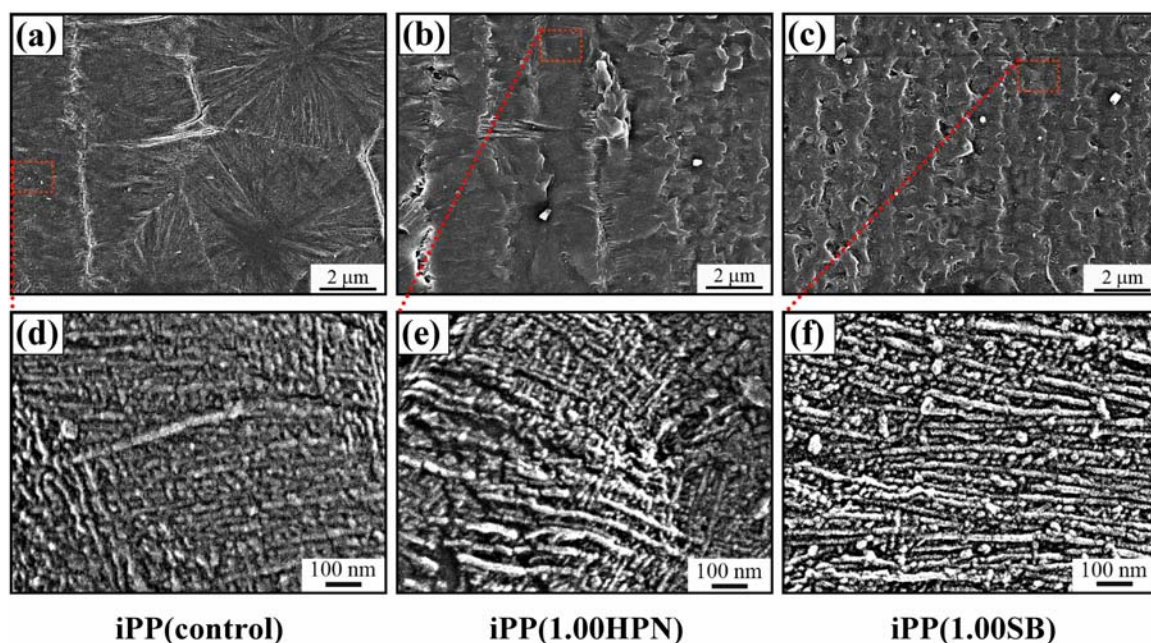


**Figure 7.10.** SEM images of permanganate etched samples after a moderate step shear (a) & (d) iPP(control), (b) & (e) iPP(1.00HPN), (c) & (f) iPP(1.00SB) (shear rate =  $80 \text{ s}^{-1}$ , shear time = 1 s, shear temperature =  $135 \text{ }^{\circ}\text{C}$ ). The red boxes in (a), (b) & (c) signify the regions of interest in (d), (e) & (f). Flow direction is vertical.

### 7.3.3 Influence of nucleant and flow condition on iPP polymorphism

In this section the combined influence of flow condition and nucleant loading level on the polymorphic morphology of iPP is investigated using ex-situ simultaneous SAXS/WAXS. To enhance consistency, the full range of shear rates was investigated within the one sample that had been sheared for 1 s at an angular velocity of  $3.3 \text{ rad/s}$ . Using the fine microbeam of the synchrotron, SAXS/WAXS measurements were taken at various points along the radius of the disk, producing images where the nominal shear rate was between  $0 - 80 \text{ s}^{-1}$ . The influence of nucleant type and shear temperature on the SAXS/WAXS images taken at a shear rate of  $80 \text{ s}^{-1}$  is shown in **Figure 7.11**. For clarity the SAXS region is enlarged relative to the WAXS region. All samples crystallised at  $135 \text{ }^{\circ}\text{C}$  contained reflections from  $\alpha$ -iPP,  $\beta$ -iPP and  $\gamma$ -iPP phases, while all samples crystallised at  $150 \text{ }^{\circ}\text{C}$  contained reflections from only  $\alpha$ -iPP and  $\gamma$ -iPP.

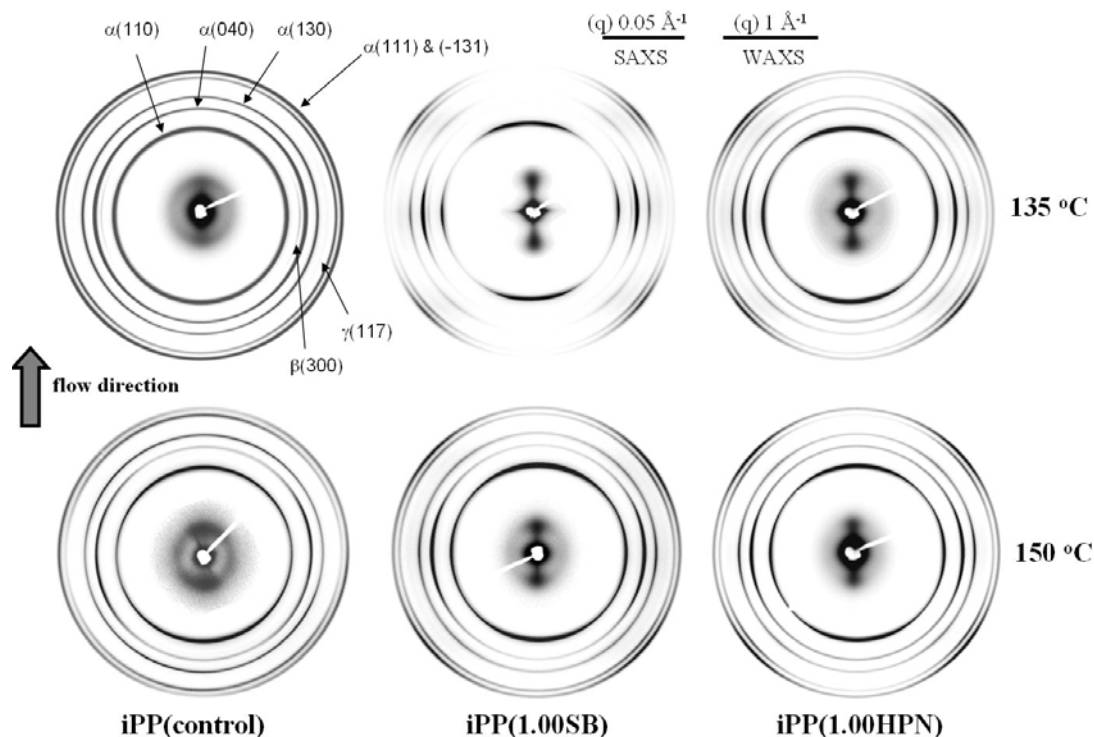


**Figure 7.11.** Influence of nucleant type and shear temperature on the simultaneous SAXS/WAXS images of sheared samples (shear rate =  $80 \text{ s}^{-1}$ , shear time = 1 s).

The influence of nucleant loading and shear rate on the  $\alpha$ -iPP ( $\chi_\alpha$ ),  $\beta$ -iPP ( $\chi_\beta$ ),  $\gamma$ -iPP ( $\chi_\gamma$ ) and volume ( $\chi_v$ ) crystallinity indices at a shear temperature of  $135 \text{ }^\circ\text{C}$  is shown in **Figure 7.12**. For reference, the crystallinity indices were determined using the method described in **Chapter 3.6.4**. The application of shear to iPP(control) led to the formation of  $\beta$ -iPP, with peak  $\chi_\beta$  occurring at  $30 \text{ s}^{-1}$ . The addition of SB resulted in a small decrease in the shear rate where peak  $\chi_\beta$  occurred. Interestingly, small quantities of SB i.e. iPP(0.01SB) created much larger fractions of  $\beta$ -iPP than iPP(control) or iPP(1.00SB). The addition of HPN suppressed the formation of  $\beta$ -iPP at low shear rates. Nevertheless, above a critical shear rate,  $30 \text{ s}^{-1}$  and  $50 \text{ s}^{-1}$  for iPP(0.01HPN) and iPP(1.00HPN) respectively, small quantities of  $\beta$ -iPP were formed. Indeed it appears that at the higher shear rates the  $\beta$ -iPP content for all samples are converging and therefore there may exist a shear rate where all samples would have the same effective  $\beta$ -iPP content. Compared to iPP(control), the addition of both SB and HPN increased  $\chi_\gamma$  under both quiescent and flow-induced crystallisation conditions. However, the addition of HPN was significantly more effective at increasing  $\chi_\gamma$  compared to SB. All samples also showed a small trend of increasing  $\chi_\gamma$  with increasing shear rate. The influence of shear rate was more pronounced in the nucleated samples compared to iPP(control).

Shear rate, nucleant type and loading level did not appreciably influence  $\chi_v$  for any samples.

**Table 7.2** shows the influence of shear temperature on the crystallinity indices. No  $\beta$ -iPP was detected when crystallisation was carried out at 150 °C. This is consistent with the unfavourable growth rate of  $\beta$ -iPP compared to  $\alpha$ -iPP and  $\gamma$ -iPP at crystallisation temperatures above 141 °C [9]. All samples crystallised at 150 °C showed significantly lower fractions of  $\gamma$ -iPP compared to samples crystallised at 135 °C. The addition of HPN raised  $\chi_\gamma$  under both quiescent and flow-induced crystallisation conditions. On the other hand, the addition of SB did not appreciably influence  $\chi_\gamma$  compared to iPP(control).

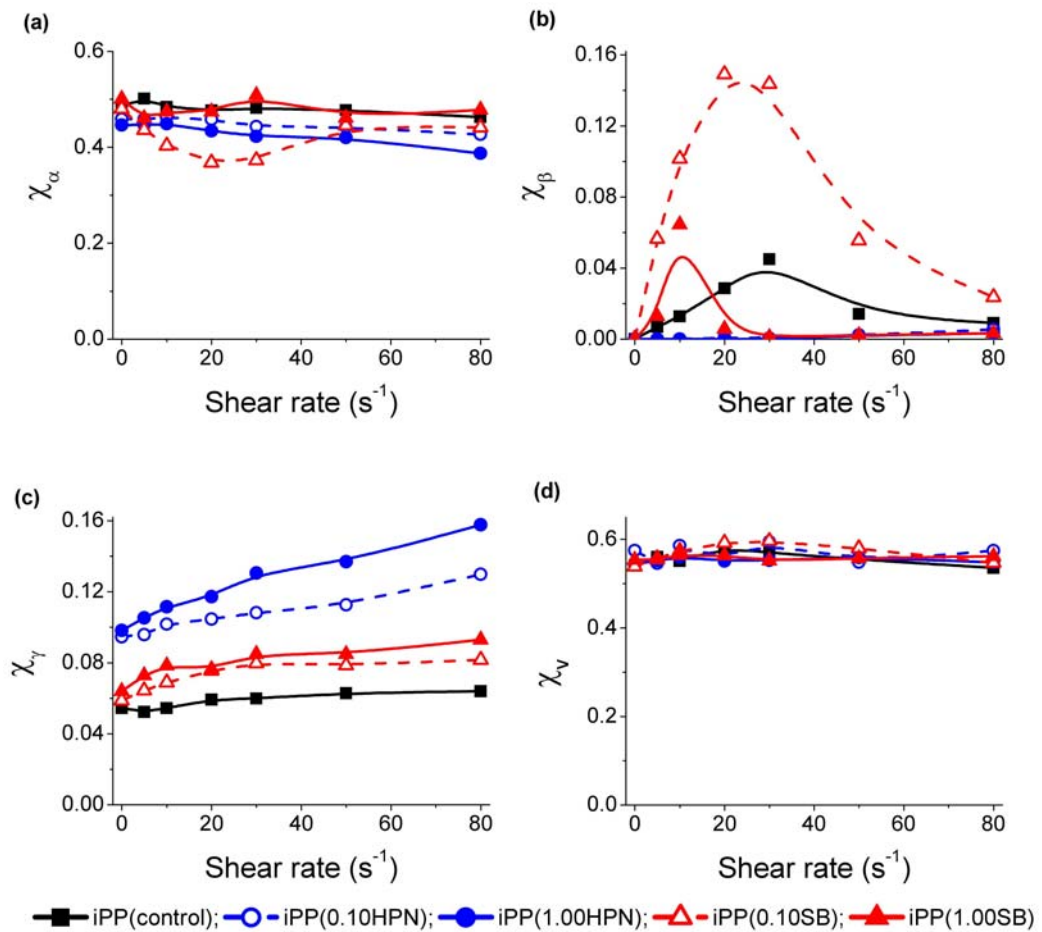


**Figure 7.12.** Influence of shear rate and loading level on (a)  $\chi_\alpha$ , (b)  $\chi_\beta$ , (c)  $\chi_\gamma$  and (d)  $\chi_v$  crystallinity indices (shear time = 1 s, shear temperature = 135 °C).



**Table 7.2.** Influence of shear temperature and shear rate on  $\chi_\alpha$ ,  $\chi_\beta$ ,  $\chi_\gamma$  and  $\chi_v$  crystallinity indices as well as the relative concentration of oriented daughter lamellae ([D]) (shear time = 1 s).

Sample	Shear Rate	$\chi_\alpha$		$\chi_\beta$		$\chi_\gamma$		$\chi_v$		[D]	
		135	150	135	150	135	150	135	150	135	150
iPP(control)	0 s <sup>-1</sup>	0.49	0.52	0	0	0.06	0.01	0.54	0.53	-	-
iPP(1.00HPN)		0.45	0.50	0	0	0.10	0.03	0.54	0.54	-	-
iPP(1.00SB)			0.54	0	0	0.07	0.01	0.57	0.55	-	-
iPP(control)	80 s <sup>-1</sup>	0.46	0.50	0.009	0	0.06	0.01	0.54	0.51	0.87	0.71
iPP(1.00HPN)		0.34	0.46	0.003	0	0.16	0.06	0.55	0.52	0.69	0.65
iPP(1.00SB)		0.48	0.52	0.003	0	0.09	0.02	0.57	0.53	0.79	0.75

The PD lamellar branching phenomenon of  $\beta$ -iPP is known to occur when crystallisation is carried out between 90 – 160 °C [134-135]. The nature of PD lamellar branching has been implicated in influencing many industrially important properties [16, 30-31]. Accordingly, the influence of shear rate on the relative concentration of oriented daughter lamellae ([D]), determined using **Equation 4.3** according to the procedure outlined in **Chapter 4.3.2**, is shown in **Figure 7.13**. In iPP(control) [D] was observed to increase up to a shear rate of 80 s<sup>-1</sup>, before decreasing at higher shear rates. The addition of SB led to the same overall trend. However, the peak [D] was at 20 s<sup>-1</sup> and 10 s<sup>-1</sup> for iPP(0.10SB) and iPP(1.00SB), respectively. With the addition of HPN, only a decrease in [D] was observed with increasing shear rate. Furthermore, compared to iPP(control) and the samples containing SB, the samples containing HPN generally had lower [D] values. The formation of daughter lamellae was further suppressed by increasing the temperature from 135 to 150 °C, **Table 7.2**.

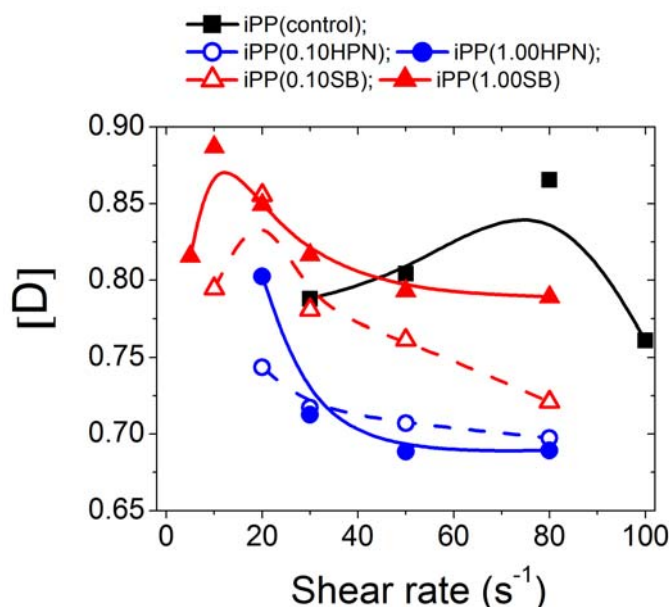


**Figure 7.13.** Influence of shear rate on the relative concentration of oriented daughter lamellae [D] (shear time = 1 s, shear temperature = 135 °C).

#### 7.3.4 Influence of nucleant and flow condition on iPP orientation

In this section the impact of flow condition and nucleant loading level on the crystalline and lamellar orientation is investigated. For all samples, when crystallisation was carried out after sufficiently intense shear flow, the crystalline ( $\alpha$ -iPP,  $\beta$ -iPP and  $\gamma$ -iPP) and lamellar scattering showed preferred orientation, **Figure 7.11**. The general distribution of scattering was similar for all samples, indicating that the same basic structural elements were present.

To further analyse the crystalline orientation present, azimuthal intensity profiles were created for the main crystalline reflections, by integrating the reflections at  $q = 0.97 \text{ \AA}^{-1}$  ( $\alpha(110)/\gamma(111)$ ),  $q = 1.15 \text{ \AA}^{-1}$  ( $\alpha(040)/\gamma(008)$ ),  $q = 1.09 \text{ \AA}^{-1}$  ( $\beta(300)$ ), and  $q = 1.38 \text{ \AA}^{-1}$  ( $\gamma(117)$ ), **Figure 7.14**. For the reflections at  $q = 0.97 \text{ \AA}^{-1}$  and  $q = 1.15 \text{ \AA}^{-1}$  an increase in scattered intensity was recorded along the equator. Furthermore, additional reflections near the meridian were recorded for the  $q = 0.97 \text{ \AA}^{-1}$  reflection. The results presented in **Figure 7.12** show that the main contribution to both reflections is from  $\alpha$ -iPP. This scattering distribution is therefore due to the branched parent-daughter structure of  $\alpha$ -iPP previously described in **Chapter 4.3.2**. An increase in scattered intensity along the equator was observed for the  $\beta(300)$  reflection, **Figure 7.14c**. As the  $\beta(300)$  plane is

perpendicular to the  $\beta$ -iPP c-axis the equatorial scattering would be consistent with the c-axis of  $\beta$ -iPP crystallites being oriented along the flow direction.

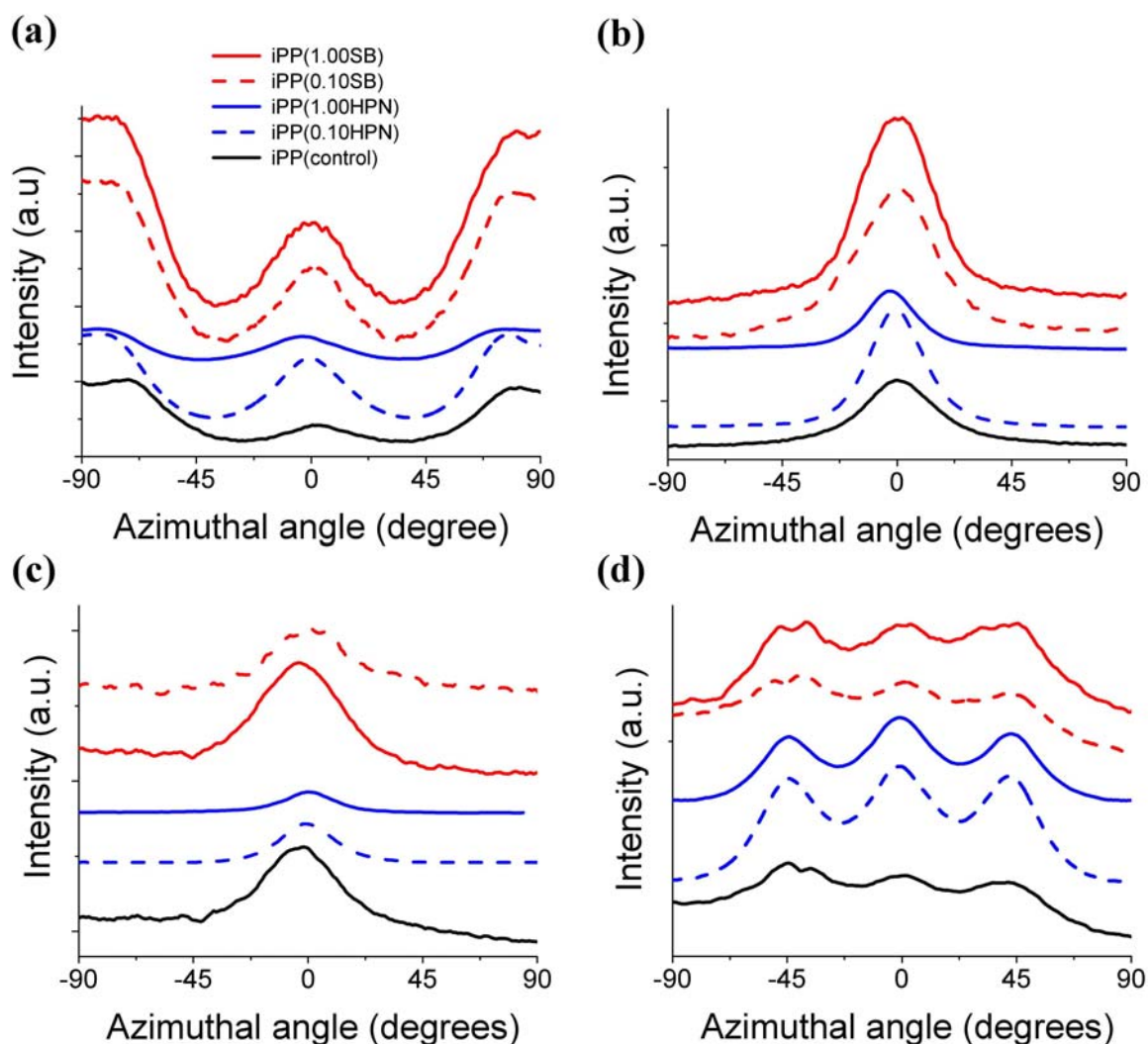


**Figure 7.14.** Influence of nucleant type and loading level on the azimuthal intensity profile centred at scattering vectors **(a)**  $q = 0.97 \text{ \AA}^{-1}$  ( $\alpha(110)/\gamma(111)$ ), **(b)**  $q = 1.15 \text{ \AA}^{-1}$  ( $\alpha(040)/\gamma(008)$ ), **(c)**  $q = 1.09 \text{ \AA}^{-1}$  ( $\beta(300)$ ), and **(d)**  $q = 1.38 \text{ \AA}^{-1}$  ( $\gamma(117)$ ) (shear rate =  $80 \text{ s}^{-1}$ , shear time = 1 s, shear temperature =  $135 \text{ }^{\circ}\text{C}$ ).

Two main orientation types are typically observed for  $\gamma$ -iPP, and are termed parallel and perpendicular (also known as cross- $\beta$ ) chain-axis orientation, respectively. Parallel chain-axis orientation is the most common and is where one half of the chain axes within the  $\gamma$ -iPP crystal are oriented along the reference direction, while the other half of the chain axes are oriented at an angle of  $\sim 81^{\circ}$  to the reference direction. Parallel chain-axis orientation has been found in a range of environments, such as: the shear zones in conventional injection moulding (CIM) and shear controlled orientation injection

moulding (SCORIM) [32-33], and the surface of pitch based carbon fibre reinforced composites [254]. Using WAXS patterns calculated from model structures, Auriemma and De Rosa showed that in the parallel axis orientation, the  $\gamma(008)$  reflection is concentrated on the equator, while the  $\gamma(117)$  reflection is confined to the equator and the first layer line [161].

Cross- $\beta$  orientation is where the c-axis (i.e. the stacking direction of the bilayers of chains) of the  $\gamma$ -iPP crystals is oriented along the reference direction. This results in the two sets of chain axes being aligned nearly normal to the reference direction. In this form the  $\gamma(008)$  reflection is concentrated on the meridian, while a very weak  $\gamma(117)$  reflection is concentrated to the first layer line only. Auriemma et al. have reported cross- $\beta$  in stretched polypropylenes at low draw ratios [161, 255]. Auriemma attributed the formation of cross- $\beta$  in these samples due to a combination of a) the near perpendicular arrangement of chain-axis in the unit cell, and (b) to the elongated shape of lamellae in the direction normal, rather than parallel to the chain axis.

The azimuthal intensity profile of the  $\gamma(008)$  reflection, which is also coincident with the  $\alpha(040)$  reflection, shows only one peak centred on the equator, **Figure 7.14d**. Furthermore, two clear peaks are observed in the  $\gamma(117)$  reflection. The centre peak is located on the equator, while the second peak is on the first layer line and is inclined at  $\sim 40^\circ$  to the equator. Similar intensity distributions were observed at all shear rates where the  $\gamma(117)$  reflection was oriented. This shows that the parallel chain-axis orientation is the dominant  $\gamma$ -iPP orientation in the present experiment.

The influence of shear rate and nucleant loading level on the  $\alpha$ -iPP orientation is shown in **Figure 7.15**. The c-axis ( $f_{c(\alpha)}$ ), b-axis ( $f_{b(\alpha)}$ ), and a-axis ( $f_{a(\alpha)}$ ) orientation parameters were determined according to the method described in **Chapter 3.3.1.5**. The addition of both nucleating particles decreased the critical shear rate required to observe  $\alpha$ -iPP orientation. The addition of SB reduced the critical shear rate from  $30 \text{ s}^{-1}$  in iPP(control) to  $10 \text{ s}^{-1}$  and  $5 \text{ s}^{-1}$  for iPP(0.10SB) and iPP(1.00SB) respectively, while the addition of HPN decreased the critical shear rate to  $20 \text{ s}^{-1}$  and  $10 \text{ s}^{-1}$  for iPP(0.10HPN) and iPP(1.00HPN) respectively. For all samples,  $f_{c(\alpha)}$  increased with increasing shear rate above the critical shear rate, indicating increased alignment of the crystalline c-axis

along the flow direction. Compared to iPP(control),  $f_{c(\alpha)}$  was increased in the presence of both nucleants, with the addition of SB being slightly more effective than HPN.

In the  $\alpha$ -iPP branched shish-kebab structure both the b-axes of the parent and daughter lamellae are perpendicular to the flow direction and therefore increasing the shear rate reduced  $f_{b(\alpha)}$ . As both parent and daughter lamellae contribute,  $f_{b(\alpha)}$  is the most sensitive to the fraction of oriented  $\alpha$ -iPP crystals. The addition of both particles decreased  $f_{b(\alpha)}$  compared to iPP(control). Interestingly, increasing the loading level of SB from 0.10 wt % to 1.00 wt% decreased  $f_{b(\alpha)}$ , while increasing the loading level of HPN over the same range increased  $f_{b(\alpha)}$ . This shows that high concentrations of HPN can decrease  $\alpha$ -iPP orientation.

Similar to  $f_{c(\alpha)}$ ,  $f_{a(\alpha)}$  is influenced by the relative amount of oriented parent and daughter lamellae. Increasing the shear rate did not appreciably change  $f_{a(\alpha)}$  for iPP(control). However, increasing the shear rate and SB loading led to an increase in  $f_{a(\alpha)}$ , while increasing shear rate and HPN loading level decreased  $f_{a(\alpha)}$ . This result further suggests that the samples containing HPN had a higher fraction of oriented parent lamellae compared to samples containing SB.

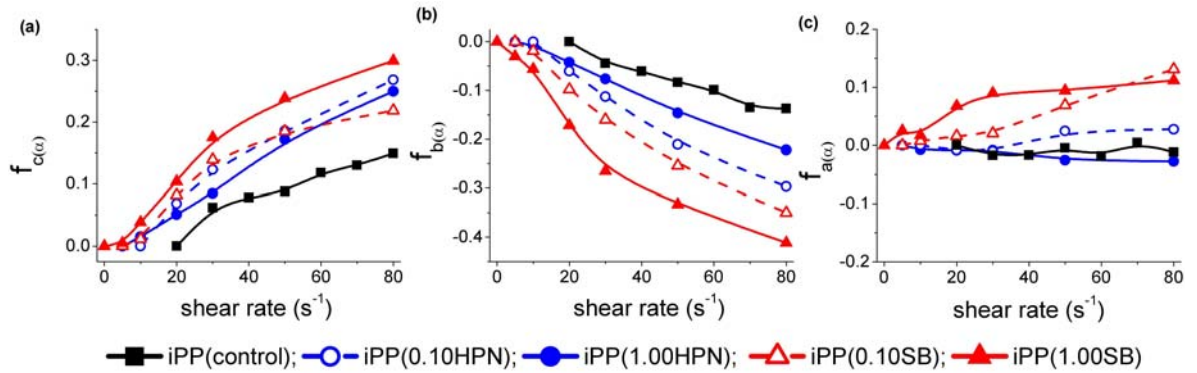


**Figure 7.15.** Influence of shear rate and nucleant loading level of the Herman's orientation function for  $\alpha$ -iPP. (a) c-axis ( $f_{c(\alpha)}$ ), (b) b-axis ( $f_{b(\alpha)}$ ), (c) a-axis  $f_{a(\alpha)}$  (shear time = 1 s, shear temperature = 135 °C).

The effect of shear rate and nucleant loading level on the  $\beta$ -iPP ( $f_{h(\beta)}$ ) and  $\gamma$ -iPP ( $f_{h(\gamma)}$ ) orientation parameters which were determined using the procedure described in **Chapter 3.3.1.5**, are provided in **Figure 7.16**. The critical shear rate required to observe  $\beta$ -iPP orientation was reduced with the addition of both nucleants. In iPP(control) a

shear rate of  $50 \text{ s}^{-1}$  was required. Increasing the SB loading reduced the shear rate to  $10 \text{ s}^{-1}$  and  $5 \text{ s}^{-1}$  for iPP(0.10SB) and iPP(1.00SB). A shear rate of  $30 \text{ s}^{-1}$  was required to induce oriented  $\beta$ -iPP crystals in iPP(0.10HPN), while a shear rate of  $50 \text{ s}^{-1}$  was required for iPP(1.00HPN). It should be noted here that no  $\beta$ -iPP crystallinity was detected in iPP(0.10HPN) and iPP(1.00HPN) samples until shear rates of  $30 \text{ s}^{-1}$  and  $50 \text{ s}^{-1}$ , respectively. The critical shear rate required to observe oriented  $\gamma$ -iPP crystals was also reduced with increasing nucleant loading. In iPP(control) the shear rate was  $60 \text{ s}^{-1}$ . Increasing the SB loading decreased the critical shear rate to  $10 \text{ s}^{-1}$  for iPP(0.10SB) and  $5 \text{ s}^{-1}$  for iPP(1.00SB). Similarly, increasing the HPN loading decreased the critical shear rate to  $20 \text{ s}^{-1}$  for both iPP(0.10HPN) and iPP(1.00HPN) samples. The addition of both nucleants also generally resulted in higher levels of both  $\beta$ -iPP and  $\gamma$ -iPP orientation.

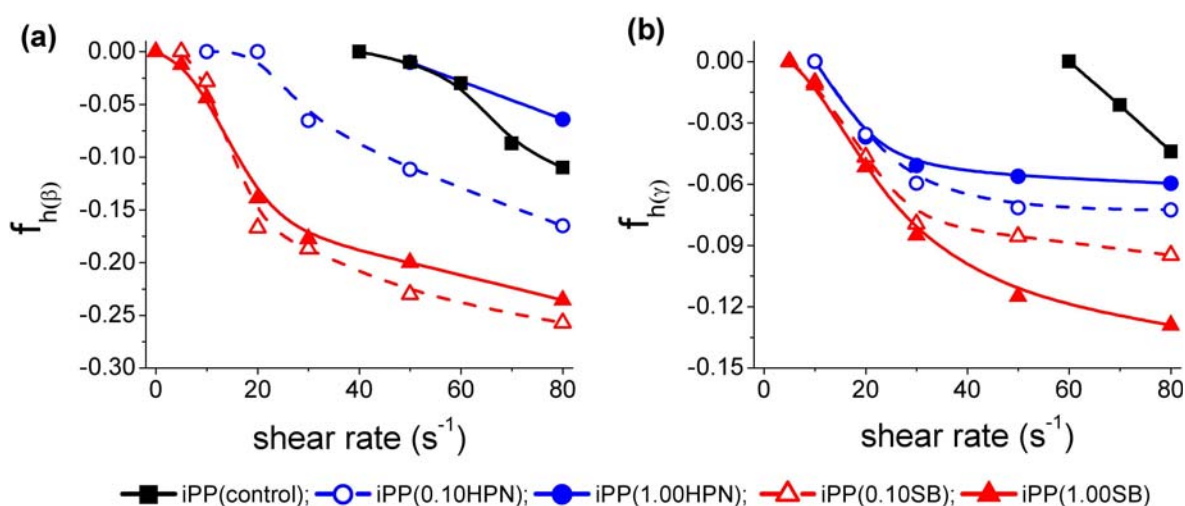


**Figure 7.16.** Influence of shear rate and nucleant loading level on the orientation of (a)  $\beta$ -iPP ( $f_{h(\beta)}$ ) and (b)  $\gamma$ -iPP ( $f_{h(\gamma)}$ ) crystals (shear time = 1 s, shear temperature =  $135^\circ\text{C}$ ).

The effect of isothermal crystallisation temperature on the  $\alpha$ -iPP,  $\beta$ -iPP and  $\gamma$ -iPP orientation is provided in **Table 7.3**. Increasing the crystallisation temperature significantly reduced the crystalline orientation for iPP(control). However, increasing the crystallisation temperature only resulted in moderate reduction in the nucleated samples.

**Table 7.3.** Influence of shear temperature on the crystalline orientation of the  $\alpha$ -iPP,  $\beta$ -iPP,  $\gamma$ -iPP crystalline phases (shear time = 1 s, shear temperature = 135 °C).

Sample	$\alpha$ -iPP						$\beta$ -iPP		$\gamma$ -iPP	
	$f_c$		$f_b$		$f_a$		$f_h$		$f_h$	
	135 °C	150 °C	135 °C	150 °C	135 °C	150 °C	135 °C	150 °C	135 °C	150 °C
iPP(control)	0.15	0.04	-0.14	-0.06	-0.01	0.02	-0.11	-	-0.05	-0.01
iPP(1.00HPN)	0.25	0.20	-0.22	-0.20	-0.03	0.00	-0.17	-	-0.06	-0.06
iPP(1.00SB)	0.30	0.27	-0.41	-0.34	0.11	0.07	-0.24	-	-0.13	-0.09

The lamellar scale orientation ( $f_{h(\text{SAXS})}$ ) was characterised using the method presented in **Chapter 3.3.1.5**. The influence of flow condition and nucleant loading level is shown in **Figure 7.17**. The addition of nucleant particles reduced the critical shear rate required to induce lamellar orientation. In iPP(control) the critical shear rate was  $30 \text{ s}^{-1}$ . Increasing SB loading reduced the critical shear rate to  $10 \text{ s}^{-1}$  for iPP(0.10SB) and to  $5 \text{ s}^{-1}$  for iPP(1.00SB). Increasing HPN loading decreased the critical shear rate to  $20 \text{ s}^{-1}$  for iPP(0.10HPN) and  $10 \text{ s}^{-1}$  for iPP(1.00HPN). Furthermore, for a given flow condition the addition of both nucleants increased the lamellar orientation. Increasing the loading of SB resulted in increased lamellar orientation. However, increasing the loading of HPN decreased the lamellar orientation.

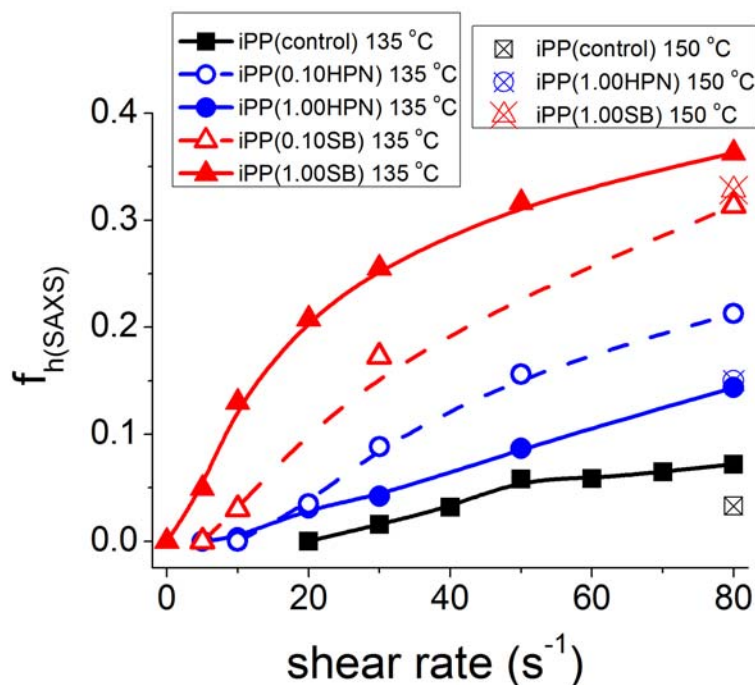


**Figure 7.17.** Influence of shear rate, shear temperature and nucleant loading level on the lamellar orientation function ( $f_{h(\text{SAXS})}$ ) (shear time = 1 s, shear temperature = 135 °C).

### 7.3.5 Morphology development during crystallisation

To gain a better understanding of the development of crystalline morphology, simultaneous rheo-SAXS/WAXS experiments were performed on samples which had been subjected to a moderate step shear. The first part of this section will seek to understand the development of crystalline morphology (WAXS) under flow-induced crystallisation conditions. This will allow the determination of the order of crystallisation and progression of the  $\alpha$ -iPP,  $\beta$ -iPP and  $\gamma$ -iPP crystalline phases. The second part of this section will examine the formation of shish and subsequent lamellar formation (SAXS) under flow-induced crystallisation conditions. This will enable the influence of SB and HPN on the initial density and alignment of shish to be probed.

**Figure 7.18** provides a “birds eye” view of the progression of crystallisation in the quiescent condition and after a moderate step shear of  $80 \text{ s}^{-1}$  and 1 s. The small arrows in the figure indicate the time where  $\alpha(110)$ ,  $\beta(300)$  and  $\gamma(117)$  reflections were first detected. In the quiescent condition reflections from only the  $\alpha$ -iPP and  $\gamma$ -iPP phases were detected, while in the sheared condition, reflections from  $\alpha$ -iPP,  $\beta$ -iPP and  $\gamma$ -iPP phases were observed. Under all conditions, the induction time for  $\gamma$ -iPP formation was always longer than the induction time for  $\alpha$ -iPP. In the sheared samples the induction time for  $\beta$ -iPP formation was greater than that for both  $\alpha$ -iPP and  $\gamma$ -iPP.

The crystallisation kinetics were further probed by separating out  $\chi_\alpha$ ,  $\chi_\beta$  and  $\chi_\gamma$  contributions to  $\chi_v$  using the procedures detailed in **Chapter 3.3.1.5**. The relative crystallinity ( $\chi_{\text{rel}}$ ) of these parameters was then determined using **Equation 4.4**. The results from this analysis for both the quiescent and sheared condition are presented in **Figure 7.19**. The data was fitted to a basic Avrami model of the form presented in **Equation 2.6**. For all samples and for  $\alpha$ -iPP,  $\beta$ -iPP and  $\gamma$ -iPP, reasonably good fits were achieved, especially for  $0.1 \leq \chi_{\text{rel}} \leq 0.9$ . The deviation at low and high conversions is not unexpected as the Avrami constant is known to vary during crystallisation [222]. In the quiescent condition,  $\gamma$ -iPP lagged behind  $\alpha$ -iPP crystallisation. Although having a greater induction time and lower crystallinity than  $\alpha$ -iPP, in the sheared condition  $\gamma$ -iPP crystallisation was comparable to  $\alpha$ -iPP crystallisation. In addition, in the sheared condition  $\beta$ -iPP crystallisation lagged both  $\alpha$ -iPP and  $\gamma$ -iPP crystallisation.



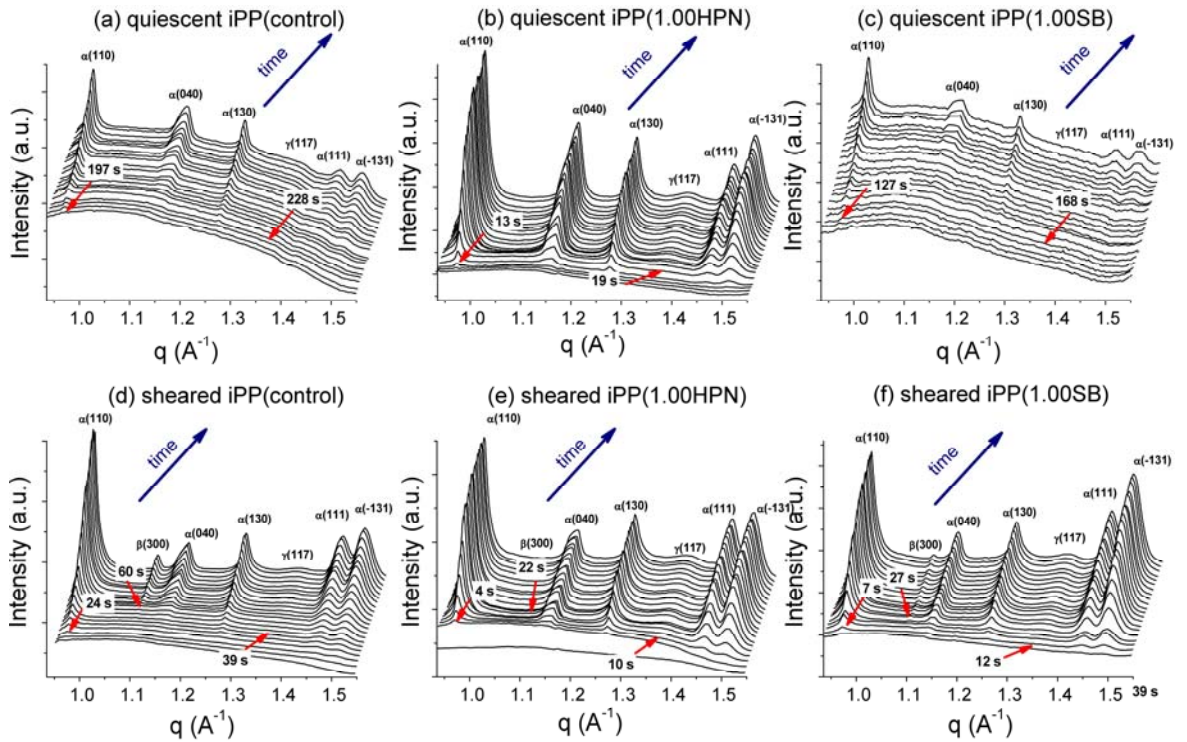


**Figure 7.18.** “Birds eye” view of the changes that occur to the WAXS intensity profiles along the scattering vector ( $q$ ) during isothermal crystallisation at  $135^\circ\text{C}$ . (a-c) quiescent (d-f) sheared condition (shear rate =  $80\text{ s}^{-1}$ , shear time = 1 s). The small arrows indicate the time where reflections from  $\alpha(110)$ ,  $\beta(300)$  and  $\gamma(117)$  are observed.

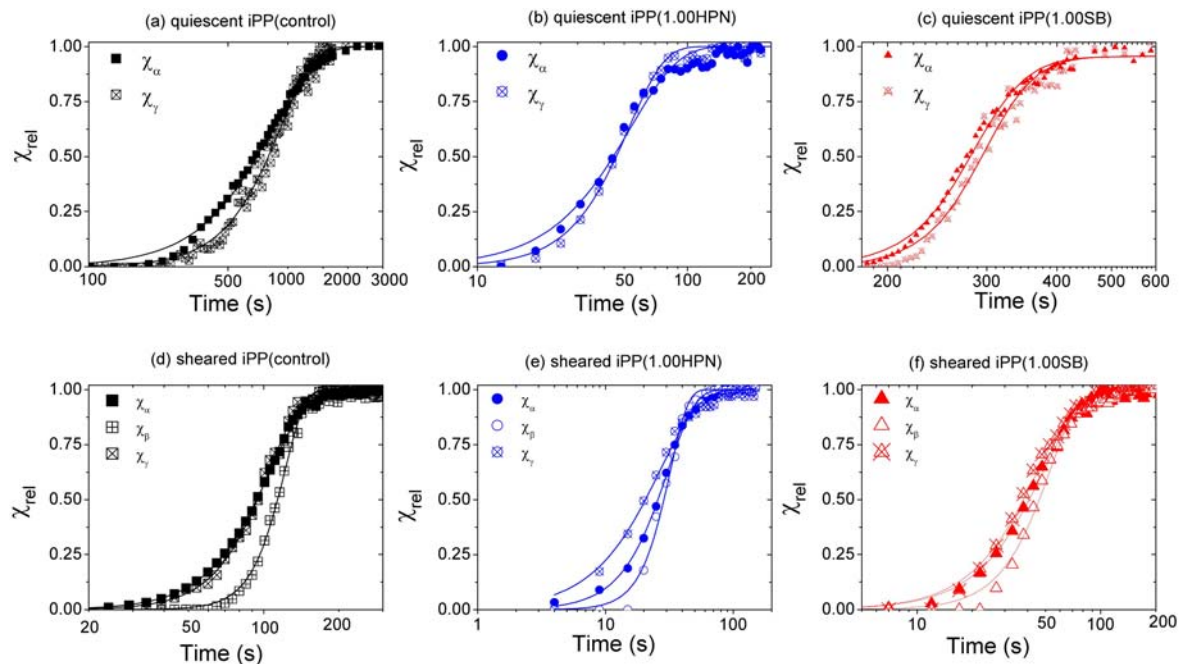


**Figure 7.19.** Changes in the relative crystallinity ( $\chi_{\text{rel}}$ ) of  $\alpha$ -iPP ( $\chi_{\alpha}$ ),  $\beta$ -iPP ( $\chi_{\beta}$ ) and total crystallinity ( $\chi_{\text{v}}$ ) during isothermal crystallisation at  $135^\circ\text{C}$  measured from WAXS. (a-c) quiescent condition (d-f) sheared condition (shear rate =  $80\text{ s}^{-1}$ , shear time = 1 s).

$t_{0.5}$  was obtained from the Avrami fits and was plotted as a function of shear rate, **Figure 7.20**. In the quiescent condition the inclusion of SB, but in particular HPN, substantially reduced the induction time for the formation of both  $\alpha$ -iPP and  $\gamma$ -iPP. This is in line with the NE and  $\Delta E$  values presented in **Table 7.1**. Increasing the shear rate over the range investigated led to a marked reduction in  $t_{0.5}$  for all samples. This is consistent with the formation of additional flow-induced nuclei.

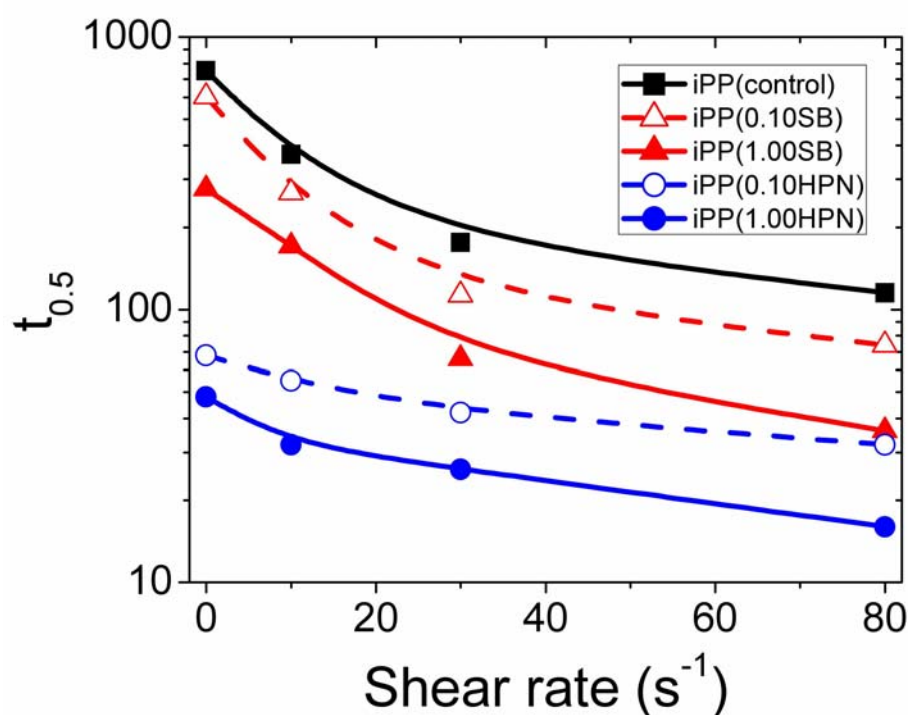


**Figure 7.20.** Influence of shear rate and nucleant loading level on the crystallisation half time ( $t_{0.5}$ ) of the volume crystallinity (shear time = 1 s, shear temperature = 135 °C).

**Figure 7.21** shows the influence of the two nucleants on the two-dimensional SAXS patterns at selected times after a step shear at a shear rate  $80 s^{-1}$  and for 1 s. In all samples flow led to the formation of equatorial streaks close to the beamstop. The appearance of equatorial streaks in flow-induced crystallisation experiments is known to signify the formation of shish aligned with their long axis along the flow direction [14]. The equatorial streaks extended to higher  $q$ -values, were sharper and became more intense with increasing loading of SB. This suggests that the density, length and alignment of shish was increased in the presence of SB. Increasing HPN loading, increased the equatorial scattered intensity but also broadened the scattered intensity

around the azimuth. This suggests that HPN additions increased the density of shish but reduced their length or alignment along the flow direction.

After an induction time meridional lobes formed in the SAXS patterns of all samples. Meridional lobes point to the formation of chain folded lamellae whose normals are aligned along the flow direction. Compared to iPP(control), the induction time for meridional scattering was significantly reduced in the nucleated samples, with the addition of HPN being somewhat more effective than the addition of SB. After the appearance of the meridional lobes, unoriented lamellar scattering was observed signifying the formation of unoriented lamellae at later stages of crystallisation.

The development of the oriented fraction of lamellae ( $\Phi_L$ ) during crystallisation is presented in **Figure 7.22a**.  $\Phi_L$  gives information about the fraction of oriented lamellae and was calculated according to the procedure specified in **Chapter 3.3.1.5**. For all samples  $\Phi_L$  was the highest in the early stages of crystallisation, and decreased as crystallisation progressed. In **Chapter 6.4.2** the decrease in  $\Phi_L$  during crystallisation was explained as arising from the competitive growth from shish and point-like nuclei. Compared to iPP(control), all nucleated samples had higher  $\Phi_L$  with the relative order being iPP(1.00SB) > iPP(1.00HPN) > iPP(control). Increasing SB loading resulted in substantially higher  $\Phi_L$  values. On the other hand, increasing the HPN loading resulted in a decrease in  $\Phi_L$  consistent with the orientation measurements presented in the previous section.

The full width at half maximum around the azimuth (FWHM( $\varphi$ )) of oriented parent lamellae (meridional scattering) was determined to get an idea of the distribution of lamellar normals. As crystallisation progressed the FWHM( $\varphi$ ) increased, **Figure 7.22b**. This can be explained by the curving and twisting of lamellae as they grow away from the shish. The direction of initial oriented parent growth can be assumed to occur perpendicular to the shish wall. Therefore the FWHM( $\varphi$ ) at the early stages of crystallisation can give information about the local shish misorientation. Compared to iPP(control) the samples containing SB had slightly smaller FWHM( $\varphi$ ) values at the start of crystallisation indicating high shish alignment along the flow direction, while the addition of HPN led to much broader FWHM( $\varphi$ ) values at the start of crystallisation. This suggests that the local shish misorientation is much higher in these samples.

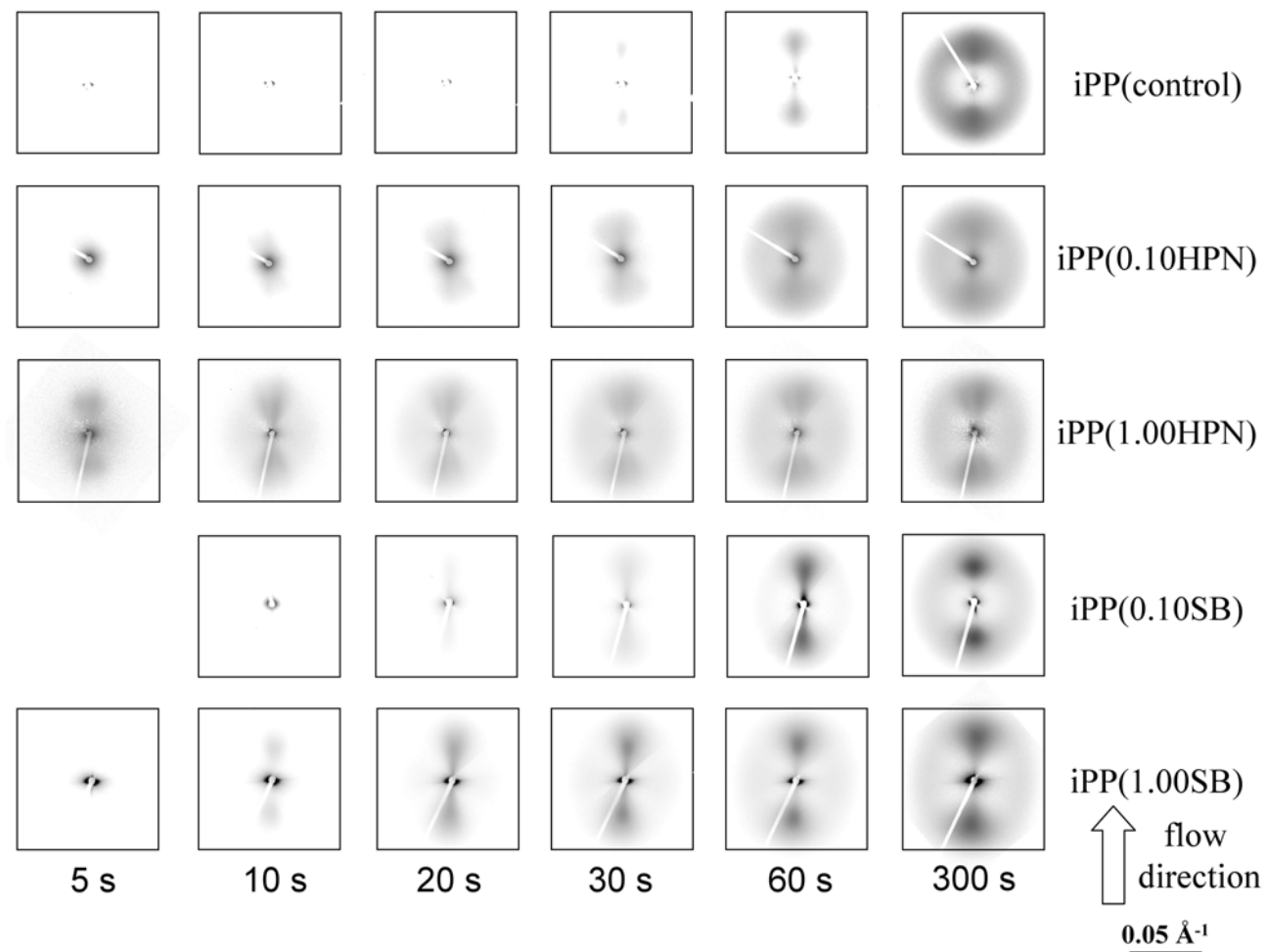


**Figure 7.21.** Two-dimensional SAXS patterns of pure iPP and iPP containing various loading levels of SB and HPN at selected times after shear (shear rate =  $80 \text{ s}^{-1}$ , shear time = 1 s, shear temperature =  $135 \text{ }^{\circ}\text{C}$ ).

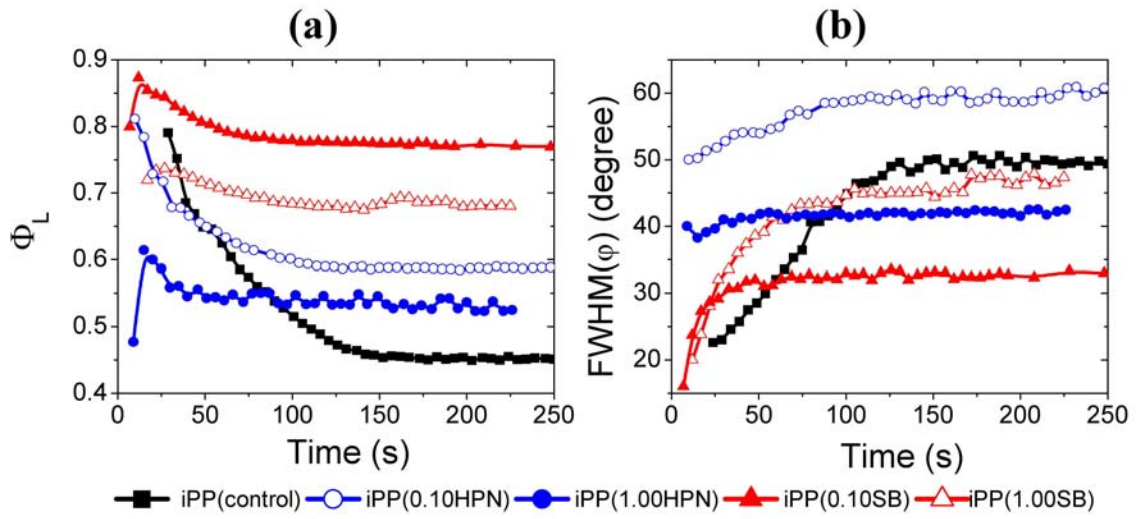


**Figure 7.22.** (a) development of the oriented fraction of lamellar ( $\Phi_L$ ) and (b) the full width at half maximum ( $\text{FWHM}(\varphi)$ ) of oriented parent lamellae during isothermal crystallisation (shear rate =  $80 \text{ s}^{-1}$ , shear time = 1 s, shear temperature =  $135^\circ \text{C}$ ).

Scattering in SAXS arises from the two phase nature of the crystalline and amorphous regions. Therefore the degree of crystallisation can also be followed using SAXS. The product of the volume fraction of the two phases has been shown to be proportional to the invariant  $\int I(q)q^2$  [256]. **Figure 7.23** shows the typical development of  $I(q)q^2$  during crystallisation. In this work the time dependence of the invariant was determined between  $0.0031 \leq q \leq 0.02$  and  $0^\circ \leq \varphi \leq 360^\circ$  according to the following relation:

$$Q_r(t) = \int_{q=0.0031\text{\AA}}^{q=0.02\text{\AA}} I(q,t)q^2 dq \quad \text{Equation 7.1}$$

As complete crystalline registration is not necessary to induce small angle scattering, this method can be expected to overestimate the crystallisation kinetics. However, a recent study performed by Byelov et al. showed that the crystallisation kinetics from this method was within 2% of that produced using WAXS data [205].

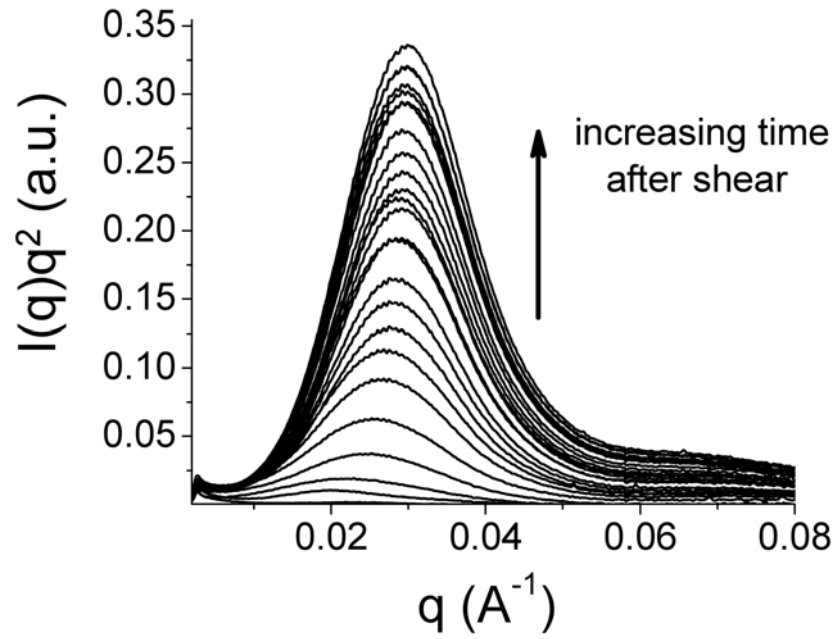


**Figure 7.23.** Plot of scattering vector ( $q$ ) versus  $Iq^2$  during isothermal crystallisation (iPP(control), shear rate =  $80 \text{ s}^{-1}$ , shear time = 1 s, shear temperature =  $135^\circ\text{C}$ ).

The two-dimensional SAXS images collected also allow the deconvolution of the oriented ( $L_{\text{oriented}}$ ) and unoriented ( $L_{\text{unoriented}}$ ) components of the total scattering to be followed during crystallisation according to:

$$Q_{\text{oriented}}(t) = Q_r(t) \times \Phi_L(t) \quad \text{Equation 7.2}$$

$$Q_{\text{isotropic}}(t) = Q_r(t) \times (1 - \Phi_L(t)) \quad \text{Equation 7.3}$$

where  $\Phi_L(t)$  is the instantaneous oriented fraction of lamellae determined over the same integral limits as that used to calculate  $Q_r(t)$ . The relative crystallinity of the unoriented ( $\chi_{\text{rel(unoriented)}}$ ) and oriented ( $\chi_{\text{rel(oriented)}}$ ) component was then determined using **Equation 4.11**. **Figure 7.24** shows the influence of the two nucleants on the development of these parameters during crystallisation. In all samples the unoriented component always lagged behind the oriented component. This shows that nucleation from shish occurs preferentially to nucleation from point-like nuclei. Interestingly, the difference in the time to reach 50% conversion for  $\chi_{\text{rel(unoriented)}}$  and  $\chi_{\text{rel(oriented)}}$  was much larger in iPP(control) and iPP(1.00SB) compared to iPP(1.00HPN). This suggests there are more or better quality point-like nuclei in samples containing HPN.

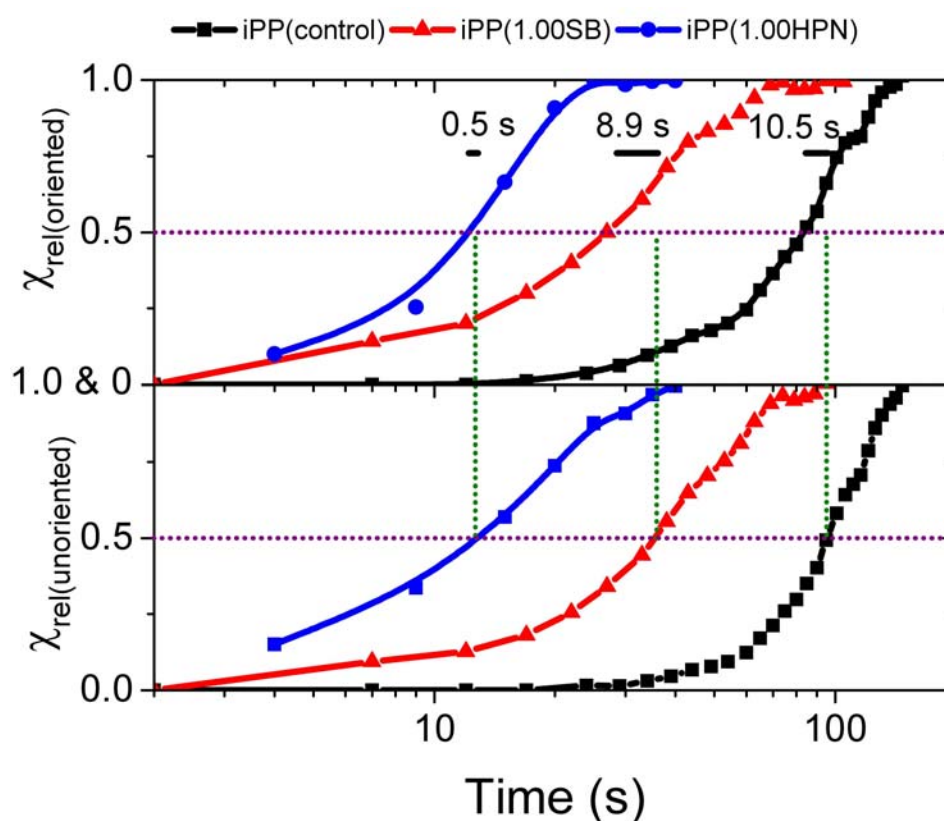


**Figure 7.24.** Crystallisation kinetics of the unoriented ( $\chi_{\text{rel(unoriented)}}$ ) and oriented ( $\chi_{\text{rel(oriented)}}$ ) crystallinity indices (shear rate =  $80 \text{ s}^{-1}$ , shear time = 1 s, shear temperature =  $135 \text{ }^{\circ}\text{C}$ ).

### 7.3.6 In-situ melting experiments

In this section the thermal stability of the microstructural constituents formed in the once sheared and crystallised samples is investigated in-situ during confined melting. In these experiments, samples which had been previously sheared and isothermally crystallised were heated from  $50 \text{ }^{\circ}\text{C}$  to  $220 \text{ }^{\circ}\text{C}$  at  $0.17 \text{ }^{\circ}\text{C/s}$ . The changes to the SAXS patterns during heating are shown in **Figure 7.25**. Lamellar melting dominated during heating up to  $180 \text{ }^{\circ}\text{C}$ . The unoriented lamellae were observed to melt first followed at higher temperatures by the melting of the oriented daughter and finally oriented parent lamellae. This relative order of melting is consistent with the findings presented in **Chapter 4.4.2**. Above  $180 \text{ }^{\circ}\text{C}$  only the equatorial scattering streak was observed. Furthermore, no associated crystalline reflections were observed in the WAXS region (not shown). This scattering suggests the sole presence of non-crystalline shish aligned along the flow direction. At a sufficiently high temperature, the equatorial scattering



disappeared indicating the dissolution of shish. Interestingly, in the latter stages of melting of iPP(1.00SB) (198 °C), the equatorial scattering streak disappeared and was replaced with an unexpected sharp meridional reflection, **Figure 7.26**.

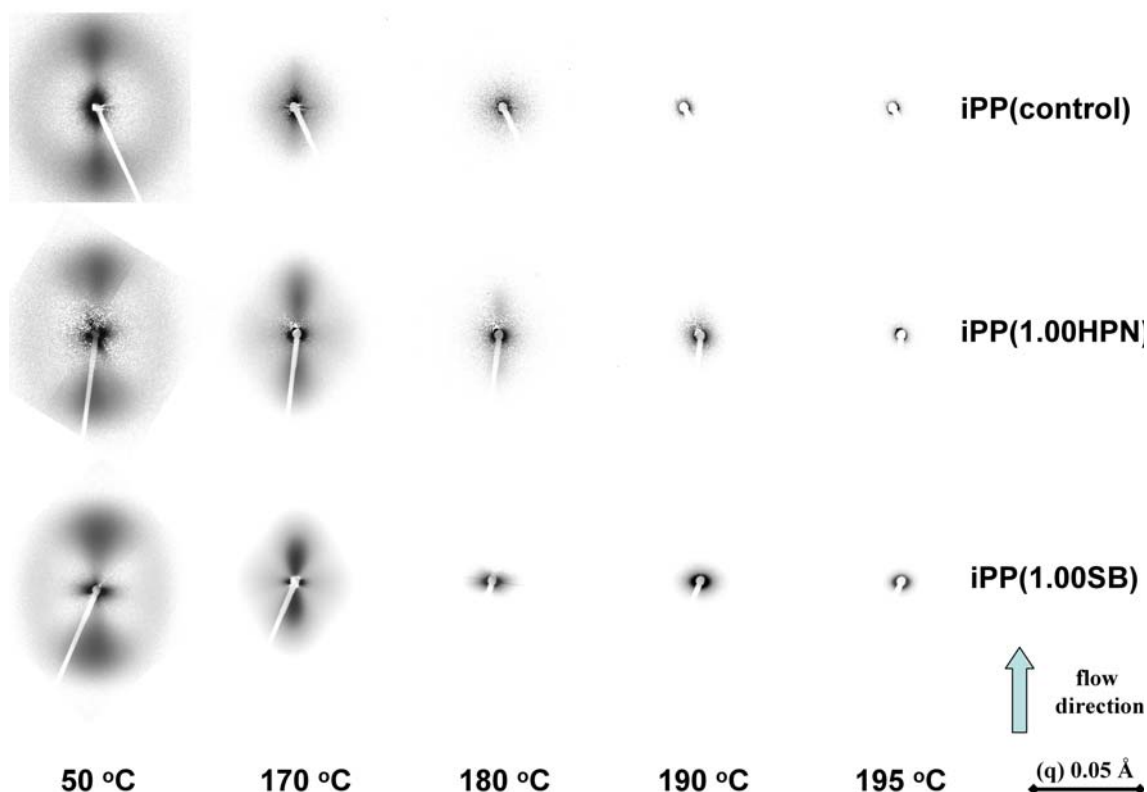


**Figure 7.25.** Selected SAXS patterns during the melting of once sheared and crystallised samples (shear rate =  $80\text{s}^{-1}$ , shear time = 1 s, shear temperature = 135 °C, heating rate = 0.17 °C/s).

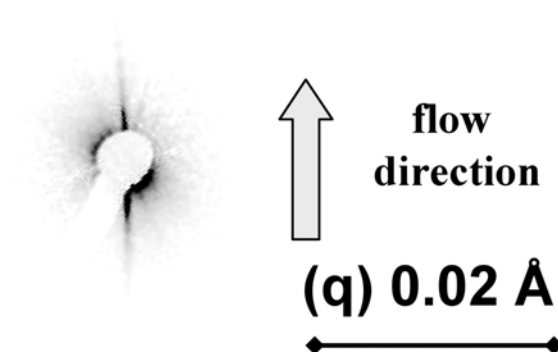


**Figure 7.26.** SAXS pattern of sheared iPP(1.00SB) taken in the last stages of shish dissolution at a temperature of 197 °C (shear rate =  $80\text{s}^{-1}$ , shear time = 1 s, shear temperature = 135 °C, heating rate = 0.17 °C/s).



The integrated intensity along the equator ( $I_0$ ) and meridian ( $I_{90}$ ) during melting was determined using **Equation 3.23** and the method presented in **Chapter 3.3.1.5**. Scattering along the meridian contains contributions from oriented parent lamellae and unoriented lamellae, while the scattering along the equatorial region contains contributions from shish, oriented daughter lamellae and unoriented lamellae. The integrated intensity along the meridian effectively decreased to zero at the same temperature ( $T_m \sim 180\text{ }^{\circ}\text{C}$ ), **Figure 7.27a**. This shows that the samples exhibited the complete melting of oriented parent lamellae around the same temperature, implying comparable oriented parent lamellae thickness distributions for all samples. This is expected from the similar thermodynamic crystallisation conditions. Scattering along the equator decreased rapidly up to  $177.5\text{ }^{\circ}\text{C}$ , but did not immediately go to zero at higher temperature, **Figure 7.27b**. This can be explained by the progressive melting of unoriented and oriented daughter lamellae but the continued stability of shish at the higher temperature. Interestingly, the shish dissolution temperature was considerably higher in iPP(1.00HPN) and iPP(1.00SB) compared to iPP(control) (i.e.  $195\text{ }^{\circ}\text{C}$  &  $198\text{ }^{\circ}\text{C}$  compared to  $189\text{ }^{\circ}\text{C}$ ). Furthermore, the magnitude of the integrated scattered intensity from shish was also much greater in iPP(1.00SB) and iPP(1.00HPN) compared to iPP(control). This further suggests higher shish density in the nucleated samples.

Once the samples reached  $220\text{ }^{\circ}\text{C}$  they were held there for a further 300 s before being isothermally crystallised under quiescent conditions at  $135\text{ }^{\circ}\text{C}$ . The corresponding SAXS/WAXS patterns are shown in **Figure 7.28**. The patterns were almost identical to samples which had originally been isothermally crystallised under quiescent conditions. Furthermore, no appreciable crystalline or lamellar orientation was detected. This showed that the remelting treatment completely eliminated the lamellar and crystalline orientation observed in the samples crystallised under flow-induced crystallisation conditions.

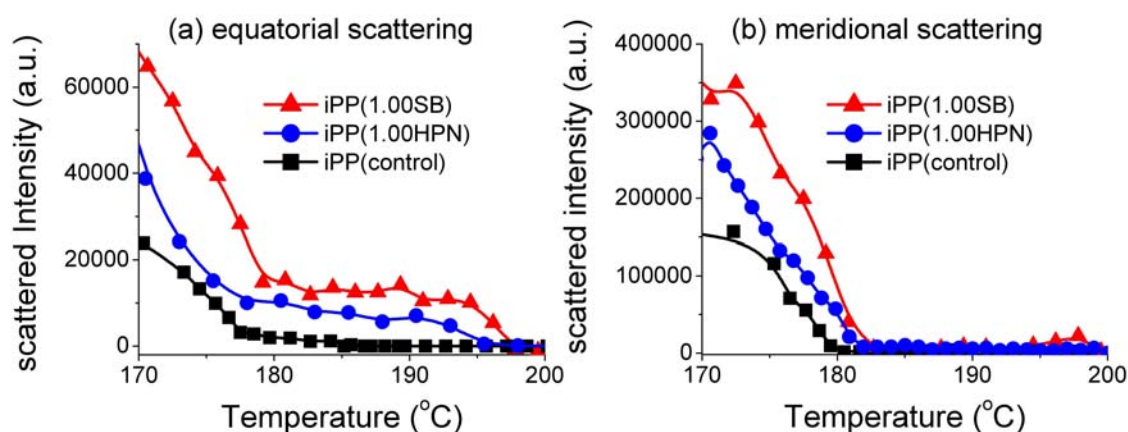


**Figure 7.27.** Changes to the scattered intensity along (a) the equator and (b) the meridian during the melting of once sheared and crystallised samples (shear rate =  $80\text{s}^{-1}$ , shear time = 1 s, shear temperature =  $135\text{ }^{\circ}\text{C}$ , heating rate =  $0.17\text{ }^{\circ}\text{C/s}$ ).

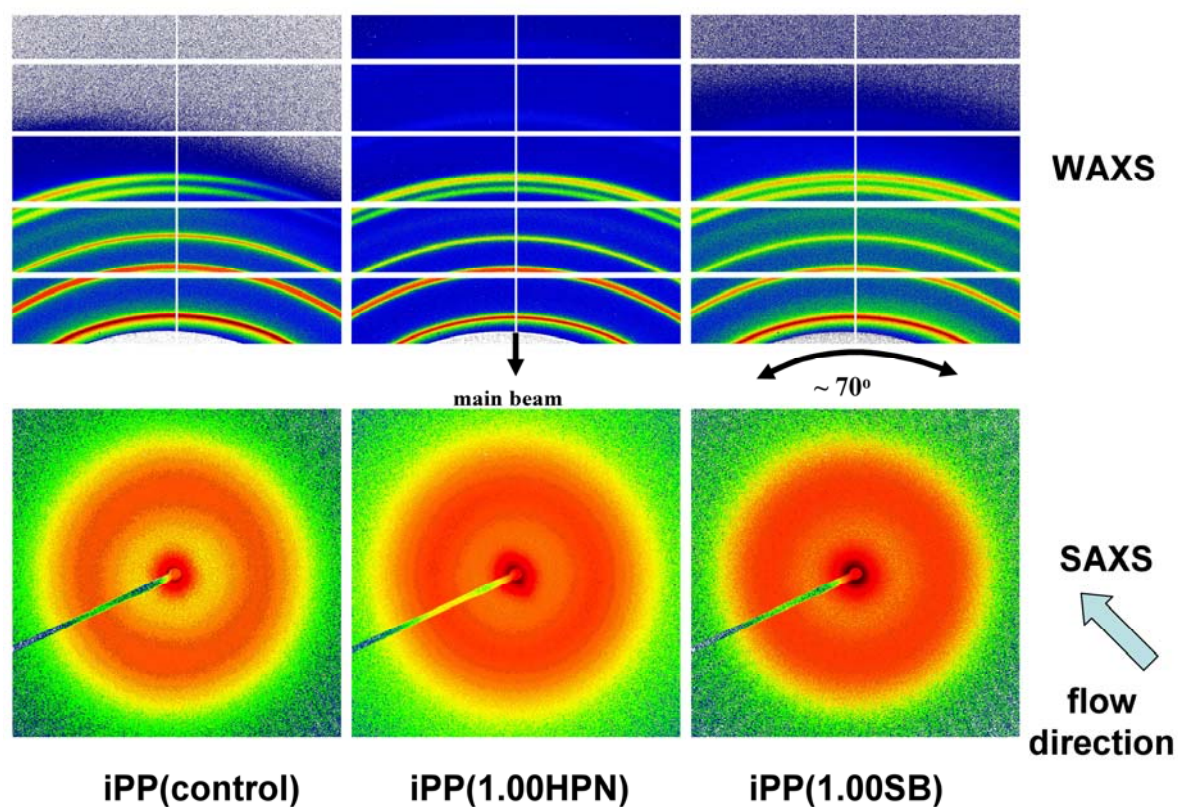


**Figure 7.28.** SAXS/WAXS patterns of once sheared and crystallised samples (shear rate =  $80\text{ s}^{-1}$ , shear time = 1 s, shear temperature =  $135^{\circ}\text{C}$ ), which had been subsequently remelted at  $220^{\circ}\text{C}$  for 300 s then isothermally crystallised at  $135\text{ }^{\circ}\text{C}$ .

## 7.4.0 Discussion

### 7.4.1 Thermal stability of shish in nucleated iPP

In the following section the influence of the two nucleants on the relative thermal stability of shish is examined. The dissolution temperature of the shish in iPP(control) was observed to be  $\sim 9$  °C higher than the lamellar melting point. This is generally comparable to the values previously reported in the literature in which the shish dissolution temperature ranges from 10-15 °C higher than the corresponding lamellar melting temperature [14, 37, 101, 257-258]. At least two reasons could account for the higher shish dissolution temperature. The first is that compared to chain folded lamellae, shish are composed of extended chains or chain segments, and therefore would have a higher effective thickness than lamellae. According to **Equation 4.1** this would yield a higher thermal stability. The second is that the interconnectivity of the chains within the shish is higher than in the lamellae. Higher interconnectivity would increase the number of effective entanglements which help stabilise the shish structure.

The addition of both nucleants did not appreciably increase the lamellar melting temperature. However, the presence of the particles significantly increased the shish dissolution temperature to 15 °C above the lamellar melting point for iPP(1.00HPN) and 18 °C for iPP(1.00SB). Therefore it can be concluded that the addition of nucleant particles stabilised the shish structure. This stabilisation may occur in a number of ways. The shish could have formed on or migrated to the surface of the particle. The surface of the particles would then provide extra contact points to stabilise the shish. However, this mechanism would appear to be unlikely as the shish shown in the SEM images in **Figure 7.10** are much longer than the average particle size. Another possibility is that the particles act as physical cross links, increasing the number of entanglement points, which help stabilise the shish. If this was the dominant mechanism, particles which strongly interact with iPP molecules would be expected to have a stronger stabilisation effect. Instead the opposite was observed. The highest shish stability was observed in the sample containing SB. However, SB was shown to have a lower affinity for the iPP molecules than HPN. **Figures 7.11, Figure 7.21 and Figure 7.25** show that addition of both nucleants increased the scattered intensity from shish. The SEM images in **Figure 7.10** show that this is primarily due to an increase in the numbers of shish. However, as

will be shown in the following chapter, the increase in scattered intensity in the nucleated samples could also indicate increased shish dimensions. Increased shish density and dimensions would be associated with a higher number of connections between neighbouring shish, as well as within the shish, which would help increase their stability. Therefore, it is proposed that the increased shish density and dimensions increased the thermal stability of shish in the nucleated samples.

In the final stages of melting iPP(1.00SB), the equatorial scattering streak disappeared and briefly gave way to an unexpected sharp meridional streak. Furthermore, no crystalline reflections were observed in the WAXS patterns. A thorough survey of the literature revealed that such a meridional streak has not previously been reported during the melting of a semicrystalline polymer. The presence of a sharp meridional streak indicates the formation of a new structural periodicity aligned along the flow direction. As the formation of the meridional streak occurred in the final stages of shish dissolution, it is speculated that it is associated with the breaking up of the shish structure. If confirmed, it would point to structural singularities along the shish length which have slightly higher thermal stability, and therefore higher order than adjacent areas within the shish. No meridional reflections were observed during shish dissolution of iPP(control) and iPP(1.00HPN). This could be associated with the much lower density of shish found in the former, which would result in the scattered intensity being too low to be detected, and the higher shish misalignment observed in the later sample, which would interrupt the necessary periodicity for scattering to occur. This aspect of shish structure will be investigated further in **Chapter 8**.

#### ***7.4.2 Orientation development in sheared iPP containing $\alpha$ -iPP nucleating particles***

Compared to iPP(control), the addition of both nucleants decreased the critical shear rate required to form oriented crystalline and lamellar structures. Furthermore, for a given flow condition, the addition of both nucleants increased both the crystalline and lamellar orientation compared to iPP(control). Similar observations were made in **Chapter 5** and **Chapter 6** for flow-induced crystallisation in the presence of  $\beta$ -iPP nucleants. Therefore, the promotion of oriented structures can be considered to be a likely consequence when foreign particles are added to sheared semicrystalline polymer melts. Nevertheless, the particle characteristics which influence the extent of this

behaviour are not well understood. Accordingly, in this section the particle characteristics which influence the development of orientation are discussed.

In this chapter orientation structures arise principally from the formation of oriented chain folded lamellae, which nucleate on or near the surface of shish that are formed during shear flow. This process is best illustrated by the formation of sharp equatorial streaks (shish) in the SAXS patterns taken immediately after the application of shear flow followed subsequently by the development of meridional lobes (oriented parent lamellae), **Figure 7.21**. Accordingly, how the two particles affect shish formation is likely to be key to understanding morphology development. However, oriented crystal growth from the surface of aligned nucleants, particularly fibrillar nucleants [51, 259-260], could also contribute to the final crystalline and lamellar orientation, **Figure 7.29**. Therefore before the influence of the two particle types on shish formation can be characterised, the contribution from oriented crystal growth on the surface of the particles needs first to be assessed. **Figure 7.4e** showed that the needle-like SB particles showed preferred alignment of their long axis along (a) radial direction before shear flow and (b) the flow direction after shear flow. No corresponding crystalline or lamellar orientation was detected before the shear was applied. Furthermore, after being annealed at 220 °C for 300 s, no corresponding crystalline or lamellar orientation was detected in the sheared sample even though the SB particles remained aligned along the flow direction. This shows that oriented crystal growth from the surface of the needle-like SB particles did not occur to an appreciable extent in these experiments.

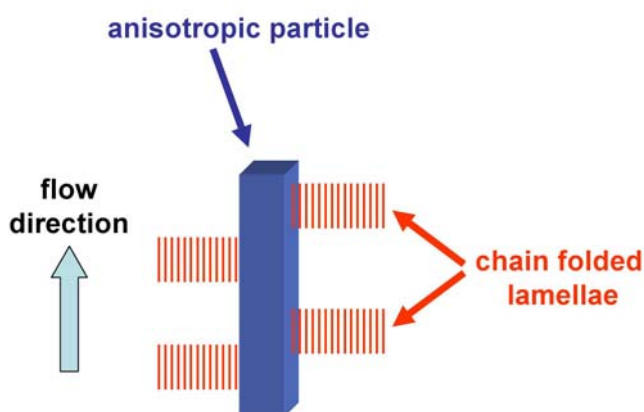


**Figure 7.29.** Schematic illustration of oriented crystal growth on the surface of an aligned anisotropic particle.

In the present experiment, the addition of both nucleants increased the intensity and resulted in an extension to high scattering angles of the equatorial streak observed in the SAXS patterns immediately after shear flow compared to iPP(control). Furthermore, the micrographs in **Figure 7.8** and **Figure 7.10** showed that the addition of both nucleants increased the density of shish. Therefore, it can be concluded that both particle types assisted the formation of shish. This higher shish density is the main reason for the higher crystalline and lamellar scale orientation observed in the nucleated samples.

Although both particles assisted the formation of shish, significant differences were observed between the two nucleant particles. The reason for these differences must lie in the different characteristics of the particles. Both particles were of similar chemical composition and size. The two particles however had different shapes, with the SB particles being needle-like with an aspect ratio near 10, and the HPN particles being relatively isotropic with an aspect ratio near 1. When compared at an equivalent surface area, it was shown that HPN had almost twice the nucleation efficiency of SB. In addition, the activation energy for crystallisation was considerably lower for samples containing HPN compared to SB. Therefore it can be concluded that HPN has a substantially greater ability to nucleate iPP crystals than SB under quiescent crystallisation conditions.

Under flow-induced crystallisation conditions, the reduction in the critical shear rate required to induce oriented structures was more pronounced with the addition of SB compared to HPN. Furthermore, when compared at a given flow condition, the addition of SB led to a higher density of shish, which then had greater alignment along the flow direction, compared to HPN. This shows that SB assisted the formation of shish to a greater extent than HPN. It has previously been reported that particles with a high affinity for the polymer molecule [3, 20] or which have a high aspect ratio [52] could aid the formation of flow-induced nuclei. Therefore in the present experiment, the particles shape can be concluded to be more important than its affinity for the polymer molecule in terms of assisting shish formation. A possible mechanism which can account for the observed influence of particle shape is proposed in **Chapter 8.4.4**.

For a given flow condition, increasing SB loading increased the crystalline and lamellar orientation. However, increasing HPN loading surprisingly decreased the crystalline and

lamellar orientation. This behaviour can be explained by the competitive growth from point-like and shish nuclei as described in **Figure 6.23**. In this experiment, point-like nuclei arise from two sources: (a) the heterogeneous sites on the surface of the nucleant and (b) the formation of flow-induced point-like nuclei. In **Chapter 6** it was noted that small shish can also be considered to act as point-like nuclei if their long dimension is considerably smaller than the distance between adjacent nuclei. In iPP(control) and iPP(1.00SB) the unoriented component of crystallisation was delayed relative to the oriented component, **Figure 7.24**. This suggests that the point-like nuclei were less numerous or not as potent as the shish nuclei. Conversely, the unoriented and oriented components for iPP(1.00HPN) were comparable, suggesting the presence of greater numbers and/or more potent point-like nuclei. Therefore the likely reason for the decreased orientation with increasing loading is the increased competition from heterogeneous nucleation off the surface of the HPN particles, which is highly effective at inducing iPP nuclei.

#### ***7.4.3 Inter-relation of shear flow and nucleant loading level on $\gamma$ -iPP formation***

$\gamma$ -iPP is widely known to form in CIM and SCORIM, particularly in the shear region and near the gate [261-262]. In these mouldings it is generally thought that the combination of high packing pressure and high molecular orientation leads to  $\gamma$ -iPP formation [261-262]. Indeed when iPP is crystallised under high pressure, samples composed almost entirely of  $\gamma$ -iPP can be obtained [158-159]. The presence of  $\gamma$ -iPP in CIM and SCORIM has been associated with the improved tensile strength and toughness of the component [261]. Recent studies which aimed to measure the individual mechanical properties of  $\alpha$ -iPP and  $\gamma$ -iPP confirmed that samples rich in  $\gamma$ -iPP will show improvements in both strength [183] and toughness [189]. Nevertheless, of the three known crystalline forms of iPP,  $\gamma$ -iPP is the least commonly observed, and accordingly the least well understood. Flow-induced crystallisation conditions [165, 169] and the addition of powerful nucleants [168] have been associated with  $\gamma$ -iPP formation. However, the combination of these factors has not yet been examined. In this section the following questions will be addressed: (a) what is the combined influence of  $\alpha$ -iPP nucleant and flow on  $\gamma$ -iPP formation?, and (b) what are the sites for  $\gamma$ -iPP nuclei in sheared iPP containing nucleants?

The  $\gamma$ -iPP content in iPP(0.10HPN) and iPP(1.00HPN) was 76% and 82% more than in iPP(control) under quiescent crystallisation conditions. Therefore it can be concluded that HPN had a  $\gamma$ -iPP nucleation effect. This result is in close agreement with the recent findings of Libster et al. [25] who observed up to a 44% increase in the  $\gamma$ -iPP content of a polypropylene/polyethylene (3% ethylene content) co-polymer with the addition of 600ppm of HPN. SB also had a mild  $\gamma$ -iPP nucleation effect, increasing the  $\gamma$ -iPP content by 9% for iPP(0.10SB) and 18% for iPP(1.00SB). A possible reason for the observed increase in  $\gamma$ -iPP in the nucleated samples is the substantially higher density of nuclei created by the presence of the nucleants. The high density of nuclei would lead to multiple nucleation events occurring near simultaneously along the one chain. This high number of nuclei would reduce the time available for the chain to properly organise during initial crystallisation. Combined with the stereo- and regio-defects already present along the main chain, this would promote shorter isotactic sequences. It has been reported that  $\gamma$ -iPP is favoured when the isotactic sequence length is interrupted [156-157]. This mechanism explains the large decrease in the  $\gamma$ -iPP content with increasing isothermal crystallisation temperature. In this case the higher temperature would reduce the number of active nuclei and slow down the kinetics of crystallisation. This would allow the chains time to properly organise, favouring the formation of the more thermodynamically stable  $\alpha$ -iPP.

Increasing shear rate was observed to have a negligible effect on the  $\gamma$ -iPP content of iPP(control), with a 6% increase over quiescent conditions for a shear rate of  $80\text{ s}^{-1}$ . A much larger increase in  $\gamma$ -iPP under flow-induced crystallisation conditions has recently been reported in a terpolymer (poly(propylene-co-ethylene-co-1-butene)) by Hong and Seo [165]. Though in that case it was considered that the defects introduced by the two co-polymer amplified the effect of the shear flow. In this study, an appreciable influence of shear rate was observed in the nucleated samples. Compared to iPP control crystallised under quiescent conditions the increase in the  $\gamma$ -iPP content of iPP(1.00SB) and iPP(1.00HPN) sheared for 1 s at a shear rate of  $80\text{ s}^{-1}$  and at shear temperature of  $135\text{ }^{\circ}\text{C}$  were 71% and 193% respectively. Therefore the combination of nucleant and shear flow produced a  $\gamma$ -iPP nucleation effect. One possible explanation for the large flow-induced  $\gamma$ -iPP formation in nucleated iPP could be due to flow around the particles



creating a local constriction of the flow field. Such a constriction would impose locally higher pressure during initial crystal nucleation, which would promote  $\gamma$ -iPP. However, the results presented in the following chapter would make this unlikely. It will be shown in **Chapter 8.3.4**, that a similar increase in  $\gamma$ -iPP was found in the same nucleant polymer system. In that experiment shear flow was applied at elevated temperature (181°C) and crystallisation was carried out after a long annealing treatment at elevated temperature (181 °C for 600 s). Considerable relaxation would be expected to occur at this temperature and thus the annealing treatment would eliminate any high pressure regions created during shear flow. Therefore it is proposed that the increased  $\gamma$ -iPP in this case is also due to increased density of nuclei. As discussed previously, shear flow leads to the formation of additional flow-induced nuclei (both point-like and shish). The resulting increased crystallisation rates would then amplify any defects present along the chain. This would disrupt the isotactic sequence length during initial crystallisation and thereby promote increased  $\gamma$ -iPP contents.

The kinetic analysis presented in **Figure 7.18** and **Figure 7.19** showed that  $\gamma$ -iPP formed around the same time or just after  $\alpha$ -iPP. This shows that  $\gamma$ -iPP formation is related to  $\alpha$ -iPP. Furthermore, at higher shear rates, an orientation relationship was found between  $\gamma$ -iPP and  $\alpha$ -iPP. The orientation relationship was the parallel chain-axis orientation which showed that  $\gamma$ -iPP lamellae formed on the surface of oriented  $\alpha$ -iPP parent lamellae. The results presented in this chapter are therefore in accord with the long held view that  $\gamma$ -iPP nuclei form on the ac surface of  $\alpha$ -iPP (i.e.  $\gamma$ -iPP lamellae branching) [9]. Interestingly, no  $\gamma$ -iPP lamellae branching was observed on the surface of daughter lamellae. However, this can be explained by the sequential formation of daughter lamellae which leads to them being thinner and less perfect and therefore they would be unlikely sites for  $\gamma$ -iPP nuclei. The proposed flow-induced structure for iPP containing  $\gamma$ -iPP is shown in **Figure 7.30**.

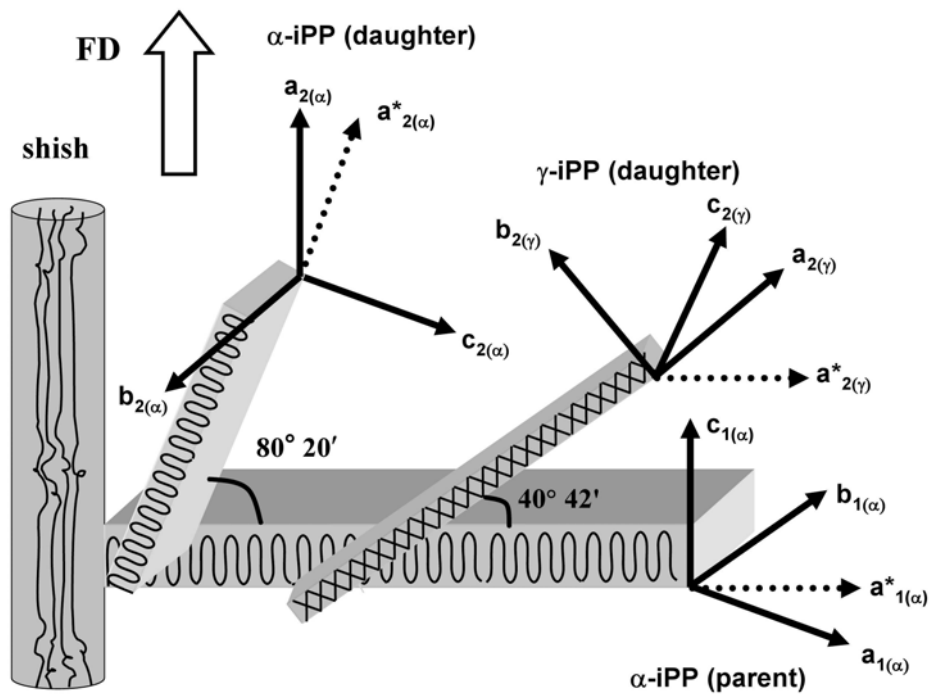


**Figure 7.30.** Schematic diagram illustrating the flow-induced crystallisation model for iPP including the orientation relationship between  $\alpha$ -iPP parent lamellae and  $\alpha$ -iPP and  $\gamma$ -iPP daughter.

The proposed structure suggests that factors which increase the amount of oriented parent lamellae should help promote a higher fraction of  $\gamma$ -iPP due to the increased number of nucleation sites available. This is indeed what was observed, with both the fraction of oriented  $\alpha$ -iPP parent lamellae and the  $\gamma$ -iPP fraction both increasing with increasing shear rate, **Figure 7.13** and **7.12c**, respectively. Therefore, the increase of oriented parent lamellae with the combined influence of shear flow and nucleant further increases  $\gamma$ -iPP formation by providing extra nucleation sites for  $\gamma$ -iPP nuclei. It should be pointed out here that in this scenario,  $\gamma$ -iPP will only form if the condition of sufficiently short isotactic helix length is reached. This point is best illustrated by comparing the two experimental crystallisation temperatures i.e. 135 °C with 150 °C. Increasing the crystallisation temperature resulted in a considerable drop in the  $\gamma$ -iPP content, but also resulted in an increase in the fraction of oriented parent lamellae. An alternative explanation for the observed relationship between the amount of oriented parent lamellae and  $\gamma$ -iPP content which cannot be ruled out, is that the increased number of  $\gamma$ -iPP nuclei simply replace and therefore reduce the amount of daughter lamellae formed.

#### ***7.4.4 Flow-induced $\beta$ -iPP formation in the presence of $\alpha$ -iPP nucleants***

$\beta$ -iPP was observed under flow-induced conditions in samples containing SB. In the case of iPP(0.10SB), the amount of  $\beta$ -iPP formed was significantly greater compared to the  $\beta$ -iPP content in iPP(control). SB has historically been considered as a good  $\alpha$ -iPP nucleant agent [28, 113, 201]. Furthermore, in the previous chapter the  $\beta$ -iPP nucleating selectivity of the CaSub particles was shown to be suppressed by the application of shear flow. The  $\beta$ -iPP nucleation effect was accordingly quite unexpected, and needs to be understood in light of the flow-induced  $\beta$ -iPP crystallisation model present in **Chapter 6.4.3**. In that model, it was proposed that a shear flow window exists for pure iPP, where mesomorphic point-like nuclei which possess the necessary internal structure to specifically nucleate  $\beta$ -iPP are formed. The addition of even a small number of SB particles was shown to amplify the influence of shear flow, assisting the formation of additional flow-induced nuclei. It is therefore conceivable that a similar mechanism as that proposed for pure iPP is in operation in the presence of SB. This assertion is supported by the reduction in the shear rate to obtain peak  $\beta$ -iPP from  $30\text{ s}^{-1}$  in iPP(control) to  $20\text{ s}^{-1}$  in iPP(0.10SB), and to  $10\text{ s}^{-1}$  in iPP(1.00SB), consistent with the higher nuclei density found in these samples.

$\beta$ -iPP was detected in the presence of HPN only at the higher shear rates examined. For iPP(0.10HPN) a shear rate of  $30\text{ s}^{-1}$  was required to induce  $\beta$ -iPP, while for iPP(1.00HPN) a shear rate of  $50\text{ s}^{-1}$  was required. The suppressed flow-induced formation of  $\beta$ -iPP at the lower shear rates can be rationalised by the high nucleation efficiency of the HPN particles dominating crystallisation. Nevertheless, a small amount of  $\beta$ -iPP was observed to form at higher shear rates. This can be explained by the formation of many additional flow-induced nuclei which may then compete with the heterogeneous nucleation from the surface of the HPN particles.

## 7.5.0 Conclusions

This chapter investigated the influence of flow condition on the morphology development of isotactic polypropylene (iPP) containing two commercial particulate nucleating agents. The two nucleating agents were sodium benzoate (SB) and bicyclo[2.2.1]heptane-2,3-dicarboxylic acid (HPN). From the results obtained the following was concluded:

When compared at an equivalent surface area, the isotropic HPN particles were found to have almost twice the nucleation efficiency of the needle-like SB particles. Furthermore, the activation energy for crystallisation was considerably lower for samples containing HPN compared to SB. These results show that HPN has a substantially greater ability to nucleate iPP crystals than SB under quiescent crystallisation conditions.

In iPP(control) the shish dissolution temperature was observed to be 9 °C higher than the melting temperature of the thickest lamellae. The relative thermal stability of the shish was further increased in the presence of both nucleating particles. The shish dissolution temperature in iPP(1.00HPN) and iPP(1.00SB) were 15 °C and 18 °C higher than the thickest lamellae respectively. This was explained by the particles' increasing the density and size of shish formed. This increased the interconnectivity within the shish which stabilised the shish structure.

Under flow-induced crystallisation conditions, the addition of both nucleating particles decreased the critical shear rate required to induce the shish-kebab structure compared to iPP(control). Furthermore, for a given flow condition, both particles increased the density of shish compared to iPP(control). This particle assisted shish formation was the main reason for the higher crystalline and lamellar orientation observed in the fully crystallised condition for the nucleated samples.

The particle characteristics which influenced the final orientation were discussed. Compared to HPN, the addition of SB led to a lower critical shear rate required to induce shish formation, a greater density of shish for a comparable flow condition, and greater shish alignment along the flow direction. These results revealed that the particle

aspect ratio was a more important factor than the nucleation efficiency of the particle in terms of assisting shish formation. Increasing SB loading increased crystalline and lamellar orientation, while increasing HPN loading surprisingly decreased the crystalline and lamellar orientation in the fully crystallised condition. This was explained by the increase in the competitive growth of unoriented lamellae from the more powerful heterogeneous sites on the surface of the HPN particles.

Under quiescent conditions the addition of HPN was found to increase the  $\gamma$ -iPP content. Compared to iPP(control) the  $\gamma$ -iPP content increased by 76% for iPP(0.10HPN) and 82% for iPP(1.00HPN). The increased  $\gamma$ -iPP content was explained by the higher density of nuclei, which disrupted the isotactic sequence length during initial crystallisation, and thereby promoted  $\gamma$ -iPP.

The combination of shear flow and nucleant was effective at inducing the  $\gamma$ -iPP phase. The increased  $\gamma$ -iPP content with increasing particle loading and shear rate was explained by (a) the increased number of nuclei which reduces the isotactic sequence length during crystallisation and (b) the accompanied increase in the fraction of parent lamellae which provide additional nucleation sites for  $\gamma$ -iPP formation.

## Chapter 8

### Shish formation and relaxation in sheared isotactic polypropylene containing nucleating particles

#### 8.1.0 Introduction

Thermoplastic polyolefins such as isotactic polypropylene (iPP) and polyethylene (PE) are typically processed into their final forms by injection moulding or extrusion technologies. If the flow intensity in these processes is sufficient, a highly anisotropic crystalline architecture termed shish-kebabs can form [10-17], which can substantially influence the final physical properties of the component [18-19]. A highly oriented thread-like core composed of extended chains (shish) is considered to form first, which then provides a template for the formation and growth of oriented chain folded lamellae (kebabs). Accordingly, the formation of shish is one of the key components to understanding morphology development under flow conditions.

For a given polymer, a critical flow intensity is necessary to form shish. However, the specific flow conditions responsible for this transition have only recently been identified [12-13]. The shear rate needs to be larger than the inverse Rouse time of the longest chains (i.e.  $\dot{\gamma} > 1/\tau_R$ ) so that the chains can become extended by the flow. Furthermore, a critical amount of mechanical work is also necessary to allow the extended chains to come together and form a stable shish entity. Although the specific flow conditions for shish formation have been identified, the mechanism responsible for the initial shish formation is still under debate as discussed in **Chapter 2.3.2**.

Recent advances in small and wide angle x-ray scattering (SAXS/WAXS) techniques have allowed shish formation and relaxation to be probed in-situ after controlled shear flow. Balzano et al. [263] investigated a high density polyethylene (HDPE), which had been specially prepared to have a bimodal molecular weight distribution, and found shish were able to be formed near to and even slightly above the equilibrium melting temperature of the unconstrained extended chain crystal. It was considered that to form the shish required the stretch of the longest chains in the molecular weight distribution. A similar conclusion was drawn by Keum et al. [257] who investigated shish formation

and relaxation in model blends of ultra high molecular weight polyethylene (UHMWPE) in HDPE. In addition Keum et al. showed that shish could grow by an autocatalytic process after the shear flow had stopped. Similar autocatalytic growth of shish was also recently observed by Patil et al. [115] in a broad molecular weight PE. Nevertheless, comparable studies have yet to be performed for other commercially important semicrystalline polymers such as iPP.

In **Chapter 5-7**, the addition of particles was shown to dramatically influence the morphology development under quiescent and flow-induced crystallisation conditions. In particular when exposed to a brief shear pulse, the particles were found to assist shish formation. The increased shish density in the samples containing the particles ultimately led to higher levels of lamellar and crystalline orientation after subsequent crystallisation. In **Chapter 7**, a range of evidence was presented which indicated that particle shape was a more important factor than the particle's nucleation efficiency in terms of assisting shish formation. Nevertheless, the underlying mechanism responsible for the strong influence of particle shape was not able to be identified. This was primarily due to a lack of observational data of shish during shish formation.

In this chapter, continuous shear flow was applied to the melt of pure iPP and melts of two iPP samples containing different commercial particulate nucleants. The shear temperature ( $T_\gamma = 181\text{ }^\circ\text{C}$ ) was selected to be well above the lamellar melting point ( $T_m = 166\text{ }^\circ\text{C}$ ) of the polymer, but below the equilibrium melting temperature of the unconstrained extended chain crystal ( $T_m^0 = 186.1\text{ }^\circ\text{C}$ ) [158]. The purpose was to investigate the influence of the two nucleants on: (a) the formation of shish under close to steady state shear flow conditions, and (b) the shish stability after shear flow was stopped. The likely mechanisms of particle assisted shish formation are discussed.

Some of the results presented in this chapter have previously been published in *Macromolecules* [264] and presented at the *Annual Meeting of the Polymer Processing Society (PPS-26)* [265]. These papers can be found in **Appendix 2**.

## 8.2.0 Experimental

### 8.2.1 Sample preparation and thermal-shear profile

Two commercial particulate nucleants which specifically nucleate  $\alpha$ -iPP were used in this chapter: sodium benzoate (SB) and bicyclo[2.2.1]heptane-2,3-dicarboxylic acid, trade name HPN-68 (HPN). The sample naming convention is described in **Table 3.2**. The compounding and sample preparation procedures are described in detail in **Chapter 3.2.2**. The thermal-shear profile is shown in **Figure 8.1a**. The previously compression moulded disks were heated to 220 °C and compressed slowly to the working distance of 0.25 mm at 0.01 mm/s. This ensures that the shear rate imposed on the sample during the compression phase is always less than 0.3 s<sup>-1</sup>. The compressed disks were held at the melting temperature for at least 300 s to erase the previous thermal history of the sample. The samples were cooled to the shear temperature and held for 60 s before a continuous shear pulse was applied to the melt for 30 s at a constant shear rate. The samples were then held at temperature for a further 600 s before being cooled at 0.5 °C/s to room temperature.

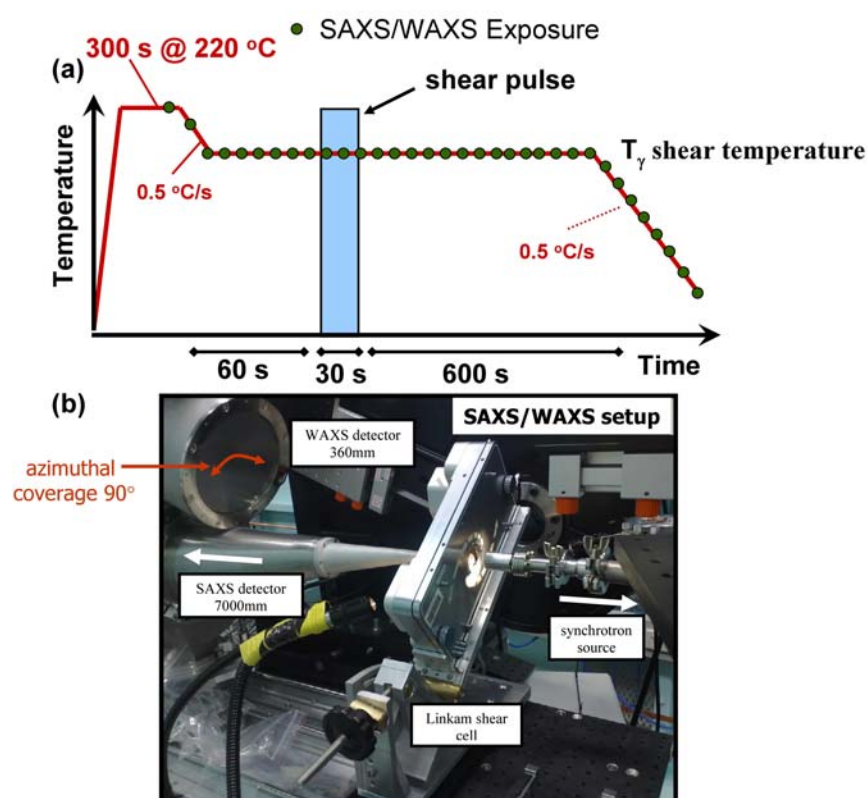


**Figure 8.1.** (a) Schematic illustration of the thermal-shear profile used in this chapter. (b) Experimental SAXS/WAXS setup on the Australian Synchrotron.



### 8.2.2 Analytical techniques

The Linkam CSS450 was adapted for use with x-ray radiation using the procedure specified in **Chapter 3.3.3**. Simultaneous two-dimensional rheo-SAXS/WAXS experiments were performed on the SAXS/WAXS beam line at the Australian Synchrotron, **Figure 8.1b**. The SAXS/WAXS(2) experimental setup used in this chapter was described in detail in **Chapter 3.6.3**. The setup allowed for in-situ investigations with a considerable amount of the scattered intensity around the azimuth ( $\varphi \sim 90^\circ$ ) in the WAXS region to be captured, whilst simultaneously capturing complete two-dimensional SAXS patterns.

Ex-situ polarised optical macro images of the sheared disks at room temperature were made using the home made polariscope described in **Chapter 3.3.4.2**. A fluorescent light box was used as the light source. The sample to be imaged was sandwiched between crossed polarising films. A 14 megapixel Olympus FE-4030 CCD camera mounted 150 mm above the light box was then used to record the images.

The Linkam CSS450 was adapted for use with infrared radiation using the procedure specified in **Chapter 3.3.3**. In-situ Fourier transform infrared spectroscopy (Rheo-FTIR) experiments were performed on a Perkin-Elmer GX. The setup was described in detail in **Chapter 3.7.0**. An empty cell was used as the background. The root mean squared intensity of the melt immediately prior to flow was used to normalise the data.

### 8.3.0 Results

#### *8.3.1 Observation of shish before, during and after shear flow*

Selected two-dimensional SAXS patterns taken using the SAXS/WAXS(2) setup before, during and after the shear profile are shown in **Figure 8.2**. The images shown before shear flow have had the empty cell data subtracted as the background. In their undeformed state, all three samples showed diffuse isotropic scattering profiles consistent with an amorphous iPP melt with no preferred orientation. To enhance scattering contrast for the subsequent two-dimensional SAXS images, both the empty cell data and the melt data immediately prior to the start of shear flow were subtracted from all subsequent images. During shear flow, a strong increase in equatorial scattering was observed as indicated by the arrows in **Figure 8.2**. The increase in equatorial scattering is consistent with the formation of shish aligned along the flow direction. The presence of fibrils in the micrographs of quenched samples verified that shish were formed by the imposed thermal-shear profile. After the shear pulse stopped, the equatorial streaks in all samples became weaker and spread around the azimuth. This indicates that the shish are not entirely stable in this temperature regime. Large differences in the scattered intensity were observed between the three samples. The addition of both nucleants increased the intensity of the equatorial streak compared to iPP(control). The equatorial streak in iPP(1.00SB) were significantly more intense, extended to a higher scattering vector ( $q$ ) and were sharper compared to those in iPP(1.00HPN). These differences in scattered intensity will be quantitatively investigated during and after shear flow in the following section.

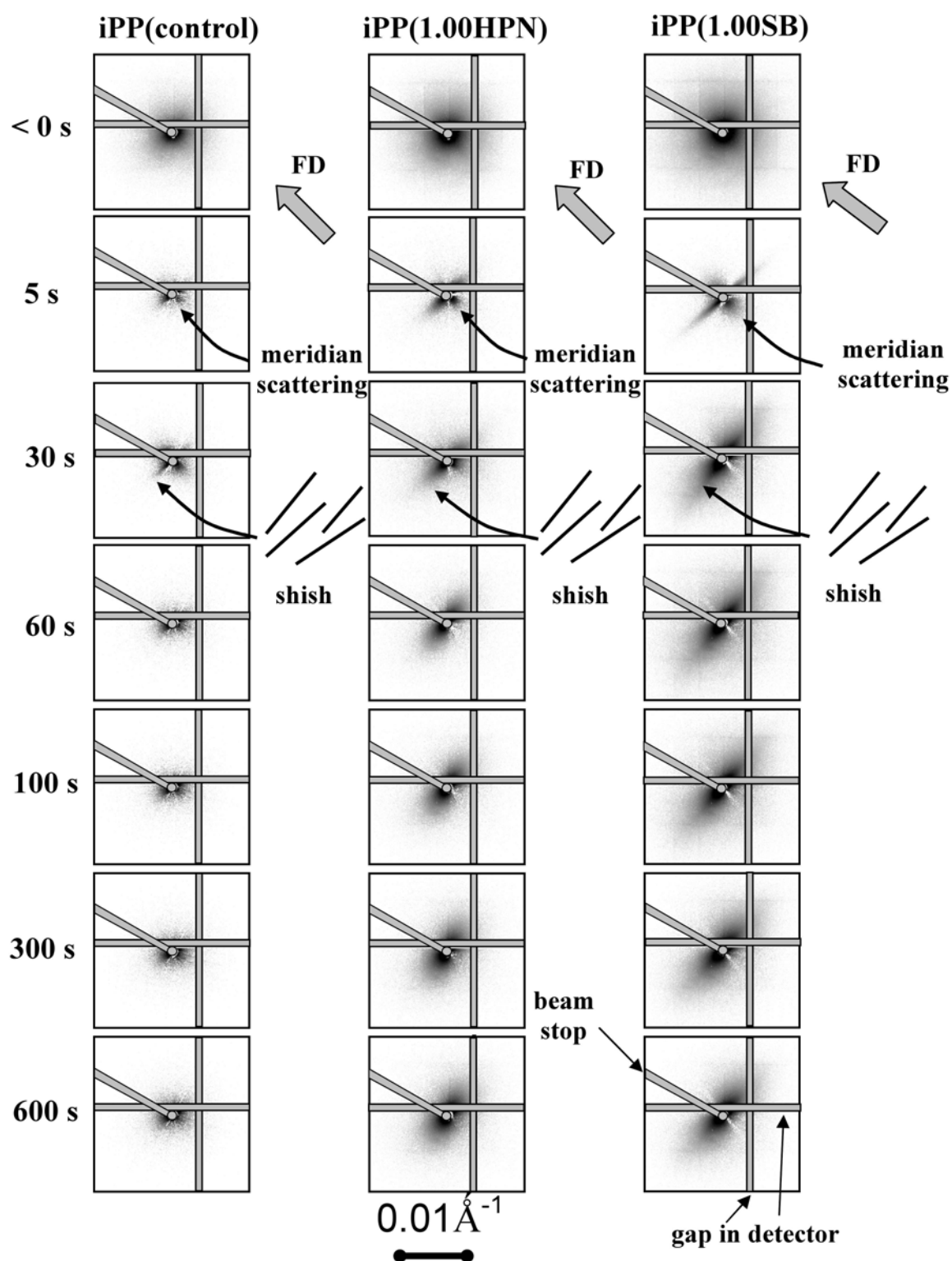


**Figure 8.2.** Selected SAXS patterns taken at various stages before, during and after continuous shear flow (shear time = 30 s, shear rate =  $80 \text{ s}^{-1}$ , shear temperature =  $181^\circ\text{C}$ ).

In addition to the equatorial scattering, a surprisingly sharp meridional streak was also observed in the SAXS patterns during shear flow. Furthermore, the meridional streak disappeared soon after the shear flow stopped. To further investigate this anomalous feature, the intensity profile around the azimuth was determined between scattering vectors  $0.003 \leq q \leq 0.01 \text{ \AA}^{-1}$ . Distinct equatorial and meridional peaks were clearly evident in all profiles during shear flow, **Figure 8.3a**. The relative amount of meridional scattering ( $[M]$ ) was estimated during shear flow using the following equation:

$$[M] = \frac{A_m}{A_m + A_e} \quad \text{Equation 8.1}$$

where  $A_m$  and  $A_e$  are the areas of the azimuthally integrated meridional and equatorial peaks. The results are plotted in **Figure 8.3b**. For all samples the amount of meridional scattering decreased steadily during shear flow and disappeared altogether soon after the flow stopped.

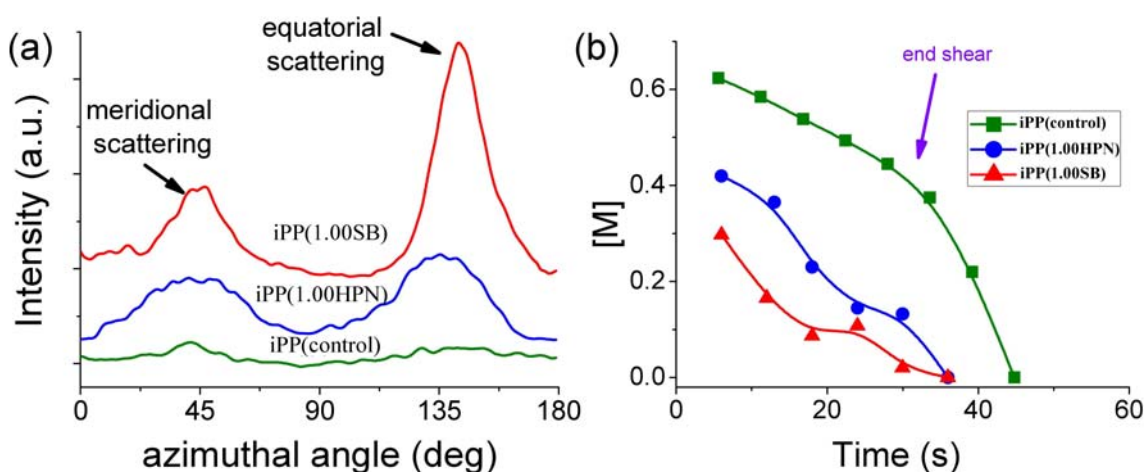


**Figure 8.3.** (a) Plot of background subtracted intensity versus azimuthal angle during the first 5 s of shear flow. (b) Relative proportion of meridional scattering ( $[M]$ ) during and immediately after shear flow (shear time = 30 s, shear rate =  $80 \text{ s}^{-1}$ , shear temperature =  $181 \text{ }^{\circ}\text{C}$ ).

To confirm the presence of the meridional reflection seen in **Figure 8.2**, additional SAXS experiments were performed using the same thermal-shear profile but using a different beam line and shear cell setup. The SAXS/WAXS(1) setup is described in **Chapter 3.6.3**. **Figure 8.4** shows the SAXS patterns immediately before, during and

after continuous shear flow of 30 s at a shear rate of  $80 \text{ s}^{-1}$  and at a shear temperature of  $181 \text{ }^{\circ}\text{C}$ . The same trend observed with the SAXS/WAXS(2) setup in **Figure 8.2** was also seen using the SAXS/WAXS(1) setup. During shear flow, sharp equatorial and meridional scattering streaks were observed which increased in intensity with increasing shear time. After the shear pulse ceased the meridional streak quickly disappeared and the equatorial streak decreased in intensity and spread around the azimuth. Minor differences were noted in the sharpness of the meridional streak between the two experimental setups. Compared to the SAXS/WAXS(2), the meridional reflections in the SAXS/WAXS(1) setup were somewhat sharper. This is not unexpected given the differences in the experimental setup.

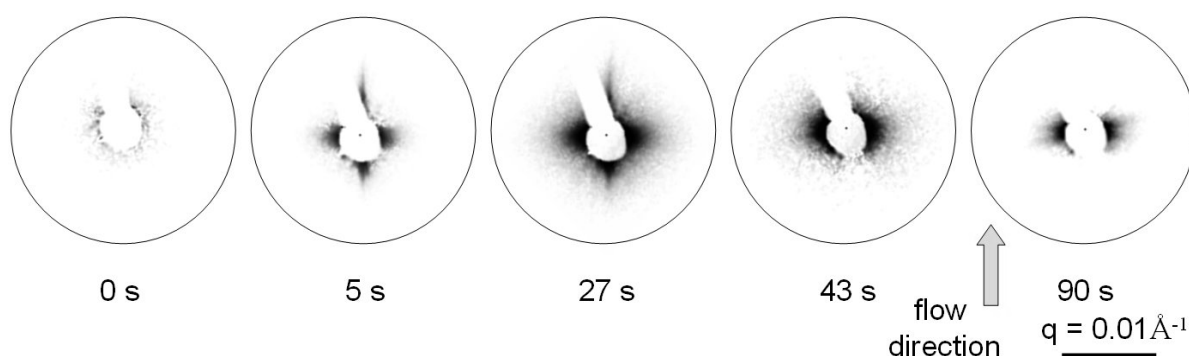


**Figure 8.4.** Selected SAXS patterns taken at various stages before, during and after continuous shear flow (shear time = 30 s, shear rate =  $80 \text{ s}^{-1}$ , shear temperature =  $181 \text{ }^{\circ}\text{C}$ ). SAXS/WAXS(1) setup described in **Chapter 3.6.3**.

The influence of continuous shear flow was further probed by varying the shear temperature between  $176 \text{ }^{\circ}\text{C}$  –  $201 \text{ }^{\circ}\text{C}$ , **Figure 8.5**. At a shear temperature of  $176 \text{ }^{\circ}\text{C}$ , the dominant scattering was a sharp equatorial streak, though a small broad increase in scattered intensity centred on the meridian was observed. As the shear temperature was increased, the intensity of the equatorial scattering streak decreased in intensity such that only a small broad streak was observed at  $191 \text{ }^{\circ}\text{C}$ . On the other hand, with increasing shear temperature the meridional streak became significantly more intense as well as sharper, such that at  $191 \text{ }^{\circ}\text{C}$  it was the dominant oriented scattering. During shear flow at  $201 \text{ }^{\circ}\text{C}$  no preferred orientation was detected in the SAXS region.

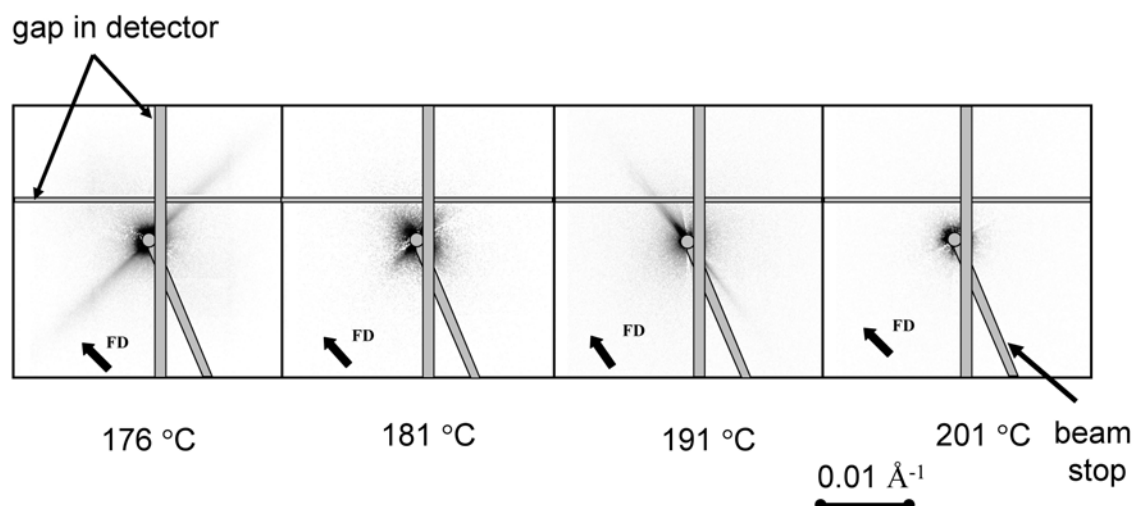


**Figure 8.5.** Influence of shear temperature on SAXS patterns taken during continuous shear flow (shear time = 30 s, shear rate = 80 s<sup>-1</sup>). SAXS/WAXS(2) setup described in **Chapter 3.6.3**.

The WAXS patterns of the undeformed melt showed an unoriented diffuse amorphous halo with peak intensity near  $q = 1 \text{ Å}^{-1}$ , further confirming that the melt was unoriented prior to shear flow. The application of shear flow did not induce any crystalline scattering during or for at least 600 s after the shear had stopped. This shows that the scattering observed in the SAXS images is due to non-crystalline entities. However, during shear flow some preferred orientation of the amorphous halo became evident with an increase in intensity occurring toward the equator at  $q \sim 1 \text{ Å}^{-1}$ , **Figure 8.6**. The interpretation of amorphous orientation from WAXS is uncertain in this case due to the complex combination of inter- and intra-chain interactions. Nevertheless, the observed increase in preferred orientation with the addition of both nucleants is consistent with the results presented in **Figure 8.2**.

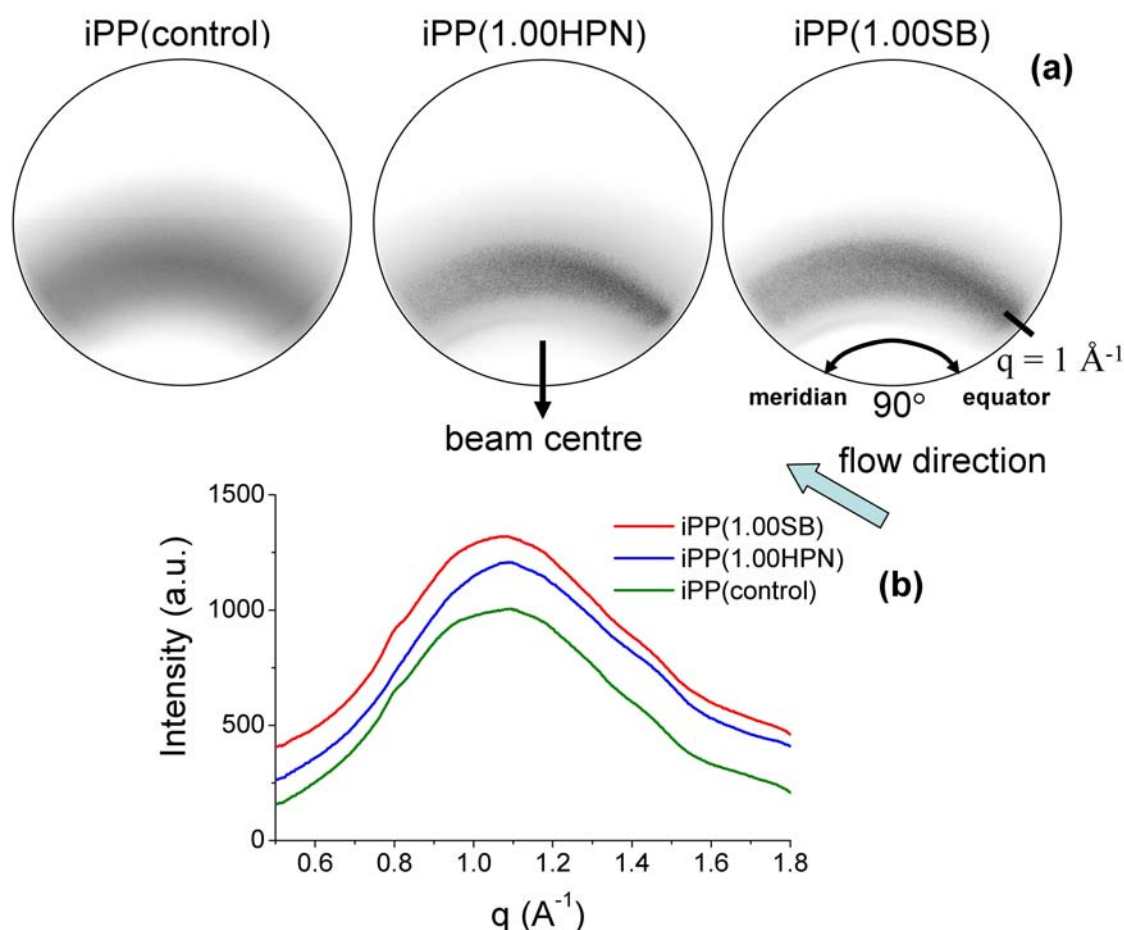


**Figure 8.6.** (a) Two-dimensional wide angle x-ray scattering patterns and (b) corresponding bragg plots for the last exposure prior to the end of continuous shear (shear time = 30 s, shear rate =  $80 \text{ s}^{-1}$ , shear temperature =  $181 \text{ }^{\circ}\text{C}$ ).

### 8.3.2 Quantitative investigation of shish during and after shear flow

SAXS arises from perturbations in the electron density within the material under investigation. In the present experiment there are two likely sources of electron density contrast. The first is the electron density contrast between the particles and the iPP matrix. The second is the electron density contrast between different localised structural elements present within the iPP matrix. In this section the equatorial scattering, which corresponds to shish, is quantitatively analysed using a number of theoretical approaches to determine the influence nucleants have on the shish structure.

Plots of the integrated SAXS intensity as a function of the scattering vector along a  $20^{\circ}$  arc centred on the equator before and during shear flow are shown in **Figure 8.7**. All

samples showed large regions at high  $q$ , where the scattered intensity obeyed a power law relation of the form:

$$I(q) \propto q^{-\alpha} \quad \text{Equation 8.2}$$

where  $\alpha$  is a positive constant. When  $q$  is large enough to satisfy the criteria  $\ell \cdot q \gg 1$  (where  $\ell$  characterises the length scale of the scatterer),  $\alpha$  can give information about the fractal dimension of the scatterers. For example,  $\alpha = 4$  indicates isotropic scatterers with smooth well defined surfaces,  $\alpha > 3$  would suggest the structure can be described as a 3D mass fractal analogous to a crunched up piece of paper,  $\alpha = 2$  would signify the scatterers were plate-like and  $\alpha = 1$  would point to rod-like scatterers being present [266]. Non-unity values of  $\alpha$  are often obtained and may be accounted for by differences in the fractal dimension, such as surface roughness, or the cumulative effect of the different scatterers present.

The scattering curves shown in **Figure 8.7a** were taken immediately before the application of shear and have had the background and empty cell data subtracted from them. Linear regression analysis was performed on the samples at large  $q$ -values ( $q \gg 0.01 \text{ \AA}^{-1}$ ) and the results are presented in **Table 8.1**. iPP(control) was found to have an exponent of  $\alpha = 2.7 \pm 1$ . The measured exponent is comparable to that recently measured for molten polyethylene terephthalate (PET) held at  $290 \text{ }^{\circ}\text{C}$  [267]. This exponent suggests that the structural elements were relatively isotropic. Increasing nucleant loading led to a reduction in the exponent with  $\alpha \approx 2$ . Given the relatively large size of both particles shown in **Figure 7.3**, the majority of scattering at these large  $q$ -values in the nucleated samples can also be considered to be due to the structural elements within the iPP matrix. Therefore one interpretation of the observed scattering is that the structural elements take on a plate-like structure in the presence of the nucleants. It is worthwhile to point out that the characteristic length scale probed here is  $63 - 8 \text{ nm}$ . In addition to the changes in the exponent, increasing the nucleant loading also increased the total scattered intensity, with the addition of HPN particles being significantly more effective than SB particles. This increase in scattered intensity suggests that the nucleant increased the volume fraction of the scatterers.



The scattering curves shown in **Figure 8.7b** were taken in the last few seconds of the 30 s shear pulse. During shear flow the scattered intensity of all samples increased. This shows that the shear flow increased the volume of scatterers. In order to get a clearer picture of the influence of shear flow on the scattering profile, the scattering data immediately prior to the imposition of shear, as well as the background and empty cell data, were subtracted. Compared to those determined under quiescent conditions, the scaling exponent was significantly reduced after shear flow, and in the nucleated materials it approached  $\alpha \approx 1$ . One interpretation of the reduction in the scaling parameter is that the additional scatterers formed by the shear flow tended to be rod-like. Furthermore, the addition of SB particles was more effective at increasing the scattered intensity during shear flow than the addition of HPN particles.

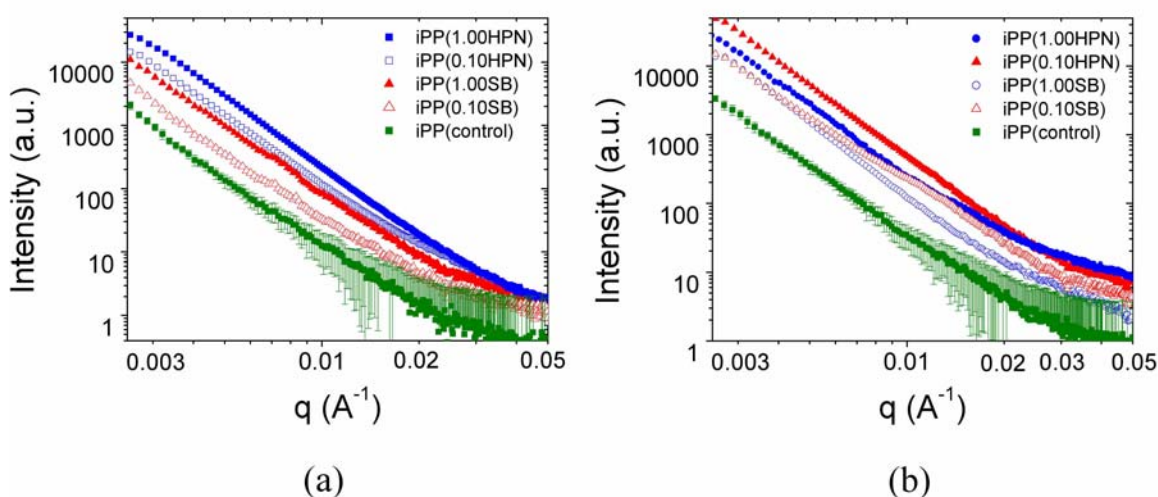


**Figure 8.7.** Intensity versus scattering vector ( $q$ ) of the polymer melt in a  $20^\circ$  arc along the equator for (a) the quiescent melt and (b) the sheared melt (shear time = 30 s, shear rate =  $80 \text{ s}^{-1}$ , shear temperature =  $181^\circ\text{C}$ ).

**Table 8.1.** Scattering exponent ( $\alpha$ ). \*sheared samples have had the isotropic melt prior to shear subtracted as background (shear time = 30 s, shear rate =  $80 \text{ s}^{-1}$ , shear temperature =  $181^\circ\text{C}$ ).

Material	Quiescent	Sheared*
iPP(control)	$-2.7 \pm 0.1$	$-2.0 \pm 0.1$
iPP(0.10HPN)	$-2.1 \pm 0.2$	$-1.7 \pm 0.2$
iPP(1.00HPN)	$-1.9 \pm 0.2$	$-1.2 \pm 0.2$
iPP(0.10SB)	$-2.3 \pm 0.2$	$-1.5 \pm 0.2$
iPP(1.00SB)	$-2.0 \pm 0.2$	$-1.0 \pm 0.2$

The behaviour of the shish during and after shear flow was probed by determining the integrated scattered intensity from the equatorial scattering streak in the SAXS images ( $I_0$ ) according to the following equation:

$$I_0 = \int_{0.003}^{0.3} \int_{0^\circ}^{20^\circ} I(q, \varphi) dq d\varphi \quad \text{Equation 3.23}$$

$I_0$  determined in this way is proportional to the total volume of shish ( $v_{\text{shish}}$ ) and the magnitude of their density contrast to the surrounding melt ( $\Delta\rho_{\text{shish-melt}}$ ). The results of this analysis are plotted in **Figure 8.8**. All samples showed the same general behaviour. During shear flow,  $I_0$  initially increased rapidly, reaching a peak value just prior to the shear pulse ending. This indicates that steady state conditions were only achieved towards the end of the shear profile. The magnitude of  $I_0$  was substantially larger in iPP(1.00HPN) and iPP(1.00SB) compared to iPP(control), raising the magnitude of  $I_0$  by a factor of 5 and 7 respectively. The higher value of  $I_0$  indicates that the addition of nucleants increased the volume fraction of shish or their density contrast. However, large changes in the density contrast of the shish is considered less likely when taken in conjunction with measurements of the shish dimensions which are discussed subsequently.

Immediately after the shear pulse stopped,  $I_0$  began to exponentially decay to an interim lower plateau level. This indicates that some shish are unstable and relax back into the melt, while other shish have some stability at the experimental temperature. The decay constant ( $\tau_1$ ) between peak  $I_0$  and the lower plateau was approximated by a simple exponential decay model:

$$h(t) = h_{eq} + \Delta h_1 e^{-\frac{t}{\tau_1}} \quad \text{Equation 8.3}$$

where  $h_{eq}$  and  $\Delta h_1$  are illustrated in **Figure 8.8**. Compared to iPP(control), the addition of both nucleants was found to decrease  $\tau_1$ .

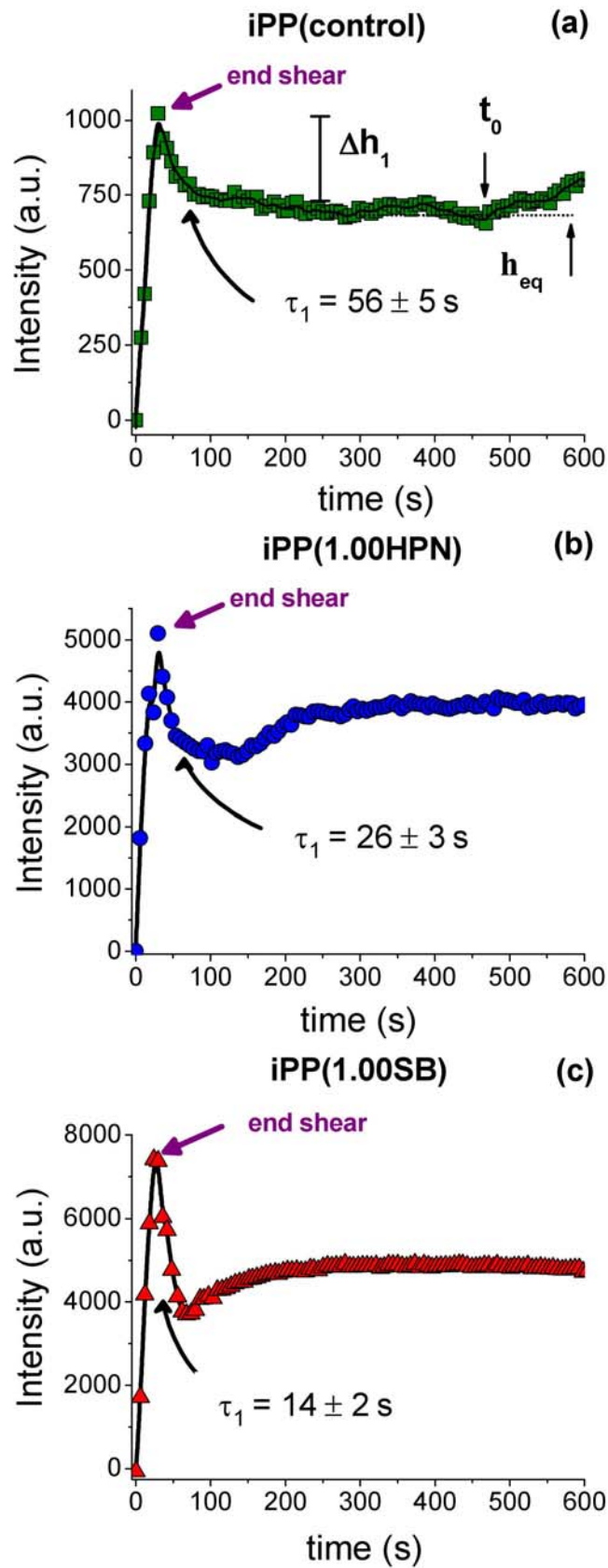


**Figure 8.8.** Scattered intensity from shish ( $I_0$ ) during and after shear for (a) iPP(control), (b) iPP(1.00HPN), and (c) iPP(1.00SB) (shear time = 30 s, shear rate =  $80 \text{ s}^{-1}$ , shear temperature =  $181 \text{ }^\circ\text{C}$ ).

After an induction time ( $t_0$ ) at the lower plateau level, the value of  $I_0$  began to increase again before reaching an upper plateau level. The value of  $I_0$  was then stable until the end of the isothermal hold. The addition of both nucleants decreased this induction time compared to iPP(control) ( $t_0 = 476 \pm 3$  s), with iPP(1.00SB) ( $t_0 = 68 \pm 3$  s) having a shorter  $t_0$  than iPP(1.00HPN) ( $t_0 = 138 \pm 3$  s). This increase in  $I_0$  could be due to an increase in the volume fraction of shish or changes in their density contrast. To further understand this interesting phenomenon, the dimensions of the shish during and after shear flow are determined next.

The diameter of the shish was estimated by applying the Guinier approximation [256] to a  $20^\circ$  arc in the azimuthal direction and centred on the maximum intensity of the equatorial scattering streak. The radius of gyration ( $R_g$ ) of rod-like scatterers can be approximated from the gradient of the linear region at low  $q$  of a plot of  $\ln(I(q)q)$  versus  $q^2$  according to the equation:

$$I \propto \frac{1}{q} e^{\frac{-R_g^2 q^2}{2}} \quad \text{Equation 8.4}$$

Assuming the shish show cylindrical symmetry, the diameter of the shish is:

$$D_{shish} = 8^{1/2} R_g \quad \text{Equation 8.5}$$

Strictly speaking, the Guinier approximation used in this way is only true for the central part of the scattering from a dilute (and therefore uncorrelated) solution of rods. However, it has been applied successfully to estimate the diameter of shish in previous studies [49, 257]. Selected Guinier plots for iPP(control) during shear flow are shown in **Figure 8.9**. For all scattering patterns the plot consisted of two linear regions with the transition occurring at  $q = 0.094 \text{ \AA}^{-1}$ . The first region (i.e.  $q < 0.094 \text{ \AA}^{-1}$ ) was used to determine  $D_{shish}$  since the second region should be discarded as the Guinier approximation is only valid in the small angle limit where the criteria  $R_g q < 1$  is maintained.

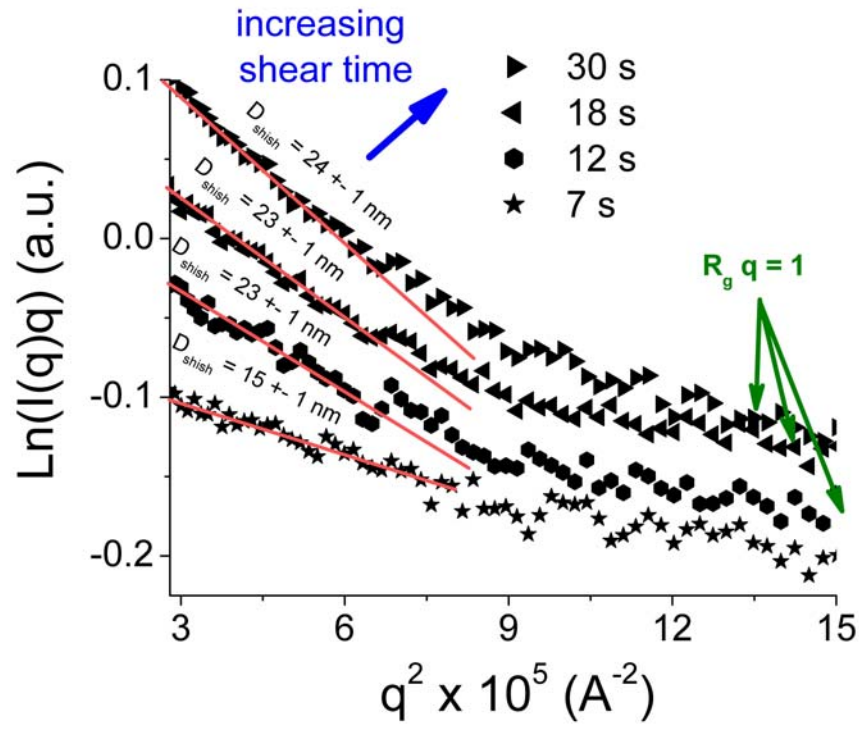


**Figure 8.9.** Guinier plot of  $\ln(I(q)q)$  versus  $q^2$  showing selected lines during shear flow for iPP(control) (shear rate =  $80 \text{ s}^{-1}$ , shear temperature =  $181 \text{ }^\circ\text{C}$ ).

The average length of the shish ( $L_{\text{shish}}$ ) and their alignment along the flow direction ( $b_\phi$ ) can be determined using the method proposed by Perret & Ruland [268]. The underlying basis for the method is that at low  $q$ , the contribution from the misorientation of the scatterers should be constant, while the contribution from the length of the scatterers should depend on  $q$ . The proposed method consists of determining the integral breadth of a series of azimuthal profiles taken at different values of  $q$  along the equator. The integral breadth ( $b_{\text{obs}}$ ) is defined according to the equation:

$$b_{\text{obs}}(q) = \frac{1}{I(q, \pi/2)} \int_{-\pi/2}^{\pi/2} I(q, \phi) d\phi \quad \text{Equation 8.6}$$

where  $\phi$  is the azimuthal angle and  $I(q, \phi)$  is the background corrected intensity. For a Cauchy-like (Lorentz) orientation distribution of scatterers,  $b_{\text{obs}}$  is then related to  $b_\phi$  and  $L_{\text{shish}}$  by:

$$b_{\text{obs}} = b_\phi + \frac{2\pi}{L_{\text{shish}} q} \quad (\text{Lorentz}) \quad \text{Equation 8.7}$$

For a Gaussian orientation distribution of scatterers the equation becomes:

$$b_{obs}^2 = b_{\phi}^2 + \frac{4\pi^2}{L_{shish}^2 q^2} \quad (\text{Gaussian}) \quad \text{Equation 8.8}$$

In the present work it was found that the Lorentz function best fit the observed azimuthal intensity profile and  $b_{\phi}$  and  $L_{shish}$  was determined from a plot of  $b_{obs}$  versus  $1/q$ , **Figure 8.10**. The magnitude of  $L_{shish}$  for all samples was below 2000 nm, which is smaller than the typical shish length observed using microscopy methods. However, it should be noted that the quantity  $L_{shish}$  represents the average coherence length of the structural units along the long axis of the shish, which will be different from that measured by microscopic methods.

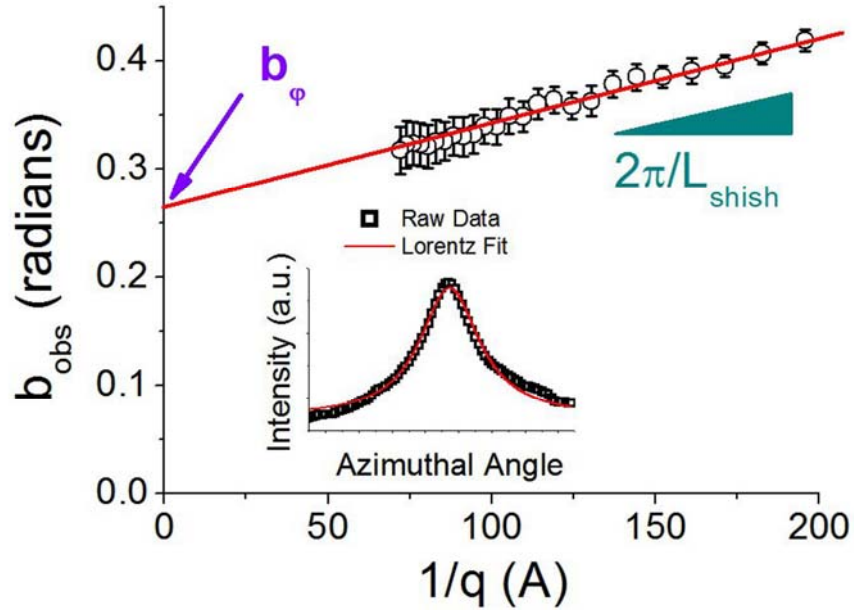


**Figure 8.10.** Plot of azimuthal integral breadth ( $b_{obs}$ ) as a function of  $1/q$  showing the method used to separate out the contributions of the misorientation of shish ( $b_{\phi}$ ) and the shish length  $L_{shish}$  at low scattering vectors ( $q$ ). Insert shows a typical background corrected azimuthal intensity profile fitted with a Lorentz function.

The time evolution of the shish dimensions,  $D_{shish}$  and  $L_{shish}$  is presented in **Figures 8.11** and **Figure 8.12**, respectively. In all three samples both  $D_{shish}$  and  $L_{shish}$  were found to increase rapidly with increasing shear time. After the shear flow stopped,  $L_{shish}$  decreased quickly to an interim value and then decreased more slowly until the end of

the isothermal hold.  $D_{\text{shish}}$  on the other hand, initially kept increasing after the shear flow had stopped, reaching an upper plateau level.  $D_{\text{shish}}$  then began to decline from the upper plateau with increasing time until the end of the isothermal hold. The addition of both nucleants led to a large increase in the value of  $L_{\text{shish}}$  and a small increase in the value of  $D_{\text{shish}}$ . The magnitude of  $D_{\text{shish}}$  and  $L_{\text{shish}}$  were larger in iPP(1.00SB) compared to iPP(1.00HPN).

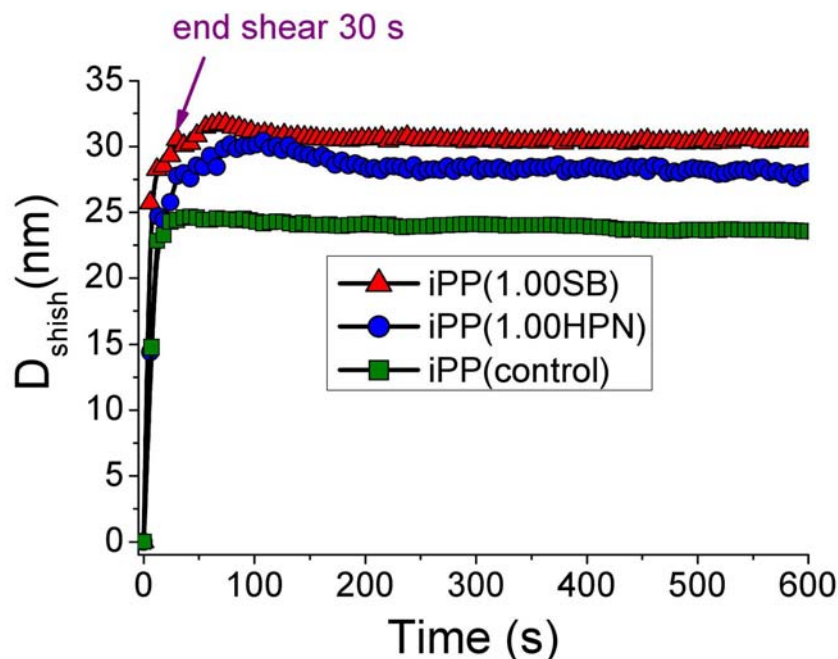


**Figure 8.11.** Calculated diameter of shish ( $D_{\text{shish}}$ ) during and after shear flow (shear time = 30 s, shear rate =  $80 \text{ s}^{-1}$ , shear temperature =  $181 \text{ }^{\circ}\text{C}$ ).

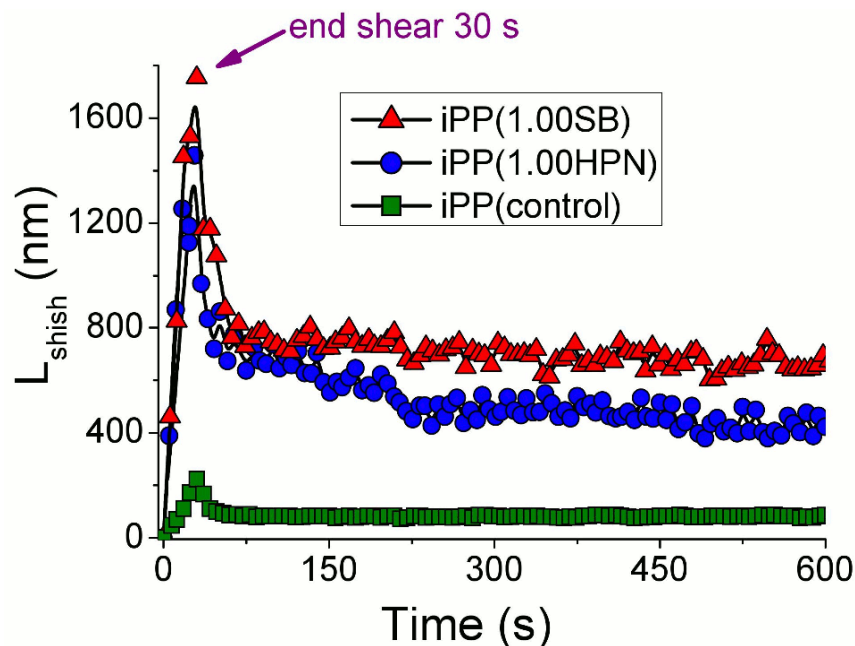


**Figure 8.12.** Calculated length of shish ( $L_{\text{shish}}$ ) during and after (shear time = 30 s, shear rate =  $80 \text{ s}^{-1}$ , shear temperature =  $181 \text{ }^{\circ}\text{C}$ ).



The alignment of shish during and after shear flow is shown in **Figure 8.13**. A line through the middle of the data is included to aid interpretation. A lower value of  $b_\phi$  indicates a higher shish alignment along the flow direction. During shear flow, iPP(control) started with high alignment along the flow direction which then increased slightly until the shear flow stopped. At the beginning of shear flow, the shish in iPP(1.00HPN) had low alignment along the flow direction. However, during shear flow their alignment increased substantially. At the beginning of shear flow, the shish in iPP(1.00SB) were highly aligned along the flow direction. Further shear flow continued to increase their alignment. After shear flow stopped, the shish alignment in iPP(control) immediately decreased. Conversely, the alignment of shish in the iPP containing both nucleants increased after shear flow stopped, reaching a lower plateau before rising again with increasing time. In general, the relative alignment of shish for the three samples was iPP(1.00SB) > iPP(control) > iPP(1.00HPN).

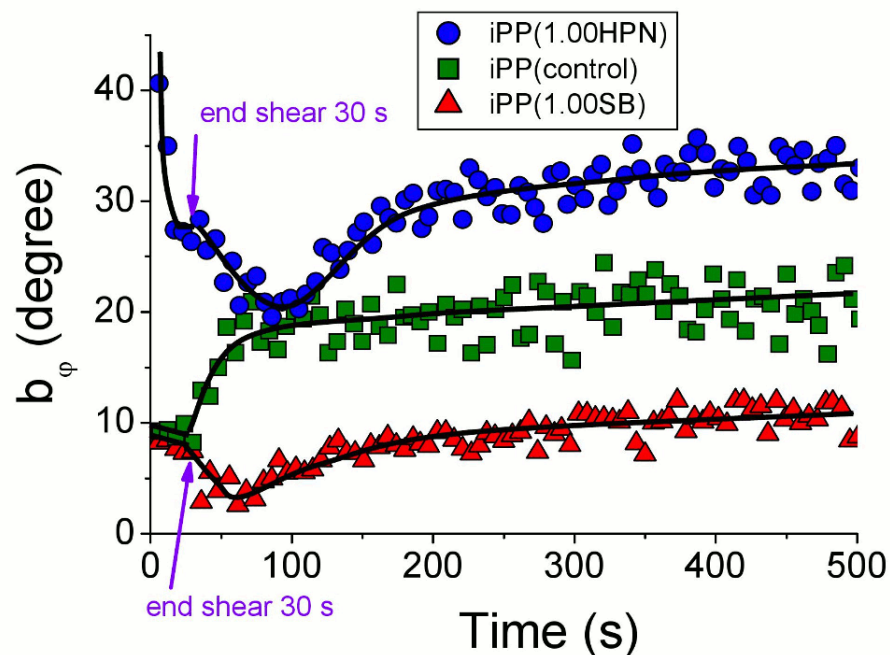


**Figure 8.13.** Calculated shish misorientation ( $b_\phi$ ) during and after shear flow (shear time = 30 s, shear rate =  $80 \text{ s}^{-1}$ , shear temperature =  $181 \text{ }^\circ\text{C}$ ).



### 8.3.3 Particle-induced and flow-induced conformational ordering

FTIR is sensitive to the conformation and local environment of the iPP molecules. In particular, information can be drawn about the length of the iPP helix with the bands at  $1100\text{ cm}^{-1}$ ,  $998\text{ cm}^{-1}$ ,  $841\text{ cm}^{-1}$  and  $1220\text{ cm}^{-1}$  having been shown to correspond to helical lengths of 6, 10, 12 and 14 monomers, respectively [269-270]. The addition of the nucleants may interfere with any conformational analysis if they show strong absorption bands which overlap with the conformational bands of iPP. The FTIR absorption spectra of crystalline iPP(control) along with ex-situ powder samples of SB and HPN particles are provided in **Figure 8.14**. The only major overlap with a conformational band was the moderate  $1220\text{ cm}^{-1}$  band of HPN. The rest of the conformational bands did not overlap with the spectra from the SB and HPN particles.

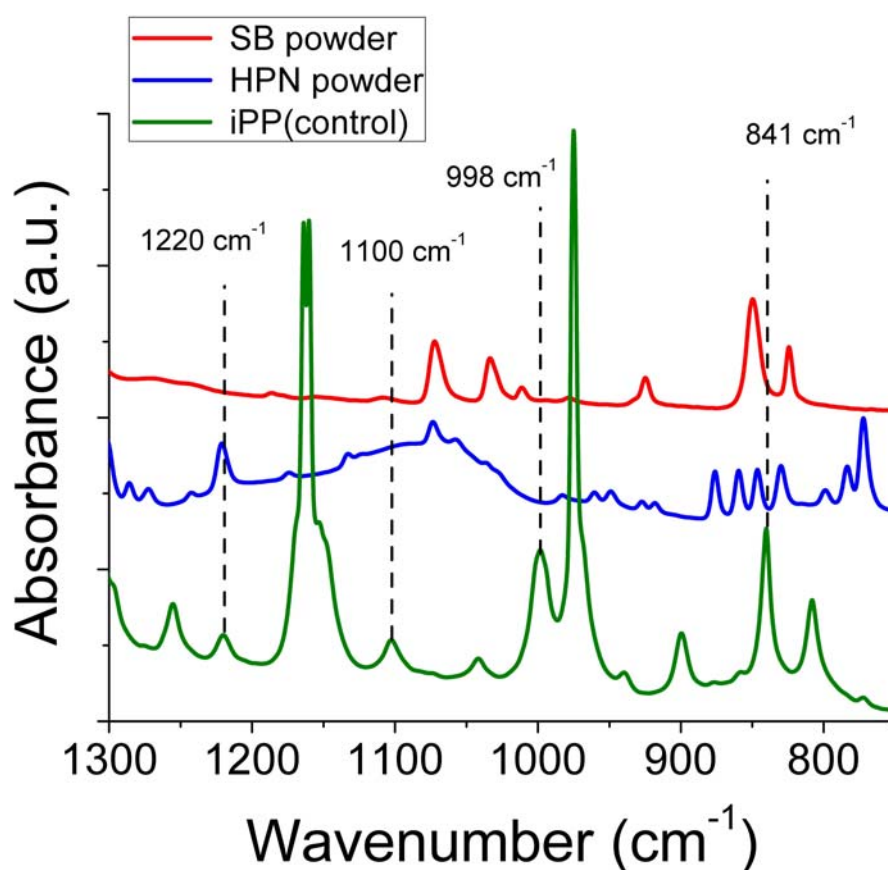


**Figure 8.14.** Comparison of the main infrared absorbance peaks between  $1300\text{-}750\text{ cm}^{-1}$  for crystalline iPP(control), SB and HPN powders.

The SAXS result presented in **Figure 8.7** revealed that the addition of both nucleants increased the scattered intensity of the quiescent melt before shear flow. To further investigate this, in-situ rheo-FTIR spectra of the quiescent melt were obtained

immediately prior to shear, **Figure 8.15a**. In iPP(control) no absorbance peak could be found at  $1220\text{ cm}^{-1}$  and  $841\text{ cm}^{-1}$ . This indicates that no long helices were present. The addition of both nucleants led to the occurrence of the  $841\text{ cm}^{-1}$  peak, with the integrated intensity being somewhat higher with the addition of HPN particles compared to SB particles. The addition of SB particles led to a very small peak at  $1220\text{ cm}^{-1}$ , while the addition of HPN particles led to a large  $1220\text{ cm}^{-1}$  peak. HPN also absorbs at  $1220\text{ cm}^{-1}$  making it difficult to properly analyse its influence on this conformational band. Nevertheless, the occurrence of the  $841\text{ cm}^{-1}$  peak shows both nucleants promoted the formation of longer helices.

The influence of shear flow on the absorbance spectra are shown in **Figure 8.15b**. Compared to iPP(control) under quiescent conditions, the application of shear increased the intensity of the  $998\text{ cm}^{-1}$  band. In addition, weak conformational bands at  $1220\text{ cm}^{-1}$  and  $841\text{ cm}^{-1}$  were also formed. This shows that shear flow can induce a coil-to-helix transition of the iPP melt. The combined influence of the particulate nucleants and shear flow increased the intensity of all conformational bands compared to the quiescent condition. Interestingly, the  $841\text{ cm}^{-1}$  band for iPP(1.00SB) was now significantly higher compared to iPP(1.00HPN). This indicates that SB particles may be more effective at inducing long helices than HPN particles during shear flow.

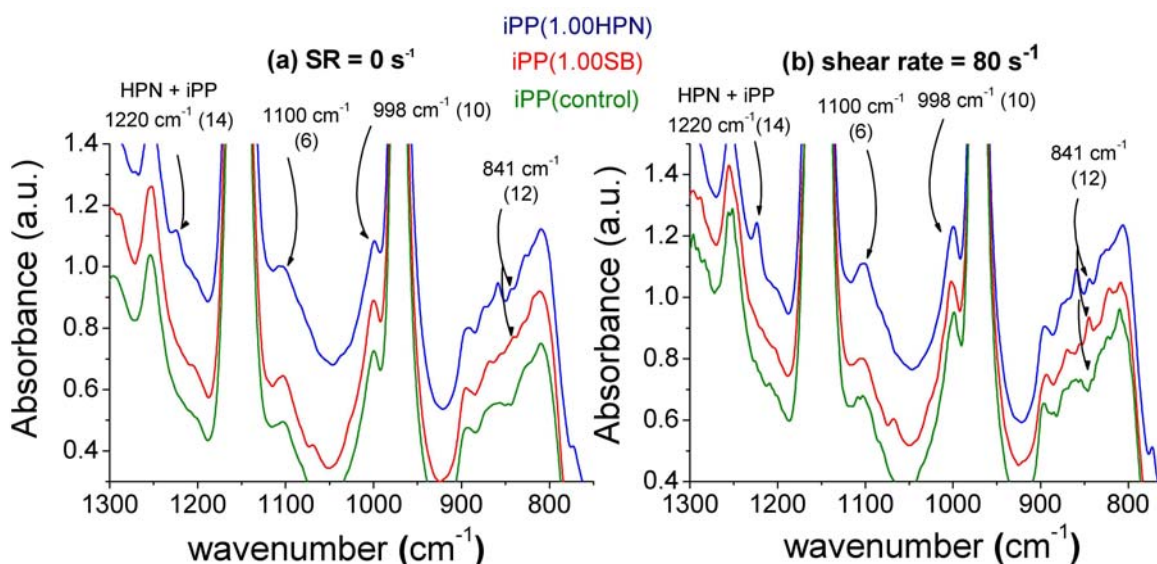


**Figure 8.15.** Influence of nucleant on the infrared absorbance spectra of (a) the quiescent melt and (b) the continuously sheared melt (shear time = 30 s, shear rate =  $80\text{ s}^{-1}$ , shear temperature =  $181\text{ }^{\circ}\text{C}$ ). The number in the brackets is the number of monomers in the iPP helix.

To further investigate the flow-induced conformational order of iPP, the integrated intensity of the  $998\text{ cm}^{-1}$  band was investigated during and after the shear profile. To allow reproducible determination of the integrated intensity, the melt immediately prior to the start of shear flow was used as a background. In addition, a baseline was constructed between the minima at  $1050\text{ cm}^{-1}$  and  $925\text{ cm}^{-1}$ , **Figure 8.16**. The results of this analysis are plotted in **Figure 8.17**. All samples showed the same trend. During shear flow the integrated intensity initially increased rapidly. The integrated intensity then level out towards the end of the flow profile. This shows that shear flow formed additional helices in the melt. Immediately after the shear pulse stopped, the integrated intensity initially decayed rapidly. The decay in intensity suggests that some helices relax. After the initial rapid decay the integrated intensity reduced much more slowly until the end of the isothermal hold. This shows that some portion of the helices were relatively stable at the experimental temperature. Reasonably good fits were obtained when the data was fitted to **Equation 8.3**. The addition of the nucleants influenced the curves in a number of ways. Their presence increased the intensity during shear, increased the initial relaxation rate, as well as increased the lower plateau level.

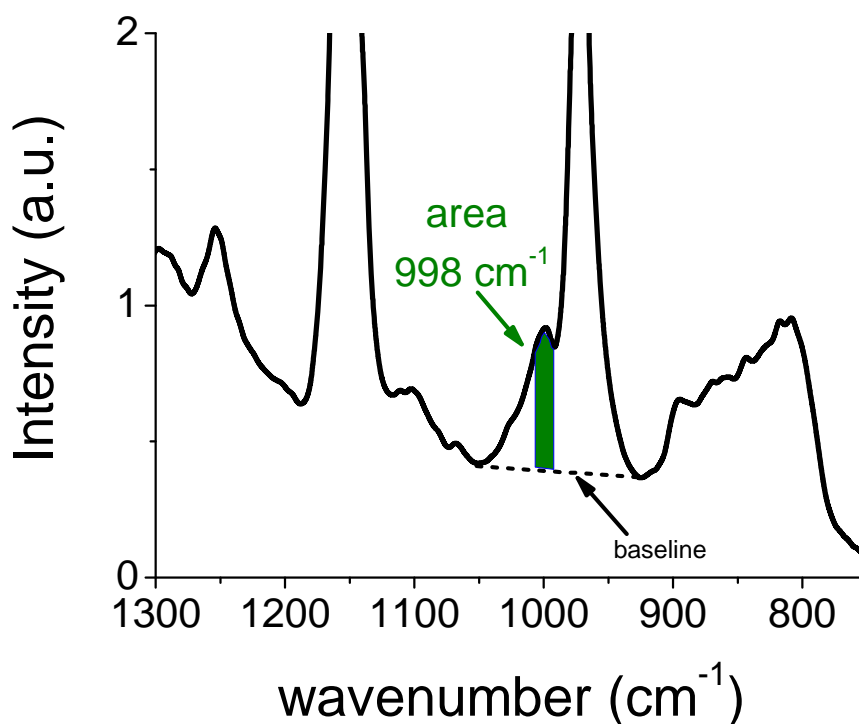


**Figure 8.16.** Example of the procedure used to determine the area of the  $998\text{ cm}^{-1}$  peak.

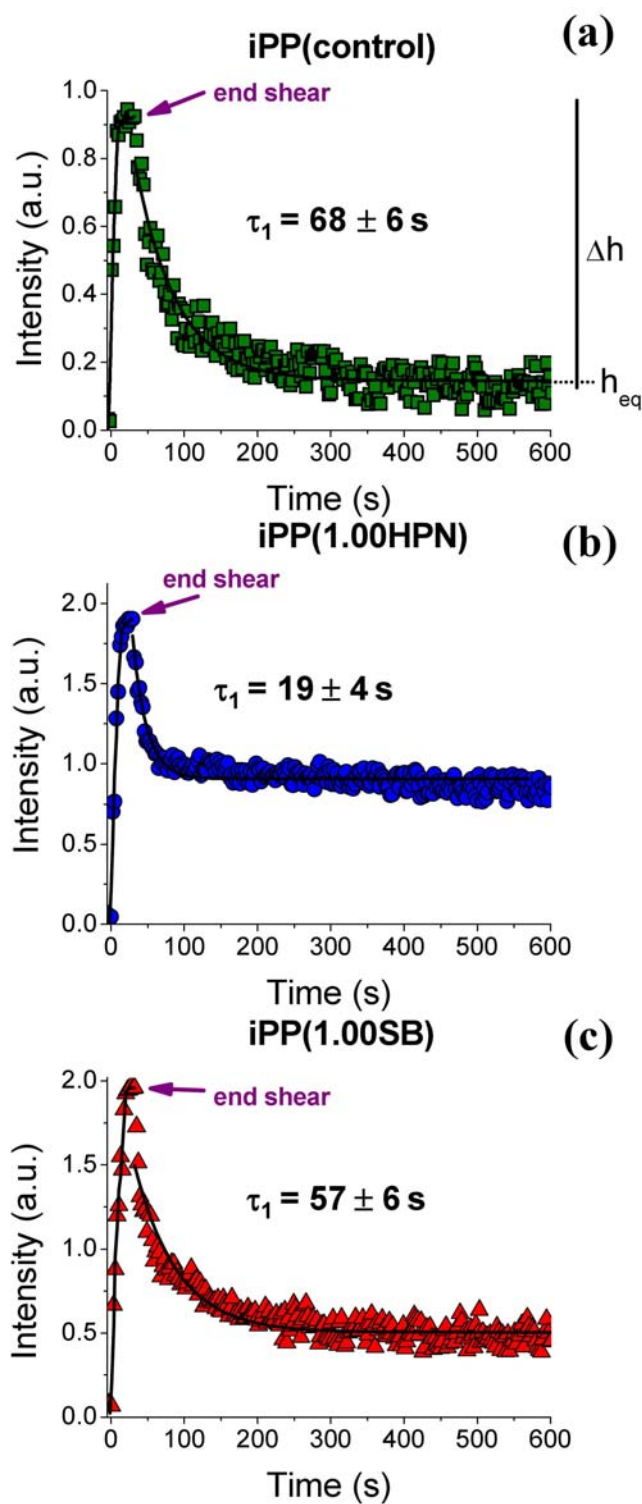


**Figure 8.17.** Intensity of the 998 cm<sup>-1</sup> band during and after shear for (a) iPP(control), (b) iPP(1.00HPN), and (c) iPP(1.00SB) (shear time = 30 s, shear rate = 80 s<sup>-1</sup>, shear temperature = 181 °C).

The influence of shear rate on the conformational ordering of the 998 cm<sup>-1</sup> band was determined by calculating the average intensity ( $\bar{I}$ ) during shear flow according to the following equation.

$$\bar{I} = \frac{1}{t_f - t_s} \int_{t_s}^{t_f} I dt$$

**Equation 8.9**

where  $t_s$  and  $t_f$  are the time at the start and end of shear flow. The results are plotted in **Figure 8.18**. For all samples, and over the range of shear rate examined, increasing the shear rate led to a general increase in the intensity of the  $998\text{ cm}^{-1}$  band. This shows that even low intensity shear flow can promote the formation of helical conformations in the iPP melt. For a given shear rate, the addition of both HPN and SB particles resulted in an increase in intensity compared to iPP(control). This shows that both varieties of particle can assist in promoting helical conformation under flow conditions.

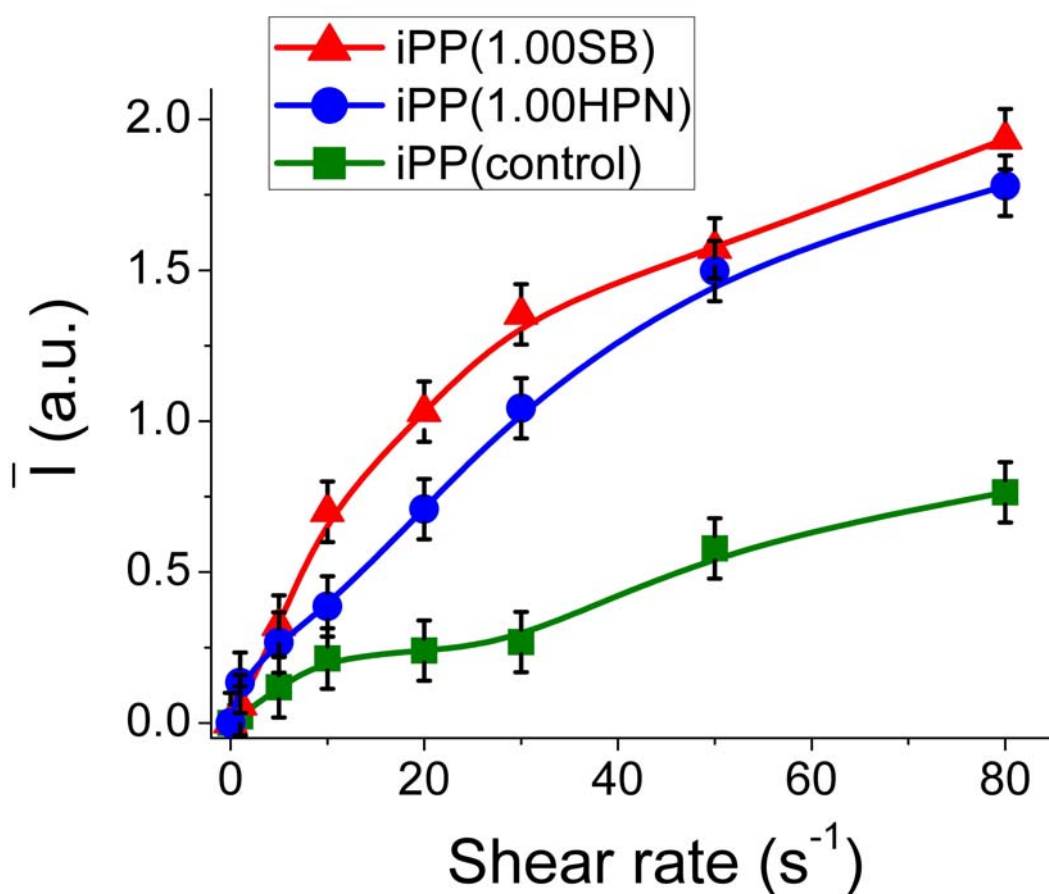


**Figure 8.18.** Influence of shear rate on the mean change in the intensity of the  $998\text{ cm}^{-1}$  band ( $\bar{I}$ ) during shear flow (shear time = 30 s, shear temperature =  $181\text{ }^{\circ}\text{C}$ ).

#### 8.3.4 Crystallisation of sheared and relaxed iPP containing nucleating particles

At the end of the 600 s hold, the samples were cooled to room temperature at  $0.5\text{ }^{\circ}\text{C/s}$ . The volume crystallinity index ( $\chi_v$ ) was measured from the circular integration of

WAXS patterns during cooling according to the method described in **Chapter 3.3.1.5**. The relative crystallinity ( $\chi_{\text{rel}}$ ), defined as the instantaneous crystallinity divided by the room temperature crystallinity, was then plotted as a function of temperature, **Figure 8.19**. The results were compared to samples which had undergone the same thermal profile but were not sheared. Without flow, the crystallisation progressed according to the relative nucleation efficiencies of the added particles. With flow, all samples showed an increased crystallisation temperature compared to the samples which had not been sheared. This is consistent with the formation of flow-induced nuclei which provide extra nucleation sites for crystal nucleation. iPP(1.00SB) showed the largest change in the crystallisation kinetics after shear flow, consistent with the higher numbers of shish observed before the onset of crystallisation. iPP(1.00HPN) exhibited the smallest change in crystallisation kinetics, which is presumably due to the high nucleation efficiency of the HPN particles swamping crystallisation under quiescent conditions.

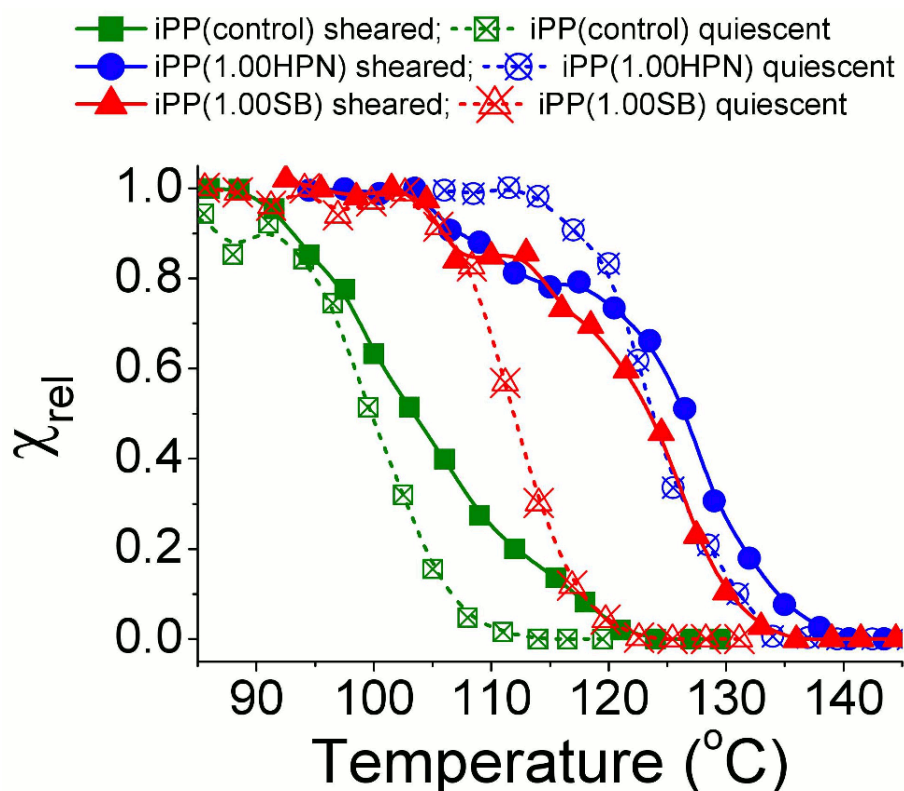


**Figure 8.19.** Influence of nucleant and shear condition on the relative crystallinity ( $\chi_{\text{rel}}$ ) during continuous cooling (shear time = 30 s, shear rate =  $80 \text{ s}^{-1}$ , shear temperature =  $181^\circ\text{C}$ , hold time = 600 s, cooling rate =  $0.5^\circ\text{C/s}$ ).

Simultaneous SAXS/WAXS patterns of the sheared samples obtained in the fully crystallised state are shown in **Figure 8.20**. The WAXS patterns of all samples showed

crystalline reflections consistent with the formation of  $\alpha$ -iPP crystals. The WAXS patterns of all samples showed crystalline reflections consistent with the formation of only  $\alpha$ -iPP and  $\gamma$ -iPP crystals. In pure iPP it is known that shear flow can induce  $\beta$ -iPP, as long as the kinetic requirement for a higher  $\beta$ -iPP growth rate than  $\alpha$ -iPP is achieved (i.e. between 105 °C – 141 °C [9]). Therefore, the absence of  $\beta$ -iPP reflections for iPP(control) in this experiment was surprising, given that crystal nucleation occurred within this temperature range. The absence of  $\beta$ -iPP is even more intriguing, given that in **Chapter 6.3.2** the flow-induced formation of  $\beta$ -iPP was observed in the same polymer. In that study, isothermal crystallisation (crystallisation temperature = 135 °C) was carried out after a moderate step shear (shear rate = 80 s<sup>-1</sup>, shear time = 1 s). These conditions are substantially different from those used in this study. Indeed it is worthwhile to note that in many of the studies presented in the literature, flow-induced formation of  $\beta$ -iPP has been investigated after the application of a brief shear pulse and where crystallisation occurred under isothermal conditions. Although not in the scope of the present study, further work is planned to clarify the reason for the absence of  $\beta$ -iPP in iPP(control).

The  $\gamma$ -iPP crystallinity ( $\chi_\gamma$ ) of the fully crystallised material was determined using the Turner-Jones method [204] according to the procedure specified in **Chapter 3.3.1.5**. The addition of both nucleants significantly increased the  $\gamma$ -iPP content from  $\chi_\gamma = 0.02$  in iPP(control) to  $\chi_\gamma = 0.11$  in iPP(1.00SB) and  $\chi_\gamma = 0.17$  in iPP(1.00HPN). The promotion of  $\gamma$ -iPP in the samples containing the nucleants is thought to be related to the substantially higher density of nuclei in these samples (both flow-induced and heterogeneous sites on the surface of the particles), combined with the relatively fast cooling rate which would further increase the number of active nuclei. The high density of nuclei would lead to multiple nucleation events occurring simultaneously along a chain, thereby reducing the time available for the chain to properly organise during the initial crystallisation. Combined with the stereo- and regio-defects already present along the polymer backbone, this would promote shorter isotactic sequences during crystallisation. It has been reported that  $\gamma$ -iPP is favoured when the isotactic sequence length is interrupted [157].



The SAXS/WAXS patterns of the samples showed preferred orientation consistent with the shish inducing the formation of shish-kebab structures. In the SAXS region broad lobes were observed along the meridian (kebabs) while equatorial scattering was observed at low  $q$  (shish). Increases in scattered intensity along the equator for the  $\alpha(110)$ ,  $\alpha(040)$  and  $\alpha(130)$  reflections in the WAXS region indicated significant crystalline c-axis orientation along the flow direction. The oriented fraction of lamellae ( $\Phi_L$ ) was determined from the SAXS pattern according to the method presented in **Chapter 5.3.2** using **Equation 5.1**. The addition of both nucleants increased  $\Phi_L$ , with SB having almost twice the number of oriented lamellae compared to HPN. The samples were reheated to 220 °C and held there for a further 300 s. Upon cooling, no preferred orientation was observed in any sample. This shows that the particles themselves did not template oriented crystal growth.

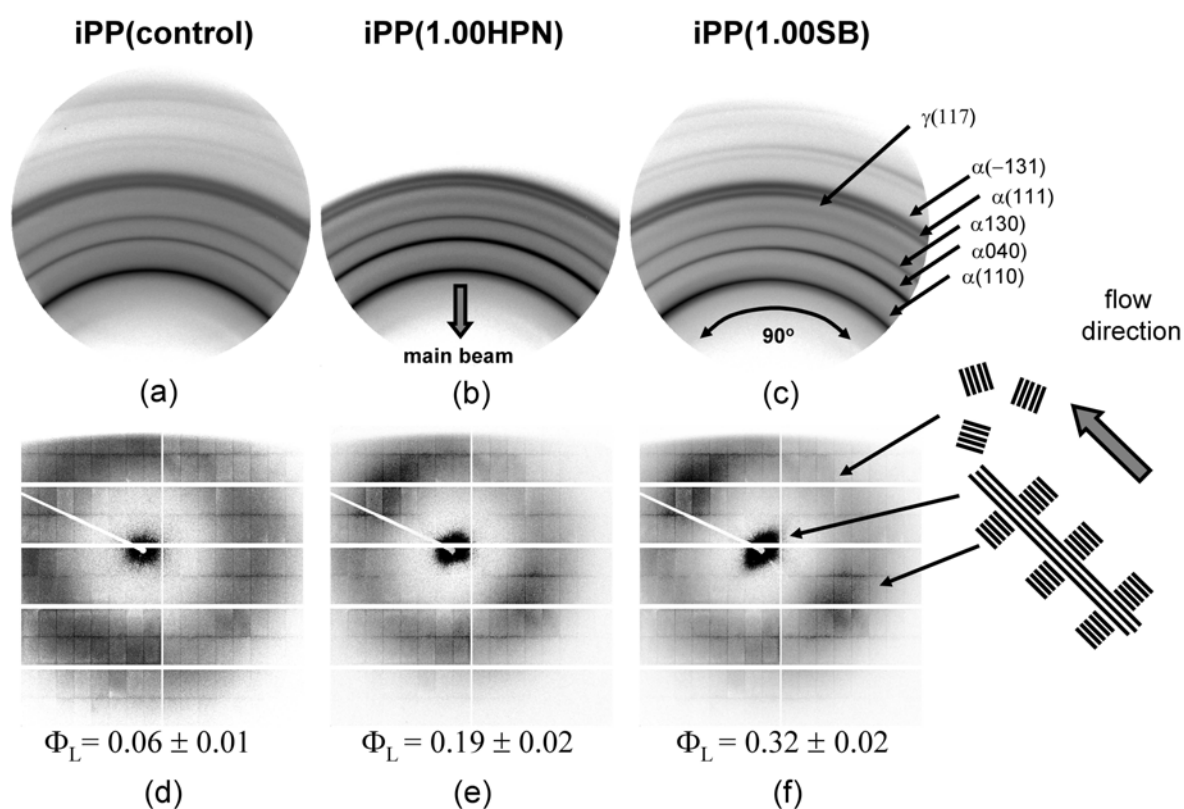


**Figure 8.20.** Small and wide angle x-ray scattering patterns in the fully crystallised condition taken at room temperature. (a) & (d) iPP(control), (b) and (e) iPP(1.00HPN), (c) and (f) iPP(1.00SB). Oriented fraction of lamellae ( $\Phi_L$ ) (shear time = 30 s, shear rate = 80 s<sup>-1</sup>, shear temperature = 181°C, hold time = 600 s, cooling rate = 0.5 °C/s).

The crystalline morphology of the samples was further investigated by viewing the entire sheared disks in the fully crystallised conditions using the homemade polariscope,



**Figure 8.21.** In the shear cell the flow direction is perpendicular to the radius of the disk and the shear rate increases linearly with increasing radius. Accordingly, this setup allows a large range of shear rates to be investigated in the one sample. At low shear rates (i.e. toward the centre of the disks) the contrast was even. The even contrast is consistent with a random orientation of lamellae and crystalline c-axis. At higher shear rates (i.e. toward the outside of the disk) the even contrast abruptly transitioned forming a characteristic Maltese cross pattern. The formation of a Maltese cross is consistent with the presence of oriented lamellae in which the c-axis (chain axis) is oriented along the flow direction. The Maltese effect is analogous, albeit on a much large scale, to that formed in iPP spherulites, such as those presented in **Figure 5.5**. The Maltese cross pattern extended almost to the edge of the disk. This result showed that stable laminar flow conditions were maintained during the applied shear flow. Compared to direct quenching after shear, holding the samples for 600 s at the shear temperature resulted in a broader and more diffuse Maltese cross pattern. This indicates the annealing treatment resulted in a broader distribution of c-axis alignment. This effect was most pronounced in the iPP(1.00HPN) sample.

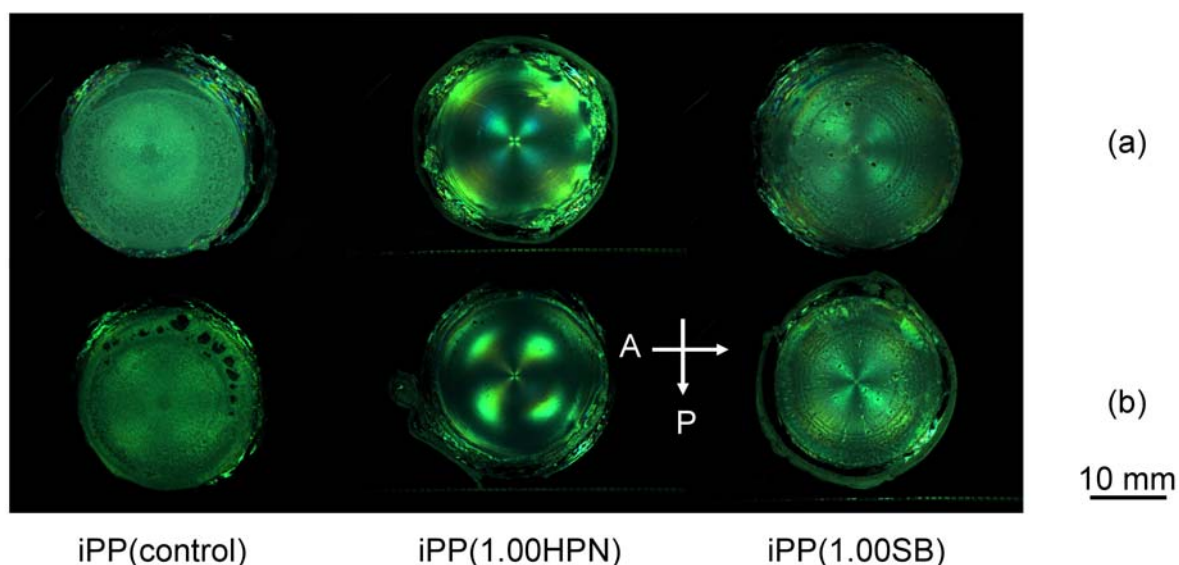


**Figure 8.21.** Polarised optical image of the sheared samples. (a) direct quench after shear. (b) Annealed at shear temperature for 600 s before quench to room temperature (shear time = 30 s, angular velocity = 2.67 rad/s, shear temperature = 181 °C, cooling rate = 0.5 °C/s). Polariser (P), Analyser (A).

The abrupt nature of the transition to the Maltese cross morphology indicates the existence of a critical shear rate to induce oriented structures [12-13]. **Figure 8.22** shows samples where the angular velocity ( $\omega$ ) during shear flow has been selected such

that the transition point can be more accurately measured. In iPP(control) this critical shear rate ( $\dot{\gamma}_{crit}$ ) was  $33 \pm 2 \text{ s}^{-1}$ . Interestingly, the critical shear rate was significantly decreased in the samples containing both nucleants with the critical shear rate in iPP(1.00HPN) and iPP(1.00SB) being,  $1.7 \pm 0.2 \text{ s}^{-1}$  and  $0.7 \pm 0.1 \text{ s}^{-1}$  respectively. This is consistent with the results presented in **Chapter 7** which showed the addition of HPN and SB particles reduced the critical shear rate required to induce oriented structures.

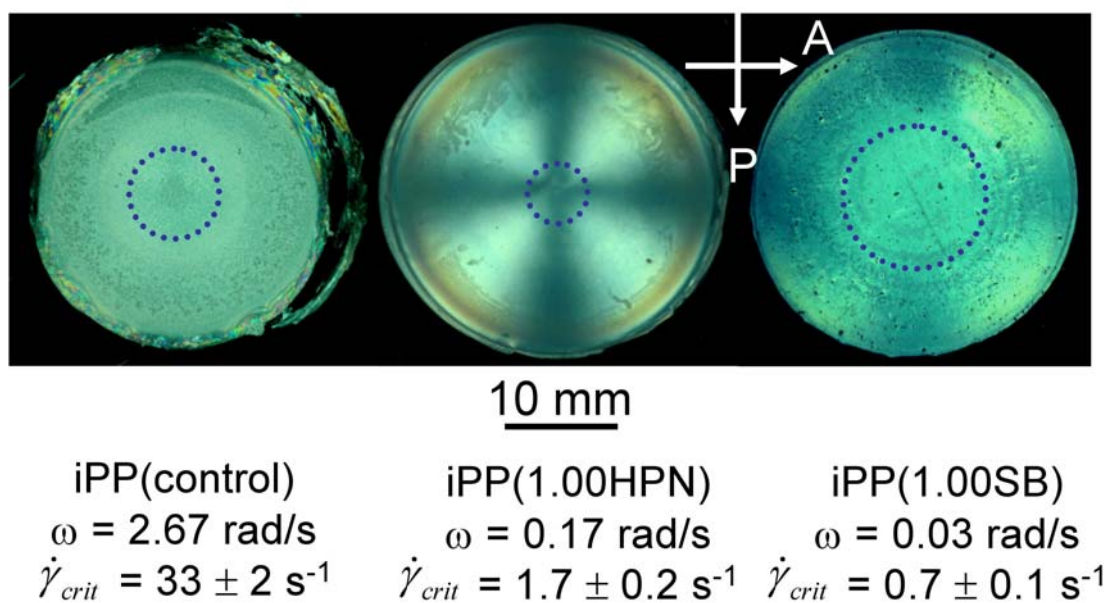


**Figure 8.22.** Polarised optical image of sheared sample showing the critical shear rate for the transition to oriented morphology ( $\dot{\gamma}_{crit}$ ) (shear time = 30 s, shear temperature = 181 °C, cooling rate). Polariser (P), Analyser (A).

## 8.4.0 Discussion

### 8.3.1 Influence of nucleants on the quiescent melt

During processing, polymers come into a contact with a variety of foreign surfaces, for instance the walls of processing equipment, substrates, and the surface of secondary phases (e.g. nucleating agents, colorants and fillers). The presence of these surfaces is well known to influence many aspects of polymer crystallisation, for instance: crystallisation rates, crystalline morphology and degree of crystallisation. Precise knowledge of the role surfaces have during crystallisation should allow for tailored microstructures and therefore properties to be produced. As discussed in **Chapter 2.3.2** it is widely thought that foreign surfaces lower the activation energy to form nuclei of critical size, thereby promoting nucleation. However, many important details about the role of the surface in nuclei formation remain to be clarified. Accordingly, this section will investigate the influence of nucleants on the structure development of the quiescent melt.

The scattering profile in **Figure 8.7a** shows that the presence of both nucleants increased the scattered intensity compared to iPP(control). This indicates that the nucleants increased the volume of structural units which give rise to the observed scattering. The power-law analysis presented in **Table 8.1** points to the shape of these structural units changing from relatively isotropic to plate-like in the presence of nucleants. Along with the increased volume of the structural units present, this would appear to indicate the preferential growth of the structural units along one or two particular directions. The FTIR analysis provides further insight into the nature of the structural units. The addition of both nucleants led to the formation of an absorbance peak at  $841\text{ cm}^{-1}$  which is due to helices which contain at least 12 monomers, **Figure 8.15**. This showed that the presence of both nucleants promoted the growth of longer helices. WAXS did not reveal any crystalline scattering and therefore these structures can be considered to have order intermediate between amorphous and crystalline. The presented evidence would therefore be consistent with the nucleants inducing the growth of small mesomorphic bundles of roughly parallel chains in helical conformation.

On the basis of the experimental results presented in this chapter, it is possible to construct a simple model to describe the influence of particles on the structure development in the quiescent melt. In pure iPP or at sufficient distances away from a particle, the polymer chain would be in a Gaussian configuration and may contain a number of short helices (**Figure 8.23a**). If the intermolecular forces are sufficient, the chain may get attracted to the surface of a particle and adsorbed onto its surface (**Figure 8.23b**). The adsorbed chain would experience a loss in entropy, which would lower the thermodynamic potential for nucleation or propagation of conformational order (**Figure 8.23c**). The entropy of single adsorbed helices could be further reduced by undergoing coalescence with neighbouring helices. This would provide a driving force for the formation bundles of roughly parallel chains in helical conformations (**Figure 8.23d**). Desorption of the bundles could take place when they reach a critical size or due to Brownian effect (**Figure 8.23e**). Depending on their size and the temperature of the melt, these bundles could relax back into the melt (**Figure 8.f**) or undergo reorganisation (**Figure 8.g**) and become crystal nuclei similar to the processes described by Allegra et al. [57].

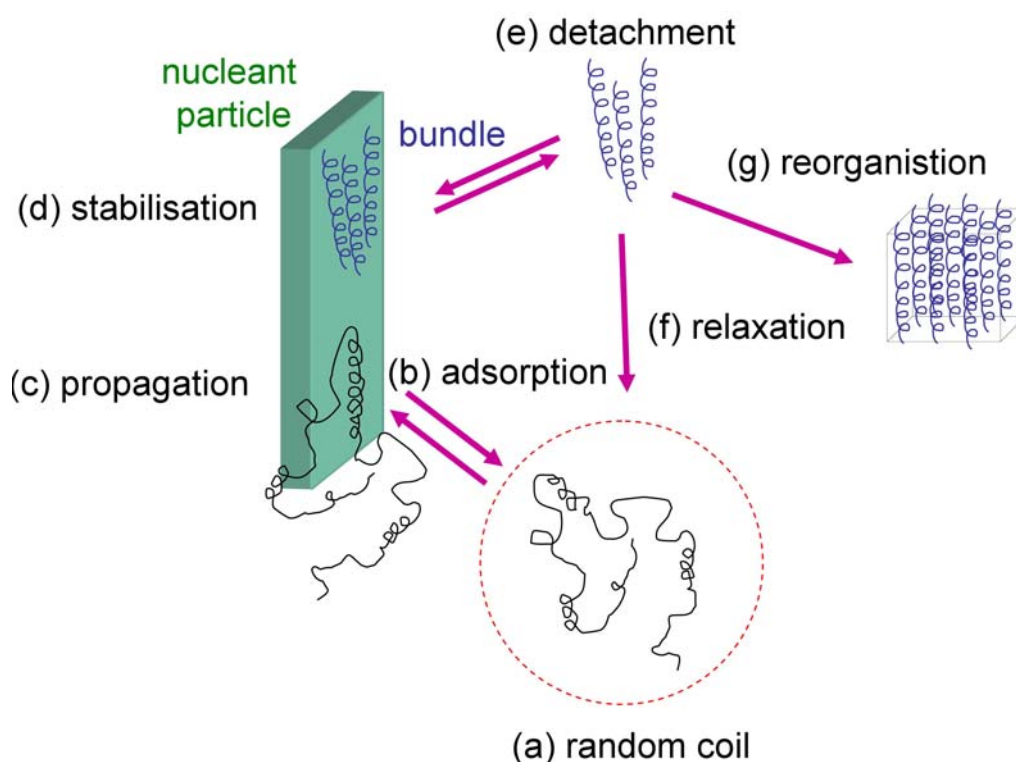


**Figure 8.23.** Influence of particle surface on quiescent melt. Refer in-text for details of the individual processes (a-e).

#### 8.4.2 Formation of shish during shear flow

Shish formation during shear flow is of considerable practical importance as shish promote oriented hierarchical structures, which significantly alter the physical, optical and mechanical properties of the solid polymer. However, the shish formation mechanism is still under intense debate. The proposed mechanisms broadly fall into three groups: shish form directly from extended chains (or chain segments) produced via an abrupt coil-to-stretch transition [10, 14-15, 87]; shish nucleate from pre-existing nuclei and then grow by the addition of new chain segments [30, 33-34, 37, 100, 102]; and shish form in discrete steps, by the aggregation of discrete nuclei into oriented threads [98, 103-106]. These three mechanisms are not necessarily mutually exclusive, and more than one mechanism could lead to shish formation under a given set of processing conditions. These mechanisms have been described in detail in **Chapter 2.3.2** and are schematically depicted in **Figure 2.9**.

In the present work, surprising sharp meridional scattering streaks were observed *during* shear flow in the SAXS patterns of all samples investigated, in conjunction with the commonly observed equatorial streaks. The absence of crystalline reflection in the WAXS region shows the scattering arose from non-crystalline entities. A review of the available literature indicates that such meridional scattering has not been previously observed during shear flow. Similar SAXS/WAXS investigations by Somani et al. [8] on sheared iPP have shown the formation of broad meridional scattering after an appreciable induction time and following the cessation of shear flow. In that work the meridional scattering was explained by the formation of non-crystalline kebabs. However, the lack of any appreciable induction time for the formation of the meridional peaks, the sharpness of the scattering, as well as the high temperature used in this experiment, which was 10 - 20 °C higher than the lamellae melting temperature, would make this scenario unlikely. Consequently, the most likely structure which fits the observed scattering are highly aligned discrete nuclei. Such a structure would be consistent with shish forming in discrete steps by the aggregation of point-like nuclei into oriented threads. The suggested sequence of events is schematically illustrated in **Figure 8.24**.

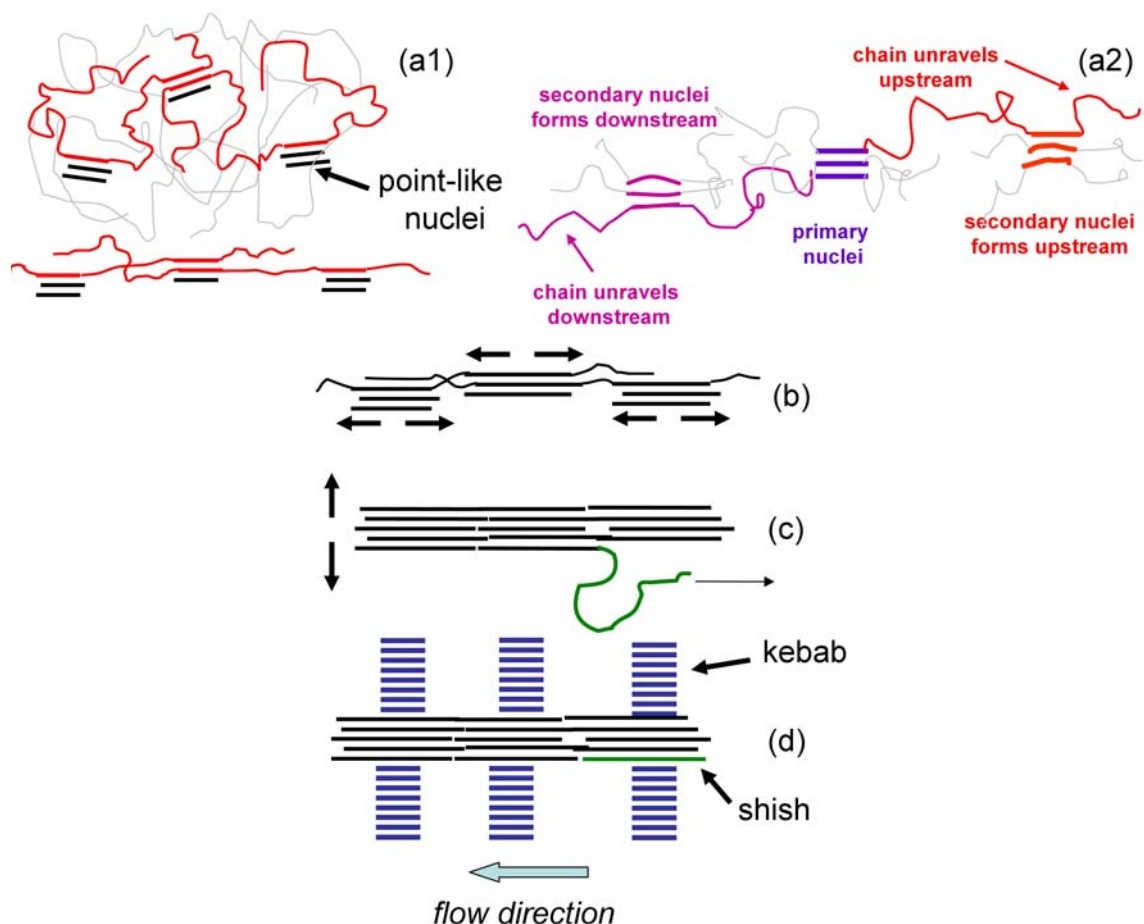


**Figure 8.24.** Proposed mechanism of shish formation. **(a1)** Flow-induced point-like nuclei form into oriented thread when their tie molecules are pulled taut by shear flow. **(a2)** Flow field causes coiled up free ends of chains attached to primary flow-induced nuclei to unravel up- and down-stream promoting secondary nuclei formation. **(b)** Infill growth of aligned point-like nuclei to form shish. **(c)** Growth of shish in the lateral direction by the unravelling of adsorbed chains along the length of the shish. **(d)** Nucleation of chain folded kebabs on lateral surface of shish.

Two possible schemes have been proposed in the literature to explain how shear flow can lead to the formation of oriented threads composed of discrete point-like nuclei. Heeley et al. suggested the point-like nuclei could act as anchor points along the length of a molecule, allowing flow to more effectively orient the molecule, and thus the attached point-like nuclei [104], **Figure 8.24a1**. An alternative mechanism was proposed by Seki et al., who suggested that molecules which adsorb onto the surface of point-like nuclei would get rapidly extended along the flow direction [103]. New point-like nuclei would then form from these extended chain segments, **Figure 8.24a2**. The

processes would then be rapidly repeated to form long threads which form the basis of the final shish structure. However, the experimental results presented here could not distinguish between these two mechanisms.

Meridional scattering is not commonly observed in the SAXS patterns of sheared semicrystalline polymers and therefore its presence in this experiment needs further explanation. The proportion and nature of the meridional streak appeared to be highly sensitive to the flow conditions. The relative proportion of meridional scattering was observed to decrease during shear flow, **Figure 8.3**. The meridional scattering then disappeared soon after the flow was stopped. At a shear temperature of 176 °C the equatorial streak was dominant. However, increasing the shear temperature reversed this and at a shear temperature of 191 °C the meridional streak was the dominant feature in the SAXS patterns. These observations can be explained by the infill of regions between neighbouring aligned point-like nuclei which would be promoted by the highly extended chains between the nuclei, **Figure 8.24b**. Such infill growth could be aided by the autocatalytic mechanism proposed by Peterman et al. [30]. This highlights that the meridional scattering may only be apparent during shear flow, while the shish are forming. However, due to the fast kinetics, many experiments previously presented in the literature investigated shish formation after shear flow stopped. Accordingly, it is the high shear temperature used in this experiment, which slows down the formation of shish, in combination with the relatively long shear times, which allows for shish formation to be probed while the shish grow.

The increase in  $D_{\text{shish}}$  during shear shows that the shish can also grow in the lateral direction during shear flow. Yamazaki et al. [33] suggested that this could occur by the repeated adsorption of chain ends to the shish surface. Once pinned on the surface, the free ends of the chain would then be rapidly elongated along the surface of the shish by the flow field, **Figure 8.24c**. This result highlights that more than one mechanism is responsible for shish growth during shear flow.

### 8.4.3 Stability of shish after shear flow

Immediately after the shear pulse ended the shish began to dissolve back into the melt. At least two separate steps are thought to be necessary for this to occur. The first step is the detachment of a stem from the surface of the shish (melting). Once detached, the extended stem can then relax in a snake-like motion along an imaginary tube formed by the constraints imposed by neighbouring molecules to restore its equilibrium conformation (reptation). The disengagement ( $\tau_d$ ) and the chain Rouse times ( $\tau_R$ ) of a stretched molecule were empirically determined using the Doi-Edwards model [89]:

$$\tau_d = 3\tau_e Z^3 [1 - \kappa Z^{-0.5}]^2 \quad \text{Equation 2.9}$$

$$\tau_R = \tau_e Z^2 \quad \text{Equation 2.10}$$

where  $\tau_e$  is the Rouse time of a single entanglement strand ( $\tau_e = 5.42 \times 10^{-8}$  s at 181 °C),  $Z$  is the number of entanglements per chain, and  $\kappa$  is a constant found to be close to unity [91]. The parameters used to calculate the theoretical reptation and Rouse times were obtained from the data assembled by Vega et al. [91], **Table 8.2**. **Table 8.3** shows the empirical disengagement and Rouse times for chains with the weight average molecular weight and the molecular weight above which 1% of the chain population by weight resides. These empirical relaxation times are expected to be an upper bound. This is due to the likely influence of constraint release from the faster relaxation of the shorter chains in the polydisperse melt, which would increase the relaxation rates. For stretched chains which are of the weight average molecular weight, relaxation occurs rapidly and within a fraction of a second. However, for the longest 1% of chains, the relaxation rates are much slower and are comparable to the relaxation rate of  $I_0$  and conformational order observed for iPP(control) shown **Figure 8.8** and **Figure 8.17**. This result is therefore consistent with the view that the dissolution of shish is controlled by the reptation of the high molecular weight component [263].

For chains to become oriented, the critical flow intensity needs to be larger than the inverse of the chain Rouse time (i.e.  $\dot{\gamma} > 1/\tau_r$ ). Therefore it is also worthwhile to point out here that the critical shear rate required to orient chains of the weight average



molecular weight is  $3700 \text{ s}^{-1}$  while for the longest 1% of chains the shear rate is  $33 \text{ s}^{-1}$ . This latter value is directly comparable to the experimentally determined critical shear rates, above which oriented structure were observed in iPP(control), for the variety of flow conditions presented in **Chapters 6-8**.

**Table 8.2.** Parameters used to calculate the Rouse time for a single entanglement strand ( $\tau_e$ ). All data taken from Vega et al.[91]

Parameter	Value
$\zeta_o$	$2.3 \times 10^{-12} \text{ kg s}$
$\langle R^2 \rangle / M$	$0.680 \text{ \AA}^2$
$M_e$	$5200 \text{ g mol}^{-1}$
T	454.15 K
$m_o$	$42.08 \text{ g mol}^{-1}$
$\tau_e$	$5.42 \times 10^{-8} \text{ s}$

**Table 8.3.** Theoretical relaxation times for stretched iPP molecules in a monodisperse entangled melt held at  $181 \text{ }^\circ\text{C}$ .

Relaxation time	$M_w (367\,000 \text{ g mol}^{-1})$	$M_{99\%} (3\,672\,823 \text{ g mol}^{-1})^a$
$\tau_d$	0.0571 s	68.5 s
$\tau_d^*$	0.0443 s	63.6 s
$\tau_R$	0.00027	0.0270 s

\*  $M_{99\%}$  calculated from a log normal fit of the molecular distribution shown in **Figure 3.2**.

Although relaxation processes have been extensively studied in a wide range of polymers, the influence of foreign particles has received comparatively little attention. Previous studies have suggested that the surface of large particles could stabilise extended chain conformations due to the surface contact points acting as physical cross-links [49-51]. Similarly, molecularly dispersed nano-particles, which have a strong affinity for the polymer molecule, could increase the number of physical cross-links in an analogous fashion [115-117]. However, in the present experiment, the addition of the nucleants increased the initial rate of relaxation of shish after shear ended, contrary to these expectations.

It is proposed that this surprising increase in shish relaxation in the presence of particles can be explained by the polydisperse nature of the iPP matrix. It is widely considered that when a polydisperse polymer is sheared, it is the longest chains which are the first to be involved in the formation of shish [14, 87, 103]. Recent small angle neutron scattering studies (SANS) have indicated that the longer chains are not necessarily over represented in the shish [37]. Rather the longer chains only act to accelerate shish formation, recruiting out chains smaller chains to the forming shish. The presence of longer molecular weight chains in the shish structure may also act to stabilise the shish structure once formed by decreasing both the rate of chain detachment from the lateral surface of the shish and subsequent chain relaxation. The molecular weight effect can be explained by the increase in the number of intra-chain contact points with increasing chain length. Higher numbers of intra-chain contact points then stabilise the extended chain conformations, retarding relaxation. Therefore, the faster relaxation of shish strongly suggests that the presence of the particles decreased the size of chains which could template shish formation. Shish formed around these lower average molecular weight chains would then have a greater propensity to relax than shish which are formed around the higher molecular weight chains.

$I_0$  was found to increase again after an appreciable induction time. Keum et al. [257] recently observed a similar phenomenon in sheared UHMWPE/HDPE, noting the shish length increased around the same time. Keum then explained the increase in  $I_0$  by the longitudinal growth of shish using the autocatalytic growth mechanism proposed by Peterman et al. [30]. However, in this experiment both  $D_{\text{shish}}$  and  $L_{\text{shish}}$  were observed to decrease over this time period. Furthermore, the in-situ FTIR experiments revealed that the conformational order also decreased over this time period. Therefore autocatalytic growth of shish after flow can not explain the observed increase in  $I_0$ . Another possible explanation for the observed increase in  $I_0$  could be the decomposition of the melt by a spinodal liquid-liquid phase separation, such as proposed by Olmsted et al. [64]. Flow would be expected to increase the kinetics of the spinodal transformation by increasing the number of segments in helical conformations available to segregate. Therefore, the observed decrease in the induction time with the addition of nucleants would support such a hypothesis, as the particle's presence appears to increase the intensity of the flow field. This will be discussed in more detail in the next section.

#### 8.4.4 Particle assisted shish formation

In the present work, both particles were found to increase the amount of shish and their dimension compared to iPP(control). This resulted in a substantially greater crystalline and lamellar orientation during subsequent crystallisation. The addition of foreign particles in a wide range of polymer/particle systems has been shown to increase the molecular orientation under flow-induced crystallisation conditions [33-34, 49-50, 84, 112-116, 242]. **Figure 2.10** in **Chapter 2.3.3** summarises six possible mechanisms proposed in the literature for how particles could assisted shish formation. In the previous section it was shown that the addition of both particles increased the relaxation rate of shish. Therefore, mechanisms where the particles stabilise extended chain conformations would appear to be unlikely to account for the observed increase in shish (**Figure 2.10a** and **Figure 2.10b**). Rather, the increased relaxation rate shows that the addition of particles allowed shorter chains to template shish formation. This implies that it is the modification of the strain environment at or near the particle surface which aids shish formation in these materials.

In **Chapter 7.3.1** it was shown that the two nucleants used in this experiment had similar chemical compositions and size but had significantly different nucleation efficiencies and aspect ratios. Particles with high affinity for the polymer molecules [84, 115] and high aspect ratios [52] have been suggested to aid the formation of flow-induced nuclei. In this experiment the HPN particles were relatively isotropic, but had a much higher nucleation efficiency than the high aspect ratio SB particles. Compared to the addition of HPN particles, the addition of SB particles resulted in more shish which also had larger dimensions. Therefore, aspect ratio appears to be the more dominant factor in aiding shish formation rather than nucleation efficiency. An appreciable influence of nucleation efficiency would have revealed that a surface mechanism may be important (**Figure 2.10e**). Hence the results presented here suggest that the addition of foreign particles assist shish formation by modifying the local strain environment near, but not necessarily on, the particle surface (**Figure 2.10c**, **Figure 2.10d** & **Figure 2.10f**).

Further information regarding how particle aspect ratio influences shish formation can be gleaned from the development of shish alignment during shear flow. At the start of shear, the shish in iPP(control) and in iPP(1.00SB) were highly aligned along the flow direction, while the shish in iPP(1.00HPN) were not. This result can be explained by how the different particles interact with, and particularly how they rotate, in the flow field.

Fibre suspensions can be classified into three regimes according to the volume fraction of fibres ( $\Phi_f$ ) and the fibre aspect ratio ( $a_r$ ), defined as the fibre length to diameter ratio  $L/D$ . The suspensions can be considered dilute when  $\Phi_f a_r^2 < 1$  is satisfied. Dilute suspensions signify the individual fibres can freely rotate in the matrix without interaction from neighbouring fibres. If the fibres interact through long range interactions then the fibres can be considered to be semi-dilute. This regime is considered when  $1 \leq \Phi_f a_r^2 \leq a_r$  and is where the fibres have only two rotating degrees of freedom. Finally, the suspensions can be considered concentrated ( $\Phi_f a_r > 1$ ) when the concentration of fibres is such that average distance between fibres is less than the fibre diameter. In this regime fibres cannot rotate without a cooperative movement of surrounding fibres, except around their symmetry axis. In the present study, all samples investigated fall into the dilute category and therefore all particles at the start of flow are able to rotate freely in the melt.

The orientation of the particle can be described by a family of closed curves known as Jeffery orbital's, which are known to depend on the initial orientation of the particles to the flow direction [271]. Furthermore, the rate of rotation is known to depend on the aspect ratio of the particle, with higher aspect ratio particles rotating less than low aspect ratio particles [272-274]. This low rotation rate is consistent with the SB particles being oriented with their long axis along the flow direction, **Figure 7.4c**. The higher rotation of the HPN particles could cause shish which are forming nearby to tumble, destabilising their formation and leading to fewer and smaller shish being formed, **Figure 8.25**. Conversely, the SB particles which adopt a more stable orientation along the flow direction, help guide shish growth. Recent reviews of the available literature suggest isotropic particles disrupt flow [250] while highly anisotropic particles stabilises flow under a range of conditions [275].

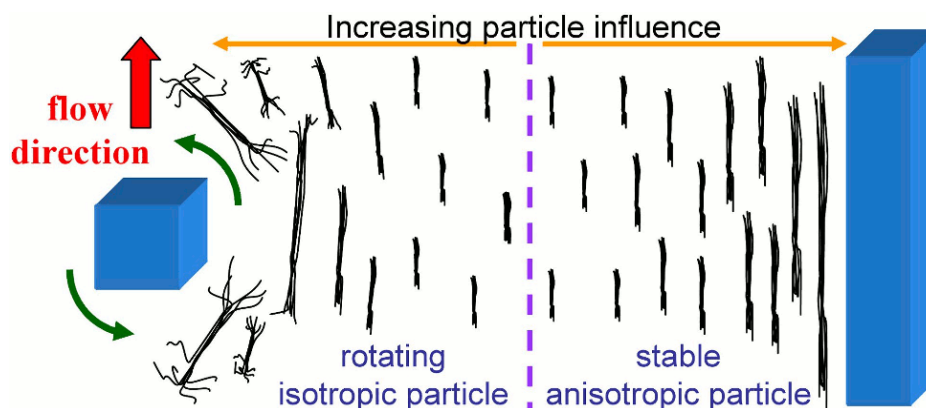


**Figure 8.25.** Influence of rotating isotropic and stable anisotropic particles on formation of shish.

It is interesting to note that the shish alignment in iPP(1.00HPN) dramatically increased during shear flow, while the shish alignment in iPP(control) and iPP(1.00SB) only slightly increased. One possible explanation is that the growing shish stabilise the rotation of the HPN particles, which would enhance shish alignment along the flow direction. Another possible explanation is that the shear flow allows the aggregation of the isotropic particles into chains. A possible mechanism based on the ability of perturbative flow to attract distant particles in the flow direction and push away particles in the other two direction has been proposed by Phillips and Talini [276]. The formation of particle chains may then lead act as a single unit or “raft”. This would allow more uniform flow to occur around the particles, enhancing shish formation and alignment.

## 8.5.0 Conclusions

In this chapter the formation and relaxation of shish was investigated in the melt of pure isotactic polypropylene (iPP(control)) and iPP containing two commercial nucleants during and after moderate continuous shear flow. The findings from this chapter are briefly summarised as follows.

In-situ SAXS/WAXS investigations of the quiescent melt, revealed that the addition of the nucleants substantially increased the scattered intensity in the SAXS region but did not lead to any detectable crystalline peaks in the WAXS region. Furthermore, in-situ FTIR experiments revealed the addition of the nucleants promoted the growth of long helices. These results provide convincing evidence that foreign particles can substantially modify the structure of quiescent semicrystalline melts at temperatures well above the lamellar melting temperature. A possible mechanism based on the adsorption of the polymer chains on the surface of the particles was put forward to account for the observed structure development.

Surprising sharp meridional streaks were observed in conjunction with equatorial streaks in the small angle x-ray scattering patterns during shear flow. As shear progressed the meridional streak decreased, and disappeared soon after the shear flow stopped. These observations provide strong evidence that the initial shish growth occurs in discrete steps, by the aggregation of point-like nuclei into oriented threads.

The addition of both nucleants increased the initial relaxation rate of shish after shear flow stopped. This result was explained by the presence of the particles inducing lower molecular weight chains to participate in shish formation. The lower molecular weight chains then destabilised the shish, accelerating their dissolution.

The addition of both nucleants resulted in a significant increase in the amount of shish and their size (length and diameter) compared to iPP(control). Possible mechanisms which could account for the particle assisted formation of shish were discussed. The most likely mechanisms were based on the particles modifying the local strain environment near the particle surface.

The amount, dimensions and alignment of the shish along the flow direction were much higher in iPP(1.00SB) compared to iPP(1.00HPN). These results imply that the shape of foreign particles can have important implications for the formation of shish. It was proposed that the needle-like SB particle adopted stable orientations along the flow direction, guiding shish growth, while isotropic HPN particles rotated during shear flow, destabilising shish forming nearby.

## Chapter 9

### Concluding remarks

Shish formation, relaxation and the subsequent crystallisation of sheared isotactic polypropylene containing a range of structurally diverse nucleant particles was characterised in this thesis. This allowed the role the nucleant particles play in morphology development to be determined. The present chapter summarises the main conclusions drawn from experimental work presented in **Chapter 4** through **Chapter 8**. In addition, possible directions for future studies are outlined.

#### 9.1 Influence of flow conditions and nucleant particles on iPP polymorphism

Polypropylene is known to crystallise in a range of polymorphic forms:  $\alpha$ -iPP,  $\beta$ -iPP and  $\gamma$ -iPP and smectic-iPP depending on the specific crystallisation conditions. The specific phases formed and their morphology can in turn have a large impact on the final properties of the produced component. Accordingly, this thesis further investigated the factors which influenced the polymorphic behaviour of iPP.

$\alpha$ -iPP exhibits a form of lamellar branching that is unique among semicrystalline polymers, where the branches have a distinct orientation relationship with the original crystalline lamellae. This is termed a parent–daughter relationship (PD). In **Chapter 4** a simple procedure was developed to follow the individual contributions of oriented PD lamella using wide angle x-ray scattering (WAXS). This allowed the formation of oriented PD lamellae to be investigated in-situ during crystallisation and melting. During crystallisation, the planes of the daughter lamellae were observed to curve towards the flow direction as they grew from their parent lamellae. This was explained by the influence of neighbouring daughter lamellae confining their growth direction. Oriented daughter lamellae were found to melt  $\sim 5$  °C lower than oriented parent lamellae. This provided a new explanation for the multiple melting behaviour typically observed in the differential scanning calorimetry (DSC) melting thermograms of sheared  $\alpha$ -iPP.



**Chapter 5** revealed that flow-induced crystallisation conditions promoted the formation of  $\beta$ -iPP in pure iPP. **Chapter 6** aimed to further understand the flow-induced formation of  $\beta$ -iPP by comparing the influence of flow condition on the  $\beta$ -iPP crystallinity with its influence on the crystalline and lamellar orientation. It was shown that a shear rate of  $30 \text{ s}^{-1}$  was necessary to induce lamellar and crystalline orientation. However, significant  $\beta$ -iPP content was formed at shear rates as low as  $5 \text{ s}^{-1}$ . This showed that the creation of oriented  $\alpha$ -iPP crystals was not necessary to form  $\beta$ -iPP crystals, contrary to the accepted view that the surface of oriented  $\alpha$ -iPP crystals provide nucleation sites for an  $\alpha$ -iPP to  $\beta$ -iPP growth transition [144, 146, 151]. Instead, the  $\beta$ -iPP content was found to initially increase with increasing shear rate up to  $30 \text{ s}^{-1}$ , before decreasing at higher shear rates, such that there was a shear rate window in which high  $\beta$ -iPP contents were produced. The existence of a shear rate window for  $\beta$ -iPP formation indicates that systematic changes occurred with increasing shear rate to the structure of the nuclei which specifically nucleate  $\beta$ -iPP. Therefore the results present in this thesis are consistent with the recent view of Li et al. [153] who proposed that the nucleation of  $\beta$ -iPP is favoured at flow-induced mesomorphic nuclei possessing intermediate order between amorphous and crystalline states.

Although the results suggest that there may be an ideal structure of mesomorphic nuclei which promotes  $\beta$ -iPP, the specific structural characteristics are unknown and remain to be determined. Consequently, further experimentation is required to probe the ideal structure of the flow-induced nuclei which can preferentially nucleate  $\beta$ -iPP.

The selectivity of the  $\beta$ -iPP nucleants used in **Chapter 5** and **Chapter 6** were suppressed under flow-induced crystallisation conditions. The suppression of the  $\beta$ -iPP nucleating activity of the particles was shown to be due to the particles assisting the formation of additional flow-induced nuclei, which specifically nucleated  $\alpha$ -iPP. These additional  $\alpha$ -iPP nuclei then overwhelmed crystallisation from the surface of the  $\beta$ -iPP nucleants. This work therefore confirms the nucleant suppression mechanism originally proposed by Huo et al. [43].

In **Chapter 7** and **Chapter 8** the combined influence of the  $\alpha$ -iPP nucleants SB and HPN and shear flow led to a dramatic increase in  $\gamma$ -iPP content, increasing  $\gamma$ -iPP content

by up to 71% and 193% respectively. Therefore, the combined influence of shear flow and  $\alpha$ -iPP nucleant has a strong  $\gamma$ -iPP nucleation effect. The surprising  $\gamma$ -iPP nucleation effect was primarily explained by the very high density of nuclei in these samples at the start of crystallisation. This high density of nuclei would lead to multiple nucleation events occurring nearly simultaneously along the one chain. The time available for the chain to properly organise during the initial crystallisation would subsequently be reduced. Combined with the stereo- and regio-defects already present along the main chain, this would lead to the isotactic sequences formed during initial crystallisation being interrupted, which is known to favour  $\gamma$ -iPP formation [157].

A further effect of the addition of the two commercial  $\alpha$ -iPP nucleants was the marked increase in the relative proportion of oriented parent lamellae produced under flow-induced crystallisation conditions. This increase in parent lamellae may further explain the observed increase in the  $\gamma$ -iPP content in these samples due to the increased number of  $\gamma$ -iPP nucleation sites which reside on the surface of parent lamellae. However, the increased proportion of parent lamellae does not necessarily mean increased numbers of parent lamellae. Therefore further experimentation is needed to clarify the combined role nucleants and shear flow have on parent-daughter structure in  $\alpha$ -iPP.

## 9.2 Influence of flow conditions and nucleant particles on shish formation

Above a critical flow intensity, shish formed with their long axis aligned along the flow direction. These shish were then found to template oriented crystalline and lamellar structures during subsequent crystallisation and consequently their presence has a large bearing on morphology development. Accordingly, one of the main themes covered in this thesis was to develop a greater understanding of the factors which govern shish formation and the associated formation of oriented crystalline and lamellar structures.

In **Chapter 7.4.1**, sharp meridional reflections were observed at high temperatures in the small angle x-ray scattering (SAXS) patterns during the final stages of shish dissolution. Furthermore, in **Chapter 8.3.1** similar sharp meridional reflections were also observed during shear flow. In both cases no associated crystalline or lamellar scattering was observed. These results therefore point to the shish containing structural singularities along their length. As the meridional reflections were only observed during

shear flow, these structural singularities, which are regions of relatively higher local order, were formed during the initial shish formation. Therefore their presence points to shish initially forming from the aggregation of point-like nuclei into oriented threads. This shish formation mechanism is in direct contrast with the classical view that shish form directly from an abrupt coil-to-stretch transition of high molecular weight chains or chain segments in an entangled network as proposed by Keller [10] and Hsiao et al. [14, 99]. However, the results support the aggregation type mechanisms which have recently been proposed by Heeley et al. [104] and Seki et al. [103]. In view of this discrepancy, further experimentation using complementary characterisation methods is required to confirm the presence of these structural singularities such that the initial mechanism of shish formation can be determined.

The experimental results presented in **Chapter 5** through **Chapter 8** revealed that the presence of nucleant particles (a) decrease the critical shear rate required to form shish and (b) for a given shear rate, increase the density and dimensions of the shish formed. Therefore the experimental results show that nucleant particles assist the formation of shish. In **Chapter 8.3.2**, it was shown that the shish relaxation rate decreased with the addition of nucleant particles. This revealed that the nucleant particles did not hinder the relaxation of shish as proposed by Zhu et al. [49-50, 113] and Garcia-Gutierrez et al. [51]. Rather, the evidence showed that the nucleant particles recruited lower molecular weight chains to participate in shish formation. This suggests that the particles intensify the local strain environment near the particle. The results presented in **Chapter 5.3.2** showed how this occurred. The particles create constrictions which required the matrix polymer to flow around the particles, leading to increased strain and strain rate near the free surface of the particles. These results therefore support the simulation work presented by Hwang et al. [118].

Although the surface of the particle was found to be important under quiescent conditions, the characteristics of the particle surface did not appear to significantly influence the formation of shish. For example, the structure of iPS particles in **Chapter 5** was varied by selective in-situ heat treatment without significantly altering the particle shape. Under quiescent conditions this change in structure resulted in a change in the epitaxial relationship, which produced different crystalline polymorphs of iPP. However, the structural change did not influence the density of shish formed. Rather, in

**Chapter 7** and **Chapter 8** it was found that the needle-like SB particles decreased the critical shear rate required to form shish as well as increased the dimensions and alignment of shish compared to the isotropic HPN particles. Therefore, particle aspect ratio was found to be an important determinate in shish formation. The influence of particle shape was explained by the manner in which the particles interact with the surrounding melt, and in particular, how they rotate during shear flow. Highly anisotropic particles adopt stable orientations which support shish formation, while isotropic particles rotate rapidly destabilising shish forming near by. Accordingly, this work furthers the recent work published by Byelov et al. [52] by introducing a mechanism to explain how different shaped particles influence structure development in sheared polymer melts.

The size range of the nucleant particles used in this thesis are typical of commercial nucleants ranging from several hundred nano-meters to tens of microns. However, it is not unreasonable to assume that deviations from the observations described here may occur when the particle size is reduced further. Accordingly, further experimentation is required to assess the influence of particle size on shish formation and relaxation.



## References

1. Piringner OG and Baner AL. Plastic Packaging. Weinheim: Verlag GmbH & Co. KGaA, 2008. pp.32.
2. Brintzinger HH, Fischer D, Mülhaupt R, Rieger B, and Waymouth RM. "Stereospecific olefin polymerization with chiral metallocene catalysts" *Angewandte Chemie International* **1995**;34:1143-1170.
3. Pino P and Mülhaupt R. "Stereospecific polymerization of propylene: An outlook 25 years after its discovery" *Angewandte Chemie International* **1980**;19:857-875.
4. Natta G. "A new class of polymers from  $\alpha$ -olefins having exceptional structural regularity" *Journal of Polymer Science* **1955**;16:143-154.
5. Kantz MR, Newman HD, and Stigale FH. "The skin-core morphology and structure-property relationships in injection-molded polypropylene" *Journal of Applied Polymer Science* **1972**;16:1249-1260.
6. Fujiyama M, Wakino T, and Kawasaki YJ. "Structure of skin layer in injection-molded polypropylene" *Journal of Applied Polymer Science* **1988**;35:29-49.
7. Katti SS and Schultz JM. "The microstructure of injection-molded semicrystalline polymers: A review" *Polymer Engineering & Science* **1982**;22:1001-1017.
8. Somani RH, Yang L, Hsiao BS, Agarwal PK, Fruitwala HA, and Tsou AH. "Shear-induced precursor structures in isotactic polypropylene melt by in-situ rheo-SAXS and rheo-WAXD studies" *Macromolecules* **2002**;35:9096-9104.
9. Lotz B and Wittmann JC. "Structure and morphology of poly(propylenes): a molecular analysis" *Polymer* **1996**;37:4979-4992.
10. Keller A and Kolnaar HW. Flow induced orientation and structure formation. In: Meijer HEH, editor. Materials Science and Technology, Processing of Polymers, vol. 18. New York: Wiley-VCH, 1997. pp. 189.
11. Janeschitz-Kriegl H and Ratajski E. "Kinetics of polymer crystallization under processing conditions: transformation of dormant nuclei by the action of flow" *Polymer* **2005**;46:3856-3870.
12. Mykhaylyk OO, Chambon P, Graham RS, Fairclough JPA, Olmsted PD, and Ryan AJ. "The specific work of flow as a criterion for orientation in polymer crystallization" *Macromolecules* **2008**;41:1901-1904.
13. Mykhaylyk OO, Chambon P, Impradice C, Fairclough JPA, Terrill NJ, and Ryan AJ. "Control of structural morphology in shear-induced crystallization of polymers" *Macromolecules* **2010**;43:2389-2405.
14. Somani RH, Yang L, Zhu L, and Hsiao BS. "Flow-induced shish-kebab precursor structures in entangled polymer melts" *Polymer* **2005**;46:8587-8623.
15. Hu W, Frenkel D, and Mathot VBF. "Simulation of shish-kebab crystallite induced by a single prealigned macromolecule" *Macromolecules* **2002**;35:7172-7174.

16. Housmans J-W, Steenbakkens RJA, Roozemon PC, Peters GWM, and Meijer HEH. "Saturation of pointlike nuclei and the transition to oriented structures in flow-induced crystallization of isotactic polypropylene" *Macromolecules* **2009**;42:5728-5740.
17. Kumaraswamy G. "Crystallization of polymers from stressed melts" *Polymer Reviews* **2005**;45:375-397.
18. Fujiyama M. Higher order structure of injection-moulded polypropylene. In: Karger-Kocsis J, editor. *Polypropylene: structure, blends and composites*, vol. 1. London: Chapman & Hall, 1995. pp. 173-174.
19. Fujiyama M, Awaya H, and Kimura S. "Mechanical anisotropy in injection-molded polypropylene" *Journal of Applied Polymer Science* **1977**;21:3291-3309.
20. Xia Z, Hartwig T, and Sue H-J. "Mechanical behavior of bulk poly(ethylene terephthalate) subjected to simple shear" *Journal of Macromolecular Science, Part B: Physics* **2004**;B43:385–403.
21. Chen X, Galeski A, and Michler GH. "Morphological alteration and strength of polyamide 6 subjected to high plane-strain compression" *Polymer* **2006**;47:3171-3185.
22. Pawlak A, Barton DC, Galeski A, and Ward IM. "Orientation of polyoxymethylene by rolling with side constraints." *Polymer* **2008**;49:303-316.
23. Clark ES and Spruiell JE. "Unlimited flex life in the molded-in hinge in polypropylene: A structural hypothesis" *Polymer Engineering & Science* **1976**;16:176-181.
24. Zheng R, Tanner RI, Wo DL, Fan X-j, Hadinata C, Costa FS, Kennedy PK, Zhu P, and Edward G. "Modeling of flow-induced crystallization of colored polypropylene in injection molding" *Korea-Australia Rheology Journal* **2010**;22:151-162.
25. Zheng R, Kennedy P, Phan-Thien N, and Fan X-J. "Thermoviscoelastic simulation of thermally and pressure-induced stresses in injection moulding for the prediction of shrinkage and warpage for fibre-reinforced thermoplastics" *Journal of Non-Newtonian Fluid Mechanics* **1999**;84:159-190.
26. Murphy J. *Modifying Processing Characteristics: Modifiers and Processing Aids. Additives for Plastics Handbook (Second Edition)*. Amsterdam: Elsevier Science, 2001. pp. 189-204.
27. Karger-Kocsis J. *Polypropylene. An A-Z Reference*. Great Britain: Kluwer Academic Press, 1999. pp.57.
28. Beck HN. "Heterogeneous nucleating agents for polypropylene crystallisation " *Journal of Applied Polymer Science* **1967**;11:673-685.
29. Beck HN. "Heterogeneous nucleating agents for the crystallization of isotactic polystyrene" *Journal of Applied Polymer Science* **1975**;19:2601-2608.
30. Petermann J, Miles M, and Gleiter H. "The crystalline core of the row structures in isotactic polystyrene. I. Nucleation and growth" *Journal of Polymer Science Part B: Polymer Physics* **1979**;17:55-62.
31. Mercier JP. "Nucleation in polymer crystallization: A physical or a chemical mechanism?" *Polymer Engineering & Science* **1990**;30:270-278.
32. Ebengou RH. "Adsorption as a mechanism for nucleating activity: A thermodynamic explanation" *Journal of Polymer Science Part B: Polymer Physics* **1997**;35:1333-1338.

33. Yamazaki S, Watanabe K, Okada K, Yamada K, Tagashira K, Toda A, and Hikosaka M. "Formation mechanism of shish in the oriented melt (II)-two different growth mechanisms along and perpendicular to the flow direction" *Polymer* **2005**;46:1685-1692.
34. Yamazaki S, Watanabe K, Okada K, Yamada K, Tagashira K, Toda A, and Hikosaka M. "Formation mechanism of shish in the oriented melt (I)-bundle nucleus becomes to shish" *Polymer* **2005**;46:1675-1684.
35. Pogodina NV, Lavrenko VP, Srinivas S, and Winter HH. "Rheology and structure of isotactic polypropylene near the gel point: quiescent and shear-induced crystallization" *Polymer* **2001**;42:9031-9043.
36. Ogino Y, Fukushima H, Takahashi N, Matsuba G, Nishida K, and Kanaya T. "Crystallization of isotactic polypropylene under shear flow observed in a wide spatial scale" *Macromolecules* **2006**;39:7617-7625.
37. Kimata S, Sakurai T, Nozue Y, Kasahara T, Yamaguchi N, Karino T, Shibayama M, and Kornfield JA. "Molecular basis of the shish-kebab morphology in polymer crystallization" *Science* **2007**;316:1014-1017.
38. Nogales A, Thornley SA, and Mitchell GR. "Shear cell for in-situ WAXS, SAXS, and SANS experiments on polymer melts under flow fields" *Journal of Macromolecular Science, Part B: Physics* **2004**;43:1161-1170.
39. An H, Li X, Geng Y, Wang Y, Wang X, Li L, Li Z, and Yang C. "Shear-induced conformational ordering, relaxation, and crystallization of isotactic polypropylene" *The Journal of Physical Chemistry B* **2008**;112:12256-12262.
40. An H, Zhao B, Ma Z, Shao C, Wang X, Fang Y, Li L, and Li Z. "Shear-induced conformational ordering in the melt of isotactic polypropylene" *Macromolecules* **2007**;40:4740-4743.
41. Li L and de Jeu WH. "Shear-induced smectic ordering in the melt of isotactic polypropylene" *Physical Review Letters* **2004**;92:075506.
42. Chen Y-H, Zhong G-J, Wang Y, Li Z-M, and Li L. "Unusual tuning of mechanical properties of isotactic polypropylene using counteraction of shear flow and  $\beta$ -nucleating agent on  $\beta$ -form nucleation" *Macromolecules* **2009**;42:4343-4348.
43. Huo H, Jiang S, and An L. "Influence of shear on crystallization behavior of the  $\beta$  phase in isotactic polypropylene with  $\beta$ -nucleating agent" *Macromolecules* **2004**;37:2478-2483.
44. Varga J, Mudra I, and Ehrenstein GW. "Highly active thermally stable  $\beta$ -nucleating agents for isotactic polypropylene" *Journal of Applied Polymer Science* **1999**;74:2357-2368.
45. Varga J. " $\beta$ -modification of polypropylene and its two-component systems" *Journal of Thermal Analysis and Calorimetry* **1989**;35:1891-1912.
46. Dong M, Guo Z, Su Z, and Yu J. "Study of the crystallization behaviors of isotactic polypropylene with sodium benzoate as a specific versatile nucleating agent" *Journal of Polymer Science Part B: Polymer Physics* **2008**;46:1183-1192.
47. Su Z-Q, Chen X-N, Yu Z-Z, and Zhang L. "Morphological distribution of polymeric nucleating agents in injection-molded isotactic polypropylene plates and its influence on nucleating efficiency" *Journal of Applied Polymer Science* **2009**;111:786-793.



48. Su Z, Dong M, Guo Z, and Yu J. "Study of polystyrene and acrylonitrile-styrene copolymer as special  $\beta$ -nucleating agents to induce the crystallization of isotactic polypropylene" *Macromolecules* **2007**;40:4217-4224.
49. Zhu P-W, Edward G, and Nichols L. "Effect of additives on distributions of lamellar structures in sheared polymer: a study of synchrotron small-angle x-ray scattering " *Journal of Physics D: Applied Physics* **2009**;42:245406.
50. Zhu P-W, Tung J, Edward G, and Nichols L. "Effects of different colorants on morphological development of sheared isotactic polypropylene: A study using synchrotron wide-angle scattering" *Journal of Applied Physics* **2008**;103:124906.
51. Garcia-Gutierrez MC, Hernandez JJ, Nogales A, Panine P, Rueda DR, and Ezquerra TA. "Influence of shear on the templated crystallization of poly(butylene terephthalate)/single wall carbon nanotube nanocomposites" *Macromolecules* **2007**;41:844-851.
52. Byelov D, Panine P, Remerie K, Biemond E, Alfonso GC, and de Jeu WH. "Crystallization under shear in isotactic polypropylene containing nucleators" *Polymer* **2008**;49:3076-3083.
53. Keller A. "A note on single crystals in polymers: Evidence for a folded chain configuration" *Philosophical Magazine* **1957**;2:1171-1175.
54. Bassett DC. "Andrew Keller: the nucleation and growth of polymer physics in Bristol" *Polymer* **2000**;41:8755-8760.
55. Magill JH. "Spherulites: A personal perspective " *Journal of Materials Science* **2001**;36:3143-3164.
56. Suñol J. Modeling polymer crystallization: DSC approach. *Polymer Crystallization*, 2003. pp. 297-311.
57. Allegra G and Valdo Meille S. "The bundle theory for polymer crystallisation" *Physical Chemistry Chemical Physics* **1999**;1:5179-5188.
58. Cahn JW and Hilliard JE. "Free energy of a nonuniform system. I. Interfacial free energy" *The Journal of Chemical Physics* **1958**;28:258-267.
59. Stribeck N, Nochel U, and Funari SS. "Melting and crystallization of differently oriented sets of crystallites in hard-elastic polypropylene" *Macromolecules* **2009**;42:2093-2101.
60. Heeley EL, Maidens AV, Olmsted PD, Bras W, Dolbnya IP, Fairclough JPA, Terrill NJ, and Ryan AJ. "Early stages of crystallization in isotactic polypropylene" *Macromolecules* **2003**;36:3656-3665.
61. Terrill NJ, Fairclough PA, Towns-Andrews E, Komanschek BU, Young RJ, and Ryan AJ. "Density fluctuations: The nucleation event in isotactic polypropylene crystallization" *Polymer* **1998**;39:2381-2385.
62. Kaji K, Nishida K, Kanaya T, Matsuba G, Konishi T, and Imai M. Spinodal crystallization of polymers: Crystallization from the unstable melt. In: Allegra G, editor. *Interphases and mesophases in polymer crystallization III*, vol. 191: Springer Berlin / Heidelberg, 2005. pp. 187-240.
63. Imai M, Kaji K, and Kanaya T. "Structural Formation of Poly(ethylene terephthalate) during the Induction Period of Crystallization. 3. Evolution of Density Fluctuations to Lamellar Crystal" *Macromolecules* **1994**;27:7103-7108.

64. Olmsted PD, Poon WCK, McLeish TCB, Terrill NJ, and Ryan AJ. "Spinodal-assisted crystallization in polymer melts" *Physical Review Letters* **1998**;81:373-376.
65. Wang Z-G, Hsiao BS, Sirota EB, Agarwal P, and Srinivas S. "Probing the early Stages of melt crystallization in polypropylene by simultaneous small- and wide-angle x-ray scattering and laser light scattering" *Macromolecules* **2000**;33:978-989.
66. Panine P, Di Cola E, Sztucki M, and Narayanan T. "Early stages of polymer melt crystallization" *Polymer* **2008**;49:676-680.
67. Wang H. "SANS study of the early stages of crystallization in polyethylene solutions" *Polymer* **2006**;47:4897-4900.
68. Hoffman JD and Miller RL. "Kinetic of crystallization from the melt and chain folding in polyethylene fractions revisited: theory and experiment" *Polymer* **1997**;38:3151-3212.
69. Mandelkern L. Crystallization of polymers, 2 ed. New York: McGraw-Hill, 2004. pp.18-27.
70. Yang H, Bhimaraj P, Yang L, Siegel R, and Schadler L. "Crystal growth in alumina/poly(ethylene terephthalate) nanocomposite films" *Journal of Polymer Science Part B: Polymer Physics* **2007**;45:747-757.
71. Durmus A and Yalçinyuva T. "Effects of additives on non-isothermal crystallization kinetics and morphology of isotactic polypropylene" *Journal of Polymer Research* **2009**;16:489-498.
72. Page AJ and Sear RP. "Heterogeneous nucleation in and out of pores" *Physical Review Letters* **2006**;97:065701.
73. Li L, Li B, Hood MA, and Li CY. "Carbon nanotube induced polymer crystallization: The formation of nanohybrid shish-kebabs" *Polymer* **2009**;50:953-965.
74. Wittmann JC and Lotz B. "Epitaxial crystallization of polymers on organic and polymeric substrates" *Progress in Polymer Science* **1990**;15:909-948.
75. Wittmann JC and Lotz B. "Epitaxial crystallization of monoclinic and orthorhombic polyethylene phases" *Polymer* **1989**;30:27-34.
76. Mathieu C, Thierry A, Wittmann JC, and Lotz B. ""Multiple" nucleation of the (010) contact face of isotactic polypropylene, [alpha] phase" *Polymer* **2000**;41:7241-7253.
77. Mathieu C, Thierry A, Wittmann JC, and Lotz B. "Specificity and versatility of nucleating agents toward isotactic polypropylene crystal phases" *Journal of Polymer Science Part B: Polymer Physics* **2002**;40:2504-2515.
78. Stocker W, Schumacher M, Graff S, Thierry A, Wittmann J-C, and Lotz B. "Epitaxial crystallization and AFM investigation of a frustrated polymer structure: isotactic poly(propylene),  $\beta$ -Phase" *Macromolecules* **1998**;31:807-814.
79. Chayen NE, Saridakis E, and Sear RP. "Experiment and theory for heterogeneous nucleation of protein crystals in a porous medium" *PNAS* **2006**;103:597-601.
80. Shin K, Woo E, Jeong YG, Kim C, Huh J, and Kim K-W. "Crystalline structures, melting, and crystallization of linear polyethylene in cylindrical nanopores" *Macromolecules* **2007**;40:6617-6623.
81. Ha J-M, Wolf JH, Hillmyer MA, and Ward MD. "Polymorph selectivity under nanoscopic confinement" *Journal of the American Chemical Society* **2004**;126:3382-3383.
82. Frenkel D. "Physical chemistry: Seeds of phase change" *Nature* **2006**;443:641-641.

83. Cacciuto A, Auer S, and Frenkel D. "Onset of heterogeneous crystal nucleation in colloidal suspensions" *Nature* **2004**;428:404-406.
84. D'Haese M, Van Puyvelde P, and Langouche F. "Effect of particles on the flow-induced crystallization of polypropylene at processing speeds" *Macromolecules* **2010**;43:2933-2941.
85. Zhu P-W, Phillips AW, Edward G, and Nichols L. "Experimental observation of effects of seeds on polymer crystallization" *Physical Review E* **2009**;80:051801.
86. de-Gennes PG. "Coil-stretch transition of dilute flexible polymers under ultrahigh velocity gradients" *The Journal of Chemical Physics* **1974**;60:5030-5042.
87. Dukovski I and Muthukumar M. "Langevin dynamics simulations of early stage shish-kebab crystallization of polymers in extensional flow" *The Journal of Chemical Physics* **2003**;118:6648-6655.
88. de Gennes PG. "Reptation of a polymer chain in the presence of fixed obstacles " *The Journal of Chemical Physics* **1971**;55:572-579.
89. Doi M and Edwards SF. *The theory of polymer dynamics* Oxford Clarendon Press, 1986.
90. Milner ST and McLeish TCB. "Reptation and contour-length fluctuations in melts of linear polymers" *Physical Review Letters* **1998**;81:725-728.
91. Vega JF, Rastogi S, Peters GWM, and Meijer HEH. "Rheology and reptation of linear polymers. Ultrahigh molecular weight chain dynamics in the melt" *Journal of Rheology* **2004**;48:663-678.
92. Watanabe H. "Viscoelasticity and dynamics of entangled polymers" *Progress in Polymer Science* **1999**;24:1253-1403.
93. Doi M. "Explanation for the 3.4 power law of viscosity of polymeric liquids on the basis of the tube model" *Journal of Polymer Science: Polymer Letters Edition* **1981**;19:265-273.
94. Bent J, Hutchings LR, Richards RW, Gough T, Spares R, Coates PD, Grillo I, Harlen OG, Read DJ, Graham RS, Likhtman AE, Groves DJ, Nicholson TM, and McLeish TCB. "Neutron-mapping polymer flow: scattering, flow visualization, and molecular theory" *Science* **2003**;301:1691-1695.
95. Mead DW. "Component predictions and the relaxation spectrum of the double reptation mixing rule for polydisperse linear flexible polymers" *Journal of Rheology* **1996**;40:633.
96. Zamponi M, Wischniewski A, Monkenbusch M, Willner L, Richter D, Likhtman AE, Kali G, and Farago B. "Molecular observation of constraint release in polymer melts" *Physical Review Letters* **2006**;96:238302.
97. Zamponi M, Monkenbusch M, Willner L, Wischniewski A, Farago B, and Richter D. "Contour length fluctuations in polymer melts: A direct molecular proof " *Europhysics Letters* **2005**;72:1039.
98. Janeschitz-Kriegl H, Ratajski E, and Stadlbauer M. "Flow as an effective promotor of nucleation in polymer melts: a quantitative evaluation" *Rheologica Acta* **2003**;42:355-364.
99. Hsiao BS, Yang L, Somani RH, Avila-Orta CA, and Zhu L. "Unexpected shish-kebab structure in a sheared polyethylene melt" *Physical Review Letters* **2005**;94:117802.
100. Lieberwirth I, Loos J, Petermann J, and Keller A. "Observation of shish crystal growth into nondeformed melts" *Journal of Polymer Science Part B: Polymer Physics* **2000**;38:1183-1187.

101. Pennings AJ and Kiel AM. "Fractionation of polymers by crystallization from solution, III. On the morphology of fibrillar polyethylene crystals grown in solution" *Kolloid-Zeitschrift und Zeitschrift für Polymere* **1965**;205:160-162.
102. Pennings AJ, van der Mark JMAA, and Booij HC. "Hydrodynamically induced crystallization of polymers from solution" *Colloid & Polymer Science* **1969**;236:99-111.
103. Seki M, Thurman DW, Oberhauser JP, and Kornfield JA. "Shear-mediated crystallization of isotactic polypropylene: The role of long chain–long chain overlap" *Macromolecules* **2002**;35:2583-2594.
104. Heeley EL, Fernyhough CM, Graham RS, Olmsted PD, Inkson NJ, Embery J, Groves DJ, McLeish TCB, Morgovan AC, Meneau F, Bras W, and Ryan AJ. "Shear-induced crystallization in blends of model linear and long-chain branched hydrogenated polybutadienes" *Macromolecules* **2006**;39:5058-5071.
105. Hoffman JD. "Formation of polymer fibrils" *Polymer* **1979**;20:1070-1077.
106. Clark EJ and Hoffman JD. "Crystallization and fibril formation in polymers" *International Journal of Thermophysics* **1990**;11:225-237.
107. Janeschitz-Kriegl H, Ratajski E, and Wippel H. "The physics of athermal nuclei in polymer crystallization " *Colloid & Polymer Science* **1999**;277:217-226.
108. Zhu P-W and Edward G. "Morphological distributions in sheared isotactic polypropylene plates with different thicknesses: Studies of simultaneous WAXS and SAXS" *Journal of Materials Science* **2008**;43:6459-6467.
109. Somwangthanaroj A, Lee EC, and Solomon MJ. "Early stage quiescent and flow-induced crystallization of intercalated polypropylene nanocomposites by time-resolved light scattering" *Macromolecules* **2003**;36:2333-2342.
110. Rozanski A, Monasse B, Szkudlarek E, Pawlak A, Piorkowska E, Galeski A, and Haudin JM. "Shear-induced crystallization of isotactic polypropylene based nanocomposites with montmorillonite" *European Polymer Journal* **2009**;45:88-101.
111. Nowacki R, Monasse B, Piorkowska E, Galeski A, and Haudin JM. "Spherulite nucleation in isotactic polypropylene based nanocomposites with montmorillonite under shear" *Polymer* **2004**;45:4877-4892.
112. Jerschow P and Janeschitz-Kriegl H. "The role of long molecules and nucleating agents in shear induced crystallization of isotactic polypropylenes" *International Polymer Processing* **1997**;12:72-77.
113. Zhu P-W, Tung J, Phillips AW, and Edward G. "Morphological development of oriented isotactic polypropylene in the presence of a nucleating agent" *Macromolecules* **2006**;39:1821-1831.
114. Zhu P-W, Phillips AW, Tung J, and Edward G. "Orientation distribution of sheared isotactic polypropylene plates through thickness in the presence of sodium benzoate" *Journal of Applied Physics* **2005**;97:104908.
115. Patil N, Balzano L, Portale G, and Rastogi S. "A study on the chain–particle interaction and aspect ratio of nanoparticles on structure development of a linear polymer" *Macromolecules* **2010**;43:6749-6759.

116. Fu BX, Yang L, Somani RH, Zong SX, Hsiao BS, Phillips S, Blanski R, and Ruth P. "Crystallization studies of isotactic polypropylene containing nanostructured polyhedral oligomeric silsesquioxane molecules under quiescent and shear conditions" *Journal of Polymer Science Part B: Polymer Physics* **2001**;39:2727-2739.
117. Kellarakis A, Yoon K, Sics I, Somani RH, Chen X, Hsiao BS, and Chu B. "Shear-induced orientation and structure development in isotactic polypropylene melt containing modified carbon nanofibres" *Journal of Macromolecular Science, Part B: Physics* **2006**;45:247-261.
118. Hwang WR, Peters GWM, Hulsen MA, and Meijer HEH. "Modeling of flow-induced crystallization of particle-filled polymers" *Macromolecules* **2006**;39:8389-8398.
119. Harlen OG and Koch DL. "Simple shear flow of a suspension of fibres in a dilute polymer solution at high Deborah number" *Journal of Fluid Mechanics* **1993**;252:187-207.
120. Natta G and Corradini P. "Structure and properties of isotactic polypropylene " *Il Nuovo Cimento* **1960**;15:40-51.
121. Bruckner S and Meille SV. "Non-parallel chains in crystalline  $\gamma$ -isotactic polypropylene" *Nature* **1989**;340:455-457.
122. Lotz B and Wittmann JC. "The molecular origin of lamellar branching in the  $\alpha$  (monoclinic) form of isotactic polypropylene" *Journal of Polymer Science Part B: Polymer Physics* **1986**;24:1541-1558.
123. Padden FJ, Jr. and Keith HD. "Crystallization in thin films of isotactic polypropylene" *Journal of Applied Physics* **1966**;37:4013-4020.
124. Binsbergen FL and de Lange BGM. "Morphology of polypropylene crystallized from the melt" *Polymer* **1968**;9:23-40.
125. Weng J, Olley RH, Bassett DC, and Jääskeläinen P. "Changes in the melting behavior with the radial distance in isotactic polypropylene spherulites" *Journal of Polymer Science Part B: Polymer Physics* **2003**;41:2342-2354.
126. Janimak JJ, Cheng SZD, Zhang A, and Hsieh ET. "Isotacticity effect on crystallization and melting in polypropylene fractions: 3. Overall crystallization and melting behaviour" *Polymer* **1992**;33:728-735.
127. Weng J, Olley RH, Bassett DC, and Jääskeläinen P. "On morphology and multiple melting in polypropylene" *Journal of Macromolecular Science, Part B: Physics* **2002**;41:891-908.
128. Mezghani K, Campbell RA, and Phillips PJ. "Lamellar thickening and the equilibrium melting point of polypropylene" *Macromolecules* **1994**;27:997-1002.
129. Khoury F. "The spherulitic crystallization of isotactic polypropylene from solution: Evolution of monoclinic spherulites from dendritic chain-folded crystal precursors." *Journal of research of the National Bureau of Standards — A. Physics and Chemistry* **1966**;70A:29-60.
130. Wang X, Hou W, Zhou J, Li L, Li Y, and Chan C-M. "Melting behavior of lamellae of isotactic polypropylene studied using hot-stage atomic force microscopy " *Colloid & Polymer Science* **2007**;285:449-455.
131. Padden Jr FJ and Keith HD. "Mechanism for lamellar branching in isotactic polypropylene" *Journal of Applied Physics* **1973**;44:1217-1223.

132. Zeng W, Wang J, Feng Z, Dong J-Y, and Yan S. "Morphologies of long chain branched isotactic polypropylene crystallized from melt " *Colloid & Polymer Science* **2005**;284:322-326.
133. Fujiyama M and Wakino T. "Distribution of higher-order structures in injection-molded polypropylenes" *Journal of Applied Polymer Science* **1991**;43:57-81.
134. Varga J. "Supermolecular structure of isotactic polypropylene " *Journal of Materials Science* **1992**;27:2557-2579.
135. Lotz B, Fillon B, Thierry A, and Whittmann JC. "Low T<sub>c</sub> growth transitions in isotactic polypropylene:  $\beta$ -to- $\alpha$  and  $\alpha$ -to-smectic phases" *Polymer Bulletin* **1991**;25:101-105.
136. Lotz B. "Molecular aspects of structure and morphology of isotactic polypropylene" *Journal of Macromolecular Science, Part B: Physics* **2002**;B41:685-709.
137. Padden FJ and Keith HD. "Spherulitic crystallization in polypropylene." *Journal of Applied Physics* **1959**;30:1479-1484.
138. Yang J. "Origin of double melting peaks of  $\alpha$ -form isotactic polypropylene: Recrystallization and lamellar thickness hierarchy" *Journal of Applied Polymer Science* **2010**;118:1520-1526.
139. Turner-Jones A and Cobbold AJ. "The  $\beta$  crystalline form of isotactic polypropylene." *Journal of Polymer Science* **1968**;6:539-546.
140. Meille SV, Ferro DR, Brueckner S, Lovinger AJ, and Padden FJ. "Structure of  $\beta$ -isotactic polypropylene: A long-standing structural puzzle" *Macromolecules* **1994**;27:2615-2622.
141. Dorset DL, McCourt MP, Kopp S, Schumacher M, Okihara T, and Lotz B. "Isotactic polypropylene,  $\beta$ -phase: a study in frustration" *Polymer* **1998**;39:6331-6337.
142. Lovinger AJ, Chua JO, and Gryte CC. "Studies on the alpha and beta forms of isotactic polypropylene by crystallization in a temperature gradient" *Journal of Polymer Science Part B: Polymer Physics* **1977**;15:641-656.
143. Thomason JL and Van Rooyen AA. "Transcrystallized interphase in thermoplastic composites" *Journal of Materials Science* **1992**;27:897-907.
144. Somani RH, Hsiao BS, Nogales A, Fruitwala H, Srinivas S, and Tsou AH. "Structure development during shear flow induced crystallization of i-PP: In-situ wide-angle x-ray diffraction study" *Macromolecules* **2001**;34:5902-5909.
145. Sun X, Li H, Wang J, and Yan S. "Shear-induced interfacial structure of isotactic polypropylene (iPP) in iPP/Fiber composites" *Macromolecules* **2006**;39:8720-8726.
146. Varga J and Karger-Kocsis J. "Rules of supermolecular structure formation in sheared isotactic polypropylene melts" *Journal of Polymer Science Part B: Polymer Physics* **1996**;34:657-670.
147. Liu G, Zhu P, and Edward G. "Morphology distribution an processing history of injection moulded polypropylene" *Macromolecular Symposia* **2002**;185:327-340.
148. Huo H, Jiang S, and An L. "Oscillation effects on the crystallization behavior of iPP" *Polymer* **2005**;46:11112-11116.
149. Ma CG, Chen L, Xiong XM, Zhang JX, Rong MZ, and Zhang MQ. "Influence of oscillatory shear on crystallization of isotactic polypropylene studied by dynamic mechanical analysis" *Macromolecules* **2004**;37:8829-8831.

150. Zhi-Qiang S, Xiao-Nong C, Zhong-Zhen Y, and Liang Z. "Morphological distribution of polymeric nucleating agents in injection-molded isotactic polypropylene plates and its influence on nucleating efficiency" *Journal of Applied Polymer Science* **2009**;111:786-793.
151. Varga J. " $\beta$ -modification of isotactic polypropylene: preparation, structure, processing, properties, and application" *Journal of Macromolecular Science, Part B: Physics* **2002**;41:1121-1171.
152. Lotz B. " $\alpha$  and  $\beta$  phases of isotactic polypropylene: a case of growth kinetics 'phase reentrancy' in polymer crystallization" *Polymer* **1998**;39:4561-4567.
153. Li L and de Jeu WH. "Shear-induced smectic ordering and crystallisation of isotactic polypropylene" *Faraday Discussions* **2005**;128:299-319.
154. Addink EJ and Beintema J. "Polymorphism of crystalline polypropylene" *Polymer* **1961**;2:185-193.
155. Briickner S, Meille SV, Sozzani P, and Torri G. "Gamma isotactic polypropylene: An MAS  $^{13}\text{C}$  NMR study of a crystalline polymer with non-parallel chains" *Die Makromolekulare Chemie, Rapid Communications* **1990**;11:55-60.
156. van der Burgt FPTJ, Rastogi S, Chadwick JC, and Rieger B. "Influence of thermal treatments on the polymorphism in stereoirregular isotactic polypropylene: effect of stereo-defect distribution" *Journal of Macromolecular Science, Part B: Physics* **2002**;41:1091-1104.
157. De Rosa C, Auriemma F, Paolillo M, Resconi L, and Camurati I. "Crystallization behavior and mechanical properties of regiodefective, highly stereoregular isotactic polypropylene: Effect of regiodefects versus stereodefects and influence of the molecular mass" *Macromolecules* **2005**;38:9143-9154.
158. Mezghani K and Phillips PJ. "The  $\gamma$ -phase of high molecular weight isotactic polypropylene: III. The equilibrium melting point and the phase diagram" *Polymer* **1998**;39:3735-3744.
159. Mezghani K and Phillips PJ. "The  $\gamma$ -phase of high molecular weight isotactic polypropylene. II: The morphology of the  $\gamma$ -form crystallized at 200 MPa" *Polymer* **1997**;38:5725-5733.
160. Angeloz C, Fulchiron R, Douillard A, Chabert B, Fillit R, Vautrin A, and David L. "Crystallization of isotactic polypropylene under high pressure ( $\gamma$  Phase)" *Macromolecules* **2000**;33:4138-4145.
161. Auriemma F and De Rosa C. "Stretching isotactic polypropylene: From "cross- $\beta$ " to crosshatches, from  $\gamma$  form to  $\alpha$  form" *Macromolecules* **2006**;39:7635-7647.
162. Agarwal PK, Somani RH, Weng W, Mehta A, Yang L, Ran S, Liu L, and Hsiao BS. "Shear-Induced Crystallization in Novel Long Chain Branched Polypropylenes by in Situ Rheo-SAXS and -WAXD" *Macromolecules* **2003**;36:5226-5235.
163. Krache R, Benavente R, Lopez-Majada JM, Perena JM, Cerrada ML, and Perez E. "Competition between  $\alpha$ ,  $\beta$  and  $\gamma$  polymorphs in a beta-nucleated metallocenic isotactic polypropylene" *Macromolecules* **2007**;40:6871-6878.
164. Foresta T, Piccarolo S, and Goldbeck-Wood G. "Competition between  $\alpha$  and  $\gamma$  phases in isotactic polypropylene: effects of ethylene content and nucleating agents at different cooling rates" *Polymer* **2001**;42:1167-1176.

165. Hong SM and Seo Y. "Crystallization of a polypropylene terpolymer made by a Ziegler-Natta catalyst: Formation of  $\gamma$ -phase" *The Journal of Physical Chemistry B* **2007**;111:3571-3575.
166. Libster D, Aserin A, and Garti N. "Advanced nucleating agents for polypropylene" *Polymers for Advanced Technologies* **2007**;18:685-695.
167. Libster D, Aserin A, and Garti N. "A novel dispersion method comprising a nucleating agent solubilized in a microemulsion, in polymeric matrix: II. Microemulsion characterization" *Journal of Colloid and Interface Science* **2006**;302:322-329.
168. Libster D, Aserin A, and Garti N. "A novel dispersion method comprising a nucleating agent solubilized in a microemulsion, in polymeric matrix I. Dispersion method and polymer characterization" *Journal of Colloid and Interface Science* **2006**;299:172-181.
169. Thomann R, Wang C, Kressler J, and Mulhaupt R. "On the  $\gamma$ -Phase of Isotactic Polypropylene" *Macromolecules* **1996**;29:8425-8434.
170. Wang Z-G, Hsiao BS, Srinivas S, Brown GM, Tsou AH, Cheng SZD, and Stein RS. "Phase transformation in quenched mesomorphic isotactic polypropylene" *Polymer* **2001**;42:7561-7566.
171. Lotz B. "What can polymer crystal structure tell about polymer crystallization processes? " *The European Physical Journal E: Soft Matter* **2000**;3:185-194.
172. Kailas L, Vasilev C, Audinot J-N, Migeon H-N, and Hobbs JK. "A real-time study of homogeneous nucleation, growth, and phase transformations in nanodroplets of low molecular weight isotactic polypropylene using AFM" *Macromolecules* **2007**;40:7223-7230.
173. Jin Y, Hiltner A, Baer E, Masirek R, Piorkowska E, and Galeski A. "Formation and transformation of smectic polypropylene nanodroplets" *Journal of Polymer Science Part B: Polymer Physics* **2006**;44:1795-1803.
174. Yamada K, Hikosaka M, Toda A, Yamazaki S, and Tagashira K. "Molecular weight dependence of equilibrium melting temperature and lamellar thickening of isotactic polypropylene with high tacticity" *Journal of Macromolecular Science, Part B: Physics* **2003**;42:733-752.
175. Yadav YS and Jain PC. "Melting behaviour of isotactic polypropylene isothermally crystallized from the melt" *Polymer* **1986**;27:721-727.
176. Juhász P, Varga J, Belina K, and Marand H. "Determination of the equilibrium melting point of the  $\beta$ -form of polypropylene" *Journal of Thermal Analysis and Calorimetry* **2002**;69:561-574.
177. Phillips AW, Zhu P-W, and Edward G. "Simple shear deformation of polypropylene via the equal channel angular extrusion process" *Macromolecules* **2006**;39:5796-5803.
178. Yamada K, Hikosaka M, Toda A, Yamazaki S, and Tagashira K. "Equilibrium melting temperature of isotactic polypropylene with high tacticity. 2. Determination by optical microscopy" *Macromolecules* **2003**;36:4802-4812.
179. Shi G-Y, Huang B, and Zhang J-Y. "Enthalpy of fusion and equilibrium melting point of the  $\beta$ -form of polypropylene" *Die Makromolekulare Chemie, Rapid Communications* **1984**;5:573-578.
180. Petraccone V, Guerra G, De Rosa C, and Tuzi A. "Extrapolation to the equilibrium melting temperature for isotactic polypropylene" *Macromolecules* **1985**;18:813-814.
181. Li JX, Cheung WL, and Jia D. "A study on the heat of fusion of  $\beta$ -polypropylene" *Polymer* **1999**;40:1219-1222.



182. Shif G-Y, Zhang X-D, and Qiu Z-W. "Crystallization kinetics of  $\beta$ -phase poly(propylene)" *Die Makromolekulare Chemie* **1992**;193:583-591.
183. Mezghani K, Gasem Z, and Faheem M. Tensile properties of the  $\gamma$  phase of isotactic polypropylene with small particles. ANTEC, vol. 3. Chicago's Navy Pier, Chicago, Illinois: Society of Plastics Engineers, 2004. pp. 2884-2891.
184. Lezak E and Bartczak Z. "Plastic deformation behavior of  $\beta$  phase isotactic polypropylene in plane-strain compression at elevated temperatures" *Journal of Polymer Science Part B: Polymer Physics* **2008**;46:92-108.
185. Lezak E and Bartczak Z. "Plastic deformation of the  $\gamma$  phase isotactic polypropylene in plane strain compression at elevated temperatures" *Macromolecules* **2007**;40:4933-4941.
186. Agarwal PK, Somani RH, Weng W, Mehta A, Yang L, Ran S, Liu L, and Hsiao BS. "Shear-induced crystallization in novel long chain branched polypropylenes by in-situ rheo-SAXS and -WAXD" *Macromolecules* **2003**;36:5226-5235.
187. Chen HB, Karger-Kocsis J, Wu JS, and Varga J. "Fracture toughness of  $\alpha$ - and  $\beta$ -phase polypropylene homopolymers and random- and block-copolymers" *Polymer* **2002**;43:6505-6514.
188. Luo F, Geng C, Wang K, Deng H, Chen F, Fu Q, and Na B. "New understanding in tuning toughness of  $\beta$ -polypropylene: The role of  $\beta$ -nucleated crystalline morphology" *Macromolecules* **2009**;42:9325-9331.
189. Na B, Lv R, and Xu W. "Effect of network relaxation on void propagation and failure in isotactic polypropylene at large strain" *Journal of Applied Polymer Science* **2009**;113:4092-4099.
190. Asano T and Fujiwara Y. "Plastic deformation of oriented lamellae: 1. Cold rolling of  $\beta$ -phase isotactic polypropylene" *Polymer* **1978**;19:99-108.
191. Xu W, Martin DC, and Arruda EM. "Finite strain response, microstructural evolution and  $\beta \rightarrow \alpha$  phase transformation of crystalline isotactic polypropylene" *Polymer* **2005**;46:455-470.
192. Aboulfaraj M, Ulrich B, Dahoun A, and G'Sell C. "Spherulitic morphology of isotactic polypropylene investigated by scanning electron microscopy" *Polymer* **1993**;34:4817-4825.
193. Karger-Kocsis J and Varga J. "Effects of  $\beta \rightarrow \alpha$  transformation on the static and dynamic tensile behavior of isotactic polypropylene" *Journal of Applied Polymer Science* **1996**;62:291-300.
194. Lezak E, Bartczak Z, and Galeski A. "Plastic deformation behavior of  $\beta$ -phase isotactic polypropylene in plane-strain compression at room temperature" *Polymer* **2006**;47:8562-8574.
195. Jacoby P, Bersted BH, Kissel WJ, and Smith CE. "Studies on the  $\beta$ -crystalline form of isotactic polypropylene" *Journal of Polymer Science Part B: Polymer Physics* **1986**;24:461-491.
196. Karger-Kocsis J, Varga J, and Ehrenstein GW. "Comparison of the fracture and failure behavior of injection-molded  $\alpha$ - and  $\beta$ -polypropylene in high-speed three-point bending tests" *Journal of Applied Polymer Science* **1997**;64:2057-2066.
197. Byelov D, Panine P, and de Jeu WH. "Shear-induced smectic order in isotactic polypropylene revisited" *Macromolecules* **2007**;40:288-289.
198. Wecker SM, Davidson T, and Cohen JB. "A structural study of glassy polystyrene" *Journal of Materials Science* **1972**;7:1249-1259.

199. Natta G, Corradini P, and Bassi I. "Crystal structure of isotactic polystyrene" *Il Nuovo Cimento* **1960**;15:68-82.
200. Hyperform HPN-68. In: (NICNAS) NICNaAS, editor. Canberra, 2004.
201. Nagasawa S, Fujimori A, Masuko T, and Iguchi M. "Crystallisation of polypropylene containing nucleators" *Polymer* **2005**;46:5241-5250.
202. Wallwork KS, Kennedy BJ, and Wang D. "The high resolution Powder Diffraction Beamline for the Australian Synchrotron" *AIP Conference Proceedings* **2007**;879:879-882.
203. Kirby N, Boldeman JW, Gentle I, and Cookson D. "Conceptual design of the Small Angle Scattering Beamline at the Australian Synchrotron" *AIP Conference Proceedings* **2007**;879:887-889.
204. Turner-Jones A. "Development of the  $\gamma$ -crystal form in random copolymers of propylene and their analysis by dsc and x-ray methods" *Polymer* **1971**;12:487-508.
205. Alexander LE. X-Ray Diffraction Methods in Polymer Science. New York: Wiley-Interscience, 1976.
206. Wilchinsky ZW. "Measuremnt of orientation in polypropylene film " *Journal of Applied Physics* **1960**;31:1969-1972.
207. Nogales A, Hsiao BS, Somani RH, Srinivas S, Tsou AH, Balta-Calleja FJ, and Ezquerra TA. "Shear-induced crystallization of isotactic polypropylene with different molecular weight distributions: in situ small- and wide-angle X-ray scattering studies" *Polymer* **2001**;42:5247-5256.
208. Somani RH, Sics I, and Hsiao BS. "Thermal stability of shear-induced precursor structures in isotactic polypropylene by rheo-X-ray techniques with couette flow geometry" *Journal of Polymer Science Part B: Polymer Physics* **2006**;44:3553-3570.
209. Fillon B, Lotz B, Thierry A, and Wittmann JC. "Self-nucleation and enhanced nucleation of polymers. Definition of a convenient calorimetric efficiency scale and evaluation of nucleating additives in isotactic polypropylene (alpha phase)" *Journal of Polymer Science Part B: Polymer Physics* **1993**;31:1395-1405.
210. Fillon B, Wittmann JC, Lotz B, and Thierry A. "Self-nucleation and recrystallization of isotactic polypropylene" *Journal of Polymer Science Part B: Polymer Physics* **2003**;31:1383-1393.
211. Olley RH, Hodge AM, and Bassett DC. "A permanganic etchant for polyolefines" *Journal of Polymer Science Part B: Polymer Physics* **1979**;17:627.
212. Olley RH and Basset DC. "An improved permanganic etchant for polyolefines" *Polymer Communications* **1982**;23:1707-1710.
213. Park J, Eom K, Kwon O, and Woo S. "Chemical etching technique for the investigation of melt-crystallized Isotactic polypropylene spherulite and lamellar morphology by scanning electron microscopy" *Microscopy and Microanalysis* **2001**;7:276-286.
214. Phillips AW, Hadinata C, Zhu P-W, and Edward G. Thermal stability of oriented Lamellae in sheared Isotactic polypropylene. PPS-25. Goa, India 2008. pp. 1-8.
215. Phillips AW, Zhu P-W, Hadinata C, and Edward G. "Crystallization and melting of oriented parent–daughter lamellae in sheared isotactic poly(propylene)" *Australian Journal of Chemistry* **2010**;63:1179-1188.

216. Paukkeri R and Lehtinen A. "Thermal behaviour of polypropylene fractions: 2. The multiple melting peaks" *Polymer* **1993**;34:4083-4088.
217. Gedde UW. Polymer Physics 1st ed ed. London: Chapman & Hall, 1995. pp.144.
218. Viana JC, Cunha AM, and Billon N. "The Thermomechanical environment and the microstructure of an injection moulded polypropylene copolymer" *Polymer* **2002**;43:4185-4196.
219. Olley RH and Basset DC. "On the development of polypropylene spherulites" *Polymer* **1989**;30:399.
220. Kakudu M and Kasai N. X-ray Diffraction by Polymers. Amsterdam: Elsevier 1972. pp.231.
221. Dean DM, Rebenfeld L, Register RA, and Hsiao BS. "Matrix molecular orientation in fibre-reinforced polypropylene composites " *Journal of Materials Science* **1998**;33:4797-4812.
222. Mubarak Y, Harkin-Jones EMA, Martin PJ, and Ahmad M. "Modeling of non-isothermal crystallization kinetics of isotactic polypropylene" *Polymer* **2001**;42:3171-3182.
223. Xu JT, Ryan AJ, Mai SM, Yuan JJ, and Cheng SY. "Diffusion control of homogeneous crystallization in nanoconfined domains of block copolymers" *Journal of Macromolecular Science, Part B: Physics* **2005**;43:685-694.
224. Zhang Z, Wu S, Ren M, and Xiao C. "Model of cold crystallization of uniaxially oriented poly(ethylene terephthalate) fibers" *Polymer* **2004**;45:4361-4365.
225. Somani RH, Yang L, and Hsiao BS. "Precursors of primary nucleation induced by flow in isotactic polypropylene" *Physica A: Statistical Mechanics and its Applications* **2002**;304:145-157.
226. Waddon AJ, Hill MJ, Keller A, and Blundell DJ. "On the crystal texture of linear polyaryls (PEEK, PEK and PPS)" *Journal of Materials Science Letters* **1987**;22:1773-1784.
227. Schultz JM. "Confinement orientation" *Journal of Polymer Science Part B: Polymer Physics* **1992**;30:785-786.
228. Scudla J, Raab M, Eichhorn K-J, and Strachota A. "Formation and transformation of hierarchical structure of  $\beta$ -nucleated polypropylene characterized by X-ray diffraction, differential scanning calorimetry and scanning electron microscopy" *Polymer* **2003**;44:4655-4664.
229. Bai H, Wang Y, Song B, Li Y, and Liu L. "Detecting crystallization structure evolution of polypropylene injection-molded bar induced by nucleating agent" *Polymer Engineering & Science* **2008**;48:1532-1541.
230. Guerra G, Petraccone V, Corradini P, Rosa CD, Napolitano R, and Pirozzi B. "Crystalline order and melting behavior of isotactic polypropylene (alpha form)" *Journal of Polymer Science Part B: Polymer Physics* **1984**;22:1029-1039.
231. Mai K, Wang K, and Zeng H. "Multiple melting behavior of nucleated polypropylene" *Journal of Applied Polymer Science* **2003**;88:1608-1611.
232. Coccorullo I, Pantani R, and Titomanlio G. "Spherulitic nucleation and growth rates in an iPP under continuous shear flow" *Macromolecules* **2008**;41:9214-9223.
233. Watanabe K, Okada K, Toda A, Yamazaki S, Taniguchi T, Koyama K, Yamada K, and Hikosaka M. "Acceleration mechanism of growth rates under shear flow due to the oriented melt: The novel morphology of spiral crystal (spiralite)" *Macromolecules* **2006**;39:1515-1524.

234. Khanna YP. "Rheological mechanism and overview of nucleated crystallization kinetics" *Macromolecules* **1993**;26:3639-3643.
235. Katada K. "Electron diffraction study on thin films of polymers of p-halogeno-styrene" *Acta Crystallographica* **1963**;16:290-301.
236. Yeh GSY. "Order in amorphous polystyrenes as revealed by electron diffraction and diffraction microscopy" *Journal of Macromolecular Science, Part B: Physics* **1972**;6:451 - 463.
237. Schubach HR, Nagy E, and Heise B. "Short range order of amorphous polymers derived by WAXS" *Colloid & Polymer Science* **1981**;259:789-796.
238. Adams R, Balyuzi HHM, and Burge RE. "The structure of amorphous polystyrene by X-ray scattering and simple conformational analysis" *Journal of Materials Science* **1978**;13:391-401.
239. Yoon DY, Sundararajan PR, and Flory PJ. "Conformational characteristics of polystyrene" *Macromolecules* **1975**;8:776-783.
240. Mitchell GR and Windle AH. "Structure of polystyrene glasses" *Polymer* **1984**;25:906-920.
241. Zhu P-W and Edward G. "Distribution of shish-kebab structure of isotactic polypropylene under shear in the presence of nucleating agent" *Macromolecules* **2004**;37:2658-2660.
242. Phillips AW, Zhu P-W, and Edward G. "Polystyrene as a versatile nucleating agent for polypropylene" *Polymer* **2010**;51:1599-1607.
243. Liu T and Petermann J. "Multiple melting behavior in isothermally cold-crystallized isotactic polystyrene" *Polymer* **2001**;42:6453-6461.
244. Hui Xu B, Ince S, and Cebe P. "Development of the crystallinity and rigid amorphous fraction in cold-crystallized isotactic polystyrene" *Journal of Polymer Science Part B: Polymer Physics* **2003**;41:3026-3036.
245. Alfonso GC and Ziabicki A. "Memory effects in isothermal crystallization II. Isotactic polypropylene" *Colloid & Polymer Science* **1995**;273:317-323.
246. Zhao S, Cai Z, and Xin Z. "A highly active novel  $\beta$ -nucleating agent for isotactic polypropylene" *Polymer* **2008**;49:2745-2754.
247. Woo E, Huh J, Jeong YG, and Shin K. "From homogeneous to heterogeneous nucleation of chain molecules under nanoscopic cylindrical confinement" *Physical Review Letters* **2007**;98:136103.
248. Vleeshouwers S. "Simultaneous in-situ WAXS/SAXS and d.s.c. study of the recrystallization and melting behaviour of the  $\alpha$  and  $\beta$  form of iPP" *Polymer* **1997**;38:3213-3221.
249. Cho K, Saheb DN, Choi J, and Yang H. "Real time in situ X-ray diffraction studies on the melting memory effect in the crystallization of  $\beta$ -isotactic polypropylene" *Polymer* **2002**;43:1407-1416.
250. Barnes HA. "A review of the rheology of filled viscoelastic systems" *Rheology Reviews* **2003**:1-39.
251. Chen Y-H, Mao Y-M, Li Z-M, and Hsiao BS. "Competitive growth of  $\alpha$ - and  $\beta$ -crystals in  $\beta$ -nucleated isotactic polypropylene under shear flow" *Macromolecules* **2010**;43:6760-6771.
252. Balzano L, Rastogi S, and Peters GWM. "Crystallization and precursors during fast short-term shear" *Macromolecules* **2009**;42:2088-2092.

253. Australian\_Standard. Methods for the Determination of Grain Size in Metals. vol. AS 1733-1976, 1976.
254. Dean DM and Register RA. "Oriented  $\gamma$ -isotactic polypropylene crystallized at atmospheric pressure" *Journal of Polymer Science Part B: Polymer Physics* **1998**;36:2821-2827.
255. Auriemma F, Rosa CD, and Corradi M. "Stereoblock polypropylene as a prototype example of elasticity via a flip-flop reorientation of crystals in a compliant matrix" *Advanced Materials* **2007**;19:871-874.
256. Guinier A. Small-angle scattering of X-rays. New York: Wiley, 1955.
257. Keum JK, Zuo F, and Hsiao BS. "Formation and stability of shear-induced shish-kebab structure in highly entangled melts of UHMWPE/HDPE blends" *Macromolecules* **2008**;41:4766-4776.
258. Zuo F, Keum JK, Yang L, Somani RH, and Hsiao BS. "Thermal stability of shear-induced shish-kebab precursor structure from high molecular weight polyethylene chains" *Macromolecules* **2006**;39:2209-2218.
259. Balzano L, Rastogi S, and Peters GWM. "Flow induced crystallization in isotactic polypropylene-1,3:2,4-Bis(3,4-dimethylbenzylidene)sorbitol blends: Implications on morphology of shear and phase separation" *Macromolecules* **2007**;41:399-408.
260. Nogales A and Mitchell GR. "Development of highly oriented polymer crystals from row assemblies" *Polymer* **2005**;46:5615-5620.
261. Kalay G, Zhong Z, Allan P, and Bevis MJ. "The occurrence of the  $\gamma$ -phase in injection moulded polypropylene in relation to the processing conditions" *Polymer* **1996**;37:2077-2085.
262. Kalay G and Bevis MJ. "Processing and physical property relationships in injection-molded isotactic polypropylene. 2. Morphology and crystallinity" *Journal of Polymer Science Part B: Polymer Physics* **1998**;35:265-291.
263. Balzano L, Kukalyekar N, Rastogi S, Peters GWM, and Chadwick JC. "Crystallization and dissolution of flow-induced precursors" *Physical Review Letters* **2008**;100:048302.
264. Phillips AW, Bhatia A, Zhu P-W, and Edward G. "Shish formation and relaxation in sheared isotactic polypropylene containing nucleating particles" *Macromolecules* **2011**;doi: 10.1021/ma200040s.
265. Phillips AW, Zhu P-W, and Edward G. Formation of shear-induced precursors in iPP containing nucleating agents Polymer Processing Society 26th Annual Meeting. Banff, Canada, 2010.
266. Brumberger H. Modern aspects of small-angle scattering. London: Kluwer Academic Publishers, 1993.
267. Hernández JJ, García-Gutiérrez MC, Nogales A, Rueda DR, and Ezquerro TA. "Small-angle X-ray scattering of single-wall carbon nanotubes dispersed in molten poly(ethylene terephthalate)" *Composites Science and Technology* **2006**;66:2629-2632.
268. Perret R and Ruland W. "Single and multiple X-ray small-angle scattering of carbon fibres" *Journal of Applied Crystallography* **1969**;2:209-218.
269. Geng Y, Wang G, Cong Y, Bai L, Li L, and Yang C. "Shear-induced nucleation and growth of long helices in supercooled isotactic polypropylene" *Macromolecules* **2009**;42:4751-4757.

270. Zhu X, Yan D, Yao H, and Zhu P. "In situ FTIR spectroscopic study of the regularity bands and partial-order melts of isotactic poly(propylene)" *Macromolecular Rapid Communications* **2000**;21:354-357.
271. Jeffery GB. "The motion of ellipsoidal particles immersed in a viscous fluid" *Royal Society of London Proceedings Series A* **1922**;102:161-179.
272. Gunes DZ, Scirocco R, Mewis J, and Vermant J. "Flow-induced orientation of non-spherical particles: Effect of aspect ratio and medium rheology" *Journal of Non-Newtonian Fluid Mechanics* **2008**;155:39-50.
273. Hobbie EK, Wang H, Kim H, Lin-Gibson S, and Grulke EA. "Orientation of carbon nanotubes in a sheared polymer melt" *Physics of Fluids* **2003**;15:1196.
274. Hinch EJ and Leal LG. "The effect of Brownian motion on the rheological properties of a suspension of non-spherical particles" *Journal of Fluid Mechanics* **1972**;52:683-712.
275. Lin J and Liang X. "A review of research on cylindrical particulate flows" *International Journal of Multiphase Flow* **2010**;36:93-99.
276. Phillips RJ and Talini L. "Chaining of weakly interacting particles suspended in viscoelastic fluids" *Journal of Non-Newtonian Fluid Mechanics* **2007**;147:175-188.



## **Appendix 1**

### **Matrix material information**

#### **Appendix 1A**

Borealis HD601CF data sheet

04/03/2009 Ed. 1.

**Pages 296-298**

#### **Appendix 1B**

Analysis of iPP matrix material, Borealis HD601CF, by Polymer Standards Services (PSS)

Report PSS#110405.

**Pages 299-302**





# Polypropylene HD601CF

## Description

HD601CF is a homopolymer film resin, suitable for the manufacturing of unoriented film on chill roll process.

## Applications

HD601CF is recommended for

Metallisable Cast film  
Inner layer in co extrusion  
Textile packaging film  
Food packaging  
Lamination films

Stationary films  
Blending with formulated grades for additive adjustments  
Manufacturing of unoriented film for producers who wish to add their own slip/antiblock/antistatic additive package

## Additives

HD601CF Free of slip and antiblock and without CaStearate.

## Special features

High gloss  
Low haze  
Excellent processability

Good mechanical properties  
Heat sterilisable  
Excellent gauge control

## Physical Properties

Property	Typical Value	Test Method
Data should not be used for specification work		
Density	900 - 910 kg/m <sup>3</sup>	ISO 1183
Melt Flow Rate (230 °C/2,16 kg)	8 g/10min	ISO 1133
Flexural Modulus <sup>1</sup>	1.450 MPa	ISO 178
Melting temperature (DSC)	162 - 166 °C	ISO 3146
Vicat softening temperature A50, (10 N) <sup>1</sup>	154 °C	ISO 306

<sup>1</sup> Measured on injection moulded specimens, conditioned at 23 °C and 50 % relative humidity.

Borealis AG | Wagramerstrasse 17-19 | 1220 Vienna | Austria  
Telephone +43 1 224 00 0 | Fax +43 1 22 400 333  
FN 269858a | CCC Commercial Court of Vienna | Website [www.borealisgroup.com](http://www.borealisgroup.com)





# Polypropylene HD601CF

## Film Properties

Property		Typical Value	Test Method
Data should not be used for specification work			
Instrumented puncture test	Total Penetration Energy	12 J	ISO 7765-2
	Force	1000 N	
Haze		< 2 %	ASTM D 1003
Gloss at 20 degree (of arc) <sup>1</sup>		> 120 %	ASTM D 2457
Tensile Strain at Break	MD	500 - 700 %	ISO 527-3
	/TD		
Tensile Strength	MD	30 - 50 MPa	ISO 527-3
Tensile Strength	TD	25 - 45 MPa	ISO 527-3
Tensile Modulus	MD	650 - 750 MPa	ISO 527-3
	/TD		
Coefficient of friction (Film/Film)		> 0,7	ISO 8295
Metal Adhesion (Tape Test)		Excellent	Borealis Method

<sup>1</sup> Specific film values evaluated on chill roll films, produced with Borealis internal standard conditions with a thickness of 50 µm. When compared to films which were produced under other conditions, it should be taken into account that the film properties are strongly dependent on the processing conditions.

## Storage

**HD601CF** should be stored in dry conditions at temperatures below 50°C and protected from UV-light. Improper storage can initiate degradation, which results in odour generation and colour changes and can have negative effects on the physical properties of this product.

## Safety

The product is not classified as a dangerous preparation.

Please see our "Safety data sheet" / "Product safety information sheet" for details on various aspects of safety of the products. For more information, contact your Borealis representative.

## Recycling

The product is suitable for recycling using modern methods of shredding and cleaning. In-house production waste should be kept clean to facilitate direct recycling.

## Related Documents

The following related documents are available on request, and represent various aspects on the usability, safety, recovery and disposal of the product.

"Safety data sheet" / "Product safety information sheet"

Statement on chemicals, regulations and standards

Statement on compliance to food contact regulations

Statement on compliance to regulations on medical use

Borealis AG | Wagramerstrasse 17-19 | 1220 Vienna | Austria  
Telephone +43 1 224 00 0 | Fax +43 1 22 400 333  
FN 269858a | CCC Commercial Court of Vienna | Website [www.borealisgroup.com](http://www.borealisgroup.com)



## Polypropylene HD601CF

### Disclaimer

**The product(s) mentioned herein are not intended to be used for medical, pharmaceutical or healthcare applications and we do not support their use for such applications.**

To the best of our knowledge, the information contained herein is accurate and reliable as of the date of publication, however we do not assume any liability whatsoever for the accuracy and completeness of such information.

**Borealis makes no warranties which extend beyond the description contained herein. Nothing herein shall constitute any warranty of merchantability or fitness for a particular purpose.**

**It is the customer's responsibility to inspect and test our products in order to satisfy itself as to the suitability of the products for the customer's particular purpose. The customer is responsible for the appropriate, safe and legal use, processing and handling of our products.**

No liability can be accepted in respect of the use of Borealis' products in conjunction with other materials. The information contained herein relates exclusively to our products when not used in conjunction with any third party materials.

Borealis AG | Wagramerstrasse 17-19 | 1220 Vienna | Austria  
Telephone +43 1 224 00 0 | Fax +43 1 22 400 333  
FN 269858a | CCC Commercial Court of Vienna | Website [www.borealisgroup.com](http://www.borealisgroup.com)



PSS Polymer Standards Service GmbH - Postfach 3368 - D-55023 Mainz

Monash University  
Dept. Of Material Engineering  
Mr. Andrew Phillips  
Wellington Road  
AUS-Clayton VIC 3800

E-mail: pmontag@polymer.de  
Fon: 06131-96239-53  
Telefax: 06131-96239-11

Mainz, 11.03.11

### Analysis report

TASK:SEC-Analysis of 1 polymer sample to determine molmass distribution

sample 1: 805-0001

PSS#110405

#### Experimental:

##### HT-SEC:

Solvent: 1,2,4-Trichlorobenzene  
Precolumn: PSS Polefin 10µm, 1000 Å, ID 8.0 mm x 50 mm  
Columns: PSS Polefin 10µm, 100 Å, ID 8.0 mm x 300 mm  
PSS Polefin 10µm, 1000 Å, ID 8.0 mm x 300 mm  
PSS Polefin 10µm, 105 Å, ID 8.0 mm x 300 mm  
PSS Polefin 10µm, 106 Å, ID 8.0 mm x 300 mm  
Pump: PolymerChar GPC-IR  
Flowrate: 1.0 ml/min  
Temperature: 150°C  
Sample concentration: see inject  
Injectionssystem: PolymerChar GPC-IR with 200 µl injectionvolumen  
Detectors: PolymerChar GPC-IR IR-4 detector with  
CH2- valence vibrationdetection  
calculation: PSS-WinGPC Unity Version 7.20



11/03/2011

**PSS** Polymer Standards Service GmbH  
In der Dalheimer Wiese 5 55120 Mainz, Germany  
Tel.: +49 6131 96239-0 Fax: +49 6131 96239-11  
Email: info@polymer.de www.polymer.de

**PSS** Polymer Standards Service USA, Inc  
43 Jefferson Blvd. Suite 3 Warwick, RI 02888 USA  
Phone: +1 401 780-8884 Fax: +1 401 780-8824  
Email: pssusa@pssgpcshop.com www.pssgpcshop.com  
Seite 1 von 4

### Sample preparation

The samples were weighted exactly and 9 ml 1,2,4-Trichlorobenzene were added. After 1 hour dissolving at 160°C the samples were injected with 200 µl into the SEC. The samples were filtered automatically with the built-in SEC-filtering system of the PolymerChar instrument.

### Calibration and calculation

A calibration curve with polystyrene standards were measured within the separation range of the column set. The calculation of molmass and -distribution was made by the slice to slice-method based on the PS-calibration curve. Calibration was classical. Samples were injected twice, the results for each single injection were similar.

### Results

Following table summarizes the results

sample	Mn (g/mol)	Mw (g/mol)	D
805-0001	91500	427000	4.7

Remark: Results are only valid for the analyzed samples

We hope, our results will help you.

If you have any question, do not hesitate to contact us.

With kindly regards



Dr. Peter Montag  
 PSS POLYMER STANDARDS SERVICE GMBH



11/03/2011

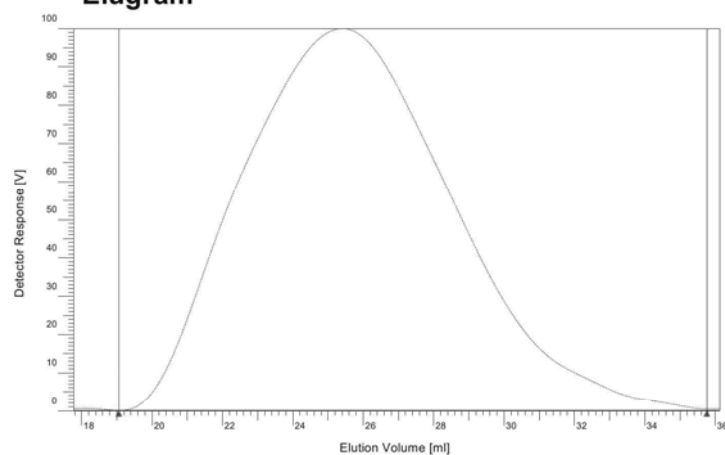
**PSS Polymer Standards Service GmbH**  
 In der Dalheimer Wiese 5 55120 Mainz, Germany  
 Tel.: +49 6131 96239-0 Fax: +49 6131 96239-11  
 Email: info@polymer.de www.polymer.de

**PSS Polymer Standards Service USA, Inc**  
 43 Jefferson Blvd. Suite 3 Warwick, RI 02888 USA  
 Phone: +1 401 780-8884 Fax: +1 401 780-8824  
 Email: pssusa@pssgpcshop.com www.pssgpcshop.com  
 Seite 2 von 4

# WINGPC Analysis Report

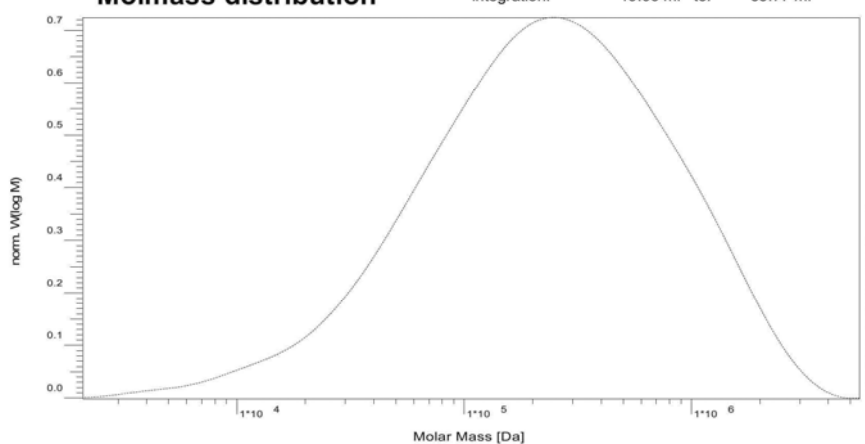
sample name **805-0001, 110405**

## Elugram



## Molmass distribution

baseline: 17.78 ml to: 36.14 ml  
integration: 19.06 ml to: 35.77 ml



Detector	Mn (D)	Mw (D)	Mz (D)	D (Mw/Mn)	Mp (D)	Area (ml*V)	w. %: 500 - 1000 D	w. %: < 500 D
GPC-IR4-CH2	91500	427000	1060000	4.66	257000	0.8131	0.00	0.00

## Method information

calibration type: Conventional

Project:	W:\GPC_DATEN\AN\LC\serv_11\serv11_1a.LD	Injection:	Wednesday 09/03/11 15:01:24
Calibration:	ps_uni_15_02_11_1_Injekt.CAL	Calibration fit:	PSS Poly 3
Int. Standard:	System	Temperature:	150.0 °C
Int. Standard - K:	46.57 ml	Int. Standard - M:	46.59 ml
Sample concentration:	2.41 g/l	Injection volume:	200 µl
Eluent:	1,2,4-Trichlorbenzol	Flowrate:	1.00 ml/min
Columns:	Polefin 1A2/guard + Polefin 1A3 + Polefin 1A5 + Polefin 1A6		
GPC instrument:	PG15 - HT-GPC-IR	Operator:	pm

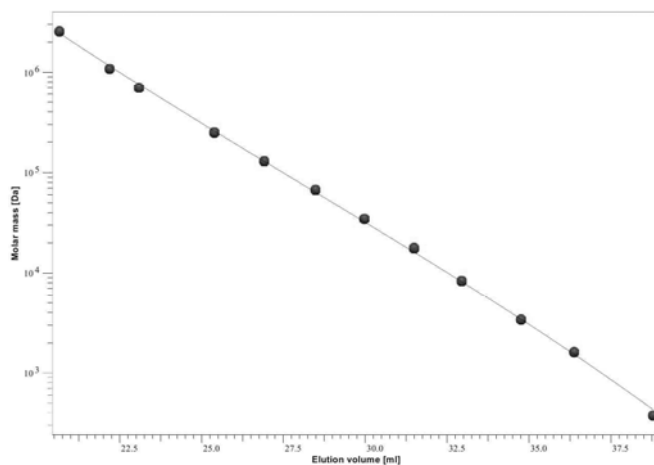
11/03/2011

Seite 3 von 4

# WINGPC Calibration

**Comment:** univ. Calibration with PS-readyCal

**Filename:** W:\GPC\_DATEN\ANL\serv\_11\Cal\_11\PG\_15\ps\_uni\_15\_02\_11\_1\_Injekt.CAL



## Calibration Parameters:

Columns: polefin, 10  $\mu$ m, guard, 100, 100  
 Mark-Houwink a: 0.650  
 Mark-Houwink k: 0.0255  
 Int. Standard: System  
 Vp int. Standard: 46.57 ml  
 Fit: PSS Poly 3  
 Operator: pm

Elutionvolume [ml]	Molar Mass Mp [D]	Sample Name	Slope	Deviation [%]
20.6550	2570000	PSS PS ReadyCal green	-0.2170	-3.8600
22.1917	1090000	PSS PS ReadyCal red	-0.2094	6.6653
23.0933	702000	PSS PS ReadyCal white	-0.2057	7.6532
25.3883	250000	PSS PS ReadyCal green	-0.1991	3.9120
26.9083	130000	PSS PS ReadyCal red	-0.1968	-0.0027
28.4767	67500	PSS PS ReadyCal white	-0.1963	-5.2425
29.9717	34800	PSS PS ReadyCal green	-0.1974	-6.6215
31.4917	17800	PSS PS ReadyCal red	-0.2003	-8.9374
32.9433	8400	PSS PS ReadyCal white	-0.2046	-1.8797
34.7550	3420	PSS PS ReadyCal green	-0.2122	1.1068
36.3750	1620	PSS PS ReadyCal red	-0.2210	-4.8025
38.7933	376	PSS PS ReadyCal white	-0.2378	14.5584

## **Appendix 2**

### **Published research**

#### **Appendix 2A**

AW Phillips, A Bhatia PW Zhu, GH Edward 2011. Shish formation and relaxation in sheared isotactic polypropylene containing nucleating particles, *Macromolecules*: doi: 10.1021/ma200040s.

**Pages 305-316**

#### **Appendix 2B**

AW Phillips, PW Zhu, GH Edward 2010. Polystyrene as a versatile nucleating agent for polypropylene, *Polymer* 51:1599.

**Pages 317-325**

#### **Appendix 2C**

AW Phillips, PW Zhu, C Hadinata, GH Edward. Crystallisation and melting of oriented parent daughter lamellar in sheared isotactic polypropylene 2010, *Australian Journal of Chemistry* 63:1179.

**Pages 327-336**

#### **Appendix 2D**

AW Phillips, PW Zhu, GH Edward 2010. Formation of shear-induced precursors in isotactic polypropylene containing nucleating agents, 26th annual meeting of the Polymer Processing Society, Banff, Canada, GO8-446, 1-5.

**Pages 337-341**

#### **Appendix 2E**

AW Phillips, PW Zhu, C Hadinata, G Edward 2009. Lamellar branching in isotactic polypropylene: An in-situ time resolved wide angle x-ray scattering study. 25th annual meeting of the Polymer Processing Society, Goa, India, GS-III: OP2, 1-8.

**Pages 343-350**



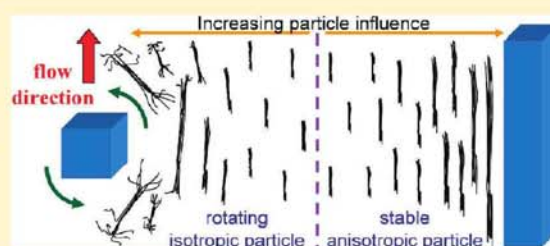


# Shish Formation and Relaxation in Sheared Isotactic Polypropylene Containing Nucleating Particles

Andrew W. Phillips,\* Amita Bhatia, Peng-wei Zhu, and Graham Edward

Department of Materials Engineering, Co-operative Research Centre for Polymers, Monash University, Clayton VIC 3800, Australia

**ABSTRACT:** The formation and relaxation of shish in molten isotactic polypropylene (iPP) and two samples containing different commercial nucleating particles was studied during and after continuous shear flow. In-situ measurements of the shish were made by simultaneous wide- and small-angle X-ray scattering (rheo-SAXS/WAXS) using synchrotron radiation. In the SAXS patterns, sharp meridional reflections were observed in all three samples during the initial stages of shear flow. Their presence indicates that shish form in discrete steps, by the aggregation of pointlike nuclei into oriented threads. Compared to pure iPP, the addition of both nucleants increased the amount and the dimensions of shish formed. However, the shish also relaxed faster in the presence of both nucleated materials. This behavior was attributed to the particles inducing lower molecular weight chains to participate in shish formation. The particle aspect ratio was observed to greatly influence shish formation. This is explained by modification of the local strain environment near the surface of the different shaped particles.



## 1. INTRODUCTION

Thermoplastic polyolefins such as isotactic polypropylene (iPP) and polyethylene (PE) are typically processed into their final forms by injection molding or extrusion technologies. If the flow intensity in these processes is sufficient, a highly anisotropic crystalline architecture termed shish-kebabs can form,<sup>1–8</sup> which can substantially influence the final physical properties of the component.<sup>9,10</sup> A highly oriented threadlike core composed of extended chains (shish) is considered to form first, which then provides a template for the formation and growth of oriented chain-folded lamellae (kebabs). Accordingly, the formation of shish is one of the key components to understanding morphology development under flow conditions.

For a given polymer, a critical flow intensity is necessary to form shish. However, the specific flow conditions responsible for this transition have only recently been identified.<sup>3,4</sup> The shear rate needs to be larger than the inverse Rouse time of the longest chains (i.e.,  $\dot{\gamma} > 1/\tau_r$ ) such that the chains can become extended by the flow. Furthermore, a critical amount of mechanical work is also necessary to allow the extended chains to come together and form a stable shish entity. Although the specific flow conditions for shish formation have been identified, the mechanism responsible for the initial shish formation is still under debate.<sup>1,5,6,11–22</sup>

Recent advances in wide- and small-angle X-ray scattering (WAXS/SAXS) techniques have allowed shish formation and relaxation to be probed in situ after controlled shear treatments. Balzano et al.<sup>23</sup> investigated a high-density polyethylene (HDPE), which had been specially prepared to have a bimodal molecular weight distribution, and found shish were able to be formed near to and even slightly above the equilibrium melting temperature of the unconstrained extended chain crystal. It was considered

that to form the shish required the stretch of the longest chains in the molecular weight distribution. A similar conclusion was drawn by Keum et al.,<sup>24</sup> who investigated shish formation and relaxation in model blends of ultrahigh molecular weight polyethylene (UHMWPE) in HDPE. In addition, Keum et al. showed that shish could grow by an autocatalytic process after the shear flow had stopped. Similar autocatalytic growth of shish was also recently observed by Patil et al.<sup>25</sup> in a broad molecular weight PE. Nevertheless, comparable studies have yet to be performed for other commercially important semicrystalline polymers such as iPP.

The crystallization of polymers is complicated by the inclusion of a wide range of particulate additives in polymer formulations such as nucleating agents, colorants, and reinforcing agents. Under quiescent conditions (i.e., without concurrent deformation) these heterogeneous particles can act as nucleation sites, enhancing crystal nucleation and thereby influencing crystallization kinetics and the final morphology of the polymer. The number of active heterogeneous nucleation sites is strongly related to factors that influence the particle surface area available for nucleation. The most common factors affecting this are the concentration and dispersion of particles in the polymer matrix. Yet many other particle characteristics have also been implicated in influencing the nucleation of polymers under quiescent conditions such as epitaxy,<sup>26,27</sup> particle size,<sup>28</sup> particle curvature,<sup>29,30</sup> and porosity.<sup>31</sup>

Foreign particles can also dramatically alter the crystallization kinetics and the development of morphology under flow conditions.

Received: January 8, 2011

Revised: February 27, 2011



The combined effects of shear and the addition of particles have been suggested to yield a synergistic increase in the number of active nuclei, raising crystallization rates further than their individual contribution.<sup>32–37</sup> Furthermore, the addition of particles has been shown to decrease the shear intensity required to form the shish-kebab structure.<sup>15,16,25,28,35,38–43</sup> A number of particle characteristics have also been suggested to influence the formation of shear-induced nuclei. Zhu and coauthors<sup>40,41</sup> suggested the surface curvature of the particles may influence the stability of shish forming on the surface of the particle. D'Haese et al.<sup>28</sup> investigated the influence of particle size under a wide range of shear rates and found that the critical shear rate for shish formation decreased with increasing particle size. However, the influence of the nucleation efficiency of the particles, which also increased with particle size, could not be entirely ruled out. Recently, Patil et al.<sup>25</sup> observed that single wall carbon nanotubes (SWCNT) led to increased shish formation, while zirconia nanoparticles destabilized shish formation. Patil explained this by the stronger chain–particle interaction of the SWCNT retarding the relaxation of extended chains compared to the weaker chain–particle interactions of the zirconia nanoparticles. Byelov et al.<sup>36</sup> showed that the shape of the particle could influence the number of shear-induced nuclei, with anisotropic particles leading to greater numbers of shear-induced nuclei compared to isotropic particles. However, the mechanism responsible for this interesting influence of particle shape was not able to be identified.

In this study, continuous shear flow was applied to the melt of pure iPP and melts of two iPP samples containing different commercial nucleating particles. The shear temperature ( $T_g = 181\text{ }^\circ\text{C}$ ) was selected to be well above the lamellar melting point ( $T_m = 166\text{ }^\circ\text{C}$ ) of the polymer but below the equilibrium melting temperature of the unconstrained extended chain crystal ( $T_m^0(\text{iPP}) = 186.1\text{ }^\circ\text{C}$ ).<sup>44</sup> The purpose was to investigate the influence of the two nucleating particles on (a) the formation of shish under close to steady-state shear conditions and (b) the shish stability after shear flow was stopped. The likely mechanisms of shish formation and the influence of nucleating particles on shish formation are discussed.

## 2. EXPERIMENTAL SECTION

**2.1. Materials.** The polymer used was an iPP homopolymer manufactured by Borealis (HD601CF). This grade was chosen as it has been extensively investigated by our group and was selected due to its low intentional additive profile. In particular, it contained no calcium stearate, which has previously been shown to induce a high-temperature smectic phase.<sup>45</sup> The average weight molecular weight ( $M_w$ ) and the average number molecular weight ( $M_n$ ) were 367 000 and 74 000 g/mol, respectively. The lamellar melting point of the polymer was determined to be  $166\text{ }^\circ\text{C}$  using differential scanning calorimetry (DSC).

Two common commercial nucleating particles which specifically nucleate the alpha phase of iPP ( $\alpha$ -iPP) were used in this study: sodium benzoate (SB) and bicyclo[2.2.1]heptane-2,3-dicarboxylic acid, trade name HPN-68 (HPN). Various loadings of the two particles were compounded into the molten iPP at  $175\text{ }^\circ\text{C}$  in a Haake Rheocord 90 batch mixer and mixed at 60 rpm for 300 s. The material was removed from the batch mixer and compression-molded to a thickness of 1.5 mm at  $190\text{ }^\circ\text{C}$  for 300 s before being cooled to room temperature. 12 mm disks were then cut from the compression-molded material for further analysis.

**2.2. Thermal–Shear Profile.** A Linkam CSS450 shear cell was used to control the thermal–shear profile. The CSS450 is a parallel plate shearing device in which a small aperture in the base and lid allows

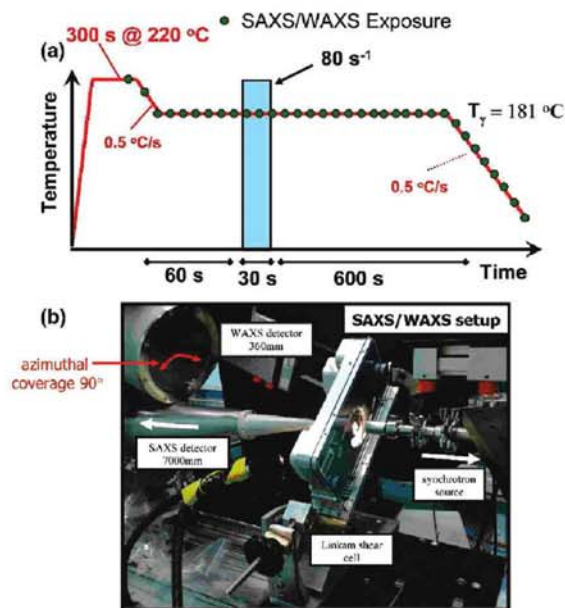


Figure 1. (a) Thermal–shear profile. (b) Experimental setup.

observation of the polymer in situ. The sample temperature was calibrated using external thermocouples inserted into the melt. The influence of wall slip and nonuniform velocity profiles through the thickness of the sample were considered to be comparable for all samples. The thermal–shear profile is shown in Figure 1a. The previously compression-molded disks were heated to  $220\text{ }^\circ\text{C}$  and compressed slowly to the working distance of 0.25 mm at 0.01 mm/s. The compressed disks were held at the melting temperature for at least 300 s to erase the previous thermal history of the sample. The samples were cooled to the shear temperature ( $T_g = 181\text{ }^\circ\text{C}$ ) and held for 60 s before a continuous shear pulse was applied to the melt for 30 s at a shear rate of  $80\text{ s}^{-1}$ . The samples were then held at temperature for a further 600 s before being cooled at  $0.5\text{ }^\circ\text{C/s}$  to room temperature.

**2.3. Wide- and Small-Angle X-ray Scattering (SAXS/WAXS).** The shear cell was adapted for use with X-ray radiation. The bottom plate had three slots allowing X-rays to be introduced to the sample. The top plate had a narrow 3 mm diameter aperture allowing scattered X-rays to pass. Thin films of Kapton  $\sim 0.05\text{ mm}$  were used to contain the sample between the top and bottom plates. Simultaneous two-dimensional SAXS/WAXS experiments were performed on the SAXS/WAXS beamline at the Australian Synchrotron (Figure 1b). The setup allowed for in situ investigations with a considerable amount of the scattered intensity around the azimuth ( $\varphi \sim 90^\circ$ ) in the WAXS region to be captured, while simultaneously capturing complete 2D SAXS patterns. Details of the SAXS and WAXS detectors used in the experiment are presented in Table 1. Beam dimensions of  $0.2\text{ mm} \times 0.1\text{ mm}$ , a wavelength of  $\lambda = 1.34\text{ \AA}$ , and an exposure time of 1 s were employed throughout the experiment. The time between successive exposures was 5.6 s. Scattering without the specimen was recorded to enable background correction. All images were normalized to the main beam intensity before subtraction. The Nika set of macros for Igor Pro was used to reduce the 2D data. The scattering vector was calculated by the relation  $q = 4\pi \sin \theta / \lambda$ , where  $2\theta$  is the scattering angle.

**2.4. DSC.** Differential scanning calorimetry (DSC) experiments were performed using a Perkin-Elmer DSC-7. Sample size was  $\sim 5\text{ mg}$ . Pure indium and zinc references were used for calibration. Samples were run in

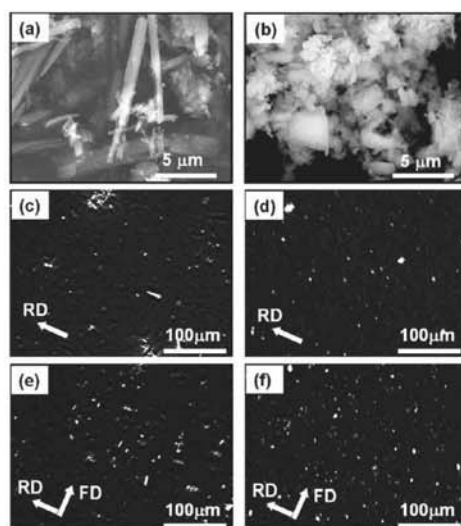
B

dx.doi.org/10.1021/ma200040s | Macromolecules XXXX, XXX, 000–000



**Table 1.** Details of the X-ray Detectors Used in This Experiment

detector	camera length (mm)	count rate (X-ray/s)	pixel size (mm)	azimuthal coverage (deg)	$q$ range ( $\text{\AA}^{-1}$ )
SAXS: Dectris-Pilatus 1M	7300	$>2 \times 10^6$	0.172	$\sim 360$	0.003–0.1
WAXS: MAR-165	320	$0.4 \times 10^6$	0.080	$\sim 90$	0.5–2.5

**Figure 2.** Scanning electron micrographs of (a) sodium benzoate (SB) and (b) bicyclo[2.2.1]heptane-2,3-dicarboxylic acid (HPN). Polarized optical micrographs of (c) iPP(1.00SB) and (d) iPP(1.00HPN) in the quiescent condition and (e) iPP(1.00SB) and (f) iPP(1.00HPN) after shear (time = 30 s, shear rate =  $80 \text{ s}^{-1}$ , shear temperature =  $181^\circ\text{C}$ ).

triplicate. Uncertainty in the parameters measured by DSC was assessed by calculating the standard error in the measurement, and the 95.4% confidence interval was reported.

**2.5. Microscopy.** Ex-situ images of the nucleating particles were taken on a JEOL JSM-7001F field emission scanning electron microscope operating in secondary electron mode. Samples were coated to 10 Å thick with gold/platinum and imaged at an acceleration voltage of 5 kV. In-situ images of the nucleating particles in the polymer matrix were made under polarized light in the Linkam shear cell using a Nikon 80i microscope and a Nikon DS-Fi1 CCD camera.

### 3. RESULTS

**3.1. Nucleant Particle Characterization.** The morphology of the two nucleant particles before being compounded into the iPP matrix is shown in Figure 2a,b. Standard metallographic techniques were employed to determine the average size and surface area of the two nucleating particles (Table 2). The SB particles were needlelike particles with an aspect ratio  $\sim 10$ . HPN particles were roughly isotropic and had an aspect ratio of  $\sim 1$ . Both SB and HPN particles exhibited flat faceted surfaces. Figure 2c,d shows both SB and HPN particles were well dispersed in the iPP

matrix by the mixing procedures employed. The SB particles showed some preferred orientation of their long axis along the radial direction of the shear cell in the quiescent condition. This alignment is presumably due to the weak flow field applied to the sample when it was compressed in the initial stages of the experiment. After a 30 s shear at a shear rate of  $80 \text{ s}^{-1}$ , both nucleant particles remained well dispersed (Figure 2e,f). After shear the SB particles showed preferred orientation of their long axis along the flow direction.

The nucleation efficiency of the particles was determined according to the method proposed by Fillon et al.<sup>46,47</sup> This method assumes the best nucleators are polymer self-seeds, i.e., small crystal fragments made from the crystals of the polymer. The peak crystallization temperature during continuous cooling of a self-nucleated polymer is considered as the upper bound ( $T_{c2}$ ), while the crystallization temperature of the pure polymer is considered the lower bound ( $T_{c1}$ ). The nucleation efficiency (NE) can then be calculated according to the following equation

$$NE = \frac{T_{cNA} - T_{c1}}{T_{c2} - T_{c1}} \quad (1)$$

where  $T_{cNA}$  is the crystallization temperature of the polymer samples containing the nucleating particles.

Table 2 shows the influence of loading level of the two nucleating particles on the NE. The NE increased with increasing loading of both nucleating particles. This is simply related to the higher number of heterogeneous sites available for nucleation. HPN was found to be a far superior nucleating particle in terms of raising NE compared to SB, when measured at an equivalent surface area. This result shows that HPN particles have a greater ability to nucleate iPP crystals than SB particles. Indeed, HPN has been shown to have one of the highest NE of all known iPP nucleating agents.<sup>48</sup>

#### 3.2. Observation of Shish during and after Shear Flow.

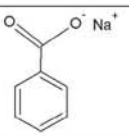
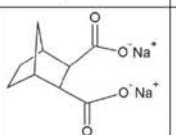
Selected 2D SAXS patterns taken before, during, and after the shear profile are shown in Figure 3. The images shown before shear have had the empty cell data subtracted as the background. Before shear all three samples showed diffuse isotropic scattering profiles consistent with an amorphous iPP melt with no preferred orientation. To enhance scattering contrast for the subsequent 2D SAXS images, both the empty cell and the melt immediately prior to the start of shear were subtracted from all subsequent images. Immediately after the application of shear, a strong increase in equatorial scattering was observed as indicated by the arrows in Figure 3. The increase in equatorial scattering is consistent with the formation of shish aligned along the flow direction. The presence of fibrils in the micrographs of quenched samples verified shish were formed by the imposed thermal–shear profile. After the shear pulse stopped, the equatorial streaks in all samples became weaker and spread around the azimuth. This indicates that the shish are not entirely stable in this temperature regime. Large differences in the scattered intensity were observed between the three samples. The addition of both nucleating particles increased the intensity of the equatorial streak compared to iPP(control). The equatorial streak in iPP(1.00SB) were significantly more intense, extended to higher  $q$  values and were sharper compared to those in iPP(1.00HPN). These differences in scattered intensity will be quantitatively investigated during and after shear in the following section.

In addition to the equatorial scattering, a surprisingly sharp meridional streak was also observed in the SAXS patterns during

C

dx.doi.org/10.1021/ma200040s | Macromolecules XXXX, XXX, 000–000

**Table 2.** Summary of the Morphology of the Sodium Benzoate (SB) and Bicyclo[2.2.1]heptane-2,3-dicarboxylic Acid (HPN) Particles Used in This Investigation and Their Influence on the Quiescent Crystallization of Isotactic Polypropylene (iPP)<sup>a</sup>

sample	chemical structure	nucleant shape	average dimension (μm)	loading (wt. %)	particle surface area (m <sup>2</sup> /g)	T <sub>c</sub> (°C)	NE (%)
iPP(control)		needle	0.43(4) x 4.70(17)	neat	-	111.3(3)	0
iPP(self seed)				self seed	-	142.7(3)	100
iPP(0.05SB)				0.05	0.005	113.3(3)	6(1)
iPP(0.10SB)				0.10	0.010	114.5(3)	11(1)
iPP(0.50SB)				0.50	0.052	119.4(3)	26(1)
iPP(1.00SB)				1.00	0.103	120.6(3)	30(1)
iPP(0.05HPN)		isotropic	0.41(4)	0.05	0.007	124.8(3)	43(1)
iPP(0.10HPN)				0.10	0.014	127.2(3)	49(1)
iPP(0.50HPN)				0.50	0.071	129.7(3)	54(1)
iPP(1.00HPN)				1.00	0.141	132.8(3)	59(1)

<sup>a</sup> T<sub>c</sub> = peak crystallization temperature, NE = nucleation efficiency.

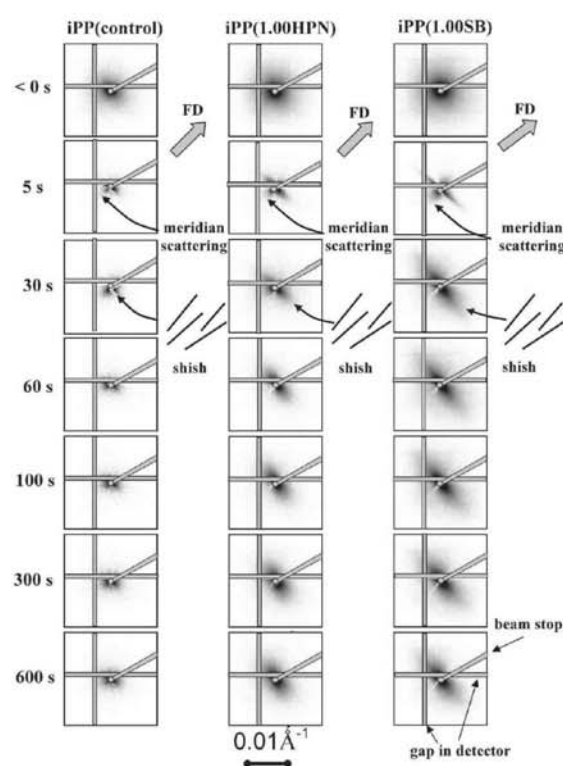


**Figure 3.** Selected small-angle X-ray scattering patterns taken at various stages before, during, and after continuous shear (shear time = 30 s, shear rate = 80 s<sup>-1</sup>, shear temperature = 181 °C).

shear for all samples. Furthermore, the meridional streak disappeared soon after the shear stopped. To further investigate this anomalous feature, the intensity profile around the azimuth was determined between scattering vectors  $0.003 \leq q \leq 0.01 \text{ Å}^{-1}$ . Distinct equatorial

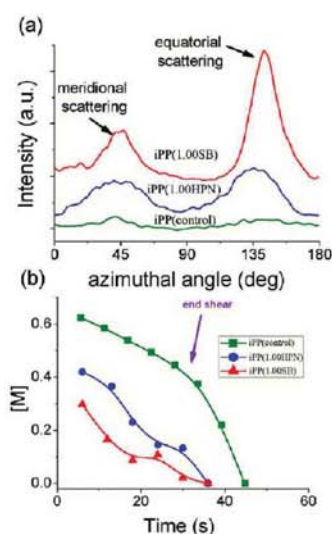


**Figure 4.** (a) Plot of background subtracted intensity versus azimuthal angle during the first 5 s of shear. (b) Relative proportion of meridional scattering ([M]) during and immediately after shear (shear time = 30 s, shear rate = 80 s<sup>-1</sup>, shear temperature = 181 °C).

and meridional peaks were clearly evident in all profiles during shear (Figure 4a). The relative amount of meridional scattering ([M]) was estimated during shear flow using the following equation

$$[M] = \frac{A_m}{A_m + A_e} \quad (2)$$

where  $A_m$  and  $A_e$  are the areas of the azimuthally integrated meridional and equatorial peaks. The results are plotted in Figure 4b. For all samples the amount of meridional scattering decreased steadily during shear and disappeared altogether soon after the shear ended.

D

dx.doi.org/10.1021/ma200040s | Macromolecules XXXX, XXX, 000–000



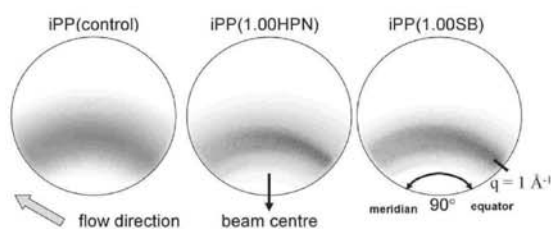


**Figure 5.** Raw wide-angle X-ray scattering patterns taken just prior to the end of continuous shear (shear time = 30 s, shear rate =  $80 \text{ s}^{-1}$ , shear temperature =  $181^\circ\text{C}$ ).

The WAXS patterns before shear showed an unoriented diffuse amorphous halo with peak intensity near  $q = 1 \text{ Å}^{-1}$ , further confirming that the melt was unoriented prior to shear. The application of shear did not induce any crystalline scattering during or for at least 600 s after the shear had stopped. This shows that the scattering observed in the SAXS images is due to noncrystalline entities. However, during shear flow some preferred orientation of the amorphous halo became evident with an increase in intensity occurring toward the equator at  $q \sim 1 \text{ Å}^{-1}$  (Figure 5). The interpretation of amorphous orientation from WAXS is uncertain in this case due to the complex combination of inter- and intrachain interactions. Nevertheless, the observed increase in preferred orientation with the addition of both nucleating particle is consistent with the results presented in Figure 3.

**3.3. Quantitative Investigation of Shish during and after Shear Flow.** The behavior of the shish during and after shear was further probed by determining the integrated scattered intensity from the equatorial scattering streak in the SAXS images ( $I_{\text{shish}}$ ) according to the following equation:

$$I_{\text{shish}} = \int_{0.003}^{0.3} \int_{0^\circ}^{20^\circ} I(q, \varphi) dq d\varphi \quad (3)$$

$I_{\text{shish}}$  determined in this way is proportional to the total volume of shish ( $v_{\text{shish}}$ ) and the magnitude of their density contrast to the surrounding melt ( $\Delta\rho_{\text{shish-melt}}$ ). The results of this analysis are plotted in Figure 6. All samples showed the same general behavior. During shear,  $I_{\text{shish}}$  initially increased rapidly, reaching a peak value just prior to the shear pulse ending. This indicates that steady-state conditions were only achieved toward the end of the shear profile. The magnitude of  $I_{\text{shish}}$  was substantially larger in iPP(1.00HPN) and iPP(1.00SB) compared to iPP(control), raising the magnitude of  $I_{\text{shish}}$  by a factor of 5 and 7, respectively. The higher value of  $I_{\text{shish}}$  indicates that the addition of nucleating particles increased the volume fraction of shish or their density contrast. However, large changes in the density contrast of the shish is considered less likely when taken in conjunction with measurements of the shish dimensions which are discussed subsequently.

Immediately after the shear pulse stopped,  $I_{\text{shish}}$  began to exponentially decay to an interim lower plateau level. This indicates that some shish are unstable and relax back into the melt, while other shish have some stability at the experimental temperature. The decay constant ( $\tau_{\text{shish}}$ ) between peak  $I_{\text{shish}}$  and the lower plateau was approximated by a simple exponential decay model:

$$I_{\text{shish}}(t) = I_{\text{shish}(0)} + \Delta I_{\text{shish}} e^{-t/\tau_{\text{shish}}} \quad (4)$$

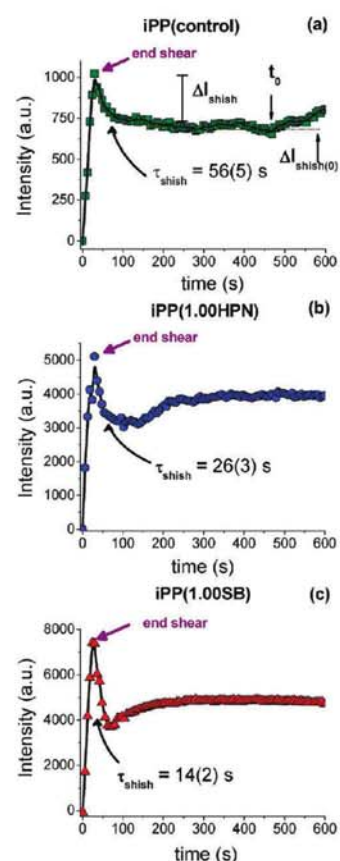


**Figure 6.** Scattered intensity from shish ( $I_{\text{shish}}$ ) during and after shear for (a) iPP(control), (b) iPP(1.00HPN), and (c) iPP(1.00SB) (shear time = 30 s, shear rate =  $80 \text{ s}^{-1}$ , shear temperature =  $181^\circ\text{C}$ ).

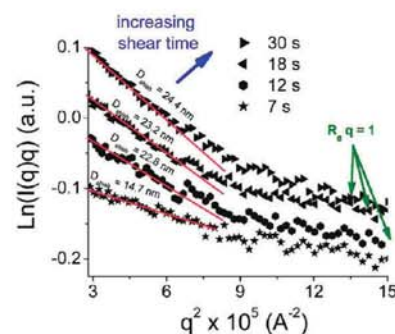


**Figure 7.** Guinier plot of  $\ln(I(q)q)$  versus  $q^2$  showing selected lines during shear flow for iPP(control) (shear rate =  $80 \text{ s}^{-1}$ , shear temperature =  $181^\circ\text{C}$ ).

where  $I_{\text{shish}(0)}$  and  $\Delta I_{\text{shish}}$  are illustrated in Figure 6. Compared to iPP(control), the addition of both nucleating particles was found to decrease  $\tau_{\text{shish}}$ .

After an induction time ( $t_0$ ) at the lower plateau level, the value of  $I_{\text{shish}}$  began to increase again before reaching an upper plateau level.

E

dx.doi.org/10.1021/ma200040s | Macromolecules XXXX, XXX, 000–000

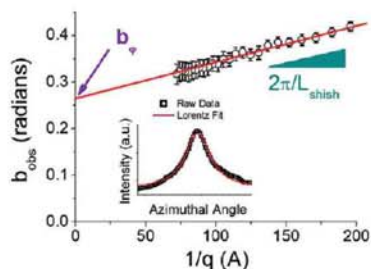


**Figure 8.** Plot of azimuthal integral breadth ( $b_{\text{obs}}$ ) as a function of  $1/q$  showing the method used to separate out the contributions of the misorientation of shish ( $b_{\phi}$ ) and the shish length  $L_{\text{shish}}$  at low scattering vectors ( $q$ ). Inset shows a typical background corrected azimuthal intensity profile fitted with a Lorentz function.

The value of  $L_{\text{shish}}$  was then stable until the end of the isothermal hold. The addition of both nucleating particles decreased this induction time compared to iPP(control) ( $t_0 = 476(3)$  s), with iPP(1.00SB) ( $t_0 = 68(3)$  s) having a shorter  $t_0$  than iPP(1.00HPN) ( $t_0 = 138(3)$  s). This increase in  $L_{\text{shish}}$  could be due to an increase in the volume fraction of shish or changes in their density contrast. To further understand this interesting phenomenon, the dimensions of the shish during and after shear flow are determined.

The diameter of the shish was estimated by applying the Guinier approximation<sup>49</sup> to a  $20^\circ$  arc in the azimuthal direction and centered on the maximum intensity of the equatorial scattering streak. The radius of gyration ( $R_g$ ) of rodlike scatterers can be approximated from the gradient of the linear region at low  $q$  of a plot of  $\ln(I(q)q)$  versus  $q^2$  according to the equation

$$I \propto \frac{1}{q} e^{-R_g^2 q^2 / 2} \quad (5)$$

Assuming the shish show cylindrical symmetry, the diameter of the shish is

$$D_{\text{shish}} = 8^{1/2} R_g \quad (6)$$

Strictly speaking, the Guinier approximation used in this way is only true for the central part of the scattering from a dilute (and therefore uncorrelated) solution of rods. However, it has been applied successfully to estimate the diameter of shish in previous studies.<sup>24,40</sup> Selected Guinier plots for iPP(control) during shear are shown in Figure 7. For all scattering patterns the plot consisted of two linear regions with the transition occurring at  $q = 0.094 \text{ \AA}^{-1}$ . The first region (i.e.,  $q < 0.094 \text{ \AA}^{-1}$ ) was used to determine  $D_{\text{shish}}$  since the second region should be discarded as the Guinier approximation is only valid in the small angle limit where the criteria  $R_g q < 1$  is maintained.

The average length of the structural units along the long axis of the shish ( $L_{\text{shish}}$ ) and their alignment along the flow direction ( $b_{\phi}$ ) can be determined using the method proposed by Perret and Ruland.<sup>50</sup> The underlying basis for the method is that at low  $q$  the contribution from the misorientation of the scatterers should be constant, while the contribution from the length of the scatterers should depend on  $q$ . The proposed method consists of determining the integral breadth of a series of azimuthal profiles taken at different values of  $q$  along the equator. The integral breadth ( $b_{\text{obs}}$ ) is defined according to the equation

$$b_{\text{obs}}(q) = \frac{1}{I(q, \pi/2)} \int_{-\pi/2}^{\pi/2} I(q, \phi) d\phi \quad (7)$$

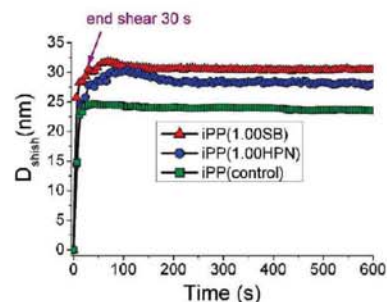


**Figure 9.** Calculated diameter of shish ( $D_{\text{shish}}$ ) during and after shear (shear time = 30 s, shear rate =  $80 \text{ s}^{-1}$ , shear temperature =  $181^\circ \text{C}$ ).

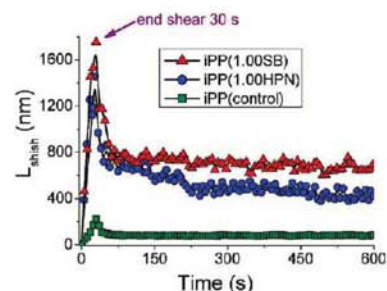


**Figure 10.** Calculated length of shish ( $L_{\text{shish}}$ ) during and after shear (shear time = 30 s, shear rate =  $80 \text{ s}^{-1}$ , shear temperature =  $181^\circ \text{C}$ ).

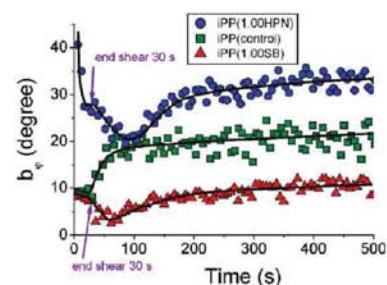


**Figure 11.** Calculated shish misorientation ( $b_{\phi}$ ) during and after shear (shear time = 30 s, shear rate =  $80 \text{ s}^{-1}$ , shear temperature =  $181^\circ \text{C}$ ).

where  $\phi$  is the azimuthal angle and  $I(q, \phi)$  is the background corrected intensity. For a Cauchy-like (Lorentz) orientation distribution of scatterers,  $b_{\text{obs}}$  is then related to  $b_{\phi}$  and  $L_{\text{shish}}$  by

$$b_{\text{obs}} = b_{\phi} + \frac{2\pi}{L_{\text{shish}} q} \quad (\text{Lorentz}) \quad (8)$$

For a Gaussian orientation distribution of scatterers the equation becomes

$$b_{\text{obs}}^2 = b_{\phi}^2 + \frac{4\pi^2}{L_{\text{shish}}^2 q^2} \quad (\text{Gaussian}) \quad (9)$$

In the present work it was found that the Lorentz function best fit the observed azimuthal intensity profile, and  $b_{\phi}$  and  $L_{\text{shish}}$  were determined from a plot of  $b_{\text{obs}}$  versus  $1/q$  (Figure 8). The

F

dx.doi.org/10.1021/ma200040s | Macromolecules XXXX, XXX, 000–000



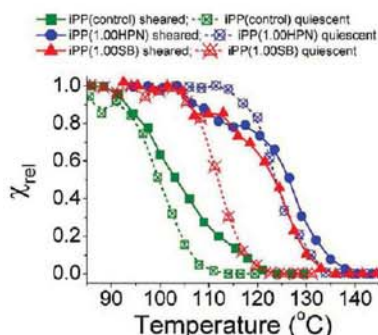


**Figure 12.** Influence of nucleating particle and shear condition on the crystallization during continuous cooling (shear time = 30 s, shear rate =  $80 \text{ s}^{-1}$ , shear temperature =  $181^\circ\text{C}$ , hold time = 600 s, cooling rate =  $0.5^\circ\text{C/s}$ ).

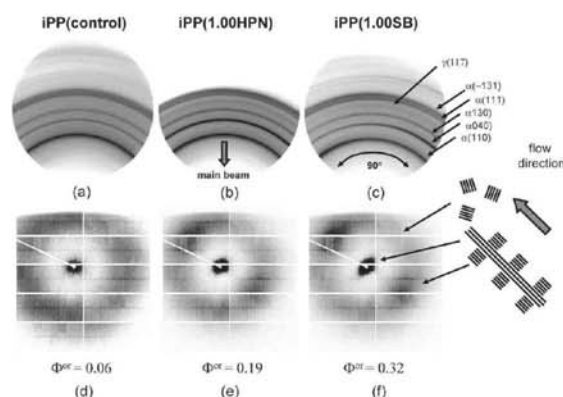


**Figure 13.** Small- and wide-angle X-ray scattering patterns in the fully crystallized condition taken at room temperature. (a, d) iPP(control), (b, e) iPP(1.00HPN), (c, f) iPP(1.00SB). Oriented fraction of lamellae ( $\Phi^{\text{or}}$ ) (shear time = 30 s, shear rate =  $80 \text{ s}^{-1}$ , shear temperature =  $181^\circ\text{C}$ , hold time = 600 s, cooling rate =  $0.5^\circ\text{C/s}$ ).

magnitude of  $L_{\text{shish}}$  for all samples was below 2000 nm, which is smaller than the typical shish length observed using microscopy methods. However, it should be noted that the quantity  $L_{\text{shish}}$  represents the average coherence length of the structural units along the long axis of the shish, which will be different from that measured by microscopic methods.

The time evolution of the shish dimensions  $D_{\text{shish}}$  and  $L_{\text{shish}}$  are presented in Figures 9 and Figure 10, respectively. In all three samples both  $D_{\text{shish}}$  and  $L_{\text{shish}}$  were found to increase rapidly with increasing shear time. After shear,  $L_{\text{shish}}$  decreased quickly to an interim value and then decreased more slowly until the end of the isothermal hold.  $D_{\text{shish}}$  on the other hand, at first kept increasing after the shear had stopped, reaching an upper plateau level.  $D_{\text{shish}}$  then began to decline from the upper plateau with increasing time until the end of the isothermal hold. The addition of both nucleating particles led to a large increase in the value of  $L_{\text{shish}}$  and a small increase in the value of  $D_{\text{shish}}$ . The magnitudes of  $D_{\text{shish}}$  and  $L_{\text{shish}}$  were larger in iPP(1.00SB) compared to iPP(1.00HPN).

The alignment of shish during and after shear is shown in Figure 11. A line through the middle of the data is included to aid interpretation. A lower value of  $b_\theta$  indicates a higher shish alignment along the flow direction. During shear, iPP(control) started with high alignment along the flow direction which then increased slightly as shear progressed. At the beginning of shear the shish in iPP(1.00HPN) had low alignment along the flow direction. However, as shear progressed, their alignment increased substantially. At the beginning of shear the shish in iPP(1.00SB) were highly aligned along the flow direction. Further shear increased their alignment further. After shear stopped, the shish alignment in iPP(control) immediately decreased. Conversely, the alignment of shish in the iPP containing both nucleating particles increased after shear stopped, reaching a lower plateau before rising again with increasing time. In general, the relative alignment of shish for the three samples went iPP(1.00SB) > iPP(control) > iPP(1.00HPN).

**3.4. Crystallization of Sheared and Relaxed iPP Containing Nucleating Particles.** At the end of the 600 s hold, the samples were cooled to room temperature at  $0.5^\circ\text{C/s}$ . The volume crystallinity index ( $\chi_v$ ) was measured from the circular integration of WAXS patterns during cooling according to the method described in a previous paper.<sup>42</sup> The relative crystallinity ( $\chi_{\text{rel}}$ ), defined as the instantaneous crystallinity divided by the room temperature crystallinity, was then plotted as a function of temperature (Figure 12). The results were compared to samples that had undergone the same thermal profile but were not sheared. Without shear, the crystallization progressed according to the relative nucleation efficiencies of the added particles. With shear, all samples showed an increase crystallization temperature compared to the samples which had not been sheared. This is consistent with the formation of shear-induced nuclei which provide extra nucleation sites for crystal nucleation. iPP(1.00SB) showed the largest change in the crystallization kinetics after shear, consistent with the higher numbers of shish observed before the onset of crystallization. iPP(1.00HPN) exhibited the smallest change in crystallization kinetics, which is presumably due to the high nucleation efficiency of the HPN particles swamping crystallization under quiescent conditions.

Simultaneous SAXS/WAXS patterns of the sheared samples obtained in the fully crystallized state are shown in Figure 13. The WAXS patterns of all samples showed crystalline reflections consistent with the formation of only  $\alpha$ -iPP and  $\gamma$ -iPP crystals. In pure iPP it is known that shear flow can induce  $\beta$ -iPP as long as the kinetic requirement for a higher  $\beta$ -iPP growth rate than  $\alpha$ -iPP is achieved (i.e., between  $105$  and  $141^\circ\text{C}$ <sup>51</sup>). Therefore, the absence of  $\beta$ -iPP reflections for iPP(control) in this experiment was surprising, given that crystal nucleation occurred within this temperature range. The absence of  $\beta$ -iPP is even more intriguing, given that in a previous study shear-induced formation of  $\beta$ -iPP was observed in the same polymer.<sup>42</sup> In that study isothermal crystallization (crystallization temperature =  $135^\circ\text{C}$ ) was carried out after a moderate step shear (shear rate =  $80 \text{ s}^{-1}$ , shear time = 1 s). These conditions are substantially different from those used in this study. Indeed, it is worthwhile to note that in many of the studies presented in the literature shear-induced formation of  $\beta$ -iPP has been investigated after the application of a brief shear pulse and where crystallization occurred under isothermal conditions. Although not in the scope of the present study, further work is planned to clarify the reason for the absence of  $\beta$ -iPP in iPP(control).

G

dx.doi.org/10.1021/ma200040s | Macromolecules XXXX, XXX, 000–000



The  $\gamma$ -iPP crystallinity ( $\chi_\gamma$ ) of the fully crystallized material was determined using the Turner-Jones method:<sup>52</sup>

$$K_\gamma = \frac{A_\gamma(117)}{A_\gamma(117) + A_\alpha(130)} \quad (10)$$

$$\chi_\gamma = K_\gamma \chi_v \quad (11)$$

where  $A_\alpha(130)$  and  $A_\gamma(117)$  are the integrated areas of the crystalline reflections indicated in Figure 13. The addition of both nucleating particle significantly increased  $\chi_\gamma$  from 0.02 in iPP(control) to 0.11 in iPP(1.00SB) and 0.17 in iPP(1.00HPN). The promotion of  $\gamma$ -iPP in the samples containing the nucleants is thought to be related to the substantially higher density of nuclei in these samples (both shear-induced and heterogeneous sites on the surface of the particles), combined with the relatively fast cooling rate which would further increase the number of active nuclei. The high density of nuclei would lead to multiple nucleation events occurring simultaneously along a chain, thereby reducing the time available for the chain to properly organize during the initial crystallization. Combined with the stereo- and regio-defects already present along the polymer backbone, this would promote shorter isotactic sequences during crystallization. It has been reported that  $\gamma$ -iPP is favored when the isotactic sequence length is interrupted.<sup>53</sup>

The SAXS/WAXS patterns in Figure 13 show preferred orientation consistent with the shish inducing the formation of kebab structures. In the SAXS region broad lobes were observed along the meridian (kebabs) while equatorial scattering was observed at low  $q$  (shish). Increases in scattered intensity along the equator for the  $\alpha(110)$ ,  $\alpha(040)$ , and  $\alpha(130)$  reflections in the WAXS region indicated significant crystalline  $c$ -axis orientation along the flow direction. The oriented fraction of lamellae ( $\Phi^{\text{or}}$ ) was determined from the SAXS pattern according to the method presented in a previous paper.<sup>42</sup> The addition of both nucleating particles increased  $\Phi^{\text{or}}$ , with SB having almost twice the number of oriented lamellae compared to HPN. The samples were reheated to 220 °C and was held there for a further 300 s. Upon cooling, no preferred orientation was observed in any sample. This shows that the particles themselves did not template oriented crystal growth.

## 4. DISCUSSION

**4.1. Formation of Shish during Shear.** Shish formation during shear flow is of considerable practical importance as shish promote oriented hierarchical structures, which significantly alter the physical, optical, and mechanical properties of the solid polymer. However, the shish formation mechanism is still under intense debate. The proposed mechanisms broadly fall into three groups: shish form directly from extended chains (or chain segments) produced via an abrupt coil-to-stretch transition;<sup>1,5,6,11</sup> shish nucleate from pre-existing nuclei and then grow by the addition of new chain segments;<sup>12–17</sup> and shish form in discrete steps, by the aggregation of discrete nuclei into oriented threads.<sup>18–22</sup> These three mechanisms are not necessarily mutually exclusive, and more than one mechanism could lead to shish formation under a given set of processing conditions.

Keller et al.<sup>1,50,54</sup> explained shish formation around the coil-to-stretch transition originally proposed by de Gennes<sup>55</sup> for dilute polymer solutions. In the model, shear flow results in the abrupt unravelling of the longest chains in the system. These extended

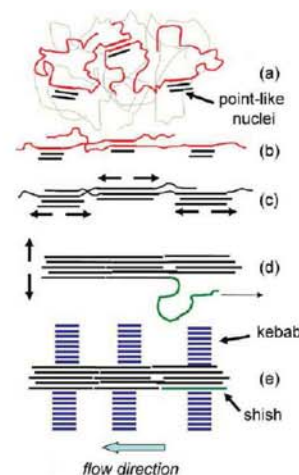


**Figure 14.** Mechanism of shish formation. (a) Formation of shear-induced pointlike nuclei. (b) Aggregation of pointlike nuclei into oriented thread when the tie molecules are pulled taut by shear flow. (c) Infill growth of aligned pointlike nuclei to form shish. (d) Growth of shish in the lateral direction by the unravelling of adsorbed chains along the length of the shish. (e) Nucleation of chain folded kebabs on lateral surface of shish.

chains then migrate together and undergo densification into the final shish structure. Chains that were not elongated by the flow field form the kebabs during subsequent crystallization. Hsiao et al.<sup>5</sup> extended this model by noting that in an entangled melt it may not be the whole chain which would become extended but rather the sections of chain between entanglement points.

Pennings et al.<sup>12,56</sup> suggested that chains adsorb onto the surface of pre-existing nuclei which then allows the free end to be extended by the flow field. This leads to longitudinal growth of the nuclei. Therefore, in the scenario an external flow field was thought to be required for shish growth. Studying deformed films of isotactic polystyrene, Petermann et al.<sup>17</sup> observed the presence of obstacles altered the shish growth direction. This observation implies that shish may also grow without a shear field by an autocatalytic process at the ends of the shish. Nevertheless, the presence of an external flow field would further enhance alignment of chain sections, increasing growth rates.

An aggregation-type mechanism for shish formation was first proposed by Hoffman,<sup>21,22</sup> who argued that kebabs are nucleated at specific sites along the core of the shish and that these provide information about structural singularities in the backbone of the shish. In this work, the shish were thought to originate with the aggregation of multiple pointlike nuclei along the length of a flow elongated molecule. In the case of iPP these pointlike nuclei can be thought of as small bundles of roughly parallel chains in helical conformations which show intermediate order between amorphous and crystalline states.<sup>57</sup> Janeschitz-Kriegl et al.<sup>2,18</sup> provided further evidence for an aggregation type mechanism by noting that the number of pointlike nuclei varied nonlinearly with the mechanical work during shear flow. This observation implies the existence of long-range interactions between pointlike nuclei. Heeley et al.<sup>20</sup> suggested this interaction could occur if the pointlike nuclei act as anchor points along the length of a molecule, allowing flow to more effectively orient the molecule, and thus the attached pointlike nuclei. An alternative mechanism

H

dx.doi.org/10.1021/ma200040s | Macromolecules XXXX, XXX, 000–000



**Table 3.** Empirical Disengagement ( $\tau_d$ ) and Chain Rouse ( $\tau_R$ ) Times for Stretched iPP Molecules in a Monodisperse Entangled Melt Held at 181 °C

relaxation times (s)	$M_w$ (367 000 g mol <sup>-1</sup> )	$M_{(>99\%)}$ (3 673 000 g mol <sup>-1</sup> ) <sup>a</sup>
$\tau_d$	0.0443	63.64
$\tau_R$	0.0003	0.0270

<sup>a</sup> Molecular weight calculated from a log–normal fit of the molecular distribution.

was proposed by Seki et al.,<sup>19</sup> who suggested that molecules which adsorb onto the surface of pointlike nuclei would get rapidly extended along the flow direction. New pointlike nuclei would then form from these extended chain segments. Nevertheless, the aggregation of pointlike nuclei into oriented threads has until now not been observed.

During shear flow, meridional scattering streaks were observed in the SAXS patterns of all samples investigated, in conjunction with equatorial streaks. A review of the available literature indicates that such meridional scattering has not been previously observed during shear flow. Similar SAXS/WAXS investigations by Somani et al.<sup>58</sup> on sheared iPP have shown the formation of meridional scattering after an appreciable induction time and following the cessation of shear. In that work the meridional scattering was explained by the formation of noncrystalline kebabs. However, the lack of any appreciable induction time for the formation of the meridional peaks as well as the high temperature used in this experiment, which was ~15 °C higher than the lamellae melting temperature, would make this scenario unlikely. Consequently, the most likely structures that fit the observed scattering are highly aligned discrete nuclei. Such a structure would be consistent with shish forming, in discrete steps by the aggregation of pointlike nuclei into oriented threads. The suggested sequence of events is schematically illustrated in Figure 14.

Meridional scattering is not commonly observed in the SAXS patterns of sheared semicrystalline polymers, and therefore its presence in this experiment needs further explanation. The relative proportion of meridional scattering was observed to decrease during shear flow (Figure 4). Furthermore, the meridional scattering disappeared soon after the shear was stopped. This can be explained by the infill of regions between neighboring aligned pointlike nuclei which would be promoted by the highly extended chains between the nuclei. Such infill growth could be aided by the autocatalytic mechanism proposed by Peterman et al.<sup>17</sup> This highlights that the meridional scattering may only be apparent during shear flow, while the shish are forming. However, because of the fast kinetics, many experiments previously presented in the literature investigated shish formation after shear flow stopped. Accordingly, it is the high shear temperature used in this experiment which slows down the formation of shish, in combination with the relatively long shear times, which allows shish formation to be investigated.

The increase in  $D_{\text{shish}}$  during shear shows that the shish can also grow in the lateral direction during shear flow. Yamazaki et al.<sup>15</sup> suggested that this could occur by the repeated adsorption of chain ends to the shish surface. Once pinned on the surface, the free ends of the chain would then be rapidly elongated along the surface of the shish by the shear field. This result highlights

that more than one mechanism is responsible for shish growth during shear.

**4.2. Stability of Shish after Shear.** Immediately after the shear pulse ended the shish began to dissolve back into the melt. At least two separate steps are thought to be necessary for this to occur. The first step is the detachment of a stem from the surface of the shish (melting). Once detached, the extended stem can then relax in a snakelike motion along an imaginary tube formed by the constraints imposed by neighboring molecules to restore its equilibrium conformation (reptation). The disengagement ( $\tau_d$ ) and the chain Rouse times ( $\tau_R$ ) of a stretched molecule were empirically determined using the Doi–Edwards model:<sup>59</sup>

$$\tau_d = 3\tau_e Z^3 [1 - \kappa Z^{-0.5}]^2 \quad (12)$$

$$\tau_R = \tau_e Z^2 \quad (13)$$

where  $\tau_e$  is the Rouse time of a single entanglement strand ( $\tau_e = 5.42 \times 10^{-8}$  s at 181 °C),  $Z$  is the number of entanglements per chain, and  $\kappa$  is a constant found to be close to unity.<sup>60</sup> Table 3 shows the empirical disengagement and Rouse times for chains with the weight-average molecular weight and the molecular weight above which 1% of the chain population by weight resides. These empirical relaxation times are expected to be an upper bound. This is due to the likely influence of constraint release from the faster relaxation of the shorter chains in the polydisperse melt, which would increase the relaxation rates. For stretched chains which are of the weight-average molecular weight, relaxation occurs rapidly and within a fraction of a second. However, for the longest 1% of chains the relaxation rates are much slower and are comparable to the relaxation rate of  $I_{\text{shish}}$ , observed for iPP(control) shown in Figure 6. This result is therefore consistent with the view that the dissolution of shish is controlled by the reptation of the high molecular weight component.<sup>23</sup>

Although relaxation processes have been extensively studied in a wide range of polymers, the influence of foreign particles has received comparatively little attention. Previous studies have suggested that the surface of large particles could stabilize extended chain conformations due to the surface contact points acting as physical cross-links.<sup>40,41,61</sup> Similarly, molecularly dispersed nanoparticles, which have a strong affinity for the polymer molecule, could increase the number of physical cross-links in an analogous way.<sup>25,43,62</sup> However, in the present experiment the addition of both nucleating particles was surprisingly found to increase the initial rate of relaxation of shish after shear ended, contrary to these expectations.

It is proposed that this surprising increase in shish relaxation in the presence of particles can be explained by the polydisperse nature of the iPP matrix. It is widely considered that when a polydisperse polymer is sheared, it is the longest chains which are the first to be involved in the formation of shish.<sup>5,11,19,63</sup> Recent small-angle neutron scattering studies (SANS) have indicated that the longer chains are not necessarily over represented in the shish.<sup>14</sup> Rather, the longer chains only act to accelerate shish formation, recruiting out chains smaller chains to the forming shish. The presence of longer molecular weight chains in the shish structure may also act to stabilize the shish structure once formed by decreasing both the rate of chain detachment from the lateral surface of the shish and subsequent chain relaxation. The molecular weight effect can be explained by the increase in the number of intrachain contact points with increasing chain length. Higher numbers of intrachain contact points then

I

dx.doi.org/10.1021/ma200040s | Macromolecules XXXX, XXX, 000–000



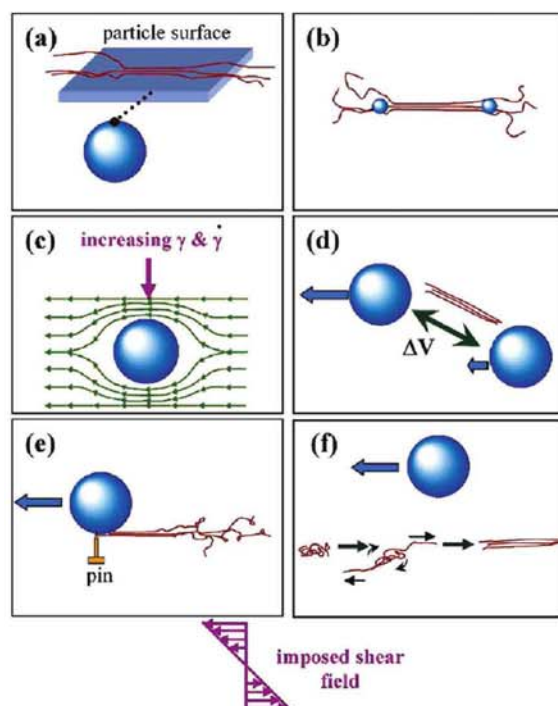


**Figure 15.** Schematic representation of six possible mechanisms for particle-assisted shish formation. (a) Stabilization of extended conformations on the surface of particles. (b) Retard relaxation of extended conformations by increasing the number of physical cross-links. (c) Increased strain and strain rate near the particle caused by flow of matrix around the particle. (d) Separation of nearby particles leading to increased elongation flow between the two particles. (e) One end of a molecule is adsorbed and pinned on the surface of particle, while the other end is extended by shear flow. (f) Long-range perturbation of a molecule's streamline by the motion of a passing particle. Refer to text for more details.

stabilize the extended chain conformations, retarding relaxation. Therefore, the faster relaxation of shish strongly suggests that the presence of the particles decreased the size of chains which could template shish formation. Shish formed around these lower average molecular weight chains would then have a greater propensity to relax than shish that are formed around the higher molecular weight chains.

$I_{\text{shish}}$  was found to increase again after an appreciable induction time. Keum et al.<sup>24</sup> recently observed a similar phenomenon in sheared UHMWPE/HDPE, noting the shish length increased around the same time. Keum then explained the increase in  $I_{\text{shish}}$  by the longitudinal growth of shish using the autocatalytic growth mechanism proposed by Peterman et al.<sup>17</sup> However, in this experiment both  $D_{\text{shish}}$  and  $L_{\text{shish}}$  were observed to decrease over this time period, and therefore autocatalytic growth of shish after shear cannot explain the observed increase in  $I_{\text{shish}}$ . Another possible explanation for the observed increase in  $I_{\text{shish}}$  could be the decomposition of the melt by a spinodal liquid–liquid phase separation, such as proposed by Olmsted et al.<sup>64</sup> Shear is considered to increase the kinetics of the spinodal transformation. Therefore, the observed decrease in the induction time with the addition of nucleating particles would support such a

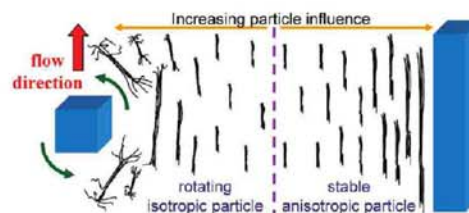


**Figure 16.** Influence of rotating isotropic and stable anisotropic particles on formation of shish.

hypothesis, as the particle's presence appears to increase the intensity of the shear field.

**4.3. Particle-Assisted Shish Formation.** In the present work, both particles were found to increase the amount of shish and their dimension compared to iPP(control). This resulted in a substantially greater crystalline and lamellar orientation during subsequent crystallization. The addition of foreign particles in a wide range of polymer/particle systems has been shown to increase the molecular orientation under shear-induced crystallization conditions.<sup>15,16,25,28,35,38–43</sup> Figure 15 summarizes six possible mechanisms for particle-assisted shish formation. The SAXS results presented in the previous section indicate that the addition of both particles increased the relaxation rate of shish. Therefore, mechanisms where the particles stabilize extended chain conformations would appear to be unlikely to account for the observed increase in shish. Rather, the increased relaxation rate shows that the addition of particles allowed shorter chains to template shish formation. This implies that it is the modification of the strain environment at or near the particle surface which aids shish formation in these materials.

The modification of the local strain environment could occur in at least four ways. Hwang et al.<sup>65</sup> advocated that polymer molecules flow around the particles, and this leads to an increase in both the strain and strain rate near the exposed sides of the particle. Furthermore, Hwang suggested the elongational component of the shear flow would be increased in the region between two separating particles. Jerschow and Janeschitz-Kriegl<sup>35</sup> proposed that polymer molecules may adsorb onto the surface of foreign particles, pinning one end of the molecule. During subsequent shear flow, the free end of the molecule becomes stretched, accelerating the formation of shish. Yamazaki et al.<sup>15,16</sup> investigated the influence of dust on shish formation and drew a similar conclusion. Under simple shear flow, the rotational component of the flow is just sufficient to counteract the elongation component from stretching out the polymer chains. Harlen and Koch<sup>66</sup> showed that polymer molecules moving past particles can tip this balance in the favor of the extensional component. As a molecule moves past a particle, the molecule gets disturbed from its initial streamline due to the slightly different flow histories along the length of the molecule. The molecule now lies over a broader range of streamlines and is able to interact more strongly with the flow and stretch along the flow direction.

The two nucleating particles in this experiment had similar chemical compositions and size. However, both particles had significantly different nucleation efficiencies and aspect ratios. Particles with high affinity for the polymer molecules<sup>25</sup> and high aspect ratios<sup>36</sup> have been suggested to aid the formation of shear-induced nuclei. In this experiment the HPN particles were

J

dx.doi.org/10.1021/ma200040s | Macromolecules XXXX, XXX, 000–000



relatively isotropic but had a much higher nucleation efficiency than the high aspect ratio SB particles. Compared to the addition of HPN particles, the addition of SB particles resulted in more shish which also had larger dimensions. Therefore, the aspect ratio appears to be the more dominant factor in aiding shish formation rather than nucleation efficiency. An appreciable influence of nucleation efficiency would have suggested a surface mechanism may be important. Hence, the results presented here suggest that the addition of foreign particles assist shish formation by modifying the local strain environment near but not necessarily on the particle surface.

Further information regarding how particle aspect ratio influences shish formation can be gleaned from the development of shish alignment during shear flow. At the start of shear, the shish in iPP(control) and in iPP(1.00SB) were highly aligned along the flow direction, while the shish in iPP(1.00HPN) were not. This result can be explained by how the different particles interact with and particularly how they rotate in the shear field. The orientation of the particle can be described by a family of closed curves known as Jeffery orbital's which depend on the initial orientation of the particles to the flow direction.<sup>67</sup> Furthermore, the rate of rotation is known to depend on the aspect ratio of the particle, with higher aspect ratio particles rotating less than low aspect ratio particles.<sup>68–70</sup> This low rotation rate is consistent with the SB particles being oriented with their long axis along the flow direction (Figure 2e). The higher rotation of the HPN particles could cause shish which are forming nearby to tumble, destabilizing their formation and leading to fewer and smaller shish being formed (Figure 16). Conversely, the SB particles, which adopt a more stable orientation along the flow direction, help guide shish growth. It is interesting to note that the shish alignment in iPP(1.00HPN) dramatically increased during shear. This could indicate that as the shish form, the growing shish stabilize the rotation of the HPN particles, further enhancing their alignment along the flow direction. However, the details of this interesting occurrence remain open for debate.

## 5. CONCLUSIONS

The formation and relaxation of shish was investigated in pure isotactic polypropylene (iPP(control)) and iPP containing two commercial nucleating particles during and after moderate shear flow. The findings from this study are briefly summarized as follows.

Surprising sharp meridional streaks were observed in conjunction with equatorial streaks in the small-angle X-ray scattering patterns during shear flow. As shear progressed, the meridional streak decreased and disappeared soon after the shear stopped. These observations provide strong evidence that the initial shish growth occurs in discrete steps by the aggregation of pointlike nuclei into oriented threads.

The two nucleating particles, needlelike sodium benzoate (SB) and isotropic bicyclo[2.2.1]heptane-2,3-dicarboxylic acid (HPN), had different nucleation efficiencies with HPN having almost twice the nucleation efficiency of SB when compared at a similar particle surface area.

The addition of both nucleating particles increased the initial relaxation rate of shish after shear flow stopped. This result was explained by the presence of the particles inducing lower molecular weight chains to participate in shish formation. The lower molecular weight chains then destabilized the shish, accelerating their dissolution.

The addition of both nucleating particles resulted in a significant increase in the amount of shish and their size (length and diameter) compared to iPP(control). Possible mechanisms that could account for the particle-assisted formation of shish were discussed. The most likely mechanisms were based on the particles modifying the local strain environment near the particle surface.

The amount, dimensions, and alignment of the shish along the flow direction were much higher in iPP(1.00SB) compared to iPP(1.00HPN). These results imply that the shape of the nucleating particle can have important implications for the formation of shish. It was proposed that the needlelike SB particle adopted stable orientations along the flow direction, guiding shish growth, while isotropic HPN particles rotated during shear, destabilizing shish forming nearby.

## ■ AUTHOR INFORMATION

### Corresponding Author

\*E-mail andyphil21@gmail.com, Ph +613 9905 53213, Fax +613 9905 4940.

## ■ ACKNOWLEDGMENT

This work was performed at the SAXS/WAXS beamline at the Australian Synchrotron, Victoria, Australia. The assistance from Dr. Jan Ilavsky at Advanced Photon Source Argonne National Laboratory for modifying the Nika software package was greatly appreciated. The authors also acknowledge George Theodossiou at the Monash Centre for Electron Microscopy (MCEM) for preparing the SEM images.

## ■ REFERENCES

- (1) Keller, A.; Kolnaar, H. W. Flow induced orientation and structure formation. In *Materials Science and Technology, Processing of Polymers*; Meijer, H. E. H., Ed.; Wiley-VCH: New York, 1997; Vol. 18, p 189.
- (2) Janeschitz-Kriegl, H.; Ratajski, E. *Polymer* **2005**, *46*, 3856–3870.
- (3) Mykhaylyk, O. O.; Chambon, P.; Graham, R. S.; Fairclough, J. P. A.; Olmsted, P. D.; Ryan, A. J. *Macromolecules* **2008**, *41*, 1901–1904.
- (4) Mykhaylyk, O. O.; Chambon, P.; Impradice, C.; Fairclough, J. P. A.; Terrill, N. J.; Ryan, A. J. *Macromolecules* **2010**, *43*, 2389–2405.
- (5) Soman, R. H.; Yang, L.; Zhu, L.; Hsiao, B. S. *Polymer* **2005**, *46*, 8587–8623.
- (6) Hu, W.; Frenkel, D.; Mathot, V. B. F. *Macromolecules* **2002**, *35*, 7172–7174.
- (7) Housmans, J.-W.; Steenbakkers, R. J. A.; Roozmond, P. C.; Peters, G. W. M.; Meijer, H. E. H. *Macromolecules* **2009**, *42*, 5728–5740.
- (8) Kumaraswamy, G. *Polym. Rev.* **2005**, *45*, 375–397.
- (9) Fujiyama, M. Higher order structure of injection-moulded polypropylene. In *Polypropylene: Structure, Blends and Composites*; Karger-Kocsis, J., Ed.; Chapman & Hall: London, 1995; Vol. 1, pp 173–174.
- (10) Fujiyama, M.; Awaya, H.; Kimura, S. *J. Appl. Polym. Sci.* **1977**, *21*, 3291–3309.
- (11) Dukovski, I.; Muthukumar, M. *J. Chem. Phys.* **2003**, *118*, 6648–6655.
- (12) Pennings, A. J.; van der Mark, J. M. A. A.; Booij, H. C. *Colloid Polym. Sci.* **1969**, *236*, 99–111.
- (13) Lieberwirth, L.; Loos, J.; Petermann, J.; Keller, A. *J. Polym. Sci., Part B: Polym. Phys.* **2000**, *38*, 1183–1187.
- (14) Kimata, S.; Sakurai, T.; Nozue, Y.; Kasahara, T.; Yamaguchi, N.; Karino, T.; Shibayama, M.; Kornfield, J. A. *Science* **2007**, *316*, 1014–1017.
- (15) Yamazaki, S.; Watanabe, K.; Okada, K.; Yamada, K.; Tagashira, K.; Toda, A.; Hikosaka, M. *Polymer* **2005**, *46*, 1685–1692.

K

dx.doi.org/10.1021/ma200040s | Macromolecules XXXX, XXX, 000–000

- (16) Yamazaki, S.; Watanabe, K.; Okada, K.; Yamada, K.; Tagashira, K.; Toda, A.; Hikosaka, M. *Polymer* **2005**, *46*, 1675–1684.
- (17) Petermann, J.; Miles, M.; Gleiter, H. *J. Polym. Sci., Polym. Phys. Ed.* **1979**, *17*, 55–62.
- (18) Janeschitz-Kriegl, H.; Ratajski, E.; Stadlbauer, M. *Rheol. Acta* **2003**, *42*, 355–364.
- (19) Seki, M.; Thurman, D. W.; Oberhauser, J. P.; Kornfield, J. A. *Macromolecules* **2002**, *35*, 2583–2594.
- (20) Heeley, E. L.; Fernyhough, C. M.; Graham, R. S.; Olmsted, P. D.; Inkson, N. J.; Embery, J.; Groves, D. J.; McLeish, T. C. B.; Morgovan, A. C.; Meneau, F.; Bras, W.; Ryan, A. J. *Macromolecules* **2006**, *39*, 5058–5071.
- (21) Hoffman, J. D. *Polymer* **1979**, *20*, 1070–1077.
- (22) Clark, E. J.; Hoffman, J. D. *Int. J. Thermophys.* **1990**, *11*, 225–237.
- (23) Balzano, L.; Kukalyekar, N.; Rastogi, S.; Peters, G. W. M.; Chadwick, J. C. *Phys. Rev. Lett.* **2008**, *100*, 048302.
- (24) Keum, J. K.; Zuo, F.; Hsiao, B. S. *Macromolecules* **2008**, *41*, 4766–4776.
- (25) Patil, N.; Balzano, L.; Portale, G.; Rastogi, S. *Macromolecules* **2010**, *43*, 6749–6759.
- (26) Mathieu, C.; Thierry, A.; Wittmann, J. C.; Lotz, B. *J. Polym. Sci., Part B: Polym. Phys.* **2002**, *40*, 2504–2515.
- (27) Mathieu, C.; Thierry, A.; Wittmann, J. C.; Lotz, B. *Polymer* **2000**, *41*, 7241–7253.
- (28) D'Haese, M.; Van Puyvelde, P.; Langouche, F. *Macromolecules* **2010**, *43*, 2933–2941.
- (29) Zhu, P.; Phillips, A.; Edward, G.; Nichols, L. *Phys. Rev. E* **2009**, *80*, 051801.
- (30) Cacciuto, A.; Auer, S.; Frenkel, D. *Nature* **2004**, *428*, 404–406.
- (31) Chayen, N. E.; Saridakis, E.; Sear, R. P. *Proc. Natl. Acad. Sci. U.S.A.* **2006**, *103*, 597–601.
- (32) Somwangthanaroj, A.; Lee, E. C.; Solomon, M. J. *Macromolecules* **2003**, *36*, 2333–2342.
- (33) Rozanski, A.; Monasse, B.; Szkudlarek, E.; Pawlak, A.; Piorkowska, E.; Galeski, A.; Haudin, J. M. *Eur. Polym. J.* **2009**, *45*, 88–101.
- (34) Nowacki, R.; Monasse, B.; Piorkowska, E.; Galeski, A.; Haudin, J. M. *Polymer* **2004**, *45*, 4877–4892.
- (35) Jerschow, P.; Janeschitz-Kriegl, H. *Int. Polym. Process.* **1997**, *12*, 72–77.
- (36) Byelov, D.; Panine, P.; Remerie, K.; Biemond, E.; Alfonso, G. C.; de Jeu, W. H. *Polymer* **2008**, *49*, 3076–3083.
- (37) Huo, H.; Jiang, S.; An, L. *Macromolecules* **2004**, *37*, 2478–2483.
- (38) Zhu, P.; Tung, J.; Phillips, A.; Edward, G. *Macromolecules* **2006**, *39*, 1821–1831.
- (39) Zhu, P.; Phillips, A.; Tung, J.; Edward, G. *J. Appl. Phys.* **2005**, *97*, 104908.
- (40) Zhu, P.; Edward, G.; Nichols, L. *J. Phys. D: Appl. Phys.* **2009**, *42*, 245406.
- (41) Zhu, P.; Tung, J.; Edward, G.; Nichols, L. *J. Appl. Phys.* **2008**, *103*, 124906.
- (42) Phillips, A.; Zhu, P.; Edward, G. *Polymer* **2010**, *51*, 1599–1607.
- (43) Fu, B. X.; Yang, L.; Somani, R. H.; Zong, S. X.; Hsiao, B. S.; Phillips, S.; Blanski, R.; Ruth, P. J. *Polym. Sci., Part B: Polym. Phys.* **2001**, *39*, 2727–2739.
- (44) Mezghani, K.; Phillips, P. J. *Polymer* **1998**, *39*, 3735–3744.
- (45) Byelov, D.; Panine, P.; de Jeu, W. H. *Macromolecules* **2007**, *40*, 288–289.
- (46) Fillon, B.; Lotz, B.; Thierry, A.; Wittmann, J. C. *J. Polym. Sci., Part B: Polym. Phys.* **1993**, *31*, 1395–1405.
- (47) Fillon, B.; Wittmann, J. C.; Lotz, B.; Thierry, A. *J. Polym. Sci., Part B: Polym. Phys.* **2003**, *41*, 1383–1393.
- (48) Libster, D.; Aserin, A.; Garti, N. *Polym. Adv. Technol.* **2007**, *18*, 685–695.
- (49) Guinier, A. *Small-Angle Scattering of X-rays*; Wiley: New York, 1955.
- (50) Perret, R.; Ruland, W. *J. Appl. Crystallogr.* **1969**, *2*, 209–218.
- (51) Lotz, B.; Wittmann, J. C. *Polymer* **1996**, *37*, 4979–4992.
- (52) Turner-Jones, A. *Polymer* **1971**, *12*, 487–508.
- (53) De Rosa, C.; Auremma, F.; Paolillo, M.; Resconi, L.; Camurati, I. *Macromolecules* **2005**, *38*, 9143–9154.
- (54) Keller, A.; MacKley, M. R. *Pure Appl. Chem.* **1974**, *39*, 195–224.
- (55) de Gennes, P. G. *J. Chem. Phys.* **1974**, *60*, 5030–5042.
- (56) Pennings, A. J.; Kiel, A. M. *Kolloid Z. Z. Polym.* **1965**, *205*, 160–162.
- (57) Janeschitz-Kriegl, H.; Ratajski, E.; Wippel, H. *Colloid Polym. Sci.* **1999**, *277*, 217–226.
- (58) Somani, R. H.; Yang, L.; Hsiao, B. S.; Agarwal, P. K.; Fruitwala, H. A.; Tsou, A. H. *Macromolecules* **2002**, *35*, 9096–9104.
- (59) Doi, M.; Edwards, S. F. *The Theory of Polymer Dynamics*; Clarendon Press: Oxford, 1986.
- (60) Vega, J. F.; Rastogi, S.; Peters, G. W. M.; Meijer, H. E. H. *J. Rheol.* **2004**, *48*, 663–678.
- (61) Garcia-Gutierrez, M.; Milner, S. T.; McLeish, T. C.; Hernandez, J. J.; Nogales, A.; Panine, P.; Rueda, D. R.; Ezquerro, T. A. *Macromolecules* **2007**, *41*, 844–851.
- (62) Kelarakis, A.; Yoon, K.; Sics, L.; Somani, R. H.; Chen, X.; Hsiao, B. S.; Chu, B. *J. Macromol. Sci., Part B: Polym. Phys.* **2006**, *45*, 247–261.
- (63) Somani, R. H.; Yang, L.; Hsiao, B. S. *Polymer* **2006**, *47*, 5657–5668.
- (64) Olmsted, P. D.; Poon, W. C. K.; McLeish, T. C. B.; Terrill, N. J.; Ryan, A. J. *Phys. Rev. Lett.* **1998**, *81*, 373–376.
- (65) Hwang, W. R.; Peters, G. W. M.; Hulslen, M. A.; Meijer, H. E. H. *Macromolecules* **2006**, *39*, 8389–8398.
- (66) Harlen, O. G.; Koch, D. L. *J. Fluid Mech.* **1993**, *252*, 187–207.
- (67) Jeffery, G. B. *Proc. R. Soc. London, Ser. A* **1922**, *102*, 161–179.
- (68) Gunes, D. Z.; Scirocco, R.; Mewis, J.; Vermant, J. *J. Non-Newtonian Fluid Mech.* **2008**, *155*, 39–50.
- (69) Hobbie, E. K.; Wang, H.; Kim, H.; Lin-Gibson, S.; Grulke, E. A. *Phys. Fluids* **2003**, *15*, 1196.
- (70) Hinch, E. J.; Leal, L. G. *J. Fluid Mech.* **1972**, *52*, 683–712.

L

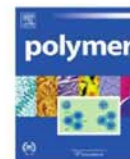
dx.doi.org/10.1021/ma200040s | Macromolecules XXXX, XXX, 000–000





Contents lists available at ScienceDirect

Polymer

journal homepage: [www.elsevier.com/locate/polymer](http://www.elsevier.com/locate/polymer)

# Polystyrene as a versatile nucleating agent for polypropylene

Andrew Phillips\*, Peng-Wei Zhu, Graham Edward

Cooperative Research Centre (CRC) for Polymers, Department of Materials Engineering, Monash University, Vic 3800, Australia

## ARTICLE INFO

**Article history:**  
Received 14 October 2009  
Received in revised form  
15 January 2010  
Accepted 3 February 2010  
Available online 10 February 2010

**Keywords:**  
Simultaneous wide and small  
angle X-ray scattering  
Time resolved  
Crystallisation

## ABSTRACT

The morphology of isotactic polystyrene (iPS) particles which had been compounded into an isotactic polypropylene (iPP) matrix was varied in-situ by selective heat treatment to be either amorphous (iPS<sub>amorphous</sub>) or semicrystalline (iPS<sub>crystalline</sub>). The influence of iPS morphology on the quiescent and shear-induced isothermal crystallisation of iPP was then studied using differential scanning calorimetry (DSC), in-situ simultaneous small and wide angle X-ray scattering (SAXS/WAXS) and polarised optical microscopy (POM). In the quiescent condition iPS<sub>crystalline</sub> was found to selectively nucleate the  $\beta$  phase while iPS<sub>amorphous</sub> nucleated the  $\alpha$  phase of iPP. Compared to the control sample (iPP<sub>control</sub>), the presence of both morphologies of iPS increased the number of shear-induced oriented crystal precursors that form as a result of the step shear. During isothermal crystallisation the shear-induced nuclei promote oriented  $\alpha$  form crystal growth, accelerate the crystallisation kinetics and ultimately swamp the effect of the nucleating particles present.

© 2010 Elsevier Ltd. All rights reserved.

## 1. Introduction

Natta and Corfidini showed that the usual crystal form of isotactic polypropylene (iPP) has each polymer molecule arranged as a  $3_1$  helix [1]. The helix is chiral and can exist in either the right or left hand configuration. This chirality allows for four different crystalline phases:  $\alpha$  (monoclinic) [1],  $\beta$  (trigonal) [2–4],  $\gamma$  (orthorhombic) [5] and the smectic phase [1].  $\alpha$ -iPP is by far the most common and occurs under a wide variety of crystallisation conditions.  $\beta$ -iPP has received considerable attention due to its promising mechanical properties, such as improved toughness and elongation at break [6–8].  $\beta$ -iPP is thermodynamically less stable and is therefore more difficult to obtain under conditions typically found in industrial processes.

Numerous methods have been developed to produce significant quantities of  $\beta$  phase such as: crystallisation in a temperature gradient [9]; shear-induced crystallisation [10–14], particularly in oscillation mode [15–17]; and by the addition of specific  $\beta$  nucleating agents [16,18–23]. Of these methods, large fractions of  $\beta$ -iPP are most easily attained by the addition of specific  $\beta$  nucleating agents. Historically these agents have been derived from low molecular weight crystallisable compounds, which can broadly be divided into two categories. The first category includes aromatic compounds such as  $\gamma$ -quinacridone [20] (Red Pigment E3B), while

the second category includes compounds derived from group IIA metal salts such as LaC and CaCO<sub>3</sub> [18] and Ca salts of pimelic and suberic acid [18,19]. The selectivity of these agents can be described by a two dimensional lattice matching theory [24–27]. Central to this theory is that a reasonable epitaxial match, at least within 10%, occurs between the repeat distance in the iPP unit cell and the corresponding nucleating surface. Recently, an amorphous polymeric nucleating agents, styrene acrylonitrile (SAN) and polystyrene (PS) were shown to also selectively nucleate  $\beta$ -iPP [22,23]. However, it is unclear how an epitaxial theory could explain the nucleation mechanism of these amorphous polymers. These polymers have the advantage of being relatively cheap and easy to process and therefore show good commercial potential. However, any explanation for the nucleation mechanism of these amorphous polymers is at best tentative.

The methyl groups of the iPP would most likely interact with the phenyl groups of PS [26] and therefore the arrangement of the phenyl groups would be important to understanding any epitaxial relationship between the two. The structure of amorphous polystyrene has been extensively studied [28–34]. The most comprehensive model proposed to date shows the phenyl groups micro-segregate into stacks [34]. Although the stacks are disordered, the phenyls within the stacks not only show significant positional registration with neighbouring phenyls within the same stack but neighbouring stacks show also significant positional registration with each other. The repeat distance between adjacent phenyl groups in the same stack is  $\sim 5$  Å. Isotactic polystyrene (iPS), being a stereoregular polymer, allows the iPS molecules to

\* Corresponding author. Tel.: +61 421 607 983; fax: +61 3 9905 4940.  
E-mail address: [andyphil21@gmail.com](mailto:andyphil21@gmail.com) (A. Phillips).

crystallise in the form of a  $3_1$  helix [35]. Micro-segregation of the phenyls into regular stacks is also a feature of crystalline iPS, with the repeat distance between adjacent phenyl groups within each stack being 6.65 Å. If epitaxy is significant, the change in the arrangement of phenyls between the amorphous and crystalline states of iPS should lead to a change in iPP crystallisation behaviour. Accordingly, in this study the morphology of iPS particles embedded in an iPP matrix were varied to be either semicrystalline (iPS<sub>crystalline</sub>) or amorphous (iPS<sub>amorphous</sub>) and their influence on the isothermal quiescent crystallisation of iPP was then studied.

Shearing the melt prior to the onset of crystallisation further complicates the crystallisation of iPP in the presence of nucleating agents. Most importantly shear increases the number of shear-induced oriented crystal precursors [36–40] which can then template the formation of oriented crystalline and lamellar structures [39,40]. The addition of common nucleating agents has been found to increase the density of the oriented crystal precursors for a given set of crystallisation conditions [41] and it is suspected that their presence can significantly reduce the activity of any nucleating agents present [16,18]. For these reasons, crystallisation after a moderate step shear was also studied.

## 2. Experimental

### 2.1. Sample preparation

The matrix polymer used in this study was an iPP homopolymer manufactured by the Borealis group with  $M_w = 367,000$  g/mol and  $M_n = 74,000$  g/mol. The polymeric nucleating agent used was a fine powder of iPS (>90% isotactic) manufactured by Scientific Polymer Products Inc. with  $M_w = 400,000$  g/mol. The iPS was heated in a vacuum oven at 180 °C for 5 h to induce a high degree of crystallinity then sieved through a 100 µm mesh to further reduce the average grain size of the particles. 2 wt% of the refined iPS powder was compounded into molten iPP at 190 °C for 10 min at 60 RPM in a Haake Rheocord 90 batch mixer. This master batch was then compression moulded into sheets 1.5 mm thick at 190 °C for 5 min.

### 2.2. Thermal–shear profile

A Linkam CSS450 shear cell was used to control the thermal–shear profile. To ensure consistent temperature between the X-ray and optical set ups, external temperature calibrations were used. Two thermal pre-treatments were applied above and below the crystalline melting point of iPS ( $T_m^0(\text{iPS}) = 242$  °C) [42] to yield samples where the morphology of the iPS was predominantly amorphous or semicrystalline. Amorphous iPS in a matrix of iPP (iPP(iPS<sub>amorphous</sub>)) was produced by heating the master batch to 280 °C for 3 min then quickly cooling it to room temperature at 30 °C/min, while crystalline iPS in a matrix of iPP (iPP(iPS<sub>crystalline</sub>)) was produced by heating the material to 200 °C for 3 min before cooling too room temperature. Control material (iPP<sub>control</sub>) containing no nucleating agent was prepared under the same conditions as iPP(iPS<sub>crystalline</sub>) and iPP(iPS<sub>amorphous</sub>). The crystallisation kinetics of the iPP<sub>control</sub> material prepared by both routes was found to be similar showing degradation of the iPP matrix was not significant under the experimental conditions. All samples were then reheated to 200 °C, compressed to the required gap thickness and held there for at least 3 min to eliminate the previous thermal history of the iPP matrix. Samples were cooled to the isothermal crystallisation temperature of 135 °C at 30 °C/min. Crystallisation from the quiescent melt and after a moderate step shear with a shear rate of  $80 \text{ s}^{-1}$  and duration of 1 s were studied. In all cases the samples were held at the crystallisation temperature for long

enough for the crystallisation rate to be effectively negligible. Samples were then cooled at 30 °C/min to room temperature.

Additional heat treatments, identical to those experienced by iPP(iPS<sub>crystalline</sub>) and iPP(iPS<sub>amorphous</sub>) were performed to prepare iPS samples of sufficient size for ex-situ X-ray analysis. The crystalline iPS material was designated (iPS<sub>crystalline</sub>), while the amorphous iPS material was designated (iPS<sub>amorphous</sub>).

### 2.3. Optical microscopy

Polarised optical micrographs (POMs) were taken on a Nikon 80i microscope using a Nikon DS-Fi1 CCD camera at a shear cell gap thickness of 50 µm.

### 2.4. Differential scanning calorimetry

Differential scanning calorimetry (DSC) experiments were performed on the fully crystallised iPP samples using a Perkin–Elmer DSC-7 at heating rates of 10 °C/s and under a nitrogen atmosphere. Sample size was ~5 mg. Pure indium and zinc references were used for calibration. Heating scans were also performed on the ex-situ iPS material which had experienced similar conditions to that which the compounded material experienced in the shear cell. Enthalpy of fusion,  $\Delta H$ , was determined by integrating the area under the baseline corrected thermogram. Percentage crystallinity of iPS was calculated from the ratio of  $\Delta H/\Delta H_f^0$  where  $\Delta H$  for iPS was taken as 86.59 J/g [43]. The density of the crystalline and amorphous phases were taken as 1.08 g/cm<sup>3</sup> [35] and 1.056 g/cm<sup>3</sup> [30] respectively.

### 2.5. X-ray scattering

Simultaneous two dimensional wide and small angle X-ray scattering experiments (SAXS & WAXS) were performed on the SAXS/WAXS beamline at the Australian Synchrotron, Fig. 1. The setup allowed for in-situ investigations with a considerable amount of the scattering intensity around the azimuth ( $\phi \sim 80^\circ$ ) in the WAXS region (Polaris CCD 2D detector) to be captured whilst simultaneously capturing complete SAXS patterns (MAR CCD 2D detector). The shear cell was adapted for use with X-ray radiation. The bottom plate had three slots allowing X-rays to be introduced to the sample. The top plate had a narrow 3 mm diameter aperture allowing scattered X-rays to pass. Thin films of Kapton™ ~50 µm were used to contain the sample between the top and bottom plates. A shear cell gap thickness of 500 µm was used. Beam dimensions of  $250 \times 150$  µm, a wavelength of  $\lambda = 1.48$  Å, and an exposure time of 1 s were employed throughout the experiment. Scattering without the specimen was also recorded to enable background correction. All images were normalised to the main

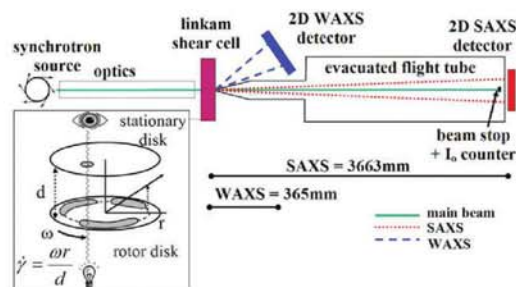


Fig. 1. Diagram of the simultaneous 2D WAXS/SAXS setup used at the Australian Synchrotron.



beam intensity which was measured by a scintillation counter mounted in the beam stop. The SAXS15id program was used to reduce the 2D data.

Additional WAXS experiments were performed on ex-situ iPS samples that had been subjected to similar thermal treatments to that experienced in the shear cell. The experiments were performed at the Australian National Beamline Facility (ANBF), a synchrotron beamline at the Photon Factory in Tsukuba, Japan. Details of the experimental setup have been reported in previous papers [40,41]. Beam dimensions were  $200 \times 200 \mu\text{m}$ , the exposure time was 300 s, and the wavelength was  $2 \text{ \AA}$ . The camera length was 111 mm and image plates were used as the detection system. The Nika software program was used to reduce the 2D data.

Uncertainty in the parameters measured by X-ray and DSC methods was assessed by calculating the standard error in the measurement and the 95.4% confidence interval was reported.

### 3. Results

#### 3.1. Morphology of iPS particles

A survey was conducted to establish the homogeneity and dispersion of iPS particles in the iPP matrix and to investigate the influence of the selective heat treatment on the morphology of the iPS particles. The distribution of equivalent spherical diameters ( $D$ ) of the  $\text{iPS}_{\text{crystalline}}$  and  $\text{iPS}_{\text{amorphous}}$  particles in the iPP matrix was determined by taking 10 POMs of each sample and applying standard image analysis techniques to determine  $D$  for each particle. The results are presented in Fig. 2a. The analysis showed a very similar distribution of diameters for iPS particles in both  $\text{iPP}(\text{iPS}_{\text{amorphous}})$  and  $\text{iPP}(\text{iPS}_{\text{crystalline}})$  material with the average equivalent spherical diameter  $D_{\text{ave}}$  for both being  $\sim 16 \mu\text{m}$ . The

influence of the selective thermal pre-treatments on the morphology of the iPS particles can be illustrated by following the changes that occurred to same iPS particle after heat treatment. Initially, the iPS particle embedded in the iPP matrix was heated to  $200^\circ\text{C}$  for 3 min ( $\text{iPP}(\text{iPS}_{\text{crystalline}})$ ), Fig. 2b. In this condition the particle showed high birefringence and was of irregular shape. The same particle was then heated to  $280^\circ\text{C}$  for 3 min ( $\text{iPP}(\text{iPS}_{\text{amorphous}})$ ), Fig. 2c. After this treatment the particle lost its birefringence and tended to become slightly more rounded in appearance.

Fig. 3 shows the scattered intensity versus 1D scattering vector ( $q = 4\pi\sin\theta/\lambda$ ; where  $\theta$  is the scattering angle and  $\lambda$  is the incident wavelength) of the two iPS samples given similar thermal profiles to that which the master batch of 2 wt% iPS in iPP was subjected in the shear cell. For clarity the  $\text{iPS}_{\text{crystalline}}$  curve is offset from  $\text{iPS}_{\text{amorphous}}$ . The WAXS profile of  $\text{iPS}_{\text{amorphous}}$  shows two broad amorphous peaks centred at  $q = 0.68 \text{ \AA}^{-1}$  and  $1.45 \text{ \AA}^{-1}$ , while seven crystalline peaks were superimposed onto the two amorphous peaks in the  $\text{iPS}_{\text{crystalline}}$  profile. A volume crystallinity index ( $\chi_v$ ) for the ex-situ iPS samples was determined by separating out the amorphous, crystalline and background contributions to scattering between  $0.4 \text{ \AA}^{-1} \leq q \leq 4 \text{ \AA}^{-1}$ , similar to the procedure outlined previously for iPP [39] and using the following equation:

$$\chi_v = \frac{A_{\text{crystalline}}}{A_{\text{crystalline}} + A_{\text{amorphous}}} \quad (1)$$

where  $A_{\text{crystalline}}$  is the area of the crystalline peaks and  $A_{\text{amorphous}}$  is the amorphous area. The crystallinity determined by X-ray was  $\chi_v = 23(1)\%$ . The crystallinity determined by DSC was in close agreement  $\chi_v(\text{DSC}) = 25(2)\%$ . No crystallinity was observed in  $\text{iPS}_{\text{amorphous}}$  by DSC or X-ray techniques.

#### 3.2. Crystalline morphology

POMs were taken while the iPP was in the molten ( $200^\circ\text{C}$ ) and crystalline states Fig. 4. During crystallisation the surface of the  $\text{iPS}_{\text{crystalline}}$  particles were covered by a negatively birefringent phase characteristic of  $\beta$ -iPP. Many nucleation points were observed and crystal growth appeared to be columnar. The identification of  $\beta$ -iPP was confirmed by heating the material in-situ. The phase covering the  $\text{iPS}_{\text{crystalline}}$  particle melted at  $\sim 155^\circ\text{C}$  while the surrounding material melted at  $\sim 169^\circ\text{C}$ . Under the same conditions no negatively birefringent phase could be observed in either the  $\text{iPP}(\text{iPS}_{\text{amorphous}})$  or  $\text{iPP}_{\text{control}}$  samples. The presence of both morphologies of iPS also substantially reduced the  $\alpha$ -iPP spherulite size when compared to the  $\text{iPP}_{\text{control}}$ .

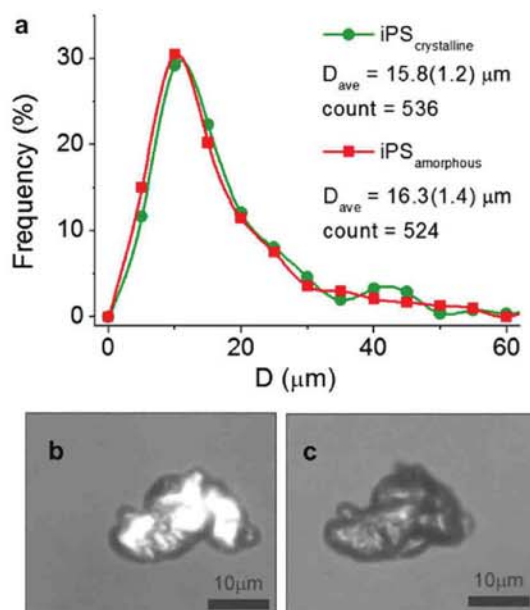


Fig. 2. (a) Distribution of the equivalent spherical diameter ( $D$ ) for iPS particles in  $\text{iPP}(\text{iPS}_{\text{crystalline}})$  and  $\text{iPP}(\text{iPS}_{\text{amorphous}})$  material. POM image of a typical iPS particle in the iPP matrix held at (b)  $200^\circ\text{C}$  for 3 min, and (c) the same particle held at  $280^\circ\text{C}$  for 3 min.

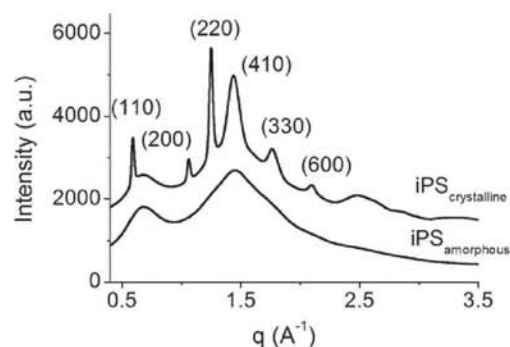


Fig. 3. 1D scattering profiles for ex-situ  $\text{iPS}_{\text{crystalline}}$  and  $\text{iPS}_{\text{amorphous}}$  material.



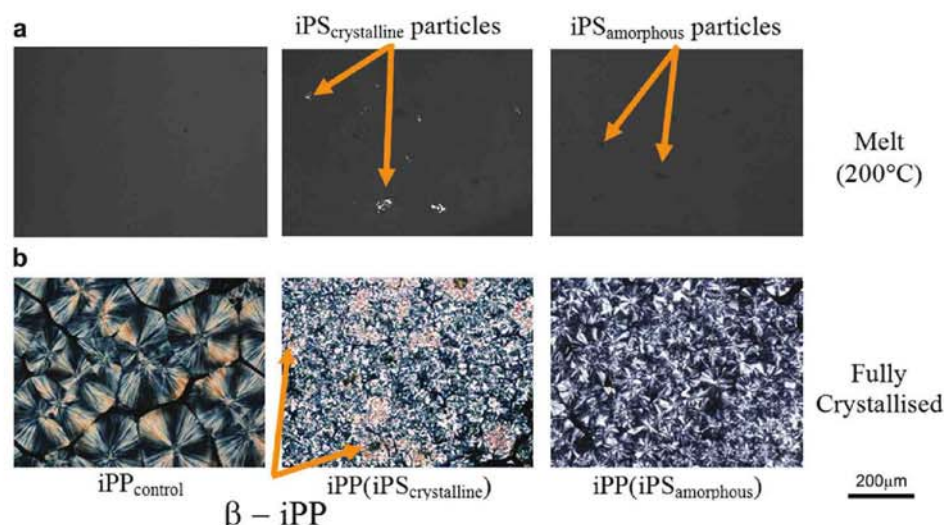


Fig. 4. Polarised optical micrographs taken of (a) the iPP melt and (b) after isothermal crystallisation at 135 °C under quiescent conditions.

1D WAXS profiles after the samples were fully crystallised from the quiescent state and after a moderate step shear are shown in Fig. 5. Automated procedures were employed to deconvolute the scattering profiles using the *fityk*® software package. Three Gaussian curves centred at  $q = 1.0 \text{ Å}^{-1}$ ,  $1.2 \text{ Å}^{-1}$  and  $1.45 \text{ Å}^{-1}$  were used to account for the amorphous scattering. Seven Gaussian

curves were used to account for the major crystalline scattering peaks observed between  $0.9 \text{ Å}^{-1} \leq q \leq 1.6 \text{ Å}^{-1}$ . The volume crystallinity index was determined using Eq. (1). The relative amount of  $\beta$  phase was determined using the Turner–Jones method [44]:

$$K_{\beta} = \frac{A_{\beta}(300)}{A_{\beta}(300) + A_{\alpha}(110) + A_{\alpha}(040) + A_{\alpha}(130)} \quad (2)$$

where  $A_{\beta}(300)$ ,  $A_{\alpha}(110)$ ,  $A_{\alpha}(040)$  and  $A_{\alpha}(130)$  are the areas of the reflections indicated in Fig. 5a. The  $\chi_v$  and  $K_{\beta}$  values are presented in Table 1. In the quiescent condition iPP(iPS<sub>crystalline</sub>) contained a mixture of  $\beta$ -iPP ( $K_{\beta} = 0.26$ ) and  $\alpha$ -iPP while both iPP(iPS<sub>amorphous</sub>) and iPP<sub>control</sub> samples did not show any  $\beta$ -iPP. This supports the POMs shown in Fig. 4. Shearing the melt prior to crystallisation led to all samples having a small amount of  $\beta$ -iPP. The samples containing both morphologies of iPS had essentially the same  $\beta$ -iPP contents with  $K_{\beta} \sim 0.08$ – $0.09$ , while iPP<sub>control</sub> had a slightly smaller value  $K_{\beta} = 0.04$ .

2D SAXS patterns after quiescent crystallisation and in the fully crystallised state are presented in Fig. 6a. These patterns show that the lamellar structure produced from quiescent conditions are essentially isotropic. SAXS patterns taken immediately after the application of shear ( $< 5 \text{ s}$ ) and after crystallisation had come to completion are shown in Fig. 6b and c respectively. For iPP<sub>control</sub> the step shear resulted in scattering at low angles in the equatorial region immediately after shear. These streaks persisted throughout the crystallisation process and were observed in the final fully

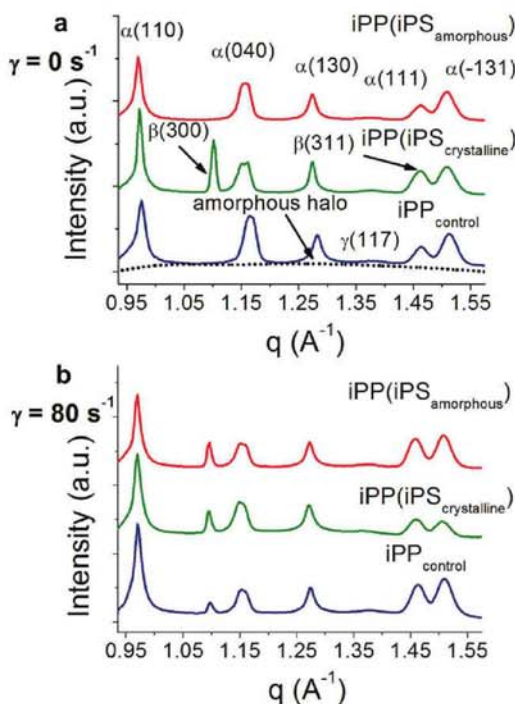
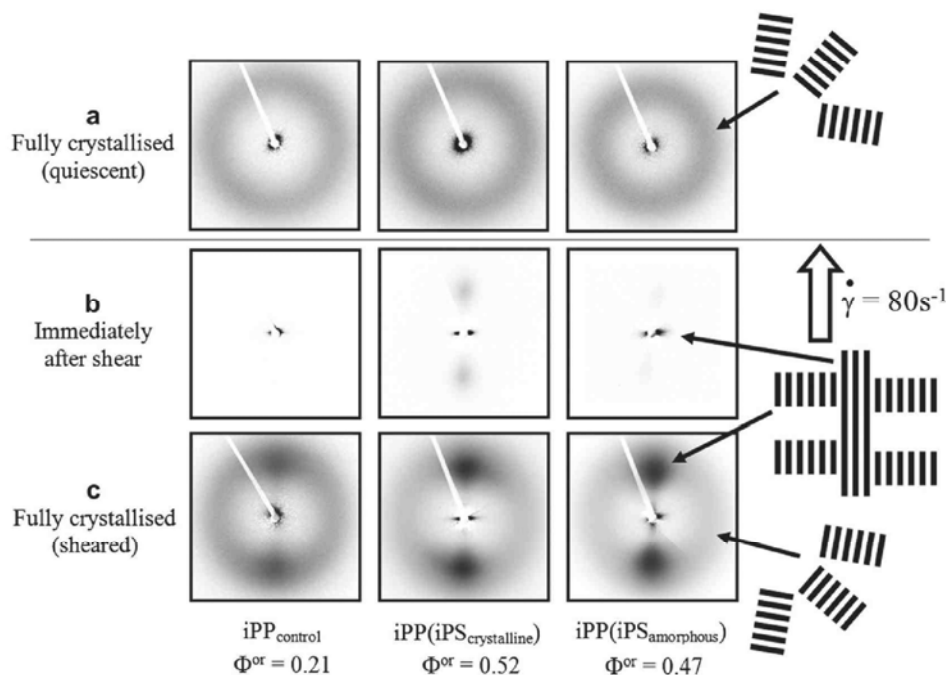


Fig. 5. 1D WAXS profiles of fully crystallised material (a) in the quiescent condition and (b) after a moderate step shear with a shear rate of  $80 \text{ s}^{-1}$  for 1 s.

Table 1

Crystallinity index ( $\chi_c$ ), relative amount of beta phase ( $k_{\beta}$ ) crystallisation half time ( $t_{0.5}$ ) and Avrami exponent ( $n$ ) under quiescent crystallisation conditions and a moderate step shear. Uncertainty in the measurement is recorded as a 95.4% confidence interval.

Material	Condition	$\chi_c$ (%)	$k_{\beta}$ (%)	$t_{0.5}$ (s)	$n$
iPP <sub>control</sub>	Quiescent	56(1)	~0	753(8)	3.0(0.2)
iPP(iPS <sub>crystalline</sub> )		63(1)	26(1)	223(3)	2.7(0.1)
iPP(iPS <sub>amorphous</sub> )		53(1)	~0	278(4)	3.1(0.1)
iPP <sub>control</sub>	Sheared	60(1)	4(1)	115(2)	2.4(0.1)
iPP(iPS <sub>crystalline</sub> )		61(1)	8(1)	73(1)	1.9(0.1)
iPP(iPS <sub>amorphous</sub> )		61(1)	9(1)	83(1)	2.0(0.1)



**Fig. 6.** Two dimensional SAXS images taken (a) in the fully crystallised condition after quiescent crystallisation, (b) immediately after the application of shear, and (c) in the fully crystallised condition after a moderate step shear with a shear rate of  $80 \text{ s}^{-1}$  for 1 s. Oriented fraction of lamellae ( $\Phi^{\text{or}}$ ) is provided for the fully crystallised material after a moderate step shear.

crystallised material. The formation of the streaks was quickly followed by an increase in scattering intensity in the meridional position. This type of scattering is consistent with a shish kebab model [36,37,39], where the equatorial scattering is due to oriented crystal precursors (shish) and the meridional scattering is due to epitaxial nucleated lamellae with their chain axis aligned along the flow direction (kebabs). Isotropic scattering was also observed and is assumed to be due to randomly oriented lamellae. The equatorial scattering formed immediately after shear was much stronger and extended to higher scattering angles for the materials containing both morphologies of iPS. Equally the meridional scattering was more pronounced and there was less isotropic scattering in these samples.

To quantify the amount of oriented lamellae formed, the oriented fraction ( $\Phi^{\text{or}}$ ) was determined from the azimuthal integration of background subtracted SAXS data according to the method proposed by Somani et al. [45]:

$$\Phi^{\text{or}} = \frac{\text{integrated area due to oriented scattering}}{\text{total integrated area}} \quad (3)$$

where the oriented and un-oriented components of scattering are defined in Fig. 7. It was found that  $\Phi^{\text{or}}$  for the material containing both iPS morphologies was more than twice that of iPP<sub>control</sub>. The material containing iPS<sub>crystalline</sub> had a slightly higher  $\Phi^{\text{or}}$  than the material containing iPS<sub>amorphous</sub>, although more detailed studies would be needed to test whether this is significant.

### 3.3. Crystallisation kinetics

The kinetics of crystallisation were probed by plotting the relative crystallinity ( $\chi_{\text{rel}}$ ) versus time, Fig. 8. The relative

crystallinity was determined by dividing the instantaneous crystallinity ( $\chi_t$ ) by the total crystallinity of the fully crystallised material ( $\chi_{\infty}$ ). Quantitative information about the crystallisation kinetics and growth geometry was obtained by fitting the crystallisation data to the Avrami model.

$$1 - \chi_{\text{rel}} = e^{-kt^n} \quad (4)$$

where  $k$  is the bulk crystallisation constant and  $n$  is the Avrami exponent. The crystallisation half time ( $t_{0.5}$ ) was taken as the time at which the model line intersected  $\chi_{\text{rel}} = 50\%$ . Compared to the iPP<sub>control</sub>,  $t_{0.5}$  was dramatically reduced in the presence of both iPS morphologies, with  $t_{0.5}$  for iPP(iPS<sub>crystalline</sub>) being slightly less than iPP(iPS<sub>amorphous</sub>), Table 1. The crystallisation kinetics from a sheared melt were significantly faster, up to 6 times for iPP<sub>control</sub>, than for the quiescent condition. The  $t_{0.5}$  for both iPS morphologies after the moderate step shear were significantly reduced compared to the iPP<sub>control</sub>. iPP(iPS<sub>crystalline</sub>) had a slightly shorter  $t_{0.5}$  than iPP(iPS<sub>amorphous</sub>).

The Avrami exponent was determined in the primary crystallisation region from the gradient of the linear region of a plot of  $\ln(\ln(1/(1 - \chi_{\text{rel}})))$  versus  $\ln(t)$ . At low conversions there is a significant uncertainty in determining  $\chi_{\text{rel}}$  by the above method. Significant deviation from the model also occurs in the latter stages of crystallisation which has been attributed to the occurrence of secondary crystallisation [46]. Therefore the Avrami exponent was determined by fitting a straight line to the linear region between these two extremes as shown in Fig. 9. In heterogeneous nucleation the Avrami exponent is related to the dimension of crystal growth: with  $n = 3$  indicating spherical growth;  $n = 2$  indicating disklike growth; and  $n = 1$  indicating rodlike growth. Often non-integer values of the Avrami exponent

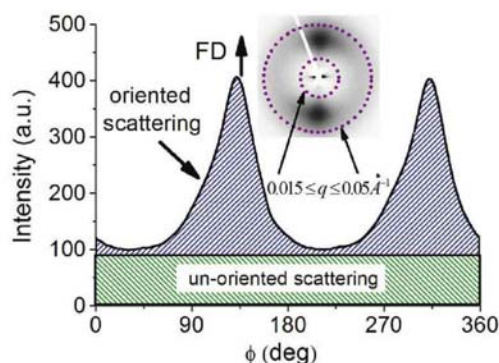


Fig. 7. Plot of background subtracted intensity versus azimuthal angle ( $\phi$ ) showing the method used to determine the oriented fraction of lamellae ( $\phi^{\text{or}}$ ) shown in Fig. 6.

are obtained indicating the presence of more than one growth geometry during crystallisation. The Avrami exponents determined by this method are summarised in Table 1. In the quiescent condition both  $\text{iPP}_{\text{control}}$  and  $\text{iPP}(\text{iPS}_{\text{amorphous}})$  had Avrami exponents close to 3 which is indicative of the spherulite growth observed in Fig. 4.  $\text{iPP}(\text{iPS}_{\text{crystalline}})$  had a slightly smaller exponent ( $n \sim 2.7$ ) which may be due to the observed columnar growth of  $\beta$ -iPP from the surface of the  $\text{iPS}_{\text{crystalline}}$  particles. After the moderate step shear the Avrami exponent of all samples was reduced with  $\text{iPP}_{\text{control}}$  having  $n \sim 2.4$  and the iPP containing both morphologies of iPS being close to  $n \sim 2$  i.e. disklike growth. This result is consistent with the SAXS results presented in Fig. 6.

#### 3.4. Thermal behaviour

Samples for DSC analysis were sectioned from the fully crystallised disks after the selected thermal-shear profile. The arc was approximately 1 mm along the radius which in the sheared samples corresponded to shear rate range of  $\sim 5 \text{ s}^{-1}$ . DSC heating scans of the three iPP samples after quiescent crystallisation are shown in Fig. 10a. All samples showed an obvious endothermic peak between 165 °C and 170 °C due to  $\alpha$ -iPP. The  $\text{iPP}(\text{iPS}_{\text{crystalline}})$  sample showed an additional peak at 156.2 °C which is in the

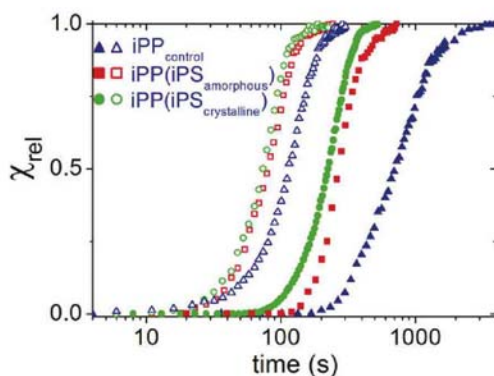


Fig. 8. Relative crystallinity ( $\chi_{\text{rel}}$ ) for the three samples during quiescent crystallisation (solid symbols) and after a moderate step shear with a shear rate of  $80 \text{ s}^{-1}$  for 1 s (open symbols).

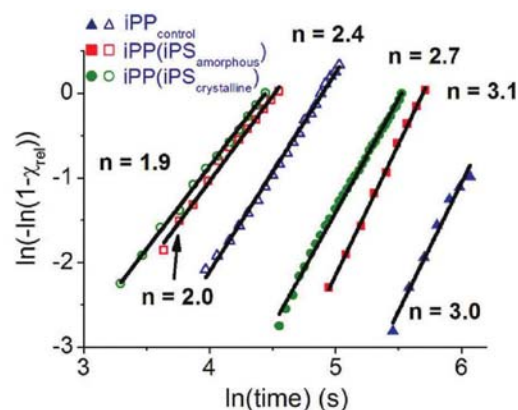


Fig. 9. Avrami plots of the crystallisation data for the three samples during quiescent crystallisation (solid symbols) and after a moderate step shear with a shear rate of  $80 \text{ s}^{-1}$  for 1 s (open symbols).

temperature range for  $\beta$ -iPP. The application of a moderate step shear complicated the heating scans further, Fig. 10b. All samples showed a similar sized shallow peak in the  $\beta$ -iPP temperature range at  $\sim 155 \text{ °C}$ . The  $\alpha$ -iPP peaks of  $\text{iPP}(\text{iPS}_{\text{crystalline}})$  and  $\text{iPP}(\text{iPS}_{\text{amorphous}})$  samples split into at least two separate endothermic peaks. It is suggested that the different lamellar components arising from oriented and un-oriented  $\alpha$ -iPP crystals are responsible for the two peaks. However, multiple melting peaks are not uncommon in  $\alpha$ -iPP and their designation remains to be confirmed. A small peak in the melting profiles at higher temperatures ( $\sim 225 \text{ °C}$ ) due to the 2 wt% crystalline iPS was observed in both the sheared and un-sheared  $\text{iPP}(\text{iPS}_{\text{crystalline}})$  samples. The position and area of these peaks were consistent with the presence of 2 wt%  $\text{iPS}_{\text{crystalline}}$ .

#### 4. Discussion

##### 4.1. Morphology of iPS

Like most polymer pairs, on blending, polypropylene and polystyrene are essentially immiscible. This results in the iPS remaining as discrete particles at the end of both heat treatments. Ex-situ X-ray analysis of material which had been given essentially the same thermal profile as experienced in the shear cell shows that the crystallinity of the  $\text{iPS}_{\text{crystalline}}$  particles was reasonably high at ( $\chi_v = 23(1)\%$ ) while  $\text{iPS}_{\text{amorphous}}$  particles showed no discernable crystallinity. The particle morphology of the originally crystalline iPS particles was irregular. Their morphology is however only slightly altered by heating them above their melting point where they tend to become more spherical. The crystalline order observed at the lower temperature is destroyed, and due to the sluggish crystallisation kinetics of iPS, they remain essentially amorphous during the subsequent isothermal crystallisation of iPP. This was confirmed by the DSC measurements presented in Fig. 10.

The non-polar methyl groups on iPP molecules would interact with iPS through their phenyl groups [26]. Therefore, the arrangement of phenyl groups in the crystal and amorphous state is important in understanding how the morphology of iPS would influence the crystallisation of iPP. Crystalline iPS has been shown to form a  $3_1$  helix with a rhombohedral unit cell (on hexagonal parameters  $a = b = 21.90 \text{ Å}$  and  $c = 6.65 \text{ Å}$ ) [35]. The phenyl groups within this crystal structure form into parallel stacks with the



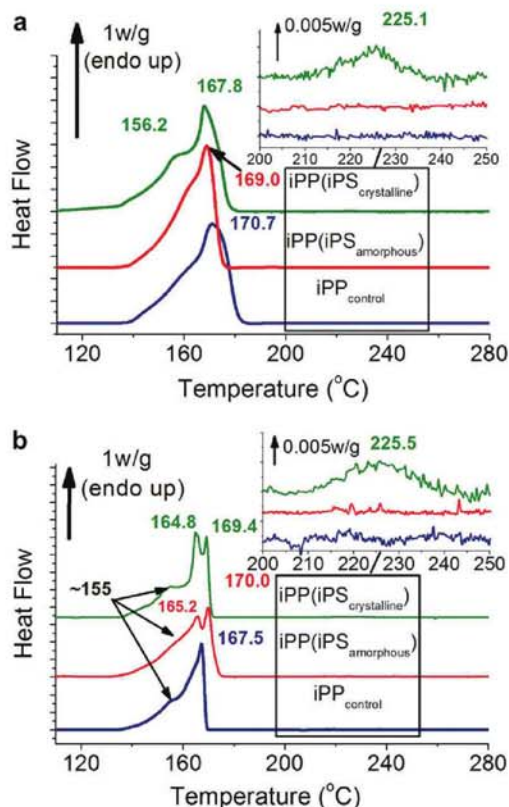


Fig. 10. Ex-situ DSC heating scans after (a) quiescent crystallisation and (b) after a moderate step shear with a shear rate of  $80 \text{ s}^{-1}$  for 1 s. The insert is a magnification of the high temperature region from  $200^\circ\text{C}$  to  $250^\circ\text{C}$ .

repeat distance between adjacent phenyl groups within the same stack being  $6.65 \text{ \AA}$  apart.

Amorphous iPS also shows considerable short range order due to the steric interactions of the bulky phenyl groups dominating chain conformation and packing. This ordering is evident by the two broad peaks centred at  $q = 0.68 \text{ \AA}^{-1}$  (polymerisation peak) and  $1.45 \text{ \AA}^{-1}$  (amorphous halo) in the WAXS profiles shown in Fig. 3. The conformation of the polystyrene chains in the amorphous state has been extensively studied, primarily by diffraction techniques [28–32]. By comparing experimentally derived radial distribution function (RDF) with those calculated from structural models, early studies, such as those by Katada [28], Yeh [29], Wecker et al. [30] and Schubach et al. [31] suggested the PS chains undergo orderly packing with neighbouring chains being roughly parallel to one another. The distance between adjacent chains was thought to be about  $9\text{--}10 \text{ \AA}$ , while the distance between adjacent phenyl groups on the same chain, as well as between neighbouring chains was  $\sim 5 \text{ \AA}$ . Adams et al. performed a detailed conformational study of amorphous PS and indicated that this type of packing could be achieved if the chain adopted a disordered helical arrangement [32], although, the conformational parameters presented were in contradiction to those indicated by conformational energy calculations [33]. Even though these models could explain broadly the features of the scattering profile of amorphous PS, they could not account for the unusual position and temperature dependence of

the polymerisation peak which increases in intensity with increasing temperature. This issue was overcome by the super chain model proposed by Mitchel and Windle [34]. In their model, micro-segregation of the phenyl groups occurs whereby the phenyls form into stacks as if they were flexible super chains. The stacks are similar to that found in crystalline iPS, being locally parallel to one another but are more highly disordered. The backbone does not form a helix but rather adopts a random configuration with as many as 6 chain segments being able to contribute to the same region of the stack. The distance between adjacent phenyls in the stacks is  $\sim 5 \text{ \AA}$ , and the distance between adjacent super chains is  $\sim 9 \text{ \AA}$ . Transmission electron microscopy suggests that the ordered regions range in size from  $15$  to  $45 \text{ \AA}$  [29]. It should be emphasised here that the order found in amorphous iPS is not long range in the accepted meaning of the term.

#### 4.2. Crystallisation from a quiescent melt

The experimental results show that the presence of both morphologies of iPS substantially influenced the quiescent crystallisation of iPP.  $\text{iPS}_{\text{crystalline}}$  particles were covered by  $\beta$ -iPP but their presence also increased the overall crystallisation kinetics and resulted in a substantial decrease in the spherulite size of  $\alpha$ -iPP spherulites further away from the particles.  $\text{iPS}_{\text{amorphous}}$  particles did not induce  $\beta$ -iPP. However, like  $\text{iPS}_{\text{crystalline}}$  their presence also resulted in increased crystallisation kinetics and smaller  $\alpha$ -iPP spherulite size. Therefore it can be concluded that morphologically,  $\text{iPS}_{\text{crystalline}}$  selectively nucleates  $\beta$ -iPP and  $\text{iPS}_{\text{amorphous}}$  nucleates  $\alpha$ -iPP. While kinetically, both  $\text{iPS}_{\text{crystalline}}$  and  $\text{iPS}_{\text{amorphous}}$  increase the crystallisation rate of iPP with the influence of  $\text{iPS}_{\text{crystalline}}$  on crystallisation kinetics of iPP being more significant.

One possible explanation for these results is as follows: the conformational changes that occur to the iPS molecule during crystallisation result in a change in the epitaxial relationship between iPS and iPP. In helical polymers such as iPP it is considered that there are two possible ways a substrate can interact with the helix: a) via the interstrand distance as found in  $\alpha$ -iPP &  $\gamma$ -iPP or b) by the repeat distance between adjacent chains as found in  $\beta$ -iPP [24]. The contact plane of  $\alpha$ -iPP (010) consists of a lozenge shaped array of methyl groups [25]. Compounds with substantially different repeat distances have been found to interact with this array and act as effective  $\alpha$ -iPP nucleants ( $4.2 \text{ \AA}$ ,  $5.0 \text{ \AA}$ , and  $6.6 \text{ \AA}$ ) [25].  $\beta$ -iPP on the other hand has been found to interact with only one repeat distance ( $\sim 6.5 \text{ \AA}$ ) but it also requires an orthogonal cell geometry [24,27]. In this case it is thought that the  $\sim 5.0 \text{ \AA}$  repeat distance between adjacent phenyls in  $\text{iPS}_{\text{amorphous}}$  would lead to nucleation of  $\alpha$ -iPP while the  $6.65 \text{ \AA}$  repeat distance between adjacent phenyls in  $\text{iPS}_{\text{crystalline}}$  would lead to nucleation of  $\beta$ -iPP.

#### 4.3. Crystallisation from a sheared melt

Over the last few years considerable effort has been focused on understanding the formation of oriented crystal precursors in sheared polymer melts. The addition of nucleating agents further complicates the process. However, a detailed explanation for the influence of nucleating agents on the formation of oriented crystal precursors is yet to be determined. In this experiment, a considerably greater intensity and an extension to high scattering angles values of the sharp equatorial streak was observed immediately after the application of shear in the presence of both iPS morphologies. This can be interpreted by an increase in the density of oriented crystal precursors. It is believed that both morphologies of the iPS particle could lead to this increased number of oriented crystal precursors in at least three ways: 1) it could increase the local strain rate in the area adjacent to the nucleating particle similar to the way

a log increases the local flow rate in a fast running stream; 2) one end of the iPP molecule could get adsorbed onto the surface of the iPS particle, while the free end gets stretched by the flow; and 3) the surface of the iPS particles could stabilise oriented molecules in the melt preventing them from relaxing back to their coiled state. The aligned segments could then drift together as suggested by Dukovski and Muthukumer [47] to form an overlap region in the flow field which could then spread over the entire chain.

The application of shear led to a similar  $\beta$  phase content for all three samples. Sheared melts are widely known to encourage the formation of  $\beta$ -iPP. It has been shown that an  $\alpha$  to  $\beta$  growth transition or  $\alpha$   $\beta$  bifurcation occurs on the surface of  $\alpha$ -iPP row nuclei [13]. Nevertheless, the nature of the nucleation sites responsible for  $\beta$ -iPP nucleation is still under debate. Sun et al. suggested that an orientation window exists for the iPP molecule in the molten state which enables the nucleation of  $\beta$ -iPP [12]; while Li et al. argued that shear can induce the formation smectic ordered domains, and that growth of  $\beta$ -iPP should be easier than  $\alpha$ -iPP from these shear-induced smectic bundles [48]. Although the application of the step shear resulted in the formation of  $\beta$ -iPP for iPP<sub>control</sub> and iPP(iPS<sub>amorphous</sub>) samples, the step shear decreased the  $\beta$  phase content for iPP(iPS<sub>crystalline</sub>) material, Fig. 5. The selective nucleation of  $\beta$ -iPP from iPS<sub>crystalline</sub> particles observed during quiescent crystallisation is therefore seemingly suppressed by the step shear. Similar behaviour has been observed by Huo et al. [18] who used WAXS and POM to investigate the influence of shear rate on the  $\beta$  content of an iPP nucleated by selective  $\beta$  nucleating agent (LaC + CaCO<sub>3</sub>). Hou argued that shear increases the number of  $\alpha$  crystal precursors which selectively nucleate  $\alpha$  phase. This seemed to be at odds with the well known increase in  $\beta$  phase content during shear-induced crystallisation of iPP that occurs through  $\alpha$   $\beta$  bifurcation [11–13]. Therefore it was unclear whether shear, in the presence of a selective  $\beta$ -iPP nucleating agent, suppressed the formation of oriented  $\alpha$  crystals or instead promoted them to the extent that that  $\beta$  phase growth from  $\alpha$   $\beta$  bifurcation would be unfavourable.

The results presented here show that the addition of both morphologies of iPS considerably increased the number of oriented crystal precursors that form immediately after the application of shear. As shown by the increase in crystallisation kinetics, which are significantly faster than found in the quiescent condition, these oriented crystal precursors are very effective at nucleating  $\alpha$ -iPP. Therefore their presence completely overwhelms the crystallisation process, resulting in high proportions of oriented  $\alpha$  form crystals. These results therefore have important implication for the processing of iPP containing intentional  $\beta$ -iPP nucleants, the addition of which can influence both the level of orientation achieved as well as the  $\beta$  phase content.

## 5. Conclusion

The morphology of isotactic polystyrene (iPS) particles which had been added to a matrix of isotactic polypropylene (iPP) were successfully varied by heat treatment to be either semicrystalline (iPS<sub>crystalline</sub>) or amorphous (iPS<sub>amorphous</sub>). Isothermal crystallisation of iPP in the presence of iPS particles of both morphologies, (iPP(iPS<sub>crystalline</sub>) and iPP(iPS<sub>amorphous</sub>)), and a control (iPP<sub>control</sub>) were then studied under quiescent conditions as well as after a moderate step shear. Under quiescent conditions iPS<sub>crystalline</sub> was found to selectively nucleate the  $\beta$ -iPP while iPS<sub>amorphous</sub> was found to nucleate  $\alpha$ -iPP. During crystallisation from a moderate step shear, both morphologies of iPS resulted in similar amounts of  $\beta$ -iPP and in increased crystallisation kinetics in comparison to iPP<sub>control</sub>. Furthermore, both iPS morphologies were found to substantially increase the number of oriented crystal precursors, compared to

iPP<sub>control</sub> which were formed as a result of the shear. These oriented precursors ultimately swamp the effect of any nucleating agent present and promote the formation of oriented  $\alpha$  form lamellae.

## Acknowledgements

This work was performed at the SAXS/WAXS beamline at the Australian Synchrotron, Victoria, Australia and the Australian National Beamline Facility (ANBF) with support from the Australian Synchrotron Research Program, which is funded by the Commonwealth of Australia under the Major National Research Facility Program. The Authors would like thank Dr Stephen Mudie, Dr Nigel Kirby and Dr Adrian Hawley for their assistance with the synchrotron experiments and modification of the SAXS15id software.

## References

- [1] Natta G, Corradini P. *Il Nuovo Cimento* 1960;15(1):40–51.
- [2] Meille SV, Ferro DR, Brueckner S, Lovinger AJ, Padden FJ. *Macromolecules* 1994;27(9):2615–22.
- [3] Dorset DL, McCourt MP, Kopp S, Schumacher M, Okihara T, Lotz B. *Polymer* 1998;39(25):6331–7.
- [4] Padden FJ, Keith HD. *Journal of Applied Physics* 1959;30:1479–84.
- [5] Addink EJ, Beintema J. *Polymer* 1961;2:185–93.
- [6] Kortek J, Raab M, Baldrian J, Grellmann W. *Journal of Applied Polymer Science* 2002;85(6):1174–84.
- [7] Varga J. *Journal of Macromolecular Science Part B Physics* 2002;41(4):1121–71.
- [8] Karger-Kocsis J. *Polypropylene. An A–Z reference*. Great Britain: Kluwer Academic Press; 1999. p. 58.
- [9] Lovinger AJ, Chua JO, Gryte CC. *Journal of Polymer Science Polymer Physics Edition* 1977;15(4):641–56.
- [10] Thomason JL, Van Rooyen AA. *Journal of Materials Science* 1992;27(4):897–907.
- [11] Somani RH, Hsiao BS, Nogales A, Fruitwala H, Srinivas S, Tsou AH. *Macromolecules* 2001;34(17):5902–9.
- [12] Sun X, Li H, Wang J, Yan S. *Macromolecules* 2006;39(25):8720–6.
- [13] Varga J, Karger-Kocsis J. *Journal of Polymer Science, Part B: Polymer Physics* 1996;34(4):657–70.
- [14] Liu G, Zhu PW, Edward G. *Macromolecular Symposia* 2002;185:327–40.
- [15] Huo H, Jiang S, An L. *Polymer* 2005;46(24):11112–6.
- [16] Chen YH, Zhong G-J, Wang Y, Li Z-M, Li L. *Macromolecules* 2009;42(12):4343–8.
- [17] Ma CG, Chen L, Xiong XM, Zhang JX, Rong MZ, Zhang MQ. *Macromolecules* 2004;37(24):8829–31.
- [18] Huo H, Jiang S, An L. *Macromolecules* 2004;37:2478–83.
- [19] Varga J, Mudra I, Ehrenstein GW. *Journal of Applied Polymer Science* 1999;74(10):2357–68.
- [20] Varga J. *Journal of Thermal Analysis* 1989;35:1891–912.
- [21] Dong M, Guo Z, Su Z, Yu J. *Journal of Polymer Science, Part B: Polymer Physics* 2008;46(12):1183–92.
- [22] Su ZQ, Chen XN, Yu ZZ, Zhang L. *Journal of Applied Polymer Science* 2009;111(2):786–93.
- [23] Su ZQ, Dong M, Guo Z, Yu J. *Macromolecules* 2007;40(12):4217–24.
- [24] Stocker W, Schumacher M, Graff S, Thierry A, Wittmann JC, Lotz B. *Macromolecules* 1998;31(3):807–14.
- [25] Mathieu C, Thierry A, Wittmann JC, Lotz B. *Polymer* 2000;41(19):7241–53.
- [26] Khanna YP. *Macromolecules* 1993;26(14):3639–43.
- [27] Mathieu C, Thierry A, Wittmann JC, Lotz B. *Journal of Polymer Science, Part B: Polymer Physics* 2002;40(22):2504–15.
- [28] Katada K. *Acta Crystallographica* 1963;16(4):290–301.
- [29] Yeh GSY. *Journal of Macromolecular Science Part B Physics* 1972;6(3):451–63.
- [30] Wecker SM, Davidson T, Cohen JB. *Journal of Materials Science* 1972;7(11):1249–59.
- [31] Schubach HR, Nagy E, Heise B. *Colloid and Polymer Science* 1981;259(8):789–96.
- [32] Adams R, Balyuzi HHM, Burge RE. *Journal of Materials Science* 1978;13(2):391–401.
- [33] Yoon DY, Sundararajan PR, Flory PJ. *Macromolecules* 1975;8(6):776–83.
- [34] Mitchell GR, Windle AH. *Polymer* 1984;25(7):906–20.
- [35] Natta G, Corradini P, Bassi I. *Il Nuovo Cimento* 1960;15(1):68–82.
- [36] Kimata S, Sakurai T, Nozue Y, Kasahara T, Yamaguchi N, Karino T, et al. *Science* 2007;316(5827):1014–7.
- [37] Somani RH, Yang L, Zhu L, Hsiao BS. *Polymer* 2005;46(20):8587–623.
- [38] Kumaraswamy G. *Journal of Macromolecular Science, Part C: Polymer Reviews* 2005;45(4):375–97.
- [39] Zhu PW, Tung J, Phillips A, Edward G. *Macromolecules* 2006;39(5):1821–31.
- [40] Zhu PW, Phillips A, Tung J, Edward G. *Journal of Applied Physics* 2005;97(10):104908.
- [41] Zhu PW, Edward G. *Macromolecules* 2004;37(7):2658–60.
- [42] Liu T, Petermann J. *Polymer* 2001;42(15):6453–61.

- [43] Hui Xu B, Ince S, Cebe P. *Journal of Polymer Science, Part B: Polymer Physics* 2003;41(23):3026–36.
- [44] Turner-Jones A, Cobbold AJ. *Journal of Polymer Science* 1968;6(8):539–46.
- [45] Somani RH, Hsiao BS, Nogales A, Srinivas S, Tsou AH, Sics I, et al. *Macromolecules* 2000;33:9385–94.
- [46] Mubarak Y, Harkin-Jones EMA, Martin PJ, Ahmad M. *Polymer* 2001;42(7):3171–82.
- [47] Dukovski I, Muthukumar M. *The Journal of Chemical Physics* 2003;118(14):6648–55.
- [48] Li L, de Jeu WH. *Faraday Discussions* 2005;128:299–319.



## Crystallization and Melting of Oriented Parent–Daughter Lamellae in Sheared Isotactic Poly(propylene)

Andrew Phillips,<sup>A,C</sup> Peng-wei Zhu,<sup>A</sup> Chitiur Hadinata,<sup>B</sup>  
and Graham Edward<sup>A</sup>

<sup>A</sup>Department of Materials Engineering, Co-operative Research Centre for Polymers,  
Monash University, Clayton, Vic. 3800, Australia.

<sup>B</sup>Autodesk Pty Ltd, 259-261 Colchester Road, Kilsyth, Vic. 3137, Australia.

<sup>C</sup>Corresponding author. Email: andyphil21@gmail.com

Alpha isotactic poly(propylene) ( $\alpha$ -iPP) exhibits a form of lamellar branching that is unique among semicrystalline polymers, where the branches have a distinct orientation relationship with the original crystalline lamellae. This is termed a parent–daughter relationship (PD). By allowing the structure to crystallize in an oriented form, a bimodal orientation of lamellae is developed and the individual contributions of PD lamellae can be observed using wide-angle X-ray scattering (WAXS). The present study investigated oriented PD lamellae during flow-induced crystallization and subsequent melting using time resolved rheo-WAXS. During crystallization the planes of the daughter lamellae were observed to curve towards the flow direction as they grew from their parent lamellae. This was explained by the influence of neighbouring daughter lamellae confining their growth direction. Oriented daughter lamellae were found to melt  $\sim 5^\circ\text{C}$  lower than oriented parent lamellae, which provides a new explanation for the multiple melting behaviour observed in the melting thermograms of sheared  $\alpha$ -iPP.

Manuscript received: 12 February 2010.

Manuscript accepted: 18 March 2010.

### Introduction

Natta and Corradini showed that the usual crystal form of isotactic poly(propylene) (iPP) has each polymer molecule arranged as a  $3_1$  helix.<sup>[1]</sup> The helix is chiral and can exist in either the right or left hand configuration. This chirality allows for four different crystalline phases:  $\alpha$ ,  $\beta$ ,  $\gamma$ , and the smectic phase. The  $\alpha$ -crystalline phase ( $\alpha$ -iPP) is by far the most common phase. Its monoclinic crystal structure is made up of alternating sheets of left- and right-handed helices. Interestingly, it appears that this regular arrangement of stems can sometimes break down and it is possible to have two adjacent sheets with the same chirality. This leads to a dramatic reorientation of the chain axis from the substrate layer (parent) by the  $\beta$ -angle of the  $\alpha$ -iPP monoclinic unit cell ( $99^\circ 80'$ ) to form a branch.<sup>[2–5]</sup> A daughter lamella ( $L_D$ ) may then form from this initial nucleus.

The orientation relation between parent lamellae ( $L_P$ ) and  $L_D$  was first determined by Keith and Padden,<sup>[6]</sup> who showed that the  $a_2$ -axis and  $c_2$ -axis of the  $L_D$  are aligned along the  $c_1$ -axis and the  $a_1$ -axis of the  $L_P$  respectively. This is termed a parent–daughter relationship (PD). In this paper, the  $a$ ,  $b$ , and  $c$  axes of the  $L_P$  are identified by the subscript 1 ( $a_1$ ,  $b_1$ ,  $c_1$ ), and the axes of the  $L_D$  by the subscript 2 ( $a_2$ ,  $b_2$ ,  $c_2$ ). PD lamellar branching has been observed over a wide range of crystallization conditions: melt,<sup>[7–12]</sup> solution,<sup>[13]</sup> thin films,<sup>[14–16]</sup> and the sheared region of injection mouldings.<sup>[17–20]</sup> PD lamellar branching is, therefore, considered a general property of  $\alpha$ -iPP crystallization. The nature of the PD structure has been thought to influence important properties such as fatigue life,<sup>[21]</sup> resistance to deformation,<sup>[22]</sup> and surface properties such as wear and adhesion.<sup>[23]</sup> Thus a greater understanding of this structure may

allow for tailored microstructures to be produced, extending the range of properties available for industrial applications.

$L_P$  and  $L_D$  are inherently difficult to study separately in in-situ environments because of their many structural similarities. However, by allowing the material to crystallize in an oriented form, such as under flow-induced crystallization (FIC) conditions, a bimodal orientation of lamellae is developed and the individual contributions of PD lamellae can be observed by wide-angle X-ray scattering (WAXS). Coupled with an appropriately designed shear cell and an intense X-ray source, this permits PD lamellae to be investigated in-situ during important physical processes like crystallization and melting. In the first part of this paper we introduce the basis and procedure for separating the individual oriented PD lamellae contributions to the two-dimensional (2D) WAXS profile. In the following section this procedure is applied to further understand oriented PD lamellar branching during isothermal crystallization from a sheared melt. In the final section of the paper, the relative thermal stability of the oriented PD lamellae are determined to identify the multiple melting peaks, which are commonly observed during non-isothermal differential scanning calorimetry (DSC) runs of sheared iPP. The melting thermograms will then be used to investigate the effect of shear conditions on lamellar thickness and perfection.

### Results and Discussion

#### PD Model in Sheared $\alpha$ -iPP

In this section the basis and procedure for the separation of the oriented PD lamellae contribution to the 2D WAXS profiles is presented. To fully understand the X-ray scattering patterns and



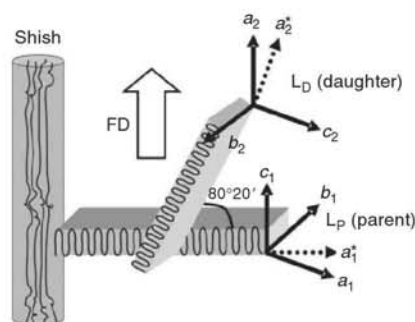


Fig. 1. Generalized model for the oriented parent-daughter structure found in sheared isotactic poly(propylene).

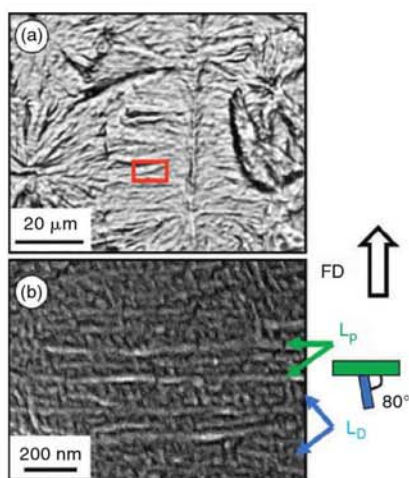


Fig. 2. (a) ROM and (b) SEM images of permanganate etched surfaces. Indicative location of (b) is shown by the small red box in (a). Shear rate  $80\text{ s}^{-1}$ .

derive quantitative information it is necessary to have a detailed structural model. A generalized model of the oriented PD lamellar structure is provided in Fig. 1. In the model, highly oriented thread-like assemblies (commonly referred to as shish), which are composed of extended chains are aligned along the flow direction (FD). Depending on a range of factors, the chains can be in an amorphous, mesomorphic, or crystalline state.<sup>[24]</sup> The shish provides nucleation sites for  $L_P$  (kebabs), which grow radially out from the shish with their  $c_1$ -axis (chain folding axis) aligned along the FD. Epitaxial nucleation of the  $L_D$  can then occur on the  $ac$  faces of the  $L_P$ . In the model, the  $c_2$ -axis of the  $L_D$  is related to the  $c_1$ -axis of the  $L_P$  by the  $\beta$ -angle of the  $\alpha$ -iPP monoclinic unit cell ( $99^\circ 80'$ ).

To confirm the proposed structural model, the surface of a sample sheared for 1 s at a shear rate of  $80\text{ s}^{-1}$  was etched in permanganate solution and investigated by reflected optical microscopy (ROM) and scanning electron microscopy (SEM). The etching procedure selectively removes the amorphous phase to leave the crystalline regions largely intact. In reflected light many highly oriented thread-like structures, consistent with the presence of a shish, were observed to be aligned along the FD, Fig. 2a. Some small spherulites were also observed between the shish. At a higher magnification the shish were heavily etched, possibly revealing that there were regions of lower order than the

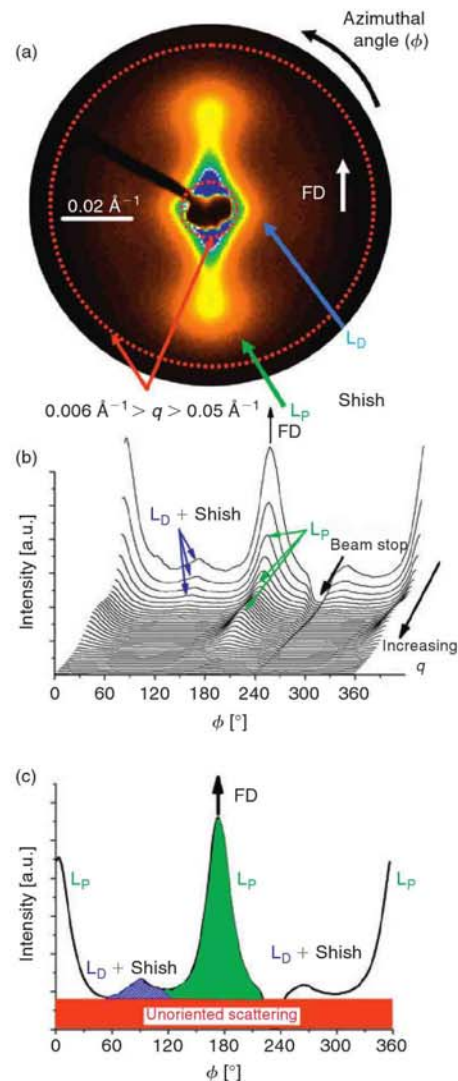


Fig. 3. (a) Typical 2D SAXS pattern of sheared  $\alpha$ -iPP. (b) Corresponding 1D azimuthal intensity profile as a function of scattering vector at  $0.0012\text{ \AA}^{-1}$  intervals and (c) average 1D azimuthal intensity profile. The scattering profiles in (b) and (c) are both between the scattering vectors indicated in (a). Oriented parent ( $L_P$ ) and daughter ( $L_D$ ) lamellae. Shear rate  $80\text{ s}^{-1}$ .

surrounding material. Extending radially from the shish were primary lamellae ( $L_P$ ), which tended to become thinner with increasing distance from the shish core, Fig. 2b. Smaller lamellae consistent with  $L_D$  filled the space between neighbouring  $L_P$ . The thickness of the oriented  $L_P$  and  $L_D$  were found to be  $126(7)$  and  $95(9)\text{ \AA}$ , respectively. The planes of the  $L_D$  were found to be inclined  $80(2)^\circ$  to the  $L_P$ . These results confirm the proposed structural model.

SAXS is a widely used and powerful technique to investigate the large-scale structures that form in semicrystalline polymers. SAXS experiments were performed to further investigate the morphology of sheared  $\alpha$ -iPP as well as to assess its potential as a tool to follow the individual contributions of PD lamellae

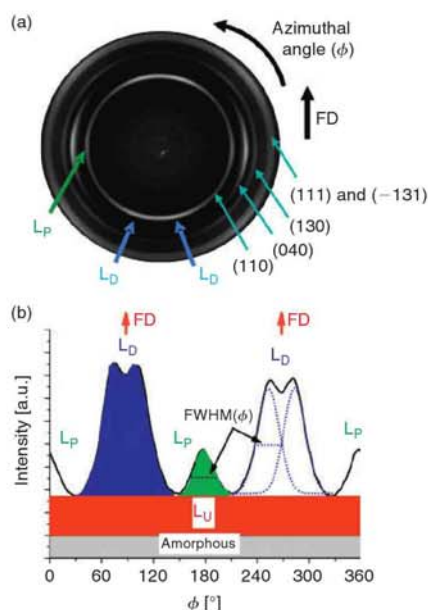


Fig. 4. (a) Typical 2D WAXS patterns and (b) 1D azimuthal intensity profile for the  $\alpha(110)$  reflection highlighting the contribution of oriented parent ( $L_P$ ) and daughter ( $L_D$ ) lamellae and unoriented ( $L_U$ ) lamellae as well as the amorphous region. Shear rate  $80 \text{ s}^{-1}$ .

during crystallization and melting. Fig. 3a shows a typical 2D SAXS pattern of a sheared  $\alpha$ -iPP ex-situ sample under fully crystallized conditions. Corresponding one-dimensional (1D) azimuthal intensity profiles as a function of scattering angle at intervals of  $q = 0.0012 \text{ \AA}^{-1}$ , as well as an azimuthal intensity profile averaged between  $0.006 \text{ \AA}^{-1} \leq q \leq 0.05 \text{ \AA}^{-1}$ , are shown in Figs 3b and 3c, respectively. The observed scattering was broadly consistent with the proposed structural model. The model predicts that the  $L_P$  should scatter along the meridian, while the  $L_D$  should scatter in a bimodal distribution either side of the equator. An increase in scattering intensity was indeed observed in the meridional regions, however, instead of the predicted bimodal distribution, a single low intensity broad peak was observed along the equator. Possible explanations for the absence of the bimodal distribution could be (a) the low azimuthal resolution of the set-up at low  $q$  where the  $L_D$  would scatter and (b) the presence of oriented shish aligned with their long axis along the FD, which would also scatter to the equatorial region. Although the low azimuthal resolution at low  $q$  values would not necessarily preclude the use of SAXS to study many aspects of PD lamellar branching, the influence of the shish on the observed scattering cannot easily be accounted for. Therefore, their presence would make accurate deconvolution of the individual parent and daughter contributions to the 2D SAXS patterns difficult, and SAXS was not pursued further.

An in-situ 2D WAXS pattern given the same thermal-shear profile as SAXS pattern is shown in Fig. 4a. The first five rings of  $\alpha$ -iPP are clearly visible. The azimuthal angle ( $\phi$ ) where scattering should occur according to the model described in Fig. 1 can be calculated using the method described by Kakudo and Kasai:<sup>[25]</sup>

$$\cos(\delta) = \cos(\theta) \cos(90 - \phi), \quad (1)$$

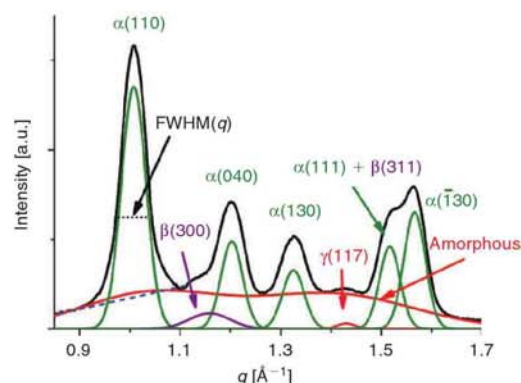


Fig. 5. WAXS intensity profile along the scattering vector ( $q$ ) showing the main isotactic poly(propylene) crystalline reflections present. Shear rate  $80 \text{ s}^{-1}$ .

where  $\delta$  is the angle the crystalline plane normal makes with the FD, and  $\theta$  is the Bragg angle. The model correctly predicts broad features of the diffraction pattern. For the  $\alpha(110)$  reflection, the  $L_P$  should scatter along the equator, while daughters should scatter close to the meridian (as diffraction occurs perpendicular to the  $c$ -axis). According to the proposed model for  $L_D$ ,  $\delta_D = 19.7^\circ$ , which equates to a predicted  $\phi_D = 70.7^\circ$ . However, the measured  $\phi_D$  was closer to  $76^\circ$ . The discrepancy can be explained if the lamellae are allowed to curve. This is discussed in further detail in the next section. For the  $\alpha(040)$  reflection, both  $L_P$  and  $L_D$  should scatter along the equator, as both their  $b$ -axes are perpendicular to the FD. Therefore, because of the clear separation of parent and daughter contributions, the  $\alpha(110)$  reflection is ideally suited to monitor oriented PD lamellae contributions to crystallization and melting. The scattering around the  $\alpha(110)$  profile can be further deconvoluted to separate out scattering attributable to the amorphous halo and scattering attributable to unoriented lamellae ( $L_U$ ). The amorphous contribution to scattering in this region was estimated by fitting a straight line to the minimum either side of the  $\alpha(110)$  peak in a WAXS intensity profile integrated along  $q$  as shown in Fig. 5. A typical  $\alpha(110)$  azimuthal intensity profile of sheared iPP is shown in Fig. 4b, and highlights the individual  $L_P$ ,  $L_D$ , and  $L_U$  contributions as well as the amorphous contribution to the total scattered intensity.

#### Crystallization of Oriented PD Lamellae

Although the structure of PD lamellae has been widely studied in a range of ex-situ samples, the crystallization of PD lamellae under conditions typical of industrial processes has received comparatively little attention. Industrial processes such as injection moulding lead to large shear gradients throughout the part. These greatly complicate crystallization kinetics and the subsequent development of morphology when compared with quiescent conditions. In this section the growth of oriented PD lamellae will be characterized in-situ during isothermal crystallization after the application of a moderate step shear. From the results obtained, the flow-induced crystallization (FIC) model for iPP will be accordingly updated.

Fig. 6 shows a bird's eye view of the changes that occur to the WAXS intensity profile along  $q$  as well as the azimuthal intensity profile of the  $\alpha(110)$  peak during crystallization after a step shear for 1 s at a shear rate  $80 \text{ s}^{-1}$ . Before the step shear no crystallinity



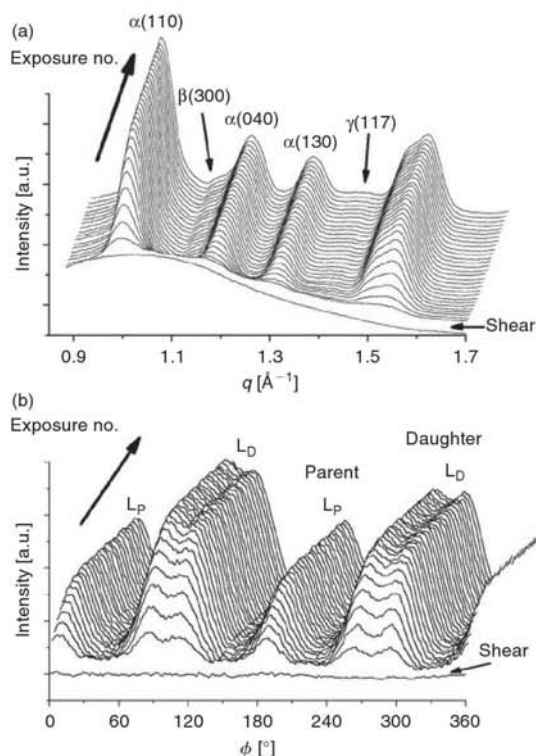


Fig. 6. Bird's eye view of the changes that occur to (a) the WAXS intensity profile ( $q$ ) and (b) the azimuthal ( $\phi$ ) intensity profile of the  $\alpha(110)$  reflection during crystallization. Shear rate  $80 \text{ s}^{-1}$ .

and no azimuthal dependence of intensity were observed. In the first exposure after the application of the step shear ( $\sim 15 \text{ s}$  after the step shear), crystallization had begun as shown by the formation of the characteristic  $\alpha$ -iPP peaks. Crystallization quickly progressed and reached saturation  $\sim 200 \text{ s}$  after the step shear. At the early stage of crystallization the azimuthal intensity profile of the  $\alpha(110)$  peak took on the characteristic appearance of the oriented PD structure described previously. The ratio of the height of the  $L_P$  to  $L_D$  was significantly more at the early stages compared with the later stages of crystallization. This confirms that  $L_P$  form before  $L_D$ .

The kinetics of crystallization were further probed by plotting the relative proportion of the parameters:  $\chi_v$ ,  $L_P$ ,  $L_D$ , and  $L_U$  defined by the ratio ( $\eta$ ) against time:

$$\eta = \frac{Q(t)}{Q(\infty)}, \quad (2)$$

where  $Q(t)$  is the instantaneous and  $Q(\infty)$  is the final value of the parameter under the fully crystallized conditions. Quantitative information about the crystallization kinetics and growth geometry were obtained by fitting the crystallization data to the Avrami model:

$$1 - \eta = e^{-kt^n}, \quad (3)$$

where  $k$  is the bulk crystallization constant and  $n$  is the Avrami exponent. The crystallization half time ( $t_{0.5}$ ) was taken as the

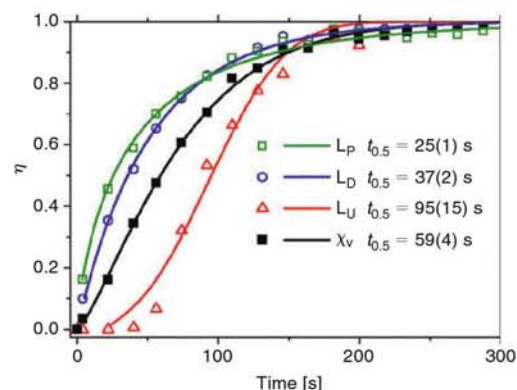


Fig. 7. Relative proportion ( $\eta$ ) of the parent ( $L_P$ ), daughter ( $L_D$ ), and unoriented ( $L_U$ ) lamellae contributions to total crystalline scattering ( $\chi_v$ ) during the initial stages of crystallization. Shear rate  $80 \text{ s}^{-1}$ .

time at which the model line intersected  $\eta = 0.5$ . The assumption used in this analysis is that the measured parameters derived from the reflected intensity (i.e.,  $Q(t)$  and  $Q(\infty)$ ) are linearly proportional to the actual volume fraction of the parameter. The results are shown in Fig. 7. Reasonably good fits were obtained for all parameters, which emphasizes the general applicability of the model to all lamellae contributions to the total crystallinity. The analysis also demonstrates that the oriented PD lamellae form well before the unoriented lamellae.

The Avrami exponent can give important information about the crystallization mechanism. The Avrami exponent was determined in the primary crystallization region from the gradient of the linear region of a plot of  $\ln[\ln(1/(1-\eta))]$  versus  $\ln(t)$ . At low conversions there is a significant uncertainty in determining  $\eta$ . Significant deviation from the model also occurs in the latter stages of crystallization, which has been attributed to the occurrence of secondary crystallization.<sup>[26]</sup> Therefore, the Avrami exponent was determined by fitting a straight line to the linear region between these two extremes. In heterogeneous nucleation where crystal growth is not diffusion controlled, the Avrami exponent is related to the dimension of crystal growth: with  $n = 3$  indicating spherical growth;  $n = 2$  indicating disk-like growth; and  $n = 1$  indicating rod-like growth. However, if growth is controlled by the diffusion of chain segments to the lamellae growth front then the crystal growth rate should be proportional to the square root of time.<sup>[27]</sup> This has been shown to lead to Avrami exponents that are less than 1.<sup>[28,29]</sup> Often non-integer values of the Avrami exponent are obtained, which can indicate the presence of more than one growth geometry during crystallization. The results of this analysis are shown in Fig. 8.

The unoriented lamellae had an Avrami exponent of 2.68(40) which indicates that they grew in an almost spherical way. This result is consistent with the unoriented lamellae being mainly in the small spherulites observed in Fig. 2, which would show three-dimensional growth characteristics. The Avrami exponent of the oriented PD lamellae was significantly less than 1. This demonstrates that both oriented  $L_P$  and  $L_D$  growth is highly constrained, which suggests athermal nucleation conditions and diffusion-controlled growth of lamellae. Similar results have been obtained from rheo-SAXS experiments that investigate the early growth of kebabs.<sup>[27,30]</sup>  $L_D$  ( $n = 0.67(8)$ ) were found to have a slightly smaller Avrami exponent than  $L_P$  ( $n = 0.78(5)$ ), which illustrates

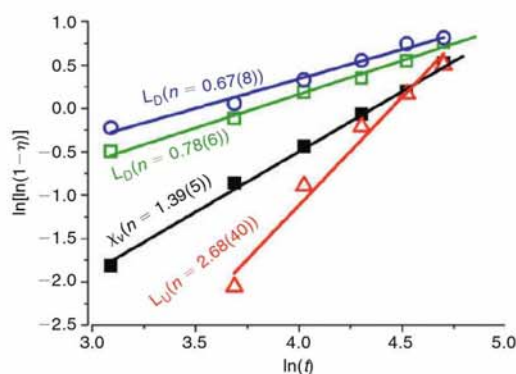


Fig. 8. Avrami plots of the crystallization data and corresponding Avrami exponent ( $n$ ) for parent ( $L_P$ ), daughter ( $L_D$ ), and unoriented ( $L_U$ ) lamellae and for total crystallinity ( $\chi_v$ ). Shear rate  $80 \text{ s}^{-1}$ .

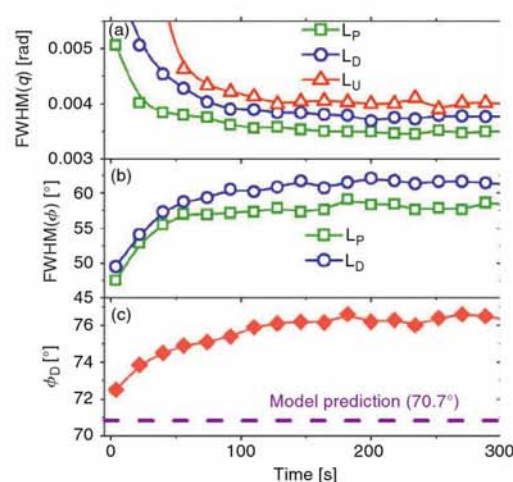


Fig. 9. (a) Full width at half maximum of the  $\alpha(110)$  reflection along (a) scattering angle  $\text{FWHM}(q)$  and (b) along the azimuthal angle  $\text{FWHM}(\phi)$  highlighting individual contributions from parent ( $L_P$ ), daughter ( $L_D$ ), and unoriented ( $L_U$ ) lamellae. (c) The azimuthal angle  $L_D$  scatter to  $\phi_D$  on the  $\alpha(110)$  reflection as a function of time during the initial stages of crystallization. Shear rate  $80 \text{ s}^{-1}$ .

that their growth is somewhat more constrained. Constraint in this case could be a result of a combination of (a) the reduced diffusion of chain segments to the crystal growth front from chains also being incorporated in neighbouring lamellae, and (b) the microstructural constraint caused by the impingement of neighbouring lamellae. The Avrami exponent determined for  $\chi_v$  was 1.39(5) and represents an average of unoriented and oriented lamellae growth.

The growth of PD lamellae during primary crystallization was further investigated by plotting the full width at half maximum of the  $L_P$ ,  $L_D$ , and  $L_U$  contributions to the  $\alpha(110)$  peak along the scattering vector ( $\text{FWHM}(q)$ ), Fig. 9a. Sectors of  $10^\circ$  width in the azimuthal direction and centred at  $0^\circ$  for  $L_P$ ,  $76^\circ$  for  $L_D$ , and  $37^\circ$  for  $L_U$  were used for the analysis. According

to Eqn 10 (see Experimental section) the  $\text{FWHM}(q)$  of the X-ray reflection from a crystal plane is inversely proportional to the number of periodic planes, which is approximated as the crystal size in the direction normal to the corresponding plane. Therefore, the  $\text{FWHM}(q)$  can give an indication of the thickness of lamellae during crystallization. During the early stages of crystallization ( $<100 \text{ s}$ ) the  $\text{FWHM}(q)$  of all lamellae decrease rapidly, which shows that as crystallization progressed the thickness of the lamellae increased substantially. This demonstrates that lamellae thickening along the chain fold direction may also be an important growth mechanism at the early stages of crystallization. The final  $\text{FWHM}(q)$  of the three lamellae indicated that  $L_U$  are thinner than  $L_D$  which are thinner than  $L_P$ . The  $\text{FWHM}$  of the parent and daughter contributions to the  $\alpha(110)$  can also be probed during crystallization along the azimuthal angle ( $\text{FWHM}(\phi)$ ), Fig. 9b. The  $\text{FWHM}(\phi)$  gives information about the angular dispersion of the crystallites, with a higher  $\text{FWHM}(\phi)$  that indicates a larger angular spread. As crystallization progressed, the  $\text{FWHM}(\phi)$  of both  $L_P$  and  $L_D$  increased. This can be explained by curving and twisting of lamellae as they grow. Further information about the curvature of  $L_D$  as they grow can be obtained by comparing the observed scattering angle with the angle where scattering should occur according to Eqn 1 and the structural model presented in Fig. 1. The results are presented in Fig. 9c and show that  $\phi_D$  increased rapidly from the model predicted value of  $70.7^\circ$  during the initial stages of crystallization before reaching an equilibrium value. The increase in the observed scattering angle shows that the planes of the  $L_D$  curve towards the FD as they grow, which further indicates highly constrained growth of the  $L_D$ .

The information presented in this section can now be used to update the PD branching contribution to the FIC model for iPP, Fig. 10.  $L_P$  radiate out from the central shish much like a flattened spherulite. Growth occurs primarily along the  $a^*$ -axis, which results in individual lamellae being much longer than they are thick. Similarly,  $L_D$  grow from the  $L_P$  with their initial growth rate being much faster along the  $a^*$ -axis direction than any other, however, because of their sequential formation, which results in reduced diffusion of chains to the crystal growth front from chains being also incorporated into nearby lamellae, the  $L_D$  are thinner and less perfect than  $L_P$ . Because of impingement on adjacent  $L_P$ ,  $L_D$  are not as long as  $L_P$ . As the  $L_D$  grow they curve towards the FD. It is thought that this occurs because of the influence of adjacent  $L_D$  which confine their growth direction. Such confinement-induced orientation has previously been observed in polymers crystallizing between inorganic fibres<sup>[31,32]</sup> or in narrow epoxy channels.<sup>[33]</sup> Amorphous and tie chains fill the space between the crystalline regions.

#### Melting of Oriented PD Lamellae

Multiple melting peaks are often observed in the DSC melting thermograms of sheared iPP. A likely explanation is that the thinner  $L_D$  melt at a lower temperature than the  $L_P$ . Experimental evidence supporting the lower thermal stability of  $L_D$  has been gained mainly in samples crystallized under quiescent conditions, which are composed predominantly of spherulites. For example by: transmission electron microscopy (TEM) measurements of the lamellar thickness of fully crystallized material<sup>[10]</sup> and partially melted samples,<sup>[8,11]</sup> and birefringence measurements made during the melting of spherulites.<sup>[12]</sup> These experiments are complicated by the unique PD structure, which leads to the thickness of radial  $L_P$  becoming thicker with increasing



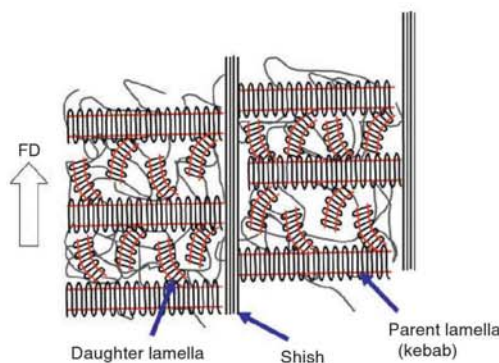


Fig. 10. Updated FIC model for iPP. Orientation relationship between parent ( $L_P$ ) and daughter ( $L_D$ ) lamellae illustrated in Fig. 1.

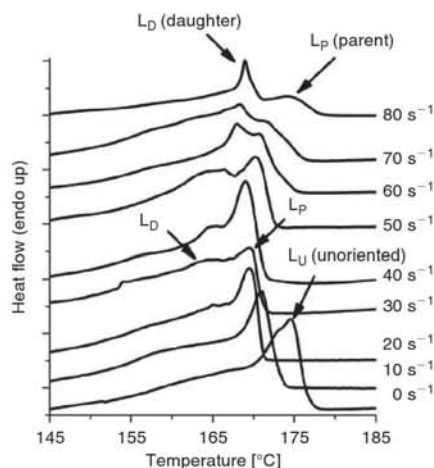


Fig. 11. Melting DSC thermograms of samples subjected to shear rates between 0 and  $80 \text{ s}^{-1}$ . Heating rate is  $10^\circ\text{C min}^{-1}$ .

distance from the core of the  $\alpha$ -iPP spherulite.<sup>[8]</sup> This is thought to be a result of the morphological constraint from the relatively higher number of branched lamellae suppressing thickening of the radial  $L_P$  towards the core of the spherulite. Nevertheless, multiple melting peaks are not uncommon in the DSC thermograms of iPP and their occurrence has been explained by several other different competing processes. For instance: different crystalline phases,<sup>[34,35]</sup> recrystallization,<sup>[36–38]</sup> and differences in crystal perfection or thicknesses.<sup>[11,14,39]</sup> Recently, Wang et al. investigated the melting behaviour of PD lamellae in thin films in-situ using environmental atomic force microscopy (AFM).<sup>[14]</sup> They concluded that PD lamellae essentially formed and melted at the same time and multiple melting was attributed to recrystallization phenomenon. However, the long time between images ( $\sim 30 \text{ min}$ ) would have substantially limited the selectivity of their experiment. In this section the relative thermal stability of the oriented PD lamellae will be determined to show the multiple melting peaks observed in the melting curves of sheared iPP are because of the oriented PD lamellar structure. The assignment of the peaks will then be used to determine the influence of shear rate on lamellar thickness and perfection.

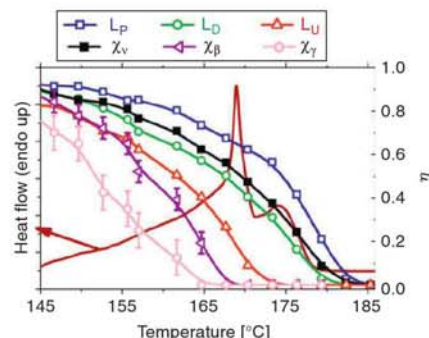


Fig. 12. Overlay of DSC thermogram with the relative proportion ( $\eta$ ) of the various contributions to the total crystallinity ( $\chi_v$ ) determined from the WAXS patterns. Parent ( $L_P$ ), daughter ( $L_D$ ), unoriented ( $L_U$ ) lamellae,  $\beta$ -iPP crystallinity ( $\chi_\beta$ ), and  $\gamma$ -iPP crystallinity ( $\chi_\gamma$ ). Shear rate  $80 \text{ s}^{-1}$ .

DSC melting thermograms of the sheared samples are shown in Fig. 11. In the sample crystallized in the absence of shear, appreciable melting was observed to begin around  $160^\circ\text{C}$ , peaking in a broad single peak centred at  $175.0^\circ\text{C}$ . Increasing the shear rate up to  $20 \text{ s}^{-1}$  decreased the peak position and also resulted in the peak becoming narrower. At  $30 \text{ s}^{-1}$  a bimodal distribution of melting temperatures was observed by the high temperature peak centred at  $169.4^\circ\text{C}$  and the lower temperature peak centred at  $165.0^\circ\text{C}$ . At this shear rate the formation of oriented structures was observed by both ROM and WAXS measurements. Increasing the shear rate above  $30 \text{ s}^{-1}$  resulted in a steady increase in both peak temperatures, in particular, the high temperature peak. In addition, the relative size of the lower temperature peak increased with respect to the high temperature peak with increasing shear rate.

Clearly the DSC melting curves of iPP are greatly complicated under FIC conditions. Using the unique evidence provided by the in-situ time-resolved rheo-WAXS technique the origin of the two melting peaks observed in the DSC thermograms can now be determined. Fig. 12 shows the DSC curve at the highest shear rate of  $80 \text{ s}^{-1}$  plotted on the same curve as the relative proportion of the different contributions to the total crystallinity. The volume fractions of both  $\beta$ -iPP and  $\gamma$ -iPP were small with  $\chi_\beta = 0.02(1)\%$  and  $\chi_\gamma = 0.03(1)\%$  and, therefore, these would be unlikely to account for the observed multiple melting behaviour. Furthermore, both  $\beta$ -iPP and  $\gamma$ -iPP melted well before the low temperature peak and, therefore, melting by  $\beta$ -iPP or  $\gamma$ -iPP can be ruled out. The smooth drop in the relative proportion of total crystallinity suggests recrystallization processes are not occurring to a significant extent in this experiment.  $L_U$  melted at too low a temperature and are, therefore, also unable to account for the observed multiple melting behaviour.  $L_D$ , however, can clearly be seen to melt at a lower temperature than  $L_P$ . In addition, the melting temperature of PD lamellae observed by WAXS closely corresponds to the melting temperature observed by DSC. This demonstrates that the bimodal distribution observed in the sheared DSC curves above  $30 \text{ s}^{-1}$  arises from two different populations of lamellar thickness. In this case the thicker  $L_P$  give rise to the high temperature peak and the thinner  $L_D$  give rise to the low temperature peak.

The clear bimodal distribution of lamellar thickness observed at shear rates greater than  $30 \text{ s}^{-1}$  is at odds with what is observed

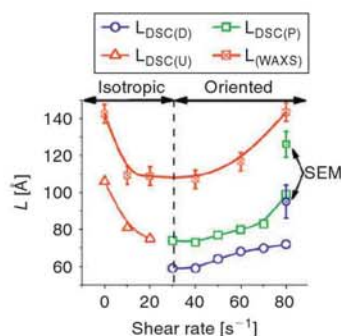


Fig. 13. Average lamellar thickness as a function of shear rate calculated using the Thompson–Gibbs equation of the melting peaks depicted in Fig. 11 along with the lamellar thickness calculated using the Scherrer equation and by SEM.

in samples crystallized below  $30 \text{ s}^{-1}$  where a single broad peak is observed. This can be explained by the unique structure of the  $\alpha$ -iPP spherulite, which leads to an increase in the lamellar thickness of radial  $L_P$  with increasing distance from the spherulite core as previously explained. The effect is evident in the lower shear rate DSC thermograms presented in Fig. 13 ( $0$ – $30 \text{ s}^{-1}$ ), which show a decrease in the peak position and, therefore, the average lamellar thickness with increasing shear rate. It is well known that shear will increase the average number of nucleation sites<sup>[40,41]</sup> thereby decreasing the spherulite size obtained. This would result in a narrowing of the difference in lamellar thickness in the spherulite morphology and, therefore, the lamellar distribution for  $L_P$  and  $L_D$  essentially overlap, which leads to one peak being observed in the DSC thermograms. FIC results in a substantially different geometrical arrangement of the crystallites and this allows the  $L_P$  to thicken relatively unhindered, which results in the observed difference in melting point.

Now that the origin of the two melting peaks observed by DSC has been confirmed, the measured peak melting temperature can be used to separate the influence of shear rate on the individual PD lamellar thickness for shear rates greater than  $30 \text{ s}^{-1}$  using Eqn 4 (see Experimental section). The results from this analysis are shown in Fig. 13 and are compared with the lamellar thickness determined from WAXS using Eqn 11 (see Experimental section) and SEM. Although the overall trends were the same between the different experimental approaches, a difference in the magnitude of the lamellae thickness between the different techniques was observed. However, this discrepancy is not unexpected because of the different theoretical approaches used in each to estimate lamellar thickness. The results show that up to a shear rate of  $30 \text{ s}^{-1}$  the lamellar thickness decreased in line with the decrease in the spherulite size as described previously. Above a shear rate of  $30 \text{ s}^{-1}$ , the  $L_P$  were found to thicken more readily than the  $L_D$ , particularly at the higher shear rates. From a thermodynamic stand point this is unexpected as an increase in the free energy would increase the degree of under-cooling achieved, and according to Eqn 4 the lamellae thickness should decrease. However, we believe the results can be explained by a mechanistic argument. The increase in shear rate leads to an increase in the number of suitably oriented chain segments aligned along the FD. This should not only increase the lamellar thickness but would also lead to increased crystal perfection by increasing the diffusion of chain segments to the crystal growth front.

Similar anisotropic behaviour of crystal growth has recently been observed during isothermal crystallization in the presence of a flow field.<sup>[42]</sup> It is unclear at this stage why the thickness of the  $L_D$  also increased slightly with increasing shear rate, although the observed change is small and could possibly be accounted for by experimental uncertainty.

## Conclusions

By allowing iPP to crystallize in an oriented form, the individual contributions from  $L_P$  and  $L_D$  were able to be observed using WAXS. The contribution of oriented PD lamellae to the crystallization, and melting of sheared  $\alpha$ -iPP, were then characterized in-situ using time-resolved rheo-WAXS. The finding from the study are briefly summarized as follows.

During crystallization, oriented  $L_P$  were observed to form before  $L_D$ , which is consistent with the long held view on their epitaxial nucleation mechanism. Growth of both oriented PD lamellae was highly constrained, indicating athermal nucleation and diffusion controlled growth conditions. Furthermore, the planes of the  $L_D$  were found to curve toward the flow direction with increasing distance from their  $L_P$ . The direction of curvature was explained by the influence of adjacent  $L_D$  confining their growth direction.

Along with their growth being more constrained than  $L_P$  during isothermal crystallization, the  $L_D$  were also observed to melt at a lower temperature because of being thinner and/or less perfect than  $L_P$ . These differences are thought to arise from their sequential formation, which results in reduced diffusion of chains to the crystal growth front because of chains also being incorporated into nearby lamellae. The difference in  $L_P$  and  $L_D$  thickness or perfection was then used to assign the multiple melting behaviour observed in the DSC thermograms.

A U-shaped dependence of lamellar thickness was observed with increasing shear rate and was explained by changes that occurred to the morphology above and below the transition to an oriented structure at a shear rate of  $\sim 30 \text{ s}^{-1}$ . Below  $30 \text{ s}^{-1}$  the decrease in lamellar thickness was related to the decrease in spherulite size consistent with the increase in radial lamellae thickness with increasing distance from the core of the spherulites, which is a characteristic of  $\alpha$ -iPP spherulites. Above  $30 \text{ s}^{-1}$  the increase in lamellar thickness was thought to be attributable to the increase in the number of suitably oriented extended chain segments aligned along the flow direction before the onset of crystallization, which increases the diffusion of chain segments to the crystal growth front.

## Experimental

### Sample Preparation and Thermal-Shear Profile

The polymer used in this study was an iPP homopolymer manufactured by the Borealis group (Borealis HD601CF). The average-weight molecular weight ( $M_w$ ) and the average-number molecular weight ( $M_n$ ) were  $367000 \text{ g mol}^{-1}$  and  $74000 \text{ g mol}^{-1}$ , respectively. Sheets  $1.5 \text{ mm}$  thick of the material were compression moulded at  $190^\circ\text{C}$  for  $5 \text{ min}$ . A Linkam CSS450 shear cell was used to control the thermal-shear profile. The CSS450 is a parallel plate shearing device in which a small aperture in the base and lid allows observation of the polymer in-situ.

The thermal-shear profile was designed to simulate, as close as practically possible, conditions found in typical industrial processes before the onset of crystallization. For example, in the injection moulding process, short-lived and intense shear



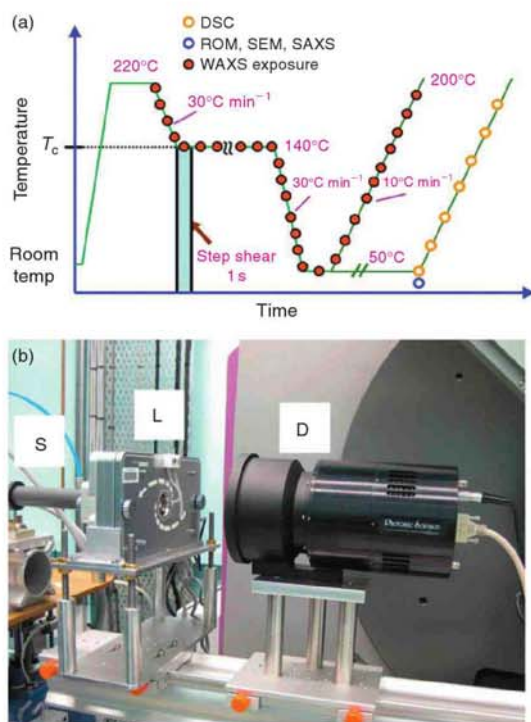


Fig. 14. (a) Thermal-shear profile used in this experiment. Coloured circles represent when WAXS, SAXS, ROM, SEM, and DSC measurements were taken. (b) Rheo-WAXS experiment on the powder diffraction beam line at the Australian Synchrotron. Synchrotron source (S), Linkam shear cell (L), and detector (D).

fields are typically imposed on the supercooled melt near the cold mould wall.<sup>[17,18]</sup> Furthermore, solidification in injection moulded parts occurs under relatively high cooling rates and large temperature gradients. However, in this study, crystallization was carried out under isothermal conditions after the application of a short step shear imposed on the supercooled melt. Isothermal conditions were chosen to allow for more simplified and detailed quantitative analysis of the crystallization kinetics and morphology development.

The thermal-shear profile used in this experiment is shown in Fig. 14a. Disks 12 mm in diameter of the compression moulded material were heated to 220°C and compressed slowly to the working distance of 500  $\mu\text{m}$  at 1 mm min<sup>-1</sup>. The relatively thick working distance was chosen to minimize the chance of edge effects that are thought to occur near the polymer-plate interface,<sup>[43,44]</sup> influencing the results. The compressed disks were held at the melting temperature for 5 min to erase any previous history. The isotropic nature of the melt after this treatment was confirmed by WAXS and polarized optical microscopy. Samples were then cooled as quickly as practically possible to the isothermal crystallization temperature ( $T_c$ ) of 135°C at 30°C min<sup>-1</sup>. A brief controlled step shear was applied for 1 s with shear rates between 0 and 80 s<sup>-1</sup> immediately after the sample reached  $T_c$ . Shear rates greater than 80 s<sup>-1</sup> were not able to be investigated in this study because of the appearance of flow instabilities (melt fracture) at shear rates greater than 80 s<sup>-1</sup>. In all cases the samples were held at the crystallization temperature

for long enough for the crystallization rate to be effectively negligible. The samples were then cooled at 30°C min<sup>-1</sup> to 50°C and held there for 5 min. The sample was then heated at constant a rate of 10°C min<sup>-1</sup> to 200°C. A heating rate of 10°C min<sup>-1</sup> was chosen to limit re-organization or recrystallization influencing the shape of the melting peaks as proposed by Paukkeri and Lehtinen.<sup>[36]</sup>

#### Microscopy

A permanganate etching technique was used to observe the lamellar structure.<sup>[45,46]</sup> Samples were immersed in a vigorously stirred solution of 3 wt-% KMnO<sub>4</sub>, 64.7 wt-% concentrated H<sub>2</sub>SO<sub>4</sub>, and 32.9 wt-% H<sub>3</sub>PO<sub>4</sub> for 7 h. An advantageous bi-product of the etching procedure is that it removes a considerable amount of material from the free surfaces, revealing the core of the samples. After etching, specimens were quenched into cold hydrogen peroxide and washed in an ultrasound bath to remove any artifacts caused by the etching procedure. ROM of the etched surfaces was performed on an Olympus PMG3 microscope with a differential interference optic attachment. Higher magnification of the etched surfaces was achieved with a JOEL JSM-7001F field emission scanning electron microscope operating in secondary electron mode. Samples were coated to 10 Å thick with gold/platinum and imaged at 50000 $\times$  magnification at an acceleration voltage of 5 kV.

#### Differential Scanning Calorimetry

DSC experiments were performed on the fully crystallized iPP samples using a Perkin-Elmer DSC-7 at heating rates of 10°C min<sup>-1</sup> and under a nitrogen atmosphere. Pure indium and zinc references were used for calibration. Samples were sectioned from the fully crystallized disk to remove enough representative material for DSC analysis (~2.5 mg). The width of the sectioned pieces along the radius of the disk was 1.5 mm, which corresponds to a shear rate resolution in the DSC samples of  $\pm 5$  s<sup>-1</sup>.

The Thompson-Gibbs relationship can be used to calculate the average lamellar thickness ( $\langle L \rangle$ ) of a polymer sample from the peak melting temperature ( $T$ ) in their DSC thermogram according to the equation:<sup>[47]</sup>

$$\langle L \rangle = \frac{2\sigma_e}{\Delta H_f \rho_c} \left( \frac{T_0}{T_0 - T} \right), \quad (4)$$

where the melting temperature of crystallites with infinite thickness,<sup>[48]</sup>  $T_0 = 187.7^\circ\text{C}$ , the lamellae surface energy,<sup>[48]</sup>  $\sigma_e = 4.8 \times 10^{-6} \text{ J cm}^{-3}$ , the density of the crystalline phase,<sup>[49]</sup>  $\rho_c = 0.91 \text{ g cm}^{-3}$ , and the melting enthalpy of a perfect crystal,<sup>[49]</sup>  $\Delta H_f = 177.6 \text{ J g}^{-1}$ .

#### Small-Angle X-ray Scattering

Small-angle X-ray scattering (SAXS) experiments were performed at the Australian National Beamline Facility (ANBF) at the Photo Factory in Tsukuba, Japan. The experimental set-up has been described in detail elsewhere.<sup>[22]</sup> The instrument has a multi-configuration vacuum diffractometer that uses image plates as its detector system. The square-shaped beam with a wavelength of 2.0 Å had dimensions of 200  $\times$  200  $\mu\text{m}^2$ . The sample-to-detector distance was 1012 mm. The scattering vector ( $q$ ) was calculated by the following formula  $q = 4\pi \sin \theta / \lambda$ ; where  $\theta$  is the scattering angle and  $\lambda$  is the incident wavelength. Scattering without the specimen was recorded as a background.

The 2D pattern was converted into polar coordinates using the *Nika* software package in Igor Pro to allow for azimuthal intensity integration.

#### *In-Situ Rheo-Wide Angle X-Ray Scattering*

2D rheo-WAXS experiments were performed on the powder diffraction beam line at the Australian Synchrotron,<sup>[50]</sup> Fig. 14b. The shear cell was adapted for use with X-ray radiation. The top plate had a narrow 3 mm diameter aperture that allowed X-rays to be introduced to the sample. The bottom plate had three slots wider than the aperture in the top plate, which allowed scattered X-rays to pass. Thin films of Kapton ~50 μm thick were used to keep the sample between the top and bottom plates. Beam dimensions of 1 mm × 1 mm, a wavelength of 0.82 Å, a camera length of 126 mm, and 15 s exposure time were employed throughout the experiment. The read out time of the detector was ~3 s. The beam current was logged every 2.5 min to allow for image normalization. A 2D Photonic Science CCT detector was used to record the WAXS patterns.

Scattering in the wide-angle regions is predominantly from crystalline planes and, therefore, WAXS is highly sensitive to the proportion of crystalline phases. A volume crystallinity index ( $\chi_v$ ) was determined by separating out the amorphous and crystalline contributions to the total scattering of a circularly integrated WAXS intensity profile along  $q$ , Fig. 5. Automated procedures were employed to deconvolute the scattering profiles using the *fity* software package. Three Gaussian curves centred at  $q = 1.0, 1.2$ , and  $1.45 \text{ Å}^{-1}$  were used to account for the amorphous scattering. Seven Gaussian curves were used to account for the major crystalline scattering peaks observed between  $0.9 \text{ Å}^{-1} \leq q \leq 1.6 \text{ Å}^{-1}$ . The volume crystallinity index was then estimated by:

$$\chi_v = \frac{A_{\text{crystalline}}}{A_{\text{crystalline}} + A_{\text{amorphous}}}, \quad (5)$$

where  $A_{\text{crystalline}}$  is the area of the seven crystalline Gaussian curves and  $A_{\text{amorphous}}$  is the area of the three amorphous Gaussian curves.

The  $\beta$ -iPP crystallinity ( $\chi_\beta$ ) and  $\gamma$ -iPP crystallinity ( $\chi_\gamma$ ) were determined using the Turner–Jones method:<sup>[51,52]</sup>

$$K_\beta = \frac{A_\beta(300)}{A_\beta(300) + A_\alpha(110) + A_\alpha(040) + A_\alpha(130)} \quad (6)$$

$$\chi_\beta = K_\beta \chi_v \quad (7)$$

$$K_\gamma = \frac{A_\gamma(117)}{A_\gamma(117) + A_\alpha(130)} \quad (8)$$

$$\chi_\gamma = K_\gamma \chi_v, \quad (9)$$

where  $A_\beta(300)$ ,  $A_\alpha(110)$ ,  $A_\alpha(040)$ ,  $A_\alpha(130)$ , and  $A_\gamma(117)$  are the areas of the reflections indicated in Fig. 5.

The lamellar thickness of the samples was also calculated from the WAXS data using the Scherrer equation:<sup>[53]</sup>

$$\langle L_{hkl} \rangle = \frac{K\lambda}{\beta_{hkl} \cos \theta_{hkl}}, \quad (10)$$

where  $L_{hkl}$  is the crystallite size in the direction perpendicular to the diffraction plane ( $hkl$ ),  $K$  is the crystallite shape factor (0.89), and  $\beta_{hkl} = (\beta_{hkl}^2 - b_0^2)^{1/2}$ , with  $\beta_{hkl}$  being the peak width at half maximum intensity and  $b_0$  the instrumental resolution. The assumption in the Scherrer equation is that all the line

broadening of reflections results from the finite crystallite size.  $\langle L_{001} \rangle$  has to be estimated from the reflections  $\alpha(111)$ ,  $\alpha(041)$ , and  $\alpha(\bar{1}31)$  because of the absence of a pure reflection of the form  $\alpha(001)$ . The thickness of crystalline lamellae,  $\langle L_{001} \rangle$ , can be calculated from the reflection  $\alpha(\bar{1}31)$  by the following equation:

$$\langle L_{001} \rangle = L_{\bar{1}31} \cos \omega = \frac{K\lambda}{\beta_{\bar{1}31} \cos \theta_{\bar{1}31}} \cos \omega, \quad (11)$$

where  $\omega$  is an angle between the lattice planes  $\alpha(001)$  and  $\alpha(\bar{1}31)$ . Using the crystal unit cell of the  $\alpha$ -form crystal ( $a = 6.66 \text{ Å}$ ,  $b = 20.96 \text{ Å}$ ,  $c = 6.5 \text{ Å}$ ,  $\beta = 99^\circ 80'$ , and  $\alpha$  and  $\gamma = 90^\circ$ ),<sup>[1]</sup> the value of  $\omega$  was calculated to be  $57.89^\circ$ .

Uncertainty in the parameters measured by X-ray analysis, SEM, and DSC were assessed by calculating the standard error in the measurement and the 95.4% confidence interval was reported.

#### Acknowledgements

This work was performed at the Powder Diffraction beamline at the Australian Synchrotron, Victoria, Australia and the Australian National Beamline Facility (ANBF) with support from the Australian Synchrotron Research Program, which is funded by the Commonwealth of Australia under the Major National Research Facility Program. The assistance from Dr Jan Ilavsky at the Advanced Photon Source Argonne National Laboratory for modifying the *Nika* software package was greatly appreciated. The authors also acknowledge George Theodossiou at the Monash Centre for Electron Microscopy (MCEM) for his invaluable assistance in preparing the SEM images.

#### References

- [1] G. Natta, P. Corradini, *Nuovo Cim.* **1960**, *15*, 40. doi:10.1007/BF02731859
- [2] B. Lotz, *J. Macromol. Sci. Part B: Phys.* **2002**, *41*, 685. doi:10.1081/MB-120013059
- [3] B. Lotz, *Eur. Phys. J. E* **2000**, *3*, 185. doi:10.1007/S101890070031
- [4] B. Lotz, J. C. Wittmann, *J. Polym. Sci., Part B: Polym. Phys.* **1986**, *24*, 1541. doi:10.1002/POLB.1986.090240712
- [5] B. Lotz, J. C. Wittmann, *Polymer* **1996**, *37*, 4979. doi:10.1016/0032-3861(96)00370-9
- [6] F. J. Padden, Jr., H. D. Keith, *J. Appl. Phys.* **1966**, *37*, 4013. doi:10.1063/1.1707968
- [7] F. L. Binsbergen, B. G. M. de Lange, *Polymer* **1968**, *9*, 23. doi:10.1016/0032-3861(68)90006-2
- [8] J. Weng, R. H. Olley, D. C. Bassett, P. Jämskeläinen, *J. Polym. Sci., Part B: Polym. Phys.* **2003**, *41*, 2342. doi:10.1002/POLB.10593
- [9] S. Kimata, T. Sakurai, Y. Nozue, T. Kasahara, N. Yamaguchi, T. Karino, M. Shibayama, J. A. Kornfield, *Science* **2007**, *316*, 1014. doi:10.1126/SCIENCE.1140132
- [10] J. J. Janimak, S. Z. D. Cheng, A. Zhang, E. T. Hsieh, *Polymer* **1992**, *33*, 728. doi:10.1016/0032-3861(92)90329-U
- [11] J. Weng, R. H. Olley, D. C. Bassett, P. Jämskeläinen, *J. Macromol. Sci., Part B: Phys.* **2002**, *41*, 891. doi:10.1081/MB-120013072
- [12] K. Mezghani, R. A. Campbell, P. J. Phillips, *Macromolecules* **1994**, *27*, 997. doi:10.1021/MA00082A017
- [13] F. Khoury, *J. Res. Natl. Bur. Stand., A Phys. Chem.* **1966**, *70A*, 29.
- [14] X. Wang, W. Hou, J. Zhou, L. Li, Y. Li, C.-M. Chan, *Colloid Polym. Sci.* **2007**, *285*, 449. doi:10.1007/S00396-006-1586-4
- [15] F. J. Padden, Jr., H. D. Keith, *J. Appl. Phys.* **1973**, *44*, 1217. doi:10.1063/1.1662331
- [16] W. Zeng, J. Wang, Z. Feng, J. Y. Dong, S. Yan, *Colloid Polym. Sci.* **2005**, *284*, 322. doi:10.1007/S00396-005-1371-9
- [17] P.-W. Zhu, A. Phillips, J. Tung, G. Edward, *J. Appl. Phys.* **2005**, *97*, 104908. doi:10.1063/1.1897072
- [18] P.-W. Zhu, J. Tung, A. Phillips, G. Edward, *Macromolecules* **2006**, *39*, 1821. doi:10.1021/MA052375G
- [19] M. Fujiiyama, T. Wakino, Y. J. Kawasaki, *J. Appl. Polym. Sci.* **1988**, *35*, 29. doi:10.1002/APP.1988.070350104



- [20] M. Fujiyama, T. Wakino, *J. Appl. Polym. Sci.* **1991**, *43*, 57. doi:10.1002/APP.1991.070430108
- [21] E. S. Clark, J. E. Spruiell, *Polym. Eng. Sci.* **1976**, *16*, 176. doi:10.1002/PEN.760160310
- [22] A. Phillips, P.-W. Zhu, G. Edward, *Macromolecules* **2006**, *39*, 5796. doi:10.1021/MA0607618
- [23] P.-W. Zhu, J. Tung, G. Edward, L. Nichols, *J. Appl. Phys.* **2008**, *103*, 124906. doi:10.1063/1.2931009
- [24] R. H. Somani, L. Yang, L. Zhu, B. S. Hsiao, *Polymer* **2005**, *46*, 8587. doi:10.1016/J.POLYMER.2005.06.034
- [25] M. Kakudu, N. Kasai, *X-ray Diffraction by Polymers* **1972** (Elsevier: Amsterdam).
- [26] Y. Mubarak, E. M. A. Harkin-Jones, P. J. Martin, M. Ahmad, *Polymer* **2001**, *42*, 3171. doi:10.1016/S0032-3861(00)00606-6
- [27] B. S. Hsiao, L. Yang, R. H. Somani, C. A. Avila-Orta, L. Zhu, *Phys. Rev. Lett.* **2005**, *94*, 117802. doi:10.1103/PHYSREVLETT.94.117802
- [28] J. T. Xu, A. J. Ryan, S. M. Mai, J. J. Yuan, S. Y. Cheng, *J. Macromol. Sci., Part B: Phys.* **2005**, *43*, 685. doi:10.1081/MB-120030014
- [29] Z. Zhang, S. Wu, M. Ren, C. Xiao, *Polymer* **2004**, *45*, 4361. doi:10.1016/J.POLYMER.2004.04.046
- [30] R. H. Somani, L. Yang, B. S. Hsiao, *Physica A* **2002**, *304*, 145. doi:10.1016/S0378-4371(01)00509-X
- [31] A. J. Waddon, M. J. Hill, A. Keller, D. J. Blundell, *J. Mater. Sci. Lett.* **1987**, *22*, 1773.
- [32] D. M. Dean, L. Rebenfeld, R. A. Register, B. S. Hsiao, *J. Mater. Sci.* **1998**, *33*, 4797. doi:10.1023/A:1004474128452
- [33] J. M. Schultz, *J. Polym. Sci., Part B: Polym. Phys.* **1992**, *30*, 785. doi:10.1002/POLB.1992.090300717
- [34] J. Seudla, M. Raab, K.-J. Eichhorn, A. Strachota, *Polymer* **2003**, *44*, 4655. doi:10.1016/S0032-3861(03)00287-8
- [35] H. Bai, Y. Wang, B. Song, Y. Li, L. Liu, *Polym. Eng. Sci.* **2008**, *48*, 1532. doi:10.1002/PEN.21125
- [36] R. Paukkeri, A. Lehtinen, *Polymer* **1993**, *34*, 4083. doi:10.1016/0032-3861(93)90670-6
- [37] V. Petraccone, G. Guerra, C. De Rosa, A. Tuzi, *Macromolecules* **1985**, *18*, 813. doi:10.1021/MA00146A037
- [38] G. Guerra, V. Petraccone, P. Corradini, C. D. Rosa, R. Napolitano, B. Pirozzi, *J. Polym. Sci.* **1984**, *22*, 1029.
- [39] K. Mai, K. Wang, H. Zeng, *J. Appl. Polym. Sci.* **2003**, *88*, 1608. doi:10.1002/APP.11652
- [40] S. S. Katti, J. M. Schultz, *Polym. Eng. Sci.* **1982**, *22*, 1001. doi:10.1002/PEN.760221602
- [41] I. Coccorullo, R. Pantani, G. Titomanlio, *Macromolecules* **2008**, *41*, 9214. doi:10.1021/MA801524T
- [42] K. Watanabe, K. Okada, A. Toda, S. Yamazaki, T. Taniguchi, K. Koyama, K. Yamada, M. Hikosaka, *Macromolecules* **2006**, *39*, 1515. doi:10.1021/MA050825Z
- [43] T. T. Dao, L. A. Archer, *Langmuir* **2002**, *18*, 2616. doi:10.1021/LA0112662
- [44] E. Polushkin, G. A. van Ekenstein, O. Ikkala, G. T. Brinke, *Rheol. Acta* **2004**, *43*, 364. doi:10.1007/S00397-003-0352-5
- [45] R. H. Olley, D. C. Basset, *Polym. Commun.* **1982**, *23*, 1710.
- [46] J. Park, K. Eom, O. Kwan, S. Woo, *Microsc. Microanal.* **2001**, *7*, 276. doi:10.1017/S1431927601010285
- [47] U. W. Gedde, *Polymer Physics* **1995** (Chapman & Hall: London).
- [48] K. Yamada, M. Hikosaka, A. Toda, S. Yamazaki, K. Tagashira, *J. Macromol. Sci., Part B: Phys.* **2003**, *42*, 733. doi:10.1081/MB-120021603
- [49] J. C. Viana, A. M. Cunha, N. Billon, *Polymer* **2002**, *43*, 4185. doi:10.1016/S0032-3861(02)00253-7
- [50] S. W. Kia, J. K. Brendan, W. David, *AIP Conf. Proc.* **2007**, *879*, 879.
- [51] A. Turner-Jones, A. J. Cobbold, *J. Polym. Sci.* **1968**, *6*, 539. doi:10.1002/POL.1968.110060802
- [52] A. Turner-Jones, *Polymer* **1971**, *12*, 487. doi:10.1016/0032-3861(71)90031-0
- [53] L. E. Alexander, *X-Ray Diffraction Methods in Polymer Science* **1976** (Wiley-Interscience: New York, NY).

# FORMATION OF SHEAR-INDUCED PRECURSORS IN IPP CONTAINING NUCLEATING AGENTS

Andrew Phillips<sup>1\*</sup>, Peng-wei Zhu<sup>1</sup> and Graham Edward<sup>1</sup>

<sup>1</sup>*Department of Materials Engineering, CRC for Polymers, Monash University, VIC 3800, Australia.  
Andrew.Phillips@eng.monash.edu.au, (Ph) +613 9905 4928, (Fax) +613 9905 4940*

The addition of nucleating agents complicate the prediction of morphology during processing of isotactic polypropylene (iPP). In this work, the formation of shear-induced precursors to crystallisation in a continuously sheared melt of iPP held at 175 °C containing two nucleants with different aspect ratios was examined by in-situ rheo-SAXS/WAXS and rheo-FTIR. Sharp equatorial streaks were observed in the SAXS patterns and a coil to helix transition was observed in FTIR spectra in all samples above a critical shear rate. However, no associated crystalline scattering was observed. These results are consistent with the formation of non-crystalline shear-induced precursors aligned along the flow direction. The critical shear rate required to induce the formation of the precursors was decreased by the presence of both nucleants compared to pure iPP. The high aspect ratio nucleant resulted in a greater number of crystal precursors, which then had a greater alignment along the flow direction when compared to the low aspect ratio nucleant. These results suggest that nucleant shape can affect the development of morphology in sheared iPP.

## Introduction

Shear flows, such as those found in injection moulding, are well known to create molecular extension and orientation in polymer melts. This leads to significant changes to crystallisation kinetics, and the development of morphology. For example, shear flow can change a spherulite structure which forms under quiescent conditions, to an oriented one containing the molecular assemblies termed 'shish-kebabs'. The shish-kebab structure is a polymer crystal assembly, which consists of chain folded lamellae (kebabs) held together by a core of highly extended chains (shish). Preceding the formation of shish must be some form of shear-induced oriented precursor structure which is associated with the transition from coiled to stretched chains that occurs above a critical shear rate (De-Gennes, 1974). Much of the evidence for the precursor structure comes from scattering experiments where sharp equatorial streaks are observed at small scattering angles (Somani et al., 2005; Kumaraswamy, 2005; Kimata et al., 2007) as well as birefringence measurements (Seki et al., 2002; Fernandez-Ballester et al., 2008). More recently, FTIR experiments show the formation of precursors is also associated with a molecular coil to helix transition (Geng et al., 2009; Xinyuan et al., 2000). However, as yet only few authors have presented combined FTIR and scattering measurements.

The formation of precursors is complicated by the addition of foreign particle such as nucleating agents and colourants. Previous studies by our group on injection moulded isotactic polypropylene (iPP) containing sodium benzoate (Zhu et al., 2005; Zhu et al., 2006) and two colourants (Zhu et al., 2008) showed their presence decreased the shear intensity required to

form the shish-kebab structure. More recently experiments by Byelov et al. (2008) showed that the shape of the nucleant may be important, with anisotropic nucleants leading to an increase in the number of nucleating sites for crystal formation compared to isotropic nucleant agents. These results show foreign particles influence the formation of precursors. However, the mechanism by which this occurs still remains a mystery.

This paper reports the results of recent small and wide angle x-ray scattering (rheo-SAXS/WAXS) and rheo-FTIR experiments on iPP containing two nucleants with widely different aspect ratios. The aim was to determine the influence of nucleant aspect ratio on the formation of the shear-induced precursor structure under continuous shear conditions. The shear temperature was chosen (175 °C) to be above the lamellae melting point to avoid artefacts from crystallisation, and long shear times (30 s) were used to allow investigation of precursor formation during shear flow. It will be shown that the high aspect ratio nucleant was more effective at forming oriented shear-induced precursors compared to the low aspect ratio nucleant.

## Experimental

The polymer used was an iPP homopolymer manufactured by the Borealis group (HD601CF). This grade was chosen as it has been extensively investigated by our group and contains almost no additives. In particular it contains no calcium stearate which has recently been shown to influence the formation of the crystal precursor structure (Byelov et al., 2007). The average weight molecular weight (Mw) and the average number molecular weight (Mn) were

367 000 and 74 000, respectively. Various loadings of two nucleating agents, sodium benzoate (SB) and bicyclo[2.2.1]heptane-2,3-dicarboxylic acid (HPN), were compounded into the iPP matrix in a Haake Rheocord 90 batch mixer. The nucleant morphology is shown in Figure 1. SB is highly elongated. Standard techniques were employed to determine the average length (2.7  $\mu\text{m}$ ), width/thickness (0.3  $\mu\text{m}$ ), and aspect ratio (10) of SB. HPN was found to have a cubic morphology which was roughly isotropic, with dimension of 0.5  $\mu\text{m}$  and aspect ratio near 1.

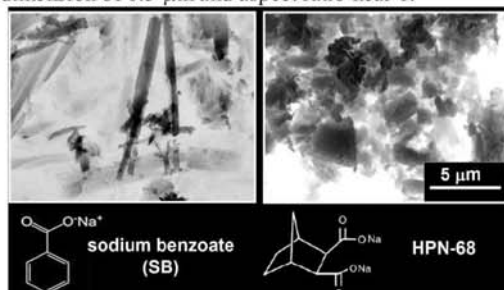


**Figure 1** – Ex-situ scanning electron microscope images of the two nucleants.

A Linkam CSS450 shear cell was used to control the thermal-shear profile, Figure 2. The CSS450 is a parallel plate shearing device in which a small aperture in the base and lid allows observation of the polymer in-situ. Samples were heated to 220 °C and compressed slowly to the working distance (x-ray = 500  $\mu\text{m}$ ; FTIR = 250  $\mu\text{m}$ ). The compressed disks were held at the melting temperature for 5 minutes to erase the samples previous thermal history. Samples were then cooled to the shear temperature (175 °C) and held there for 5 minutes to allow the sample to equilibrate. A series of controlled continuous shears of increasing shear rate between 0 – 80  $\text{s}^{-1}$  was then applied to the melt. The step shears were applied for 30 s with a 60 s relaxation time between each successive shear.

Simultaneous 2D rheo-SAXS/WAXS experiments were performed on the SAXS/WAXS beamline at the Australian Synchrotron. The set up allowed for in-situ investigations with a considerable amount of the scattering intensity around the azimuth ( $\phi \sim 80^\circ$ ) in the WAXS region (Polaris CCD 2D detector) to be captured whilst simultaneously capturing complete SAXS patterns (MAR CCD 2D detector). Exposure times were 1 s with successive exposures being 4.8 s apart. Details of the apparatus have been reported in a previous paper (Phillips et al., 2010). Data analysis was performed with the aid of the SAXS15iD program.

FTIR is sensitive to the conformation and local environment of the iPP molecules. In particular, information can be drawn about the length of the iPP helix (Geng et al., 2009; Xinyuan et al., 2000). The bands at 1100  $\text{cm}^{-1}$ , 998  $\text{cm}^{-1}$ , 841  $\text{cm}^{-1}$  and 1220  $\text{cm}^{-1}$  correspond to helical lengths with monomers of 6, 10,

12 and 14 respectively. The CSS450 was adapted for use with IR radiation by fitting it with 1 mm thick ZnSe windows. Rheo-FTIR experiments were performed on a Perkin-Elmer GX FTIR over a wavenumber range of 2000–500  $\text{cm}^{-1}$ , and resolution of 4  $\text{cm}^{-1}$ . An empty cell was used as the background.

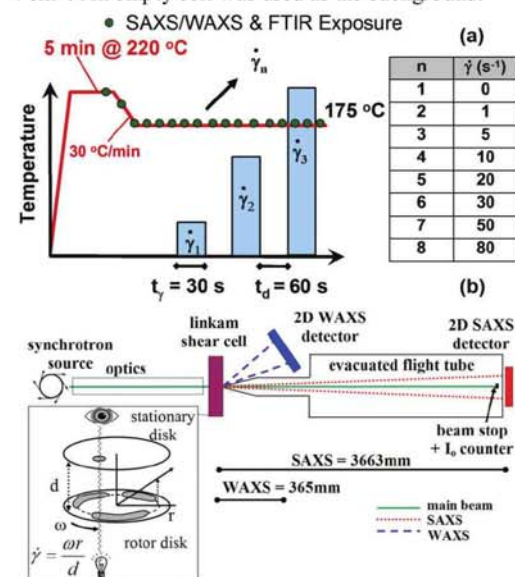


**Figure 2** – Schematic diagrams of (a) the thermal-shear profile and (b) the simultaneous 2D WAXS/SAXS setup.

## Results & Discussion

### Influence of nucleants on the quiescent melt

In-situ 2D SAXS patterns of pure iPP and iPP containing the two nucleants in the quiescent melt at 175 °C are shown in Figure 3a. In all patterns the scattering profile was isotropic. The addition of both nucleants led to an increase in the overall amount of scattering. In particular, the addition of the HPN nucleant led to a significant increase in the amount of scattering compared to pure iPP and iPP containing SB. This increase in scattering intensity could be due to the effect of the nucleant particles themselves or the effect of the nucleants on the structure of the melt. To further investigate this, in-situ rheo-FTIR spectra of the quiescent melt were obtained, Figure 4a. In pure iPP no absorbance could be found at 841  $\text{cm}^{-1}$  indicating that no long helices were present. The addition of both nucleants led to the occurrence of the 841  $\text{cm}^{-1}$  peak. The addition of HPN also led to the occurrence of the 1220  $\text{cm}^{-1}$  peak, however pure HPN also absorbs at this frequency. This indicates that both nucleants could promote the coil to helix transition without shear. It is unclear at this stage the mechanism by which this occurs. However, it may be that an appropriate nucleant surface can stabilise the conformation of shorter iPP helices allowing them to reach a greater length than would otherwise be obtainable in the melt.



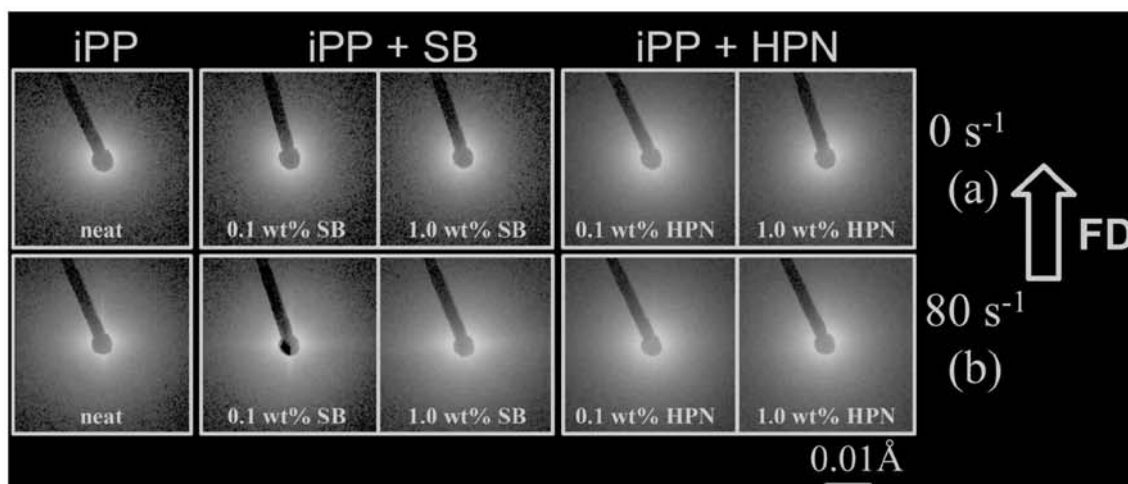


**Figure 3** – In-situ small angle x-ray scattering patterns showing the influence of the two nucleants on (a) the quiescent melt and (b) the continuously sheared melt held at 175 °C.

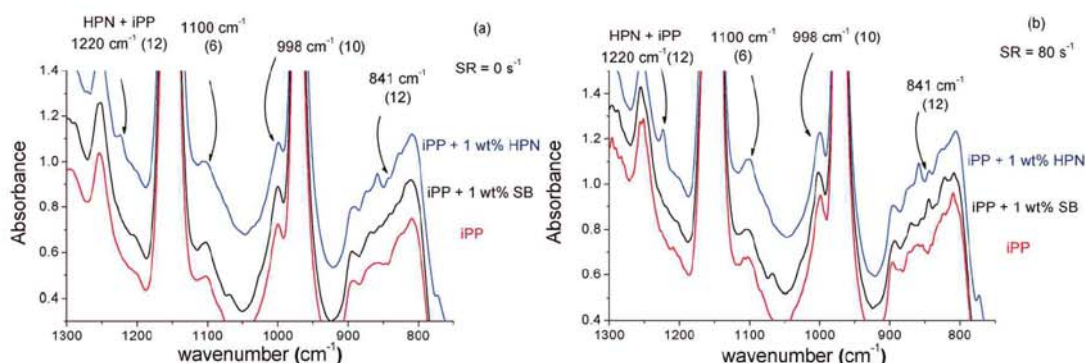


**Figure 4** – (a) FTIR spectra showing the influence of the addition of the two nucleants on (a) the quiescent melt and (b) the continuously sheared melt held at 175 °C. The number in the brackets is the number of monomers in the iPP helix.

#### *Influence of nucleants on the sheared melt*

Figure 3b shows the last frame before the end of a continuous shear of shear rate 80 s<sup>-1</sup> for 30 s at 175 °C. Sharp equatorial scattering was observed in all samples above a critical shear rate. This is consistent with the formation of oriented crystal precursors aligned along the flow direction. Recent studies by Balzano et al. (2009) found crystals formed during short fast shears in super-cooled iPP at a shear temperature of 145 °C. However, in these experiments no crystalline scattering could be discerned in the WAXS profiles. This suggests that the precursors at this temperature are primarily non-crystalline entities. Corresponding FTIR spectra to the SAXS results shown in Figure 3b are provided in Figure 4a. A critical shear rate above which an increase in the absorbance of the 998 cm<sup>-1</sup> and 841 cm<sup>-1</sup> peaks compared to their quiescent state was also observed. This suggests a shear induced coil to helix transition is associated with the formation of the precursors. Using criteria proposed by Doi et al. (1988), the critical persistence length for a shear-

induced isotropic to nematic transition in iPP has been found to be 11 monomer units (Geng et al., 2009; Li and de Jeu, 2004). Therefore in combination with the SAXS results the shear-induced occurrence of the 841 cm<sup>-1</sup>, which corresponds to helices greater than 12 monomer units long, indicates that structure of the precursors may be liquid crystalline in origin.

The addition of both nucleants significantly influenced the formation of the precursor structure. In the SAXS patterns the sharpness of the equatorial streak can be interpreted as the level of alignment of the precursors along FD while its intensity can be related to precursor density. The addition of SB increased both the sharpness and intensity while the addition of HPN appeared to reduce the sharpness and only mildly increase the intensity of the equatorial peak when compared to pure iPP. The critical shear rate identified in the SAXS patterns and the FTIR spectra was also investigated. The results are presented in Table 1 along with the nucleation efficiency of the nucleants at the various loading calculated using the method proposed by Fillon et al. (1993). Both

nucleating agents decreased the critical shear rate for precursor formation and coil to helix transition compared to pure iPP. SB was slightly more effective at reducing the two critical shear rates than HPN even though its nucleation efficiency was less.

**Table 1** – The critical shear rate for the occurrence of equatorial scattering in the SAXS patterns and the 841  $\text{cm}^{-1}$  (helix of 12 monomers) and 998  $\text{cm}^{-1}$  (helix of 10 monomers) peaks in the FTIR spectra.

Material	Loading (wt%)	Nucleation Efficiency (%)	SAXS ( $\text{s}^{-1}$ )	998 $\text{cm}^{-1}$ ( $\text{s}^{-1}$ )	841 $\text{cm}^{-1}$ ( $\text{s}^{-1}$ )
iPP	0	0	30	30	50
iPP + SB	0.1	11	5	5	10
	1	30	1	5	10
iPP + HPN	0.1	49	10	10	30
	1	59	5	5	5

These interesting results can be explained by the effect of the nucleant on the local flow of iPP molecules near the nucleant particles. Assuming the velocity of the particle is lower than the velocity of melt ( $V_{\text{particle}} < V_{\text{melt}}$ ) then the presence of the nucleants would result in an increase in the local flow rate near the particle, amplifying the shear field. Additionally, the flow constriction imposed by the particles would result in a greater elongational component to the shear flow (Hwang et al., 2006). Both would lead to the observed decrease in the critical shear rate required to form the precursor structure. Compared to high aspect ratio particles, low aspect ratio particles are known to tumble considerably more in shear fields (Zettner and Yoda, 2001). This leads to increased vortices which resulting in more uneven flow near the particles (Majhi and Vasudevaiah, 1982). The uneven flow field near the low aspect ratio nucleant is then thought to lead to the observed higher critical shear rate for precursor formation as well as their reduced alignment along the flow direction compared to the high aspect ratio nucleant.

## Conclusions

Two nucleating agents with different aspect ratios were added to an iPP matrix and the formation of crystal precursor structures was investigated in-situ by simultaneous rheo-SAXS/WAXS and rheo-FTIR. In the quiescent melt the addition of nucleating agents induced some iPP molecules to undergo a coil to helix transition. In the continuously sheared melt oriented crystal precursor structures were formed in all samples above a critical shear rate. The critical shear rate for precursors formation was reduced in the presence of both nucleating agents compared to the pure iPP. The high aspect ratio nucleant reduced the critical shear rate more than the low aspect ratio nucleant. These results were explained by what happens to the flow of material around the nucleant particle.

## Acknowledgements

This work was performed at the SAXS/WAXS beamline at the Australian Synchrotron, Victoria, Australia. The authors would also like to acknowledge George Theodossiou at the Monash Centre for Electron Microscopy (MCEM) for his invaluable assistance in preparing the SEM images.

## References

- Balzano, L., Rastogi, S. & Peters, G. W. M. Crystallization and Precursors during Fast Short-Term Shear. *Macromolecules*, **42**, 2088-2092 (2009).
- Byelov, D., Panine, P. & De Jeu, W. H. Shear-Induced Smectic Order in Isotactic Polypropylene Revisited. *Macromolecules*, **40**, 288-289 (2007).
- Byelov, D., Panine, P., Remerie, K., Biemond, E., Alfonso, G. C. & De Jeu, W. H. Crystallization under shear in isotactic polypropylene containing nucleators. *Polymer*, **49**, 3076-3083 (2008).
- De-Gennes, P. G. Coil-stretch transition of dilute flexible polymers under ultrahigh velocity gradients. *The Journal of Chemical Physics*, **60**, 5030-5042 (1974).
- Fernandez-Ballester, L., Gough, T., Meneau, F., Bras, W., Ania, F., Balta-Calleja, F. J. & Kornfield, J. A. Simultaneous birefringence, small- and wide-angle X-ray scattering to detect precursors and characterize morphology development during flow-induced crystallization of polymers. *Journal of Synchrotron Radiation*, **15**, 185-190 (2008).
- Fillon, B., Lotz, B., Thierry, A. & Wittmann, J. C. Self-nucleation and enhanced nucleation of polymers. Definition of a convenient calorimetric efficiency scale and evaluation of nucleating additives in isotactic polypropylene (alpha phase). *Journal of Polymer Science Part B: Polymer Physics*, **31**, 1395-1405 (1993).
- Geng, Y., Wang, G., Cong, Y., Bai, L., Li, L. & Yang, C. Shear-Induced Nucleation and Growth of Long Helices in Supercooled Isotactic Polypropylene. *Macromolecules*, **42**, 4751-4757 (2009).
- Hwang, W. R., Peters, G. W. M., Hulsen, M. A. & Meijer, H. E. H. Modeling of Flow-Induced Crystallization of Particle-Filled Polymers. *Macromolecules*, **39**, 8389-8398 (2006).
- Kimata, S., Sakurai, T., Nozue, Y., Kasahara, T., Yamaguchi, N., Karino, T., Shibayama, M. & Kornfield, J. A. Molecular Basis of the Shish-Kebab Morphology in Polymer Crystallization. *Science*, **316**, 1014-1017 (2007).

Kumaraswamy, G. Crystallization of Polymers from Stressed Melts. *Polymer Reviews*, **45**, 375 - 397 (2005).

Li, L. & De Jeu, W. H. Shear-Induced Smectic Ordering in the Melt of Isotactic Polypropylene. *Physical Review Letters*, **92**, 075506 (2004).

Majhi, S. & Vasudevaiah, M. Flow separation in a viscous parabolic shear past a sphere. *Acta Mechanica*, **45**, 233-249 (1982).

Doi, M., Shimada, T. & Okano. Concentration fluctuation of stiff polymers. II. Dynamical structure factor of rod-like polymers in the isotropic phase. *The Journal of Chemical Physics*, **88**, 4070-4075 (1988).

Phillips, A., Zhu, P. & Edward, G. Polystyrene as a versatile nucleating agent for polypropylene. *Polymer*, **51**, 1599-1607 (2010).

Seki, M., Thurman, D. W., Oberhauser, J. P. & Kornfield, J. A. Shear-Mediated Crystallization of Isotactic Polypropylene: Shear-Mediated Crystallization of Isotactic Polypropylene: The Role of Long Chain-Long Chain Overlap. *Macromolecules*, **35**, 2583-2594 (2002).

Somani, R. H., Yang, L., Zhu, L. & Hsiao, B. S. Flow-induced shish-kebab precursor structures in entangled polymer melts. *Polymer*, **46**, 8587-8623 (2005).

Xinyuan, Z., Deyue, Y., Hongxi, Y. & Pingfang, Z. In situ FTIR spectroscopic study of the regularity bands and partial-order melts of isotactic poly(propylene). *Macromolecular Rapid Communications*, **21**, 354-357 (2000).

Zettner, C. M. & Yoda, M. Moderate-aspect-ratio elliptical cylinders in simple shear with inertia. *Journal of Fluid Mechanics*, **442**, 241-266 (2001).

Zhu, P., Tung, J., Edward, G. & Nichols, L. Effects of Different Colorants on Morphological Development of Sheared Isotactic Polypropylene: A Study Using Synchrotron Wide-Angle Scattering. *Journal of Applied Physics*, **103**, 124906 (2008).

Zhu, P., Phillips, A., Tung, J. & Edward, G. Orientation distribution of sheared isotactic polypropylene plates through thickness in the presence of sodium benzoate. *Journal of Applied Physics*, **97**, 104908 (2005).

Zhu, P., Tung, J., Phillips, A. & Edward, G. Morphological development of oriented isotactic polypropylene in the presence of a nucleating agent. *Macromolecules*, **39**, 1821-1831 (2006).



# Thermal Stability of Oriented Lamellae in Sheared Isotactic Polypropylene

Andrew Phillips<sup>1</sup>, Peng-wei Zhu<sup>1</sup>, Chitiur Hadinata<sup>2</sup>, Graham Edward<sup>1</sup>

<sup>1</sup>*Department of Materials Engineering, CRC for Polymers, Monash University, VIC 3800, Australia.*

<sup>2</sup>*Moldflow Pty. Ltd., 259-261 Colchester Rd., Kilsyth VIC 3137, Australia*

*Andrew.Phillips@eng.monash.edu.au, (Ph) +613 9905 8064, (Fax) +613 9905 4940*

## Abstract

$\alpha$  isotactic polypropylene ( $\alpha$ -iPP) exhibits a form of lamellar branching that is unique amongst semi-crystalline polymers, where the branches have a distinct orientation relationship with the original crystalline lamellae. This is termed a parent-daughter relationship (PD). By allowing the structure to crystallise in an oriented form, a bimodal orientation develops and the individual contributions of PD lamellae can be observed using wide angle x-ray scattering (WAXS). The present study investigated the thermal stability of oriented PD lamellae using differential scanning calorimetry (DSC) and in-situ time resolved WAXS. Increasing the shear rate above a critical value ( $SR = 30s^{-1}$ ) resulted in two distinct melting peaks in the DSC thermograms. Daughter lamellae were observed to melt at lower temperatures than parent lamellae providing an explanation for the multiple melting peaks observed by DSC.

**Keywords:** isotactic polypropylene, melting, wide angle x-ray scattering (WAXS), differential scanning calorimetry (DSC), lamellae

## 1.0 Introduction

External flow fields, such as those produced during injection moulding, are well known to create molecular extension and orientation in polymer melts. This leads to significant changes in the crystallisation kinetics and in the development of morphology<sup>1</sup>. Crystallisation of  $\alpha$  isotactic polypropylene ( $\alpha$ -iPP) is further complicated by a lamellae branching phenomenon that is unique amongst semicrystalline polymers, where the branches have a distinct orientation relationship with the original crystals<sup>2</sup>. The orientation relationship is such that the  $a_2$ -axis and  $c_2$ -axis of the daughter lamellae ( $L_D$ ) are aligned along the  $c_1$ -axis and the  $a_1$ -axis of the parent lamellae ( $L_P$ ). This is termed a parent-daughter relationship (PD). The nature of the PD structure has been thought to influence important properties such as fatigue life<sup>3</sup>, resistance to deformation<sup>4</sup>, and surface properties such as wear and adhesion<sup>5</sup>.

Parent and daughter lamellae are inherently difficult to study separately in in-situ environments due to their many similarities. However, by allowing the material to crystallise in an oriented form, such as that found in the skin of injection mouldings, the individual contributions of PD lamellae can be observed by wide angle x-ray scattering (WAXS)<sup>3,6</sup>. Coupled with an appropriately designed shear cell and an intense x-ray source this permits PD lamellae to be investigated in-situ during important processes like crystallisation and melting.

The sequential formation of daughter lamellae should result in their reduced thickness and therefore reduced thermal stability compared to their parent lamellae due to: a) their lower temperature of formation in continuously cooled material and b) that chains already incorporated into parent lamellae will hinder their diffusion to the crystal growth front. It is the aim of this work to investigate the thermal stability of oriented PD lamellae formed by flow-induced crystallisation to confirm the expected relative thickness of PD lamellae. This is achieved using a combination of differential scanning calorimetry (DSC) and in-situ time resolved WAXS.

## 2.0 Experimental

The polymer used in this study was an iPP homopolymer manufactured by the Borealis group. A Linkam CSS450 shear cell was used to control the thermal-shear profile. The CSS450 is a parallel plate shearing device in which small apertures in the base and lid allow observation of the polymer in-situ, Figure 1. The generic thermal-shear profile used in this experiment is shown in Figure 2. Disks 12 mm in diameter of the material were heated to 220 °C and compressed to the working thickness of 500  $\mu m$ . The compressed disk was held at the melting temperature for 3 minutes to erase any previous history. The sample was cooled to the crystallisation temperature ( $T_c$ ) of 140 °C at 30 °C/min. A controlled shear rate ( $SR$ ) between 0-80  $s^{-1}$  was applied for 1s immediately after the sample reached  $T_c$ . To ensure consistency of results, the time each sample was held at  $T_c$  was set at  $2.5 \times t_{0.5}$ , where  $t_{0.5}$  is



the time for crystallisation to reach 50% completion as measured by birefringence (Table 1). Samples were then cooled at 30 °C/min to 50 °C and held there for 3mins.

Experiments were performed in duplicate. One sample was immediately heated in-situ at 10 °C/min for time resolved WAXS studies. The second sample was removed from the shear cell and sectioned to obtain enough representative material for DSC analysis ~2.5 mg. The width of the sectioned pieces corresponds to a shear rate resolution of  $\pm 5 \text{ s}^{-1}$ . DSC experiments were performed using a Perkin-Elmer DSC-7.

2D WAXS experiments were performed on the powder diffraction beam line at the Australian Synchrotron, Figure 3. The shear cell was adapted for use with x-ray radiation. The top plate had a narrow 3 mm diameter aperture allowing x-rays to be introduced to the sample. The bottom plate had three slots wider than the aperture in the top plate allowing scattered x-rays to pass. Thin films of Kapton™ ~50  $\mu\text{m}$  were used to keep the sample between the top and bottom plates. A 15 KeV ( $\lambda = 0.82 \text{ \AA}$ ) beam of dimensions of 1 mm x 1 mm, a camera length of 126 mm, and a 15s exposure time were employed throughout the experiment. The read-out time of the detector was approximately 3s. Beam current was logged every 2.5 minutes to allow for image normalisation. A 2D Photonic Science CCT detector was used to record the WAXS patterns.

### 3.0 Results and Discussion

#### 3.1 DSC

DSC melting thermograms of the sheared samples are shown in Figure 4. In the sample crystallised in the absence of shear, appreciable melting was observed to begin around 160 °C, peaking in a broad single peak centred at 175.0 °C ( $L_1$ ). Increasing shear rates up to 20  $\text{s}^{-1}$  decreased the peak position and also resulted in the peak becoming narrower. At 30  $\text{s}^{-1}$  a second lower temperature peak was observed at 165 °C ( $L_2$ ). Increasing the shear rate above 30  $\text{s}^{-1}$  resulted in a steady increase in both peak temperatures, but particularly  $L_1$ . Additionally, the relative size of the  $L_2$  peak increased while the relative size of the  $L_1$  peak decreased with increasing shear.

It is suspected that the two melting peaks are due to the oriented PD structure, with the thinner daughter lamellae melting at a lower temperature than the thicker parent lamellae. However, multiple melting peaks are not uncommon in the DSC thermographs of iPP and their occurrence has been explained by a number of different processes. For instance: different crystalline phases, recrystallisation<sup>7, 8</sup> and differences in crystal perfection / thicknesses<sup>9, 10</sup>. Unfortunately, DSC results alone are unable to provide definitive information as to which process/es are responsible.

WAXS can give invaluable information on many important morphological parameters such as: the crystallinity, crystalline phases present and morphology. Therefore to determine the origin of the multiple melting peaks observed in the DSC thermograms, sheared samples were melted in-situ whilst continually recording WAXS patterns. A highly intense synchrotron source was used to reduce the time required for a satisfactory exposure to be taken and increase the temperature selectivity of the experiment. To further increase the temperature selectivity, the condition which produced the greatest difference in peak position ( $\text{SR} = 80 \text{ s}^{-1}$ ) was used.

#### 3.2 wide angle x-ray scattering (WAXS)

Figure 5a shows a typical 2D image crystallised after a shear rate of 80  $\text{s}^{-1}$ . In the figure the flow direction (FD) is vertical. Orientation is clearly evident with an azimuthal intensity distribution characteristic of oriented PD lamellae. A generalised model of the oriented PD lamellae structure which gives rise to this pattern is provided in Figure 5b. In the model parent lamellae have their  $c_1$ -axis (chain folding axis) aligned along FD. Epitaxial nucleation of daughter lamellae may then form with the orientation relationship mentioned earlier. This model correctly predicts broad features of the diffraction pattern. For the 110 reflection, parent lamellae should diffract along the equator whilst daughters should diffract close to the meridian (as diffraction occurs perpendicular to the c-axis). For the 040 reflection, both parent and daughter lamellae diffract along the equator as their b-axes are perpendicular to FD.

Post processing of the 2D raw WAXS images and data reduction was performed using the Nika SAS macros in Igor Pro. Images were first normalised using the measured beam current before empty cell and dark field images were subtracted. A reduced circular 1D integration of the 2D pattern was

performed and is shown in Figure 6. The 5 most intense reflections of  $\alpha$ -iPP were clearly evident showing that the crystalline material was almost entirely composed of the  $\alpha$  phase.

The oriented PD lamellae were reheated at 10 °C/min until the polymer had completely melted. During this heating regime WAXS patterns were continually measured. A volume crystallinity index ( $\chi_v$ ) was determined for each exposure by separating the amorphous and crystalline contributions to scattering between  $7^\circ \leq (2\theta) \leq 13^\circ$  and  $0^\circ \leq \psi \leq 360^\circ$ . The amorphous contribution, ( $A_{\text{amorp}}$ ), was determined by fitting a smooth curve to 50 points selected to define the shape; the crystalline contribution, ( $A_{\text{cryst}}$ ), was determined by integrating the scattering above this amorphous halo. The volume crystallinity index was then estimated by:

$$\chi_v = \frac{A_{\text{cryst}}}{A_{\text{cryst}} + A_{\text{amorp}}} \quad (1)$$

The results are plotted in Figure 7 and they show that the volume crystallinity begins to drop appreciably above 144 °C. The rate of decline increases at 160 °C and drops until the material has completely melted at a temperature of 183 °C.

Figure 8 shows plots of the intensity ( $I(\psi)$ ) vs azimuthal angle ( $\psi$ ) for the (110) reflection as a function of temperature. Initially, increasing temperature led to a decrease in the intensity from daughter lamellae while the intensity from parent lamellae stayed relatively constant. It was not until a temperature of 173 °C that the intensity from the parent lamellae began to decrease appreciably. At this stage the peak heights of both parent and daughter lamellae were roughly similar.

To further analyse the temperature dependence of the oriented PD lamellae, the individual contributions from both parent and daughter lamellae were deconvoluted by fitting the observed (110) azimuthal scattering with Gaussian functions in the fityk package. Before deconvolution, isotropic scattering was subtracted from the plots by fitting a linear horizontal baseline. The integrated intensities from the parent (P) and daughter (D) lamellae are presented in Figure 9a. Both show a slight decrease in intensity with increasing temperature above 100 °C. This is presumably due to the melting of small and imperfect lamellae stacks. Appreciable melting did not occur until greater than 156 °C for D and 161 °C for P, a difference of ~5 °C.

An idea of the relative concentration of the daughter lamellae [D] can be obtained by calculating the ratio of the integrated intensity under the (110) reflection according to the following equation<sup>11</sup>:

$$[D] = \frac{D}{D + P} \quad (2)$$

This analysis does not provide an absolute concentration value but rather an indication of the change in relative concentration<sup>12</sup>. The results are presented in Figure 9b and show that initially as the temperature increases above 100 °C, [D] remains constant. However, with increasing temperature above 140 °C, [D] begins to drop significantly and is zero by 177 °C. At this temperature a small amount of parent lamellae are still present. This analysis shows definitively that the daughter lamellae melt at lower temperatures than the parent lamellae.

The change in azimuthal angle between the 110 peaks due to parent and daughter lamellae ( $\delta$ ) as they melt was determined by calculating the relative change in the centre of the fitted Gaussian curves in the 110 reflection, Figure 9c.  $\delta$  stayed relatively constant at 77° until 140 °C where it was observed to decrease steadily until the daughter lamellae had completely melted.

### 3.3 Discussion

From the results obtained, the origin of the two melting peaks observed in the DSC thermographs of material with shear rates greater than  $30\text{s}^{-1}$  can now be determined. X-ray scattering revealed that the morphology was predominantly  $\alpha$  phase and therefore melting by  $\beta$  phase can be ruled out. The smooth drop in both D and P with increasing temperature as well as the absence of multiple melting behaviour at low shear rates makes the presence of a recrystallisation phenomenon unlikely. Daughter lamellae however can clearly be seen to melt at a lower temperature than parent lamellae. The difference in melting temperature observed by WAXS also corresponds to the difference observed by DSC (~5 °C).

The melting temperature of semi-crystalline polymers can be related to the lamellae thickness (L) using the well known Thompson-Gibbs equation<sup>13</sup>:

$$L = \frac{2\sigma_e}{\Delta H_f \rho_c} \left( \frac{T_0}{T_0 - T} \right) \quad (3)$$

where  $T_0$  is the melting temperature of crystallites with infinite thickness,  $\sigma_e$  is the lamellae surface energy,  $\rho_c$  is the density of the crystalline phase, and  $\Delta H_f$  is the melting enthalpy of perfect crystal. The equation shows thicker lamellae melt at higher temperatures than thinner lamellae. Therefore it is proposed that the bimodal distribution observed in the sheared DSC curves above 30 s<sup>-1</sup> arises from two different populations of lamellae thickness. In this case the thicker parent lamellae give rise to the high temperature peak and the thinner daughter lamellae gives rise to the low temperature peak. The daughter lamellae are thinner as a result of their sequential formation which leads to reduced diffusion of chains to the crystal growth front due to the constriction of chains being also incorporated in nearby lamellae.

Figure 9c shows the angle between the parent and daughter contributions to the 110 peaks gets smaller as the daughter lamellae melt. This can be explained by the daughter lamellae getting thinner and curving as they grow away from their parent lamellae. The azimuthal angle ( $\delta$ ) from the model described in Figure 5b can be calculated according to the method described by Kakudo and Kasai<sup>14</sup>:

$$\cos(\phi) = \cos(\theta)\cos(90 - \delta) \quad (4)$$

where  $\phi$  is the angle the 110 plane normal makes with FD and  $\theta$  is the Bragg angle. For the model described in Figure 5b  $\phi = 19.7^\circ$  which equates to  $\delta = 70.7^\circ$ . At low temperatures, before any melting has occurred the measured  $\delta$  is much higher than predicted at  $\delta = 77^\circ$ . According to Dean<sup>12</sup> curving of the lamellae can lead to an asymmetric shift in  $\delta$  explaining the observed discrepancy from the predicted value. During melting  $\delta$  drops closer to the predicted value, reaching  $71.5^\circ$  before the sample had completely melted. At high temperatures only the thicker regions close to the parent lamellae remain. As curvature would not be significant over these short lamellae lengths the predicted and measured values of  $\delta$  should be similar as was observed. This shows that the daughter lamellae curve and get thinner as they grow away from their parent lamellae. In this experiment melting occurs at the extremities first, progressing at higher temperatures toward their parent lamellae.

From the experimental results obtained in this investigation an updated model of the oriented structure formed by flow-induced crystallisation in  $\alpha$ -iPP is proposed, Figure 10. A small amount of highly oriented extended chain crystals are oriented along FD (shish). These penetrate crystalline lamellae which also have their crystalline c-axis oriented along FD (kebabs). Kebabs from nearby shish can also interpenetrate each other. Epitaxially nucleated daughter lamellae grow from the surface of the kebabs and due to their sequential formation and/or constriction of chains being incorporated into nearby lamellae are less perfect but particularly are thinner than the kebabs. Daughter lamellae get thinner and curve as they grow away from their parent lamellae. Amorphous and tie chains fill the space between the crystalline regions.

#### 4.0 Conclusions

By allowing isotactic polypropylene to crystallise in an oriented form, the individual contributions of parent and daughter lamellae were able to be observed during melting in an in-situ environment using wide angle x-ray scattering(WAXS). The relative thermal stability of the oriented PD lamellae was then determined by a combination of DSC and time resolved WAXS. Daughter lamellae were observed to melt at a lower temperature showing that they are thinner and less perfect than parent lamellae. The difference in parent and daughter lamellae thickness was used to explain the multiple melting behaviour observed in the DSC thermograms.

#### 5.0 Acknowledgments

The authors would like to acknowledge the funding support provided by the Australian Synchrotron, the Cooperative Research Centre for Polymers (CRCP) and the Moldflow Corporation. The assistance from Dr Jan Ilavsky at Advanced Photon Source Argonne National Laboratory for modifying the Nika software package was also greatly appreciated.

## 6.0 References

1. Keller, A.; Kolnaar, H. W. H., *Processing of Polymers*, VCH, New York, **18**, p. 189, (1997).
2. Lotz, B.; Wittmann, J. C. *J. Polym. Sci., Part B: Polym. Phys.*, **24**, 1541, (1986).
3. Clark, E. S.; Spruiell, J. E. *Polym. Eng. Sci.*, **16**, 176, (1976).
4. Phillips, A.; Zhu, P.-w.; Edward, G. *Macromolecules*, **39**, 5796, (2006).
5. Zhu, P.-w.; Tung, J.; Edward, G.; Nichols, L. *J. Appl. Phys.*, **103**, 124906, (2008).
6. Fujiyama, M.; Wakino, T.; Kawasaki, Y. *J. Appl. Polym. Sci.*, **35**, 29, (1988).
7. Petraccone, V.; Rosa, C. D.; Guerra, G.; Tuzi, A. *Die Makromolekulare Chemie, Rapid Communications*, **5**, 631, (1984).
8. Paukkeri, R.; Lehtinen, A. *Polymer*, **34**, 4083, (1993).
9. Weng, J.; Olley, R. H.; Bassett, D. C.; Jääskeläinen, P. *J. Macromol. Sci., Phys.*, **41**, 891, (2002).
10. Wang, X.; Hou, W.; Zhou, J.; Li, L.; Li, Y.; Chan, C.-M. *Colloid Polym. Sci.*, **285**, 449, (2007).
11. Fujiyama, M.; Wakino, T. *J. Appl. Polym. Sci.*, **43**, 57, (1991).
12. Dean, D. M.; Rebenfeld, L.; Register, R. A.; Hsiao, B. S. *J. Mater. Sci.*, **33**, 4797, (1998).
13. Karger-Kocsis, J., *Polypropylene. An A-Z Reference*. Kluwer Academic Press: Great Britain, p. 381, (1999).
14. Kakudu, M.; Kasai, N., *X-Ray Diffraction by Polymers*. Elsevier Amsterdam, p. 245, (1972).

## 7.0 List of Tables

Table 1: Crystallisation times used in the experiment.  $t_{0.5}$  is the time for crystallisation to reach 50%.

SR (s <sup>-1</sup> )	2.5 x $t_{0.5}$ (min)
0	68
10	25
20	23
30	21
40	20
50	18
60	17
70	16
80	15

## 8.0 List of Figures

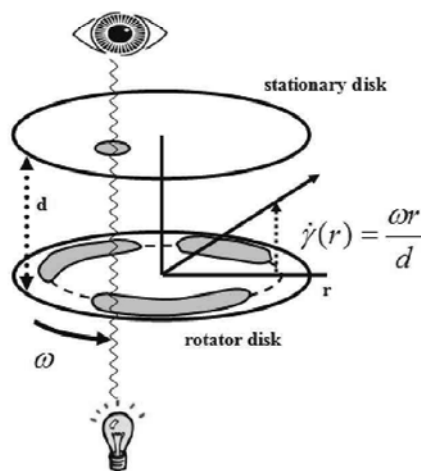


Figure 1: Schematic diagram of the basic operation of the Linkam parallel plate shear cell.

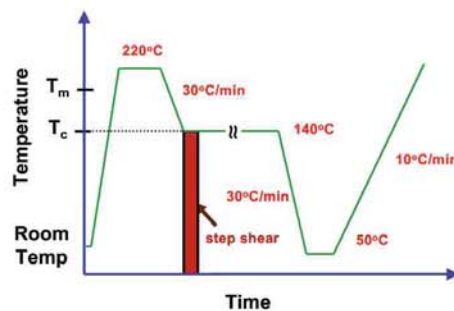


Figure 2: Thermo-mechanical profile used in this experiment.

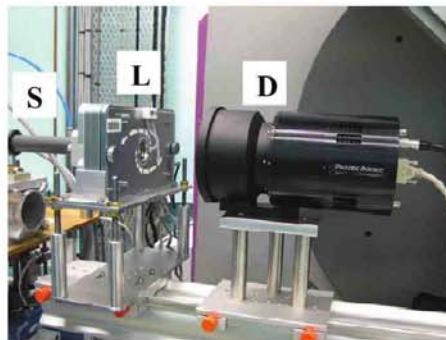


Figure 3: Wide Angle X-ray Scattering (WAXS) experiment on the powder diffraction beam line at the Australian Synchrotron. Synchrotron source (S), Linkam shear cell (L) and detector (D).

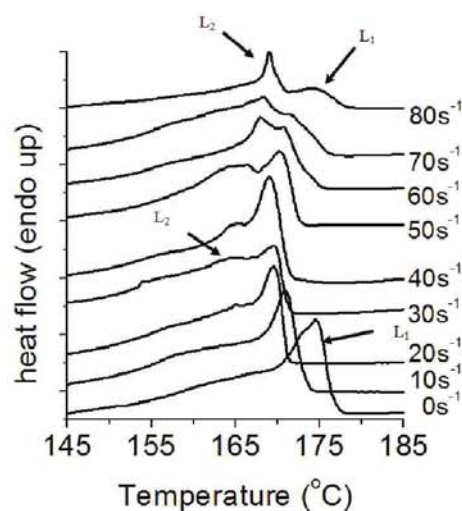


Figure 4: Melting thermograms of samples subjected to shear rates between 0-80s<sup>-1</sup>.

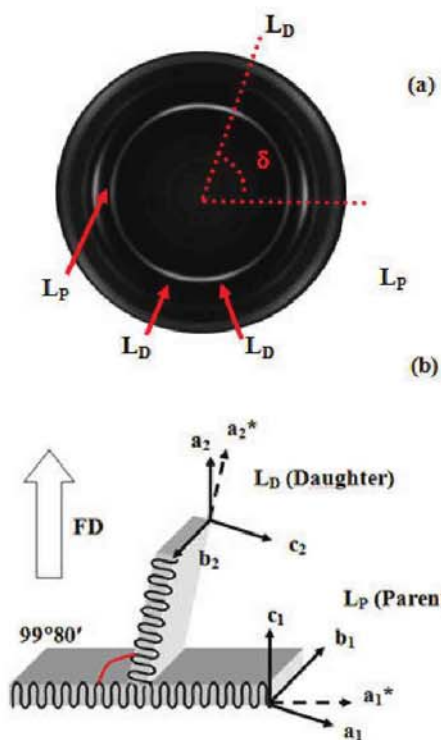


Figure 5: a) Typical raw 2D wide angle x-ray scattering (WAXS) pattern of sheared  $\alpha$  isotactic polypropylene, highlighting the contributions to the  $\alpha(110)$  ring from parent ( $L_P$ ) and daughter ( $L_D$ ) lamellae.  $SR = 80 \text{ s}^{-1}$ . Flow direction (FD) vertical. b) Generalised model used to describe the azimuthal intensity distribution in a).

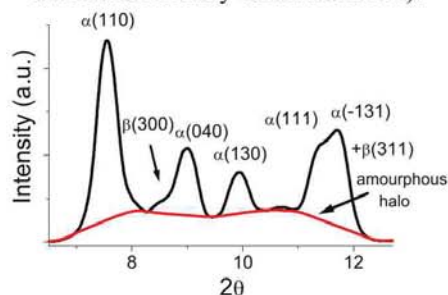


Figure 6: Circular integration of Figure 5a showing the main iPP crystalline reflections present. Shear rate  $SR = 80 \text{ s}^{-1}$ .

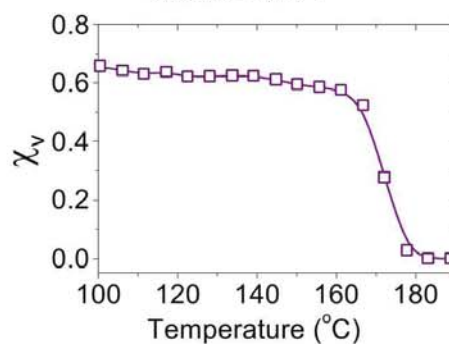


Figure 7. Temperature dependence of the volume crystallinity index ( $\chi_v$ ). Shear rate  $SR = 80 \text{ s}^{-1}$ , heating rate is  $10 \text{ }^\circ\text{C}/\text{min}$ .



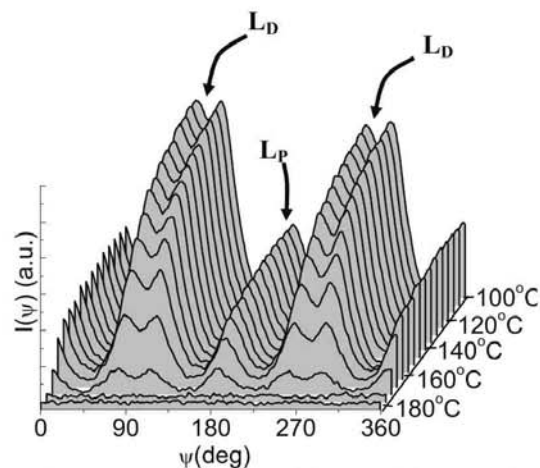


Figure 8: Temperature dependence of intensity for the (110) reflection  $I(\psi)$  as a function of azimuthal angle  $\psi$ . Shear rate  $SR = 80 \text{ s}^{-1}$ , heating rate is  $10 \text{ }^{\circ}\text{C/min}$ .

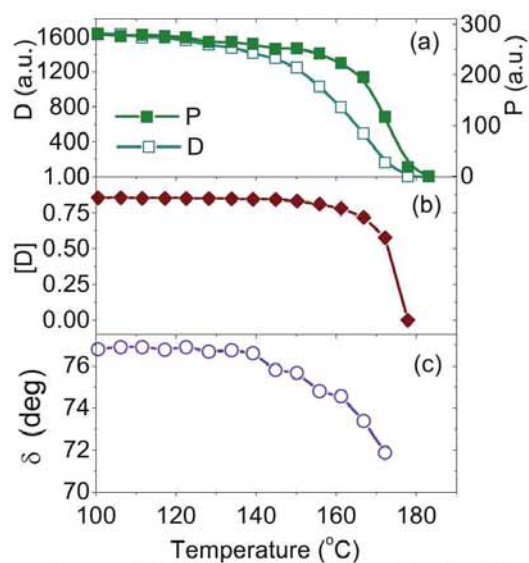


Figure 9: Temperature dependence of a) the integrated area under the 110 reflection of daughter (D) and parent (P) lamellae. b) Relative concentration of the daughter lamellae ( $[D]$ ). c) Azimuthal angle between the parent and daughter contributions to the 110 reflection ( $\delta$ ). Shear rate  $80 \text{ s}^{-1}$ , heating rate is  $10 \text{ }^{\circ}\text{C/min}$ .

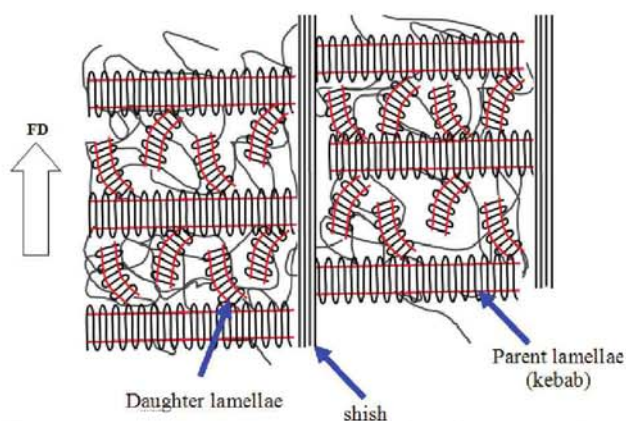


Figure 10: Updated model for the oriented structure produced by flow-induced crystallisation in isotactic polypropylene.